

**The chromite-garnet peridotite
assemblages and their role in the
evolution of the mantle lithosphere**

Tim Ivanič

PhD Thesis

University of Edinburgh

2007



DECLARATION

I certify that the thesis has been composed by myself, the work is my own and the work has not been submitted for any other degree or professional qualification except as specified.

Contents

Abstract	i
Acknowledgements	iii
Chapter 1 – Introduction	1
1.1 Background	1
1.2 Overall Aims of the Thesis	3
1.3 Thesis Layout	4
1.4 Chapter Synopsis	4
1.5 References	8
Chapter 2 – Previous Work and Project Rationale	9
2.1 Early Knowledge of the Mantle	9
2.2 Diamond Inclusions	11
2.3 KIMs (Kimberlite Indicator Minerals)	13
2.4 Mantle Xenoliths	16
2.5 Summary of Key Areas of Current Research	22
2.6 Formulation of a Tractable Problem	26
2.7 References	31
Chapter 3 – Sampling and Petrography	37
3.1 Sampling	37
3.2 Petrography	43
3.3 Discussion	68
3.4 References	75
Chapter 4 – Major Element Compositions	77
4.1 Introduction	77
4.2 Barkly West Kimberlite Concentrate	83
4.3 Newlands, Bobbejaan and Leicester Samples	123
4.4 Summary	128
4.5 References	130
Chapter 5 – Major Element Zonation Patterns in Minerals	133
5.1 Objectives	133
5.2 Garnet Zonation Patterns	134
5.3 Cr-Spinel Zonation Patterns	156
5.4 Cr-Diopside Zonation Patterns	158
5.5 Summary	160
5.6 References	161
Chapter 6 – Phase Relations	163
6.1 Objectives	163
6.2 Equilibria	163
6.3 Phase Relations	165
6.4 Newlands and Bobbejaan Samples	168
6.5 Summary	179
6.6 References	181
Chapter 7 – Geothermobarometry	183
7.1 Objectives	183
7.2 Application	183
7.3 Results	186
7.4 ‘Perplex’ Computations	200

7.5	Conclusions	205
7.6	References	208
Chapter 8	– Garnet Major Element Diffusion	211
8.1	Introduction	211
8.2	Results	217
8.3	Limitations	226
8.4	Summary	227
8.5	References	229
Chapter 9	– Trace Element Mineral Chemistry	231
9.1	Introduction	231
9.2	Aims	234
9.3	Results	235
9.4	Summary	253
9.5	Discussion	257
9.6	Conclusions	269
9.7	References	271
Chapter 10	– Synthesis, Wider Implications and Further Work	273
10.1	Synthesis	273
10.2	Wider Implications	282
10.3	Further Work	289
10.4	References	290
Appendix I	– Analytical Techniques	I-1
I.1	Optical Microscopy	I-1
I.2	Electron Microprobe	I-2
I.3	Ion Microprobe (SIMS)	I-12
I.4	Chromite Standard Preparation and Use in Analysis	I-21
I.5	References	I-28
Appendix II	– Summary Tables and EMPA Traverses	CD & II-1
Appendix III	– X-ray Maps	CD & III-1
Appendix IV	– EBSD Results	IV-1
Appendix V	– Trace Element Analyses	CD & V-1
Appendix VI	– Data CD	Inside Back Cover

Abstract

Newlands and Bobbejaan kimberlites, South Africa, contain suites of highly chromian, garnet-rich peridotites amongst their xenolith population and an investigation of these xenoliths has been targeted because there is an overlap of mineral compositions with the garnet-chromite-olivine paragenesis found as inclusions in diamonds. A high proportion of garnets and chromites in these rocks plot in the diamond facies fields on Cr₂O₃-CaO and Cr₂O₃-MgO wt. % plots respectively. However, it has also been found that many Cr-rich assemblages are clinopyroxene-bearing (lherzolitic) as well as harzburgitic (i.e. forming a range of chromite-garnet peridotite assemblages). Many samples have garnets with inclusions of serpentine ± chromite (+ clinopyroxene in lherzolitic samples) whose arrangement are sometimes indicative of exsolution or annealed exsolution textures. Initial bulk REE patterns were calculated for the pre-exsolution, pre-metasomatism, high-Cr garnets. The patterns found are humped for harzburgitic samples and relatively flat for lherzolitic ones. These appear to be closely linked to the concentration of Ca in garnet indicative of a single-stage formation process for the humped profiles. The profiles were later modified by exsolution of pyroxenes (with a clear link between Ca content of garnet and the garnet/clinopyroxene partition coefficients) and, in a few cases, by metasomatism causing a zonation of REE.

Most of the garnets have strongly developed zonation patterns which are a result of diffusion towards the matrix (external zonation) followed by zonation towards inclusions (internal zonation). Cr-Al and Mg-Ca inter-diffuse in both types of zonation; Ti may also be strongly zoned, whereas Fe is not distinctly zoned in any sample. External zonation may be divided into 'P-T re-equilibration' and 'metasomatic' types, where the former type conforms to down-P-T garnet-spinel transition reaction simulations and the latter does not. All internal zonations conform to down P-T reaction simulations. All the zonation profiles conform well to diffusion controlled reaction models. External P-T re-equilibration is modelled to have occurred on an order of magnitude greater timescale than internal zonation (~5 Ma compared to ~0.5 Ma using $D_{Mg} = 10^{-20} \text{m}^2/\text{s}$). Metasomatic zonation occurs over the longest diffusion distances and is modelled to have timescales up to 20 Ma. Based upon the geometries of chemical heterogeneity in the minerals analysed, a sequence of events has been proposed for the evolution of the Newlands and Bobbejaan samples: (1) Earliest known mineralogy. There is little evidence for the events prior to and during this stage. However, the modal mineralogy is postulated to have been more garnet and olivine-rich than seen in the samples and the crystals more chemically homogeneous. The P and T in samples are modelled to have the highest Ps and Ts of all stages (potentially > 65kb and > 1350°C). (2) Exsolution. This stage represents the initiation of an event which significantly lowered P and T where spinel and pyroxene exsolved from garnet. (3a) External zonation - P-T re-equilibration and metasomatism. These events are contiguous with stage 2 and P-T estimates for this stage indicate further lowering of P and T. This is accompanied by modification of a few samples by the infiltration of metasomatic fluid. (3b) Internal zonation - P-T re-equilibration. This stage represents the final lowering of P and T, yielding final P-T estimates on clinopyroxene inclusion-garnet boundaries of 38-50 kb and 900-1150°C. These P-T estimates place samples plot on a relatively cool continental steady state geotherm. (4) Kimberlite eruption.

The initial formation of the garnet-rich rock types with their (calculated) highly chromian composition and particular initial REE compositions appears to be related to a major depletion event with subsequent burial. Differential interaction with a CO₂-bearing fluid would generate the range of harzburgitic and lherzolitic compositions found. However it is acknowledged that this is difficult to determine and constrain because of the lack of preservation of evidence prior to Stage 2. The down-P-T event has a similar timescale and associated uplift rate to be related to continent-continent collision according to the timescales for diffusion. The contemporaneous metasomatism leads to postulation that the event may have been related to the continental accretion of the eastern and western parts of the Kaapvaal craton in the late Archaean. In terms of the relation to diamond, it was found that samples with high-Cr harzburgitic garnets tended to yield P-T estimates that were most substantially into the diamond stability field based upon the Cr-Al partitioning between garnet and spinel and also modelling the samples using the computer programme known as 'Perplex'. Clinopyroxene-bearing samples (i.e. those with a bulk rock composition higher in Ca) tended to indicate higher temperatures of equilibration. Cr-spinels from the harzburgitic paragenesis have higher Mg and lower Ti than the lherzolitic Cr-spinels, but overlapping Cr compositions at high Cr and may be differentiated on Cr-Mg and Cr-Ti compositional plots.

Acknowledgements

I am hugely grateful to Ben Harte for providing carefully considered advice throughout the duration of the project. Ben also helped to train me to think about the mantle as a metamorphic rock and he encouraged me to take important opportunities such as a field trip to the diamond mines of Northwest Territories, Canada and the International Mineralogy Association conference in Kobe, Japan. I thank John Gurney for the project samples, the conception of the project and also his inspiring charisma – I think John's rock collection is ever so slightly bigger than mine! I also thank John for two fantastic Kimberley collecting trips and a truly memorable time in Lesotho. Great thanks to my family, Mum, Dad and Suz, who have always been supportive. I also acknowledge a NERC studentship which has made this project possible.

Pete Hill and David Steele have been very patient and helpful with my (sometimes incessant) use of the Electron Microprobe at EMMAC (Edinburgh Materials and Microanalysis Centre). Thanks to Richard Hinton, Simone Kasemann and John Craven at the Ion Microprobe Unit, EMMAC and Richard especially for the tutoring and patience with various calculations. Rob Ellam, Valerie Olive and Anne Kelly worked hard to help me with the diverse range of tasks I had for them and they did a brilliantly efficient job at the chemistry labs and ICP-MS unit, SUERC, East Kilbride.

At the Grant Institute, thanks to Barry Dawson who has had an unrequited enthusiasm for kimberlites and xenoliths which has continually spurred me on. He has also livened up every coffee break in the museum with his great African stories. Thanks also to Stephan Klemme for the valuable discussions on phase equilibria. I very much appreciate Mike Hall's efforts in finding a way to deal with my peculiar samples so that I could end up with great polished mounts to analyse. Brian Upton has provided enthusiasm and continued to convey a wide knowledge of alkaline igneous rocks to me. Dodie James helped during my use of the XRF furnace and Ann Menim made sure all was in place to carry out mineral separation. Lisa, Ian, Heather, Helena and Nikki have provided an unfaltering service sorting all finance and admin tasks effectively – much appreciated. Bill has also manned the door and administered a fine dose of sarcasm each morning. In Chemistry Lorna Eades helped analyse samples on ICP-OES only days before going on maternity leave.

At University of Cape Town, I shared many interesting ideas with Ben Garden and also a few samples. Anton LeRoex and Hartwig Frimmel let me help on a great field trip to Namibia even if I did have to break my nose to examine the nepheline syenite. Also in Cape Town, the guys at Mineral Services, Andrew Menzies and Kalle Westerlund must be thanked moral support during conferences and Andrew for samples, 'xenolith chat' and conducting some analyses for me on the SEM. During my time at UCT, Robin Lee and David Reid also donated some of their Bushveld chromite samples.

Mark Huchison and Julie Hollis have put me up in Denmark three times in the last three years now. Simon Harley has not only talked about a lot of minerals to me (mainly cordierite) but has also supplied many rockin' Inch and Kinlochleven trips, Ian Parsons is thanked for a legendary Mull 2004.

Last, and by no means least, thank you for putting up with my 'offensive minerals', the attic crews past and present (sorry I can't name you all): First of all there is Caroline, Alex, Sarah B, Ira, Nick, Dan and Nigel; the 'Hard Rock Corner' folk (again past and present) Fahad, Conor, Emma, Sarah A (*The Germanator*), Rich and Jenny; the A.R.C. desk mates, Gwilym, Ciaran (*el presidente*) and Pete. Also: Clare W, Clare B, Simon, Kev, Mikael, Zana, Dave P, Silje, Jon H, Robin, Shaggy, Theo, J Mac, Gavin, Helen D, Sam, Jason, JD, Janette, Natasha, Antoine, Andy, Hannah, Natalie, Gillian (*Chakra*), Dave H and Adam W (*Scooby*). Adam S and John, thanks for a great time in Greenland, 2005.

1. Introduction

1.1 Background

After discovery of the 'type-locality' kimberlite in Kimberley, South Africa, 120 years ago, it was noted that a particular suite of minerals were associated with kimberlites. Wagner (1914) used the principles of crystal chemistry and crystal structure to suggest that some of these minerals were high-pressure phases that likely crystallised in the upper mantle. These crystals and associated rounded ultramafic inclusions were interpreted as accidental inclusions (i.e. xenocrysts and xenoliths) in the kimberlite magma because of their ultrabasic nature compared to the K-, CO₃-rich host. The controversy arose as to whether diamond was a xenocryst in kimberlite or a kimberlite phenocryst.

The discovery of diamondiferous xenoliths was made by Bonney (1899), which confirmed that most diamond is likely to be derived from disaggregated mantle material and thus a xenocryst in kimberlite. Further strong evidence for a xenocrystal origin came with dating evidence (e.g. Richardson et al., 1984) that diamonds were thousands of millions of years older than their host kimberlites. Kimberlite-hosted diamondiferous xenolith rock types have been described petrographically in Williams (1932) and more recent chemical data are as follows for different diamond-bearing rock types:

- eclogite, e.g. Rickwood et al. (1969)
- garnet lherzolite, e.g. Dawson and Smith (1975)
- garnet dunite, e.g. Sobolev et al. (1969)
- garnet harzburgite, e.g. Viljoen et al. (1994)

Diamond inclusion mineral sets broadly conform to these main parageneses with a major distinction between eclogitic and peridotitic parageneses (Meyer, 1975).

However, in detail the dominant peridotitic inclusion suite in diamonds is more refractory than that seen in many peridotite xenoliths – it commonly lacks clinopyroxene and contains chromite together with other minerals characterised by low Ca, high Cr and high Mg/(Mg+Fe). Thus explanations of the origin of these refractory compositions have been sought (e.g. Harte et al., 1980; Schulze, 1986; Sobolev et al., 1969). The distinctive peridotitic paragenesis in diamond may be referred to as the *diamond-chromite-garnet harzburgite assemblage*. This project has been concerned with a wider range of *chromite-garnet peridotite assemblages* where peridotite may be harzburgitic or lherzolithic.

High pressure and temperature experimental studies on mantle rock compositions have given rise to an ever expanding set of geothermometers and geobarometers that utilise temperature- and pressure-sensitive compositional parameters in minerals to estimate temperature and pressure. More recent studies have been successful at linking pressure and temperature estimates from suites of mantle xenoliths to geophysical heat flow models for the change in temperature with depth e.g. McKenzie et al. (2005).

The development of highly sensitive analytical techniques has allowed investigators to accurately determine the concentrations of major and trace elements and isotopes in mantle minerals. The electron microprobe (EMP) and ion microprobe (secondary ionisation mass spectrometry (SIMS) technique) have the advantage of being able to measure major and trace element concentrations (respectively) in situ on a polished rock surface with a < 30 μm diameter analysis volume. This means that the spatial context of chemical variation in minerals can be recorded with high precision and minimal contamination effects. The harzburgitic diamond inclusion paragenesis has been analysed by these techniques (e.g. Harte et al., 1980 by EMP and Shimizu and Richardson, 1987 by ion microprobe SIMS). Additionally, isotope ratios have been determined by means of mass spectrometry techniques for syngenetic inclusions (e.g.

Sm-Nd by Richardson et al., 1984 and Re-Os by Pearson et al., 1997) which have yielded isochron and model ages for the harzburgitic diamond inclusion paragenesis.

The thrust of this thesis is to define and account for the formation of the chromite-garnet peridotite assemblages (CGPA) in terms of their petrography and geochemistry utilising modern analytical techniques. This is achieved by the study of collections of xenoliths from Newlands and Bobbejaan kimberlites that commonly contain chromite and, in some cases, minerals of comparable composition to those found as diamond inclusions. The application of phase equilibria and thermodynamic models to the emergent data allows further appreciation of the nature of the diamond-chromite-garnet harzburgite paragenesis and an appreciation of the role it plays in a wider mantle context.

1.2 Overall Aims of the Thesis

The aims of the thesis are as follows:

1. To establish the petrographic constraints of the CGPA. i.e. modal mineralogy, texture, grain size of the rocks.
2. To quantify the composition of the CGPA. i.e. major, minor trace element chemistry of minerals and any zonation that may be present.
3. To interpret compositional information in its spatial/petrographic context and in relation to coexisting phases. This will be done using major and trace element concentrations analysed in coexisting minerals to estimate P-T conditions of formation and equilibration. Trace elements will also be used to assess the role of melts/fluids as modifying agents in the CGPA of the mantle.
4. To assess existing models for their ability to explain compositional and petrographic features noted for the CGPA, and clarify which mechanisms should be invoked for generating and modifying Archaean sub-continental lithospheric mantle.

5. Endeavour to supplement information for identifying regions of diamond stability in the lithosphere and identifying distinctive geochemical trends.

1.3 Thesis Layout

The thesis comprises 10 chapters each having figures embedded into the text. Each chapter has an introductory part designed to give the reader an idea of the particular focus and aims of the chapter and any relevant literature that the chapter builds on. Additionally, comment is made on the importance the chapter has for understanding the chromite-garnet-peridotite assemblages. At the end of each chapter is a summary of the main emergent points that are used for synthesis in the final chapter. Since the chapters are reasonably specific, a reference list is provided at the end for each individual chapter.

1.4 Chapter Synopsis

Chapter 2 – Previous Work and Project Rationale

An overview of the current state of knowledge about the sub-continental mantle lithosphere is presented. This includes methods for estimating the composition of the upper mantle, the depth of the lithosphere-asthenosphere boundary, the variation of temperature with depth (and hence the constraints on diamond stability), the age and modifying processes acting on the mantle rocks themselves. The way in which this thesis relates to previous studies is explained and the aims of the thesis justified in terms of the new information it will add to existing mantle knowledge.

Chapter 3 – Sampling and Petrography

Information about the sampling localities is presented and a description of the style of sampling is made. The petrography section starts with a guide to the nomenclature used for rock type definition. Then the quantification of the grain size, mineralogy, modal mineralogy and texture of the samples is presented. These data are used to define rock types (i.e. garnet harzburgite/lherzolite) and to make a necessary classification of ‘sample types’, which is important for justifying chemical

relationships in later chapters. Individual samples that illustrate the differences between each of the sample types are described in more detail.

Chapter 4 – Major Element Compositions

The chapter compares electron microprobe analyses of garnet, spinel, clinopyroxene, olivine and orthopyroxene from Newlands and Bobbejaan kimberlite concentrate to analyses from other kimberlites in the 'Barkly West region' (Leicester and Frank Smith kimberlites). These are compared with databases of analyses from southern African kimberlite concentrate and also a concentrate from glacial till in a diamondiferous source region in the Northwest Territories of Canada. Existing compositional classifications are used and compared with the petrology and major element chemistry of the Newlands and Bobbejaan samples.

Chapter 5 – Major Element Zonation in Minerals

Electron microprobe traverses across minerals in samples are described with particular profiles and X-ray maps being referred to in Appendix II and III (on data CD). A subset of samples that display clear examples of garnet zonation trends are selected and described systematically in terms of the sample types that are affected, the chemical substitution that occurs, and the core-rim direction of zonation shown on a Ca vs. Cr plot. The zonation types are classified using terminology that relates to the sample type classification in Chapter 3. The zonation types are compared to previous studies of mantle garnet zonation illustrating the overlap between classification schemes.

Chapter 6 – Phase Relations

Firstly the equilibria associated with garnet peridotite are defined. Analyses of coexisting garnet, clinopyroxene and spinel are calculated as cation concentrations and cation ratios and are plotted in Cr-present compositional space using tie line on triangular and tetrahedral plots. The relationships discovered in the range of rock compositions present for Newlands and Bobbejaan samples are shown to conform to particular equilibria utilising specific reactions. The chapter provides grounds for the geothermobarometry in Chapter 7.

Chapter 7 – Geothermobarometry

Several appropriate, existing geothermometers and geobarometers are applied to the samples and the results plotted relative to major reaction lines and isopleths from experimental studies on peridotitic systems. The relation of coexisting mineral compositions to estimates of pressure and temperature for the samples is made with a suggestion as to potential use of a geothermobarometer for coexisting garnet-spinel and garnet-spinel-clinopyroxene in the system CMASCr. Additionally the result of thermodynamic modeling using a newly developed computer programme known as 'Perplex' is presented.

Chapter 8 – Diffusion in Garnet

Diffusion profiles are shown for particular zoned and unzoned initial garnets using information from experimental studies. An appraisal of existing major element diffusion coefficients in garnet from experimental studies is made. An error function model for diffusion is used in conjunction with a suitable diffusion coefficient for pressures and temperatures relevant to the samples (Chapter 7) and applied to their zonation profiles. Finally, the likely range of timescales over which diffusion is thought to operate is calculated and discussed.

Chapter 9 – Trace Element Compositions

The range of trace element analyses of minerals from a subset of samples (described in chapter 3 and 5) by ion microprobe is documented. Data is presented as concentration/chondritic concentration spidergrams and also as divariant plots with samples divided into harzburgitic and lherzolithic groups, with the high-Ca varieties differentiated. Existing models for generating humped REE (rare earth element) profiles in garnets are reviewed and assessed and then compared to the garnet and clinopyroxene compositions in Newlands and Bobbejaan samples.

Chapter 10 – Synthesis, Wider Implications and Further Work

In the final chapter the main emergent conclusions of the thesis are synthesised into a multi-stage history for the Newlands and Bobbejaan samples. The main conclusions are discussed with their relevance to current areas of mantle research and also to

commercial diamond exploration strategies. Finally there is discussion of the potential new lines of investigation that this study has uncovered in the 'Further Work' section.

Appendices

Appendix I - Analytical techniques comprises a summary of the analytical techniques including detailed documentation of the techniques involved in petrography, electron microprobe analysis and ion microprobe (SIMS) analysis. There is also documentation of the preparation procedure followed for the generation of a chromite standard.

Appendix II – EMP Traverses comprises tabulated sample classification based on petrography and also tabulated measured diffusion distances from the EMP traverses. A summary of the core and rim compositions in garnets and of coexisting mineral compositions are shown. Annotated EMP traverses across minerals in samples are included on the data CD (see back cover).

Appendix III – X-ray Maps comprises a description of the technique and all the major element X-ray maps for samples with the individual analytical operating conditions for the EMP are included on the data CD (see back cover).

Appendix IV – EBSD (electron backscatter diffraction) comprises the EBSD data used to establish mineral orientation in samples whose grain size was indeterminable from light microscopy.

Appendix V – Trace Element Compositions comprises a summary table of trace element data for the samples analysed by ion microprobe SIMS with the complete analyses included on the data CD (see back cover).

Appendix VI – Raw Data is a data CD-ROM (pocket at end of Appendices, inside the back cover) containing all EMP and IMP data obtained for the thesis in the form of Excel spreadsheets. Corel Draw files are provided for the X-ray map images for each sample analysed by this technique and the accompanying raw images may also be found in this folder. All petrographic photographs of the samples are also included on the CD.

1.5 References

- Bonney, T. G. (1899). The parent rock of the diamond in South Africa. *Proceedings of the Royal Society*. **65**. 223-226.
- Dawson, J. B. and Smith, J. V. (1975). Occurrence of diamond in a mica-garnet lherzolite in kimberlite. *Nature*. **254**. 580-581.
- Harte, B., Gurney, J. J. and Harris, J. W. (1980). The formation of peridotite suite inclusions in diamonds. *Contributions to Mineralogy & Petrology*. **72**. 181-190.
- McKenzie, D., Jackson, J. and Priestley, K. (2005). Thermal structure of oceanic and continental lithosphere. *Earth and Planetary Science Letters*. **233**. 337-349.
- Meyer, H. O. A. (1975). Chromium and the genesis of diamond. *Geochimica et Cosmochimica Acta*. **39**. 929-936.
- Pearson, D. G., Shirey, S. B., Bulanova, G. P., Carlson, R. W. and Milledge, H. J. (1997). Single crystal Re-Os isotopic dating of sulphide inclusions within a zoned Siberian diamond. 7th Goldschmidt Conference, Tucson, AZ.
- Richardson, S. H., Gurney, J. J., Erlank, A. J. and Harris, J. W. (1984). Origin of diamonds in old enriched mantle. *Nature*. **310**. 198-202.
- Rickwood, P. C., Gurney, J. J. and White-Cooper, D. R. (1969). The nature and occurrences of eclogitic xenoliths in the kimberlites of South Africa. Upper Mantle Project. Geological Society of South Africa, Special Publication. **2**. 371-393.
- Schulze, D. J. (1986). Calcium anomalies in the mantle and a subducted metaserpentinite origin for diamonds. *Nature*. **319**. 483-485.
- Shimizu, N. and Richardson, S. H. (1987). Trace element abundance patterns of garnet inclusions in peridotite-suite diamonds. *Geochimica et Cosmochimica Acta*. **51**. 755-758.
- Sobolev, V. S., Nay, B. S., Sobolev, N. V., Lavrent'ev, Y. G. and Pospelova, L. N. (1969). Xenoliths of diamond-bearing pyrope serpentinite from the "Aykhal" pipe, Yakutia. *Doklady Akademii Nauk SSSR*. **188**. 1141-1143.
- Viljoen, F., Robinson, D. N., Swash, P. M., Griffin, W. L., Otter, M. L., Ryan, C. G. and Win, T. T. (1994). Diamond- and graphite-bearing peridotite xenoliths from the Roberts Victor kimberlite, South Africa. 5th International Kimberlite Conference, South Africa, CPRM. 285-303.
- Wagner, P. A. (1914). The diamond fields of southern Africa. Transvaal Leader. Johannesburg.
- Williams, A. F. (1932). The genesis of the diamond. London, Ernest Benn, Ltd.

2. Previous Work and Project Rationale

This chapter aims to summarise the types of studies that have established the current understanding of the mineralogy, rock types, thermal structure and age of the mantle lithosphere. Previous work is summarised by looking at early knowledge of the mantle and then focussing on particular mantle samples such as diamond inclusions, kimberlite concentrate and mantle xenoliths. Particular emphasis is placed on the peridotitic minerals and mineral assemblages from diamond inclusions, kimberlite concentrate and mantle xenoliths.

The current areas of mantle research are outlined subsequently with brief descriptions of the types of scientific advances that are currently being made. Lastly, the studies that specifically led up to this project are discussed with reference to the new questions they raise and, hence, providing the rationale for this study.

2.1 *Early knowledge of the mantle*

2.1.1 Seismic evidence – boundary layers

In 1909 Mohorovičić discovered the boundary between the earth's crust and mantle, now called the Moho. It was discovered by the way that seismic P waves increase in velocity below this boundary. Therefore the mantle had to be primarily composed of solid material of a higher density than the crust. The depth of the Moho varies from 5 km beneath mid ocean ridges to 75 km beneath continents. The uppermost mantle is relatively cold, cools by conduction and behaves in a rigid fashion and is called the mantle lithosphere. The lithosphere-asthenosphere boundary (LAB) was originally identified by a low seismic velocity zone at about 200 km beneath continents (Fig. 2.1), thought to represent a region of partial melting, hence a slowing of seismic waves. The asthenospheric upper mantle temperature-depth profile was modelled to as conductive and convective in 1950s and found to conform to the convective model in the 1960s according to Turcotte and Oxburgh (1972). McKenzie (1989) and McKenzie et al. (2005) provide models for the continental geotherm which takes into

account conduction and convection and also a model for the thermal conductivity of different crust and upper mantle rock compositions.

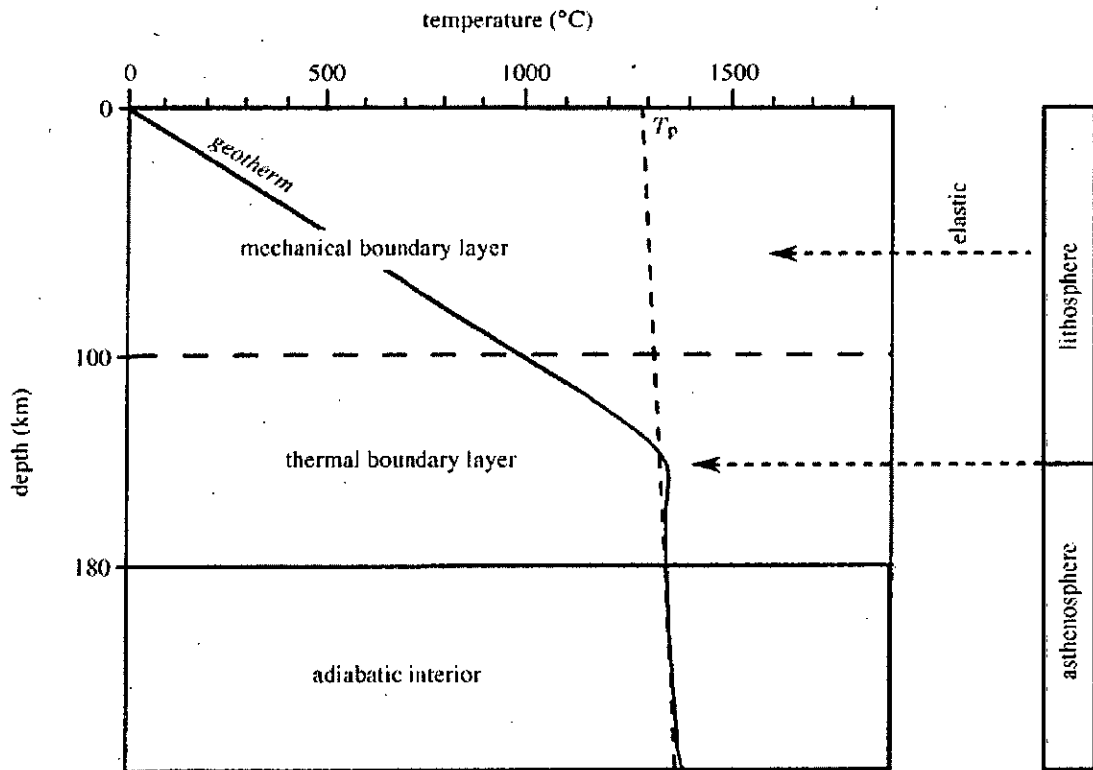


Figure 2.1: Diagram from Hawkesworth et al. (1999), based on the model continental geotherm of McKenzie (1989). Summary of temperature variation with depth for the sub-continental lithosphere and asthenosphere. Note that the asthenosphere has a temperature that does not deviate far from a single potential temperature (T_p) and lies along an adiabatic decompression line. The rigid lithosphere is not able to cool convectively and so has a conductive geotherm and hence becomes cooler at a faster rate with decreasing depth.

The lower mantle is separated from the upper mantle by a transition zone which represents another change in density associated with several phase transitions between 440 km and 670 km. Including garnet and pyroxene forming a solid solution in the mineral majorite and olivine transforming to a cubic spinel structure (ringwoodite). These phase transitions have been determined experimentally using high-pressure apparatus (e.g. Ringwood, 1956; Ringwood and Major, 1971)

The core-mantle-boundary was identified at approximately 2900 km depth by analysing the passage of earthquake wave paths through the earth. Here there is a

discontinuity in seismic wave velocities reflecting a distinct density change from solid silicate rock to liquid iron. The outer core is thought to be made of liquid because S waves appear to be strongly attenuated at these depths.

2.1.2 Models for the mantle

Whether the mantle convects as a whole, as two separate layers (upper and lower) or in a way defined by an alternative model has been a matter of debate for some time. Ringwood's megalith model (Ringwood, 1982) involves the ascent of plumes derived from the lower mantle and the descent and eventual detachment of subducted oceanic lithosphere until impingement on the 660 km discontinuity. This is where megaliths of eclogite are thought to reside. Using seismic tomography the lower velocity, cooler subducted slabs have been imaged in the mantle and there is evidence for both penetration of the transition zone and also for deflection of slabs to low angles at the transition zone (Kárason and van der Hilst, 2000).

2.2 Diamond Inclusions

2.2.1 Mineral suites and compositions

Analysis of diamond inclusions by electron microprobe (EMP) identified two main suites of inclusions: peridotitic (P-type) and eclogitic (E-type) e.g. Meyer and Tsai (1976a). Other rare suites such as a wehrlitic and a calc-silicate suite have also been identified. Multiple inclusions in single diamonds do not contain minerals from both suites. Harris and Gurney (1979) noted that peridotitic minerals in diamonds had more depleted compositions than minerals found in the most depleted peridotitic xenoliths. i.e. Lower $\text{Ca}/(\text{Ca}+\text{Mg})$, higher $\text{Cr}/(\text{Cr}+\text{Al})$ and high $\text{Mg}/(\text{Mg}+\text{Fe})$ cation ratios which is suggestive that included minerals and host diamond equilibrated at high pressure and medium (900-1100°C) and in the absence of clinopyroxene (Harte et al., 1980). P-type inclusions were also noted for their low clinopyroxene abundance compared to common peridotite xenoliths.

More specifically the peridotitic paragenesis identified in many studies of peridotitic suites of inclusions in diamonds is therefore one of a harzburgite (olivine and orthopyroxene) together with low-Ca, high-Cr garnet. Magnesiochromite is a common member of this assemblage and clinopyroxene is typically absent. This therefore forms the characteristic *diamond-chromite-garnet harzburgite assemblage*.

Trace element analyses of P-type garnets found as inclusions in diamond by Shimizu and Richardson (1987) identified very high Sr concentrations (> 20 ppm) accompanied with light rare earth element (REE) enrichment. These features suggest alteration by incompatible element-enriched fluids and were ascribed to ancient metasomatic processes. A disequilibrium process involving the differential diffusion of the rare earth elements into garnet was the mechanism invoked for this metasomatism. A review of this and other models is presented in the final section of Chapter 9.

2.2.2 Dating diamond inclusions

Diamond inclusions have the potential to provide chemical isolation from interaction with their surroundings for long periods of time. Richardson et al. (1984) analysed diamond hosted P-type (Cr-rich, Ca-poor) garnets from Finsch and Kimberley pipes for Sm-Nd isotopic composition and yielded model ages of 3.2-3.3 Ga. Octahedral garnet crystal morphology in these inclusions is indicative of growth controlled by diamond structure (e.g. Harte et al., 1999). Therefore this date represents both inclusion mineral growth age and diamond growth age.

More recent studies dating sulphides from diamond inclusions using the Re-Os isotope system have revealed that sulphide crystallisation has likely occurred over a wide range of ages from 1.1 – 2.9 Ga (Pearson et al., 1998, underneath the Koffiefontein pipe, Kaapvaal Craton).

2.2.3 P-T estimates from diamond inclusions

Isolated inclusions are unlikely to represent equilibrium mineral compositions but multiple minerals from the same diamond may be used in addition to touching mineral pairs to estimate the range of Ps and Ts of formation and equilibration respectively. 29 garnet-olivine inclusion pairs from Finsch kimberlite yield temperatures of 900-1100°C at around 50kb (Boyd et al., 1985) which plot close to a 40 mW/m² geotherm in the diamond stability field. Diamondiferous lherzolite xenoliths also plot close this geotherm, given that they equilibrated much more recently (Davis, 1977). Therefore in the Archaean the lithospheric root of the Kaapvaal craton must have been at least 150 km deep, extending into the diamond stability field and similar to low dT/dP geotherms to present day Precambrian shields (Boyd and Gurney, 1986).

The studies of the inclusion suites found inside diamonds, including isotopic studies of their ages, have concluded that diamonds and their host kimberlites have separate origins. Many diamonds appear to be Precambrian (and even Archaean) in age, whilst most kimberlites belong to the Phanerozoic.

2.3 KIMs (Kimberlite Indicator Minerals)

Minerals that crystallise in the kimberlite magma are numerous. The principal minerals are olivine, phlogopite, calcite, perovskite and ilmenite but each are not always present (Mitchell, 1986). Of these only the ilmenite survives in the surface environment sufficiently to be used in kimberlite prospecting. There are two subsets of KIMs (i.e. minerals that are also indicative of kimberlite): Mantle indicator minerals and diamond indicator minerals (DIMs).

Mantle minerals erupted as xenocrysts in kimberlite are not stable with respect to the kimberlite magma since the kimberlite liquid is highly volatile and mantle minerals

are highly depleted in volatiles. The minerals are able to survive, preserved in the crystalline matrix of the kimberlite rock, because of the short time between entrainment and magma crystallisation. They are also physically mantled by reaction rims e.g. the kelyphite rim, which is commonly present around garnet xenocrysts. The compositions of these minerals are highly magnesian and are indicative of a high-P, high-T origin in the mantle rather than the crust. Xenocrysts outweigh xenoliths 100:1 (Boyd and Gurney, 1986) and form concentrates due to their relatively high density in surface systems like alluvial gravels (hence their importance in kimberlite prospecting); they can also be found in great abundance in diamond mining concentrates.

The other subset of kimberlite indicator minerals is the diamond indicator minerals. These are those minerals that have overlapping compositions with diamond inclusions. Peridotitic olivine, orthopyroxene, clinopyroxene, garnet and chromite in diamondiferous kimberlite concentrates show a range of compositions i.e. from that common in peridotitic xenoliths to that of P-type diamond inclusions (Gurney and Switzer, 1973; Gurney and Zweistra, 1995).

Therefore olivine, orthopyroxene, clinopyroxene, garnet and Cr-spinel are the main diamond indicator minerals. However, only garnet and chromite have major element compositions that do not overlap strongly with non diamondiferous sources. They are also the two most resilient minerals mentioned and may survive transport away from a kimberlite source region.

In southern Africa, the presence of low-Ca garnets in kimberlites coincides with the extent of Archaean cratons, indeed correlating with the presence of diamonds as well (see "Clifford's Rule"). Gurney (1984) correlated particular low-Ca garnets with the presence of diamond in kimberlites reinforcing this connection. Both low-Ca garnet and diamond appear to have originated in the same harzburgitic host rock beneath

Archaean crust. Additionally Fipke et al. (1995) shows compositions of chromite that have ‘diamond inclusion affinity’ on Cr-Ti and Cr-Mg plots.

Due to their high abundance compared to diamonds, low-Ca garnets similar in composition to P-type diamond inclusions are thought to have crystallised in rocks rather than to represent escapees from diamonds. Furthermore, on consideration of the $\text{CaSiO}_3\text{-MgSiO}_3\text{-Al}_2\text{O}_3$ phase triangle (Fig. 2.1), low-Ca garnet is likely to be in equilibrium with enstatite and without clinopyroxene, thereby indicating a harzburgitic rather than lherzolitic host rock, and thus reinforcing the notion of the *diamond-chromite-garnet harzburgite paragenesis*.

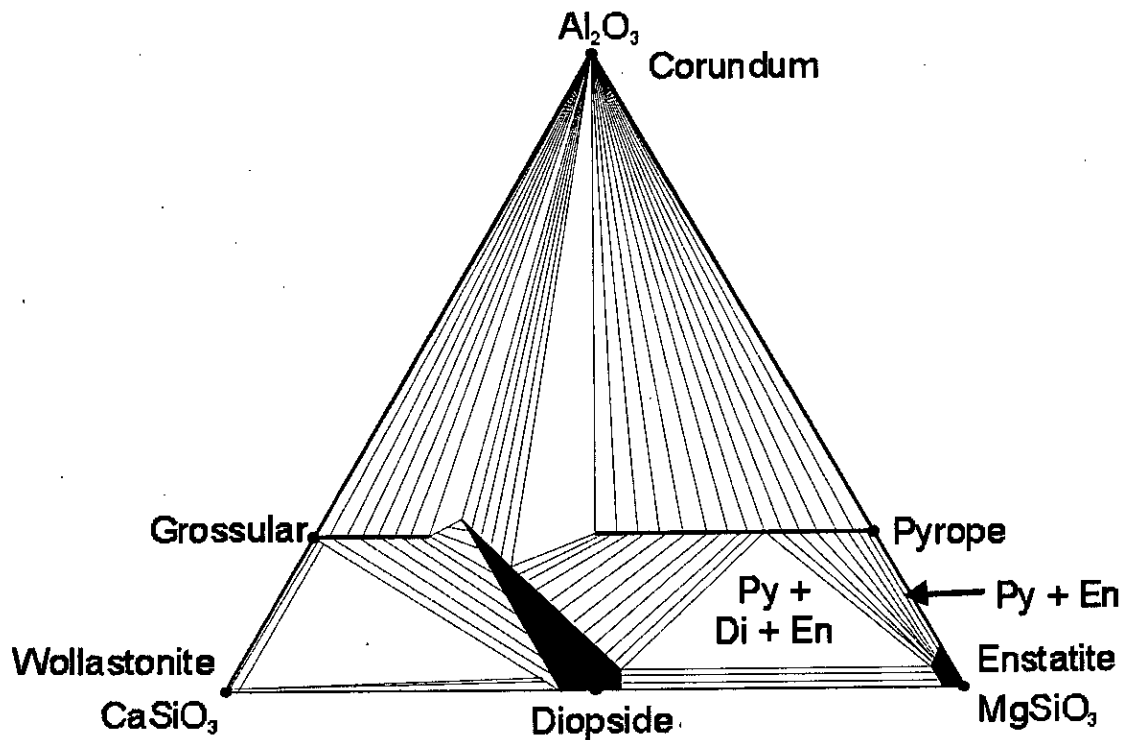


Figure 2.2: Schematic $\text{CaSiO}_3\text{-MgSiO}_3\text{-Al}_2\text{O}_3$ phase triangle at 1200°C and 50 kb illustrating the wide range of Ca compositions in pyrope for common lherzolitic compositions, compared to restricted low-Ca compositions for harzburgites. Py = pyrope, Di = diopside, En = enstatite. Modified from Boyd (1970).

2.4 Mantle Xenoliths

Ultramafic mantle xenoliths are found predominantly as rounded discrete nodules within kimberlites, lamproites and alkali basalts. They are comprised essentially of the minerals found as xenocrysts (see last section on kimberlite indicator minerals) but with a petrological relationship to the other rock forming minerals evident. They range in size from a cluster of several minerals (1 cm diameter) to larger xenoliths up to 1 m diameter which may indicate cross-cutting 'field' relations (e.g. Harte et al., 1993). Mantle xenoliths form the basis for defining the assemblages and modal proportions of minerals within mantle rocks, hence defining the larger scale composition and structure of the lithospheric mantle. A thermal and lithological upper mantle structure may be suggested by pressure and temperature estimates via geothermobarometry involving the coexisting minerals present in xenoliths.

2.4.1 Mantle rock types: Current nomenclature

Peridotite is by far the most common mantle rock type found as xenoliths with eclogite being abundant in particular kimberlites. Table 2.1 summarises currently accepted definitions of the mantle xenolith types found in kimberlites with the main petrological and compositional features described.

Type	Description
I - Coarse, Mg-rich cold peridotites	Universal distribution and abundant (the common 'granular' peridotites xenoliths from kimberlite series eruptive rocks). Rocks largely of olivine and orthopyroxene with little clinopyroxene and garnet; may be with chromite. Grains typically > 2mm with equant or tabular shapes and somewhat irregular grain boundaries, but rarely granuloblastic (Harte, 1977). Depleted major-minor element compositions, often with very small range in bulk and mineral compositions (but exceptions occur, e.g. Premier (Danchin, 1979). Estimated temperatures of formation below 1100-1150°C. $Mg/(Mg+Fe)*100 = 91-95$. $Ca/(Ca+Mg)*100 = 43-51$.
II - Coarse, Fe-rich cold peridotites and pyroxenites	Widespread but usually very rare, mainly garnet lherzolites and garnet websterites. Micro-structures and temperatures of formation as Type I, but sometimes layered. Wide bulk and mineral compositional range, with relatively high Fe, Ca, Al and Na compared with Type I, but variable Cr and low Ti and K. Possibly cumulates (sensu lato) (Gurney et al., 1975).

III – Dunites	Widespread, sometimes common. Two varieties: (a) $Mg/(Mg+Fe)*100 = 93-95$ and often coarse; (b) $Mg/(Mg+Fe)*100 = 88-90$ and usually fine-grained. Of these (a) may be the most depleted rocks (restites) and (b) may be either cumulates or recrystallised megacrysts.
IV - Deformed, cold peridotites and pyroxenites	Widespread and sometimes common. Micro-structures are porphyroclastic or mosaic-porphyroclastic (Harte, 1977), but modal and chemical characteristics and estimated temperatures of formation are usually similar to those of Type I.
V - Hot peridotites	Widespread, but abundance highly variable, rare-absent in Group II kimberlites. Usually deformed and showing porphyroclastic and mosaic-porphyroclastic textures typically with very small neoblasts; rarely coarse and little deformed. Rocks and minerals commonly enriched with Fe and Ti by comparison with Type I and overlap with megacrysts (Type IX). Estimated temperatures of formation above 1150-1200°C. $Mg/(Mg+Fe)*100 = 87-92$. $Ca/(Ca+Mg)*100 = 28-43$.
VI - Marid suite	Widespread, sometimes common. Rocks consisting of: mica, amphibole (richterite), rutile, ilmenite, diopside and zircon. Probable igneous origin. Related to certain kimberlite and lamproitic magmas (Dawson & Smith, 1977; Waters 1986).
VII - Pyroxenite sheets rich in Fe-Ti	Only reported from Matsoku (Harte et al., 1977; 1987). Orthopyroxene- and clinopyroxene-rich rocks with widely variable olivine and garnet, often with ilmenite and phlogopite. From magmatic intrusions (<16 cm thick) into Type I rocks which are metasomatised.
VIII - Modal metasomatic groups	Diverse, usually coarse, cold peridotites showing evidence of modal metasomatism in the form of minerals developing within pre-existing rock. Different types seen at different pipes: ilmenite-rutile-phlogopite-sulphide (IRPS) association at Matsoku; richterite-phlogopite-Cr-titanite association at Bultfontein; edenite-phlogopite association at Jagersfontein.
IX – Eclogites and grosopydites	Universal distribution; usually rare but occasionally very common. Diamond and graphite accessory minerals: no olivine. Very wide range in bulk and mineral compositions. Increasingly thought to come from oceanic crust by subduction. Wide range in equilibration temperature.
X - Megacrysts or discrete nodules	(a) Cr-poor variety: widespread, occasionally very common, particularly involving the minerals orthopyroxene, clinopyroxene and garnet, sometimes olivine and ilmenite. Wide range in chemistry and equilibration temperature, which correlates with $Mg/(Mg+Fe)$. Hotter megacrysts show chemical similarities to Type V; cooler megacrysts sometimes intergrown with ilmenite. Magmatic origin. (b) Cr-rich variety: uncertain distribution and overall features. Mineral compositions overlap those of Type I (Eggler et al., 1979). (c) Various minerals (with or without exsolution features) which are not clearly associated with (a) or (b) and might represent disrupted peridotites and eclogites etc.

XI - Diamonds and inclusions in diamonds	Widespread; in southern Africa distribution related to cratons. Inclusion suites divided into peridotitic and eclogitic. Peridotitic inclusions have restricted and depleted chemistry (Fo: 93-94, i.e. olivine $Mg/(Mg+Fe)*100$) and low-medium equilibration temperatures. Eclogitic inclusions have a wide range in chemistry and equilibration temperatures.
---	---

Table 2.1: Major types of rock and mineral inclusions in kimberlite series eruptive rocks. (Largely based on descriptions and summaries given by Gurney and Harte (1980) and Harte (1983). Reproduced from Table 1.2 in Harte and Hawkesworth (1989), (see also Pearson et al., 2003).

Mineralogically, the paragenesis of mantle xenoliths can be determined initially by the proportion of each of its constituent minerals (Fig. 2.3). When garnet is added to these minerals, garnet peridotite and eclogite may be considered and only rare phlogopite-, ilmenite-, amphibole-bearing rocks are not represented.

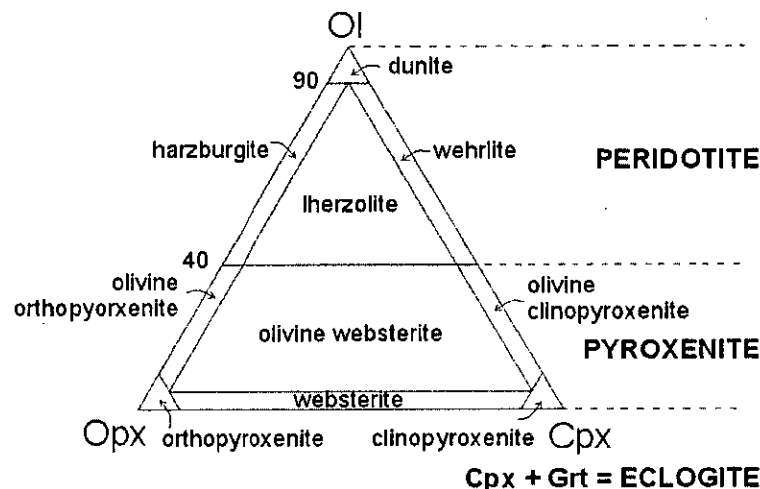


Figure 2.3: Ultramafic rock type nomenclature based on olivine (Ol), orthopyroxene (Opx) and clinopyroxene (Cpx) modal abundance.

Texturally the xenolith may be coarse with no foliation evident, fine-grained with coarse porphyroclasts indicative of deformation or structured on a large scale. Structured xenoliths may contain veins or possess modal layering. Major element chemical analysis allows determination of cation ratios and the application of geothermobarometry and thus confirmation of xenolith origin. However, most classification is possible in hand specimen.

2.4.2 Compositional variation and trace element data

Trace elements vary from depleted to primitive (pyrolitic) to enriched compositions in peridotite xenoliths. Normal peridotitic garnets tend to have low (<1*chondrite) LREE to medium (~50*chondrite) HREE concentrations. If modal metasomatic minerals such as phlogopite, ilmenite, rutile, edenite, richterite are present then peridotitic minerals may be locally affected by having increased Ca, Al, Fe^{III}, Ti and LREE concentrations. Garnet is the most useful of the peridotitic minerals in this case since it may attain measurable quantities of most of these elements.

Recent studies (e.g. Burgess and Harte, 2004; Griffin et al., 1999b) indicate that bulk rock major element depleted harzburgitic xenoliths with minerals of similar composition to P-type diamond inclusions have low-Ca and high-LREE garnets. Particular garnet zonation from the low-Ca core to a high-Ca, high-Ti rim is recorded. Therefore the authors attribute these features to ancient major element depletion and subsequent trace-element enrichment within certain harzburgitic garnets derived from kimberlite xenoliths. This is an example of cryptic metasomatism, and these studies indicate it's accompaniment with incompatible trace element enrichment in these garnets expressed as humped REE patterns.

2.4.3 Peridotitic xenoliths that conform to P-type diamond inclusion compositions

Rocks fitting diamond inclusion-based constraints (type XI in Table 1) and with chemistries like those described in Gurney (1984) and Fipke et al. (1995), for garnets and chromites respectively, are very rarely found. The recognised localities are: Newlands, Kaapvaal craton (this project; Clarke and Carswell, 1977; Menzies, 2001), Udachnaya, Siberian craton (Pokhilenko et al., 1977) and Arnie kimberlite, Northwest Territories, Canada (Doyle, 2002). Some mechanism, therefore, has to be invoked for the disruption of these rocks so that they are not so commonly preserved as articulated xenoliths in kimberlite. Several workers (e.g. Wyllie et al., 1983; Luth, *indirect communication*) suggest that some form of disseminated magnesite may have been present in these harzburgites prior to eruption. Magnesite is modelled to

undergo explosive decomposition during decompression in kimberlitic systems, however no magnesite has been reported in these rocks on examination at the surface.

The discovery of diamondiferous xenoliths was made by Bonney (1899), who described a diamondiferous eclogite. More recently described diamondiferous xenoliths include: Eclogite by Rickwood et al. (1969), garnet lherzolite by Dawson and Smith (1975), garnet dunite by Sobolev et al. (1969) and garnet harzburgite by Viljoen et al. (1994) and Menzies (2001). The minerals in these peridotitic xenoliths conform closely to the compositions found as P-Type diamond inclusions. Menzies (2001) confirms that diamond inclusions from garnet-chromite harzburgite hosted diamonds conform to the *diamond-chromite-garnet harzburgite paragenesis*. Since these inclusions have been armoured potentially for up to 3.3 billion of years Richardson et al. (1984), the question arises as to how compositionally different minerals inside diamond are compared to the rock-forming minerals. This provides a pre- and post-diamond formation geochemical history to examine.

2.4.4 P-T estimates and mantle xenoliths-derived geotherms

Coexisting minerals in equilibrium within xenoliths are modelled through geothermobarometric formulations to originate at various temperatures and pressures within the mantle, forming 'xenolith geotherms' for particular kimberlites and sometimes larger kimberlitic regions (e.g. Northern Lesotho, Carswell and Gibb, 1987). The xenoliths can be divided on this basis into ones that have equilibrated at low (< 900°C), medium (900-1100°C) and high temperatures (> 1100°C). Low-T xenoliths tend to plot close to model cratonic geotherms of 40mW/m², whereas high-T xenoliths tend to plot to the high-temperature side of this geotherm as though perturbed to higher temperatures (Fig. 2.4).

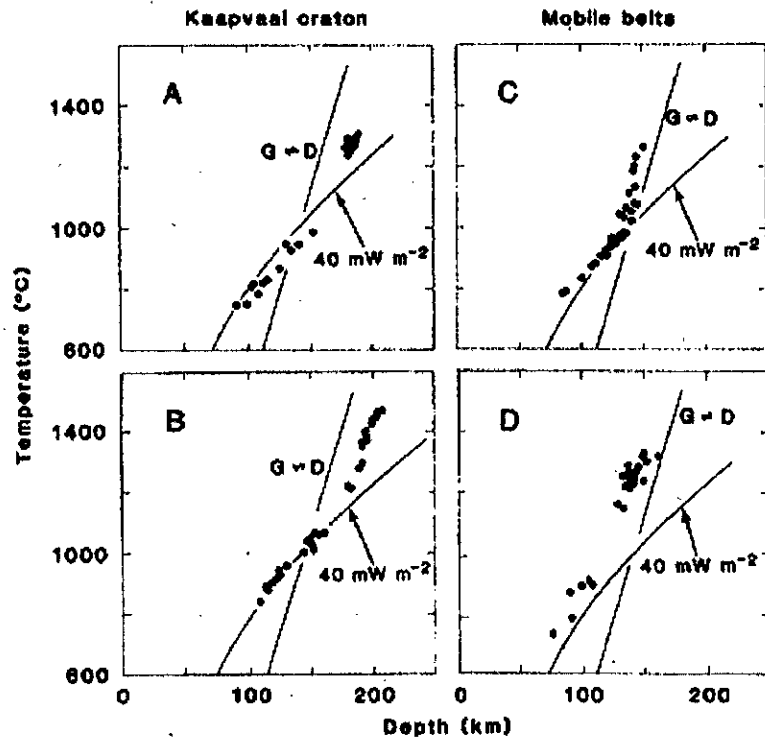


Figure 2.4: Temperature-depth profiles derived from xenolith suites. On craton suites: A from Finsch, B from Northern Lesotho, are perturbed at ~180 km. Off craton profiles from adjacent mobile belts: C & D are perturbed at depths > 120 km. Duplicated from Boyd and Gurney (1986) using conductive geotherm of 40 mW m^{-2} of Pollack and Chapman (1977).

Calculated depths for high-T xenoliths within craton margins are greater than those outside the margins and the transition between low- and high-T xenoliths is also deeper (170-190 km rather than ~140 km for low-Ts) within the cratons e.g. Kaapvaal craton, Boyd and Gurney (1986). Fig. 2.5 illustrates how xenoliths are derived from the diamond stability field underneath the Kaapvaal cratonic root in southern Africa i.e. a theoretical plane exists within the mantle separating rocks that have equilibrated above and below about 1100°C , which corresponds to the volatile-present mantle solidus at close to 50 kb. Nixon and Boyd (1973) and Gurney et al. (1979) point out that megacrysts may reflect pre-kimberlitic melting at the base of the lithosphere, hence Harte (1983) suggested that this may be metamorphosing low-T xenoliths at temperatures above 1100°C prior to eruption. Previous authors have suggested temperature perturbation by convective asthenospheric overturn and incorporated this into a conductive-convective geotherm model (e.g. McKenzie, 1989).

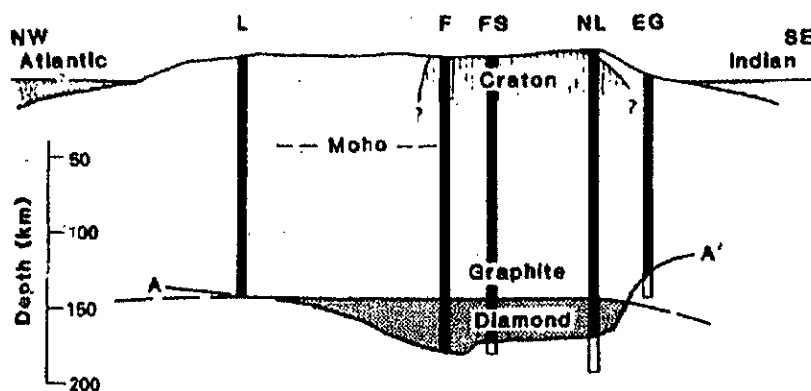


Figure 2.5: NW-SE cross-section through southern African lithosphere based on kimberlite xenolith-derived geothermometry indicating the diamond stability field in the craton root. F = Finsch, FS = Frank Smith in the Barkly-West district, NL = Northern Lesotho, EG = East Griqualand. Line A-A' = postulated lithosphere-asthenosphere boundary based on high-T/low-T xenolith division. From Boyd and Gurney (1986).

2.5 Summary of Key Areas of Current Research

Approximately 70 new kimberlites per year are discovered with ~1/100 being economic for gem diamond production. More xenolith data is becoming available from previously unrepresented parts of the globe and more extensive databases are being set up to document the range of mineral compositions found as xenoliths, xenocrysts, diamond inclusions and diamonds themselves. There are several key areas of research that workers are attempting to resolve by further study of these new and also existing sample sets. High micro-scale spatial resolution is also possible with the latest analytical techniques such as the electron and ion microprobes that can be used for in situ major and trace element and isotopic analysis.

2.5.1 Thermal structure of the mantle lithosphere

The aim of this area of research is to establish more accurate knowledge of the temperature variation of rocks with depth. This aids diamond exploration since it is able to make predictions about whether particular kimberlites can sample material from the diamond stability field and hence assess the diamond-carrying potential of kimberlites. Therefore finding and analysing more samples that have well equilibrated minerals suitable for geothermobarometric calculations will help to delineate a pre-kimberlitic geotherm.

The formulation of additional barometers and thermometers enables more mantle material to be characterised in terms of P and T. But major element equilibria between mineral pairs has been thoroughly assessed as to their P-T dependence so single grain techniques (e.g. Ni-in-garnet and Cr-in-clinopyroxene) are enabling more diamond inclusions and single minerals in alluvial concentrate to be given P-T estimates. Although there is less accuracy involved in the single grain techniques, since they rely on a coexisting mineral of assumed composition, they are especially applicable to alluvial and glacial gravel samples.

The addition of new end member molecules and hence the ability to compute more components in thermodynamic models allows the potential to explore a wider range of bulk rock compositions and their behaviour on changing pressure and temperature more accurately. Further experimental studies in relevant systems will also help to refine these techniques and improve accuracy.

2.5.2 Lithological structure

Further descriptions of obducted peridotitic and eclogitic massifs discovered on land will add to the current understanding of larger scale cross cutting and lithological layering expected in the mantle lithosphere. On a larger scale Schulze (1986), for example, associated wedges of cratonic crust seen in the field in Ontario with lower lithosphere accretion mechanisms. This is echoed in South Africa by Re-Os studies that date Kimberley block accretion of the Kaapvaal craton with its crustal expression being the Colesberg magnetic lineament (Shirey et al., 2002). However it is the mantle sample of kimberlites that is still relied upon to provide multiple 'pseudo bore holes' through the sub-continental mantle lithosphere. Therefore further data on geobarometric depth estimates for particular rock types will give resolution to ± 5 or 10 km on the lithological layering. Improved resolution on seismic

reflectors should aid delineation of underplated and layered regions of the sub-continental lithospheric mantle with strong density contrasts.

Large scale, cross-craton correlations have been used to identify differences and similarities in worldwide mantle properties. Two such examples are: The composition of worldwide diamond inclusions as a marker for pre- and syn-diamond, depleted peridotite lithologies and appears to be relatively consistent worldwide. A second example is the identification and extent of development of potentially underplated pyroxenitic horizons e.g. xenoliths from alkali basalts in xenolith suites from Scotland (Halliday et al., 1993). Many institutes and companies have started collating large-scale databases of kimberlite indicator mineral analyses in an attempt to produce estimates of mantle conditions underneath cratons using a 'mantle mapper' approach.

Many similarities have been found between different cratons, but because of the vast amount of data and the lack of accompanying petrography, interpretations are still at an early stage. Large-scale investigations are important in indicating the extent of the occurrence of diamond-harzburgite and diamond-eclogite assemblages especially.

2.5.3 Composition of metasomatic fluids affecting mantle rocks

The effect of metasomatism has been an important line of investigation ever since its widespread occurrence was identified in 1970s by authors such as Harte et al. (1975) and Bailey (1982). Classifications such as Dawson and Smith (1975) and Harte (1983) separated metasomatism into modal (i.e. the addition of a phase) and cryptic (i.e. major element enrichment or isolated trace element enrichment) types. Therefore current studies, through the study of xenoliths and the characterisation of these types of metasomatism, are gathering data on the range of compositions expected to be introduced into peridotitic/eclogitic mantle by fluid infiltration. Partition coefficients for elements between minerals and melt are required for modelling this process and

preliminary experimental results are being examined and assessed in current literature.

The quantification of the oxygen fugacity of metasomatic fluids is also important in order to assess the stability of diamond compared to different types of metasomatic melt. i.e. whether the melt will consume diamond by being too reduced or oxidised for the diamond buffer. e.g. studies by Deines (1980); McCammon et al. (1998); Luth (1993).

2.5.4 Timescales for craton formation, diamond growth phases, metasomatism and pressure-temperature re-equilibration

Establishing timescales for processes in the mantle has always been a problem given that most isotopic systems are reset at mantle temperatures. At high temperatures diffusion is also faster so only chemical information from relatively recent events are likely to be preserved.

Os is extremely compatible in mantle rocks and its concentration remains effectively constant once trapped in mantle phases even if partial melting and metasomatism were to occur. Therefore the Re-Os isotope system is relatively robust compared to Sm-Nd and has the ability to provide an isotope ratio that will reflect the timing of original melt extraction and mantle rock formation (Walker and Morgan, 1989b; Pearson et al., 1995). If reliable mineral or whole rock isochrons can be obtained, an age can be derived, otherwise a model age may be derived (see Pearson et al., 1995).

Diamond inclusion sulphides may be dated using the Re-Os isotope system to date diamond formation events (e.g. Westerlund et al., 2004). This timing has been compared to large scale events such as subduction and craton suturing affecting the Kaapvaal and Zimbabwe cratons. Shirey et al. (2002) combine deep seismic structural information with ages of major crustal events in the Archaean and Proterozoic (De Wit et al., 1992). At least three diamond formation events seem to

correspond to various parts of southern African craton formation, stabilisation and modification history. Whether diamond formation is truly episodic or actually relatively continuous is a current debate that is being resolved from study of diamond and xenoliths in African and worldwide cratonic regions.

Diffusion coefficients for major and trace elements have been established experimentally (Ganguly et al., 1998; van Orman et al., 2002) and refined empirically (Carlson, 2006) in recent years. This has allowed researchers to examine 'stranded' diffusion profiles in minerals to estimate the timescale for chemical heterogeneity more accurately. Bulk modification of harzburgite by fluids may be tracked and the extent of its conversion to lherzolite is being documented e.g. in Griffin et al. (1999b) and in Burgess and Harte (1999). These issues will continue to be debated.

2.6 Formulation of a Tractable Problem

2.6.1 Previous studies on high-Cr, low-Ca garnet-bearing xenoliths

The Barkly-West district of kimberlites comprises Newlands, Frank Smith, Leicester and Bellsbank situated 40-80 km northwest of Kimberley (Fig. 2.6). All of these kimberlites are currently being mined for diamonds. The discovery of diamondiferous garnet–chromite harzburgite xenoliths by John Gurney at Newlands kimberlite prompted preliminary analysis by Menzies (2001) who additionally studied diamondiferous eclogites and a wide variety of mantle material from the pipe in a detailed initial survey. Menzies' (AH) study yielded promising comparisons to the harzburgitic diamond inclusion suite in terms of the major and minor elements compositions of minerals from garnet harzburgite xenoliths. Two of the diamondiferous peridotites studied are shown in Fig. 2.7a and b. Doyle (2002) also describes xenoliths from Arnie kimberlite, Canada, showing similar properties but they are not diamond-bearing (Fig. 2.7c-e).

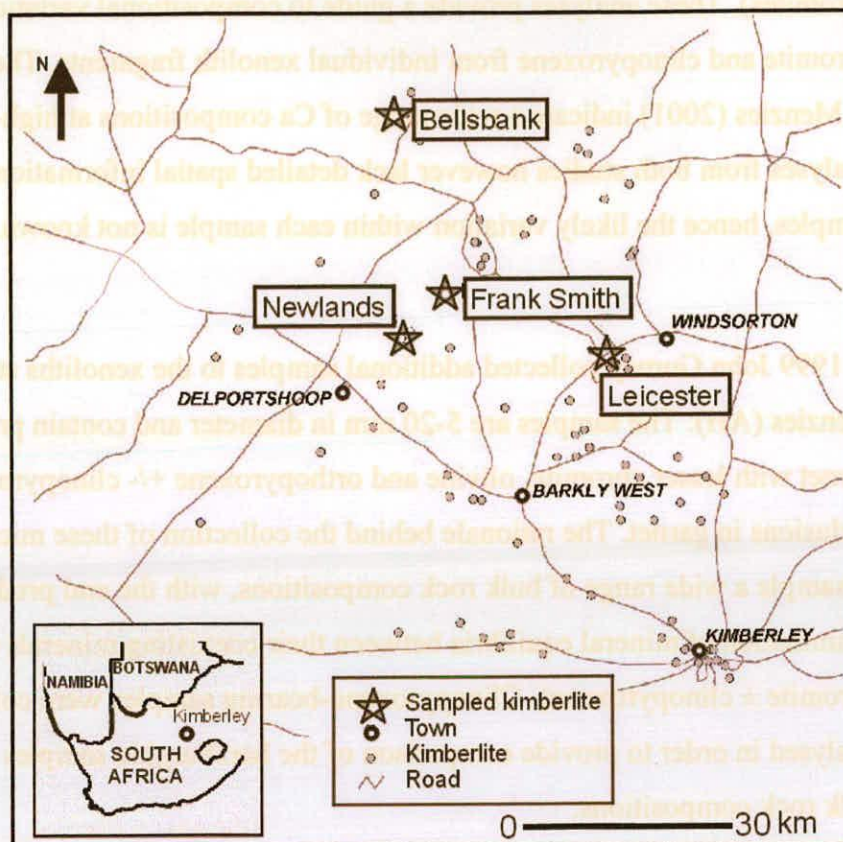


Figure 2.6: Map of the sampled kimberlites in the area north of Kimberley, Western Cape Province, Republic of South Africa (Figure adapted from Menzies, 2001).

Clarke and Carswell (1977) first announced the presence of unusual garnets with both high-Cr and high-Ca (i.e. rich in the uvarovite end member) from Newlands kimberlite and noted that garnets of these compositions are relatively scarce, being only known from Newlands and some of the Yakutian kimberlites. It is now known from mining concentrate analysis that several other southern African kimberlites also possess these garnets (Bellsbank included).

Newlands garnet macrocrysts have been analysed by electron probe spot analyses by Menzies (2001) (310 garnets with 30 coexisting clinopyroxenes and 31 coexisting chromites) and Bobbejaan garnet macrocrysts by van der Westhuizen (1992) (53 garnets, 10 coexisting clinopyroxenes, 1 coexisting orthopyroxene and 18 coexisting

chromites). These analyses provide a guide to compositional variation of garnet, chromite and clinopyroxene from individual xenolith fragments. The garnet analyses of Menzies (2001) indicate a wide range of Ca compositions at high-Cr values. The analyses from both studies however lack detailed spatial information within the samples, hence the likely variation within each sample is not known.

In 1999 John Gurney collected additional samples to the xenoliths studies by Menzies (AH). The samples are 5-20 mm in diameter and contain predominantly garnet with lesser chromite, olivine and orthopyroxene +/- clinopyroxene often as inclusions in garnet. The rationale behind the collection of these microxenoliths was to sample a wide range of bulk rock compositions, with the end product being the examination of mineral equilibria between their coexisting minerals (garnet and chromite \pm clinopyroxene). Clinopyroxene-bearing samples were collected and analysed in order to provide comparison of the harzburgitic samples to higher-Ca bulk rock compositions.

(a)



(b)



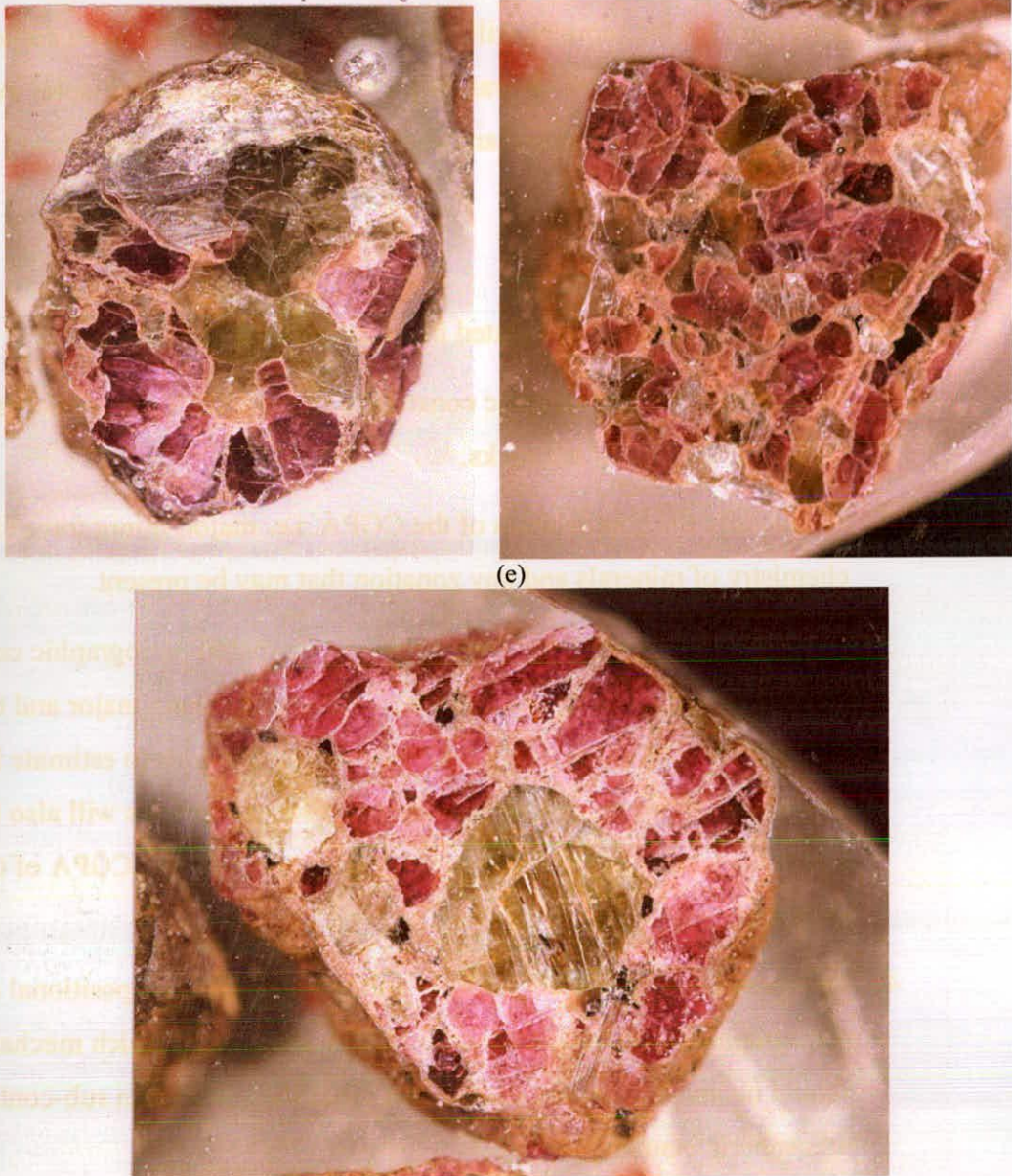


Figure 2.7: (a) and (b) Photos of fresh surfaces of diamond-chromite-garnet harzburgites from Newlands kimberlite, RSA by Menzies (2001). In (b) . (c), (d) and (e) Photos of chromite-garnet harzburgites from Arnie kimberlite, NWT, Canada by Doyle (2002). Photograph widths are (a) 90 mm, (b) 100 mm, (c) 100 mm, (d) 110 mm, (e) 80 mm.

2.6.2 Formulation of a tractable problem

Therefore, given the extent of previous studies, it is clear that a detailed petrographic and geochemical study of the polymineralic assemblages present in the Newlands

and Bobbejaan high-Cr garnet-rich samples is required in order to gain information on the chromite-garnet peridotite assemblages (CGPA). This knowledge will provide a P-T framework for the samples will allow general mantle-evolution context to be placed upon this rock type which was only known from isolated mineral inclusions in diamond and isolated geochemical analyses of single grains over a narrow range of bulk rock compositions.

Hence, the aims of the thesis (as stated in Chapter 1) are as follows:

1. To establish the petrographic constraints of the CGPA. i.e. modal mineralogy, texture, grain size of the rocks.
2. To quantify the composition of the CGPA. i.e. major, minor trace element chemistry of minerals and any zonation that may be present.
3. To interpret compositional information in its spatial/petrographic context and in relation to coexisting phases. This will be done using major and trace element concentrations analysed in coexisting minerals to estimate P-T conditions of formation and equilibration. Trace elements will also be used to assess the role of melts/fluids as modifying agents in the CGPA of the mantle.
4. To assess existing models for their ability to explain compositional and petrographic features noted for the CGPA, and clarify which mechanisms should be invoked for generating and modifying Archaean sub-continental lithospheric mantle.
5. To endeavour to supplement information for identifying regions of diamond stability in the lithosphere and identifying distinctive geochemical trends.

2.7 References

- Bailey, D. K. (1982). Mantle metasomatism - continuing chemical change within the Earth. *Nature*. **296**. 525-530.
- Bonney, T. G. (1899). The parent rock of the diamond in South Africa. *Proceedings of the Royal Society*. **65**. 223-226.
- Boyd, F. R. (1970). Garnet peridotites and the system $\text{CaSiO}_3\text{-MgSiO}_3\text{-Al}_2\text{O}_3$. *Mineralogical Society of America, Special Publication*. **3**. 63-75.
- Boyd, F. R. and Gurney, J. J. (1986). Diamonds and the African lithosphere. *Science*. **232**. 472-477.
- Burgess, S. R. and Harte, B. (1999). Tracing lithosphere evolution through the analysis of heterogeneous G9/G10 garnets in peridotite xenoliths, I: Major element chemistry. 7th International Kimberlite Conference, Cape Town, Red Roof Designs. 66-80.
- Burgess, S. R. and Harte, B. (2004). Tracing lithosphere evolution through the analysis of heterogeneous G9-G10 garnets in peridotite xenoliths, II: REE chemistry. *Journal of Petrology*. **45**. 609-634.
- Carlson, W. D. (2006). Rates of Fe, Mg, Mn and Ca diffusion in garnet. *American Mineralogist*. **91**. 1-11.
- Carswell, D. A. and Gibb, F. G. F. (1987). Garnet lherzolite xenoliths in the kimberlites of northern Lesotho: revised P-T equilibration conditions and upper mantle Palaeogeotherm. *Contributions to Mineralogy and Petrology*. **97**. 473-487.
- Clarke, D. B. and Carswell, D. A. (1977). Green garnets from the Newlands kimberlite, Cape Province, South Africa. *Earth and Planetary Science Letters*. **34**. 30-38.
- Dawson, J. B. and Smith, J. V. (1975). Occurrence of diamond in a mica-garnet lherzolite in kimberlite. *Nature*. **254**. 580-581.
- De Wit, M. J., De Ronde, C. E. J., Tredoux, M., Roering, C., Hart, R. J., Armstrong, R. A., Green, R. W. E., Peberdy, E. and Hart, R. A. (1992). Formation of an Archaean continent. *Nature*. **357**. 553-562.
- Deines, P. (1980). The carbon isotopic composition of diamonds: relationship to diamond shape, color, occurrence and vapor composition. *Geochimica et Cosmochimica Acta*. **44**. 943-961.
- Doyle, P. M. (2002). A petrographic and petrochemical study of selected peridotitic and pyroxenitic xenoliths from three kimberlite localities in the Lac de Gras region, Northwest Territories, Canada. Department of Geological Sciences. Cape Town. University of Cape Town. *Unpublished Masters Thesis*

- Fipke, C. E., Gurney, J. J. and Moore, R. O. (1995). Diamond exploration techniques emphasising indicator mineral geochemistry and Canadian examples. *Geological Survey of Canada*. **423**. 1-86.
- Ganguly, J., Cheng, W. and Chakraborty, S. (1998). Cation diffusion in aluminosilicate garnets: experimental determination in pyrope-almandine diffusion couples. *Contributions to Mineralogy and Petrology*. **131**. 171-180.
- Griffin, W. L., Shee, S. R., Ryan, C. G., Win, T. T. and Wyatt, B. A. (1999b). Harzburgite to lherzolite and back again: metasomatic processes in ultramafic xenoliths from the Wesselton kimberlite, Kimberley, South Africa. *Contributions to Mineralogy and Petrology*. **134**. 232-250.
- Gurney, J. J. (1984). A correlation between garnets and diamonds in kimberlites. In: Ed. Glover, J. E., Harris, P. G. *Kimberlites: Occurrence and origin: A basis for conceptual models in exploration*. Perth, University of Western Australia, Extension Services. **8**. 143-166.
- Gurney, J. J. and Harte, B. (1980). Chemical Variations in Upper Mantle Nodules from Southern African Kimberlites. *Philosophical Transactions of the Royal Society of London*. **293**. 273-293.
- Gurney, J. J., Jakob, W. R. O. and Dawson, J. B. (1979). Inclusions in kimberlites and other volcanics. In: Eds.: Boyd, F. R. and Meyer, H. O. A. *The mantle sample*. Washington D.C, American Geophysical Union. 227-234.
- Gurney, J. J. and Switzer, G. S. (1973). The Discovery of Garnets Closely Related to Diamonds in the Finsch Pipe, South Africa. *Contributions to Mineralogy & Petrology*. **39**. 103-116.
- Gurney, J. J. and Zweistra, P. (1995). The interpretation of the major element compositions of mantle minerals in diamond exploration. *Journal of Geochemical Exploration*. **53**. 293-309.
- Halliday, A. N., Dickin, A. P., Hunter, R. N., Davies, G. R., Dempster, T. J., Hamilton, P. J. and Upton, B. G. J. (1993). Formation and composition of the lower continental crust: Evidence from Scottish xenolith suites. *Journal of Geophysical Research*. **98**. 581-608.
- Harris, J. W. and Gurney, J. J. (1979). Inclusions in diamonds. In: Ed. Fields, J. E. *The Properties of Diamond*. New York, Academic Press. 555-594.
- Harte, B. (1983). Mantle peridotites and processes: the kimberlite sample. In: Ed. Hawkesworth, C. J. N., M. J. *Continental Basalts and their Xenoliths*. Nantwich, Shiva. 46-92.
- Harte, B. (1983). Mantle peridotites and processes: The kimberlite sample. In: Eds.: Hawkesworth, C. J. and Norry, M. J. *Continental basalts and mantle xenoliths*. Nantwich, Shiva. 46-92.
- Harte, B., Cox, K. G. and Gurney, J. J. (1975). Petrography and geological history of upper mantle xenoliths from the Matsoku kimberlite pipe. *Physics and Chemistry of the Earth*. **9**. 477-506.

- Harte, B., Gurney, J. J. and Harris, J. W. (1980). The formation of peridotite suite inclusions in diamonds. *Contributions to Mineralogy & Petrology*. **72**. 181-190.
- Harte, B. and Hawkesworth, C. J. (1989). Mantle domains and mantle xenoliths. In: Eds.: Ross, J., Jaques, A. L., Ferguson, J. et al. *Kimberlites and Related Rocks*. Geological Society of Australia, Special Publication. **2**. 649-686.
- Harte, B., Hunter, R. H. and Kinny, P. D. (1993). Melt geometry, movement and crystallization, in relation to mantle dykes, veins and metasomatism. *Philosophical Transactions of the Royal Society of London*. **342**. 1-21.
- Harte, B., Hutchison, M. T., Watt, G. R. and Wilding, M. C. (1999). Lower mantle mineral associations in diamonds from São Luiz, Brazil. *The Geochemical Society Special Publication*. **6**.
- Hawkesworth, C. J., Pearson, D. G. and Turner, S. P. (1999). Chemical and temporal variations in the Earth's lithosphere. *Phil. Trans. R. Soc. Lond. A*. **357**. 647-669.
- Kárason, H. and van der Hilst, R. D. (2000). Constraints on mantle convection from seismic tomography. In: Eds.: Richards, M. R., Gordon, R. and van der Hilst, R. D. *The History and Dynamics of Global Plate Motion*. Washington DC, American Geophysical Union, Geophysics Monographs. **121**. 277-288.
- Luth, R. W. (1993). Diamonds, eclogites, and the oxidation state of the earth's mantle. *Science*. **261**. 66-68.
- McCammon, C. A., Chinn, I. L., Gurney, J. J. and McCallum, M. E. (1998). Ferric iron content of mineral inclusions in diamonds from George Creek, Colorado determined using Mossbauer spectroscopy. *Contributions to Mineralogy and Petrology*. **133**. 30-37.
- McKenzie, D. (1989). Some remarks on the movement of small melt fractions in the mantle. *Earth and Planetary Science Letters*. **95**. 53-72.
- McKenzie, D., Jackson, J. and Priestley, K. (2005). Thermal structure of oceanic and continental lithosphere. *Earth and Planetary Science Letters*. **233**. 337-349.
- Menzies, A. (2001). A detailed investigation into diamond-bearing xenoliths from Newlands kimberlite, South Africa. Department of Geological Sciences. Cape Town. University of Cape Town. *Unpublished PhD Thesis*
- Meyer, H. O. A. and Tsai, H.-M. (1976a). Mineral inclusions in natural diamond: their nature and significance. *Mineral Science and Engineering*. **8**. 242-261.
- Mitchell, R. H. (1986). *Kimberlites- Mineralogy, geochemistry, and petrology*. New York, Plenum.
- Nixon, P. H. and Boyd, F. R. (1973). Petrogenesis of the granular and sheared ultrabasic nodule suite in kimberlites. *Lesotho Kimberlites*.
- Pearson, D. G., Canil, D. and Shirey, S. B. (2003). Mantle Samples Included in Volcanic Rocks: Xenoliths and Diamonds. In: Eds.: Holland, H. D. and Turekian, K. K. *Treatise on Geochemistry, Volume 2*. Elsevier. 171-275.

- Pearson, D. G., Shirey, S. B., Carlson, R. W., Boyd, F. R., Pokhilenko, N. P. and Shimizu, N. (1995). Re-Os, Sm-Nd, and Rb-Sr isotope evidence for thick Archaean lithospheric mantle beneath the Siberian craton modified by multistage metasomatism. *Geochimica et Cosmochimica Acta*. **59**. 959-977.
- Pearson, D. G., Shirey, S. B., Harris, J. W. and Carlson, R. W. (1998). Sulphide inclusions in diamonds from the Koffiefontein kimberlite, S Africa: constraints on diamond ages and mantle Re-Os systematics. *Earth and Planetary Science Letters*. **160**. 311-326.
- Pokhilenko, N. P., Sobolev, N. V. and Lavrent'ev, Y. G. (1977). Xenoliths of diamondiferous ultramafic rocks from Yakutian kimberlites. 2nd International Kimberlite Conference, Santa Fe, USA, Extended Abstracts.
- Pollack, H. N. and Chapman, D. S. (1977). On the regional variation of heat flow, geotherms, and lithospheric thickness. *Tectonophysics*. **38**. 279-296.
- Richardson, S. H., Gurney, J. J., Erlank, A. J. and Harris, J. W. (1984). Origin of diamonds in old enriched mantle. *Nature*. **310**. 198-202.
- Rickwood, P. C., Gurney, J. J. and White-Cooper, D. R. (1969). The nature and occurrences of eclogitic xenoliths in the kimberlites of South Africa. Upper Mantle Project. Geological Society of South Africa, Special Publication. **2**. 371-393.
- Ringwood, A. E. (1956). The olivine-spinel transition in the earth's mantle. *Nature*. **178**. 1303-1304.
- Ringwood, A. E. (1982). Phase transformations and differentiation in subducted lithosphere: Implications for mantle dynamics, basalt petrogenesis and crustal evolution. *Journal of Geology*. **90**. 611-643.
- Ringwood, A. E. and Major, A. (1971). Synthesis of majorite and other high pressure garnets and perovskites. *Earth and Planetary Science Letters*. **12**. 411-418.
- Schulze, D. J. (1986). Calcium anomalies in the mantle and a subducted metaserpentinite origin for diamonds. *Nature*. **319**. 483-485.
- Shimizu, N. and Richardson, S. H. (1987). Trace element abundance patterns of garnet inclusions in peridotite-suite diamonds. *Geochimica et Cosmochimica Acta*. **51**. 755-758.
- Shirey, S. B., Harris, J. W., Richardson, S. H., Fouch, M. J., James, D. E., Cartigny, P., Deines, P. and Viljoen, F. (2002). Diamond genesis, seismic structure, and evolution of the Kaapvaal-Zimbabwe craton. *Science*. **297**. 1683-1686.
- Shirey, S. B., Harris, J. W., Richardson, S. H., Fouch, M. J., James, D. E., Cartigny, P., Deines, P. and Viljoen, F. (2002). Diamond Genesis, Seismic Structure, and Evolution of the Kaapvaal-Zimbabwe Craton
10.1126/science.1072384. *Science*. **297**. 1683-1686.
- Sobolev, V. S., Nay, B. S., Sobolev, N. V., Lavrent'ev, Y. G. and Pospelova, L. N. (1969). Xenoliths of diamond-bearing pyrope serpentinite from the "Aykhal" pipe, Yakutia. *Doklady Akademii Nauk SSSR*. **188**. 1141-1143.

- Turcotte, D. L. and Oxburgh, E. R. (1972). Mantle convection and the new global tectonics. *Annual Review of Fluid Mechanics*. **4**. 33-66.
- van der Westhuizen, A. (1992). The Bellsbank kimberlites, with special reference to a suite of purple garnet megacrysts from the Bobbejaan mine. University of the Orange Free State. *Unpublished Masters Thesis*
- van Orman, J. A., Grove, T. L., Shimizu, N. and Layne, G. D. (2002). Rare earth element diffusion in a natural pyrope single crystal at 2.8 GPa. *Contributions to Mineralogy and Petrology*. **142**. 416-424.
- Viljoen, F., Robinson, D. N., Swash, P. M., Griffin, W. L., Otter, M. L., Ryan, C. G. and Win, T. T. (1994). Diamond- and graphite-bearing peridotite xenoliths from the Roberts Victor kimberlite, South Africa. 5th International Kimberlite Conference, South Africa, CPRM. 285-303.
- Walker, R. J. and Morgan, J. W. (1989b). Rhenium-osmium isotope systematics of carbonaceous chondrites. *Science*. **243**. 519-522.
- Westerlund, K. J., Gurney, J. J., Carlson, R. W., Shirey, S. B., Hauri, E. H. and Richardson, S. H. (2004). A metasomatic origin for late Archean eclogitic diamonds: Implications from internal morphology of diamonds and Re-Os and S isotope characteristics of their sulfide inclusions from the late Jurassic Klipspringer kimberlites. *South African Journal of Geology*. **107**. 119-130.
- Wyllie, P. J., Huang, W.-L., Otto, J. and Byrnes, A. P. (1983). Carbonation of peridotites and decarbonation of siliceous dolomites represented in the system CaO-MgO-SiO₂-CO₂ to 30 kbar. *Tectonophysics*. **100**. 359-388.

3. Sampling and Petrography

3.1 Sampling

3.1.1 Locality selection

As a premise for the project the concentrates from Newlands and Bobbejaan were known to contain a significant number of G10 garnets (i.e. with diamond-garnet-chromite harzburgite affinity) (John Gurney pers. comm.). Previous work on Newlands by Menzies (2001) and on Bobbejaan by van der Westhuizen (1992) also indicated that G10 garnets existed in polymineralic samples. During field work other kimberlites in the Kimberley area were examined but found not to contain the same abundance of samples with G10 garnets. In particular the concentrates from the nearby Frank Smith and Leicester kimberlites were found to contain individual red 'megacryst suite' garnets and only very rarely lilac G9/G10 garnets. Only one of the lilac garnet-bearing samples from Leicester was polymineralic and displayed phase relations. Thus this study has focused on material from Newlands and Bobbejaan.

3.1.2 Newlands and Bobbejaan kimberlite xenolith population

The xenoliths from Newlands and Bobbejaan investigated here are not the common coarse peridotite xenoliths of many localities. Thus the question that arises of whether the samples suggest something markedly different from other kimberlites in South Africa or the rest of the world? In other words, have Newlands and Bobbejaan kimberlites sampled a different type of mantle to other kimberlites?

Considering broad petrographic definitions the answer to this question in general seems to be no. Variations in percentages of a few rock types and the presence of some rare rock types are expected for most kimberlites. Menzies (2001) notes the abundance of various xenolith rock types in general at Newlands (see Fig. 3.1).

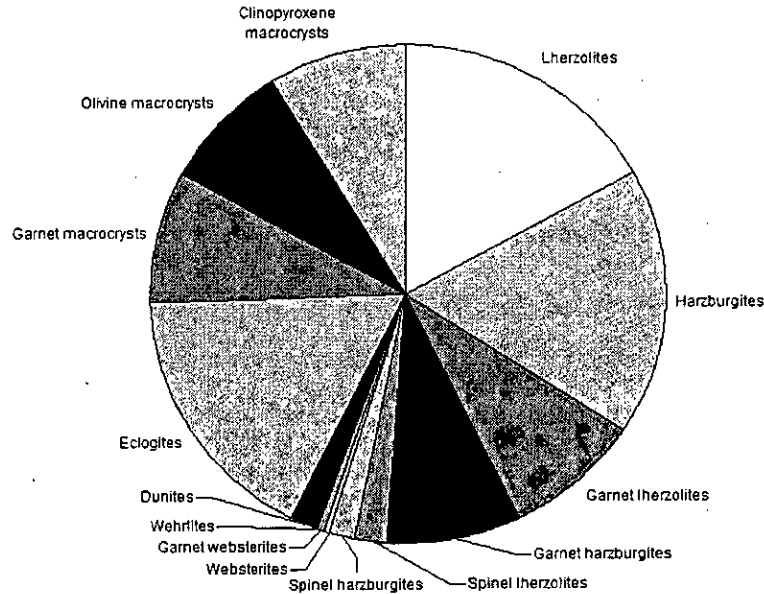


Figure 3.1: $n = \sim 500$, data reprocessed from Menzies (2001). Note that all rock types are relatively well represented (most $> 10\%$) except for websterites ($< 1\%$). The Bobbejaan xenolith population is thought to be similar to Newlands.

The xenolith population at Newlands and Bobbejaan is similar to the average South African kimberlite in that they have a reasonably normal proportion of harzburgite, lherzolite, garnet harzburgite, eclogites and spinel peridotites. However Newlands and Bobbejaan clearly have distinctive features; namely:

- Garnet lherzolite xenoliths containing extensive amounts of olivine and orthopyroxene are much lower in abundance at Newlands and Bobbejaan.
- Newlands has no recorded deformed peridotite or marid-suite peridotites.
- Newlands and Bobbejaan kimberlites have high proportions of ‘peridotitic garnet macrocrysts’¹.

¹ Macrocrysts are generally < 1 cm and megacrysts are generally > 1 cm (Mitchell, R. H. (1986). Kimberlites- Mineralogy, geochemistry, and petrology. New York, Plenum Press.)

3.1.3 Newlands

Sampling at Newlands was undertaken initially by John Gurney and Trish Doyle in 1999 and in March 2003 by the author, John Gurney, Ben Harte and Ben Garden. Sampling permission was granted by the mine owner who also took John Gurney and the author on a tour of the underground workings. The two sessions made collections predominantly from several piles of heavy concentrate. Additional samples of kimberlite and other xenoliths were gathered from dumps containing newly mined kimberlite. The concentrate piles are known to be derived from 'Blow 2' (Fig. 3.2). Newlands is currently owned by Dwyka Diamonds Limited as of 2004.

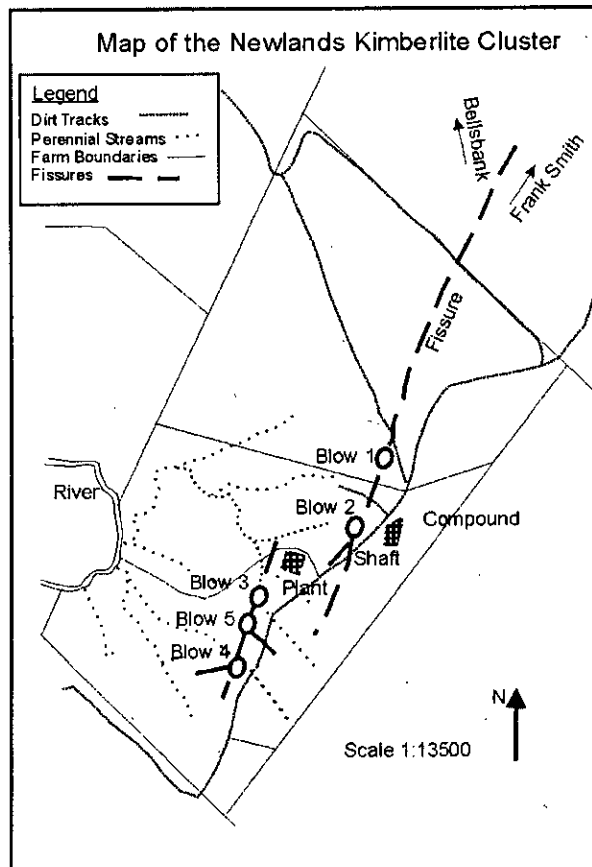


Figure 3.2: Reproduced from Van Heerden and Gurney (1994) showing the en-echelon style of the fissures at Newlands and the compass direction to nearby kimberlites.

3.1.4 Bellsbank

Sampling at Bellsbank was undertaken with the owner's permission (Mr. J. Davison) in March 2003 by the author, John Gurney, Ben Harte and Ben Garden. Heavy concentrate piles (obtained by reworking former dumps on the mine floors) were sampled from close to the plant and are known to be derived from the Bobbejaan Fissure (Fig. 3.3).

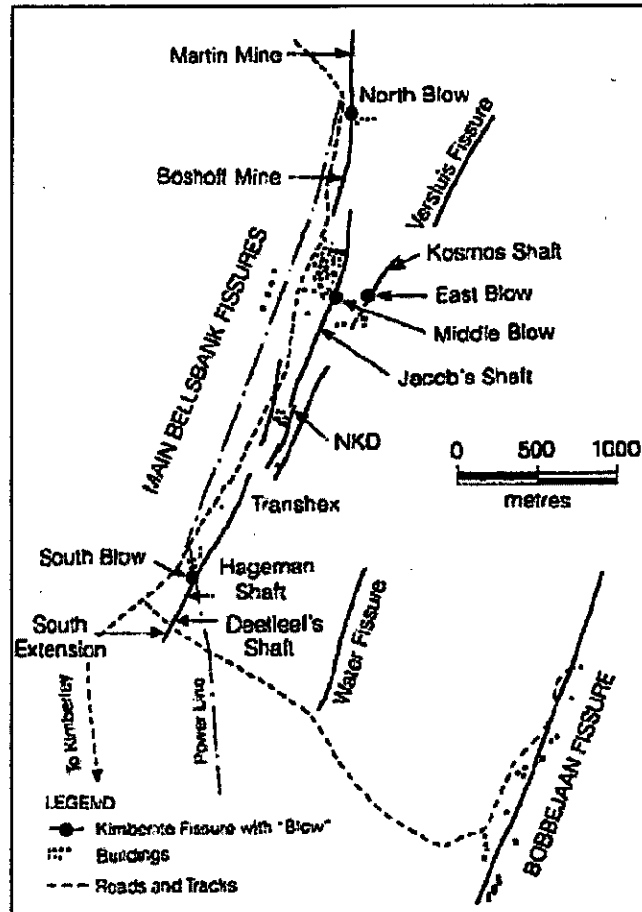


Figure 3.3: Map of the surface exposures of the Bellsbank fissures from Gurney (1997). North is vertical towards the top of map. NNE-trending Bobbejaan fissure to SE of map.

3.1.5 Sampling strategy

During the sampling procedure all mantle rocks/minerals were collected and the following types were yielded:

- Garnet peridotites (additionally containing one or more of: Cr-spinel, serpentine and Cr-diopside)

- Lilac garnet macrocrysts (derived from peridotites)
- Eclogites (containing omphacitic clinopyroxene and orange garnet)
- Cr-diopside megacrysts (derived from 'megacryst suite' magmatic rock)
- Orthopyroxene megacrysts (derived from 'megacryst suite' magmatic rock)
- Red garnets (derived from 'megacryst suite' magmatic rock)
- Individual orange garnets (derived from eclogites)

Fresh orthopyroxene is dark grey-brown and is only found as megacrysts and not within the peridotites. Altered orthopyroxene is a dark green-brown colour in transmitted light. Fresh olivine is only found as kimberlite xenocrysts rather than part of the garnet macrocryst mineralogy and is light green-yellow in colour. Altered olivine (mainly serpentine) is found as part of the garnet macrocryst assemblage and is pale yellow and not as translucent as fresh olivine. Garnet, chromite, clinopyroxene, olivine and orthopyroxene were collected from concentrates at Newlands, Bobbejaan and Leicester. Newlands concentrate was readily available for analysis from Mineral Services sampling (Gurney, pers. com.) and therefore made up the majority of concentrate grains.

3.1.6 Sample size

Since the average specimen size from concentrate was small (< 0.5 cm long dimension) effort was made to search for larger samples (~ 1 cm) that were more likely to contain mineral grain boundaries and textural information. Larger specimens were given sample numbers and saved for textural examination and sectioning before commencement of microanalysis. The smaller specimens were put into labelled bags for their particular collection locations and reserved for direct mounting for concentrate analysis by electron microprobe.

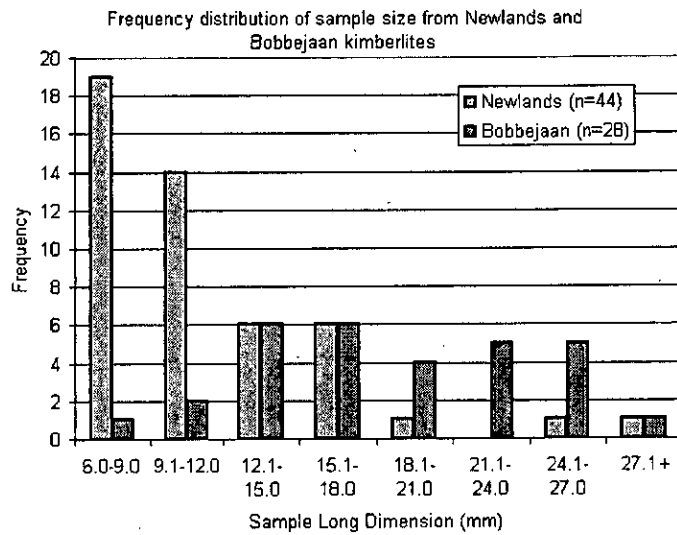


Figure 3.4: Size distribution of samples chosen for textural analysis from Newlands and Bobbejaan kimberlites.

Fig. 3.4 illustrates that Newlands samples have a strong preponderance of finer material and Bobbejaan has a more normal distribution across the size range. The data of Fig. 3.4 are controlled by a combination of factors:

1. Actual xenolith size in the natural kimberlite – some samples have not been changed by any subsequent mining factors.
2. Crush size at the mines (which is known to be smaller at Newlands) and the varieties of concentrate from various stages of processing available for collection during field work.
3. Sample selection from concentrate at the mines where grains > 5 mm were preferentially picked.
4. Sample selection where by larger samples were preferred to smaller ones for textural analysis.

The resultant average long dimension of samples investigated in this chapter is 11.4 mm for Newlands and 18.9 mm for Bobbejaan.

3.2 Petrography

3.2.1 Introduction

Petrographic observations are principally all the features observable by transmitted or reflected light using petrographic and fixed-stage microscopes at 20X to 200X magnification. These observations provide the basis for definition of rock types, modal mineralogy and texture. In addition the textures allow some assessment of the state of equilibrium to be made and provide the spatial context for electron and ion microprobe analysis. Information may also be gained about the effect of fluids (metasomatism) on the samples either in the igneous or metamorphic environment or by surface weathering processes.

The modal mineralogy of the samples was recorded to define bulk rock compositions. A textural classification scheme was devised to differentiate the samples as effectively as possible using simple criteria without necessarily implying the presence of particular processes. It was very important to use these methods carefully in the case of many of the present samples because the sample size was often similar to the original crystal size.

Use of geothermobarometry (see chapter 7) requires thermodynamic equilibrium to be the case. It is therefore beneficial to note whether the samples show a good approach to textural equilibrium or not. Samples showing disequilibrium features such as exsolution or recrystallisation have to be described with care to know whether use of thermodynamic equations to make geothermobarometric predictions is justified.

3.2.2 Methodology

300 samples from Newlands, 200 from Bobbejaan and 40 from Leicester were selected for their large size (> 0.5 cm) and potential for displaying phase relations.

The samples were then examined using a binocular microscope at low magnification in their sampled state and notes made on approximate modal proportions of minerals and any texture of note observable at the surface. Certain features were photographed and then a selection of about 100 samples from Newlands, about 70 from Bobbejaan and 15 from Leicester were made to either break in half for further examination or to directly mount and polish ready for electron probe analysis. Certain samples (e.g. NEWSP) were ground to a particular level to expose inclusions for analysis.

The polished surfaces of all mounted samples were examined so that the mineralogy, modal proportions and texture could be recorded. The samples were then photographed in transmitted and/or reflected light to record mineral spatial information and to provide navigation sheets for microanalytical purposes (electron and ion microprobe).

Additionally EBSD (Electron Backscatter Diffraction) was carried out on some polished samples by SEM to gain garnet crystal orientation information and to determine whether the samples were polygranular or monogranular (see Appendix I). This was particularly useful on samples that had suffered veining and cracking which made it impossible to be sure of the garnet grain size from reflected/transmitted light microscopy alone.

3.2.3 Nomenclature adopted

Fig. 3.5 shows the basic IUGS classification of ultramafic rock types based on modal mineralogy. Peridotitic rock compositions are those that contain more than 40 % olivine and pyroxenitic rocks are those with less than 40 % olivine. > 90% of one of olivine, orthopyroxene and clinopyroxene requires a different rock name as shown. <5 % of one mineral also requires a unique rock name as shown.

This classification scheme does not cater for the minerals garnet and chromite², however, and so poses a problem given that garnet is always present and in many of the samples garnet is predominant. Therefore the rock types 'garnet-harzburgite' or 'garnet-chromite-harzburgite' and 'garnet-lherzolite' or 'garnet-chromite-lherzolite' are used depending on the presence or absence of clinopyroxene and chromite for most samples. These rock types often show substantial alteration of their olivine and pyroxene phases, but are considered to be peridotitic rather than pyroxenitic because the alteration material is always serpentine rich. However, again it must be emphasized that, because of the small size of the samples and the common abundance of garnet, the use of the term peridotite, harzburgite and lherzolite does not imply 60% or more olivine. Because of its petrogenetic importance 'diamond' is added as a prefix to the above rock names if present.

It is often the convention in mantle petrology to refer to rocks with any clinopyroxene as lherzolites and only those completely without evident clinopyroxene as harzburgites, unlike the 5 % clinopyroxene limit shown in Fig. 3.5. This system will be used in the present study to be consistent with other similar studies in the academic literature. One has to bear in mind that there may be a few instances where clinopyroxene is present in very small amounts and not exposed on the surface of a sample; therefore a sample may be recorded as harzburgitic when it should be lherzolic.

² 'chromite' and 'diopside', referred to in this chapter and Chapter 2, are end member names from the spinel and pyroxene mineral groups. These are often referred to in the diamond exploration-related literature as 'chromite' and 'Cr-diopside' but note that they will be referred to specifically depending on their compositions in later chapters (e.g. see section 4.2.1.2, Chapter 4).

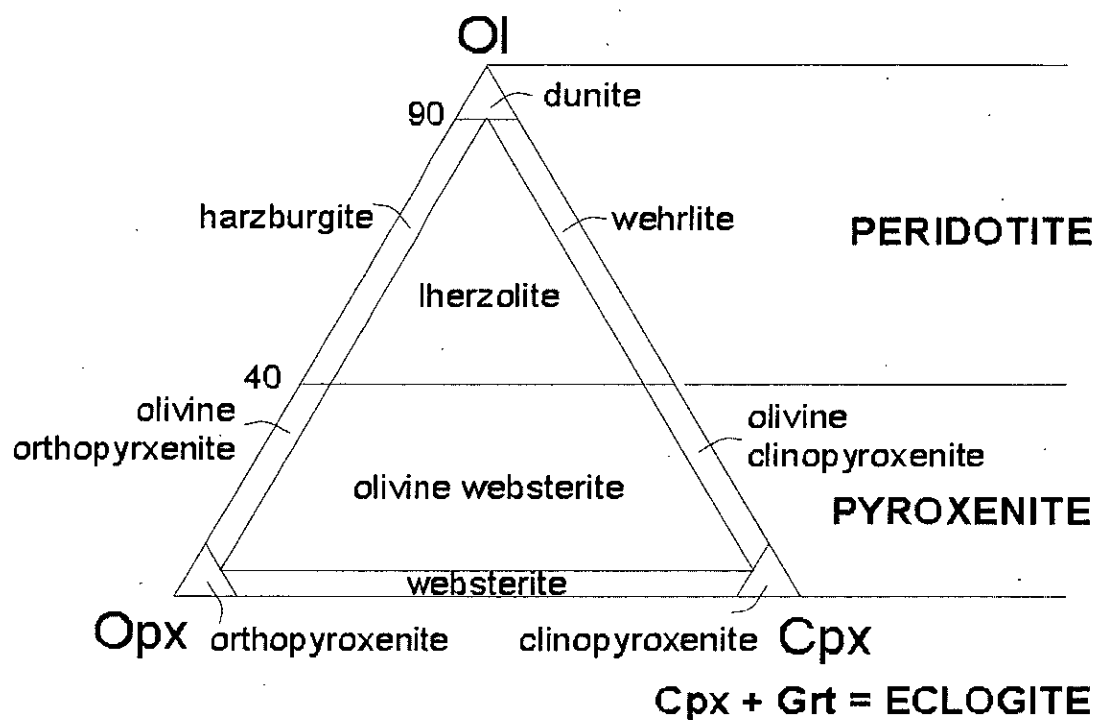


Figure 3.5: Modified from Streckeisen (1980). Ol = Olivine, Opx = orthopyroxene, Cpx = clinopyroxene, Grt = garnet.

Because the sample size is usually small compared to crystal size the samples have been divided into those where the garnet crystal size is \geq sample size (monogranular garnet samples) from those where it is $<$ sample size (polygranular garnet samples). This distinction simply divides those samples that have the appearance of a rock from those that are largely a single garnet crystal, and does not imply at the outset any differences in mineral abundances or composition. Having made these and subsequent subdivisions (below) some tentative comments will be made about the nature of the original rock textures and their overall mineralogy.

For polygranular (P) garnet samples subdivisions are made according to types of matrix present (see also Fig. 3.6):

- **Ps** Serpentine \pm chromite (i.e. harzburgitic): the matrix may contain serpentine alone but it never contains chromite alone and is therefore defined

as having serpentine \pm chromite mineralogy. Matrix chromite is sometimes a separate grain to serpentine but may be attached to it in the matrix.

- **Pd** Diopside, serpentine \pm chromite (i.e. lherzolitic): the matrix may contain diopside alone with both serpentine and chromite being accompaniments to diopside either together or alone.
- **Pg** Garnet-garnet grain boundaries are present as a continuous network and thus garnet dominantly resides in a matrix of garnet.

Note that in polygranular samples the matrix constituents always relate to mineralogy of the inclusions in garnets (i.e. a case was not observed of a lherzolitic matrix to the garnet with only harzburgitic inclusions inside garnet or vice versa).

Monogranular garnet samples are subdivided according to the mineralogy of inclusions present (see also Fig. 3.6):

- **Ms** Serpentine \pm chromite (i.e. harzburgitic): Inclusions may be serpentine alone but only very rarely (2 examples) chromite alone and is therefore defined as having serpentine \pm chromite inclusions. When chromite is present it is nearly always contained within a serpentine inclusion and very rarely occurs as isolated, monomineralic inclusions.
- **Md** Diopside \pm serpentine \pm chromite (i.e. lherzolitic): Inclusions may be monomineralic with any combination of minerals present (i.e. di, di+serp, di+chr or di+srp+chr). Polymineralic inclusions may be present in any combination in addition or exclusively to monomineralic inclusions.
- **M** Monogranular garnet with no inclusions (i.e. no affinity observable)

x:y:z, of 0.8:1:1.3. This is indicative of a uniform erosive/reactive action attributed to the kimberlite magma. The Newlands samples have mean $z = 8$ mm (11.4 mm for those used to provide textural information) given the ~ 5 mm lower cut off size. At Bellsbank however the mean $z = 11$ mm (18.9 mm for those used to provide textural information).

Samples possess a 1-3 mm radial thickness of kelyphite rim at the contact with kimberlite (where it is preserved). Many show kelyphitic rims without attached kimberlite. Also evident on the surface is the presence of many fractures and veins filled predominantly with white calcite.

The minority ($\sim 20\%$) of the samples show evidence for the nature of the grain boundaries present in the original rock where garnets are bounded by serpentine (probably once olivine/orthopyroxene). From this it is clear that estimates of modal proportion are not likely to be reliable and that olivine and orthopyroxene may well have been higher in the larger rocks samples prior to eruption.

3.2.4.2 MINERAL COLOURATION

Garnets from concentrate from Newlands and Bobbejaan show a wide variety of colouration. Eclogitic garnets associated with green omphacitic clinopyroxene vary from yellow-orange to red-orange; whereas peridotitic garnets tend to be purple-lilac but may vary from salmon pink to lilac to deep magenta (see Fig. 3.8a). Deep red garnets occur rarely and have been found to have chemical composition characteristics of the megacryst suites found at many kimberlite pipes.



Figure 3.8: (a) 2.54 cm round mount of peridotitic garnet concentrate in transmitted light. Note subtle variations in hue and the abundance of fractures in most garnets. (b) 2.54 cm round mount of green minerals from concentrate in transmitted light. Lighter yellow-green is olivine, darker grey-green is omphacitic clinopyroxene associated with orange garnet at bottom. Darker varieties of deep green are Cr-diopsides.

Some garnets within samples display the 'alexandrite effect' where high levels of chromium in combination with high-calcium are probably responsible for the shift from green-blue under sunlight or fluorescent light to purple under incandescent light. (Alexandrite is a Cr^{3+} -bearing beryl which displays this effect). About 1 % of concentrate garnets from Newlands and Bobbejaan clearly display this effect.

Slight variation in the deepness of green in Cr-diopsides was also evident and may also be due to certain samples having particularly elevated chromium contents.

Olivine and orthopyroxene crystals have nearly entirely been pseudomorphed by yellow serpentine and a brownish green bastite respectively (see Fig. 3.8b).

3.2.4.3 MODAL PROPORTIONS

Proportions of minerals observable on polished sample surfaces were recorded. Both poly- and monogranular samples are divided into clinopyroxene present (Iherzolithic) assemblages and clinopyroxene absent (harzburgitic) assemblages in the proportions

shown in Fig. 3.9. This indicates sample affinity to a harzburgitic or lherzolitic paragenesis.

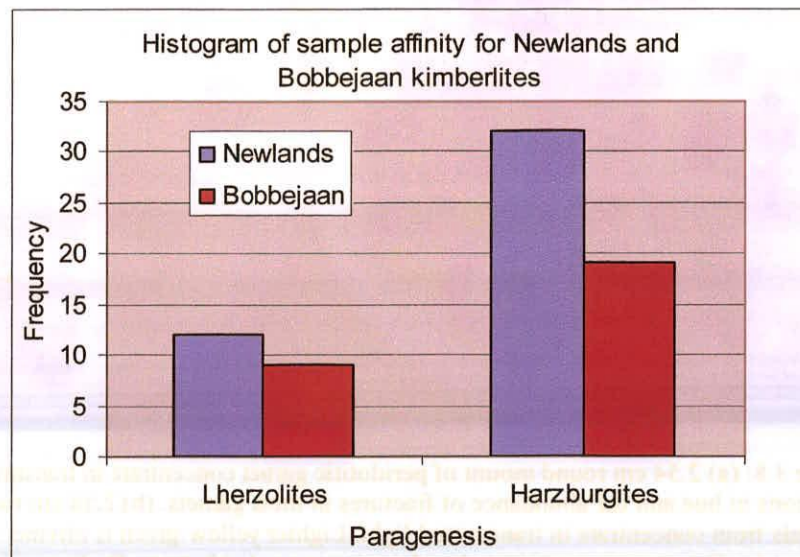


Figure 3.9: Number of lherzolitic and harzburgitic garnet samples from Newlands and Bobbejaan kimberlites (for both P and M sample types).

The modal mineralogy of polygranular samples from both kimberlites is shown in Fig. 3.10. Most samples therefore fall into either garnet (\pm chromite) harzburgite or lherzolite categories. Four samples may be classed as garnetite since they have > 90 % garnet.

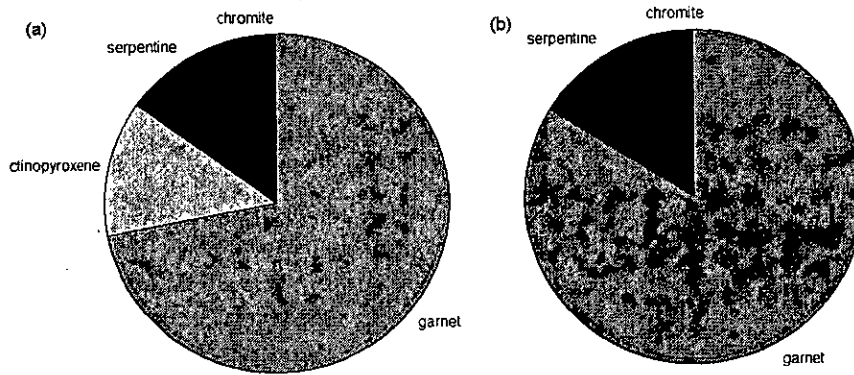


Figure 3.10: Average modal mineralogy of harzburgitic (a) and lherzolitic (b) polygranular samples.

The modal mineralogy of inclusions present in garnets from all samples with inclusions present is shown in Fig. 3.11. It is possible to call these samples garnet samples with lherzolitic or harzburgitic affinity based on the inclusion mineralogy because this is observed to correspond to matrix mineralogy in polygranular samples. However a rock name cannot be applied because only one crystal is present, but the samples do indicate affinity to a peridotitic paragenesis rather than an eclogitic one. Inclusions present within garnets in P samples have similar proportions to those from M samples. This is indicative of M (single crystals) being derived from P rocks. This data is not graphed because of the low number of P samples. Additionally the presence of diamond was noted in sample BOB404. The diamond is a filamentous aggregate of white octahedra growing in a vein within garnet and is $\sim 300 \mu\text{m}$ long.

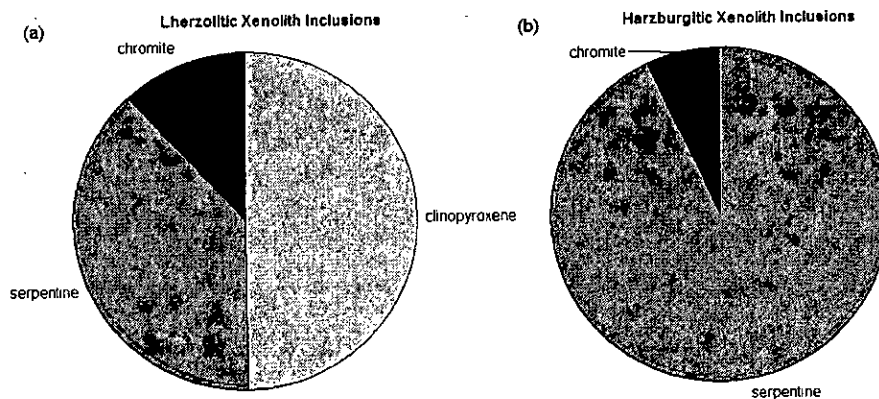


Figure 3.11. Modal mineralogy of inclusions present within garnets from polygranular and monogranular samples of harzburgitic (a) and lherzolitic (b) affinity.

A check was made to see whether there was a significant sample size effect on the number of phases (in garnet and matrix and inclusions) seen per sample. Fig. 3.12 illustrates that polygranular samples are, in general larger than monogranular samples, but that there is not a substantial bias towards larger samples of either type having more phases observable.

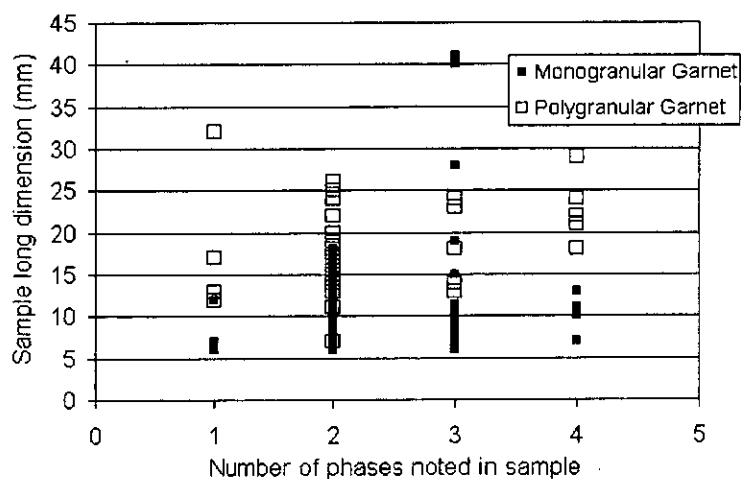


Figure 3.12: Number of phases noted vs. size of monogranular and polygranular samples.

3.2.4.4 PETROGRAPHIC EXAMPLES

3.2.4.4.1 Polygranular Garnet Samples

Polygranular garnet samples have multiple garnet crystals and other minerals forming a matrix around the garnets (section 3.2.2.2). This leads to a garnet-, serpentine- or clinopyroxene-rich matrices and examples of these types are described below.

Ps (NEW308 and BOB063)

NEW308 (Fig. 3.13) possesses garnet-garnet and garnet-serpentine grain boundaries. Each of the three large garnets possesses its own rounded serpentine inclusion < 1 mm diameter. The areas of serpentine have reasonably smooth grain boundaries suggestive of 120° grain triple junctions with garnet. Although the sample size is limited, these observations suggest a coarse polygonal-granoblastic or granuloblastic texture (see Harte, 1977).

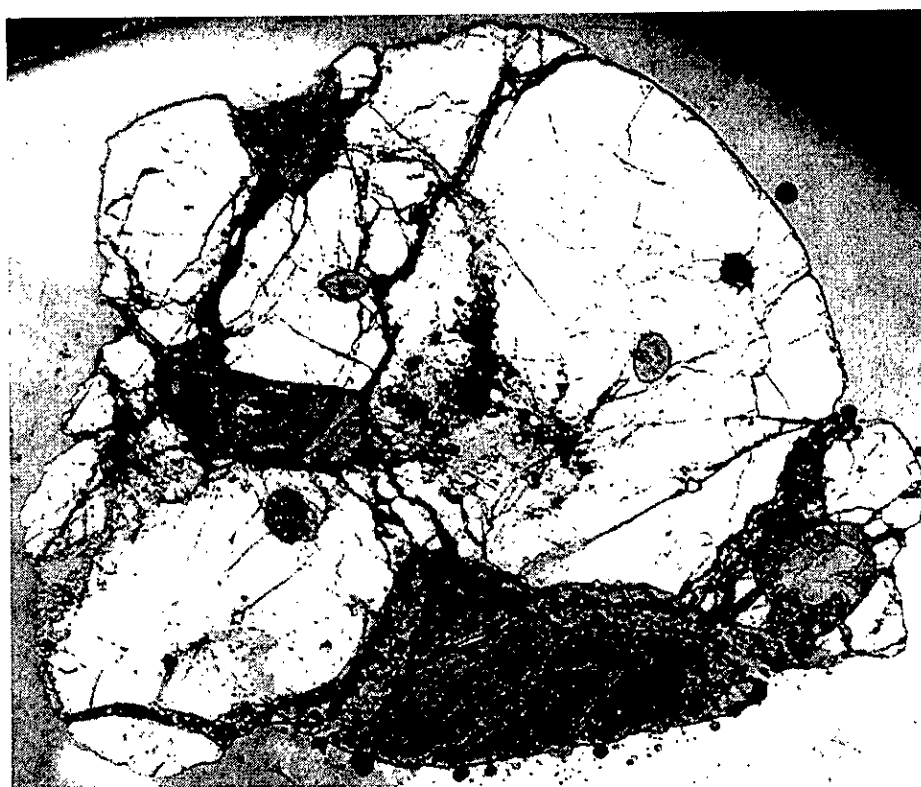


Figure 3.13: Reflected light photo of sample NEW308 (long dimension 11.5 mm). Palest grey is garnet, dark grey is serpentine, and black areas are veins/cracks.

Serpentine is more abundant in samples such as BOB065 where it forms more of a continuous network that surrounds garnets. Serpentine-serpentine-garnet contacts are distinctly granuloblastic in this sample (see Fig. 3.14).

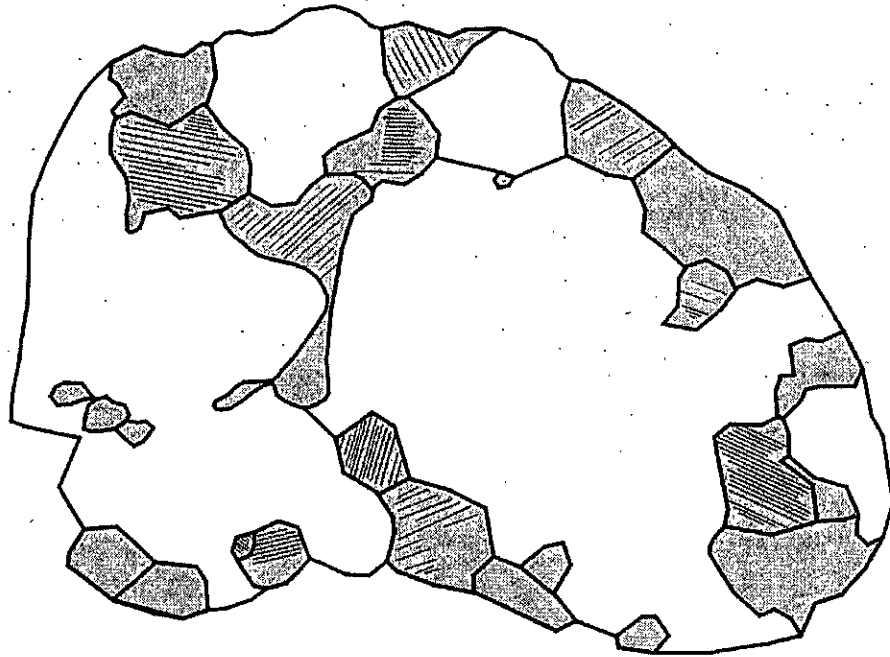


Figure 3.14: Tracing of photograph³ of BOB065 (long dimension 18 mm). Garnet is in white and serpentine is in grey with striations (potentially cleavage) of different orientations (thin lines) reflecting different original crystal orientations. Thick lines represent interpreted grain boundaries.

Pd (NEW303)

Fig. 3.15 shows sample NEW303 which comprises approximately equal proportions of serpentine, clinopyroxene and garnet as matrix minerals. Garnet and clinopyroxene appear euhedral and the serpentine appears more interstitial but may have been formed from several orthopyroxene crystals prior to alteration. Note the presence of rounded inclusions of both serpentine and clinopyroxene within the garnet as millimetre to sub-millimetre crystals.

³ Note that full quality photographs of all samples are included in Appendix VI (data CD).

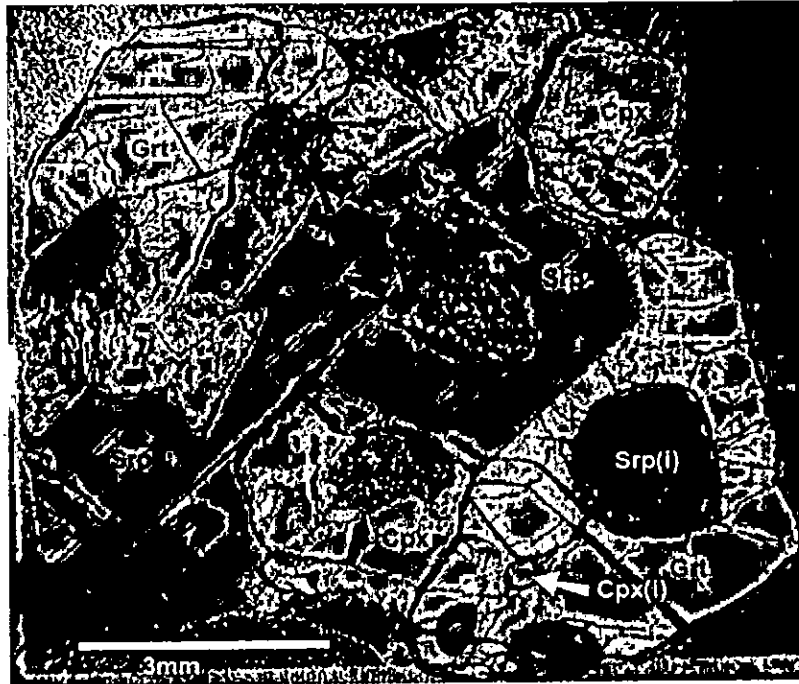


Figure 3.15: Reflected light image of NEW303. Serpentine forms both as a matrix mineral (dark grey with cleavage in the centre of the sample, Srp) and as an inclusion in garnet (black, Srp(i)). Clinopyroxene also forms as significant part of the matrix (Cpx) in lighter grey and as an inclusion in garnet (Cpx(i)). Garnet (Grt) is lightest grey in reflected light and has two differently orientated crystals (EBSD results) to the top left and bottom right of the sample.

Pg (NEW059)

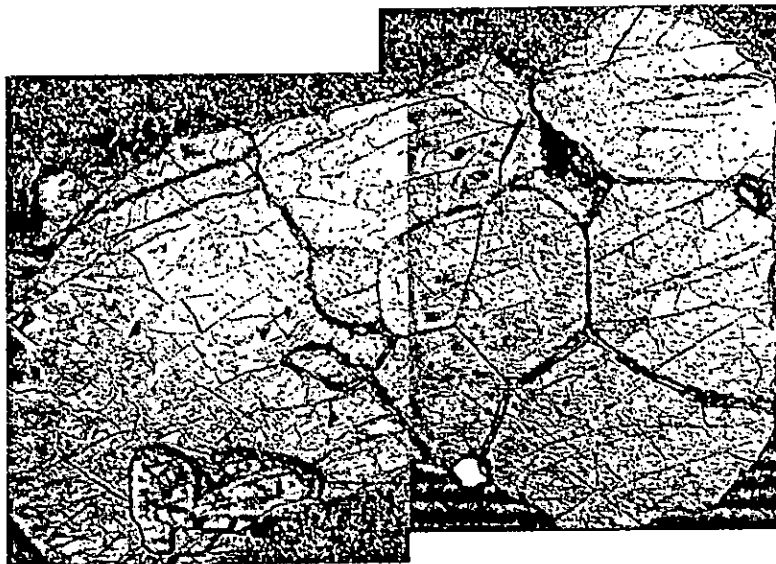


Figure 3.16: Composite image of two reflected light photographs of NEW059 (long axis = 10.5 mm). Bright white is chromite, light grey is garnet and darker grey is serpentine. There are at least 10 garnet crystals with different crystallographic orientations according to EBSD work. Their grain boundaries are picked out by veins. Ignore speckled nature of the garnet (relic of sition polishing).

NEW059 illustrates the garnet-rich nature of the **Pg** rocks in a relatively fine-grained example where garnet grains size varies from > 1 to < 5 mm (Fig. 3.16). Garnet is the predominant matrix mineral whereas the serpentine and chromite grains are small and isolated. A granuloblastic texture is particularly well expressed in NEW059.

3.2.4.4.2 Monogranular Garnet Samples

Monogranular garnet samples comprise one garnet crystal which may or may not enclose inclusions of other minerals. The maximum size of inclusions within garnet is 3 mm down to sub-millimetre size. The inclusions may be monomineralic or a composite of 2-3 minerals (i.e. either serpentine + chromite, clinopyroxene + chromite or all three). The inclusions are normally rounded to subhedral but may have straight crystal contacts with garnet. When chromite is part of a rounded or subhedral polymineralic inclusion it is usually euhedral inwards to the inclusion and rounded at the contact with the garnet. Examples of samples from each monogranular type are presented below.

Ms (NEW074, BOB304)

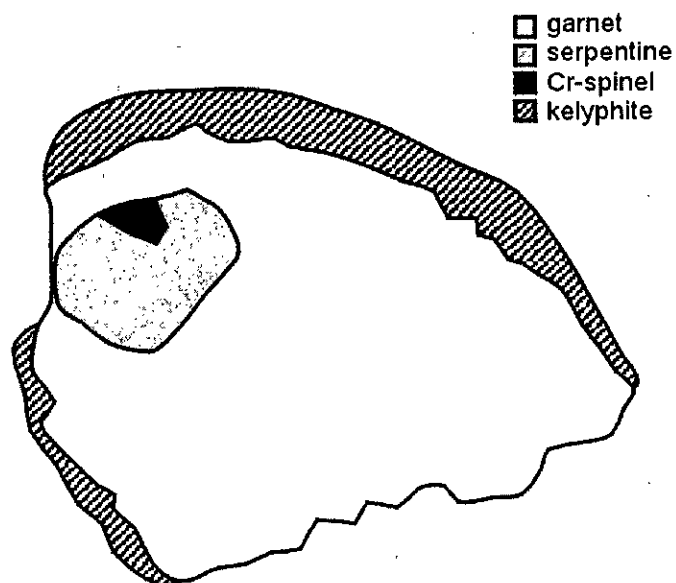


Figure 3.17: Tracing of photograph of NEW074 (long dimension 11 mm).



Figure 3.18: Thin section scan of BOB304 (width = 24 mm). A single garnet crystal makes up the majority of the slide in medium grey and poikilitically encloses serpentine inclusions which are darker grey on the image. Note the serpentine inclusions to the right of the slide that appear to show evidence for previous Mg-silicate-Mg-silicate grain boundaries now altered to serpentine.

NEW074 is a monogranular garnet sample containing a subhedral inclusion of serpentine which itself encloses a smaller euhedral chromite at its margin (Fig. 3.17). Other examples, such as BOB304, have as many as 20 angular to rounded serpentine inclusions dispersed throughout the 20 mm garnet host crystal. Some of the serpentine inclusions appear to have been composed of multiple olivine crystals due the presence of 'ghost grain boundaries' (see Fig. 3.18).

Md (NEWSP, B55, BOB403, NEW078)

Monogranular samples with inclusions of clinopyroxene, serpentine and chromite vary from those with polyminerally inclusions such as NEWSP containing diopside, serpentine and chromite (Fig. 3.19) to those with only monomineralic inclusions (e.g NEW107). Inclusions are predominantly rounded.

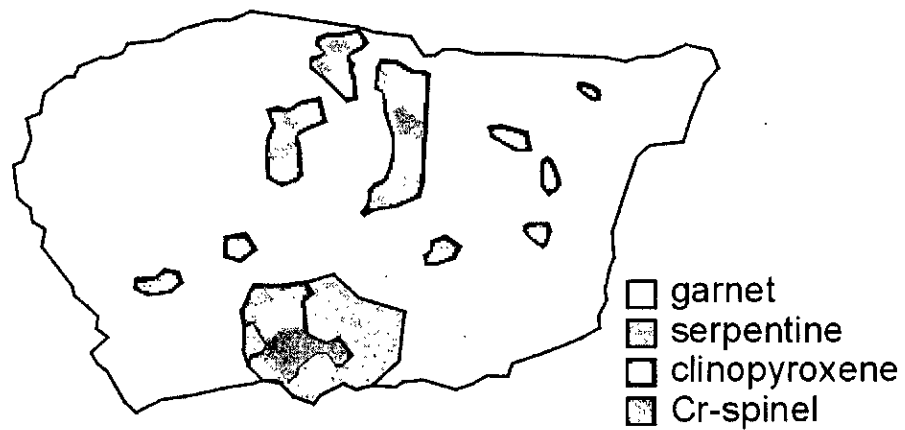


Figure 3.19: Tracing of photograph of sample NEWSP (long dimension = 19 mm). The host garnet has inclusions of predominantly rounded and biminerally containing clinopyroxene and chromite (or Cr-spinel black). The serpentine at the bottom of the photograph is part of a relatively straight-edged inclusion also containing clinopyroxene and euhedral chromite.

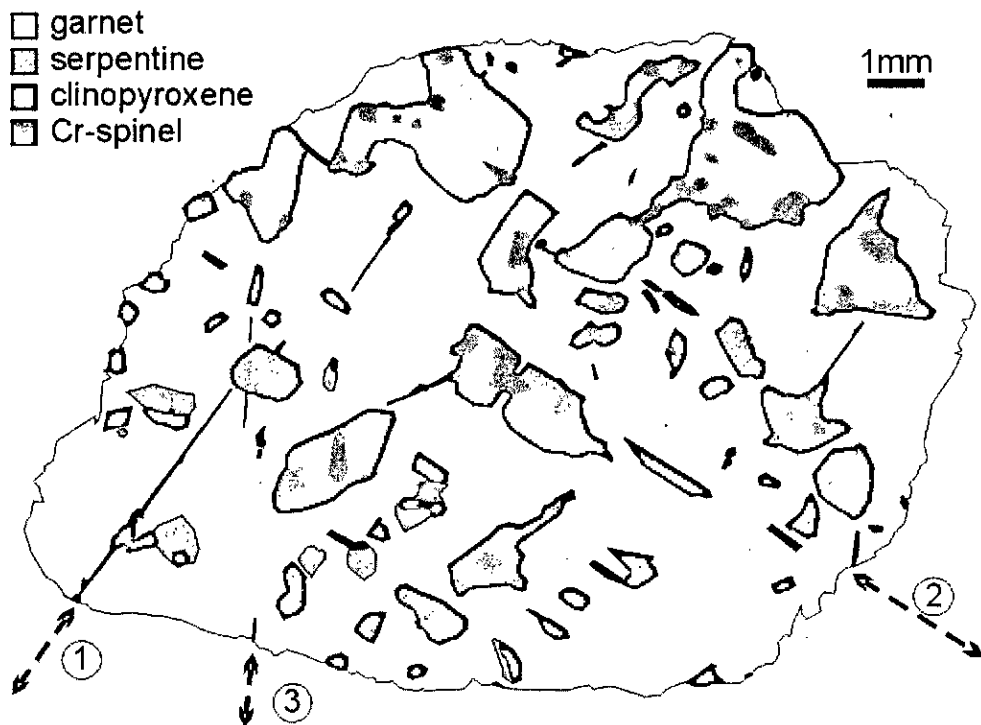


Figure 3.20: Tracing mineral arrangement in sample B55 from back scattered electron mosaic of images. The single garnet crystal is host to inclusions of its clinopyroxene, chromite (or Cr-spinel) and serpentine (a darker brown serpentine that appears to have been orthopyroxene). Directions of the three main Cr-spinel mineral orientations are shown with dashed arrows (1-3).

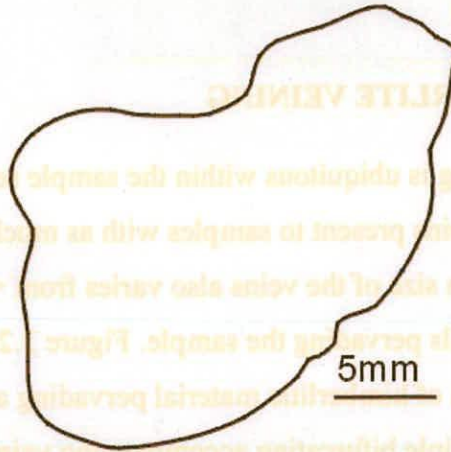
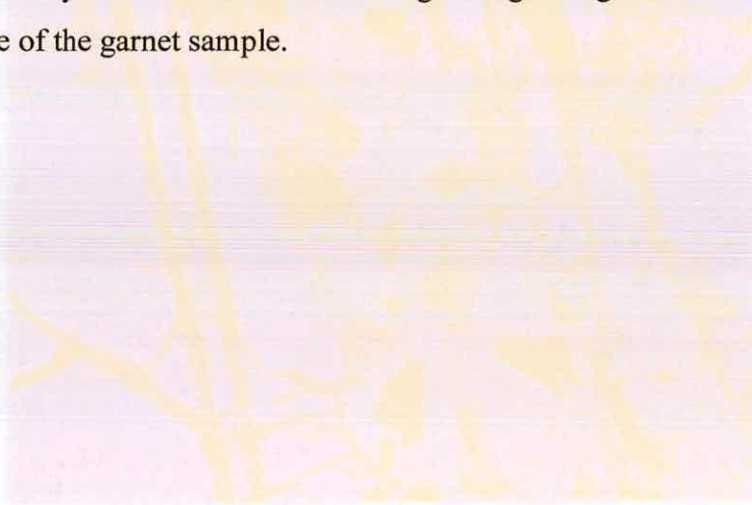


Figure 3.23: Tracing of photograph of NEW003 (long dimension = 12 mm). Single garnet crystal.

The outline shape of many of the monogranular garnet samples appears to be controlled mainly by the kimberlitic erosive force which has rounded most samples approximately into oblate spheroids. Samples such as NEW003 (see Fig. 3.23) show modified sample outlines that appear to be shaped in similar ways to garnets from polygranular samples e.g. NEW059 (see Fig. 3.16) i.e. with curvy-planar surfaces. These may therefore have once been garnet-garnet grain boundaries affecting the shape of the garnet sample.



3.2.5 Alteration

3.2.5.1 KIMBERLITE VEINING

Kimberlite veining is ubiquitous within the sample set. Variation exists from samples with a few fine veins present to samples with as much as 30 % volume occupied by veining. The grain size of the veins also varies from $< 50 \mu\text{m}$ in fine veins to $> 1 \text{ mm}$ with coarse crystals pervading the sample. Figure 3.24 shows a typical instance of a $200 \mu\text{m}$ wide vein of kimberlitic material pervading a garnet crystal with finer scale ($\sim 10\text{-}50 \mu\text{m}$) multiple bifurcating accompanying veins. Veins are often phlogopite-rich and may also contain chrome-spinel, serpentine, calcite and other minor phases (Fig. 3.25).



Figure 3.24: PPL thin section photograph of kimberlite vein intruding pink garnet from NEW301. The brown, cleaved mineral is phlogopite and opaque mineral is an Fe oxide. Fov = 1 mm.



Figure 3.25: Photograph of garnet macrocryst B47 showing extensive kimberlitic intrusion (black (phlogopite) and white (calcite) areas). Fov width = 13 mm.

When samples are still set in kimberlite it is apparent that the veins are aligned with the strike of veining in the host kimberlite in Blow 2 at Newlands (Fig. 3.26). Veins in kimberlite follow a strike to NNE. This aligns with the dominant dextral trend of en-echelon kimberlite dykes at Newlands and Bellsbank (see Figs. 3.3 and 3.4).



Figure 3.26: North-north-easterly view of a tunnel roof inside the Newlands mine at Blow 2. Blue-grey host rock is kimberlite. White veins oriented approximately NNE are calcite-filled. Top of picture is close to 1 m across; veins are 1-20 mm wide and en-echelon along strike.

3.2.5.2 KELYPHITISATION

Many samples (all those with attached kimberlite) display a kelyphite rim at their margins between garnet and kimberlite. These range in thickness from 200 μm to 1 mm and occur all or most of the way around the sample unless chipped off by the mine crushing procedure. The kelyphite is composed of phlogopite and other accessory phases forming fibrous crystals radially disposed around the sample (see Figs. 3.27 and 3.28 for details). The kelyphite is clearly distinguishable from the sample itself by its fine grained radial texture, its green appearance in transmitted light and its light brown appearance in reflected light.

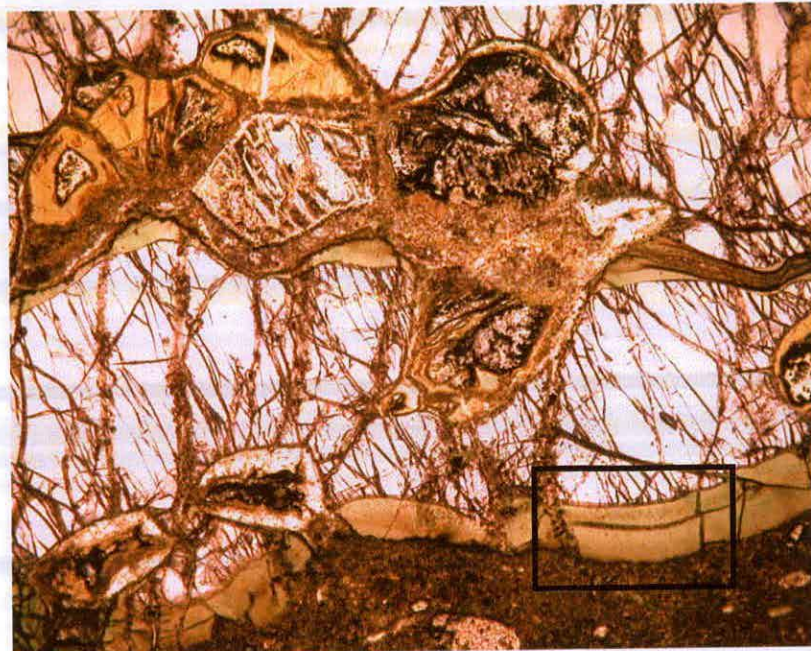


Figure 3.27: Thin section photograph in plain polarised light of the edge of sample BOB302 with kimberlite at the bottom (brown is fine grained groundmass, yellow rounded shape is altered olivine macrocryst). A kelyphite rim can be seen as a green band separating kimberlite from garnet (note the absence of kelyphite where a serpentine inclusion is exposed to kimberlite magma). Note second band of kelyphite along region of more intense kimberlitic invasion through the middle of the field of view. The black box indicates the field of view for Fig.3.28.

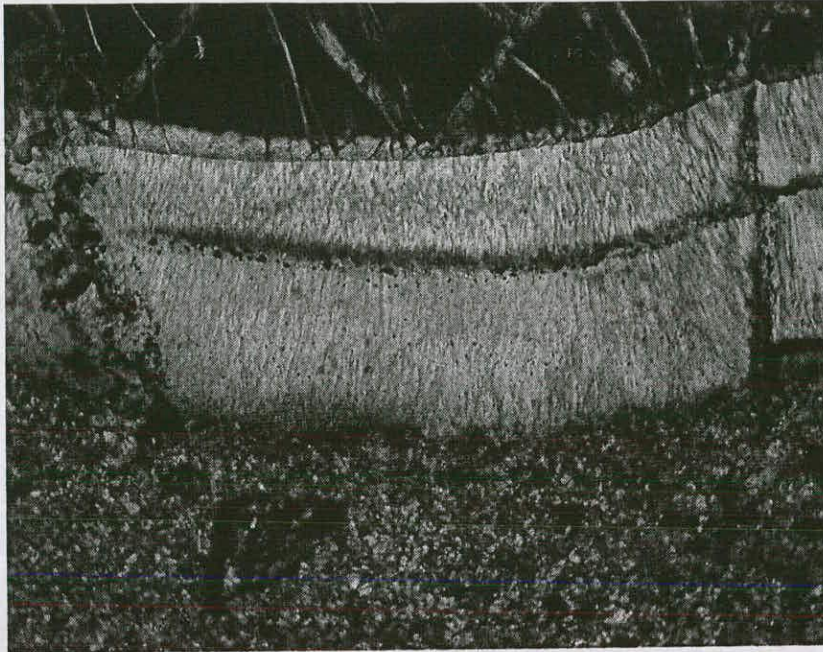


Figure 3.28: Enlargement from Fig. 3.27 of kelyphite rim (XPL). Fibrous radial growth can be seen within the kelyphite along with included euhedral fine oxide minerals. Note displacement of kelyphite rim and garnet contact by intruding kimberlite veins to the left and right of the image.

3.2.5.3 SERPENTINISATION

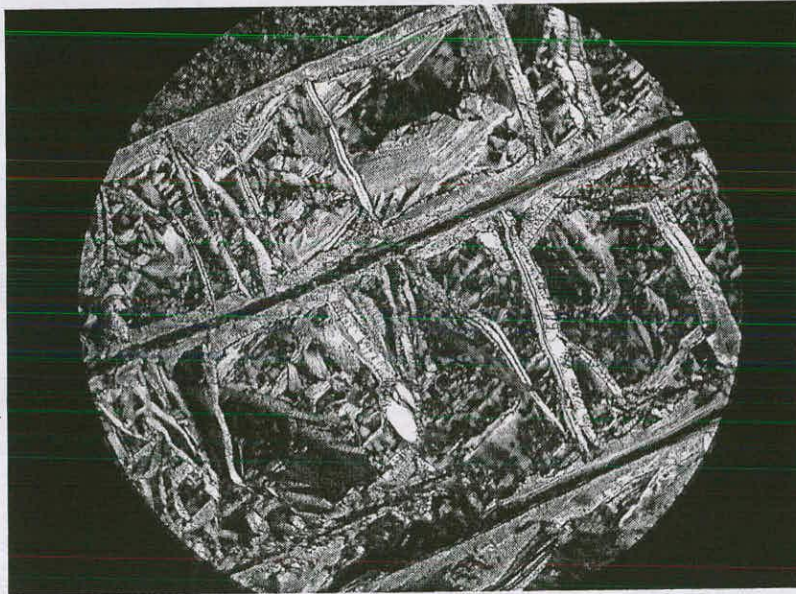


Figure 3.29: XPL thin section photograph of serpentine 'window-texture' replacing a magnesium silicate mineral (most likely olivine) at the edge of sample BOB302. Circle field of view is 500 μm .

Serpentine group minerals pervasively replace olivine in kimberlite (Fig. 3.29) and olivines and orthopyroxenes within samples. Clinopyroxene is also replaced by serpentine in a few cases (see Fig. 3.23). Serpentinisation has occurred to such an extent as to leave no fresh olivine/orthopyroxene in any sample in this study.

3.3 Discussion

3.3.1 Modal mineralogy: Worldwide localities with similarities

With regard to the garnet-rich xenoliths in this study it is important to note any similarities with previously studied samples from other kimberlites and to assess how unique they are. This should provide a means to place the samples in context if there appears to be a continuum of rock types with similar bulk rock compositions.

3.3.1.1 PREVIOUS NEWLANDS SAMPLING

Menzies (2001) studied a selected xenolith population which comprised diamond-bearing and diamond-free eclogites and peridotites. The mineralogy of the diamondiferous garnet macrocrysts that Menzies studied can be seen to be very similar to mineral modes recorded for all harzburgitic polygranular samples in this study (compare Fig. 3.30 to Fig 3.10b). 11/18 of these are harzburgitic garnet-chromite samples with the rest being garnets with harzburgitic affinity. Menzies' samples were on average larger (1-3 cm in diameter) and polygranular. Diamond is present in these samples with an average concentration of 1 % which is several orders of magnitude greater than most diamondiferous kimberlites.

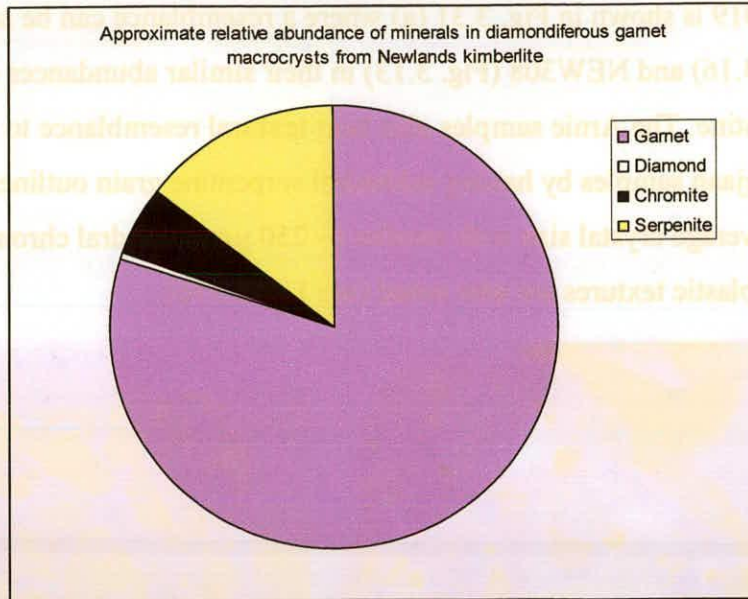


Figure 3.30: n = 18, data reprocessed from Menzies (2001)

The diamond-free samples in this study at Newlands and Bobbejaan produce similar modal proportions to Fig. 3.30 but have the additional feature of clinopyroxene in approximately 30 % of garnet macrocryst samples.

3.3.1.2 PREVIOUS BOBBEJAAN SAMPLING

23 samples from Bobbejaan were studied petrographically by van der Westhuizen (1992) and he recognized the equivalent of polygranular and monogranular sample types distinguished here. One mode for a polygranular sample was made and recorded as 2 % clinopyroxene, 3 % phlogopite, 40 % spinel and 55 % garnet. This mode is similar, disregarding alteration products such as phlogopite, to lherzolites from Newlands and Bobbejaan examined in this study and appears to have come from the same kimberlite sample set as those from Bobbejaan in this study.

3.3.1.3 COMPARISON TO ARNIE SAMPLES

The modal mineralogy of the samples in this study is exceptionally garnet-rich compared to the majority of xenoliths from kimberlite. The only locality in the literature with similar garnet-rich, chromite-bearing harzburgite samples are those that have been noted at Arnie kimberlite in Canada by Doyle (2002). Sample

ARN019 is shown in Fig. 3.31 (a) where a resemblance can be seen to NEW059 (Fig. 3.16) and NEW308 (Fig. 3.13) in their similar abundances of garnet and serpentine. The Arnie samples also bear textural resemblance to the Newlands and Bobbejaan samples by having subhedral serpentine grain outlines and a similar 2-3 mm average crystal size with smaller (~ 250 μm) euhedral chromites. Some more granoblastic textures are also noted (see Fig. 3.31b).

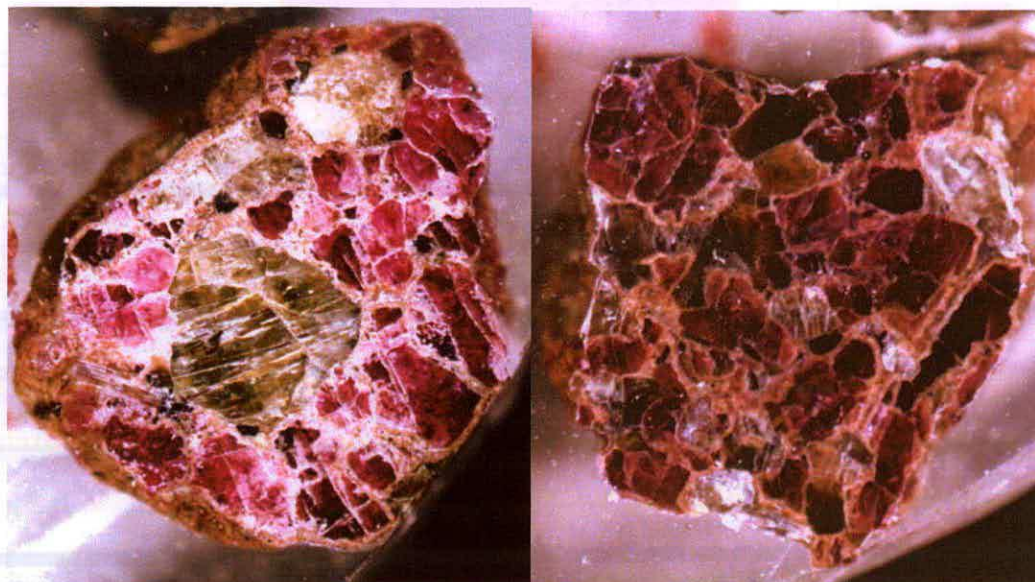


Figure 3.31: (a) Photograph of garnet sample ARN019 from Arnie kimberlite, NWT, Canada from Doyle (2002) (width of photo = 7 mm). The altered Mg-silicate is serpentine (yellow-brown), the garnet is the host mineral comprising 60 % of the sample surface (magenta) and chromite occurs at the margins of the serpentine inclusions as small, euhedral black crystals. (b) Photograph of garnet sample ARN0059 from Arnie kimberlite, NWT, Canada from Doyle (2002) (width of photo = 7 mm). Purple garnet and brown serpentine with a granular appearance.

3.3.1.4 COMPARISON TO RUSSIAN LOCALITIES

Some xenoliths from the Yakutian kimberlites show some features of similarity to the Newlands and Bobbejaan samples. Of the 18 diamondiferous specimens from Udachnaya pipe studied by Pokhilenko and Sobolev (1986), 16 have 95 % olivine (i.e. dunites) and they record 6 olivine-pyrope assemblages, 6 olivine-pyrope-chromite, 3 olivine-pyrope-enstatite-chromite and 1 olivine-enstatite-chromite. The rocks are said to be megacrystalline implying a large (> 5 mm) crystal size. However, 16 out of 18 samples have > 95 % olivine and fresh olivine is present in

most samples and fresh orthopyroxene is present in two. A similar sample set is apparent at the Aykhal pipe also from Yakutia, Sobolev et al. (1969). Therefore these samples are different to Newlands and Bobbejaan samples in their high percentage olivine present, but they do contain garnet macrocrysts and relatively commonly have chromite and diamond.

3.3.1.5 COMPARISON TO ALKREMITES

Alkremites are spinel-garnet rocks high in Al, Si and Mg (Ponomarenko, 1975). Garnet is high in all these elements (even given their chromium-rich nature, see Chapter 4) and, in the Newlands and Bobbejaan samples garnet can comprise around 90 % of polygranular samples the bulk compositions of the samples imply Al_2O_3 -rich rocks. It is therefore worth comparing the modal mineralogy and to some extent the resultant bulk rock chemistry with some aluminous assemblages identified by various authors, e.g. the corundum-bearing assemblages identified in the Jagersfontein xenolith suite by Mazzone and Haggerty (1986), which are similar to some of the Newlands and Bobbejaan samples in having 50-80 % garnet. However the alkremite bulk rock compositions plot in very Ca-undersaturated compositional space i.e. to the low-Ca area of the basalt field. In terms of Al, the alkremites are far richer in Al than basalts and plot to higher Al than eclogites. Interestingly the Udachnaya pipe in Yakutia also has xenoliths of this unusual nature.

Alkremites also contain spinel but the abundance of the spinel phase is very high and is also a different (Al-rich, Cr-poor) composition. Alkremites also lack appreciable amounts of olivine and pyroxenes which are noted in this study. One High-Cr garnet has been mentioned as part of the Alkremite-suite xenoliths from Bellsbank by Nixon et al. (1978) which seems to overlap the Bobbejaan sample set from this study in terms of modal mineralogy, texture and composition (see chapter 4). By and large samples referred to as alkremitic in the literature do not bear as close resemblance to the samples in question because of their high spinel modal abundance and distinct bulk compositions. Therefore Newlands and Bobbejaan samples are unique in that

they are the only sample set to display garnet-rich harzburgitic/lherzolitic mineralogy \pm chromite and diamond.

3.3.2 Textures

GENERAL FEATURES

The samples from Newlands and Bobbejaan are divided into monogranular and polygranular samples, but we have seen that because of inclusions within garnets, both possess a similar range of mineralogy and textural features and they appear to be inherently derived from the same set of rocks. Essentially the textures are coarse; garnets are equant with curvy-linear grain boundaries and from polygranular samples the crystal contacts usually approach equilibrium ($\sim 120^\circ$). Only a small proportion of samples display distinctly cusped grain boundaries. Inclusion textures vary from rounded to equant and poly- to mono-mineralic.

As mentioned in section 3.3.1.3 there is a textural resemblance of some Newlands and Bobbejaan samples to small xenoliths from the Arnie kimberlite, which are defined by Doyle (2002) as 'equilibrium textures'. Most of her samples do show evidence for a good approach to textural equilibrium in their having 120° grain boundaries.

Compared to textures described by Harte (1982), the samples would most closely fall into the 'Type I, Coarse, Mg-rich, cold' category with grains typically > 2 mm with equant or tabular shapes and showing smooth to more irregular grain boundaries (referred to as the common 'granular' peridotites xenoliths from kimberlite series eruptive rocks). There is no evidence in the Newlands and Bobbejaan sample set for deformed textures comprising porphyroclasts and neoblasts.

3.3.2.1 AN EXSOLUTION ORIGIN FOR TEXTURES

Some samples show evidence for the exsolution of chromite, clinopyroxene and sometimes olivine or orthopyroxene (now serpentine) from garnet. This is most clearly suggested in sample B55 (Fig. 3.20). These samples are readily identifiable where chromite and sometimes clinopyroxene show a preferred orientation within a single garnet crystal. According to Haggerty and Sautter (1990) the cubic crystallography of garnet and its cylindrical stacking produces rods that connect Al^{VI} sites in the structure oriented at 0°, 120° and 240° (when looking down a triad axis) that are compositionally amenable to the exsolution of clinopyroxene. The size of the clinopyroxenes in B55 is much greater than those noted by Haggerty and Sautter (1990) for their Jagersfontein samples (up to 2 mm rather than a maximum of 200 μm). B55 also contains abundant chromite that is orientated in three main directions that correspond to some of the clinopyroxene lamellae and, therefore, also seem to be controlled by the garnet structure in an exsolution process. The lamellar chromites appear to originate from more euhedral chromites within the polymineralic clinopyroxene-chromite inclusions, which could imply that there is a polyphase exsolution where a secondary chromite growth phase is more lamellar. However, both morphologies of chromite have the same chemical composition as analysed by electron microprobe. Haggerty and Sautter (1990) infer that the Jagersfontein exsolved garnets have an ultra-deep origin at 120-130 kbar and have compositionally re-equilibrated at 45 kbar at about 900°C over millions of years.

Sample BOB301 has smaller, well-formed chromites with less marked preferred orientation and no evidence for exsolved clinopyroxene. Therefore potentially different exsolution chemistries are apparent in the present samples: One suggests chromite alone and another suggests clinopyroxene and chromite ± orthopyroxene. On the other hand the preservation of obvious lamellae with marked preferred orientation depends upon the absence of textural maturing or annealing processes which might be expected at mantle temperatures. Partial annealing may be evident in sample NEW078 as rounded lamellar chromites. Some samples such as BOB065

have rounded serpentine inclusions evenly spaced through the single garnet host. This has the appearance of 'blebby exsolution' in minerals such as pyroxene and alkali feldspar.

3.3.3 Conclusions

- 1) The samples in this study are unique in their garnet-rich and identifiably peridotitic mineralogy and display a relatively narrow range of modal abundances and textures.
- 2) The samples fall into two categories: Those possessing multiple garnet crystals (polygranular garnet samples) and those comprising one garnet crystal (monogranular); though inclusions are common in the garnets of both types. However these two categories do not appear to be intrinsically different; most probably they reflect the degree of disaggregation (grain dissolution and separation) from their source rock.
- 3) The samples are garnet-rich rocks with distinctive modal mineralogy that includes olivine, orthopyroxene, clinopyroxene and chromite. Their closest comparison is to certain harzburgitic samples from Arnie kimberlite in Canada. Their broad peridotitic mineralogy and megacrystalline aspect is similar to Yakutian garnet-dunitites but their modal abundances are very different.
- 4) The samples are divided into lherzolitic or harzburgitic samples based on the presence or absence, respectively, of clinopyroxene. The Newlands sample set is unique in having a strong bias towards harzburgitic rock types (i.e. without clinopyroxene).
- 5) The following samples types are recognized: Polygranular (Ps, Pd, Pg) and monogranular (Ms, Md, M), see Fig. 3.6.

- 6) Texturally the majority of the samples appear to be derived from rocks of coarse grain size with reasonably smooth (granuloblastic) grain boundaries. Coarse garnet grains may poikilitically enclose inclusions of serpentine, clinopyroxene or chromite either as mono- or poly-mineralic inclusions.
- 7) A small subset of the samples show large garnets enclosing inclusions that have preferred orientation which suggest an origin by exsolution.

3.4 References

- Doyle, P. M. (2002). A petrographic and petrochemical study of selected peridotitic and pyroxenitic xenoliths from three kimberlite localities in the Lac de Gras region, Northwest Territories, Canada. Department of Geological Sciences. Cape Town. University of Cape Town. *Unpublished Masters Thesis*
- Haggerty, S. E. and Sautter, V. (1990). Ultradeep (greater than 330 kilometers), ultramafic upper mantle xenoliths. *Science*. **248**. 993-996.
- Harte, B. (1977). Rock nomenclature with particular relation to deformation and recrystallisation textures in olivine-bearing xenoliths. *Journal of Geology*. **85**. 279-288.
- Mazzone, P. and Haggerty, S. E. (1986). Corangites and corgaspinites: Two new types of aluminous assemblages from the Jagersfontein kimberlite pipe. Fourth International Kimberlite Conference. **Volume 2**. 795-808.
- Menzies, A. (2001). A detailed investigation into diamond-bearing xenoliths from Newlands kimberlite, South Africa. Department of Geological Sciences. Cape Town. University of Cape Town. *Unpublished PhD Thesis*
- Mitchell, R. H. (1986). Kimberlites- Mineralogy, geochemistry, and petrology. New York, Plenum Press.
- Nixon, P. H., Chapman, N. A. and Gurney, J. J. (1978). Pyrope-spinel (alkremite) xenoliths from kimberlite. *Contributions to Mineralogy & Petrology*. **65**. 341-346.
- Pokhilenko, N. P. and Sobolev, N. V. (1986). Xenoliths of diamondiferous peridotite from Udachnaya kimberlite pipe, Yakutia. Fourth International Kimberlite Conference, Extended Abstracts, Geological Society of Australia Abstract Volume. 16:309-311.
- Ponomarenko, A. I. (1975). Alkremite — a new variety of aluminous hyperbasite xenoliths from the kimberlites of the Udachnaya pipe. *Doklady Akademii Nauk SSSR*. **225**.

Sobolev, V. S., Nay, B. S., Sobolev, N. V., Lavrent'ev, Y. G. and Pospelova, L. N. (1969). Xenoliths of diamond-bearing pyrope serpentinite from the "Aykhal" pipe, Yakutia. *Doklady Akademii Nauk SSSR*. **188**. 1141-1143.

Streckeisen, A. (1980). Classification and nomenclature of volcanic rocks, lamprophyres, carbonatites and melilitic rocks IUGS Subcommittee on the Systematics of Igneous Rocks, recommendations and suggestions. *Geologische Rundschau*. **69**. 194-207.

van der Westhuizen, A. (1992). The Bellsbank kimberlites, with special reference to a suite of purple garnet megacrysts from the Bobbejaan mine. University of the Orange Free State. *Unpublished Masters Thesis*

Van Heerden, L. A. and Gurney, J. J. (1994). Diamond grades at Newlands Kimberlite, Part 1: Blow 2:. Unpubl. Report for Gem Mining.

4. Major Element Compositions

4.1 Introduction

4.1.1 Aims and objectives

The first aim is to assess the chemical composition of peridotitic mineral concentrate from the kimberlites in this study relative to that from other southern African diamondiferous kimberlites. General context for concentrate will be provided by a database of heavy mineral concentrate from till sampling for diamond exploration in Northwest Territories of Canada. The second aim is to judge how the chemistry of minerals from the samples differs from the concentrate datasets.

The Newlands, Bobbejaan and Leicester concentrate essentially consists of single crystals of garnet, chromite¹, clinopyroxene, orthopyroxene and olivine (< ~ 5 mm). These grains were mounted in bulk and analysed on 1-2 points per grain by electron microprobe. An appraisal of the deviation of their compositions from other kimberlite concentrate was made to provide a means to discriminate sample types and parageneses and further broaden the basis for diamond prospecting via major element analysis.

In particular, analysis of Newlands concentrate minerals adds to the Kimberlite Research Group (KRG, Univ. of Cape Town) database of kimberlitic mantle minerals from the Barkly West area. The KRG database includes kimberlite heavy mineral concentrate analysis from many kimberlites in southern Africa and provides

¹ 'Chromite' is the Fe-Cr end member spinel and is used in literature to denote a chromium-rich spinel. See section 4.2.1.2 for the terminology used for this mineral in this study.

worldwide diamond inclusion analyses for multiple phases from published work. The comparison of the bulk mantle sample from Newlands and Bobbejaan kimberlites with this data should provide a means to assess the usefulness of various chemical discriminants in diamond exploration.

4.1.2 Geochemical classification

Systems for classifying mineral compositions are discussed in Chapter 2. In this chapter the '85 % line' imposed by Gurney (1984) onto the garnet Cr_2O_3 -CaO plot shall be utilised to differentiate G9 from G10 garnets. This line essentially equates to the line of Sobolev (1973) that separates harzburgitic, clinopyroxene-free garnet bearing xenoliths from lherzolitic, clinopyroxene present ones. Grütter et al. (2004) provide compositional parameters for many of the garnet classes, G1 through to G12, of Dawson and Stephens (1975) (see Table 4.1). Grütter's classification takes Cr, Ca, Mg, Fe, Ti and Na into account and adds the 'diamond-graphite constraint' (DGC) which is a sub-horizontal line on CaO vs. Cr_2O_3 graph positioned to divide the G10 garnets into those occurring in diamond-bearing peridotite xenoliths and those occurring in graphite-bearing peridotite xenoliths. This formulation is based upon the Cr and Ca compositions of garnets from diamond and graphite-bearing xenoliths largely using data from Roberts Victor in Viljoen et al. (1994).

Fields from Fipke et al. (1995) are used to identify potential diamond facies chromites in Cr-Mg and Cr-Ti space. A broader appraisal of chromites, based on the spinel prism, will also be made. Clinopyroxenes can be given an initial compositional assessment based on their location in the pyroxene quadrilateral in CaO-MgO-FeO space. Cr-Al and Cr-Na plots shall be used to assess jadeite (NaAlSiO_3) and kosmochlor (NaCrSiO_3) end-member activities. Due to the absence of fresh orthopyroxene and olivine in samples it is only for the concentrate that the compositional classification of these minerals shall be required. The Mg:Fe ratio is the most commonly cited factor plotted in the literature for both minerals since it provides information as to the degree of depletion of the parent rock. Ni-in-olivine

and Ca-in-orthopyroxene shall also be discussed since these minor constituents bear some relation to the P-T conditions of formation (see chapter 7).

Class	Paragenesis	Cr ₂ O ₃	CaO	TiO ₂	MgO	FeO
G0	Unclassified	0.00-1.00	0.00-2.00	n/a	n/a	n/a
G1	Low-Cr Megacrysts	0.00-3.67	3.74-6.83	0.31-0.87	16.2-22.2	6.15-12.18
G2	High-Ti Peridotitic	0.21-2.80	4.20-5.30	0.89-1.28	19.5-21.7	6.62-11.17
G3	Eclogitic	0.00-3.96	2.50-14.00	0.00-0.57	8.46-18.60	11.27-22.95
G4	Pyroxenitic & websteritic	0.00-0.20	5.35-16.20	0.64-1.38	2.95-13.70	14.50-30.54
G5	Pyroxenitic	0.00-0.13	1.07-5.66	0.00-0.35	5.26-10.90	24.96-29.94
G6	Eclogitic	0.08-0.51	9.15-9.10	0.08-0.51	5.17-16.19	5.71-13.95
G7	Wehrlitic	7.16-14.90	18.80-26.00	0.18-0.47	5.86-10.50	4.56-6.43
G8	Eclogitic	0.00-0.12	19.92-30.13	0.01-0.65	2.94-7.01	4.32-8.74
G9	Lherzolithic	0.24-9.15	3.67-8.36	0.00-0.45	13.60-24.2	5.42-11.80
G10	Harzburgitic	3.01-15.90	0.27-3.80	0.00-0.25	20.70-25.58	4.71-8.46
G11	High-TiO ₂ Peridotitic	5.60-13.55	5.90-15.40	0.21-0.80	11.40-20.44	4.65-11.35
G12	Wehrlitic	12.20-18.90	5.89-19.80	0.00-0.54	10.30-19.20	6.45-8.57

Table 4.1: Summary of garnet classes from Dawson and Stephens (1975). Paragenetic terms are taken from Schulze (2003) and Grütter et al. (2004). Concentrations of oxides expressed in weight percent.

4.1.3 Processing of spot analysis data

For full operating conditions and summary of the Electron Microprobe technique used see Appendix I: Analytical Techniques. Using weight percent oxide values output from the electron probe, the number of cations for each mineral analysis was calculated on a cation basis so that they summed to 6 in spinel, 8 in Cr-diopside and 8 in garnet². The advantage of this method is that the mineral formulae are satisfied most closely since there are always a total of 8 cations and 12 oxygens in garnet for

² Two main differences between the 'sum to 12 oxygens' and 'sum to 6 cations' methods emerge on cation plots: Firstly, a tighter distribution is present in garnet and chromite from concentrate using the latter method (Fig. 4.19 shows this for chromites). Secondly there is a better fit to total site occupancy e.g. for garnets (Fig.I.1, Appendix I).

example. To make a stoichiometric estimate of $\text{Fe}^{2+} : \text{Fe}^{3+}$ ratios the number of charges was then summed assuming all Fe as Fe^{2+} . Then the charges were corrected by creating the appropriate amount of Fe^{3+} . The formulation adopted follows Ryburn et al. (1975) using the formula for clinopyroxenes (garnet and chromite use a similar method) where:

$$\text{Fe}^{3+} = 4 - (2\text{Si} + 2\text{Ti} + \text{Al} + \text{Cr}) + (\text{Na} + \text{K})$$

$$\text{and } \text{Fe}^{2+} = \text{Fe}_t - \text{Fe}^{3+}$$

This method was preferred to that of Droop (1987) because it means the number of cations and oxygens do not deviate away from their whole number values. However it was found that the Fe^{3+} estimates varied markedly with some negative values being generated. This variation is attributed to the known inaccuracies of measuring major elements especially abundant like Si on electron microprobe. Therefore, in the appendices and in all calculations of compositional parameters, all Fe analyses are expressed as Fe_t (total iron).

In this thesis cation concentrations are generally calculated and used for further processing and assessment of compositional variation. However, much current literature quotes concentrations in weight percent for particular parameters. This is a product of diamond exploration companies quoting electron microprobe analyses in their raw form of weight percent when investigating kimberlite indicator minerals. In order to make direct comparisons with other work certain weight percent (wt. %) plots shall also be made in this chapter. Figure 4.1a shows a cation plot of $\text{Cr}/(\text{Cr}+\text{Al})$ vs. $\text{Ca}/(\text{Ca}+\text{Fe}+\text{Mg})$ for garnets and shows that it is virtually identical spatially to a standard Cr_2O_3 vs. CaO garnet wt. % plot. This is indicative of the fact that for the garnets considered, cation Cr is directly proportional to (2-Al) and Ca directly proportional to (2-Mg) since Fe (presumably both Fe^{2+} and Fe^{3+}) remains relatively constant.

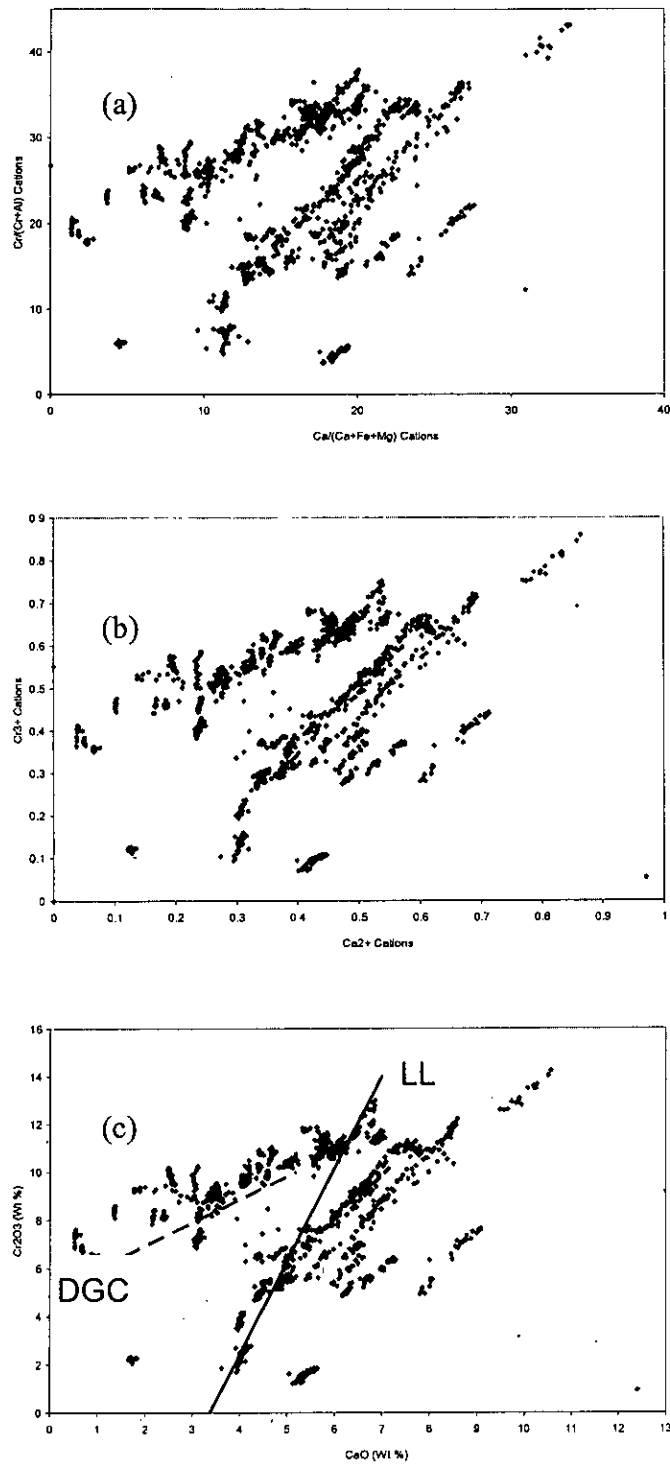


Figure 4.1: Garnet traverses from this study. (a) Cr/(Cr+Al) vs Ca/(Ca+Mg+Fe) cations plot compared to (b) Cr vs Ca cation plot and (c) Cr₂O₃ vs CaO wt. % plot for Newlands garnet sample traverses. The Iherzolite line (LL, solid, Gurney (1984), which has G10 garnets to the low-Ca side and G9 garnets to the high-Ca side) and diamond-graphite constraint (DGC, dashed, Grütter et al. (2004), which has diamond facies garnets plotting to the high Cr side of the line) are shown in (c).

Using the method of Rickwood (1968) garnet end member calculation was made assuming low Fe^{3+} , Ti, Y and V (< 0.1 formula unit) in the calculation, values for pyrope, almandine, spessartine, uvarovite and knorringite were calculated for selected garnets to show the range of end-member compositions present and to compare with diamond inclusion garnet compositions and previously reported compositions. Low-Ca harzburgites are expected to have a relatively high knorringite ($\text{Mg}_3\text{Cr}_2\text{Si}_3\text{O}_{12}$) component and high-Cr, high-Ca garnets are expected to have a high uvarovite ($\text{Ca}_3\text{Cr}_2\text{Si}_3\text{O}_{12}$) component.

The samples display little variation in almandine end member compared to uvarovite, pyrope and knorringite. The cation ratio plot of $\text{Cr}/(\text{Cr} + \text{Al})$ vs. $\text{Ca}/(\text{Ca} + \text{Fe} + \text{Mg})$ vs. $\text{Mg}/(\text{Mg} + \text{Fe})$ turns out to be essentially equivalent to a garnet end member plot of knorringite vs. uvarovite vs. pyrope. The three cation ratios mentioned are, therefore, proxies for the ratios of respective end member compositions.

4.2 Major Element Composition of Barkly West Kimberlite Concentrate

Three main datasets of concentrate analyses are compared in this section:

- 1) NWT - A large dataset of concentrate from North West Territories of Canada glacial till sampling (Open Report 2001-2002 conducted by John Armstrong, <http://www.nwtgeoscience.ca>). This dataset was chosen for its large size and diverse source material, which is known to include diamondiferous kimberlites. This dataset will provide the widest range as a much greater number of parageneses are represented than in other datasets.
- 2) SAK - Southern African diamondiferous kimberlite concentrates from the Kimberlite Research Group, University of Cape Town (KRG database). This dataset was chosen to provide a widespread southern African concentrate example for comparison with those found from the kimberlites in this study from the Barkly West region. This dataset should have a higher proportion of material from the diamond stability field than dataset 1 since only kimberlitic material is being analysed.
- 3) BWK - A Barkly West dataset that includes Newlands, Bellsbank, Frank Smith and Leicester kimberlites was compiled from KRG database, Menzies (2001), van der Westhuizen (1992) and data collected in this study. The Newlands dataset is most numerous and is examined separately on occasion. Of these kimberlites, Frank Smith is known to have mainly peridotitic and megacrystic garnets in its concentrate, whereas the other three may have relatively high percentages of eclogitic garnets and for these three a bias towards analysis of purple garnets (and hence peridotitic garnets) was made so the resultant population of all four kimberlites is predominantly a peridotitic one. Opaque minerals, pyroxenes and olivine do not have any bias. Mineral compositions present in this small group of localities that are not present in datasets 1 and 2 will indicate unique material present.

The number of analyses in each dataset and subsets are shown in Table 4.2. Finsch garnet concentrate and diamond inclusion garnets analysed by KRG are highlighted for additional comparison.

	Garnet	Chromite	Clinopyroxene	Orthopyroxene	Olivine	Total
1 NWT	30462	3659	2156	166	1219	37662
2 SAK	3738	921	267	129	0	5055
3 BWK NEW	1139 (494T, 277A, 368K)	546 (197T, 141A, 208K)	111 (87T, 24K)	158 (121K, 37T)	98T	2052
3 BWK BELL	426 (53W, 134T, 239K)	19W	11W	0	0	456
3 BWK FSM	138	139	31	0	0	308
3 BWK LEI	167	0	0	0	0	167
TOTAL	36070	5284	2576	453	1317	45700

Table 4.2: Number of analysed minerals from concentrate in datasets 1 (NWT = Northwest Territories of Canada till sampling), 2 (SAK= southern African diamondiferous kimberlite concentrate from KRG Research Group database) and 3 from four Barkly West region kimberlites (BWK); NEW = Newlands (T = analyses from this study, A = analyses from Menzies (2001) and K = analyses from KRG database), BELL = Bellsbank kimberlite concentrate (T and K as above, W = number of analyses from van der Westhuizen, 1992). FSM = Frank Smith kimberlite concentrate from KRG database and LEI = Leicester kimberlite concentrate garnets analysed in this study.

Numbers in Table 4.2 illustrate the large number of analyses in the NWT dataset with the ratios between the minerals reflecting the degree to which they are preserved in the Canadian tundra. Orthopyroxene is therefore the least common, weathering relatively quickly. Garnet and chromite are known to survive particularly well and so the ratio between them reflects the high proportion of garnet present in the source rock sample relative to chromite. Olivine is known to be much more common than garnet in kimberlite but is readily weathered and its source characteristics not so distinctive as garnet.

The KRG database lacks many olivine analyses, which reflects sampling bias and does not imply rarity in southern African kimberlites. It is the Newlands olivine analyses from this study that are used for comparison to the NWT dataset. Within the

Barkly West kimberlite concentrates a special effort was made, in this study, to assemble a representative sample of concentrate from Newlands that included all peridotitic minerals and that may be compared directly to the assemblages of interest in the larger samples studied (see Chapter 3).

4.2.1 Garnet

The garnets discussed in this section fall into several categories ranging from almandine-pyrope for crustal garnets, grossular-pyrope-almandine for eclogitic compositions, chrome-pyrope (knorringitic-pyrope) for low-Ca, high-Cr peridotitic garnets and high-Cr, high-Ca (uvarovitic) garnet for 'websteritic' and wehrlitic compositions.

Dawson and Stephens (1975), Gurney (1984), Grütter et al. (2004) and Schulze (2003) have devised classification schemes in order to define compositional discriminants for garnets. They attempt to relate compositional variation to particular mantle/crustal paragenesis (see discussion in chapter 2). The classification scheme of Grütter et al. (2004) is used here because it takes into account the previous two systems and is also widely used in diamond exploration today. This classification mainly relates to discrete regions on the CaO vs. Cr₂O₃ (wt. %) diagram but also takes other elements such as Ti into account (see section 4.1.2). Other standard plots for garnet will also be made to see how garnets deviate from crustal compositions e.g. Ca-Fe-Mg cation plot and Na₂O plots for high-pressure garnets. Plots for other elements analysed will be made to check for additional variation e.g. Ti, Na.

4.2.1.1.1 *Ca-Fe-Mg*

Fig. 4.2a shows a Ca-Fe-Mg cation plot of garnets from the NWT indicator mineral prospecting in Canada and illustrates the full range of mantle garnets present. Low-Mg, high-Fe and intermediate Ca garnets form a cluster that represents crustal garnet compositions. The plot therefore serves to differentiate garnet paragenesis based on these three important substituting divalent ions.

By comparing the three plots below (Fig. 4.2) several features emerge: (1) Finsch diamond inclusions form two clusters; one eclogitic at intermediate Fe:Mg and low-moderate Ca; and one peridotitic at high Mg and low Ca and forms a unique area relative to indicator mineral sampling in Canada but merges with the low-Ca concentrate from Newlands and to some extent Bellsbank (Fig. 4.2b). (2) A trend forms from the Finsch peridotitic diamond inclusions at constant low Fe to higher Ca values (i.e. a Mg-Ca substitution) at Newlands and Bobbejaan. This trend is not so evident in the 5000 garnets from NWT indicator mineral prospecting. (3) A more dispersed trend is seen emerging from the most concentrated peridotitic cluster (probably lherzolitic) in Newlands and Bellsbank concentrate towards higher Fe values (i.e. a Fe-Mg substitution) and eclogitic compositions. This is also seen in the SAK dataset but not clear in the NWT dataset. (4) The indicator mineral sample (Fig.4.2a) has two clusters not apparent in diamond inclusions or in Newlands and Bellsbank concentrate, which is at high Fe and intermediate Ca. The other cluster is at low Ca and intermediate Fe:Mg. These probably represent crustal garnets not sampled by kimberlite. Fifthly, kimberlite concentrate from southern Africa has less high-Ca garnets than shown in the Canadian sampling and Barkly-West concentrate. It also has a strong extension into the peridotitic diamond inclusion field unlike the Canadian sampling.

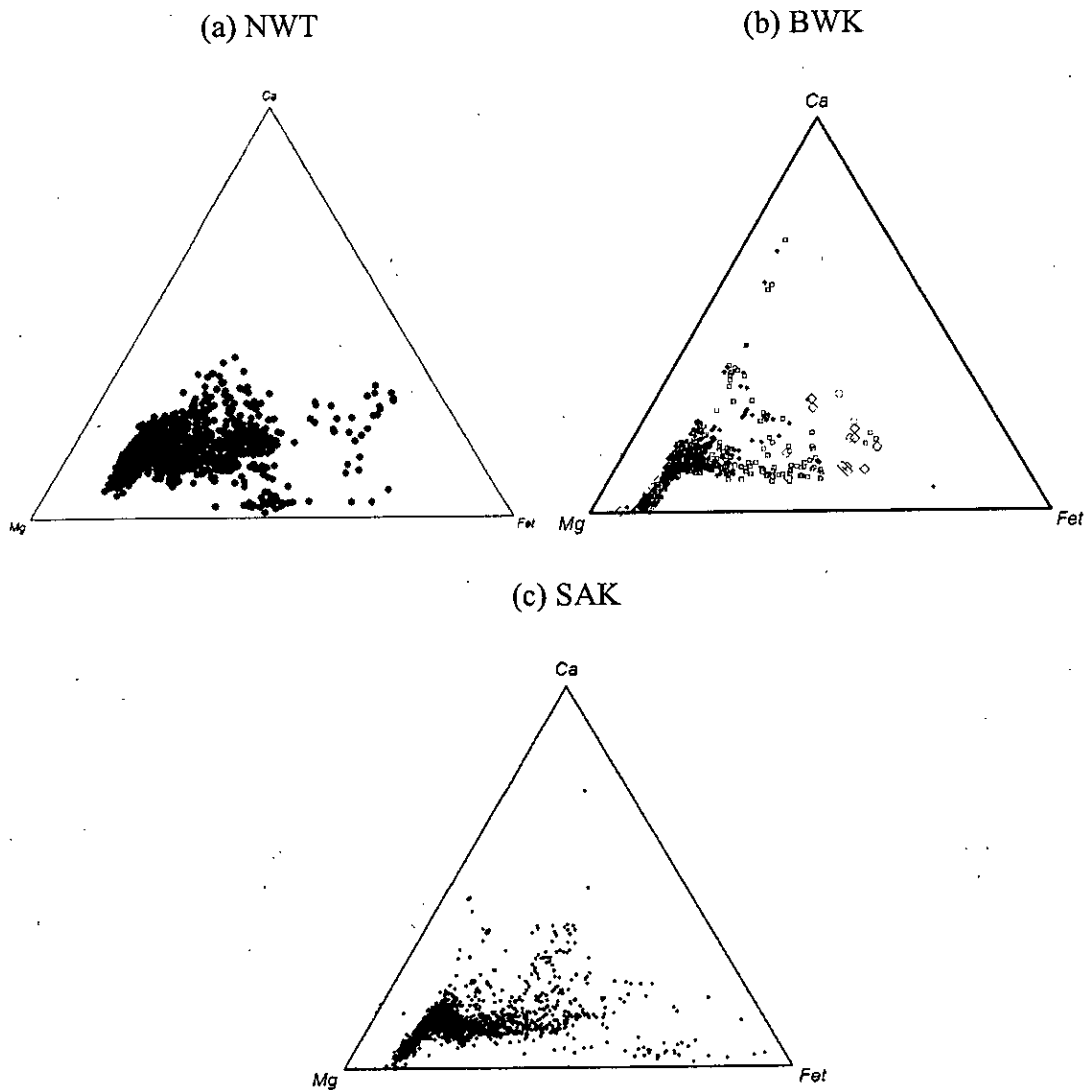


Figure 4.2: Cation plots of Ca-Fet-Mg (Fet is total Fe) of garnets from (a) NWT till sampling ($n = 5000$, a random sample of $\sim 30,000$ data points), (b) Newlands (open circle symbols) and Bellsbank (grey square symbols) kimberlite garnet concentrate, Finsch diamond inclusions (open diamond symbols), (c) SAK concentrate ($n = 2500$) data from KRG Database.

Additionally the NWT dataset shows extensions to the lherzolitic and megacrystic cluster to higher CaO values which are thought to represent pyroxenitic and wehrlitic compositions (G11, G12 fields from Grütter et al., 2004). The distribution of G10 garnets appears to be strongly limited at low Cr₂O₃. There is a high density region above 4 wt. % Cr₂O₃ and between 1.5 and 4 wt. % CaO above the diamond-graphite constraint (DGC); the abundance falls away and becomes very sparse above about 12 wt. %.

The garnet concentrate analysis from Newlands kimberlite is shown in Fig. 4.3c. Here the lherzolitic cluster is seen once again, but it is observed to extend towards higher Cr₂O₃ than in the NWT dataset (Fig. 4.3b). The Newlands lherzolite cluster is comparatively dispersed adjacent to the lherzolite line. Some lower Cr₂O₃ garnets are observed in the Newlands data, but preferential analysis of purple garnets has meant that crustal, megacrystic and eclogitic garnets are under-represented. The G10 field at Newlands possesses a trend, which is not immediately evident from bulk indicator mineral sampling elsewhere. This trend is relatively narrow, conspicuously parallel to and continuously above the DGC, extending from 0.5 to 7 wt. % CaO. G10 garnets also exist at lower Cr₂O₃ values than the DGC but are less abundant at Newlands than elsewhere. The trend of high-Cr₂O₃ garnets above the DGC line extends across the lherzolite line at Newlands. The Newlands concentrate appears to contain high-Cr G10 garnets, high-Cr G9 garnets and high-Cr, high-Ca garnets in excess of the proportion seen in large scale sampling from a diamondiferous source region such as NWT, Canada.

Though the total number of analyses is not high, Fig. 4.4 shows that concentrate from the other Barkly West region kimberlites has far fewer garnets with more than 7 wt. % Cr₂O₃ than Newlands. This is evident in the lower percentage of G10D garnets at Bellsbank, with even lower percentages at Frank Smith and Leicester compared to

Newlands (see pie charts, Fig. 4.5). The bulk of the Frank Smith garnet concentrate is offset from the Bellsbank lherzolitic concentrate to higher CaO values by approximately 0.5 wt. %, with Leicester approximately between the two. Bellsbank concentrate has a significant proportion of G10D garnets and also shares Newlands' feature of a greater proportion of high-Cr, high-Ca garnets.

Fig. 4.5 shows the proportions of peridotitic kimberlite concentrate garnet classes found at the 4 Barkly West localities and, in addition, from general indicator mineral sampling from recent Canadian exploration. It is evident from this figure that Newlands has the highest proportion of G10D garnets and also G10+G10D garnets. It is also clear that Newlands and Bellsbank have similar proportions of garnet classes, the only significant difference being that Bellsbank has more G9 lherzolitic garnets (~ 2/3, compared to < 1/2 at Newlands) at the expense of other classes. Frank Smith has general proportions similar to Newlands except there is a higher proportion of G1 megacryst garnets present (~1/3, compared to 2 % at Newlands) at the expense of high-Cr garnets such as G10s, G11s and G12s. Leicester is different to all other datasets in that it comprises 95 % lherzolitic G9 garnet. Compared to the Barkly West kimberlites excluding Leicester, the bulk Canadian till sampling from NWT is similar except it has a larger G11 and an intermediate G1 population with a lower G10D:G10 ratio.

The concentrate derived from southern African kimberlites is most similar to Frank Smith except for the higher proportion of G9s at the expense of G1s. G10+G10D and G9 proportions are similar for both SAK and NWT datasets, the only significant difference is the higher proportion of G1s present in SAK.

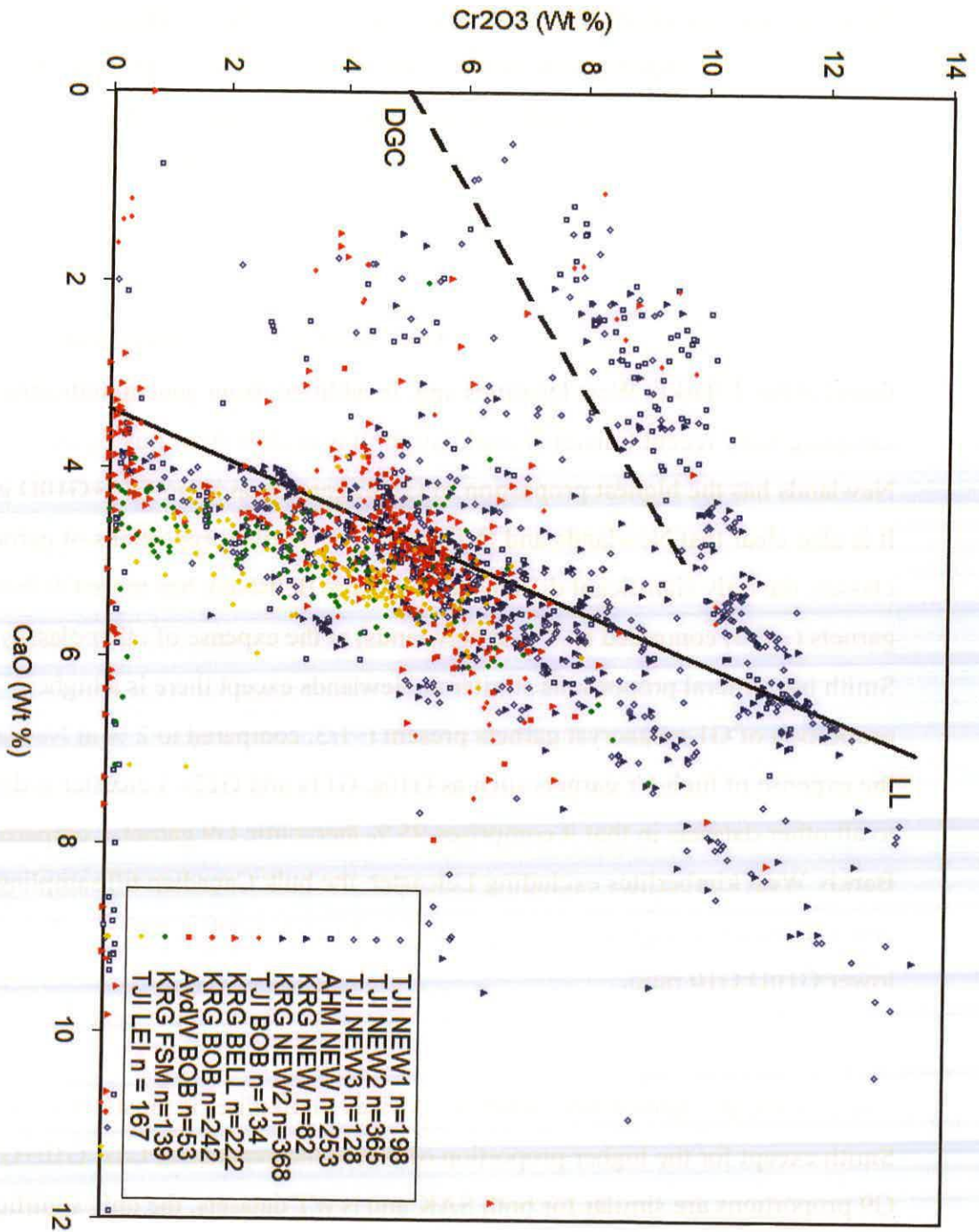


Figure 4.4: CaO vs. Cr₂O₃ (Wt. %) of garnet concentrate analyses from this study (TJI NEW, TJI BOB, TJI LEI), the Kimberlite Research Group Database (KRG NEW, KRG BELL, KRG BOB, KRG FSM), Menzies (2001) (AHM NEW) and van der Westhuizen (1992) (AvdW BOB). The prefixes 'NEW' = Newlands kimberlite concentrate (dark blue symbols), 'BOB' = Bobbejaan kimberlite concentrate, 'BELL' = undifferentiated Bellsbank concentrate (red symbols), 'FSM' = Frank Smith kimberlite concentrate (bright green symbols) and 'LEI' = Leicester kimberlite concentrate (yellow symbols). Reference lines as for Fig.4.3.

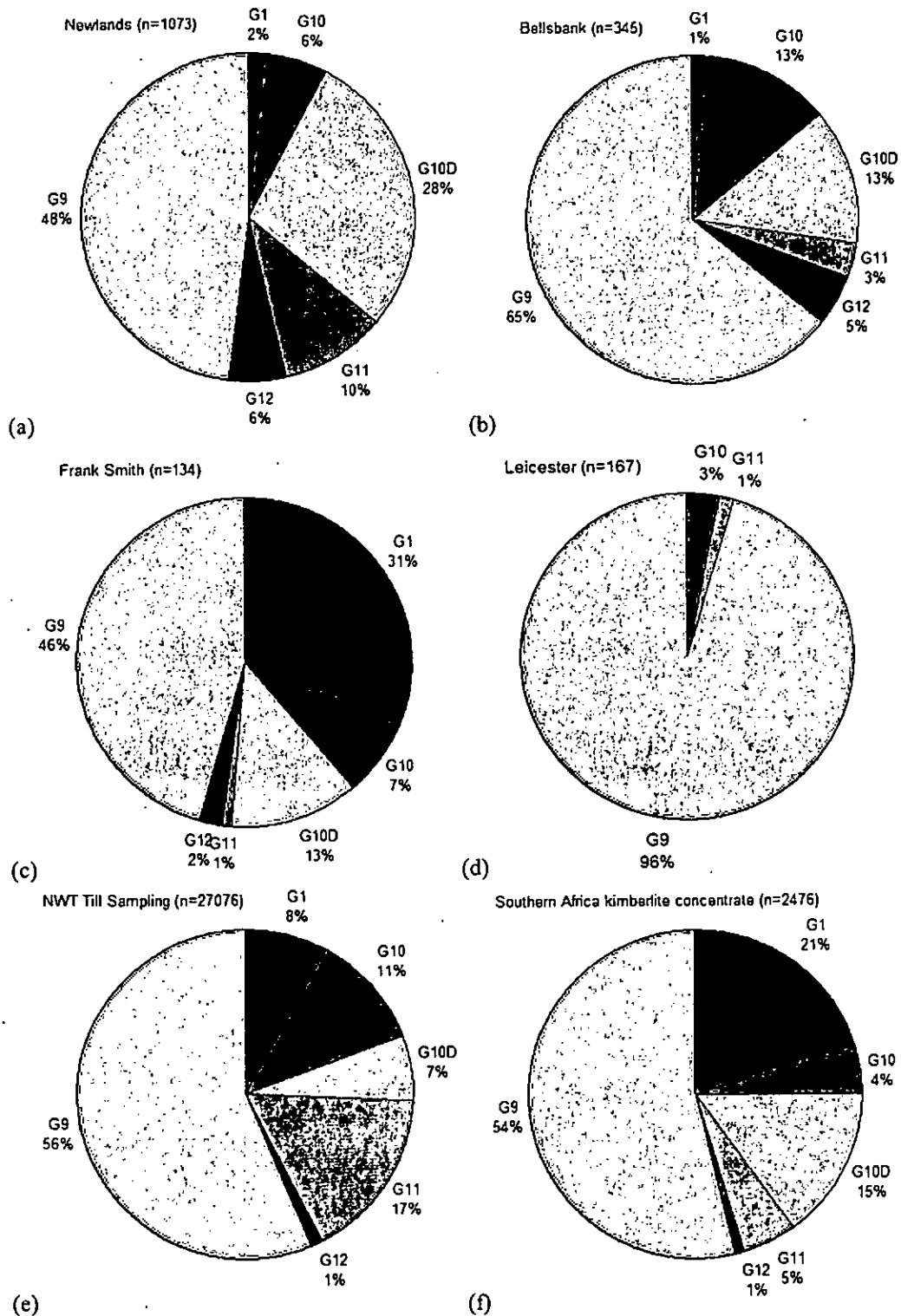
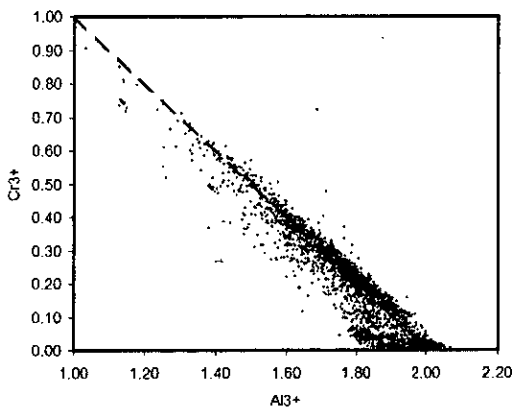


Figure 4.5: Pie charts illustrating the proportions of garnets from particular compositional classes as defined by Grütter et al. (2004) from (a) Newlands kimberlite concentrate (data from this study, KRG database, Menzies, 2001), (b) Bellsbank kimberlite concentrate (data from this study, KRG database,

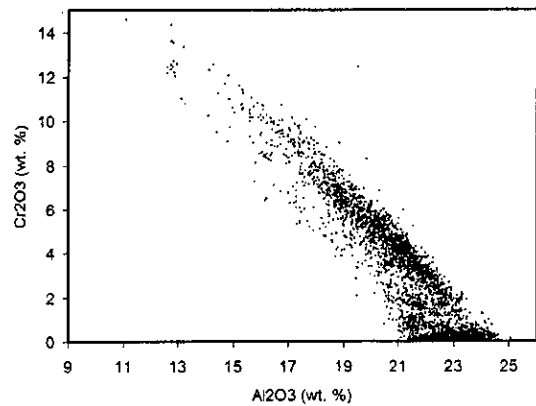
van der Westhuizen, 1992), (c) Frank Smith kimberlite concentrate (data from KRG database), (d) Leicester kimberlite concentrate (data from this study), (e) Northwest Territories of Canada till sampling (data from open file: <http://www.nwtgeoscience.ca>) and (f) Southern Africa kimberlite concentrate (data from KRG database). Low Cr_2O_3 garnets are removed from the datasets (i.e. those with $< 1\%$ Cr_2O_3) so that only peridotitic-affinity garnets are shown.

4.2.1.1.3 Al vs. Cr

(a) SAK



(b) SAK



(c) NWT

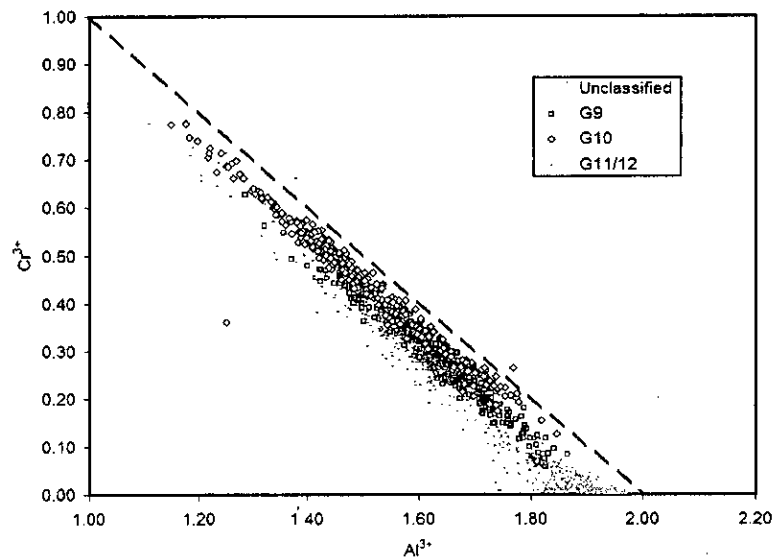
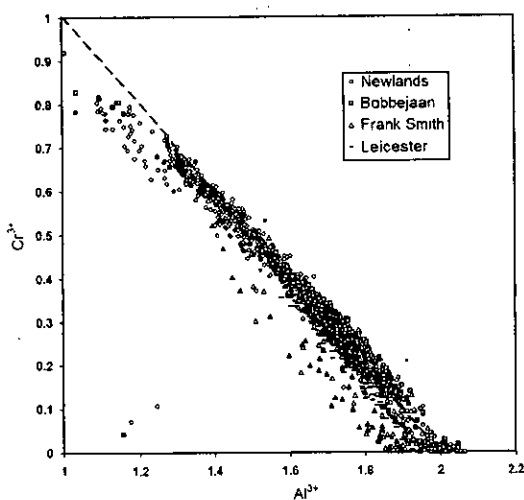


Figure 4.6: (a) Al vs. Cr cations for SAK garnet concentrate. (b) Al_2O_3 vs. Cr_2O_3 wt. % for the same dataset as (a). (c) Al^{3+} vs. Cr^{3+} cation plot of garnets from NWT till sampling. G9 garnets are open square symbols, high Cr, high-Ca G11/12s are dark grey bar symbols, G10s are white filled diamond symbols and other garnets including eclogitic, megacryst and unclassified (probably crustal) are the light grey dot symbols. All cations calculated so that they sum to 8. The dashed lines in (a) and (c) show the sum of 2 R^{3+} cations in the common 8 cation garnet formula of $\text{R}^{+3}_2\text{R}^{+2}_3\text{Si}_3\text{O}_{12}$.

Figure 4.6a illustrates the inverse relationship between aluminium and chromium in garnet. At low-Cr the spread away from the sum of 2 cation line is probably due to the increased abundance of Fe^{3+} and occasionally Ti at the expense of Al and Cr in eclogitic and crustal garnets. The cluster between 2 and 6 wt. % Cr_2O_3 is composed of the peridotitic garnets with megacrysts and eclogites plotting at low Cr_2O_3 .

From Fig. 4.6 it is clear that there is more detail to be observed as to the different amounts of potential Fe^{3+} present. A broad area is occupied by G9 garnets, which encompasses most of the G11/12- and G10-rich regions. G11/12 garnets fall to the low-Cr side of this G9 field indicating presence of more Fe^{3+} whereas the harzburgitic garnets (G10s) appear to be confined to only the highest Cr for a given Al indicating that the garnets are saturated in 3+ ions without taking Fe^{3+} into account.

(a) BWK



(b) BWK This Study

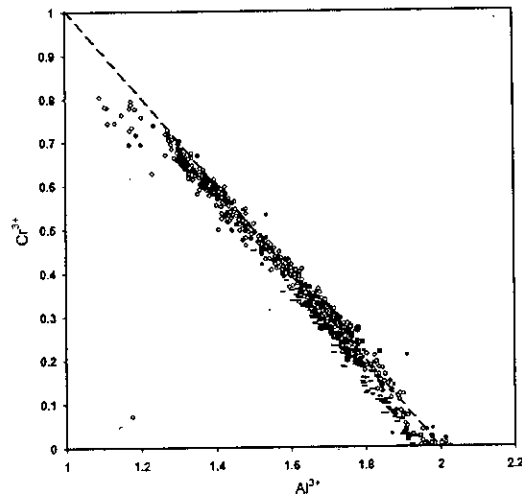


Figure 4.7: (a) Al^{3+} vs. Cr^{3+} cation plot (cations summed to 8) of Barkly West kimberlite garnet concentrate from Newlands open circle symbols, Bellsbank filled grey square symbols, Frank Smith open triangle symbols and Leicester black bar symbols. (b) as for (a) except only analyses from this study shown. Dashed line as for Fig. 4.6.

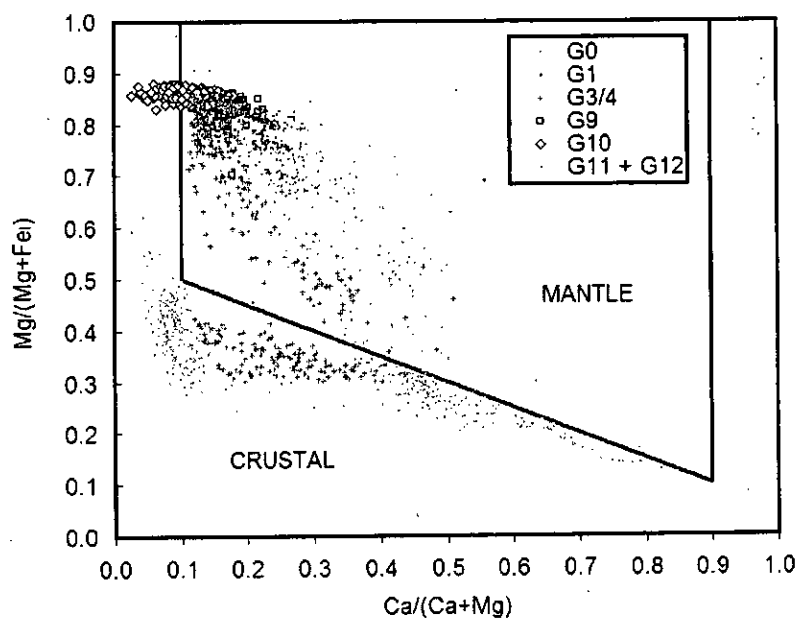
Fig. 4.7 above shows a particularly high relative density at the elevated Cr region of the cation plot by comparison with NWT till analyses (Fig.4.6). Newlands dominates

in this high-Cr, low-Al part of the array with Bellsbank plotting close to the $3+$ cation sum = 2 line but at lower Cr and higher Al concentrations. Leicester and Frank Smith have compositions more akin to low-Cr lherzolitic compositions. Deer et al. (1962) suggest that titanium may substitute into the Y site (with Al and Cr) because of its ionic radius rather than the Z site (Si). This would allow further deviation from the ideal $Cr + Al = 2$ sum.

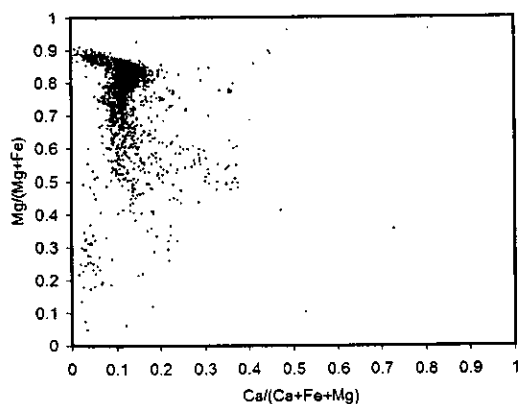
4.2.1.1.4 *Ca vs. Mg*

Low-Ca, high-Mg garnets occur at the extension of a negative Ca-Mg trend in all mantle garnet concentrate analysed (see pink G10 field in NWT till concentrate Fig. 4.8a). Eclogitic garnets can be seen to plot to lower $Mg/(Mg+Fe)$ values and extend to intermediate $Ca/(Ca+Fe+Mg)$. Crustal garnets have low to intermediate $Mg/(Mg+Fe)$ and low $Ca/(Ca+Fe+Mg)$ (and $Ca/(Ca+Mg)$) as shown in the classification of Schulze (2003) (Fig. 4.8b). Fig. 4.8c shows that SAK concentrate has a similar distribution to NWT till garnets except there is a smaller eclogitic and crustal component in the SAK dataset. The Barkly West group kimberlites have a similar pattern to the SAK dataset except Newlands and Bellsbank display a unique Ca-enrichment trend away from the dense G9 cluster. This particular trend is not observed in the NWT dataset.

(a) NWT



(b) SAK



(c) BWK

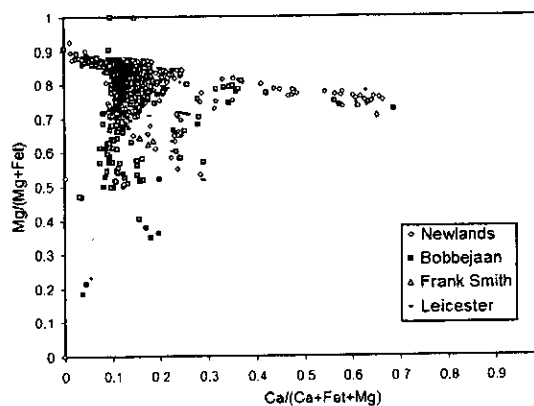
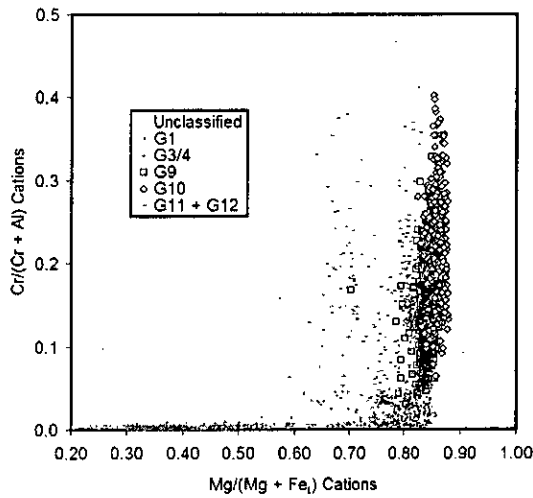


Figure 4.8: (a) $\text{Ca}/(\text{Ca}+\text{Fe}+\text{Mg})$ vs. $\text{Mg}/(\text{Mg}+\text{Fe})$ cation plot (cations summed to 8 and Fe is total Fe) of garnet concentrate analyses from NWT till sampling. G10 garnets are open diamond symbols, G9s open square symbols, G1s black dot symbols, G11/12 grey bar symbols, G3, G4 and G0 (unclassified) garnets are plotted as light grey dots symbols. $n=30435$. Crustal and mantle garnet fields from Schulze (2003) are shown in (a). (b) as for (a) except SAK concentrate plotted. (c) as for (a) except Barkly West kimberlite concentrates plotted (Note: symbols as for Fig. 4.7b).

4.2.1.1.5 Mg vs. Cr

(a) NWT



(b) BWK

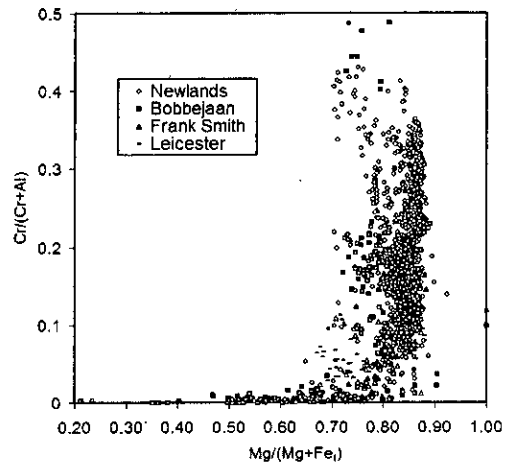
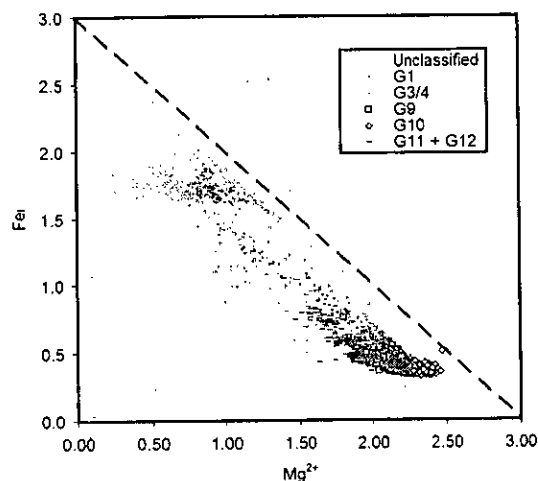


Figure 4.9: (a) Mg/(Mg+Fe) vs. Cr/(Cr+Al) (calculated on the basis of 8 cations with Fe representing total Fe) for NWT garnets, symbols as for Fig. 4.8 (a). (b) as for (a) except Barkly West kimberlite concentrate plotted, symbols as for Fig. 4.7 (b).

Fig. 4.9a shows the marked maximum Mg/(Mg+Fe) for garnets from indicator mineral sampling in NWT, G10 garnets possess marginally higher Mg/(Mg+Fe) than other classes of garnet. In addition, G10s have higher Cr/(Cr+Al) and overlap more significantly with G11/12 and G9 garnets at high Cr/(Cr+Al). The G11/12 population extends to lower Mg/(Mg+Fe) while at higher Cr/(Cr+Al); G9s exhibit this weakly and G10s only have Mg/(Mg+Fe) < 0.8 once Cr/(Cr+Al) is below ~0.2.

4.2.1.1.6 Mg vs. Fe

(a) NWT



(b) BWK

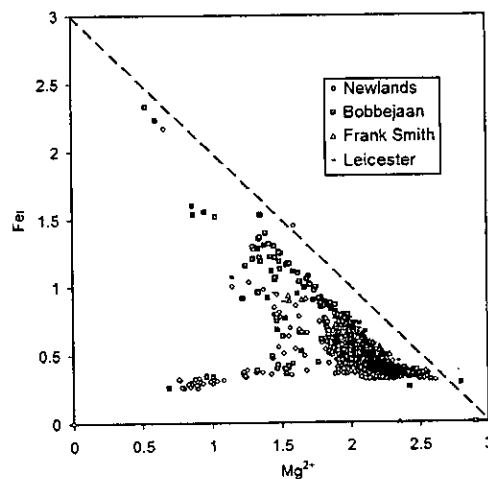


Figure 4.10: (a) Mg vs. Fet cations (calculated on the basis of 8 cations) for NWT till sampling garnets, symbols as for Fig. 4.8 (a), the sum of 3 cations line is shown. (b) as for (a) except Barkly West kimberlite concentrate plotted, symbols as for Fig. 4.7 (a). The dashed lines in (a) and (b) show the sum of 3 R²⁺ cations in the common 8 cation garnet formula of R+3R²⁺+23Si₃O₁₂.

Fig. 4.10a shows a marked separation of different garnet classes according to their combined abundance of Fe+Mg (the converse of their abundance in Ca). Eclogitic garnets are high in Fe, low in Mg and high in Ca. G9/11/12 garnets plot to higher Mg+Fe and Mg/(Mg+Fe) values with G10 garnets approaching the 2+ ion saturation line of 3. Unclassified G0 garnets appear to be mainly almandine-rich crustal garnets since they plot at high Fe and close to the 3 cation saturation line (implying small amounts of other 2+ cations). In the same way as in the CFM triangular plot (Fig. 4.2), Newlands and Bellsbank garnets form a trend away from the 3 cation line indicating extensive Ca-Mg substitution, which is only very weakly present in the NWT dataset in the G11/12 category. Leicester and Frank Smith concentrates are similar to the G9 and G10 populations from NWT.

4.2.1.1.7 CaO vs. TiO₂

Fig. 4.11 shows that different Barkly West kimberlites have different Ti-Ca characteristics. Newlands and Bellsbank are the only localities to occupy the low-Ca,

low-Ti region. These garnets are the low-Ca harzburgitic garnets from the Cr-Ca plots. All BWKs produce a cluster at 4-6 wt. % CaO with wt. % TiO₂ ranging from 0 to 0.6 which represents the lherzolitic G9 garnets. Frank Smith is the only kimberlite to possess a large fraction of megacryst garnets (see pie chart Fig. 4.5c) which are at lherzolitic CaO contents but have between 0.5 and 1 wt. % TiO₂. All BWKs have garnets enriched in CaO and TiO₂, relative to the bulk lherzolitic cluster. This is thought to correspond to the higher-Cr, higher-Ca garnets found at the top of the 'lherzolite trend' on the Cr-Ca graphs.

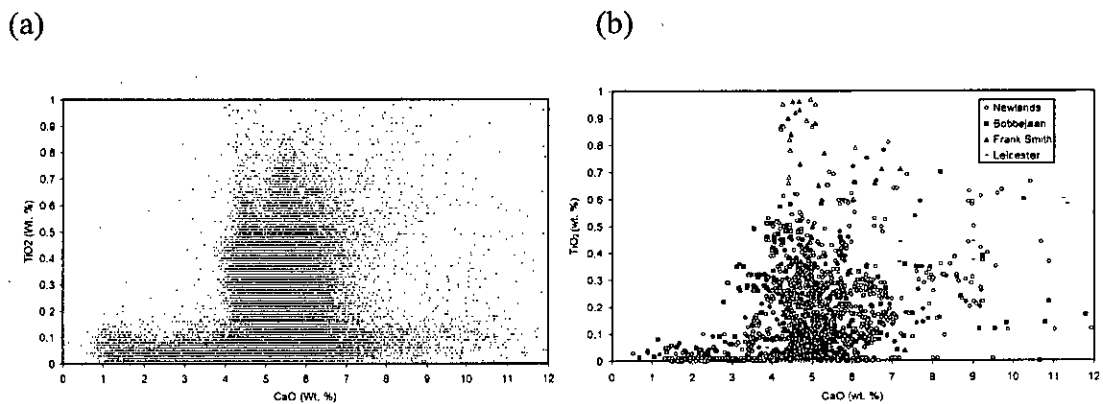


Figure 4.11: (a) CaO vs. TiO₂ plot for garnet concentrate from NWT till sampling. (b): CaO vs. TiO₂ plot for garnet concentrate from Newlands, Bellsbank, Frank Smith and Leicester.

When comparing individual kimberlite concentrates to bulk NWT sampling several differences are apparent (see Fig. 4.11b). Newlands and Bellsbank concentrates pick out the low-TiO₂ low-CaO extremities of the NWT data, with Bellsbank having a unique cluster at 3-4 wt. % CaO and 0.25-0.35 wt. % TiO₂. Eclogitic garnets from NWT are present in abundance at high-Ca and low-Ti. The megacryst population is much more abundant in the till sampling.

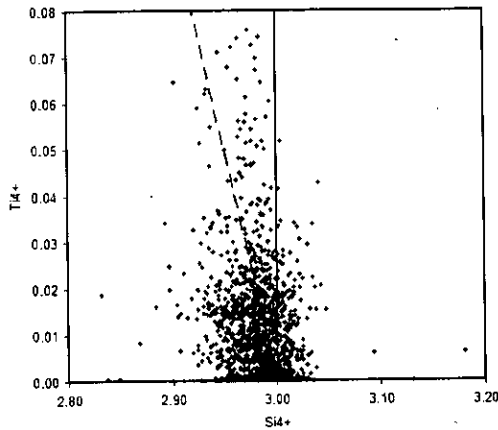


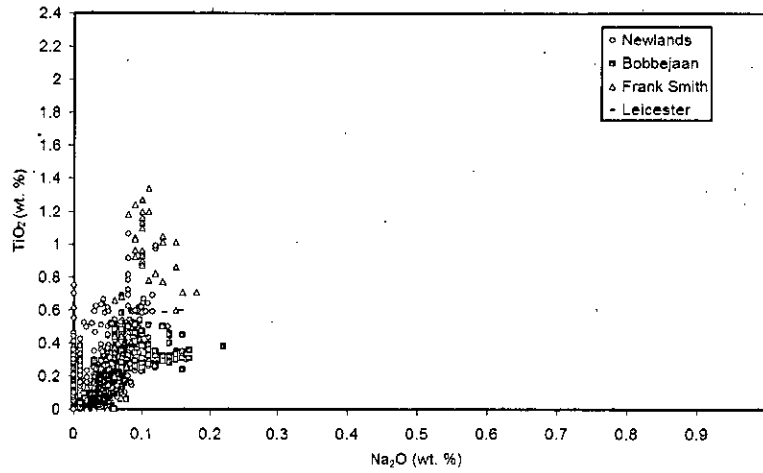
Figure 4.12: Si^{4+} cations vs. Ti^{4+} cations for all BWK concentrate. The dashed line is for $\text{Ti} + \text{Si}$ equal to a total of 3 cations. Solid line for Si equal to 3 cations.

Fig. 4.12 illustrates that there is no discernable correlation between the 4+ ions suggesting that Ti is substituting on the Y site rather than the Z site, but relatively large errors on Si analysis and the low absolute values of Ti make this conclusion uncertain. It appears that Ti^{4+} substitution on the Y site is charge balanced by small quantities of Na (see positive correlation in next subsection, Fig. 4.13).

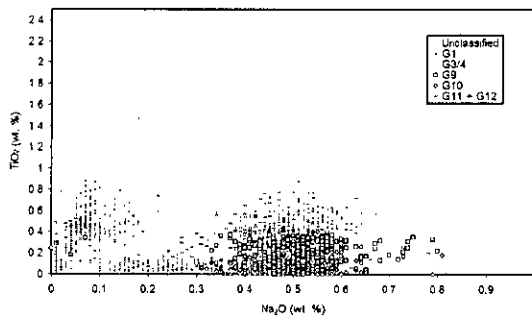
4.2.1.1.8 Na_2O vs. CaO and TiO_2

The majority of concentrate analysed in the KRG database and from other studies records 0.00 wt. % values for Na_2O and largely reflects a lack of careful analysis for this element. The majority of 'good' analyses are < 0.1 wt % and show a slight positive correlation with TiO_2 (Fig. 4.13a). Slightly higher Na_2O values are recorded for the unique cluster from Bellsbank between 0.25 and 0.35 % TiO_2 . Compared to the NWT till samples (Fig. 4.13b), the Na_2O range is greatly reduced in the analyses from Barkly West.

(a) BWK



(b) NWT



(c) NWT

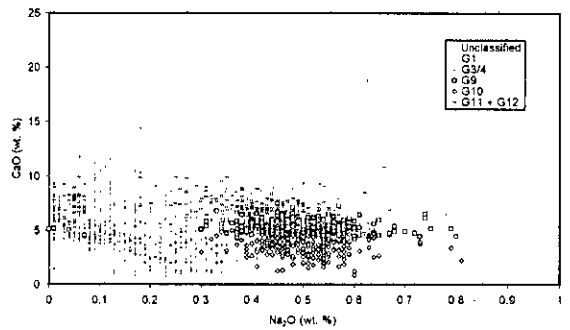


Figure 4.13: (a) Na_2O vs. TiO_2 wt. % for Barkly West kimberlite concentrate garnet analyses. Symbols as for Fig. 4.7 (b). SAK garnet concentrate has often not been analysed for Na within the KRG database and is therefore not shown. (b) Na_2O vs. TiO_2 plot for NWT till garnet analyses. (c): Na_2O vs. CaO plot for NWT till garnet analyses.

Due to differences in analytical conditions, Barkly West concentrate Fig. 4.13a does not extend into the fields shown by the NWT dataset Fig. 4.13b. However, a positive correlation exists, between BWK and NWT, from zero up to 1 wt. % TiO_2 and 0.15 wt. % Na_2O (Fig. 4.13b). For the latter, it is the crustal, eclogitic and megacrystic compositions that occupy this trend. Peridotitic garnets from NWT plot at high Na_2O (0.3-0.8 wt. %) which has not been reported before. This dataset also records low (G10), medium (G9) and high (G11+12) TiO_2 contents (Fig. 4.13b) in peridotitic garnets. Similar regions exist in the Na_2O vs CaO plot (Fig. 4.13c) with the high- Na_2O region being occupied by peridotites with low- CaO being mainly G10,

medium CaO being G9 and high CaO being G11+12. The high Na₂O is thought to be an analytical artefact.

4.2.1.2 Cr-SPINEL

The oxide phase present in samples was referred to as 'chromite' in chapter 3 because no knowledge of the major element chemistry was known at the time of examination. 'Chrome-spinel' (Cr-spinel) and 'chromite' are common terms in mantle-related literature and will only be used here when a chromium-rich spinel or a true chromite, respectively, is being referred to. However, within the spinel prism, the majority of kimberlitic 'chromite' concentrate plots in the magnesiochromite region with relatively low Fe_t (total Fe) and Al and relatively high Mg and Cr compositions (see Fig.4.14 shaded region).

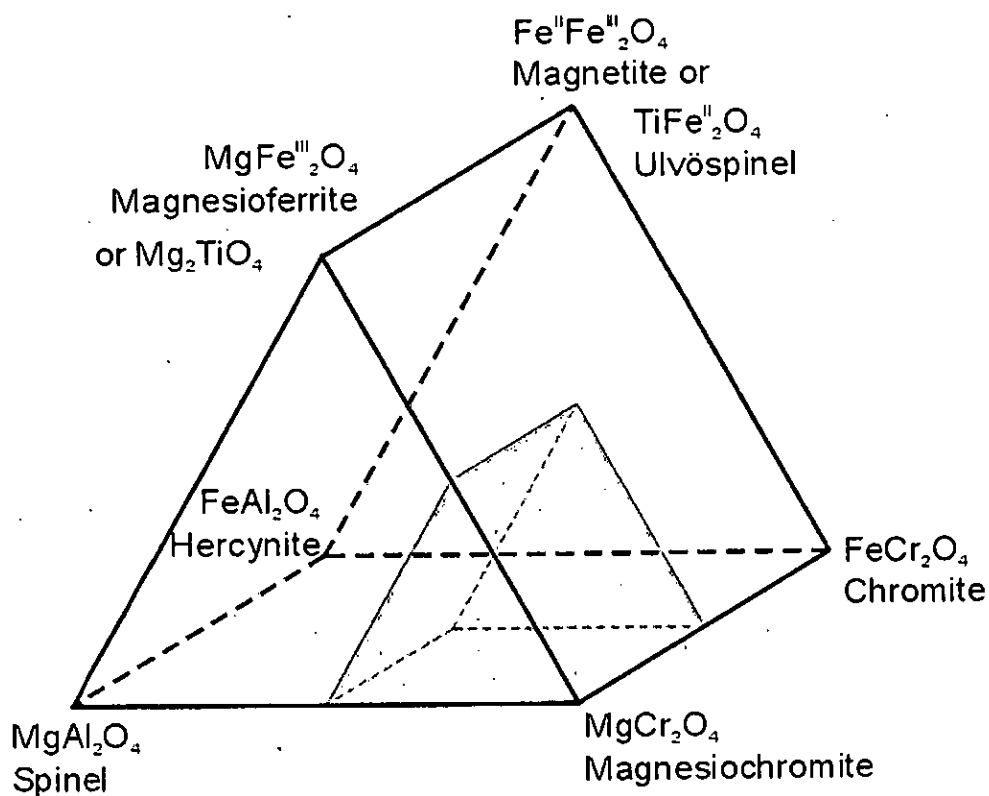


Figure 4.14: Spinel multi-component compositional prism after Deer et al. (1962) illustrating spinel group end members. Shaded region indicates the region of the spinel prism where the majority of kimberlitic spinel from concentrate plots i.e. towards the magnesiochromite end member.

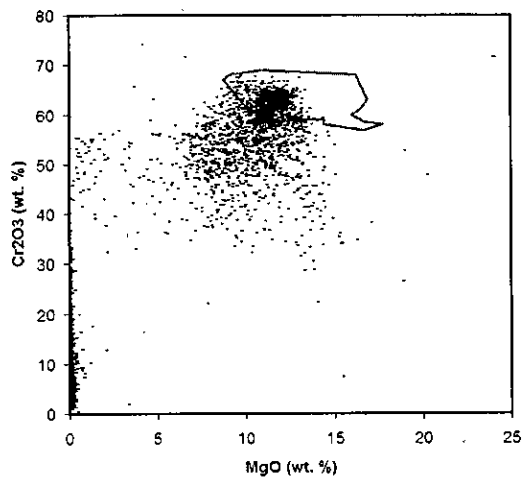
In this section additional comparison is made by plotting Dokolwayo concentrate along with the SAK concentrate since it has been commented on specifically as being especially similar to diamond inclusion Cr-spinel by Daniels (1991).

4.2.1.2.1 Cr_2O_3 vs. MgO

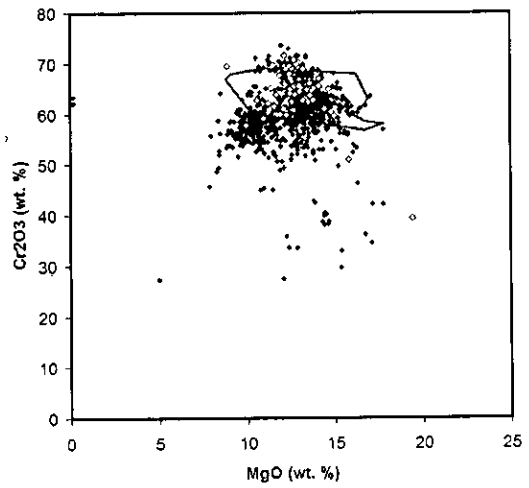
The Cr_2O_3 vs. MgO plot is the most useful divariant plot for distinguishing parageneses in mantle-derived Cr-spinels. Fig. 4.15 illustrates that the three concentrate datasets occupy subtly different areas of the plot. The NWT data (Fig. 4.15a) is the only dataset to possess a low-Cr, low-Ti cluster, which would probably correspond to part of the continental layered intrusion field shown in the cation plot (Fig. 4.16). The majority of the NWT data occupies a diffuse cluster between 5 to 15 wt. % MgO and 40 to 70 wt. % Cr_2O_3 with a high density region in the low- MgO part of the DI field. There is a diffuse extension from the DI field towards low Cr_2O_3 and high MgO .

The SAK concentrate (Fig. 4.15b) does not have the low MgO spinels present as for NWT and has a high density region in the central part of the DI field. The Dokalwayo spinels are exceptionally high in Cr_2O_3 . BWK concentrate (Fig. 4.15c) is similar to the SAK concentrate except for the Newlands dataset analysed by Menzies which extends from the diamond inclusion field of Fipke et al. (1995) towards high MgO and low Cr_2O_3 .

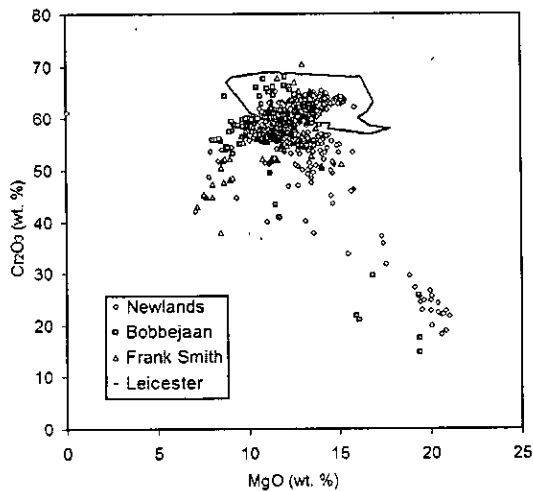
(a) NWT



(b) SAK



(c) BWK



(d) NEW

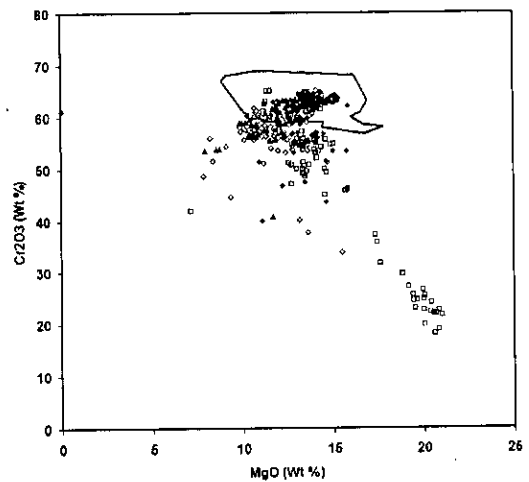


Figure 4.15: (a) MgO vs. Cr_2O_3 plot of NWT till spinels ($n=3766$) with the diamond inclusion field of Fipke et al. (1995) outlined. (b) as for (a) but with SAK concentrate ($n=1001$) (data from KRG Database), Dokolwayo concentrate is highlighted in open symbols ($n=58$). (c) as for (a) but data plotted from Newlands concentrate (open circle symbols), Bobbejaan concentrate (grey square symbols) from van der Westhuizen (1992) and KRG database and Frank Smith concentrate (open triangle symbols) from KRG database. Number of analyses at Newlands $n = 1161$, Bellsbank $n = 295$, Frank Smith $n = 139$, Leicester did not yield sufficient spinel in the concentrate sample taken. (d) as for (a) but just Newlands concentrate plotted (total $n=378$). Data from this study (diamond symbols), Menzies (2001) (open square symbols) and the KRG database (filled triangles).

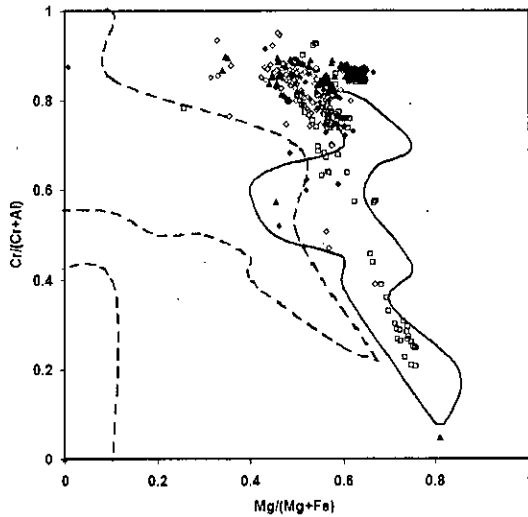


Figure 4.16: Cr/(Cr+Al) 3+ cations vs. Mg/(Mg+Fe) 2+ cations for Newlands kimberlite concentrate spinels. Approximate 90% fields adapted from Barnes and Roeder (2001) for podiform chromites in ophiolites shown as field outlined with a solid black line, continental layered intrusions shown as dashed black line. Symbols as for Fig. 4.15d.

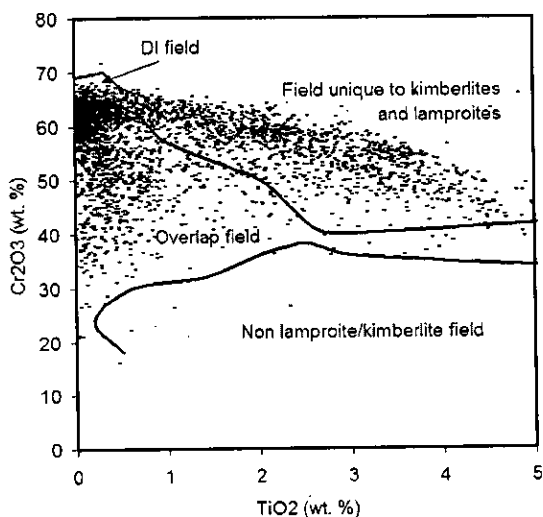
Fig. 4.16 indicates the compositional variation on data derived from Newlands, based on cation ratios rather than weight percent (Fig. 4.15d). It is clear that the extension to high Mg/(Mg+Fe) at lower Cr/(Cr+Al) is a linear trend picked out in data from Menzies (2001) (open square symbols) which follows the region indicated for podiform chromites in ophiolites along the so called 'Cr-Al trend' of Barnes and Roeder (2001). Newlands concentrate has an extension towards more Mg-rich compositions at high Cr (seen within the DI field in Fig. 4.15d) which would correspond to the Fe-Ti trend of Barnes and Roeder (2001).

4.2.1.2.2 Cr_2O_3 vs. TiO_2

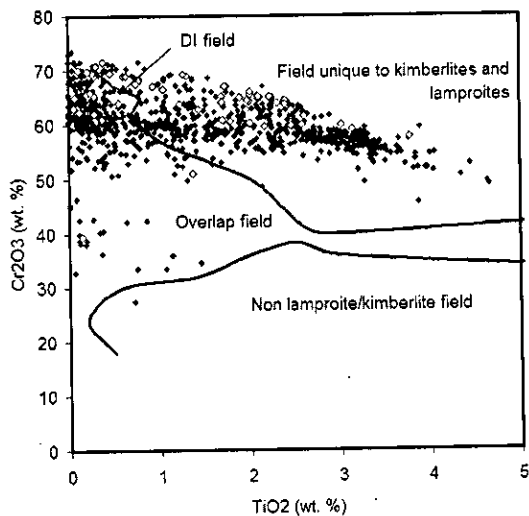
As a whole the concentrate produces two trends in Cr-Ti space (Fig.4.17). The first trend forms a negative Cr:Ti correlation that emerges from the diamond inclusion field and extends towards higher Ti and lower Cr. This trend is elevated to higher Cr in the SAK concentrate especially in the Dokalwayo concentrate (Fig. 4.16b) compared to the NWT dataset. The second trend is a low-Ti trend that varies in Cr content that is apparent in the 'overlap field' of Fipke et al. (1995) and especially evident in NWT concentrate. These spinels mainly correspond to compositions in the

podiform chromites from ophiolites and continental layered intrusion chromites (see fields in Fig. 4.16).

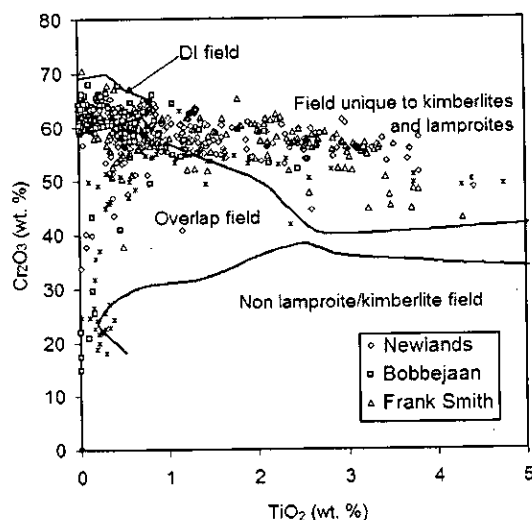
(a) NWT



(b) SAK



(c) BWK



(d) BWK

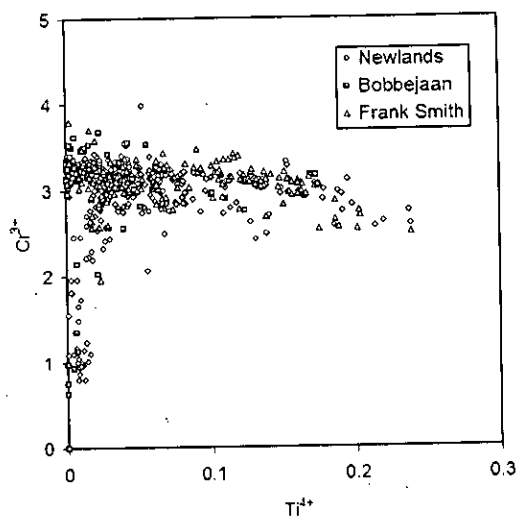
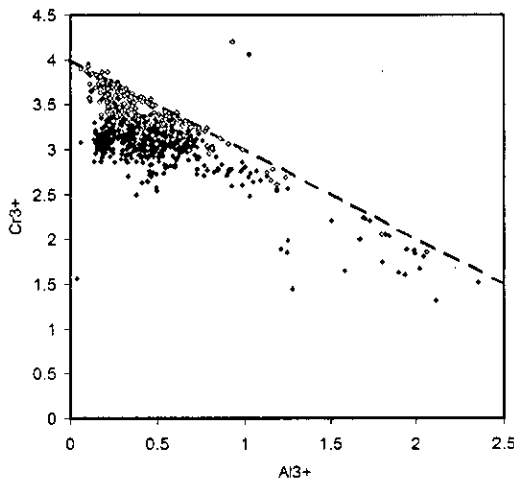


Figure 4.17: (a) TiO_2 vs. Cr_2O_3 wt. % plot of spinels from NWT till sampling $n=3766$, Fields from Fipke et al. (1995). (b) as for (a) but with SAK concentrate spinel, Dokolwayo concentrate is highlighted in open symbols. (c) as for (a) but for BWK spinel concentrate with Menzies (2001) Newlands spinels plotted as "*" symbols. (d) as for (c) except Cr and Ti calculated as cations where the cations are summed to 6.

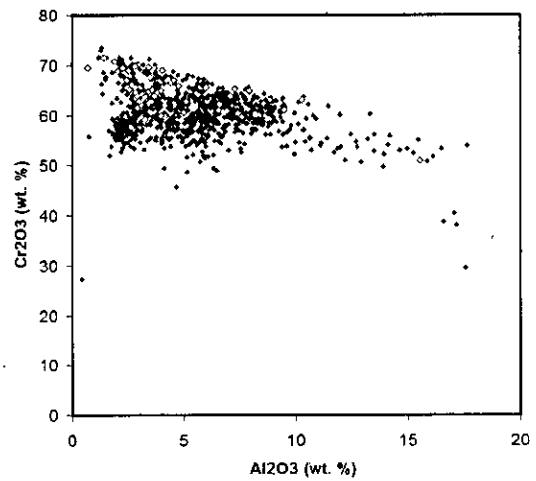
Cr₂O₃ and TiO₂ compositions of BWK concentrate spinel can be seen to overlap significantly with the DI field (Fig. 4.17c). The negative Cr-Ti trend is expressed in all Barkly West kimberlites with only Newlands expressing the low-Ti trend. This low TiO₂ and low Cr₂O₃ trend is likely to correspond to compositions in the podiform chromites from ophiolites field (see fields in Fig. 4.16).

4.2.1.2.3 Al vs. Cr

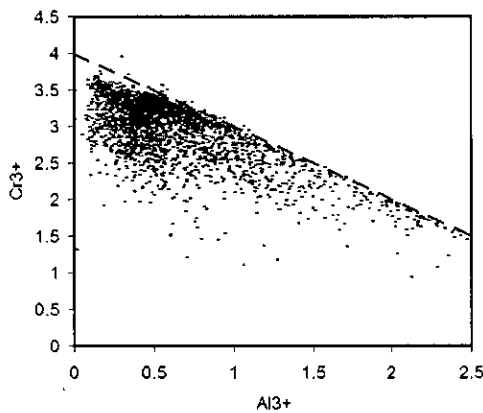
(a) SAK



(b) SAK



(c) NWT



(d) BWK

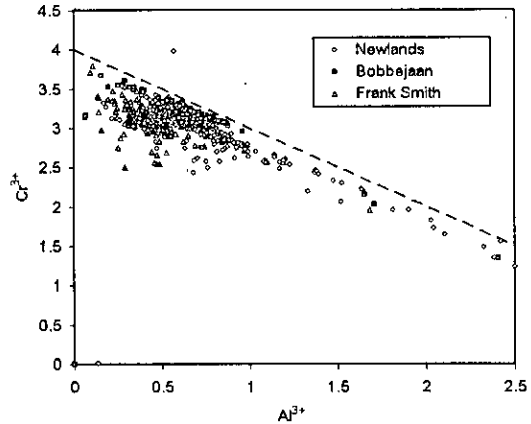


Figure 4.18: (a) Al³⁺ vs. Cr³⁺ cations calculated for 6 cations for spinels from SAK (Dokalwayo plotted as open diamond symbols). (b) as for (a) except Al and Cr are shown as weight percent. (c) as for (a) but with NWT till analyses. (d) as for (a) except for BWK concentrate. The dashed lines in (a) and (b) show the sum of 4 R³⁺ cations in the common 6 cation formula of R⁺²₂R⁺³₄O₈.

Fig. 4.18a shows that the Dokalwayo concentrate has very high Cr at low Al, close to 4 cations of Cr and 0 cations of Al, which is not present within any of the other datasets. Much of the Dokolwayo concentrate plots on the sum of 4^{3+} cation line and a few points plot above it. Both Fig. 4.18a and b show a negative correlation between aluminium and chromium with increased diffusivity at the lower aluminium end. The graph (Fig. 4.18c) also displays the upper limit to Cr + Al as a more continuous line (due to the larger dataset) across compositional space with a slight kink towards lower Cr at the high-Cr end.

Bellsbank spinels are seen to be at elevated chromium at low-Al concentrations (Fig. 4.18d) and form a shallower slope than the more abundant Newlands data. The Newlands compositions occupy the full range from the high-Cr to high-Al along this negative correlation trend and they cluster at $\text{Cr}^{3+} > 2.5$. Frank Smith spinels occupy a similar compositional space to Bellsbank but extend to lower Al for a particular Cr concentration indicating a greater concentration of a substituting ion.

Fig 4.19a and b indicate a significant deviation from the ideal formula along a decreasing $3+$ and increasing $2+$ trend. Fig. 4.19c shows that Ti^{4+} is substituting for $3+$ ions on the Y site by means of the ulvöspinel component ($\text{TiFe}^{2+}_2\text{O}_4$), hence increasing the $2+$ ion concentration and the negative correlation in Fig. 4.19a and b. This conforms to the Fe-Ti trend of Barnes and Roeder (2001).

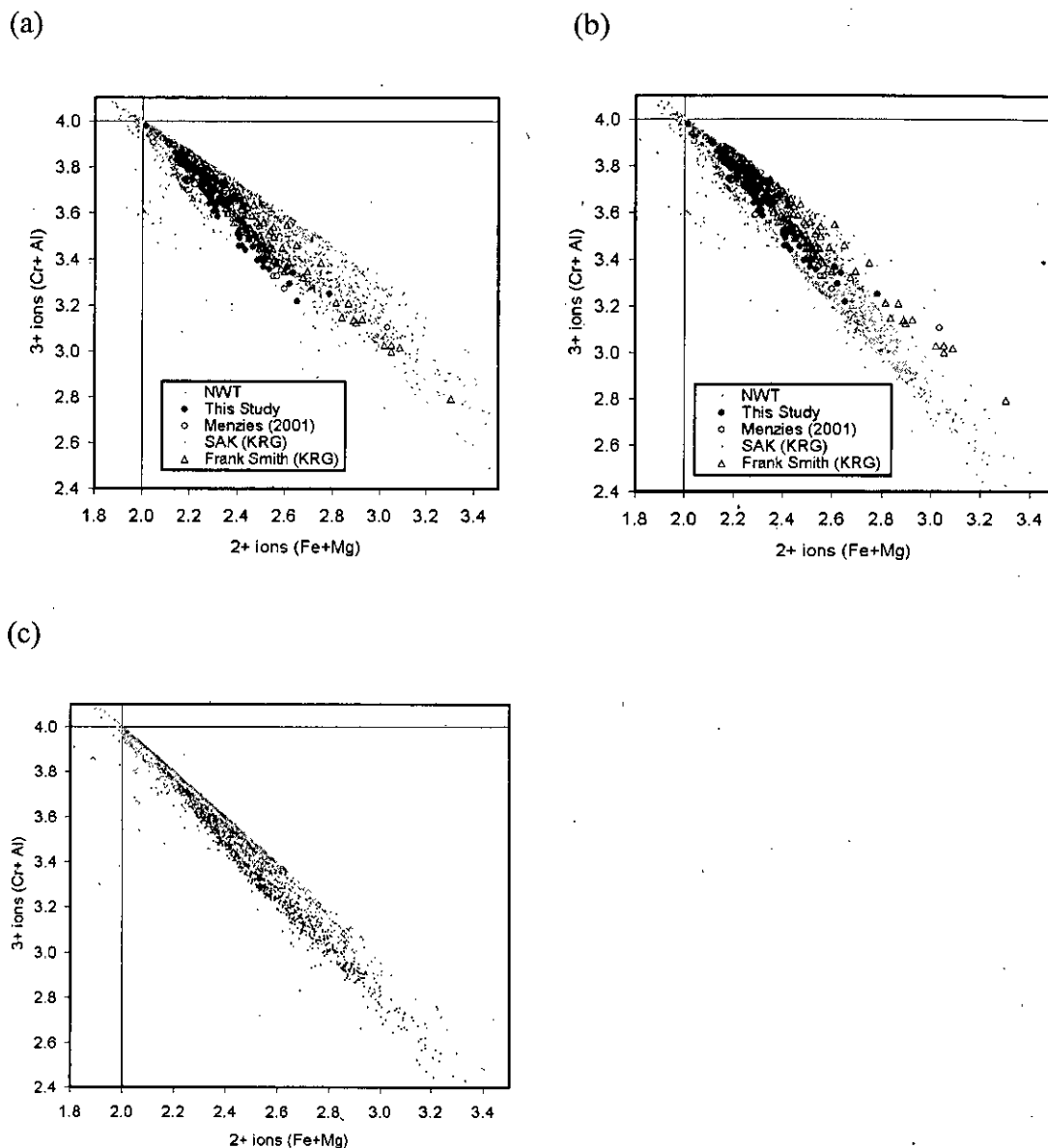


Figure 4.19: (a) 2+ ions vs. 3+ ions (calculated on a 8 oxygens basis) for concentrate from NWT till, SAK concentrate, Newlands concentrate from this study and from Menzies (2001) and Frank Smith concentrate. Reference lines for ideal formula numbers of 4 per 6 cations for 3+ ions and 2 per 6 cations for 2+ ions. (b) as for (a) except cations calculated on a 6 cation basis. (c) as for (a) except only NWT concentrate subdivided into Ti < 0.5 wt. % (pale grey diamond symbols), 0.5 < Ti < 1 wt. % (light grey dots), 1 < Ti < 2 wt. % (dark grey dots) and Ti > 2 wt. % (black dots).

4.2.1.2.4 Mg vs. Fe

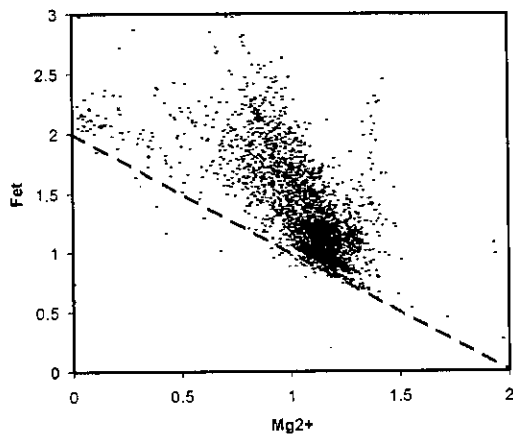
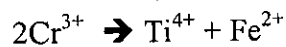


Figure 4.20: Fet vs. Mg cation plot of NWT till sampling chromites, cations summed to 6. The dashed lines shows the sum of 4 R³⁺ cations in the common 6 cation spinel formula of R²⁺₂R³⁺₄O₈.

Fig. 4.20 shows that the majority of chromites from indicator mineral sampling in the case of the NWT have > 2 cations' worth of Fe + Mg. This may indicate the presence of Fe³⁺, which would increase the amount of Fe expressed as Fet. The presence of Ti⁴⁺ would allow more 2+ ions to be present by a substitution such as:



which would increase the ulvöspinel component.

4.2.1.3 CLINOPYROXENE

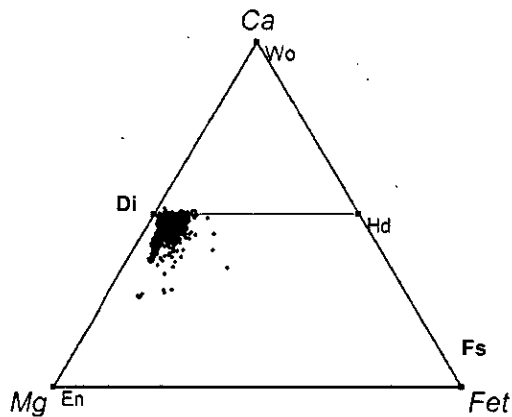
Clinopyroxenes are usually classified as chromium-diopsides (Cr-diopside) for peridotitic compositions and omphacites for the more jadeite-rich eclogitic compositions.

4.2.1.3.1 Ca-Fe-Mg

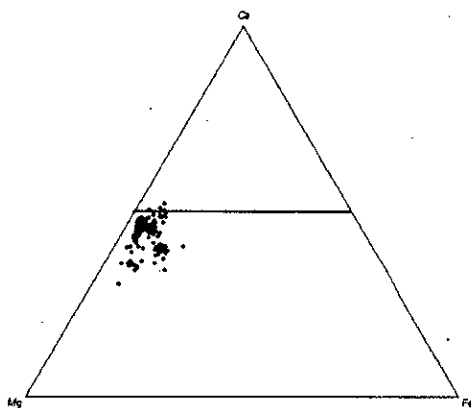
The Ca-Fe-Mg plot is used to classify pyroxenes. Clinopyroxenes occupy the lower trapezium shape of the triangle. The baseline is reserved for orthopyroxenes (see 4.2.1.4). The end members diopside (Di), hedenbergite (Hd), enstatite (En) and .

ferrosilite (Fs) are located at the top left, top right, bottom left and bottom right corners of this trapezium respectively.

(a) NWT



(b) SAK



(c) BWK

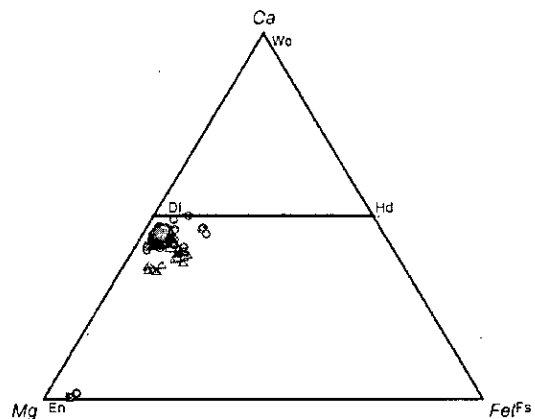


Figure 4.21: (a) Ca-Fe-Mg cation plot of clinopyroxenes from NWT till sampling (n=2155). Wo = wollastonite, Di = diopside, Hd = hedenbergite, En = enstatite and Fs = ferrosilite. (b) as for (a) but for SAK concentrate (n=267). (c) as for (a) but for Newlands (open circle symbols, data from this study, n=119 and KRG database, n=24), Bellsbank (grey square symbols, data from van der Westhuizen (1992), n= 11) and Frank Smith (open triangle symbols, data from KRG database, n=31).

For the most part it is clear that NWT till sampled clinopyroxene (Fig. 4.21a) and SAK concentrate clinopyroxene (Fig. 4.21b) are very close to diopside in composition although there appears to be an upper Mg limit to the data. Newlands and Bellsbank concentrate (Fig. 4.21c) appears to be more closely packed into the diopside corner of the graph with Bellsbank being especially close to diopside in

composition. The Frank Smith concentrate has higher Fe/Mg and Ca/(Fe+Mg) values. Lower temperature crustal clinopyroxenes are probably responsible for the extension to lower Mg/Ca and higher Fe/Mg ratios seen in the NWT till sampling and SAK concentrate.

4.2.1.3.2 ACF

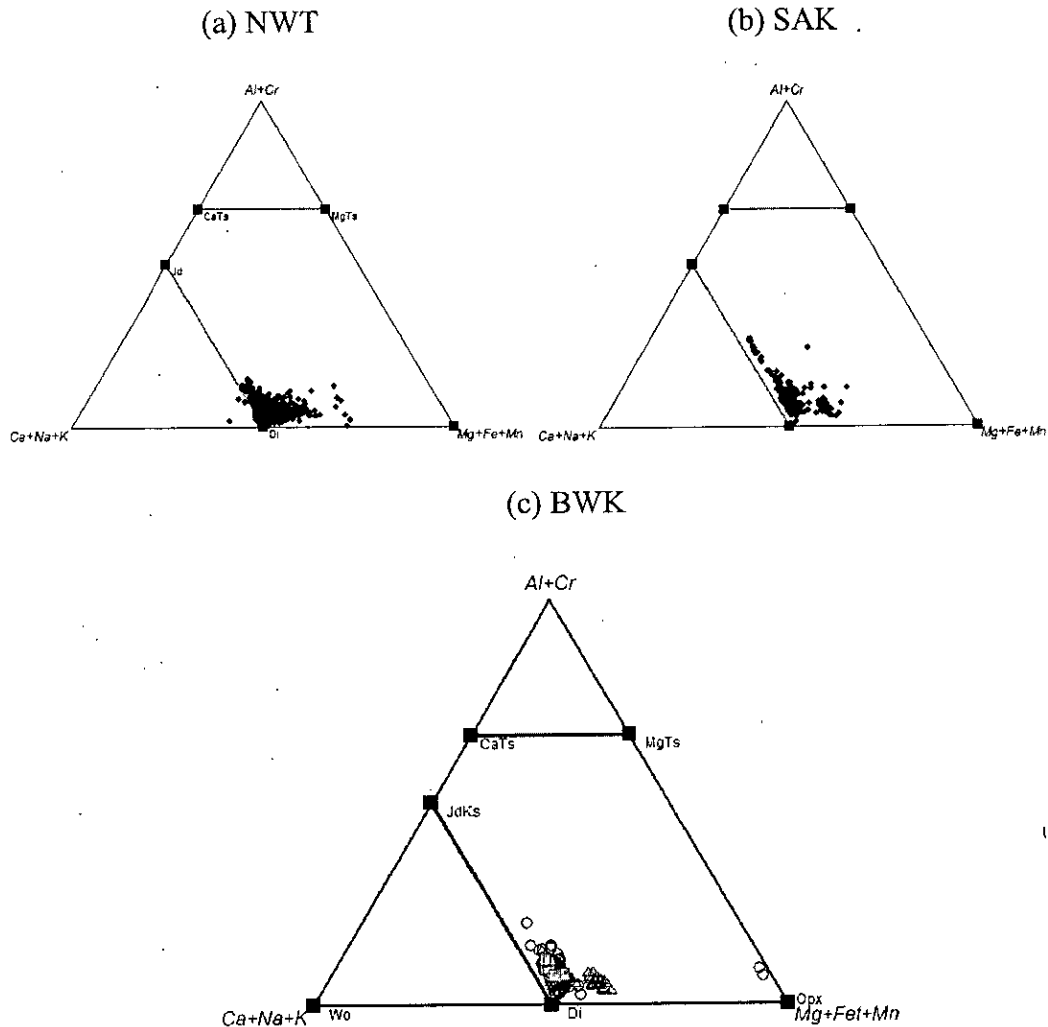


Figure 4.22: (a) ACF cation plot for clinopyroxenes from NWT till sampling. (b) as for (a) but with SAK concentrate plotted. (c) as for (a) except BWK concentrate plotted (symbols as for Fig. 4.21c). JdKs = jadeite-kosmochlor solid solution, Di = diopside, CaTs = Ca-Tschermak's pyroxene end member, MgTs = Mg-Tschermak's pyroxene end member, Opx = enstatite-ferrosilite solid solution and Wo = wollastonite.

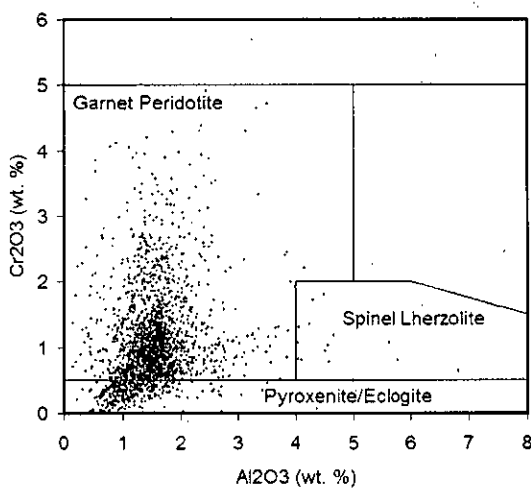
Di-Jd substitution is apparent in all datasets towards omphacitic compositions (those lying on the Jd-Di tie line, Fig. 4.22a-c). A minimum level of Al+Cr is apparent for

the En-Di substitution towards low Ca. Since omphacitic clinopyroxenes are often found in eclogites it is to this paragenesis that these compositions are attributed. The kosmochlor ($\text{NaCrSi}_2\text{O}_6$) end member plots in the same position as jadeite and also forms a component in higher-Na clinopyroxenes. Frank Smith concentrate is lower in Ca+Na+K and higher in Mg+Fe+Mg indicating Mg-Ca substitution (Fig. 4.22c).

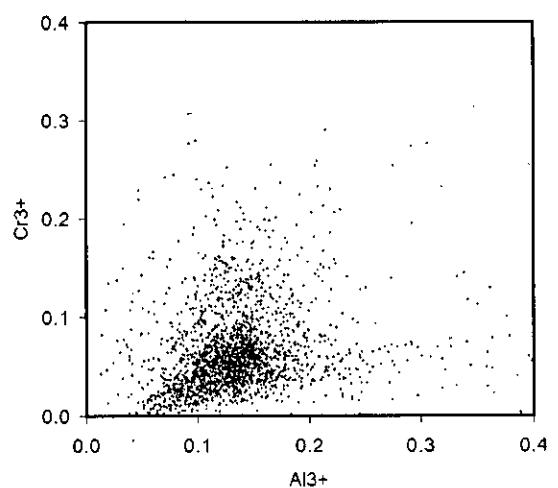
4.2.1.3.3 Al vs. Cr

Ramsay (1992) studied the geochemistry of diamond indicator minerals and classified clinopyroxenes into garnet peridotite, spinel lherzolite and low-Cr compositional fields according to their Al and Cr content. Fig. 4.23a shows how NWT till clinopyroxenes fall mainly into the garnet peridotite field at elevated Cr/Al and eclogite across low-Cr compositions. Hence two positively correlated trends emerge, one towards high-Cr and the other towards high-Al. Garnet peridotite and eclogite clinopyroxenes are present in the Barkly West kimberlites (Fig. 4.23c) with Newlands and Bobbejaan possessing the highest Cr_2O_3 and Al_2O_3 concentrations, high even compared to the more numerous dataset in 4.23a. The cation plot for the same data as that in Fig. 4.23a is shown in Fig. 4.23b, and a similar spatial organisation can be seen. Fig. 4.23d shows the cation values for SAK concentrate where a more L-shaped distribution can be seen.

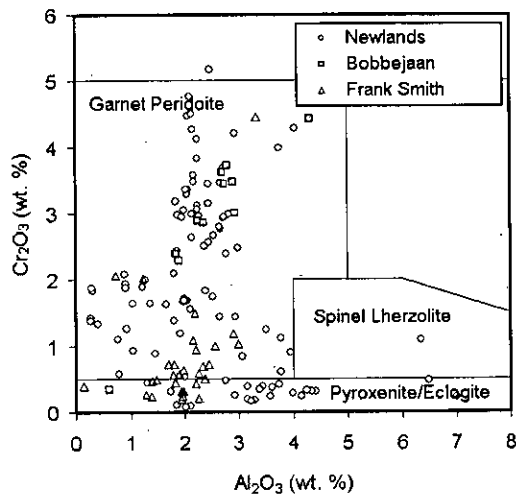
(a) NWT



(b) NWT



(c) BWK



(d) SAK

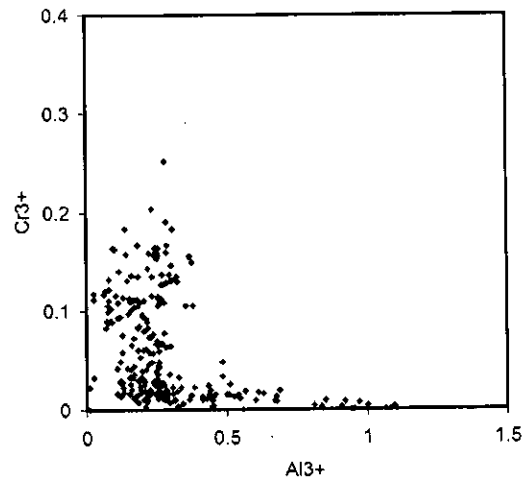
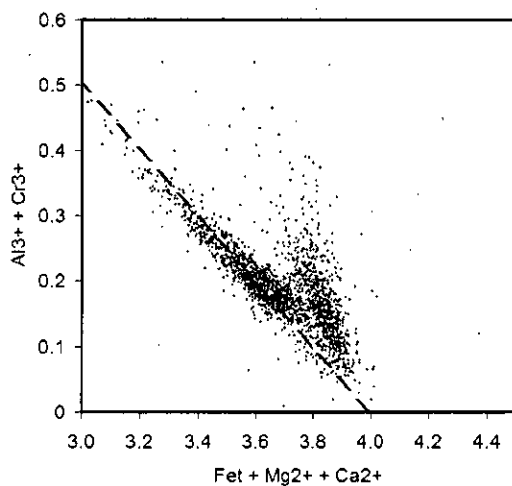


Figure 4.23: (a) Al_2O_3 vs. Cr_2O_3 wt. % plot with fields from Ramsay (1992), for NWT till clinopyroxenes. (b) as for (a) except Al vs. Cr cations are plotted where cations are summed to 8. (c) as for (a) except BWK concentrate plotted. (d) as for (b) except clinopyroxenes from SAK concentrate plotted.

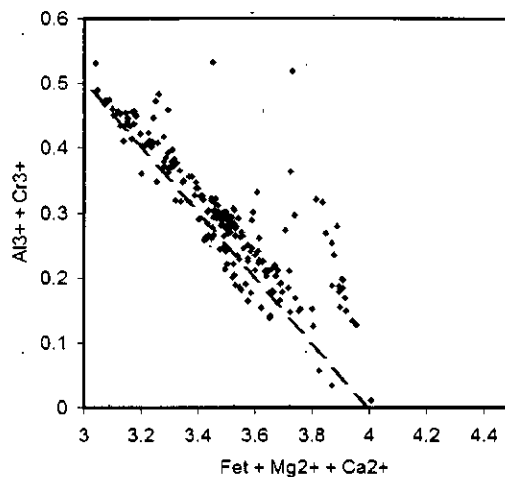
4.2.1.3.4 2+ cations vs. 3+ cations

Two groupings of clinopyroxenes are apparent from the plots in Fig. 4.24. The first trend lies along a 2:1 (2+:3+ ratio) mixing line that would be expected for a tschermakitic substitution (i.e. for every 3+ ion substituted and an accompanying Na^+ , two 2+ ions would be required to balance the charge, hence the negative 2:1 trend as shown). The area of data to higher 2+ ion values lies on a 1:1 line forming a trend which corresponds to a sharper rise in 3+ ions with reduction of 2+ ions as shown in the ACF diagram (Fig. 4.22a) associated with tschermakitic substitution. Fig. 4.24b shows how southern African kimberlite concentrate has a trend of pronounced jadeitic substitution which is also seen at Newlands and Bellsbank kimberlites (Fig. 4.24c). Frank Smith has a higher proportion of clinopyroxenes away from this main trend.

(a) NWT



(b) SAK



(c) BWK

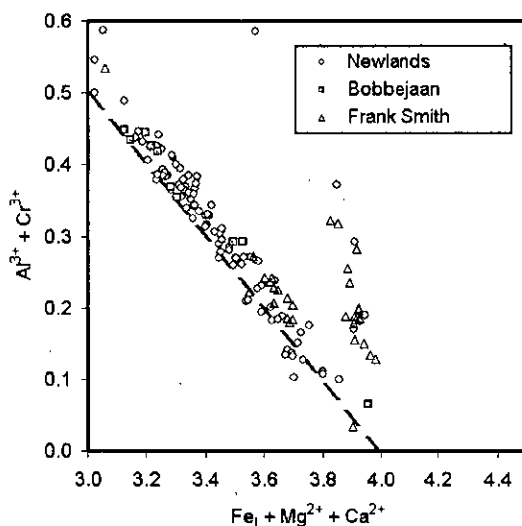


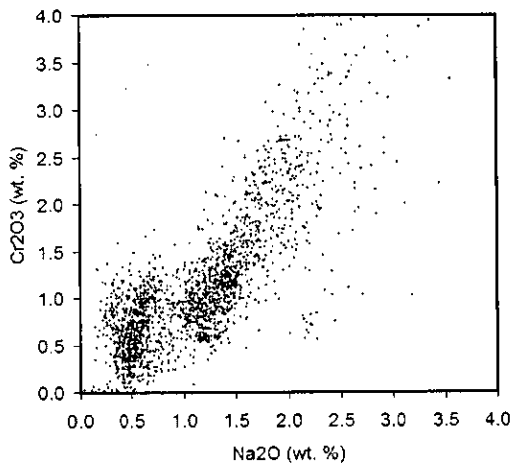
Figure 4.24: (a) $\text{Fe} + \text{Mg}^{2+} + \text{Ca}^{2+}$ cations vs. $\text{Al}^{3+} + \text{Cr}^{3+}$ cations for clinopyroxene concentrate from NWT till sampling, 1:2 trend line shown. (b) as for (a) but with SAK concentrate plotted. (c) as for (a) but with BWK concentrate plotted.

4.2.1.3.5 1+ ions vs. 3+ ions

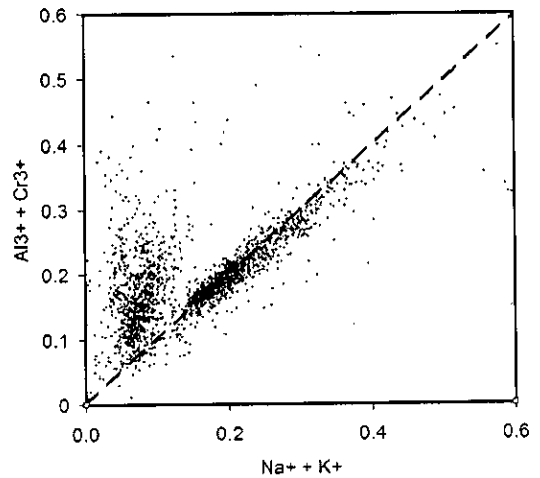
Jadeite + kosmochlor substitution is picked out as a positive 1:1 line on a Na^+ vs. $\text{Cr}^{3+} + \text{Al}^{3+}$ plot. One of the two main clusters in the NWT concentrate conforms to this line well (Fig. 4.25b) with the other cluster forming above the line to higher Cr +

Al values (see discussion in samples section 4.3.3). This feature is not observed as clearly using a weight percent plot (Fig. 4.25a). SAK concentrate in Fig. 4.25c (including the Barkly West kimberlites, Fig. 4.25d) also conform to this line but with a higher degree of scatter that may be attributed to inaccuracies in electron probe Na determination for Na + K plots.

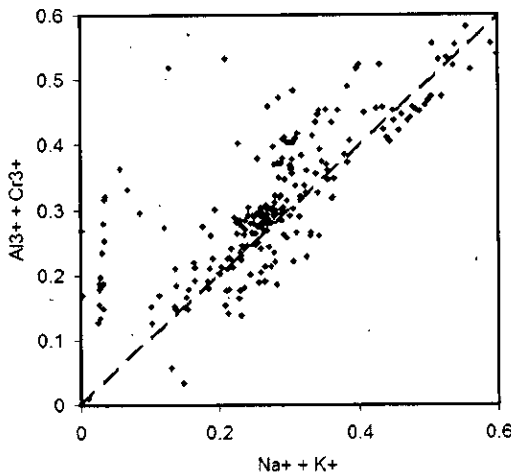
(a) NWT



(b) NWT



(c) SAK



(d) BWK

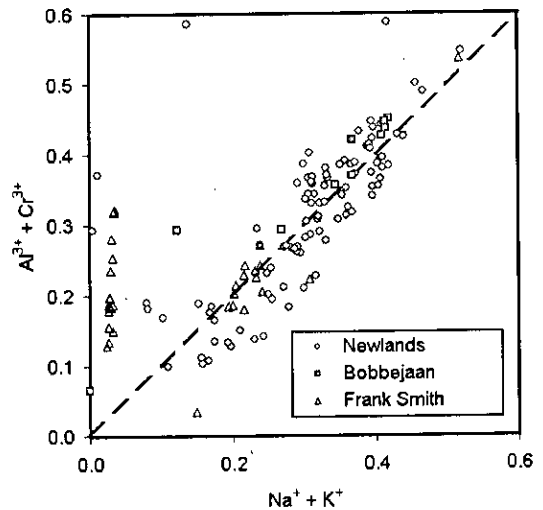
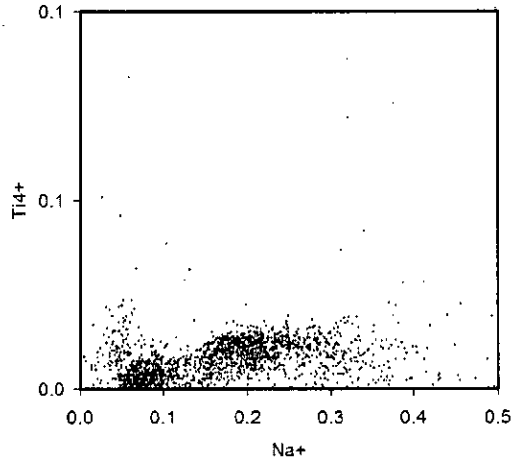


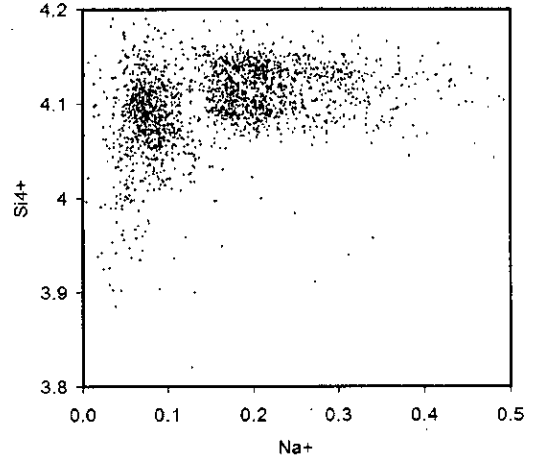
Figure 4.25: (a) Na_2O vs. Cr_2O_3 wt. % plot for clinopyroxenes (b) $\text{Na}^+ + \text{K}^+$ cations vs. $\text{Al}^{3+} + \text{Cr}^{3+}$ cations for clinopyroxene concentrate from NWT till sampling, 1:1 trend line shown. (c) as for (b) but with SAK concentrate plotted. (d) as for (b) but with BWK concentrate plotted.

4.2.1.3.6 Na vs. Ti and Si

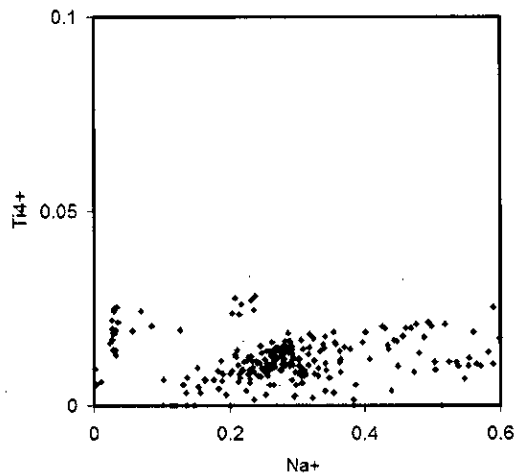
(a) NWT



(b) NWT



(c) SAK



(d) BWK

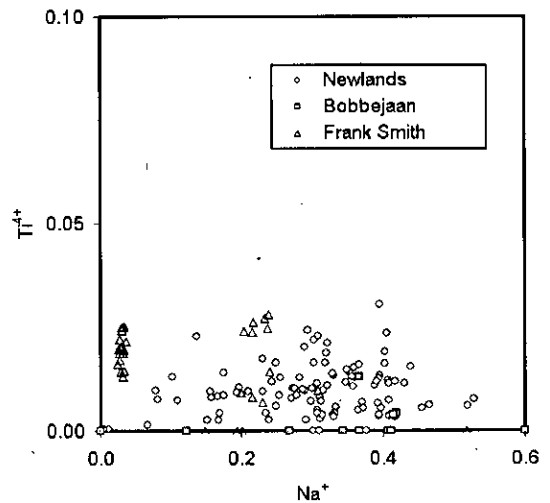
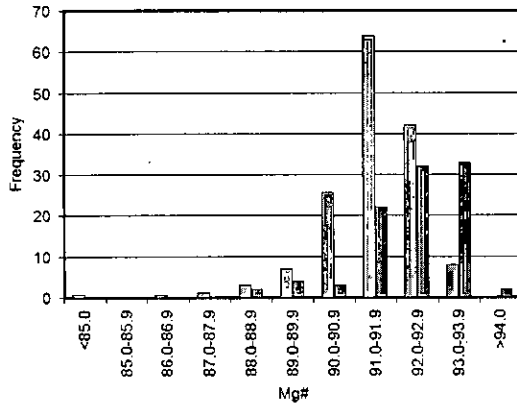


Figure 4.26: (a) Na^+ vs. Ti^{4+} for NWT till sampling clinopyroxene concentrate (b) as for (a) except Si^{4+} vs. Ti^{4+} . (c) as for (a) except plotting data from SAK. (d) as for (a) except plotting BWK concentrate clinopyroxenes.

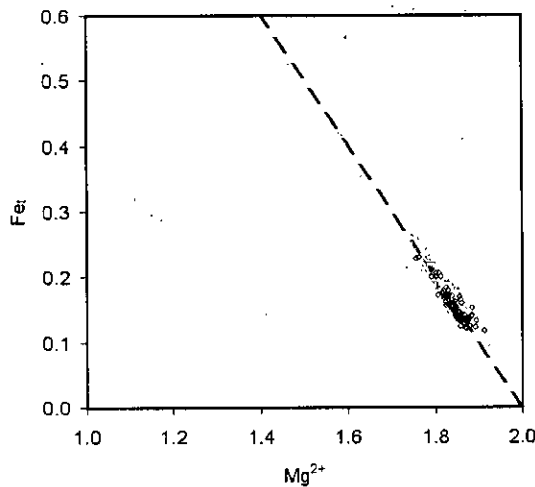
No clear relationships exist between Na and Ti or Si, although a slight positive correlation between Na and Ti may be seen in NWT and SAK concentrate (Fig.4.26a-d).

4.2.1.4 OLIVINE

(a)



(b)



(c)

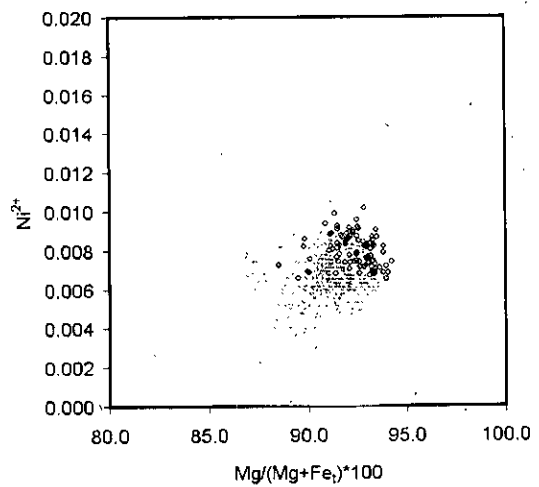


Figure 4.27: (a) Olivine Mg# ($Mg/(Mg+Fe) \cdot 100$ (cations calculated on an 8 cation basis) vs. frequency of occurrence for NWT till sampling olivines (grey points, $n=1219$) and for Newlands kimberlite concentrate olivines (open black diamond symbols, $n=98$). (b) dataset as for (a) but Mg²⁺ vs. Fet cations. (c) as for (a) except Mg# vs. Ni²⁺ cations.

Newlands concentrate olivines have a bias towards a high Mg# (Fig. 4.27a) with a large proportion of olivines falling in between Mg# 93 and 94 ($\bar{x} = 92.36$), whereas NWT olivines have a large proportion falling between Mg# 91 and 92 ($\bar{x} = 91.51$). This can also be seen on the Mg-Fe cation plot (Fig. 4.27b) with Newlands olivines

plotting at the high-Mg, low-Fe end of the 1:1 substitution line. All olivines adhere to the Fe-Mg 1:1 negative correlation, hence only very minor substitutions such as with Ni may be anticipated. No relationship was found given the accuracy of the electron microprobe for Cr, Al or Ca in olivine.

4.2.1.5 ORTHOPYROXENE

In a similar way to the olivine concentrate, the Newlands orthopyroxene concentrate has a higher average $Mg/(Mg+Fe)*100$ of 93.22 than the NWT till (Fig. 4.28b) ($\bar{x} = 92.98$). SAK has $\bar{x} = 92.25$. Values are higher than for olivine with most orthopyroxene being 92-94 $Mg/(Mg+Fe)*100$. The diamond inclusion field of Fipke et al. (1995) is shown based on Al_2O_3 and $Mg/(Mg+Fe)$ in Fig. 4.28a. All datasets have a trend extending to high Al_2O_3 wt. % values at approximately constant $Mg/(Mg+Fe)$. The southern African dataset is the only one to have a definite trend at ~ 1 wt. % Al_2O_3 to lower values of $Mg/(Mg+Fe)$. The NWT dataset has the lowest Al_2O_3 value whilst at $Mg/(Mg+Fe)*100$ of 93, locating a large proportion of the dataset within the diamond inclusion field.

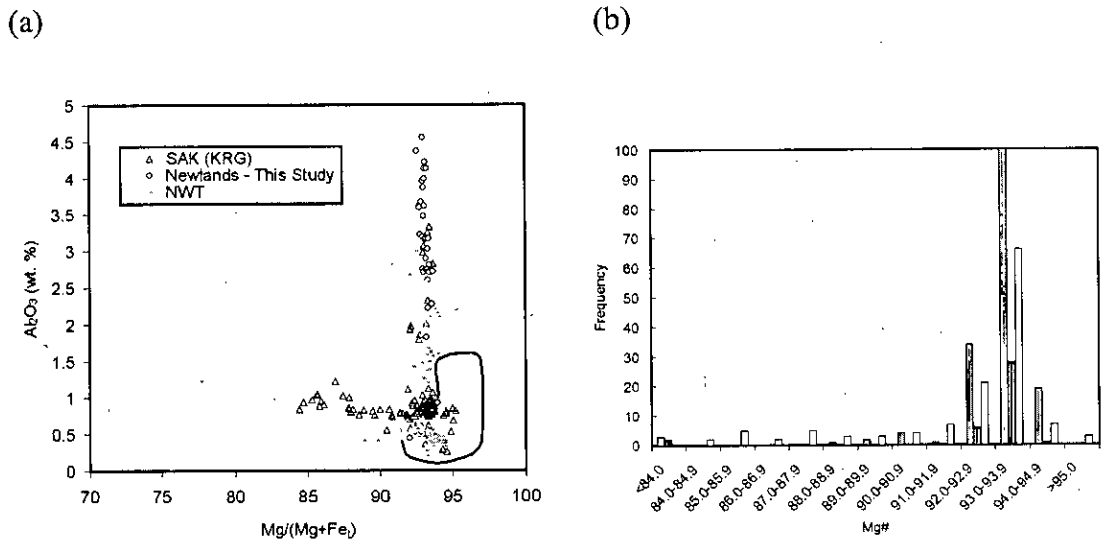


Figure 4.28: (a) $Mg\#$ ($Mg/(Mg+Fe)*100$ cations) vs. Al_2O_3 wt. % for orthopyroxene concentrate from NWT till sampling ($n=363$), SAK concentrate ($n=127$) and Newlands kimberlite concentrate ($n=36$). Diamond inclusion field is outlined in a solid black line of Fipke et al. (1995). (b) $Mg\#$ groups vs. frequency for the same dataset as (a). Medium grey is NWT till sampling, dark grey is Newlands orthopyroxene concentrate from this study and light grey is SAK concentrate orthopyroxene.

4.2.1.5.1 2+ and 3+ ions

Fig. 4.29a shows a positive correlation between Cr^{3+} and Al^{3+} , of $\sim 1:5$ ratio in all orthopyroxene concentrate. A negative trend can be seen when comparing 3+ ions to 2+ ions indicating the presence of a jadeitic style of substitution as evident in the extension of the cluster in the ACF diagram (Fig. 4.29b). Some of the SAK analyses are low and scattered since they are likely to be below detection limits for the analysis setup (Appendix I).

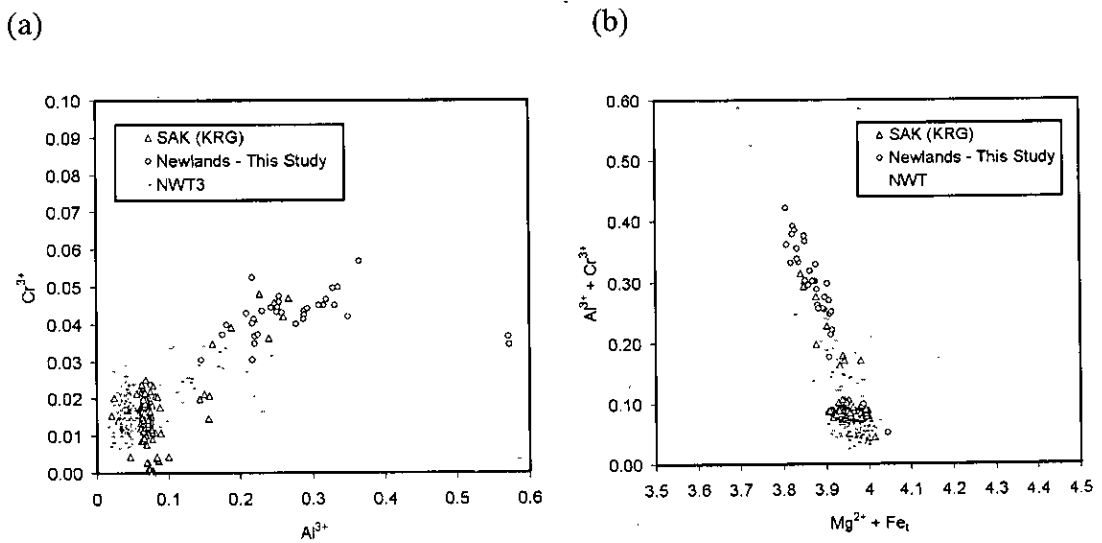


Figure 4.29: (a) Al^{3+} vs. Cr^{3+} cations for orthopyroxene concentrate. (b) $(\text{Mg}^{2+} + \text{Fe}_t)$ vs. $(\text{Cr}^{3+} + \text{Al}^{3+})$ cations for the same datasets as (a).

4.2.1.5.2 ACF & CFM

Orthopyroxene from concentrate plots close to the baseline of the pyroxene quadrilateral with a range in $\text{Mg}/(\text{Mg} + \text{Fe})$ from 0.85 to 0.94 (Fig. 4.30a). Suggestion of MgTs, CaTs and small JdKs substitutions away from En end member are apparent especially in the southern African dataset (Fig. 4.30b and c).

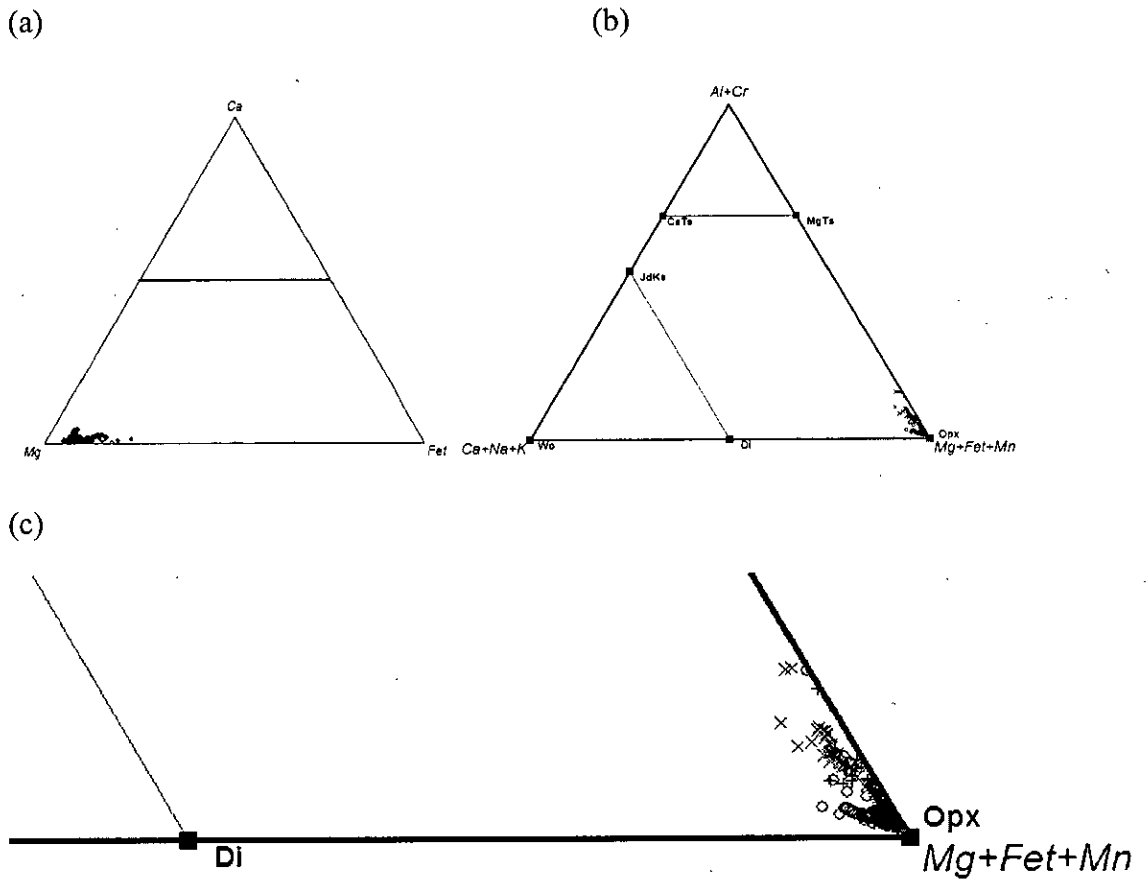


Figure 4.30: (a) Ca-Fet-Mg cation plot (calculated by summing to 8 cations) illustrating the range of compositions for orthopyroxenes from all available concentrate. (b) ACF (Al+Cr, Ca+Na+K and Mg+Fe_T+Mn) plot for orthopyroxene. (c) zoom of Mg+Fe+Mg apex in (b). 'x' symbols are for SAK concentrate (KRG database), open circles are Newlands kimberlite concentrate from this study and '+' symbol are NWT till orthopyroxene compositions.

4.3 Major Element Composition of the Newlands, Bobbejaan and Leicester Composite Samples

The samples were all collected from heavy concentrate piles at diamond mines and the spread of compositions observed at each locality is expected to reflect the concentrate compositions from that particular kimberlite (see section 4.2). The primary sample selection bias was in favour of garnet-rich samples with purple garnets and against red or orange colours.

4.3.1 Garnet

Fig. 4.31 shows how lherzolitic and harzburgitic sample affinity correlates to the composition of the samples in Cr-Ca space from each kimberlite. Lherzolites are confined to the high-Ca side of the lherzolite line (LL), except for a few cases in Newlands samples where G10 garnet compositions had clinopyroxene present. This presents a case for caution to be used when referring to a 'lherzolite line' and using the term 'G10' synonymously with harzburgitic garnet. At Newlands and Bobbejaan there are cases where apparently harzburgitic samples plot clearly within the G9 field. This is justified since, as mentioned in Chapter 3, there may be a few cases where clinopyroxene is present in a sample but not exposed at the analysis surface and not visible on the outer surface.

All kimberlites studied have some, inclusion-free, monogranular garnets types. The Leicester samples are predominantly of this type, presumably because of their small size. Only a single polyphase sample was analysed and this contained clinopyroxene and is therefore lherzolitic in affinity. It would be expected that all the Leicester samples are lherzolitic given their G9 affinity. The Newlands and Bobbejaan samples have many of their inclusion-free monogranular garnet samples (yellow symbols Fig. 4.31) plotting very close to the lherzolite line. They therefore effectively straddle lherzolite/harzburgite affinity. Few samples of this type plot in the G10 field; these

are usually small samples and might be too small to display any coexisting mineral in the same way that most of the Leicester samples probably do.

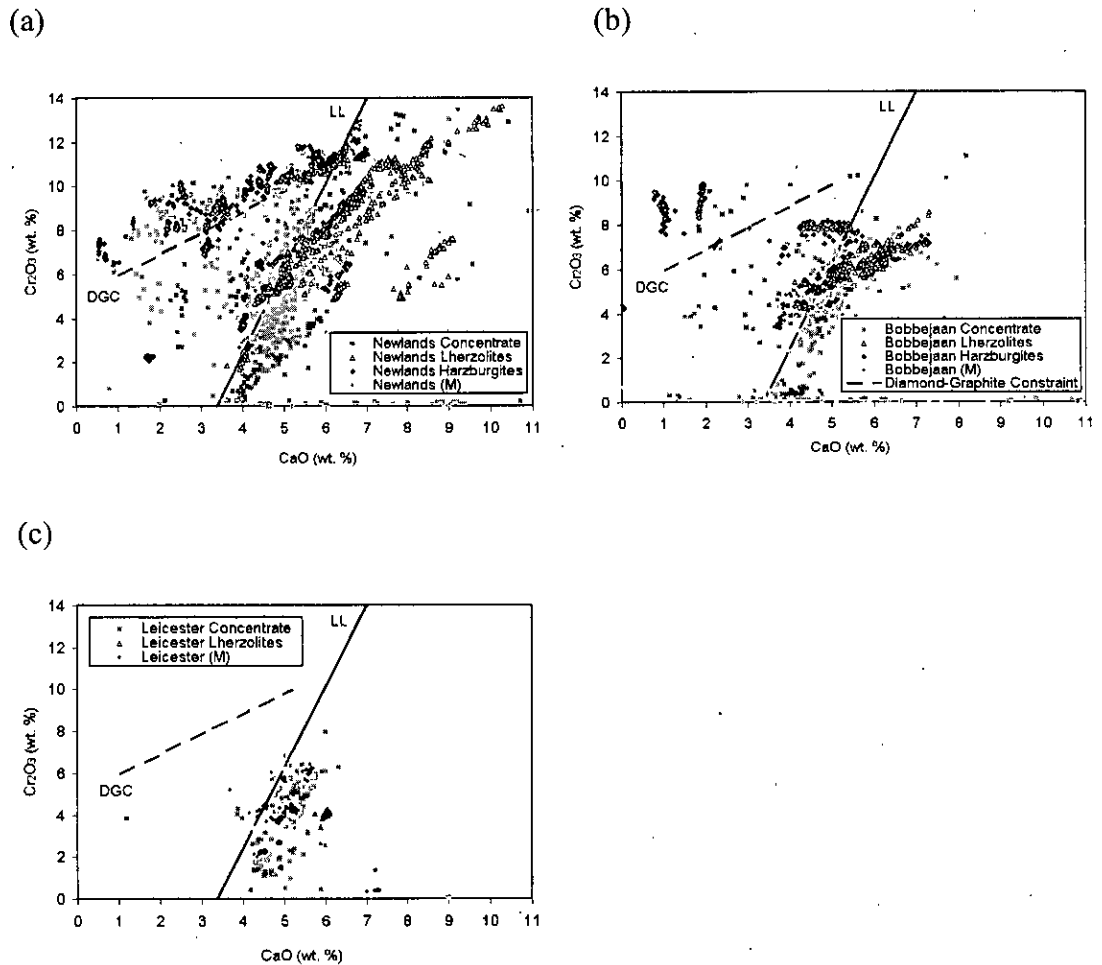


Figure 4.31: Garnet Cr_2O_3 vs. CaO wt. % diagrams showing analyses of Newlands (a), Bobbejaan (b) and Leicester (c) samples relative to concentrate compositions from those kimberlites. 'M' denotes the monogranular garnets with no inclusions (classified as M in chapter 3). Reference lines of Gurney (1984) (LL = Iherzolite line) and Grütter et al. (2004) (DGC = diamond-graphite constraint) are shown.

Compared to the Newlands concentrate shown in Fig. 4.31a the Newlands samples are evidently displaced towards the high-Cr parts of the range of compositions present at the kimberlite. A shallow positive slope is present in the G10 field where few garnets plot below the diamond-graphite constraint. A steeper trend is present in the G9 field with the samples occupying the high-Cr regions of the large G9 cluster evident in the concentrate. High-Cr, high-Ca Iherzolites are particularly well

represented at Newlands compared to other kimberlites worldwide. Two features associated with these have not been reported from other kimberlites:

- 1) A continuum of compositions connects the high-Cr, high-Ca concentrate garnets to the high-Cr parts of the dense lherzolite cluster.
- 2) Garnets at the top of the 'harzburgitic trend' (6-7 wt. % CaO and 10-13 wt. % Cr₂O₃) straddle the 85% line and appear to be associated with high-Cr, high-Ca garnets forming another potential continuum in compositional space.

Garnets from Bellsbank samples conform well to Cr-rich concentrate with fewer samples of the high-Cr, high-Ca nature described at Newlands. A harzburgitic trend is present but only 2-3 samples were found with garnets of these compositions. Leicester samples relate to relatively Cr-rich G9 concentrate but these compositions would form only the very lowest Cr garnets from Newlands and Bobbejaan.

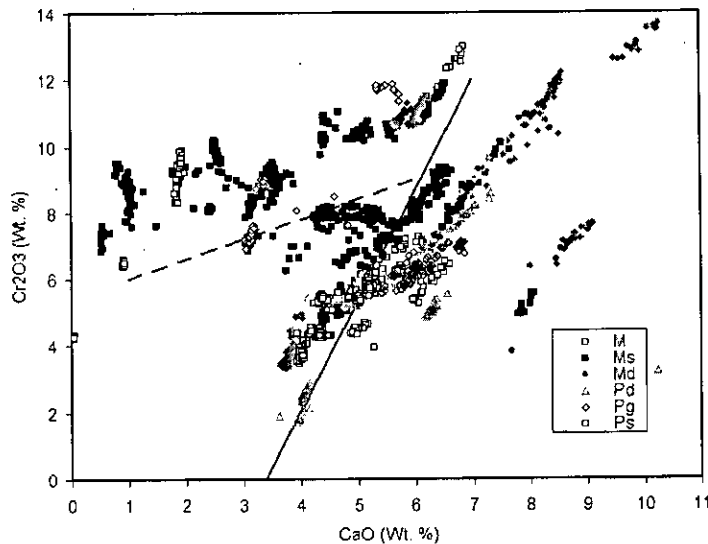


Figure 4.32: Sample type (Chapter 3) compared to garnet CaO vs Cr₂O₃ wt. % composition for Newlands and Bobbejaan samples.

Sample type does not appear to show any correspondence with garnet composition in samples (Fig. 4.32) except that clinopyroxene-bearing samples (Md and Pd) tend to plot more frequently in the G9 field as seen in Fig. 4.31. This indicates that polygranular and monogranular garnet samples are not chemically different.

4.3.2 Cr-spinel

The samples form a broadly positive Cr-Mg slope in Fig. 4.33a indicating a depletion trend towards high-Cr and high-Mg concentrations. The harzburgites from Newlands and Bobbejaan samples tend to plot at the more depleted part of this trend with most occurring within the diamond inclusion field. The one harzburgitic Cr-spinel from Newlands that plots at a lower Cr_2O_3 concentration can be seen to be of higher TiO_2 (Fig. 4.33b indicating a different) paragenesis (probably affected by kimberlitic fluids). Cr-spinels from clinopyroxene-bearing (lherzolitic) samples from Newlands and Bobbejaan plot at lower Cr_2O_3 and MgO concentrations, including several within the diamond inclusion field. It can be seen from Fig. 4.33b that the lherzolitic samples are also higher in TiO_2 and not within the diamond inclusion field. Cr-spinels do not have differing compositions dependent on whether they are in the matrix or as inclusions in garnet.

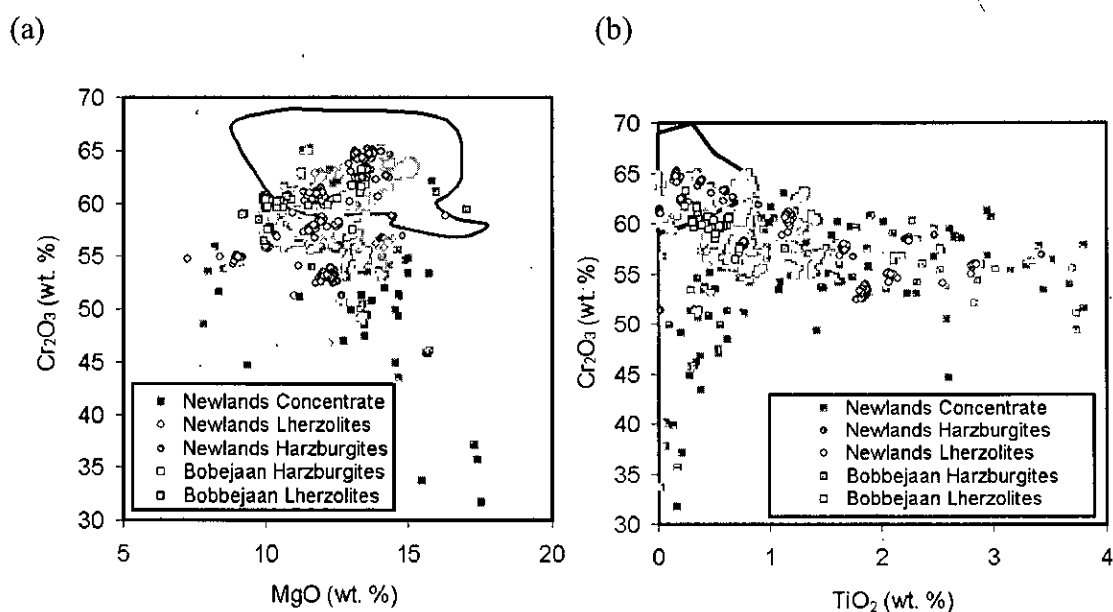


Figure 4.33: (a) MgO vs. Cr_2O_3 wt. % plot for chromites in samples from Newlands and Bobbejaan kimberlites compared to the Newlands chromite concentrate. (b) as for (a) except TiO_2 vs. Cr_2O_3 wt. % plotted. The diamond inclusion field of Fipke et al. (1995) is shown in each case as a solid black line.

4.3.3 Clinopyroxene

Lherzolitic samples from Newlands and Bobbejaan have clinopyroxene compositions in the ‘garnet peridotite’ field of Ramsay (1992) and conform to peridotitic concentrate compositions (Fig. 4.34a). Fig. 4.34b illustrates that the samples (which are petrographically peridotitic, see Chapter 3) fall along the Jd_{50} - Ks_{50} substitution line, which conforms to the kimberlitic ‘sheared nodules’ and ‘granular nodules’ fields of Kornprobst (1981). This field has tentatively been encircled and named ‘peridotitic’.

The ‘discrete nodules’ field of Kornprobst (1981) appears to contain eclogitic and megacrystic compositions with pronounced jadeitic substitution, hence the ‘E’ field encircled in Fig. 4.34b defined predominantly by the SAK concentrate. NWT concentrate is the only dataset to generate a low-Na, low-Cr cluster and is labelled ‘C’ for crustal clinopyroxenes. This field conforms to a small part of the ‘sub-oceanic’ field of Kornprobst (1981).

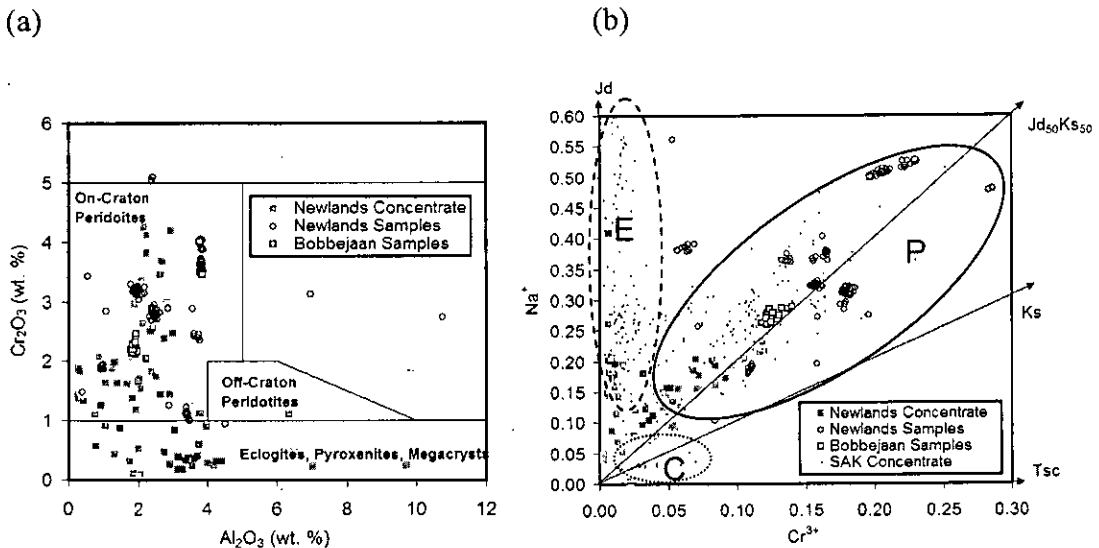


Figure 4.34: (a) Al_2O_3 vs. Cr_2O_3 wt. % plot for clinopyroxenes in samples from Newlands and Bobbejaan compared to Newlands clinopyroxene concentrate. (b) Cr vs. Na cation plot for Newlands samples, Bobbejaan samples compared to Newlands and SAK clinopyroxenes from kimberlite concentrate. Jd = jadeite substitution along Na axis, Jd_{50} - Ks_{50} = 50 % jadeite, 50 % kosmochlor substitution line, Ks = kosmochlor substitution line and Tsc Ca-Cr Tschermak’s molecule substitution along Cr axis. Approximate fields indicating peridotitic compositions (oval, solid line labelled ‘P’),

eclogitic and megacryst suite compositions (oval, dashed line labelled 'E') and megacryst compositions (oval, dotted line labelled C) have been inserted on inspection.

4.4. Summary

4.4.1 General observations

The use of several different electron microprobes under different analytical conditions in collection of the datasets described has necessitated the need to observe the data critically. The emergent features are as follows:

- 1) ~150-200 analyses per concentrate phase are required in a dataset to show the extent and clustering of major element compositions present.
- 2) Cation plots of compositional parameters are preferable to weight percent plots for assessment of mineral elemental constituents. However garnet CaO vs Cr₂O₃ and spinel MgO vs Cr₂O₃ weight % plots provide spatially very similar plots to the equivalent cation versions (see Figs. 4.1, 4.15 and 4.16).
- 3) Due to the diverse heavy mineral sources present in northwest Canada, NWT till concentrate provided a useful standard with which to compare southern African kimberlite and individual kimberlite concentrates. Additionally this dataset is particularly numerous but contains some poor analysis data points. Na-in-garnet seems to be too high compared to existing data.
- 4) Cr-Ca plots discriminate the peridotitic garnet classes of table 1 the most effectively. This is because the Cr correlates negatively with Al and Ca with Mg, which covers variation in the four most variable elements in mantle garnets leaving only Ti unaccounted for.

4.4.2 Garnet

- 1) Southern African diamondiferous kimberlite (SAK) garnet concentrate has major element compositions slightly higher in Cr compared to the Northwest Territories dataset (NWT) (Fig. 4.3a and b). SAK also has far fewer crustal garnets.

- 2) Of the Barkly West kimberlites Newlands and Bobbejaan garnets appear markedly higher in Cr, on average, compared to the NWT and SAK datasets (Fig. 4.4) and hence have higher proportions of G10 garnets (Fig. 4.5). Leicester is unique in having such high prevalence of G9 garnets (Fig. 4.5). Frank Smith is similar to the NWT and SAK datasets (Fig. 4.5) but has a higher proportion of G1 garnets.
- 3) All concentrate datasets have a cluster of G9 garnets with a positive Cr:Ca slope. SAK and NWT have significant proportions of G10 garnets but Newlands kimberlite concentrate is the only dataset to have a well defined cluster of G10 garnets at high-Cr (Fig. 4.3c).
- 4) Newlands and Bobbejaan samples have garnet compositions that are effectively a subset of compositions defined by concentrate from the two kimberlites. The samples are however biased to the high-Cr part of this spread of data, which is most probably due to original sampling bias towards samples with garnets that have a purple colour, avoiding orange, eclogitic and red, megacryst suite garnets.

4.4.3 Cr-spinel

- 1) SAK spinels are more Cr- and Mg-rich compared to NWT and BWK concentrate (Fig. 4.15a-c), hence high in magnesiochromite end member. The Dokolwayo spinels are exceptionally Cr-rich (Fig. 4.15b) reaching Cr₂O₃ wt. % concentrations > 70.
- 2) Newlands is the only individual locality to have an extension of spinel concentrate towards the Mg-rich part of the diamond inclusion field (Fig. 4.15d). Other BWK concentrate conforms to a subset of SAK concentrate.
- 3) Newlands and Bobbejaan harzburgitic samples plot to higher Mg and Cr compositions. Most lherzolithic samples do not plot in the diamond inclusion field when both Mg, Cr and Ti are taken into account (Fig. 4.33a and b).
- 4) An ulvöspinel substitution is evident in concentrate spinels (Fig. 4.19) which is responsible for the Ti variation.

4.4.4 Clinopyroxene

- 1) The ACF plot (Fig. 4.22) reveals that SAK has a population of clinopyroxenes with a more pronounced jadeite substitution trend than other datasets.
- 2) The jadeite + kosmochlor substitution is particularly visible on Na + K vs. Al + Cr plot as a 1:1 line (Fig. 4.25).
- 3) Tentative discrimination between peridotitic and eclogitic clinopyroxenes has been made on a Cr vs. Na plot (Fig. 4.34b). This discrimination appears to be more appropriate on a Cr vs. Na plot than on the more common Al₂O₃ vs. Cr₂O₃ wt. % plot.
- 4) Newlands and Bobbejaan clinopyroxene concentrate plots at high-Cr compared to NWT and SAK concentrate (Fig. 4.23).
- 5) 90 % of clinopyroxene in samples from this study plot in the garnet peridotite field of Ramsay (1992) (Fig. 4.34) which forms a cluster at 2-3 wt. % Cr₂O₃.

4.4.5 Olivine and orthopyroxene

Newlands olivine and concentrate has higher Mg/(Mg+Fe) values on average compared to NWT dataset; Newlands has an average of 92.36 Mg/(Mg+Fe)*100 cations whereas the NWT value is 91.51 (Fig. 4.27). Average Newlands orthopyroxene Mg/(Mg+Fe)*100 is 93.22, NWT = 92.98 and SAK is 92.25. Most orthopyroxene at Newlands and in the NWT and SAK datasets are between 93 and 94 Mg/(Mg+Fe)*100 cations (Fig. 4.28b) with NWT and SAK having a larger spread of data towards sub-90 values. A jadeitic substitution trend is evident in orthopyroxene concentrate (Fig. 4.29).

4.5 References

- Barnes, S. J. and Roeder, P. L. (2001). The range of spinel compositions in terrestrial mafic and ultramafic rocks. *Journal of Petrology*. **42**. 2279-2302.
- Daniels, L. R. M. (1991). Diamonds and related minerals from the Dokolwayo kimberlite, Kingdom of Swaziland. Department of Geological Sciences. Cape Town. University of Cape Town. *Unpublished PhD*

- Dawson, J. B. and Stephens, W. E. (1975). Statistical classification of garnets from kimberlite and associated xenoliths. *Journal of Geology*. **83**. 589-607.
- Deer, W. A., Howie, R. A. and Zussman, J. (1962). *Rock Forming Minerals*. London, Longmans.
- Droop, G. T. R. (1987). A general equation for estimating Fe^{3+} concentrations in ferromagnesian silicates and oxides from microprobe analyses, using stoichiometric criteria. *Mineralogical Magazine*. **51**. 431-435.
- Fipke, C. E., Gurney, J. J. and Moore, R. O. (1995). Diamond exploration techniques emphasising indicator mineral geochemistry and Canadian examples. *Geological Survey of Canada*. **423**. 1-86.
- Grütter, H. S., Gurney, J. J., Menzies, A. H. and Winter, F. (2004). An updated classification scheme for mantle-derived garnet, for use by diamond explorers. *Lithos*. **77**. 841-857.
- Gurney, J. J. (1984). A correlation between garnets and diamonds in kimberlites. In: Ed. Glover, J. E., Harris, P. G. *Kimberlites: Occurrence and origin: A basis for conceptual models in exploration*. Perth, University of Western Australia, Extension Services. **8**. 143-166.
- Kornprobst, J. (1981). Na and Cr contents in clinopyroxenes from peridotites: A possible discriminant between "sub-continental" and "sub-oceanic" mantle. *Earth and Planetary Science Letters*. **53**. 241-254.
- Menzies, A. (2001). A detailed investigation into diamond-bearing xenoliths from Newlands kimberlite, South Africa. Department of Geological Sciences. Cape Town. University of Cape Town. *Unpublished PhD Thesis*
- Ramsay, R. R. (1992). *Geochemistry of diamond indicator minerals*. Perth. University of Western Australia. *Unpublished PhD*
- Rickwood, P. C. (1968). On recasting analyses of garnet into end-member molecules. *Contributions to Mineralogy & Petrology*. **18**. 175-198.
- Ryburn, R. J., Råheim, A. and Green, D. H. (1975). Determination of P,T paths of natural eclogites during metamorphism - record of subduction. *Lithos*. **9**. 161-164.
- Schulze, D. J. (2003). A classification scheme for mantle-derived garnets in kimberlite: a tool for investigating the mantle and exploring for diamonds. *Lithos*. **71**. 195-213.
- van der Westhuizen, A. (1992). The Bellsbank kimberlites, with special reference to a suite of purple garnet megacrysts from the Bobbejaan mine. University of the Orange Free State. *Unpublished Masters Thesis*
- Viljoen, F., Robinson, D. N., Swash, P. M., Griffin, W. L., Otter, M. L., Ryan, C. G. and Win, T. T. (1994). Diamond- and graphite-bearing peridotite xenoliths from the Roberts Victor kimberlite, South Africa. 5th International Kimberlite Conference, South Africa, CPRM. 285-303.

5. Major Element Zonation Patterns in Minerals

5.1 Objectives

In this chapter empirical observations are made based on spatial major element data collected for the Newlands and Bobbejaan samples. Interpretations are presented in subsequent chapters. For details on the electron microprobe analysis (EMPA) technique see Appendix I.

Samples were selected for EMPA using petrographic criteria such as large size and multi-mineral assemblages (see Chapter 3). Initially spot analyses of cores and rims were made. Samples with any significant chemical variation were then analysed on a smaller scale by means of a finely-spaced electron microprobe traverse. From petrographic information and traverses certain samples exhibiting a variety of chemical trends were selected for 5-element, X-Ray mapping. Some X-ray maps revealed areas of zonation that were not captured by previous traverses. These particular areas were targeted for extra traverses, thus recording the additional variation.

The main aims of the major element analysis programme of larger samples (i.e. not kimberlite concentrate) was to: (1) identify garnet-rich samples whose compositions are analogous to those of the harzburgitic diamond inclusion suite; (2) define chemical differences in garnets and chromites in harzburgitic and lherzolitic samples; (3) determine the direction of any zonation trends and relate them to trends found by other workers e.g. Griffin et al. (1999b) and Burgess and Harte (1999); (4) analyse clinopyroxenes, where possible; (5) use this information to make an overall assessment of garnet-chromite equilibria for the harzburgites and garnet-chromite-clinopyroxene equilibria for lherzolites; (6) to provide a framework for the interpretation of trace element analyses. In no case was it possible to obtain good analyses of orthopyroxene and olivine because they have been serpentinised in the Newlands and Bobbejaan samples (see Chapter 3).

5.2 Garnet Zonation Patterns

Analyses of garnets by means of electron microprobe traverses are presented as profiles in Appendix II showing distance (μm) vs. cation concentrations for traverses with > 10 analysis points. Chromite and clinopyroxene profiles are discussed in the next section and are also shown in Appendix II (see data CD). Accompanying X-ray maps were made for certain samples and are presented in Appendix III (see data CD). Figures from both of these Appendices will be referred to in the text in order to illustrate zonation in minerals from the garnet-rich samples.

5.2.1 Overall variety of garnet zonation patterns

A total of 72 samples from Newlands, 27 from Bobbejaan and 12 from Leicester were analysed by means of selected linear traverses (in some cases over 3 traverses per sample) across parts of samples. The traverses were chosen to record garnet core-rim compositional trends so that in polygranular (and potentially in many monogranular) garnet samples a core-to-matrix trend was recorded. Monogranular and polygranular garnet samples with included phases (namely serpentine, Cr-diopside and Cr-spinel) were analysed along traverses towards inclusions. Analyses of inclusions themselves were also made along these traverses in order to gain coexisting mineral compositions with a close analysis separation. Cr-spinel and clinopyroxene analyses are described in the subsequent two sections.

External zonation in garnet is that which occurs towards a matrix which may be: Serpentine \pm Cr-spinel (harzburgitic, Es), diopside \pm serpentine \pm Cr-spinel (lherzolitic, Ed), garnet (garnetite, Eg) or an unknown matrix (Eu). It is only within the few polygranular samples that external zonation towards a matrix may be defined (i.e. Eg, Es and Ed) and therefore not classed as Eu.

Internal zonation in garnet is divided into that which occurs towards inclusions which may be: Serpentine \pm Cr-spinel (harzburgitic, Is), Cr-diopside \pm serpentine \pm Cr-spinel (lherzolitic, Id) and monomineralic Cr-spinel (Ic) (Fig. 5.1). 'Is' zonation

may be towards monomineralic serpentine or bimineralic serpentine + Cr-spinel. All three internal zonation types may be towards a monomineralic inclusion and Id zonation may be towards a monomineralic diopside inclusion or towards diopside + serpentine or diopside + Cr-spinel, if bimineralic, and all three of diopside, serpentine and Cr-spinel if trimineralic. Based simply upon the location and orientation of zonation trends relative to petrographic features the zonations may be classified as shown in Fig. 5.1:

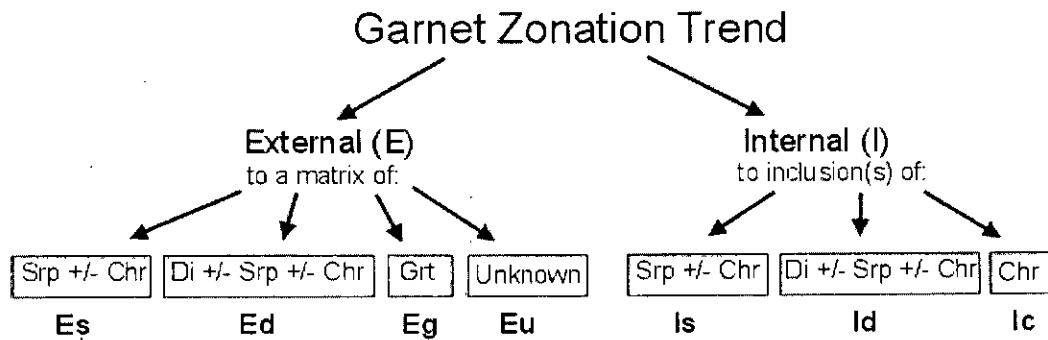


Figure 5.1: Garnet zonation trend classification based on matrix and inclusion mineralogy, where s/Srp = serpentine, d/Di = Cr-diopside, c/Chr = Cr-spinel, g/Grt = garnet.

The zonation types are illustrated on Cr₂O₃ vs. CaO wt. % plots with selected examples in Fig. 5.2 (a) and (b), with directional arrows indicating trends towards garnet boundary in Fig. 5.2 (b). In harzburgitic (low Ca) samples two trajectories are seen: a steep trajectory (i.e. mainly Cr-variation) and a sub-horizontal trajectory (i.e. mainly Ca-variation) that appears to be present in four samples. Garnets to the high-Ca side of the lherzolite line have positive Cr-Ca trends.

At Newlands and Bobbejaan the majority (~ 80 %) of samples display some external zonation with ~ 40 % showing both external and internal zonation (see Table II.I in Appendix II). ~ 15 % show evidence for internal zonation alone and around another 5 % do not show evidence for either external or internal zonation. Few samples were traversed and found to be almost chemically homogeneous and therefore with little or no manifestation of either zonation type.

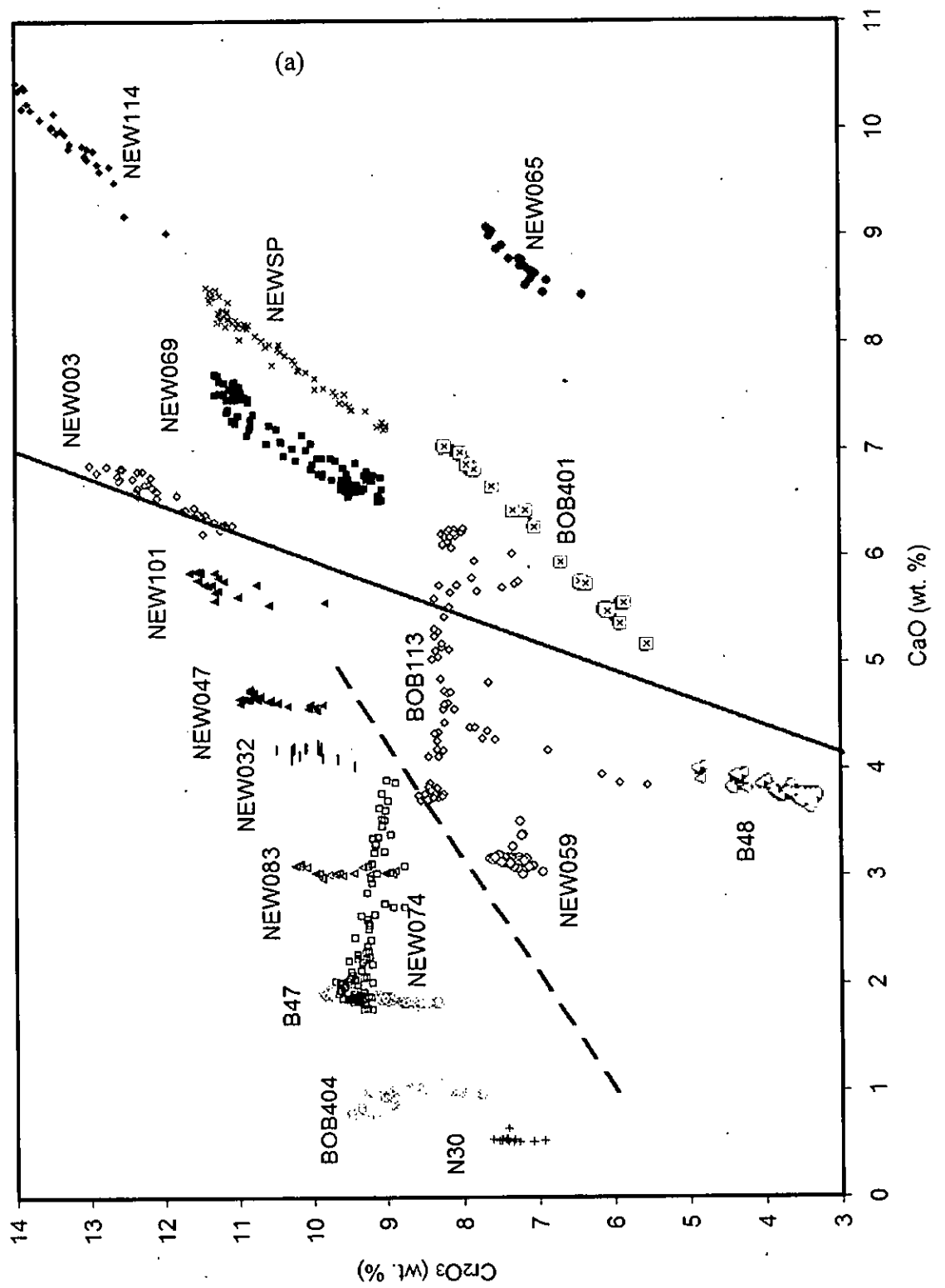
Some difficulty exists in determining whether each zonation type is present. For example internal zonation may be caused by an inclusion that is not quite exposed at the analysis surface and will therefore appear as a hump/dip on a traverse or an island of different intensity on an X-ray map. In some cases this may be mistaken for external zonation. A second example is from small monocranular garnet samples exhibiting apparent core to rim zonations. These might have had inclusions present outside the current edge of the sample causing a concentric zonation pattern with a similar appearance to an external zonation. In general these problems are not thought to cause misidentification in many of the samples.

Fig. 5.2 shows selected data illustrating the major compositional trends. For completeness Fig. 5.3a and b shows the Cr-Ca distribution of all the garnet traverses carried out on Newlands (a) and Bobbejaan (b) samples (i.e. all those in Appendix II and additional analyses, Appendix VI). There is a larger compositional variety in the Newlands samples with greater representation at the high-Cr parts of the harzburgitic and lherzolitic trends. Zonations in some samples cross the lherzolite line (LL) and the diamond-graphite constraint (DGC). The two kimberlites have individual samples with a similar magnitude of chemical variation.

Fig. 5.3 emphasises that, despite involving two localities (Newlands and Bobbejaan) and a variety of matrix and inclusion minerals, there are only three main trajectories in Cr-Ca space: (1) The sub-vertical trend that is to the low-Ca side of LL and close to DGC, (2) the trend parallel with LL which is in the vicinity of LL or with slightly shallower slope at high Ca and (3) the sub-horizontal trend in a few samples usually plotting in the harzburgite field. (1) and (2) appear to be continuous with each other since the internal zonation trajectories swing to more diagonal as more Ca is involved. Ic zonation has a different direction to Id and Is zonations whilst still conforming to the neighbouring trajectories.

As shown in Chapter 4, Cr typically substitutes directly for Al and Mg for Ca in terms of cations in garnet, therefore the Cr-Ca diagram effectively accounts for the

major variations in the most common substituting cations in garnets. Thus the features seen in Figs 5.2 and 5.3 would be largely reproduced in plots with the axes $\text{Cr}/(\text{Cr}+\text{Al})$ and $\text{Ca}/(\text{Ca}+\text{Mg})$ (see Fig. 4.1). Ti is the only significantly variable element not accounted for by Cr-Ca plots (plots of Ti-variation are shown in section 5.2.5). Of the other analysed elements Si and Fe are the only elements that are high in concentration (Si > 37 wt. % and Fe usually > 5 wt. %) and that do not show any evidence of zonation in garnets from Newlands and Bobbejaan samples. Other elements that are relatively constant across the zonations are Mn and Na; whilst Ni and K are usually in sub-detection limit concentrations (with EMPA at normal counting times).



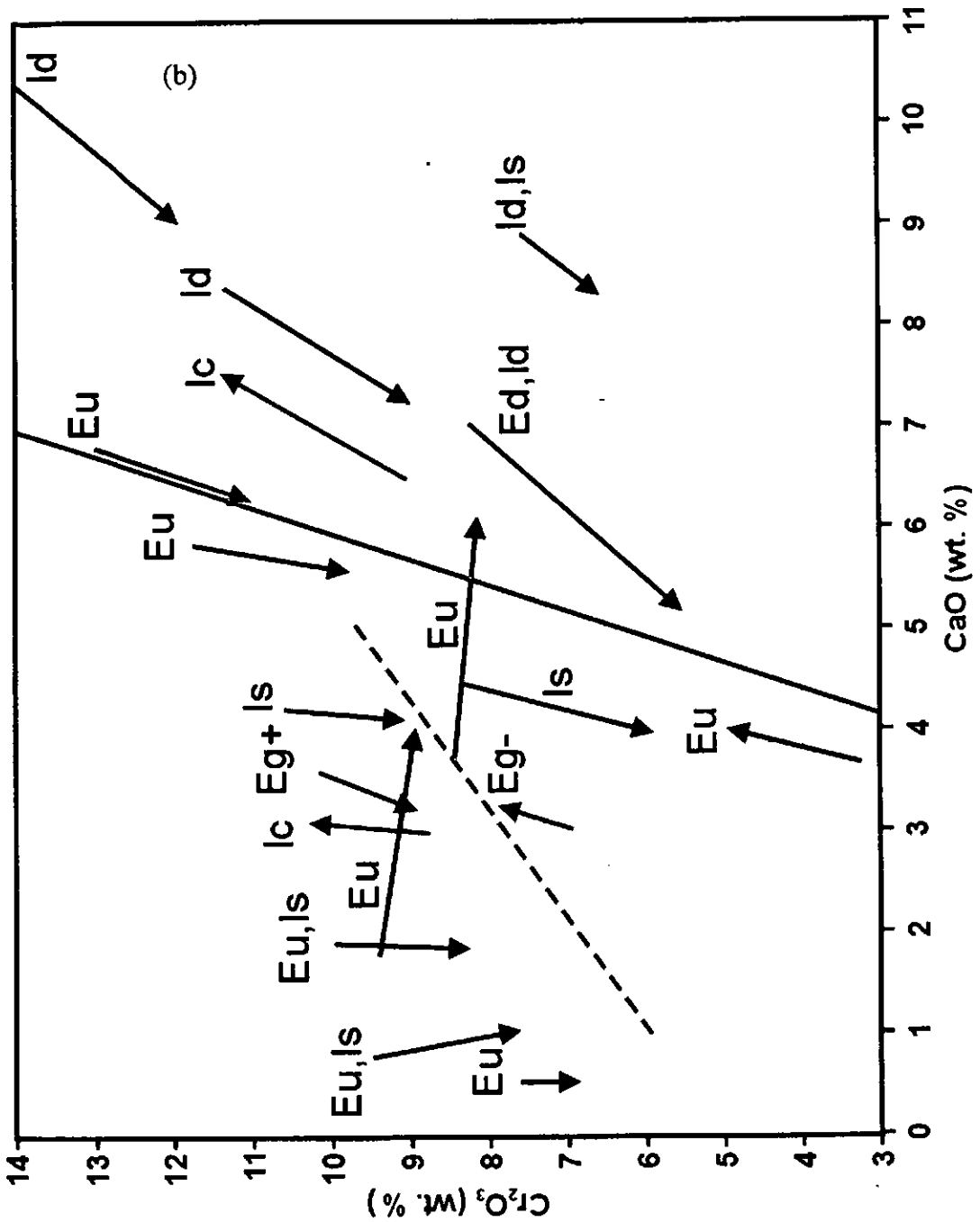
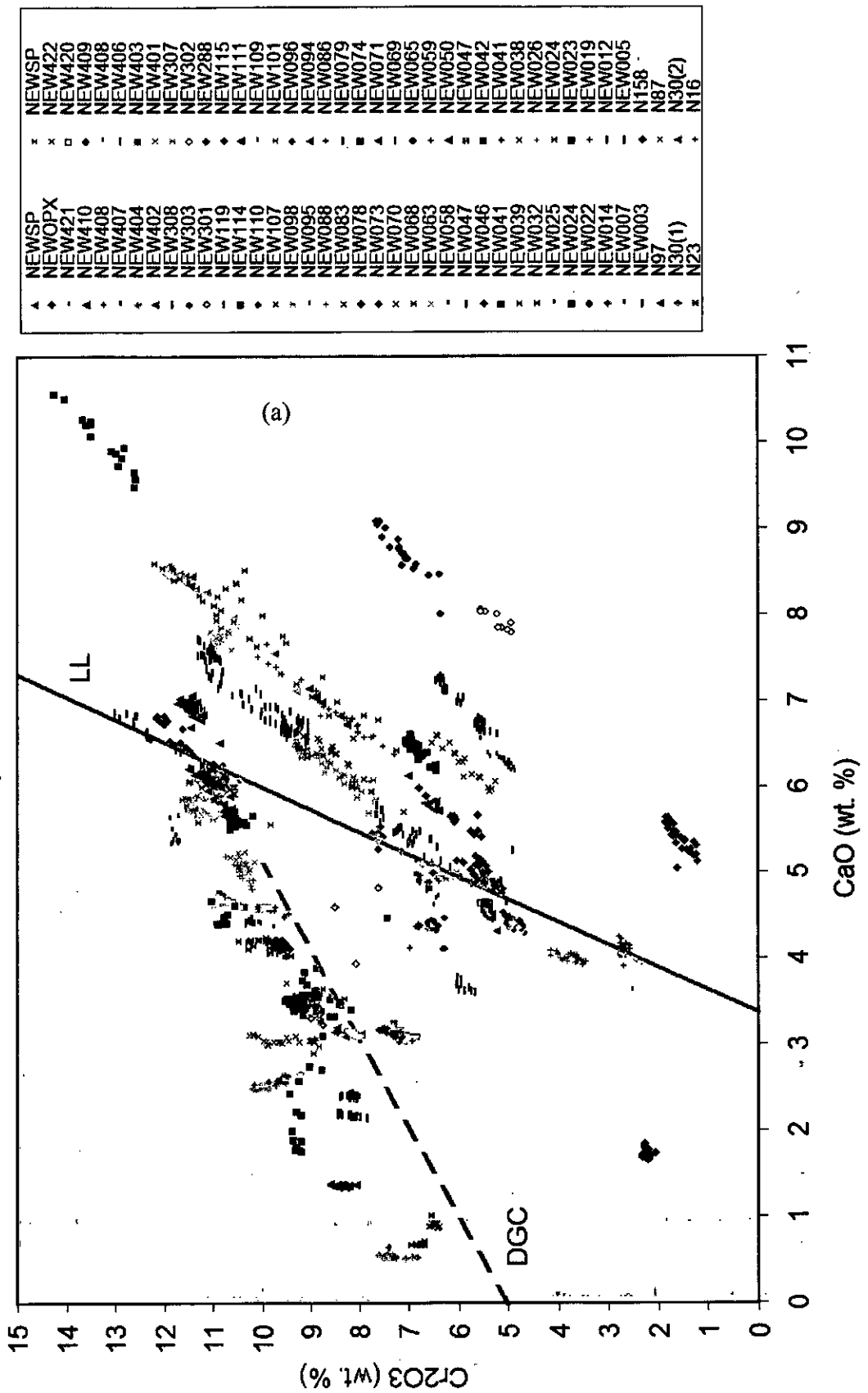


Figure 5.2: (a) CaO vs. Cr₂O₃ wt. % plot of selected Newlands (black symbols) and Bobbejaan (white symbols) garnet traverses. Note Cr₂O₃ scale starts at 3 wt. %. (b) as for (a) with the same samples plotted (with the addition of Eg⁺ trend of NEW301), arrows shown indicating direction of zonation for internal zonation towards an inclusion (Is=blue, Id=green, Ic=grey) and for external zonation. When external zonation alone is present it is shown in red for an unknown matrix and in purple for one with garnet as the matrix. The lherzolite line (solid line, Gurney, 1984) and the diamond-graphite constraint (dashed line, Grütter et al., 2004) are shown on each diagram.



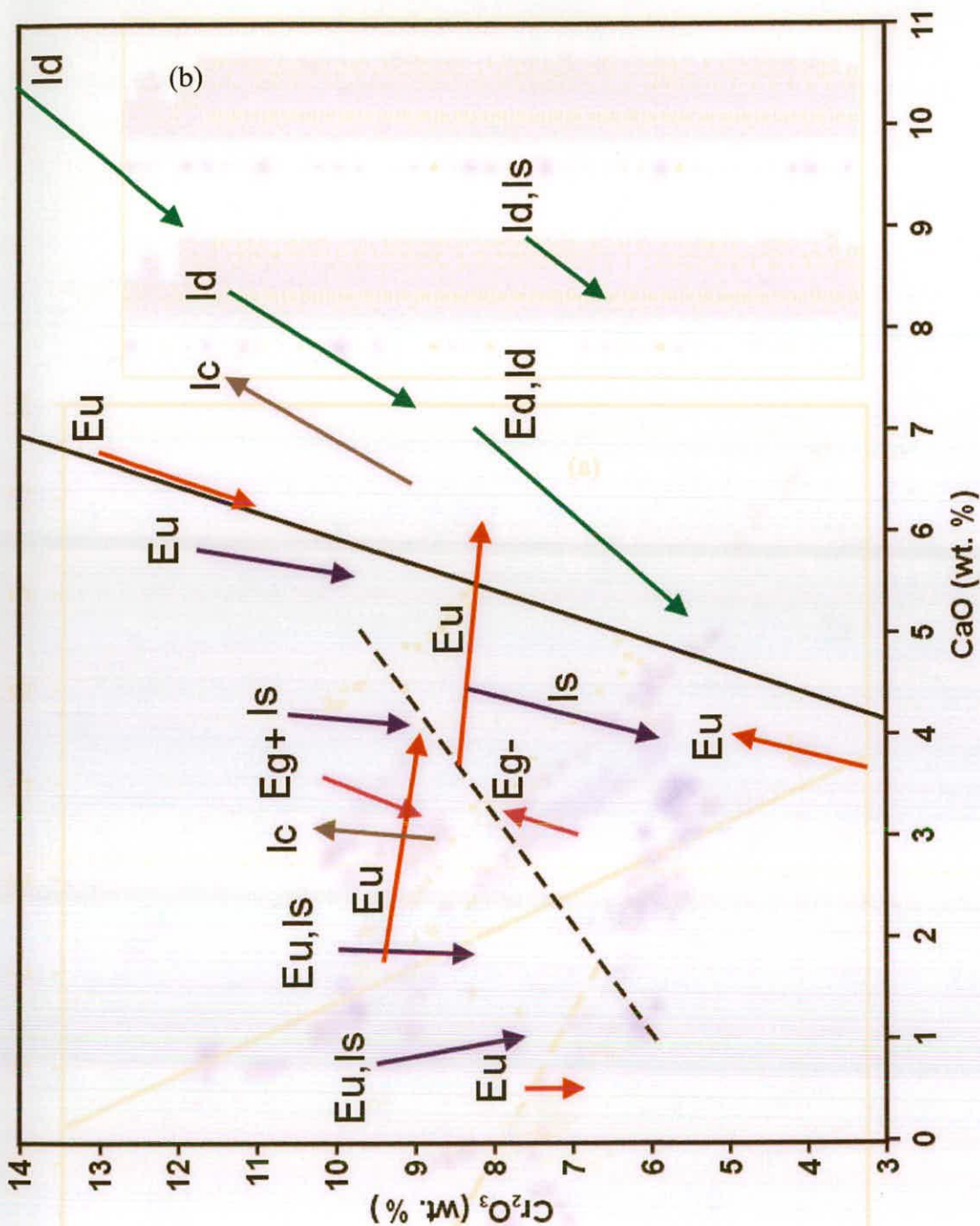
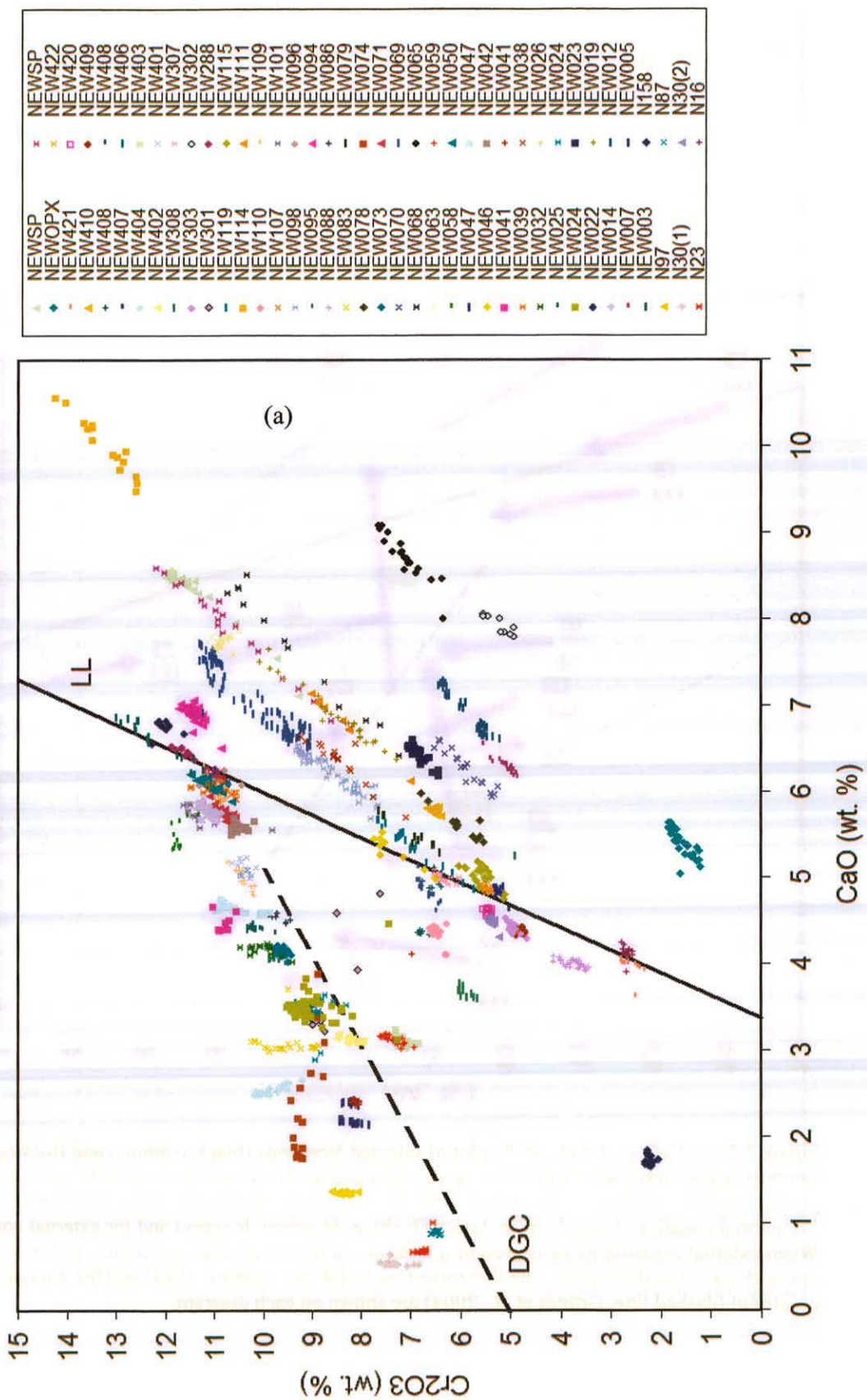


Figure 5.2: (a) CaO vs. Cr₂O₃ wt. % plot of selected Newlands (black symbols) and Bobbejaan (white symbols) garnet traverses. Note Cr₂O₃ scale starts at 3 wt. %. (b) as for (a) with the same samples plotted (with the addition of Eg+ trend of NEW301), arrows shown indicating direction of zonation for internal zonation towards an inclusion (Is=blue, Id=green, Ic=grey) and for external zonation. When external zonation alone is present it is shown in red for an unknown matrix and in purple for one with garnet as the matrix. The Iherzolite line (solid line, Gurney, 1984) and the diamond-graphite constraint (dashed line, Grütter et al., 2004) are shown on each diagram.



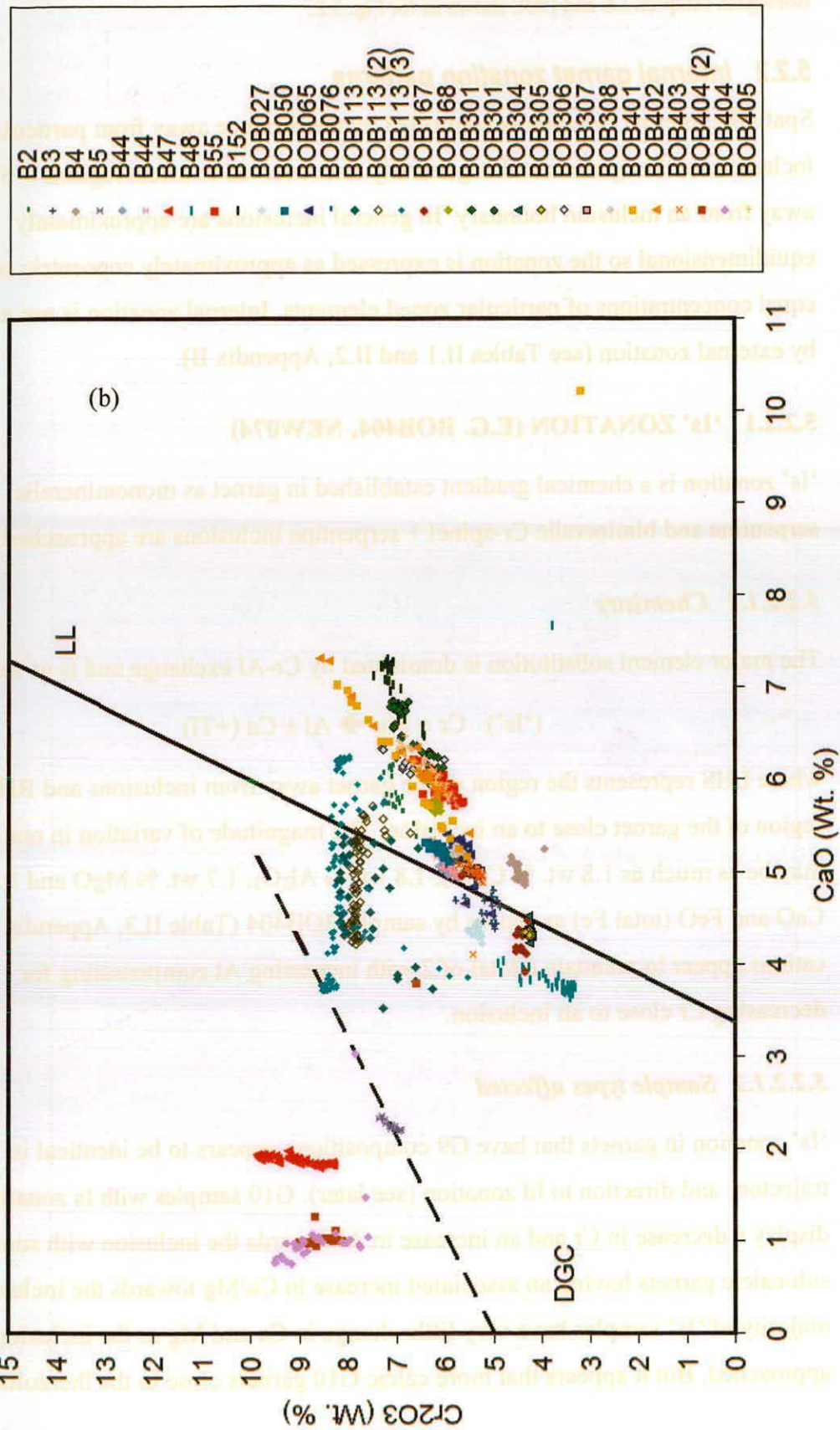


Figure 5.3: (a) Cr₂O₃ vs. CaO wt. % plots of all Newlands garnet traverses. (b) as for (a) but for Bobbejaan samples. LL and DGC shown as for Fig. 5.2.

5.2.2 Internal garnet zonation patterns

Spatially, internal zonation is controlled by the distance away from particular inclusions within garnets and is generally not observed to affect regions > 500 μm away from an inclusion boundary. In general inclusions are approximately equidimensional so the zonation is expressed as approximately concentric zones of equal concentrations of particular zoned elements. Internal zonation is not affected by external zonation (see Tables II.1 and II.2, Appendix II).

5.2.2.1 'Is' ZONATION (E.G. BOB404, NEW074)

'Is' zonation is a chemical gradient established in garnet as monomineralic serpentine and bimineralic Cr-spinel + serpentine inclusions are approached.

5.2.2.1.1 Chemistry

The major element substitution is dominated by Cr-Al exchange and is as follows:



where LHS represents the region of the garnet away from inclusions and RHS the region of the garnet close to an inclusion. The magnitude of variation in one sample may be as much as 1.8 wt. % Cr₂O₃, 1.8 wt. % Al₂O₃, 1.7 wt. % MgO and 0.3 wt. % CaO and FeO (total Fe) as shown by sample BOB404 (Table II.3, Appendix II). 3+ cations appear to maintain a total of 2 with increasing Al compensating for decreasing Cr close to an inclusion.

5.2.2.1.2 Sample types affected

'Is' zonation in garnets that have G9 compositions appears to be identical in trajectory and direction to Id zonation (see later). G10 samples with Is zonation display a decrease in Cr and an increase in Al towards the inclusion with some highly sub-calcic garnets having an associated increase in Ca/Mg towards the inclusion. The majority of 'Is' samples have very little change in Ca and Mg as the inclusion is approached. But it appears that more calcic G10 garnets close to the Iherzolite line

possess larger reductions in Ca associated with reductions in Cr towards the inclusion.

5.2.2.1.3 Examples

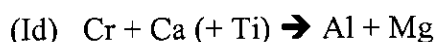
NEW074 X-ray map¹ shows reduced Cr and increased Al as the serpentine + Cr-spinel inclusion is approached with a small increase in Ca and Ti and a small decrease in Mg. The zonation appears to be contained within a 200 μ m radius of the inclusion contact with garnet as can be seen in the first 500 μ m of the traverse. The external zonation will be discussed later. BOB404 X-ray map shows localised reductions in Cr and increases in Al close to inclusions; Ca-Mg variation does not appear to correspond to the proximity of the garnet to inclusions and is part of the external zonation (see later). Sub-500 μ m variations in Cr and Al can be seen close to inclusions in the profile. All other elements remain constant in concentration as the inclusions are approached.

5.2.2.2 ID ZONATION (E.G. NEWSP, BOB402, B55)

Id zonation is a chemical gradient established in garnet as Cr-diopside + Cr-spinel + serpentine, Cr-diopside + serpentine, Cr-diopside + Cr-spinel and monomineralic Cr-diopside inclusions are approached.

5.2.2.2.1 Chemistry

The major element substitution is one where Cr and Ca have a clear positive correlation and is as follows:



where LHS represents the region of the garnet away from inclusions and RHS the region of the garnet close to an inclusion with Ti variation being greater in the high-Cr high-Ca garnets. The magnitude of this variation in one sample may be as high as 3.5 wt. % Cr₂O₃, 3.3 wt. % Al₂O₃, 2.5 wt. % MgO and 2.1 wt. % CaO, 0.5 wt. % FeO and 0.12 wt. % TiO₂ as shown by sample NEWSP. Sample BOB401 is notable

¹ X-ray maps and profiles may be found on the data CD (Appendices III and II respectively).

in Fig. 5.2a for having a shallower Cr/Ca slope than other Newlands and Bobbejaan samples showing Id zonation.

5.2.2.2.2 *Sample types affected*

Id zonation is restricted to lherzolitic samples (due to its definition) and is therefore mainly restricted to the G9 field (Fig. 5.2b). Few samples plot a short way into the G10 field.

5.2.2.2.3 *Examples*

Sample NEWSP is monogranular and contains multiple bimineralic inclusions of Cr-diopside + serpentine + Cr-spinel and Cr-diopside + Cr-spinel. All zonation appears to be controlled by the proximity of the garnet to inclusions and no evidence of external zonation is present (see X-ray map). Traverses adjacent to inclusions reveal close to symmetrical chemical variation according to the Id substitution. In a similar way to samples with 'Is' zonation, NEWSP has Id zonation distributed with radial symmetry all the way around polymineralic inclusions suggesting that the inclusion behaves as a whole when interacting with garnet.

The polygranular sample BOB402 has Id zonation visible on a sub-millimetre scale near inclusions (see BOB402-Zoom X-ray map). Larger-scale zonation is apparent and attributed to manifestation of external zonation.

Most inclusions in sample B55 are platy bimineralic Cr-spinel + Cr-diopside inclusions (chapter 3) with Id zonation isopleths equidistant from the garnet-inclusion interface (maximum distance of ~ 500 μm). No external zonation is apparent. X-ray maps B55 and B55-Zoom show this distribution of Id zonation.

5.2.2.3 IC ZONATION (E.G. NEW069, NEW083)

Ic zonation is a chemical gradient established in garnet as monomineralic Cr-spinel inclusions are approached. There is a rarity of monomineralic chromite inclusions and so there are only two analysed examples of Ic zonation manifestation.

5.2.2.3.1 Chemistry

The major element substitution is essentially opposite in direction to Id zonation and is as follows:



where LHS represents the region of the garnet away from inclusions and RHS the region of the garnet close to an inclusion. The magnitude and chemical vector of variation is similar to that of Is if the sample is in the G10 field and similar to that of Id if in the G9 field e.g. NEW083 and NEW069 respectively.

5.2.2.3.2 Sample types affected

All the samples with Ic are found to be at high-Cr (> 6 wt. %). Ti variation is greatest in NEW069 which is a high-Cr, high-Ca G9 garnet sample. Ca-Mg exchange is less apparent in G10 garnets such as NEW083.

5.2.2.3.3 Examples

NEW069 plots as a high-Cr part of the Iherzolite trend for Newlands garnets in Fig. 5.2a. Internal zonation towards monomineralic Cr-spinel is particularly clear on the X-ray map and profile and can be seen to occur over a distance of ~ 500 μm . The NEW083 X-ray map shows that close to the Cr-spinel inclusion, the style and magnitude of sample-scale variation is concentrated into an approximately 500 μm zone around the inclusion. However, the trajectory of Cr-Ca space is steeper and like that of Is zonation (the traverse does not pass directly over the Cr-spinel inclusion).

5.2.3 External garnet zonation patterns (E)

Spatially, external zonation is controlled by the distance away from the garnet matrix and affects regions next to the matrix and usually penetrating > 500 μm away from the garnet rim, which may reach to the core of the garnet. In no case was it possible to discriminate between differences in zonation next to different matrix minerals. In polygranular samples external zonation concentration isopleths can be seen to be parallel to garnet grain boundaries, whereas in monogranular samples the external zonation concentration isopleths are normally parallel to the sample edge except

where the sample has been broken by mine processing activities (e.g. NEW024 X-ray map). External zonation is affected by internal zonation and is therefore 'overprinted' by inclusion-controlled chemical variation in nearly every externally zoned sample where garnet has inclusions.

5.2.3.1 ES ZONATION (E.G. NEW308)

Es zonation is a chemical gradient established in garnet as a serpentine ± Cr-spinel matrix is approached. The zonation may be present in many harzburgitic samples but is only unmistakably identifiable in polygranular samples such as NEW308.

5.2.3.1.1 Chemistry

The major element substitution is similar in nature to Is zonation and is as follows:



where the LHS is the garnet core and the RHS is the garnet rim. The magnitude of variation has only been recorded as small (i.e. < 1 wt. % for Cr₂O₃ and Al₂O₃, and < 0.3 wt % CaO and MgO). Ca-Mg variation is always less than with Ed zonation.

5.2.3.1.2 Sample types affected

Es zonation affects samples that are predominantly harzburgitic both petrographically and geochemically (i.e. they are samples with no diopside and have G10 garnet chemistry). Occasionally lherzolitic samples with apparently monomineralic serpentine or bimineralic serpentine + chromite matrix have been designated with Es zonation but chemically the trend is that of Ed/Id indicative of diopside being present somewhere in the matrix.

5.2.3.1.3 Examples

NEW308 X-ray map indicates that Es zonation occurs to rim-core distances of about 1000 μm in garnet away from a serpentine-rich matrix. Internal zonation next to inclusions overprints this core-rim external zonation. NEW059 has a similar zonation pattern, chemistry and garnet composition but it is classified as Eg zonation since the matrix is nearly 100 % garnet. However, the chemical substitution appears to be the same and the variation about the same magnitude.

5.2.3.2 ED ZONATION (E.G. BOB402)

Ed zonation is a chemical gradient established in garnet as a Cr-diopside ± serpentine ± Cr-spinel matrix is approached. Again, this type of zonation is only unmistakably identifiable in polygranular samples.

5.2.3.2.1 Chemistry

The substitution components are identical to those of Id zonation with the addition of Mn and Fe:



where the LHS is the garnet core and the RHS is the garnet rim next to matrix. The magnitude of variation may be large as shown in sample BOB401 which has Cr₂O₃ and Al₂O₃ variation in the order of 2.5 wt. % (equating to close to 0.2 cation formula units of both Cr and Al) and CaO and MgO vary approximately 1.5 wt. % each (equating to close to 0.2 cation formula units for Ca and Mg). Ti, Mn and Fe variation is generally small.

5.2.3.2.2 Sample types affected

Polygranular lherzolitic samples are observed to be affected by Ed zonation. Since the matrix is not identifiable in monogranular samples, many of these may be derived from a diopside-present matrix. Therefore many monogranular samples with sample-wide zonation that does not correspond to I zonation has been recorded as Eu zonation (i.e. unidentified) but may have been derived from a diopside-present matrix. This is justifiable since inclusions in garnets from polygranular samples usually reflect the composition of the matrix (Chapter 3).

5.2.3.2.3 Examples

BOB401 shows E zonation over a distance of 4000 μm (see X-ray map BOB401). X-ray map 'BOB401 zoom' shows that internal zonation adjacent to inclusions overprints the external zonation but the substitution chemistry is very similar. Only one of potentially three garnets in the sample show strongly developed E zonation which is expressed as a decrease in Cr and Ca from the core towards the direction of the matrix.

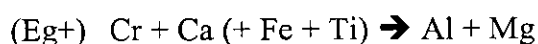
The Cr-Ca slope is shallower in BOB401 than other Newlands and Bobbejaan garnet zonation trends (Fig. 5.1a). BOB401 is also the only sample where Fe and Mn can also be seen to vary in correspondence with the Cr and Ca (therefore correlating negatively with Al and Mg). Their variation is smaller in magnitude than the four main elements (Fe = 0.03 and Mn = 0.01 cation formula units).

5.2.3.3 EG ZONATIONS (E.G. NEW059, NEW301)

Eg zonation is a chemical gradient established in garnet as a matrix of garnet is approached. This type of zonation is only unmistakably identifiable in polygranular samples. A positive and negative Eg zonation are described here because there are two chemical directions to which the substitution is observed to occur depending on garnet composition.

5.2.3.3.1 Chemistry

The major element substitution is similar to Id and Ed except that Ca-Mg exchange is less well pronounced and hence a steeper Cr-Ca trajectory is produced very close to the slope of the Iherzolite line of Gurney (1984). The substitution may be positive (i.e. in the same direction as Id and Ed) or negative (reversed direction to Id and Ed) and is as follows:



where the LHS is the garnet core and the RHS is the garnet rim next to matrix. The magnitude of variation is small in sample NEW059 but may be larger (around 1.5 wt. % Cr₂O₃ rather than 0.6) in unconfirmed Eg samples such as B48 and NEW003. In NEW059 however Cr₂O₃ and Al₂O₃ variation is in the order of 0.6 and 0.4 wt. % respectively (equating to close to 0.02 cation formula units for both Cr and Al) CaO and MgO vary approximately 0.2 wt. % each (equating to close to 0.02 cation formula units for Ca and Mg).

5.2.3.3.2 *Sample types affected*

Only one sample is unambiguously defined as Eg+ (NEW301) and one Eg- (NEW059), therefore it is not possible to be sure how diverse the sample types are with this zonation, However both samples are polygranular garnetite with minor serpentine and chromite in the matrix and their garnets are G10 in composition.

Monogranular samples with few to no inclusions often have the same substitution from core to rim. Even though a matrix cannot be defined in NEW003 its shape appears to be part of a garnetite rock rather than garnet in a matrix of other minerals (see Chapter 3). These samples also tend to be very close to the lherzolite line and have a slope very similar to this line with Cr₂O₃ decreasing markedly with decreasing CaO. They are also usually garnet-only samples with no other coexisting minerals. None of the above-mentioned samples possess inclusions, which is a common feature of many of the samples just to the Ca-poor side of the lherzolite line.

5.2.3.3.3 *Examples*

NEW059 is a sample that contains multiple garnet grains with garnet-garnet grain boundaries. This sample displays the way that each individual garnet has concentric core-rim zonation from Cr-poor at the core to Cr-rich at the rims. Ca varies in the same sense to Cr and Al and Mg vary in the opposite sense to Cr. Zonation does not conform to the edge of the sample (NEW059 X-ray map). The shape of the zones depends on the shape of the particular garnet grain margin.

NEW301 contains three separate garnet crystals (EBSD Appendix IV). The garnet that comprises most of the sample (garnet 1, see NEW301 X-ray map and profile) is zoned from high- to low-Cr (and Ca, although Ca zonation is less pronounced) as matrix minerals are approached. Garnet 2 is a smaller garnet (~7 mm across) that has a Cr-rich core and becomes lower in Cr as garnet 1 is approached over a distance of ~1500 μm to attain the same Cr concentration as garnet 1 at the contact. The substitution is therefore the opposite of NEW059 even though the samples have similar overall Cr-Ca compositions (see Fig. 5.2) and designated Eg+ (Fig. 5.2b)

B48 has clearly increasing Cr + Ca to the rim and is therefore Eg- (B48 X-ray map). This sample is within the G10 field but at low-Cr₂O₃ (3-4 wt. %) and has a slope steeper than but close to the lherzolite line and is also garnet-only. It seems that the zonation relates to the edge of the sample and hence probably the edge of the original crystal margin in contact with matrix.

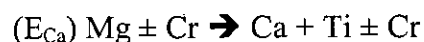
With NEW003 the zonation pattern is such that the highest Cr and Ca region is located to one side of the centre of the grain (NEW003 X-ray map, NEW003 profile). The sample, chemically, would fall into the Eg+ category. Given external zonation is dependent on distance from matrix, this implies that the centre of the analysed surface was closer to the rock matrix than the high-Cr and Ca region. Since the sample is rounded and not broken at the edges it is assumed that the edge of the sample represents the edge that was transported in the kimberlite and not a mining artefact. Therefore the zonation is a primary feature where the major element distribution within the garnet has not been affected by kimberlitic activity to any detectable extent.

5.2.3.4 E_{Ca} ZONATION (E.G. NEW074, BOB113)

E_{Ca} zonation is a chemical gradient established in garnet where there is an extreme enrichment in Ca as the edge of the grain is approached. This zonation was not identified in any polygranular samples so there is no knowledge of matrix composition in the samples discussed.

5.2.3.4.1 Chemistry

The substitution is essentially a Ca- and Ti enrichment at the expense of Mg and is as follows:



where the LHS is the garnet core and the RHS is the garnet rim presumably next to matrix, but in the case of the examples it is the edge of the sample. The magnitude of

variation may be up to 2.5 wt. % CaO change from core to rim and is often accompanied by a TiO₂ change of up to 0.1 wt. %.

5.2.3.4.2 *Sample types affected*

This type of zonation generally occurs in samples whose cores are in the G10 field and away from the lherzolite line. The zonation moves samples from sub-calcic regions of Cr-Ca space towards the lherzolite line with the change in Ca being much greater than that in Cr. Four, possibly five samples have been identified from Newlands and Bobbejaan that conform to this style of zonation. Cr variation is usually small.

5.2.3.4.3 *Examples*

NEW074 displays clear ECa zonation with a Ca-poor core and Ca, Ti-rich rim (X-ray map NEW074). There is a plateau at the centre (2000-3000 μm on NEW074 profile) and a zonation occurring over a distance of at least 3000 μm towards the edge of the sample from this core. 3000 μm is a minimum distance to the true contact with matrix. This external zonation is overprinted by an internal zonation adjacent to the serpentine + Cr-spinel inclusion.

BOB113 displays flat parts to its profile that are established at the edge of garnet crystals as well as at the core (BOB113 X-ray map and profile). On the full-sample Ca X-ray map, sample BOB113 displays the core as blue, transitional regions as green and the plateau region at the rim as yellow. Modification of the external zonation occurs adjacent to serpentine ± Cr-spinel inclusions where there is Cr-Al exchange occurring in Is zonation. Profile BOB113 (b) clearly shows how Mg-Ca external zonation is independent of Cr-Al internal zonation since Ca continuously increases along the profile regardless of proximity to inclusions whereas Cr is reduced as the inclusions are approached with no discernable trend from the start to the end of the profile.

5.2.4 Comparison to other garnet zonation studies

Table 5.1 indicates how the classifications of external zonation patterns in other studies relate to those described above. Some elements in brackets needed to be added to the core/rim compositions in order to contain all elements mentioned in other studies.

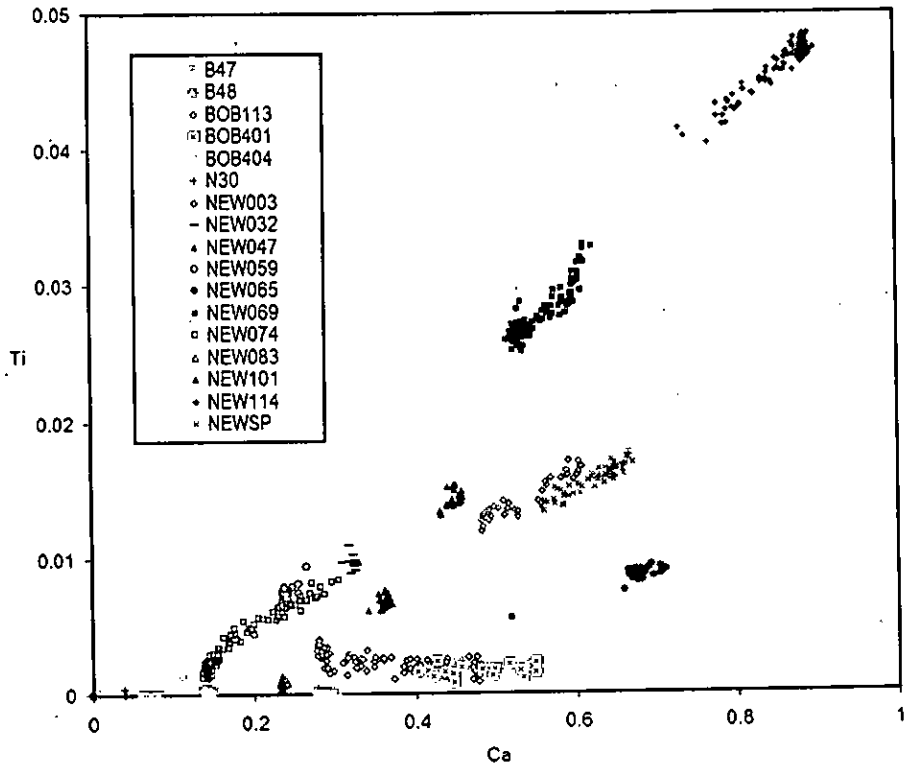
Core rich in	Cr + Ca	Al + Mg	Mg (\pm Cr)	Cr (\pm Ca)	Cr+Al+Mg	Cr + Ti	Homog.
Rim rich in	Al + Mg	Cr + Ca	Ca + Ti	Al (\pm Mg)	Ca+Fe+Na+Ti	Lower Cr + Ti	Homog.
This study	Ed	Eg-	E _{Ca}	Es	-	Seen in Ed	-
BH98	Type I	Type II	Type IIIb	-	Type IIIa	Seen in Ib	-
SB92	Group III (V?)	-	Group VI	-	Group I (\pm Cr)	Group IV	Group II
G99	Yes	-	Yes	-	-	-	-

Table 5.1: Table showing the classifications of different garnet external (core to rim) zonations from this study compared to the classifications in Burgess and Harte (1999) (BH98) and Smith and Boyd (1992) (SB92) and whether the type of zonation is present in garnets analysed by Griffin et al. (1999b).

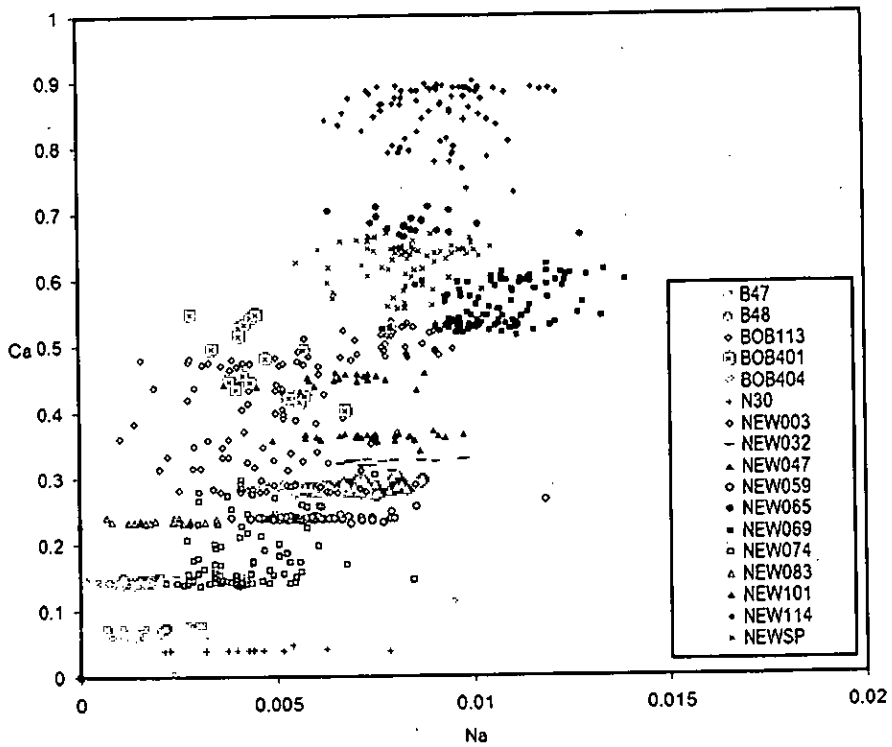
5.2.5 Covariation plots for sample traverses

The garnet zonation trends at Newlands and Bobbejaan show extreme major element variation (Fig. 5.3 a & b) both as a suite of samples (0-11 wt. % CaO and 0-15 wt. % Cr₂O₃) and within individual samples (up to 2.5 wt % CaO and 3 wt. % Cr₂O₃). This combination of features is not previously reported for mantle garnets from kimberlites worldwide. Menzies (2001) reported on the variation of the sample suite at Newlands and van der Westhuizen (1992) reported a limited number of analyses illustrating some of the variation found at Bobbejaan. Burgess (1997) provides a detailed study of multiple zonation trends from Jagersfontein that illustrate a maximum of 1 wt. % variation within individual garnets but over a restricted range of garnet compositions (4-6 wt. % CaO and 0-8 wt. % Cr₂O₃) compared to this study.

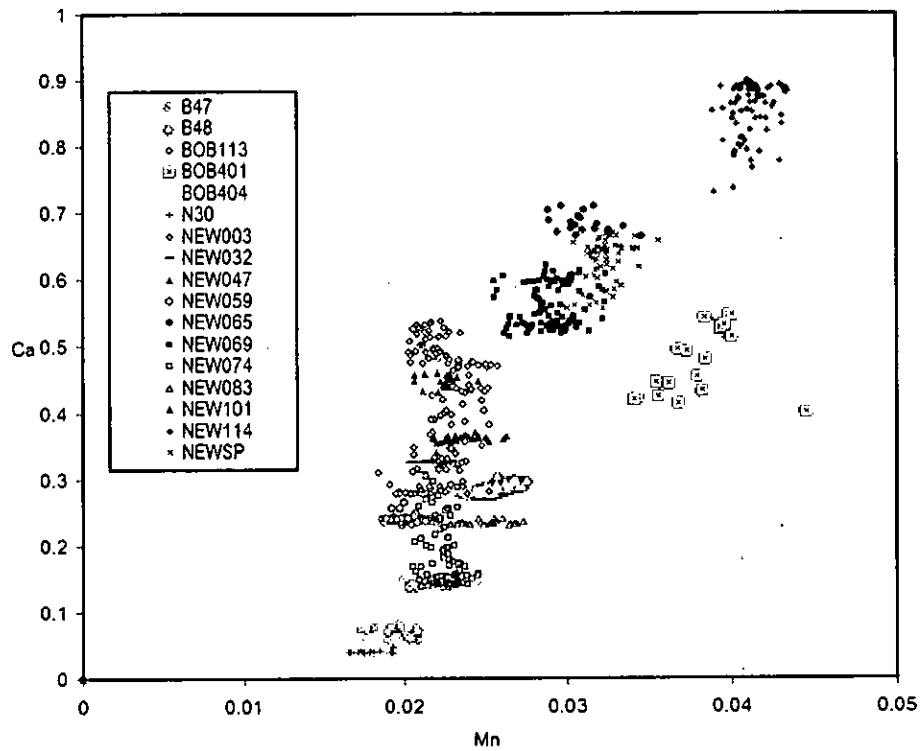
(a)



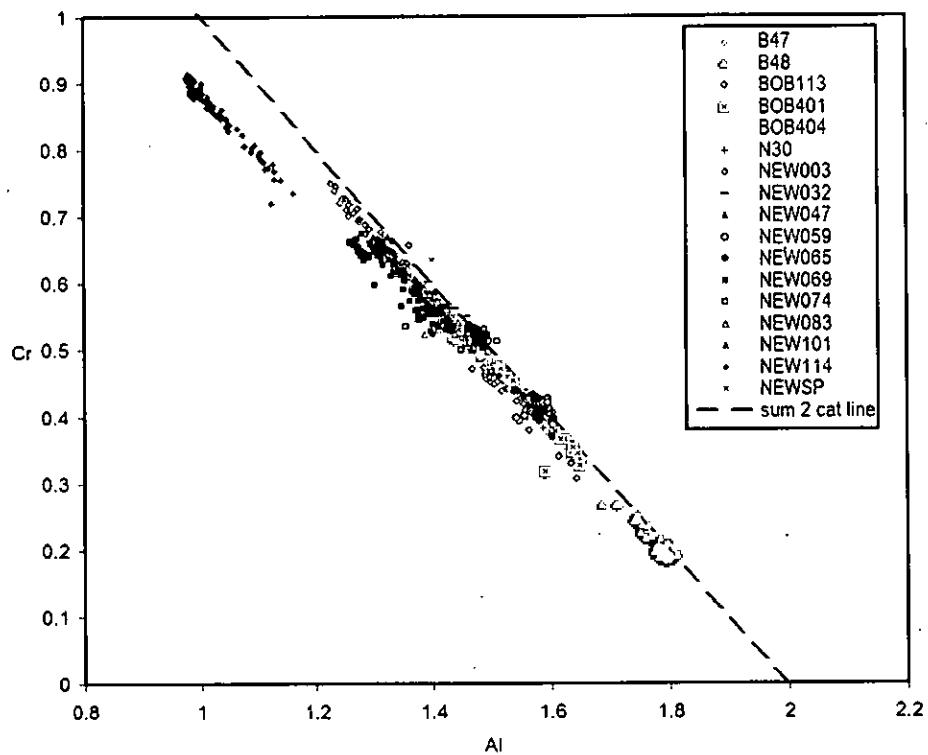
(b)



(c)



(d)



(e)

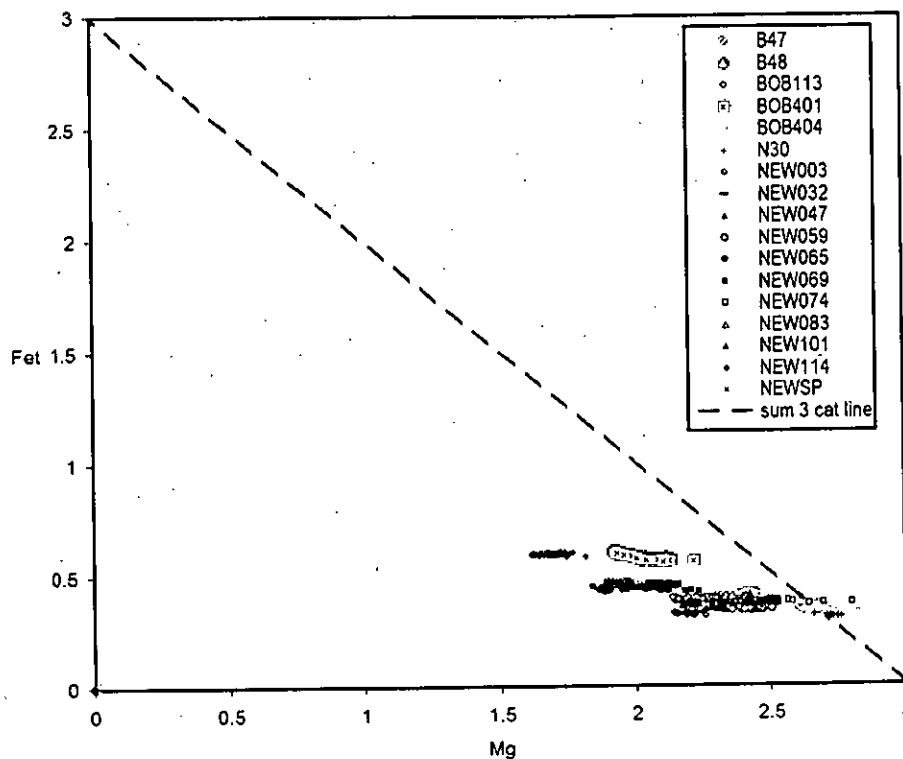


Figure 5.4: (a) Ca vs. Ti cation plot for the selected Newlands (black-grey symbols) and Bobbejaan (white symbols) sample traverses of Fig. 5.2 (a). (b) as for (a) but with Na vs. Ca cations plotted. (c) as for (a) but with Mn vs. Ca cations plotted. (d) as for (a) but with Al vs. Cr cations plotted including a sum of 2 cations line. (e) as for (a) but including a sum of 3 cations line.

Figure 5.4 illustrates additional plots that were used in Chapter 4 to differentiate types of concentrate garnets. Fig. 5.4a shows that there is a strong positive correlation between Ca and Ti in zoned garnets, both as a whole and in some individual garnets. This trend is not visible in garnets from the concentrate datasets (Fig. 4.11a). The Bobbejaan samples (white symbols) do not reach high-Ti concentrations as visible in many Newlands garnets such as the high-Cr, high-Ca garnets (e.g. NEW114, NEWSP and NEW069). NEW065 plots to high Ca side of the trend and many harzburgitic samples plot to very low-Ti and lower Ca parts of the trend. BOB113 and BOB401 show variation in Ca without significant change in Ti.

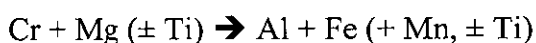
Fig. 5.4b indicates that the variation in Na in the peridotitic garnet samples studied does not correlate with Ca (the same is true for Na vs. Cr). Therefore it appears to be varying independently of other zoned variables and may correspond to parts of the

sample that have been enriched in highly incompatible elements (see trace element chapter). Fig. 5.4c shows garnet compositions forming a broadly positive Mn-Ca trend but individual samples are not significantly zoned in Mn since diffuse clusters are produced. Some of the lower Ca samples appear to have significant Mn variation that is independent of Ca.

Fig. 5.4d has the tight Cr-Al relationship where Cr + Al is close to 2 of the G10 garnets from concentrate. Only sample NEW114 strays from this trend towards lower values, which is indicative of the presence of a small amount of Fe³⁺. Mg vs. Fet (total Fe) shows that the samples have little Fe-Mg substitution occurring with Mg-Ca dominant (Fig. 5.4e). The low-Ca harzburgitic garnets clearly plot close to the sum of 3 cations line indicative of high Mg content and very low other 2+ ion content.

5.3 Cr-spinel Zonation Patterns

Cr-spinel appears homogeneous in the samples on X-ray maps and most profiles (see appendix III and II respectively and also Fig. 5.5) since the majority of crystals are small and are inclusions in garnet. However, few Cr-spinels have been noted as showing external zonation towards a matrix of garnet ± serpentine ± clinopyroxene on profiles (Appendix II, and occasionally in Fig 5.5). The major element substitution is as follows:



Where LHS is core, RHS is rim. The magnitude of this variation may be as high as 1.1 wt. % Cr₂O₃, 0.3 wt. % Al₂O₃, 0.4 wt. % MgO and wt. % CaO, 0.9 wt. % FeO and 0.12 wt. % TiO₂ is as shown by sample NEW063 (see profile in Appendix II). The composition is moved away from the high Cr values typical of diamond inclusions. All examples of zonation in Cr-spinel occur in the outer 300 μm of the crystal.

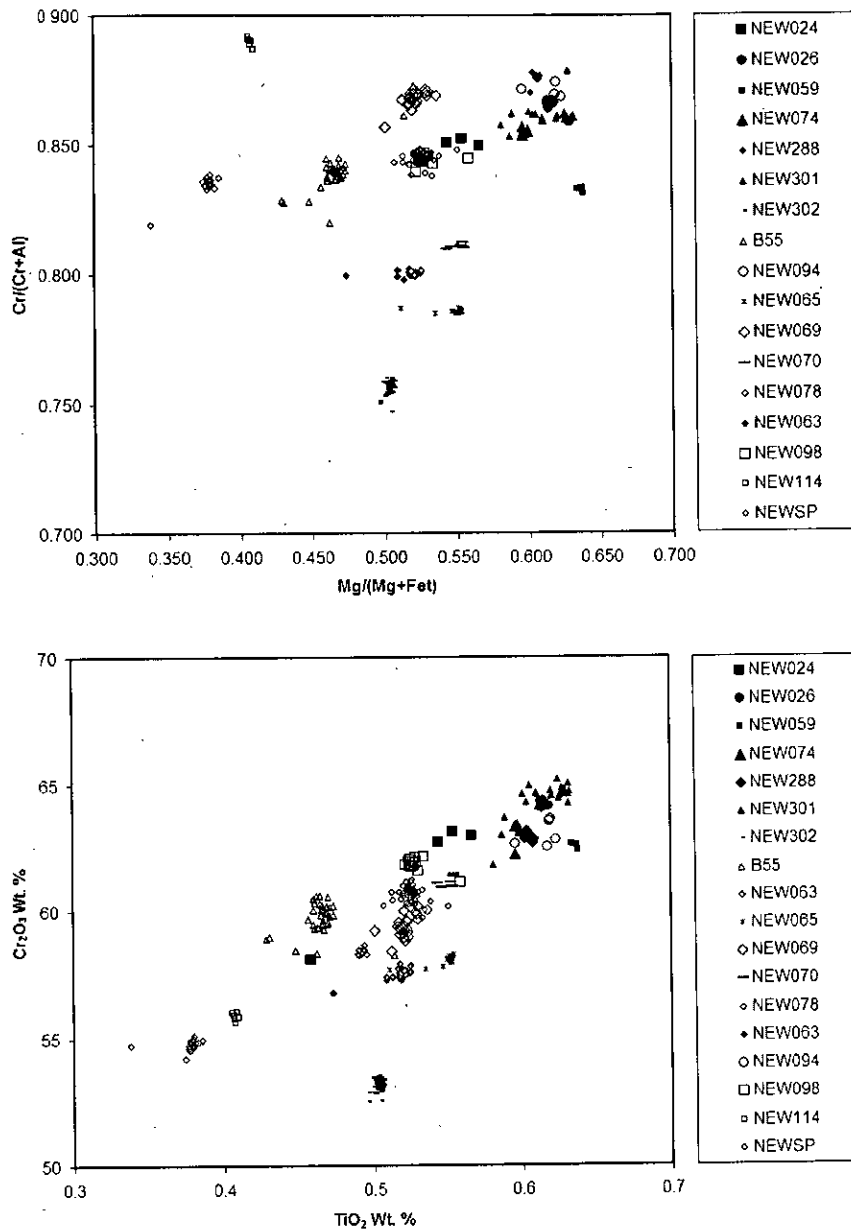


Figure 5.5: (a) Mg/(Mg+Fet) vs. Cr/(Cr+Al) for samples with multiple analyses on Cr-spinels in Newlands and Bobbejaan samples. (b) as for (a) but TiO₂ vs Cr₂O₃ in weight percent. Note: the diamond inclusion fields are not shown due to expansion of the scales on the graphs e.g. refer to Fig. 4.17a.

NEW098 also shows this type of zonation but it is towards the garnet host that the chromite is included in rather than a matrix. NEW302 shows an example of an Fe-Ti-rich chromite overgrowth which appears to be associated with the kimberlitic veining of the sample (Fig. 5.6). It is therefore interpreted to be a secondary feature (similar to the kelyphitic rims on many garnets).

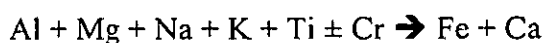


Figure 5.6: Backscattered electron image of chromite in NEW302 illustrating the high-Fe rim in contact with kimberlitic vein minerals. Black is the edge of the sample, dark grey is phlogopite, medium grey is chromite, light grey is chromite and white is the high-Fe chromite rim.

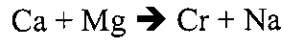
Menzies (2001) ascribes the first zonation style to be due to ‘edge effects’ during analysis but analysis in this study reveals that there is a consistent trend in the crystal that could not be produced by a bad analysis at the edge of the grain. Daniels (1991) finds that most Dokolwayo Cr-spinels are homogeneous with some low-Ti Cr-spinels having an Al → Cr core to rim zonation.

5.4 Cr-Diopside Zonation Patterns

In the same way to Cr-spinel, most Cr-diopsides in samples are small inclusions in garnets and are observed to be close to homogeneous on X-ray maps and profiles. It is only in a few cases that profiles have revealed any *external* zonation towards a matrix. The first of these is zonation towards a matrix of garnet ± serpentine ± Cr-spinel and is as follows:



where LHS is the core and RHS is the rim. The second zonation style seen in sample NEW421 contains a clinopyroxene that displays this substitution. BOB301 and NEW303 have a zonation that is as follows:



where LHS is the core and RHS is the rim. This is effectively a kosmochlor-jadeite component increase to the rim relative to diopside (see Fig 5.7). Both these zonations are evident towards a garnet host and occur only at the outer 800 μm of the clinopyroxene crystals.

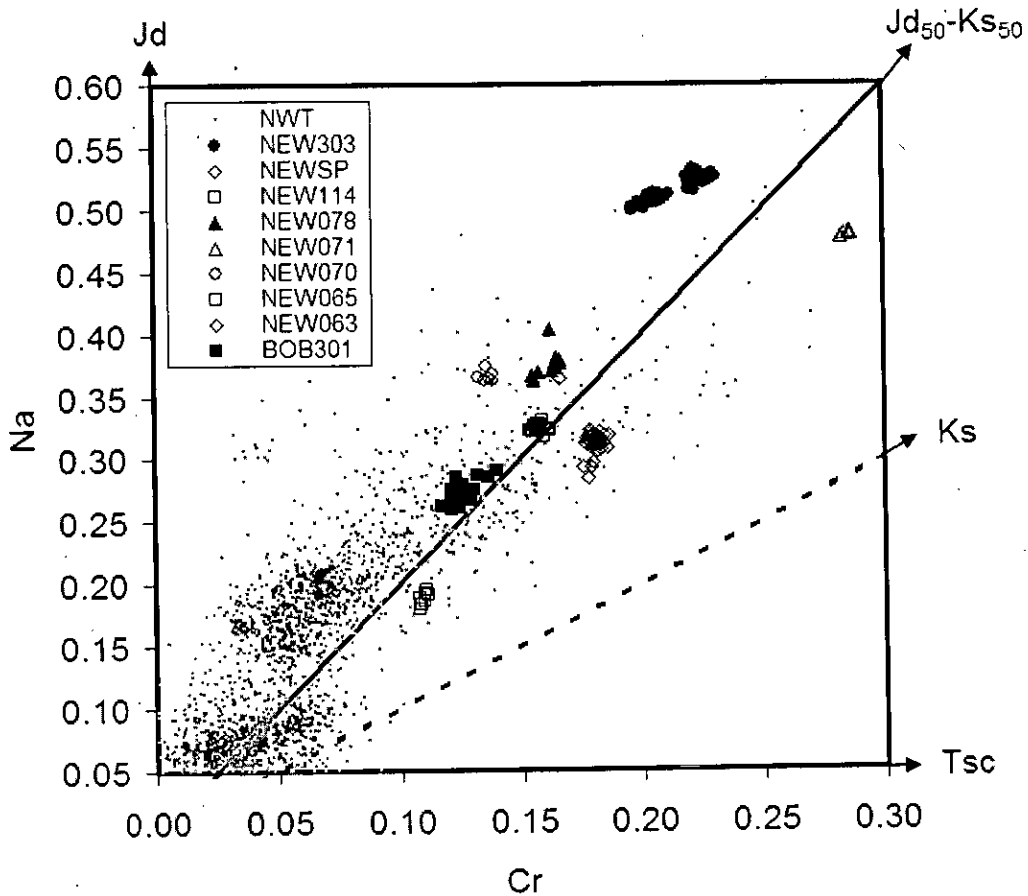


Figure 5.7: Cr vs. Na cation plot (calculated to a sum of 8 cations) for traversed clinopyroxenes indicating the presence of zoned samples NEW303, BOB301 and potentially in NEW078. Other samples are shown as open symbols and Northwest Territories Till (NWT dataset, Chapter 4) clinopyroxene concentrate is plotted in grey.

5.5 Summary

Internal garnet zonation is found to occur in the 500 μm adjacent to inclusions in a high proportion of samples. External garnet zonation is found to occur in the outer 2000 μm of garnet crystals adjacent to matrix minerals in a high proportion of samples. A summary of garnet substitutions and the strengths to which they exist is shown in Table 5.2:

Substitution	Cr/Al	Ca/Mg	Ti	Garnet type affected
Is	Strong -ve	Weak \pm ve	No variation	G9 and G10
Id	Strong -ve	Strong -ve	Strong -ve	G9
Ic	Strong +ve	Weak +ve	Weak +ve	High-Cr G9 and G10
Es	Weak -ve	Weak \pm ve	No variation	G9 and G10
Ed	Strong -ve	Strong -ve	Weak \pm ve	G9
Eg (-)	Weak +ve	Weak +ve	Weak -ve	G10 & G9/G10 boundary
Eg (+)	Strong -ve	Weak -ve	No variation	G10 & G9/G10 boundary
ECa	Weak -ve	Strong +ve	Strong +ve	G10

Table 5.2: Major element substitutions occurring in each garnet zonation type with Cr-Ca garnet compositions affected. (weak means approximately <1 wt. % Cr_2O_3 , <1 wt. % CaO and <0.05 wt. % TiO_2 , strong is greater than these values).

Cr-spinel and clinopyroxenes are not commonly zoned but some samples do contain crystals with evidence for primary zonation that is not due to kimberlitic alteration/rim growth.

5.6 References

- Burgess, S. R. (1997). The evolution of the sub-cratonic mantle seen in mantle xenoliths. Grant Institute of Earth Science. Edinburgh. University of Edinburgh. *Unpublished PhD*
- Burgess, S. R. and Harte, B. (1999). Tracing lithosphere evolution through the analysis of heterogeneous G9/G10 garnets in peridotite xenoliths, I: Major element chemistry. 7th International Kimberlite Conference, Cape Town, Red Roof Designs. 66-80.
- Daniels, L. R. M. (1991). Diamonds and related minerals from the Dokolwayo kimberlite, Kingdom of Swaziland. Department of Geological Sciences. Cape Town. University of Cape Town. *Unpublished PhD*
- Fipke, C. E., Gurney, J. J. and Moore, R. O. (1995). Diamond exploration techniques emphasising indicator mineral geochemistry and Canadian examples. Geological Survey of Canada. **423**. 1-86.
- Griffin, W. L., Shee, S. R., Ryan, C. G., Win, T. T. and Wyatt, B. A. (1999b). Harzburgite to lherzolite and back again: metasomatic processes in ultramafic xenoliths from the Wesselton kimberlite, Kimberley, South Africa. Contributions to Mineralogy and Petrology. **134**. 232-250.
- Grütter, H. S., Gurney, J. J., Menzies, A. H. and Winter, F. (2004). An updated classification scheme for mantle-derived garnet, for use by diamond explorers. Lithos. **77**. 841-857.
- Gurney, J. J. (1984). A correlation between garnets and diamonds in kimberlites. In: Ed. Glover, J. E., Harris, P. G. Kimberlites: Occurrence and origin: A basis for conceptual models in exploration. Perth, University of Western Australia, Extension Services. **8**. 143-166.
- Menzies, A. (2001). A detailed investigation into diamond-bearing xenoliths from Newlands kimberlite, South Africa. Department of Geological Sciences. Cape Town. University of Cape Town. *Unpublished PhD Thesis*
- Smith, D. and Boyd, F. R. (1992). Compositional zonation in garnets in peridotite xenoliths. Contributions to Mineralogy & Petrology. **112**. 134-147.
- van der Westhuizen, A. (1992). The Bellsbank kimberlites, with special reference to a suite of purple garnet megacrysts from the Bobbejaan mine. University of the Orange Free State. *Unpublished Masters Thesis*

6. Phase Relations

6.1 Objectives

In this chapter the coexisting minerals in samples will be assessed as to their state of equilibrium. Petrographic criteria (Chapter 3), mineral chemistry (e.g. Cr₂O₃-CaO garnet composition, Chapter 4) and mineral zonation (Chapter 5) shall be used to divide samples into different assemblages (i.e. whether the sample has clinopyroxene/serpentine/chromite in addition to garnet), different parageneses (i.e. lherzolithic/harzburgitic) and different facies (i.e. diamond/graphite) and also to identify any secondary minerals present.

Coexisting minerals will be plotted and joined with tie lines in compositional space diagrams. This will enable an assessment of the effects of bulk rock composition on the coexisting phase chemistry and the extent of equilibrium between phases and phase assemblages. Once this is known, then the role of P-T may be determined. The assemblages will be examined in simple systems initially and then in terms of a variety of compositional parameters. Finally, compositional trends will be related to important reactions between mantle minerals by means of calculating distribution coefficients for particular cations.

6.2 Equilibria

The important minerals in peridotitic mineral assemblages are as follows: olivine, clinopyroxene, orthopyroxene, garnet, Cr-spinel for lherzolites; and olivine, orthopyroxene, garnet, Cr-spinel for harzburgites. Table 6.1 shows the nearest end member formulae for these minerals in Newlands and Bobbejaan samples and indicates the main chemical substitutions that may occur. Accessory minerals may also be present i.e. diamond or phlogopite.

Primary mineral end-members	Formula	Main Substitutions
Forsterite	MgSiO ₄	Fe-Mg
Enstatite	Mg ₂ Si ₂ O ₆	Fe-Mg
Diopside	CaMgSi ₂ O ₆	Fe-Mg, Na-Ca, Al-Cr
Pyrope	Mg ₃ Al ₂ Si ₃ O ₁₂	Fe-Mg-Ca, Al-Cr
Magnesiochromite	MgCr ₂ O ₄	Fe-Mg, Cr-Al
Accessory mineral end-members		
Diamond	C	B-C, N-C (aggregation)
Phlogopite	KMg ₃ AlSi ₃ O ₁₀ (OH) ₂	Fe-Mg

Table 6.1: Peridotitic minerals with end member formulae and the main major element substitutions associated. Other secondary minerals occur due to the infiltration of kimberlite e.g. calcite, serpentine etc. see Chapter 3.

Therefore the main reactions that are important concerning mineral stability are as follows:

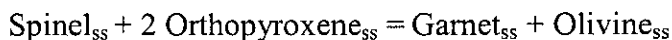
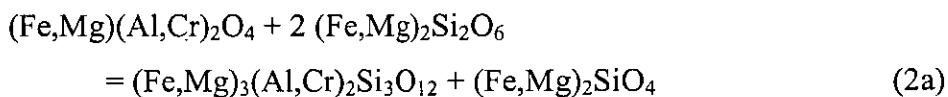
6.2.1 Univariant equilibria:



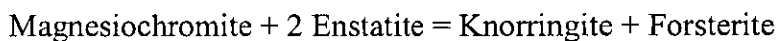
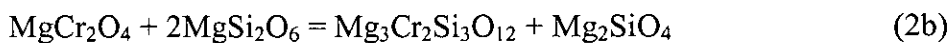
Diamond = Graphite, Kennedy and Kennedy (1976).

6.2.2 Reactions in harzburgites:

FMASCr system:

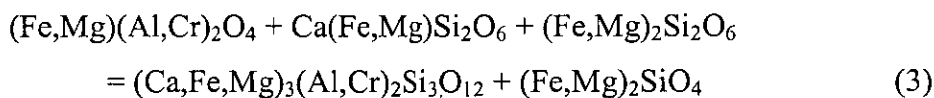


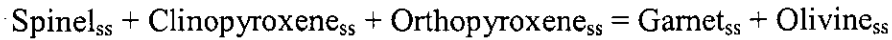
CrMS system:



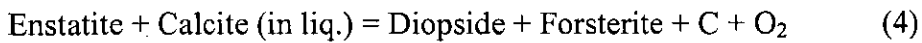
6.2.3 Reactions in lherzolites:

CFMASCr system:





6.2.4 Reactions in carbonate-bearing peridotites:



Reactions (2a), (2b) and (3) may be represented in CFMAS diagram which shows the discontinuous configuration (Fig. 6.1). Also note that the diamond producing side of reaction (4) will be favoured by having a low-CaO protolith which is more oxidised than the interacting carbonatite liquid (Luth, indirect communication via H. Grütter).

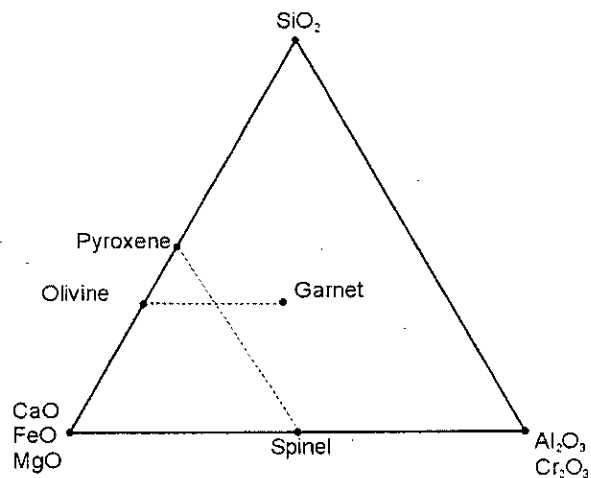


Figure 6.1: CFMAS(Cr) triangle (in cation + oxide molecular proportions, as are all the following diagrams in this chapter) illustrating the two configurations of tie lines involved in reactions (2) and (3).

6.3 Phase Relations

Fig. 6.2 indicates that for a given pressure and temperature, higher Ca rock compositions will form lherzolites and lower Ca rock compositions will form harzburgites in the system CMAS.

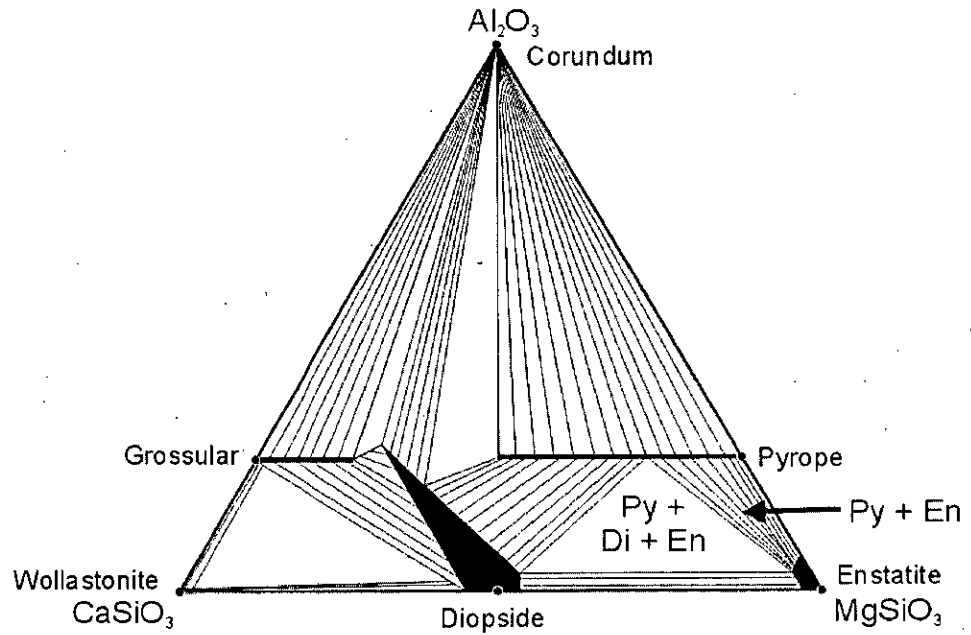


Figure 6.2: $\text{CaSiO}_3\text{-MgSiO}_3\text{-Al}_2\text{O}_3$ system for 3 GPa and 1200°C reproduced from Boyd (1970). Harzburgitic rock compositions form from two phase tie lines between pyrope and enstatite (Py + En). Lherzolic rock compositions plot within the 3 phase field indicated by Py + Di.

Considering the addition of Cr (CMASCr), garnets are observed to increase in Ca content with increasing Cr (this gives the positive slope of the lherzolite line - Fig. 5.2a). Therefore the tie lines would move in the way illustrated in Fig. 6.3 so that the garnet composition shifts with clinopyroxene to higher Ca contents. This effect appears to be irrespective of the addition of chromite.

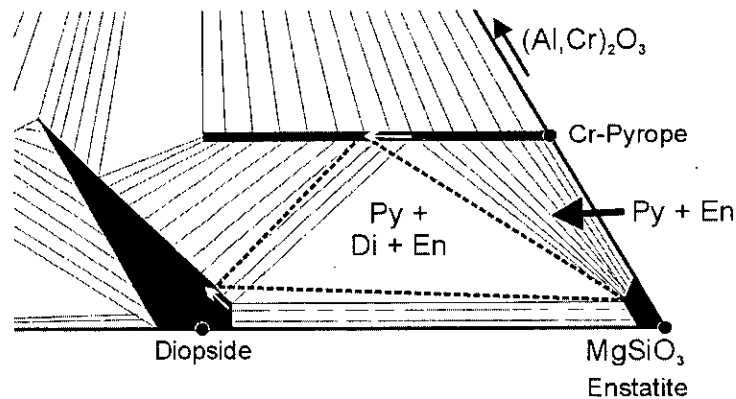


Figure 6.3: Zoom of the enstatite apex of the $\text{CaSiO}_3\text{-MgSiO}_3\text{-Al}_2\text{O}_3$ triangle with the thin tie lines as in Fig. 6.2. The effect of adding Cr to the system is shown by the bold dashed 3-phase field. The clinopyroxene are displaced to higher Ca, Cr, Al-rich and the garnet becomes more Ca-rich (white arrows).

In order to plot the main phases concerned a compositional tetrahedron was set up with the components $(\text{Mg,Fe})\text{Al}_2\text{O}_4$ - $(\text{Mg,Fe})\text{Cr}_2\text{O}_4$ - $(\text{Mg,Fe})_2\text{Si}_2\text{O}_6$ - $\text{Ca}(\text{Mg,Fe})\text{Si}_2\text{O}_6$ at the apices which means that garnet plots equidistant between spinels and pyroxenes. $(\text{Mg,Fe})\text{O}$ is treated as a single component and the tetrahedron projects from olivine. Therefore plotting parameters are as follows:

Apex	Apex percentage proportional to molecular proportion of:
$(\text{Mg,Fe})\text{Al}_2\text{O}_4$	Al_2O_3
$(\text{Mg,Fe})\text{Cr}_2\text{O}_4$	Cr_2O_3
$(\text{Mg,Fe})_2\text{Si}_2\text{O}_6$	$((\text{FeO}+\text{MgO})-(\text{Cr}_2\text{O}_3+\text{Al}_2\text{O}_3+\text{CaO}))/2$
$\text{Ca}(\text{Mg,Fe})\text{Si}_2\text{O}_6$	CaO

Table 6.2: Calculation of phase tetrahedron apex proportions.

The garnet formulae at the corners of the garnet plane are therefore:

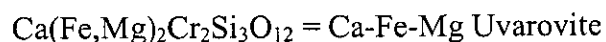
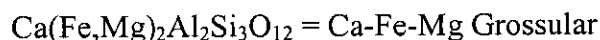
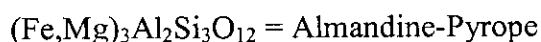
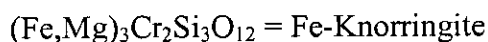


Fig. 6.4 shows the tetrahedron with all end members labelled and looking onto the garnet plane. Fig. 6.4b shows the appearance when looking down the pyroxene join, looking edge on to the garnet plane. Garnets plot on the garnet plane and never have $> 0.5 \text{ Cr}/(\text{Cr}+\text{Al})$ and therefore plot in the lower half of this square. Cr-spinels plot on the magnesiochromite-spinel join and are usually between 0.6 and 0.9 $\text{Cr}/(\text{Cr}+\text{Al})$ and therefore plot in the top half of this line. Clinopyroxenes plot slightly away from the clinopyroxene apex since they are not pure Ca end members and they also contain considerable concentrations of Cr and Al (Chapter 4).

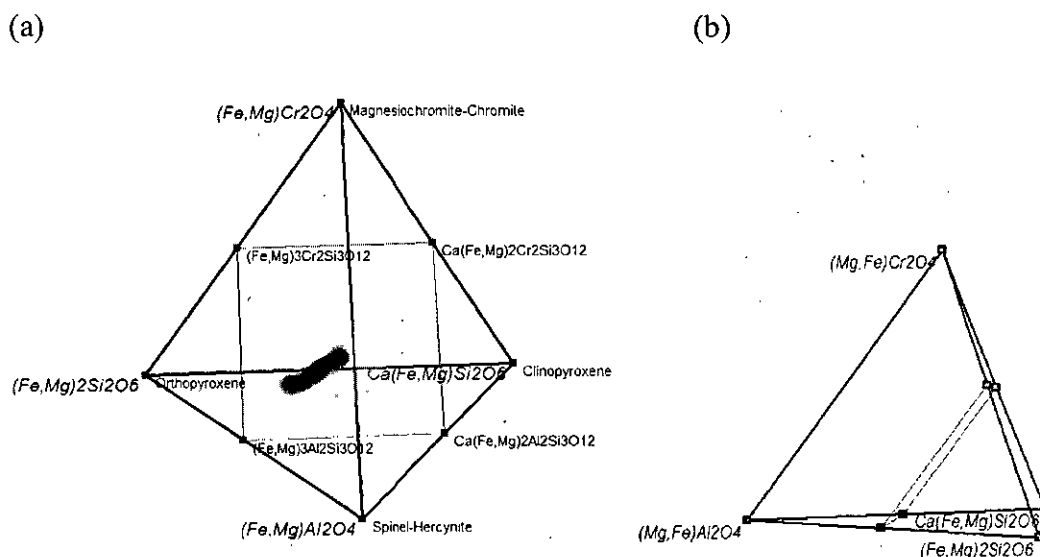


Figure 6.4: The 'garnet-spinel-pyroxene tetrahedron'. (a) Facing onto the garnet plane (thin square outline) which has Newlands and Bobbejaan harzburgitic garnets plotting in the dark grey patch and Iherzolitic garnets in the light grey patch. Garnet compositions for the corners of the garnet plane are shown and are as defined above. (b) Tetrahedron rotated 70° clockwise about the vertical axis, looking edge on to the garnet plane and nearly down the pyroxene join.

The Ca-free system FMACr shall also be examined in order to see the full range of spinel compositions in particular. This is because the Cr-Mg diagram (Chapter 4) is capable of discriminating the Cr-spinels reasonably well into parageneses.

6.4 Newlands and Bobbejaan Samples

6.4.1 Treatment of internal and external mineral compositions

From Chapter 5, we can say that the observation of internally zoned garnet is common and externally zoned garnet is less common. Zoned clinopyroxene and Cr-spinel inclusions in garnet have not been observed. Clinopyroxene and Cr-spinel in the matrix are uncommonly preserved in the Newlands and Bobbejaan samples (see Chapter 3) but when present it is only the clinopyroxene that has been observed to be strongly externally zoned in a primary fashion (Cr-spinel has been observed to be zoned but in a fashion consistent with secondary kimberlitic modification).

Therefore, when 'coexisting minerals' are joined with tie lines on the following plots, it is the composition of the homogeneous Cr-spinel and clinopyroxene inclusions within garnet and the garnet adjacent to the inclusion that are used.

Additionally some of the plots show the interior garnet composition to illustrate the compositional direction of the internal garnet zonation. This avoids the influence of any potential metasomatic chemical modification.

Sample NEW303, which clearly shows both internal and external clinopyroxene (Fig. 3.15), has revealed that the internal and external compositions are similar with minor substitution occurring in the external clinopyroxene (Chapter 5). Both the internal clinopyroxene-garnet and external (both core and rim compositions) clinopyroxene-garnet pairs are consistent with P-T re-equilibration and not metasomatism (see Chapter 7 for more details).

6.4.2 $(Mg,Fe)Cr_2O_4$ - $(Mg,Fe)Al_2O_4$ - $Ca(Fe,Mg)Si_2O_6$ - $(Fe,Mg)_2Si_2O_6$

Fig. 6.5 shows the distribution of tie lines between coexisting spinel, garnet and clinopyroxene in lherzolitic (green lines) and spinel and garnet in harzburgitic (black lines) assemblages in the spinel-garnet-pyroxene tetrahedron. Orthopyroxene compositions are not plotted because alteration has made them unavailable however one value is obtained for NEW088. The orientation shown allows garnets to be viewed in the same spatial arrangement as on a Cr-Ca diagram with a harzburgite trend and lherzolite trend evident within the garnet plane.

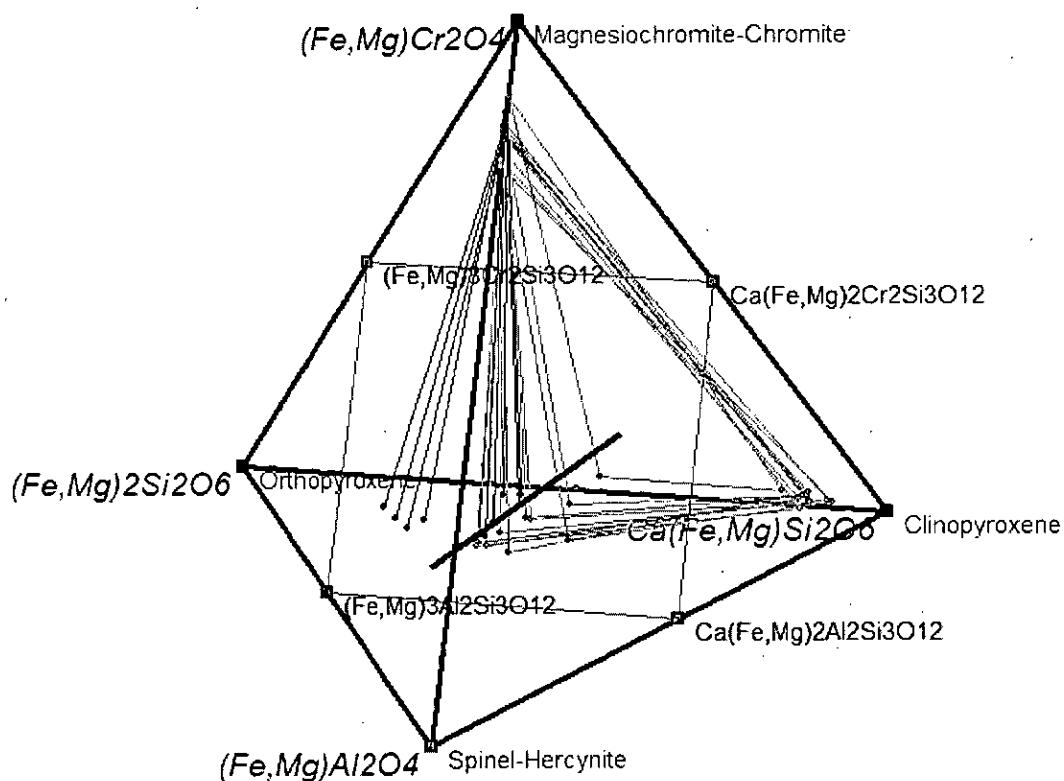
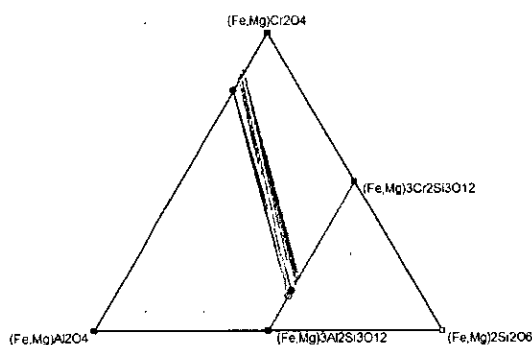


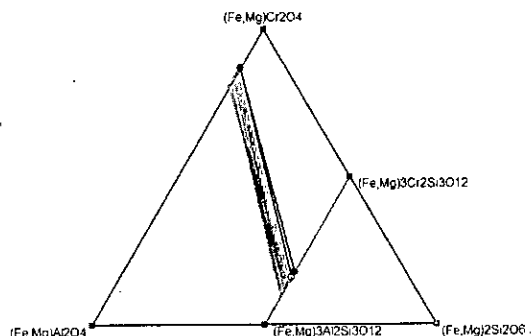
Figure 6.5: The spinel-garnet-pyroxene tetrahedron (SGPT, Fig. 6.6) for samples with coexisting minerals from Newlands and Bobbejaan. 3 phase (spinel-clinopyroxene-garnet) combinations for lherzolite assemblages are plotted with grey tie lines, 2 phase (spinel-garnet) combinations for harzburgites in black. All garnets plot in the garnet plane outlined as a thin square shape. The black line separates harzburgitic garnets (left) from lherzolitic garnets (right) and approximates the lherzolite line.

Numerous 2 and 3 phase tie lines are approximately parallel, i.e. those involving garnet + spinel, garnet + clinopyroxene and spinel + clinopyroxene. Also evident is the overlap in harzburgitic and lherzolitic spinels with regard to their Cr/Al ratio. Independently though, the higher Cr-Ca lherzolitic garnets tend to coexist with higher Cr spinels and clinopyroxenes. Garnet-pyroxene pairs tend to involve low-Cr garnets at the base of the lherzolite trend.

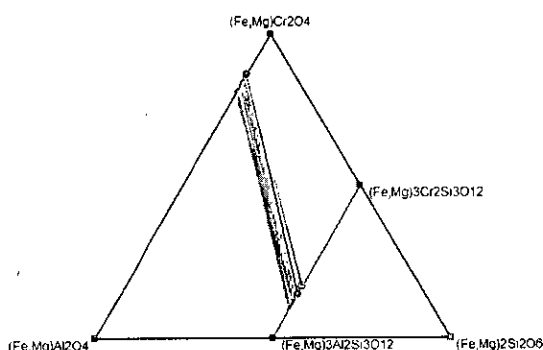
(a) B47



(b) NEW288



(c) NEW069



(d) NEW088

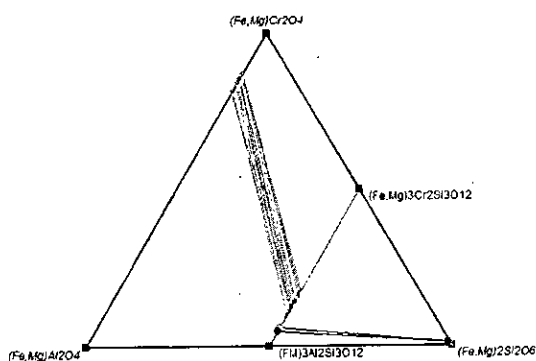


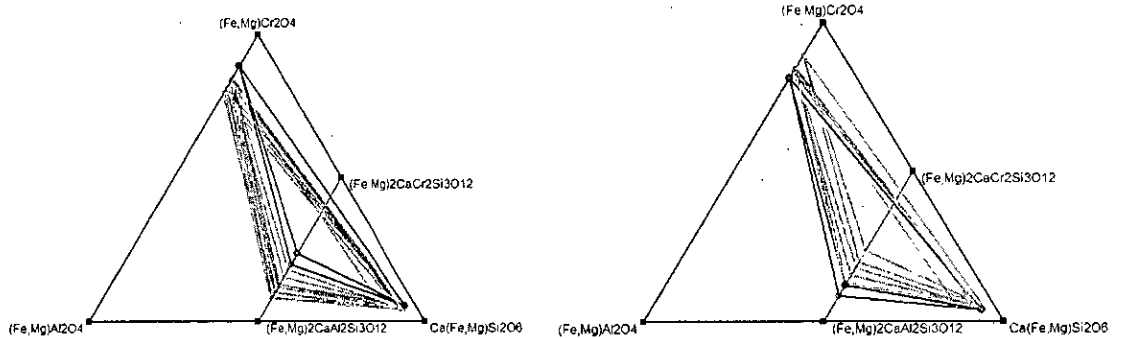
Figure 6.6: Harzburgitic samples plotted onto the spinel-chromite-orthopyroxene plane of SGPT. Garnet core compositions are plotted as a grey circle and the composition of garnet adjacent to coexisting minerals is plotted as filled black circle, the range of harzburgitic garnet-spinel tie lines from all samples are shown in each for comparison in grey. (a) sample B47, a low-Ca G10 garnet. (b) NEW288, a high-Ca G10 garnet. (c) NEW069 a high-Cr, high-Ca G9 garnet-chromite sample. (d) NEW088 a low-Cr G10 garnet with coexisting orthopyroxene.

Fig. 6.6 shows the way that low Ca garnets with moderate Cr in harzburgitic field at Newlands and Bobbejaan coexist with the lowest Cr spinels (B47) whereas the high Ca, high-Cr garnets in the harzburgitic field coexist with the highest Cr spinels (NEW288). In both cases if garnet core compositions are joined to the Cr-spinel composition present they produce tie lines sub-parallel to the majority of garnet-spinel pairs since they are effectively out of equilibrium at too high Cr. NEW069 however has its garnet core composition at low-Cr relative to the majority of these tie lines which is in accordance with its I_c trend that is in the opposite direction with respect to the majority of internal zonation trends I_d and I_s (chapter 5). Sample NEW088 contains a particularly low-Cr garnet for the range displayed at Newlands

and Bobbejaan and lacks chromite. Therefore this represents a low-Cr bulk rock composition which belongs to the garnet-orthopyroxene field without spinel-chromite. For most of the other garnet-spinel pairs lines it can be expected that orthopyroxene will also coexist forming 3 phase triangles (not shown), however, since the orthopyroxene would not deviate far from $(\text{Fe,Mg})_2\text{Si}_2\text{O}_6$, one can assume that the triangles shown in Fig. 6.6 would rotate around this apex.

(a) NEW114

(b) BOB402



(c) B48

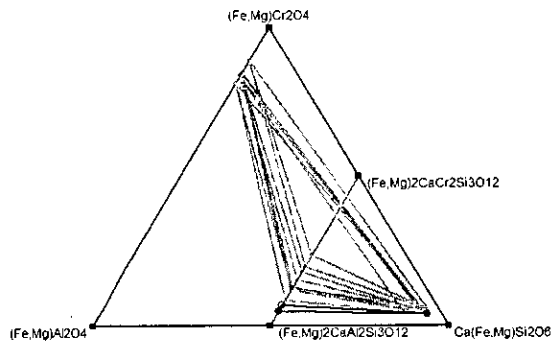


Figure 6.7: Lherzolitic samples in chromite-spinel-clinopyroxene triangles projecting from orthopyroxene in the SGPT. Garnet core compositions are plotted as a grey circle and the garnet adjacent to coexisting minerals is plotted as a filled black circle, the whole range of lherzolitic garnet-clinopyroxene-spinel tie lines from all samples are shown for comparison in grey. (a) sample NEW114 a high-Cr, high-Ca G9 garnet. (b) BOB402, an intermediate Cr-Ca G9 garnet. (c) B48 a chromite-free, low Cr, low-Ca G10 garnet with coexisting clinopyroxene (too small to analyse so shown as an average clinopyroxene composition).

Fig. 6.7 illustrates the range of compositions in coexisting minerals from clinopyroxene-bearing samples. High-Cr, high-Ca garnets tend to coexist with high-Cr spinels and clinopyroxenes (NEW114) whilst lower Cr, lower Ca garnets (e.g.

BOB402) tend to coexist with lower Cr spinels and clinopyroxenes. As with NEW288 and B47 harzburgites, it is apparent that the core compositions (grey circle symbols) of NEW114 and BOB402 are Cr-rich compared to the garnet compositions adjacent to inclusions (filled black circle symbols in Fig. 6.7). Sample B48, in a similar way to NEW288 has a low-Cr bulk rock composition and the garnet coexists with a pyroxene (this time clinopyroxene) without chromite.

Fig. 6.8 shows the triangles from Figs 6.6 and 6.7 with relation to the garnet zonation trends in Cr-Ca space. A lowering of bulk rock Cr reduces the likelihood of Cr-spinel being present; thus garnets with below about 5 wt. % Cr₂O₃ do not contain chromite in the Newlands and Bobbejaan samples recorded in this study. Garnet interior to inclusion contact trends are visible in the triangular graphs in the same sense as they are as arrows from interior to contact on the Cr-Ca plot.

The Iherzolite line (Gurney, 1984) as indicated in Fig. 6.8 does not apply strictly to differentiate Iherzolic from harzburgitic garnets in the Newlands and Bobbejaan samples. The line that separates clinopyroxene-bearing from clinopyroxene free samples is a shallower line (i.e. rotated clockwise). It is parallel to the Iherzolic zonation arrows shown (e.g. BOB402) and parallel to the zonation trends close to the Iherzolite line at high Cr values.

The line that indicates chromite-present from chromite free samples is not well constrained but seems to lie at about 4 wt. % Cr and is shown in Fig. 6.8. The triangles with just garnet-pyroxene tie lines have major element compositions below this line. This is the line of 'Cr saturation'.

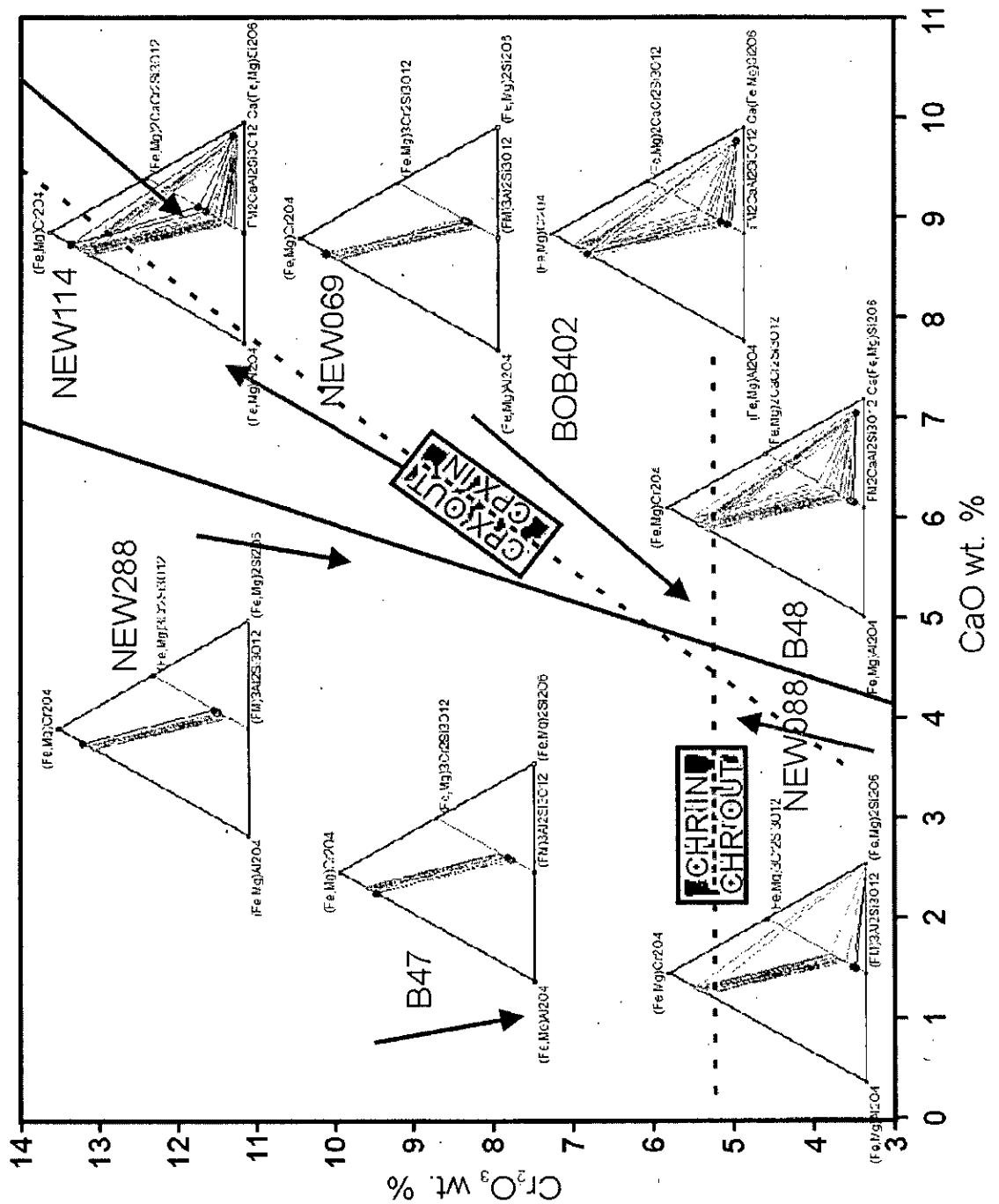


Figure 6.8: The spinel-garnet-pyroxene triangles from Figs 6.6 and 6.7 arranged according to garnet location on the Cr-Ca wt. % plot (see chapter 5). NEW088 (orthopyroxene-garnet pair) and B48 (clinopyroxene-garnet pair) have a similar zonation trend (upward pointing arrow at low Cr and is shown as one trend for clarity). Garnet compositions adjacent to inclusions are plotted with filled grey circles for clarity, with interiors as filled black circles. The clinopyroxene-in line (short, dashed) is shown for Newlands and Bobbejaan samples relative to the Iherzolite line of Gurney (1984). The spinel-in line (or chromite-in line) is shown as a horizontal, dashed line at ~ 5 wt. % Cr_2O_3 .

6.4.3 Sliding reaction simulations

One may simulate the effect of consuming spinel and pyroxenes as garnet and olivine are generated in reactions (2a) and (3) (see first part of this chapter) on the composition of garnet. Using different proportions Ca: Fe+Mg in garnet and bulk pyroxene one may simulate the real data in terms of cation ratios. The precise reactions simulated are as follows:

1.
$$\text{Ca(Fe,Mg)}_2\text{Al}_2\text{Si}_3\text{O}_{12} + (\text{Fe,Mg})(\text{Al,Cr})_2\text{O}_4 + 2 (\text{Fe,Mg})_2\text{Si}_2\text{O}_6$$

$$= \text{Ca(Fe,Mg)}_2\text{Al}_2\text{Si}_3\text{O}_{12} + (\text{Fe,Mg})_3(\text{Al,Cr})_2\text{Si}_3\text{O}_{12} + (\text{Fe,Mg})_2\text{SiO}_4$$
2.
$$\text{Ca(Fe,Mg)}_2\text{Al}_2\text{Si}_3\text{O}_{12} + (\text{Fe,Mg})(\text{Al,Cr})_2\text{O}_4 + 2 \text{Ca(Fe,Mg)Si}_2\text{O}_6 +$$

$$(\text{Fe,Mg})_2\text{Si}_2\text{O}_6$$

$$= \text{Ca(Fe,Mg)}_2\text{Al}_2\text{Si}_3\text{O}_{12} + \text{Ca}_2(\text{Fe,Mg})(\text{Al,Cr})_2\text{Si}_3\text{O}_{12} + (\text{Fe,Mg})_2\text{SiO}_4$$
3.
$$\text{Ca(Fe,Mg)}_2\text{Al}_2\text{Si}_3\text{O}_{12} (\text{Fe,Mg})(\text{Al,Cr})_2\text{O}_4 + 2 \text{Ca}_{0.5}(\text{Fe,Mg})_{1.5}\text{Si}_2\text{O}_6 +$$

$$(\text{Fe,Mg})(\text{Al,Cr})_2\text{O}_4$$

$$= \text{Ca(Fe,Mg)}_2\text{Al}_2\text{Si}_3\text{O}_{12} + \text{Ca(Fe,Mg)}_2(\text{Al,Cr})_2\text{Si}_3\text{O}_{12} + (\text{Fe,Mg})_2\text{SiO}_4$$

The starting garnet compositions plot at zero Cr/(Cr+Al) and the final compositions (RHS of the reactions above) are all at 0.25 Cr/(Cr+Al). Therefore, in words, the simulations are as follows:

1. garnet + spinel + 2 opx → lower Ca, higher Cr garnet + olivine.
2. garnet + spinel + 2 cpx → much higher Ca, higher Cr garnet + olivine.
3. garnet + spinel + opx + cpx → higher Cr garnet + olivine.

Fig. 6.9 shows these results of these simulations on a Ca/(Ca+Mg+Fe) vs. Cr/(Cr+Al) plot. In Fig. 6.9 the simulations are run with realistic starting garnet composition which is lower in Ca/(Ca+Mg+Fe) and involve a realistic spinel composition which is higher in Cr/(Cr+Al) than the values shown in the generalised equations above. This generates trajectories that coincide with the Newlands and Bobbejaan garnet zonation trends. Several points emerge from this diagram: Firstly, the clinopyroxene-only simulation [2] is parallel to many of the lherzolitic garnet zonation trends ('Id' from chapter 5). Secondly this line is parallel to the CCGE of Kopylova et al. (2000) although they occur to higher Cr and Ca values. Thirdly,

simulation [1] provides a good approximation to some of the harzburgitic zonation trends ('Is' from chapter 5) and the range of slopes of these trends may be generated by adding various proportions of clinopyroxene component into the sliding reactions (i.e. the range of trajectories lying in between simulation [1] and [3] which would be able to match the zonations of NEW047 and NEW088). Fourthly, simulation [3] produces a line with a slope parallel to garnet zonations that conform to the lherzolite line in a CaO vs. Cr₂O₃ wt. % plot.

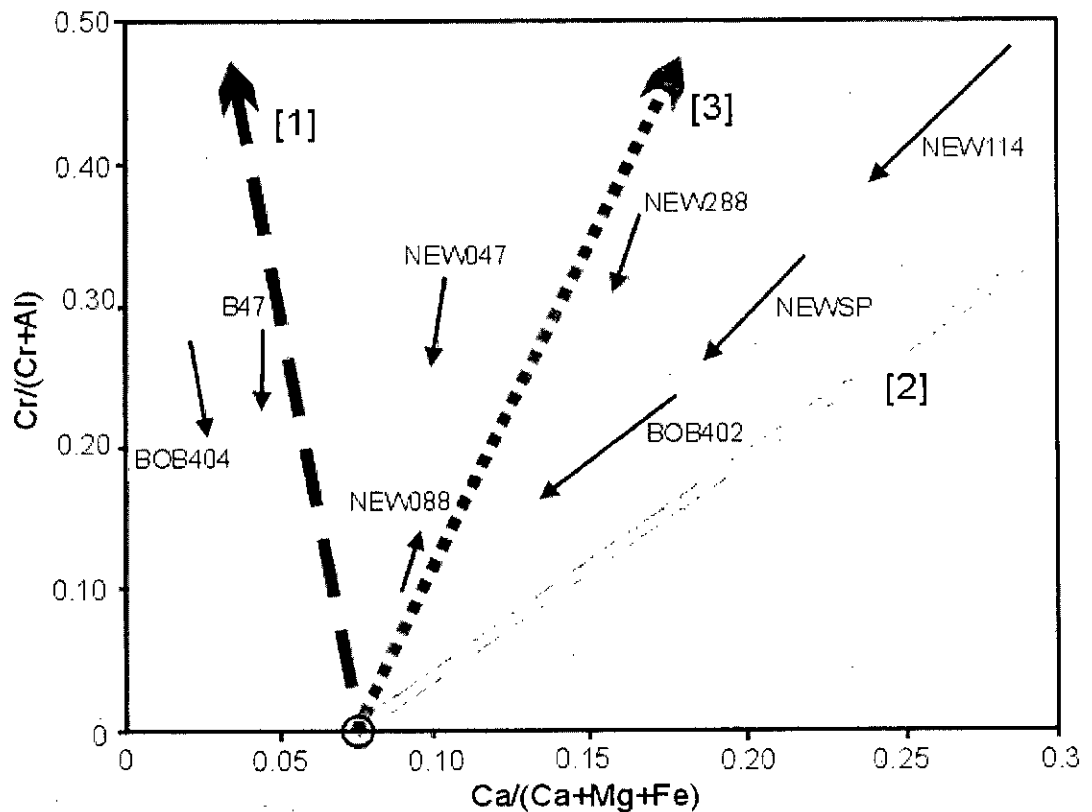


Figure 6.9 Ca/(Ca+Mg+Fe) vs. Cr/(Cr+Al) cation plot illustrating the results of the three simulations on garnet compositions from an initial starting garnet composition at zero Cr/(Cr+Al) (black circle). Several garnet zonations from Fig. 5.3 (a and b) are shown to indicate the trends of natural garnets. The CCGE line of Kopylova et al. (2000) corresponds to the clinopyroxene reaction of simulation [2] (thick light-grey solid arrow). Simulation [1] representing the orthopyroxene reaction is shown as thick grey dashed arrow. Simulation [3] representing the 1:1 clinopyroxene:orthopyroxene reaction is shown as a medium grey, square, dotted arrow.

6.4.4 FeO-MgO-Al₂O₃-Cr₂O₃

In order to see the full range of spinel compositions, the Fe:Mg ratio has to be taken into account. Fig. 6.10 shows that the harzburgitic garnets have tie lines to high-Mg spinels whereas the lherzolitic garnets and clinopyroxenes may be at similar Cr:Al ratios but are at higher Fe:Mg.

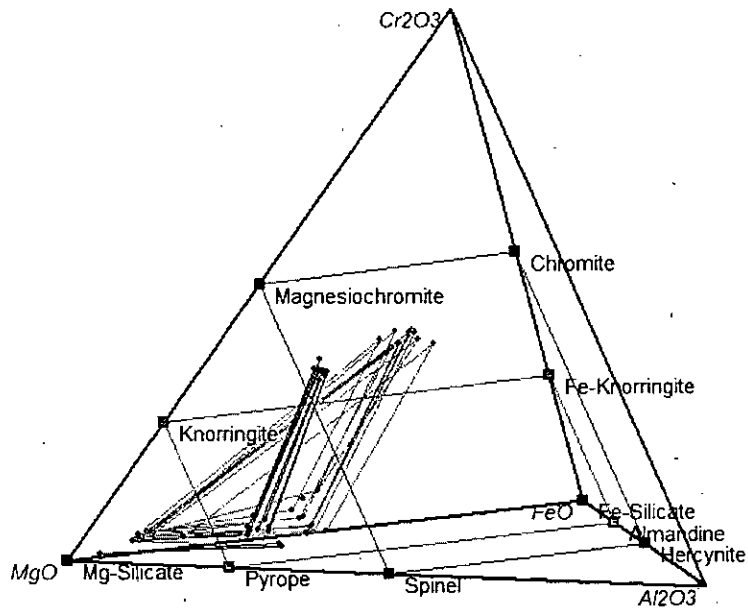


Figure 6.10: FMACr Tetrahedron with the square spinel plane and the rectangular garnet plane outlined in thin lines. Black tie lines are harzburgitic samples with garnet-spinel pairs. Grey lines are lherzolitic samples with garnet-spinel-clinopyroxene. Clinopyroxene compositions plot closest to the MgO apex.

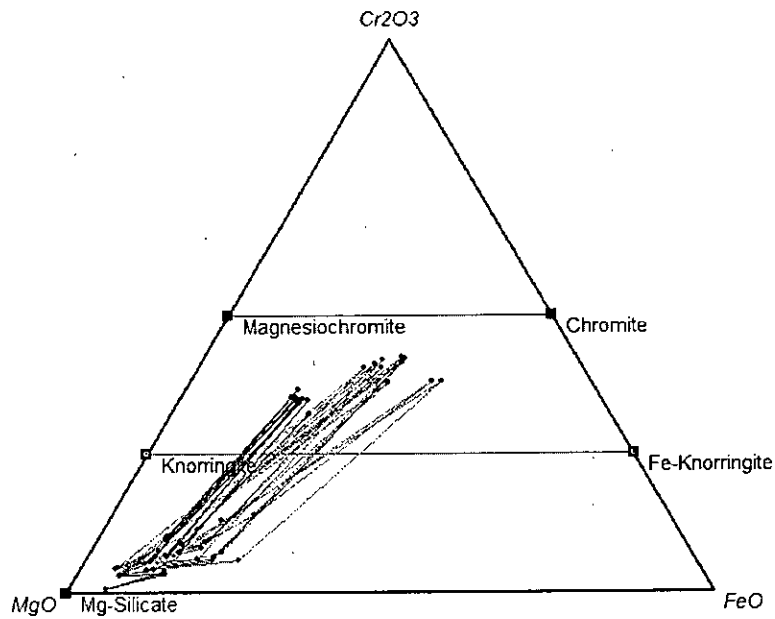


Figure 6.11: FMCr triangular plot of selected lherzolitic (grey tie lines) and harzburgitic (black tie lines) samples. All points above the knorringite-Fe-knorringite join are Cr-spinels. The garnets plot in two clusters with the harzburgitic cluster almost overlapping with the clinopyroxenes which plot closest to the MgO apex.

Fig. 6.11 again shows that the harzburgitic spinels have higher MgO contents and lower Cr₂O₃ contents than lherzolitic spinels. Harzburgitic garnets are less distinct

from lherzolitic ones but they are higher in MgO and on average slightly lower in Cr₂O₃. On this graph clinopyroxenes plot very close to garnets so it is most useful for distinguishing chromites. Orthopyroxene plots at lowest Cr₂O₃ value. Note that spinels and garnets do not plot on their lines (horizontal tie-lines, Fig. 6.11) because Al₂O₃ is not considered.

6.4.5 Exsolution and phase relations

The modal proportions of minerals were measured using a 100 μm grid for the monogranular garnet sample B55, which contains well developed exsolved pyroxene and spinel. The modal proportion of minerals is as follows: garnet 72 %, clinopyroxene 18 %, Cr-spinel 9 % and serpentine 1 %. The serpentine was treated as orthopyroxene since it has relict cleavage. These modes were multiplied by the major element analyses of the constituent minerals to achieve a precise bulk rock composition using a typical harzburgitic orthopyroxene composition (see Table 6.3).

Oxide	SiO ₂	TiO ₂	Al ₂ O ₃	Cr ₂ O ₃	FeO	MnO	MgO	CaO	Na ₂ O	Total	Mode
Grt	39.599	0.041	18.941	6.408	9.412	0.628	19.505	6.059	0.027	100.64	72.16
Cpx	52.996	0.012	1.693	2.506	2.299	0.107	17.273	20.480	1.961	99.38	17.98
Crt	0.066	0.498	7.825	60.337	20.877	0.426	10.010	0.016	0.013	100.20	8.63
Opx	55.000	0.000	2.000	0.000	4.000	0.000	39.000	0.000	0.000	100.00	1.23
Bulk	38.783	0.075	14.672	10.284	9.057	0.509	18.523	8.056	0.373	100.36	
Cations	Si	Ti	Al	Cr	Fet	Mn	Mg	Ca	Na	Total	
Bulk Cations	2.905	0.004	1.295	0.609	0.567	0.026	2.069	0.647	0.027	8.15	

Table 6.3: mineral compositions in sample B55, with calculated bulk rock (calculated on a 12 oxygen basis) composition based on the mineral modes.

The resultant composition is higher in Cr/(Cr+Al) and higher in Ca/(Ca+Fe+Mg). The weight % oxide values appear to be consistent with a garnet formula in terms of cations calculated. Therefore the bulk rock composition was calculated as a garnet (Table 6.3 and Fig. 6.12). Both the overall trend from bulk rock composition to core to inclusion and the core to inclusion trend can be seen to match well in slope to simulation [3], which fits with the presence of orthopyroxene (above). Therefore sliding reactions explain the increase in modal spinel and two pyroxenes in the rocks and the exsolution texture noted in Chapter 3. This is a process expected to be operating in many samples but they show a range from partial to nearly complete annealing of the exsolution textures.

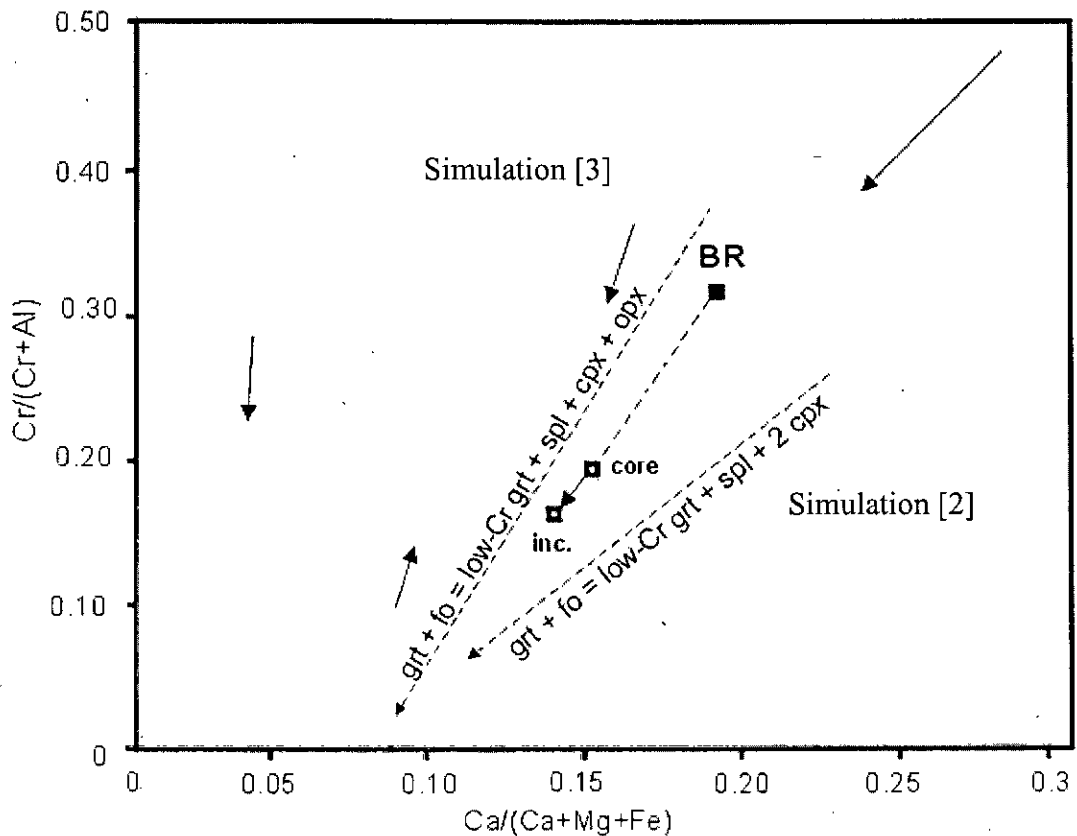


Figure 6.12: Ca/(Ca+Fe+Mg) vs. Cr/(Cr+Al) plot for B55 'bulk rock' (i.e. bulk sample) composition (BR). The garnet core and region adjacent to inclusion (inc.) are shown from the actual analyses on electron probe. Simulation [3] is the steeper reaction line and simulation [2] is the shallower reaction line. Several other garnet zonation trends are shown from Fig. 6.9 for comparison.

6.5 Summary

The system CMASCr yields a tetrahedron with apices Fe-Mg chromite, Fe-Mg spinel, clinopyroxene and orthopyroxene that defines a garnet plane in its interior. In this plane harzburgitic garnets plot in a field that may be differentiated from lherzolitic garnets by a dividing line. This line is essentially a clinopyroxene-in/out line that can be indicated on a garnet Cr-Ca plot.

The system FMASCr yields a tetrahedron with apices FeO, MgO, Cr₂O₃ and Al₂O₃ which defines the spinel and garnet planes. Harzburgitic garnets and spinels are differentiated from lherzolitic garnets and spinels by having consistently higher MgO concentrations and on average lower Cr₂O₃ concentrations.

In Cr-spinel-garnet lherzolites, higher Cr and Ca garnets are in equilibrium with higher-Cr spinels and higher Cr clinopyroxenes. These garnets show compositions plotting along a general 'clinopyroxene-chromite-garnet equilibrium' (CCGE) first noted by Kopylova et al. (2000). Some Cr-spinel-garnet lherzolites show a steeper trend on a Cr-Ca diagram and these samples plot close to the lherzolite line of Gurney (1984). The zonation profiles in garnets are parallel to these trends because they reflect progress along the sliding reaction: garnet + forsterite \rightarrow garnet + spinel + 2 clinopyroxene (simulation [2]) and garnet + forsterite \rightarrow garnet + spinel + orthopyroxene + clinopyroxene (simulation [3]) towards lower P and T. Garnet zonation trends in Newlands and Bobbejaan samples are found parallel to the CCGE trend but displaced to both lower and higher Ca e.g. NEW065 and NEW069 in Fig. 5.3a.

In chromite-garnet harzburgites higher Cr and Ca garnets are in equilibrium with higher-Cr spinels. The general trend of these garnet compositions plots along a 'harzburgitic trend' of bulk rock compositions - a band of compositions of shallow slope in the harzburgite field of a Cr-Ca diagram is thought to represent a line of equal pressure. This also conforms to the line of equal pressure represented by the diamond-graphite constraint of Grütter et al. (2004).

The garnet zonation trends in the harzburgite field are much less Ca-dependent than for clinopyroxene-bearing samples and reflect the progress of the sliding reaction garnet + forsterite \rightarrow garnet + spinel + 2 orthopyroxene (simulation [1]) towards lower P and T. Samples with higher Ca bulk compositions have garnets that are displaced to higher Ca and have approximately similar although a little shallower zonation trends as would be explained by including small proportions of a clinopyroxene component in the reaction above (e.g. simulation [3]).

Therefore from the simulations in both harzburgitic and lherzolitic garnets the spinel controls the Cr/(Cr+Al) ratio and the pyroxenes control the Ca/(Ca+Fe+Mg) ratio. Since higher Cr spinels coexist with higher Cr higher Ca garnets, the larger change in

Cr for the lherzolitic trends is explained by the resultant relative change in $Cr/(Cr+Al)$ in the reactions. The way that garnet zonation trends change in trend from steep to those with a positive slope on a $Cr/(Cr+Al)$ vs. $Ca/(Ca+Fe+Mg)$ cation plot is strongly dependent on bulk pyroxene $Ca/(Ca+Fe+Mg)$.

The sliding reactions rely on an increase in modal spinel and pyroxene in the rocks. This would conform to the presence of exsolution textures noted in several samples in Chapter 3 (especially evident in sample B55).

6.6 References

Boyd, F. R. (1970). Garnet peridotites and the system $CaSiO_3$ - $MgSiO_3$ - Al_2O_3 . Mineralogical Society of America, Special Publication. **3**. 63-75.

Grütter, H. S., Gurney, J. J., Menzies, A. H. and Winter, F. (2004). An updated classification scheme for mantle-derived garnet, for use by diamond explorers. *Lithos*. **77**. 841-857.

Gurney, J. J. (1984). A correlation between garnets and diamonds in kimberlites. In: Ed. Glover, J. E., Harris, P. G. *Kimberlites: Occurrence and origin: A basis for conceptual models in exploration*. Perth, University of Western Australia, Extension Services. **8**. 143-166.

Kennedy, C. S. and Kennedy, G. C. (1976). The equilibrium boundary between graphite and diamond. *Journal of Geophysical Research*. **81**. 2467-2470.

Kopylova, M. G., Russell, J. K., Stanley, C. and Cookenboo, H. (2000). Garnet from Cr- and Ca-saturated mantle: implications for diamond exploration. *Journal of Geochemical Exploration*. **68**. 183-199.

7. Geothermobarometry

7.1 Objectives

Pressure and temperature (P-T) estimates in Newlands and Bobbejaan samples will be calculated using appropriate existing geothermometer and geobarometer formulations from the literature for mineral compositions determined by electron microprobe (Chapter 5). The relative merits of particular thermometers and barometers will be assessed in the context of Newlands and Bobbejaan samples. Any consistent P or T bias for these calibrations will be highlighted. The conformism of the samples to model geotherms will also be addressed. A new method for measuring Ni-in-garnet has been developed (see Appendix I, McDade et al., *unpubl.*) and is implemented on garnets from 16 samples in order to derive Ni-in-garnet thermometry estimates.

The objective of the last part of this chapter is to establish P-T behaviour of the samples and to identify mineral compositional parameters that conform to P-T trends. The garnet-spinel-2pyroxene-olivine equilibria and the garnet-spinel-clinopyroxene-olivine equilibria (CCGE of Kopylova et al., 2000) from Chapter 6 will be related to coexisting mineral compositional parameters and their independent P-T estimates. The garnet-spinel-orthopyroxene-olivine equilibria identified in Chapter 6 will be related to harzburgitic P-T estimates and again related to coexisting mineral compositional parameters. Cr/(Cr+Al) values for coexisting garnet, spinel (and clinopyroxene where present) will be examined and compared to existing experimental data.

The P-T estimates will be plotted and compared to the constraints shown in Figure 7.1. The diamond-bearing sample (BOB404) identified in Chapter 3 will provide a clear marker for the diamond stability field. The level of Cr saturation of the minerals in the samples can be compared to the progressive effect of Cr on the spinel-garnet transition, which can dramatically increase the stability of spinel from around 10 kb to a maximum of about 70 kb according to the MCrS stability line of Klemme (2004)

for a normal cratonic geotherm. Different sets of Cr/(Cr+Al) isopleths have been experimentally determined for garnet and spinel in MASCr by Malinovsky and Doroshev (1977), and FMASCr by Girmis and Brey (1999). Therefore one of the objectives is to compare the P-T estimates for the samples with Cr/(Cr+Al) isopleths.

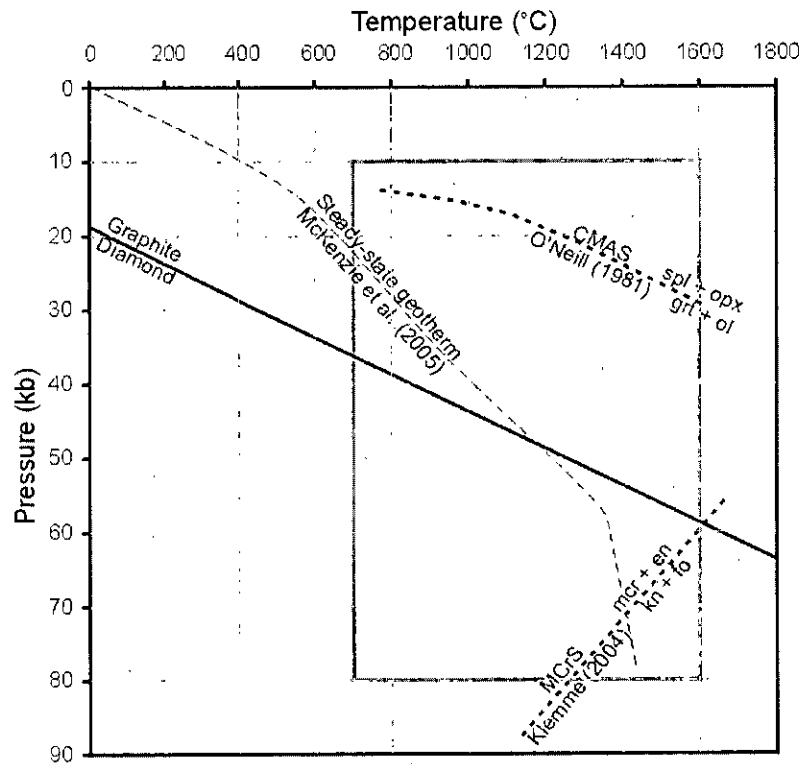


Figure 7.1: P-T diagram with the graphite-diamond line of Kennedy and Kennedy (1976), the steady state geotherm for old, cold lithosphere of McKenzie et al. (2005), the spinel-garnet transition for the CMAS system of O'Neill (1981) and the spinel-garnet transition for MCrS of Klemme (2004). spl = spinel, opx = orthopyroxene, grt = garnet, ol = olivine, mcr = magnesiocromite, en = enstatite, kn = knorringite, fo = forsterite. Grey box indicates the P-T region shown in Fig. 7.6.

Finally, the Perplex thermodynamic modelling program (Connolly and Petrini, 2002) will be used to model a range of Newlands and Bobbejaan sample compositions. These models will then be used to calculate changes in mineral assemblage, mode and composition with variations in P and T. An appraisal of its success will be made.

7.2 Application

Due to the serpentinisation of olivine and orthopyroxene in Newlands and Bobbejaan samples, it is only garnet, Cr-spinel and clinopyroxene that are available for

geothermobarometry. This limits the barometers and thermometers to those shown in Table 7.1. Garnet-spinel equilibria are not shown in this table because the authors chose not to formulate an algorithm for treating the equilibria as a geothermobarometer, rather than as a presentation of the particular isopleths generated for their specific experimental systems.

Shorthand	Distribution of Element/molecule in mineral(s)	Reference	1 σ Error
T _{EG79}	D _{Fe/Mg} Cpx-Grt	Ellis and Green (1979)	50 °C
T _{KR88}	D _{Fe/Mg} Cpx-Grt	Krogh (1988)	50 °C
T _{AI94}	D _{Fe/Mg} Cpx-Grt	Ai (1994)	50 °C
T _{CA94}	D _{Ni/Mg} Ol-Grt*	Canil (1994)	50 °C
T _{CA99}	D _{Ni/Mg} Ol-Grt*	Canil (1999)	50 °C
T _{GR89}	[Ni] Ol-Grt* or Grt (Ol)	Griffin et al. (1989)	50 °C
T _{RY96}	[Ni] Grt (Ol)	Ryan et al. (1996)	50 °C
T _{NT00}	a _{En} Cpx (Grt)	Nimis and Taylor (2000)	50 °C
P _{NT00}	a _{Ca-Cr-Ts} Cpx (Grt)	Nimis and Taylor (2000)	2.3 kbar
P ₃₈	[Cr,Ca] Grt (Chr)	Grütter et al. (2006)	2 kbar

Table 7.1: Summary of existing geothermometers, geobarometers suitable for use with Newlands and Bobbejaan samples. The single grain techniques at the bottom of the table assume equilibrium with a mineral indicated in brackets. 1 σ errors are the errors quoted by the authors for replicating experimental/natural calibration data. The propagation of analytical errors from electron and ion microprobe techniques used in this project yield additional 1 σ errors of < 10°C and < 1 kbar. '*' indicates the thermometers where olivine Ni concentrations will have to be assumed in for the case of Newlands and Bobbejaan samples.

Since garnets are often zoned towards coexisting minerals in the matrix and/or inclusions (see Chapter 5), care was taken to use analyses close to mineral contacts for use in geothermobarometric formulations. These locations are most likely to yield equilibrium compositions between minerals. Unlike garnet, other minerals as inclusions in garnet are typically unzoned. Only NEW303 has clinopyroxene both as an inclusion in garnet and present in the matrix. No samples have both matrix and inclusion spinel. Garnet is never included in other minerals.

In harzburgites only single-garnet techniques are available. The Cr/Ca barometer of Grütter et al. (2006) was applied to all harzburgitic samples and the Ni-in-garnet thermometer of Ryan et al. (1996) applied to those samples analysed for Ni by SIMS.

Other Ni-in garnet thermometer formulations require knowledge of Ni and Mg in olivine (Table 7.1) which is not known in Newlands and Bobbejaan samples, therefore application of these uses assumed concentrations in olivine of Ni (3000 ppm) and MgO (40 wt. %) following the suggestion of Griffin et al. (1989). T_{R96} should be regarded as the most accurately constrained.

In lherzolitic samples, temperatures were calculated based on garnet-clinopyroxene Fe-Mg exchange thermometers. Further T_s and, additionally, P_s for these samples were estimated using the single clinopyroxene geothermobarometer formulation of Nimis and Taylor (2000). The single-garnet techniques of the Ni-in garnet thermometer of Ryan et al. (1996) and the Cr/Ca barometer of were applied to those analysed for Ni by SIMS and to all samples analysed by electron microprobe respectively.

7.3 Results

7.3.1 Analysis of the different P-T formulations

Table 7.2 shows the range in P-T estimates and Fig. 7.2 shows the estimates in P-T space for the different existing thermometers and barometers. Table II.4 in Appendix II has the coexisting mineral compositions for all samples analysed by electron microprobe.

Sample	T_{EG79}	T_{K88}	T_{AI94}	P_{NT00}	T_{NT00}	T_{G89}	T_{C94}	T_{R96}	T_{C99}	P_{38}
NEW021	1036	1033	937	36	859					26
NEW056	1007	966	914	38	925					27
NEW007						938	985	948	970	27
NEW070	1353	1379	1398	40	1210					28
NEW071	1010	960	949	50	1220					28
NEW063	1149	1136	1139	50	1150	1091	1067	1105	1064	28
NEW065	1016	1007	931	40	1000					29
BOB403	973	896	881	45	1120					30
B55	990	932	927	48	1080	906	966	914	949	30
NEW407						883	953	890	934	30
B48						835	924	841	901	30
NEW303 cores	1013	931	909	40	1050					30

Sample	T _{EG79}	T _{K88}	T _{Al94}	P _{NT00}	T _{NT00}	T _{G89}	T _{C94}	T _{R96}	T _{C99}	P ₃₈
NEW303 rims	984	896	864	38	1025					30
NEW303 internal	1006	924	890	37	1010					30
NEW078	1046	995	979	38	1250					30
BOB402	986	931	929	50	1180					31
NEW011	1139	1117	1102	42	920					31
BOB301	961	912	888	45	960					31
B44	927	842	803	40	965					32
NEW406	1016	947	920	40	1050	895	960	903	941	32
NEW116	997	942	906	43	1035					32
BOB401	986	939	926	48	1110	804	904	809	879	33
NEW079	1097	1060	1099	52	1130					34
NEW018	1135	1128	1122	50	1150					35
BOB113						859	939	866	918	37
NEW013	1115	1124	1071	45	1150					37
NEW051	1049	1020	1004	47	1040					37
NEW068						940	986	949	971	38
NEW009	1112	1115	1090	48	1040					38
NEW114	1234	1276	1261	45	1255	1073	1057	1086	1053	40
NEW052	1128	1142	1166	60	1220					41
NEWSP	1118	1128	1082	44	1130	979	1008	990	996	41
NEW101						990	1014	1001	1003	42
NEW029	1140	1123	1107	48	1210					43
NEW107	1104	1073	1063	49	1170					44
NEW401	1358	1375	1371	34	1270					45
NEW032						1006	1022	1017	1013	46
NEW074						994	1016	1005	1005	47
B47						996	1017	1007	1007	50
BOB404						1040	1041	1053	1034	53

Table 7.2: P-T estimates for all samples using appropriate geothermometers and geobarometers. Samples are arranged with increasing P₃₈ pressures (kb) (i.e. essentially increasing Cr/(Cr+Al) in garnet.

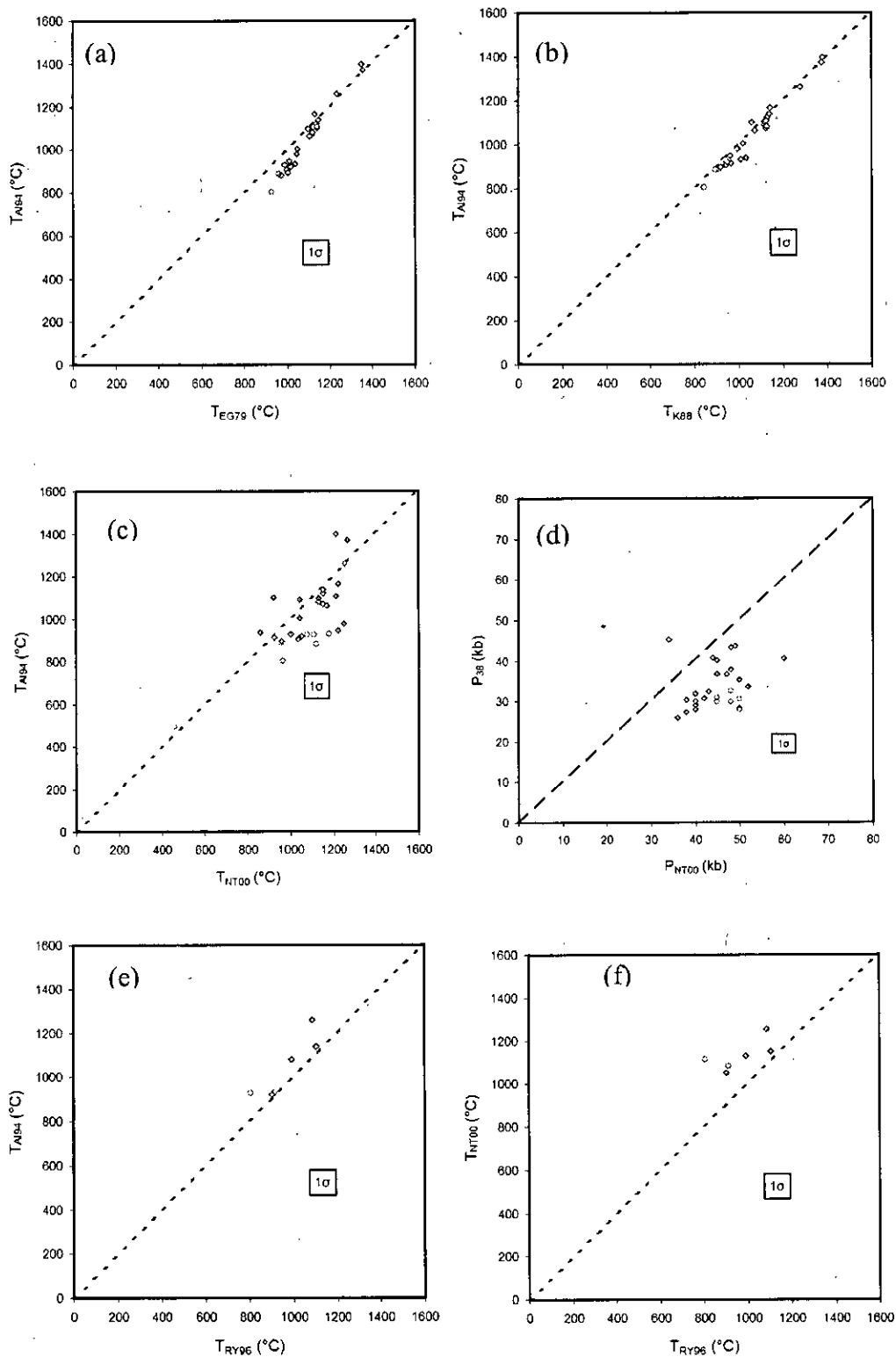


Figure 7.2: (a) T_{A194} vs. T_{EG79} . (b) T_{A194} vs. T_{K88} . (c) T_{A194} vs. T_{K88} . (d) P_{NT00} vs. P_{38} . (e) T_{RY96} vs. T_{A194} . (f) T_{RY96} vs. T_{NT00} . Dashed lines are 1:1 lines. All data calculated from analysis of garnet-clinopyroxene pairs from Newlands (filled symbols) and Bobbejaan (open circular symbols) samples. Boxes show the combined effects of 1 σ errors from the thermometer/barometer formulation and propagated analytical errors.

Relative to T_{AI94} , the thermometers T_{EG79} , T_{KR88} and T_{NT00} consistently overestimate temperatures (Fig. 7.2a, b and c, respectively). T_{EG79} estimates are higher particularly at lower temperatures but in general the differences between T_{KR88} , T_{AI94} and T_{EG79} are within error. T_{AI94} vs. T_{NT00} (Fig. 7.2c) produces a larger scatter due to the latter's single grain technique having less compositional constraints. P_{38} consistently underestimates pressures relative to P_{NT00} (Fig. 7.2d) even though the majority of the samples are known to be Cr-saturated. This is because the formulation for P_{38} suggests that the pressures it generates are a minimum P estimate (Grütter et al., 2006). The Ni-in-garnet, single garnet thermometer T_{RY96} tends to be higher but within error of T_{AI94} and about 100°C low compared to T_{NT00} (Fig. 7.2e and f, respectively).

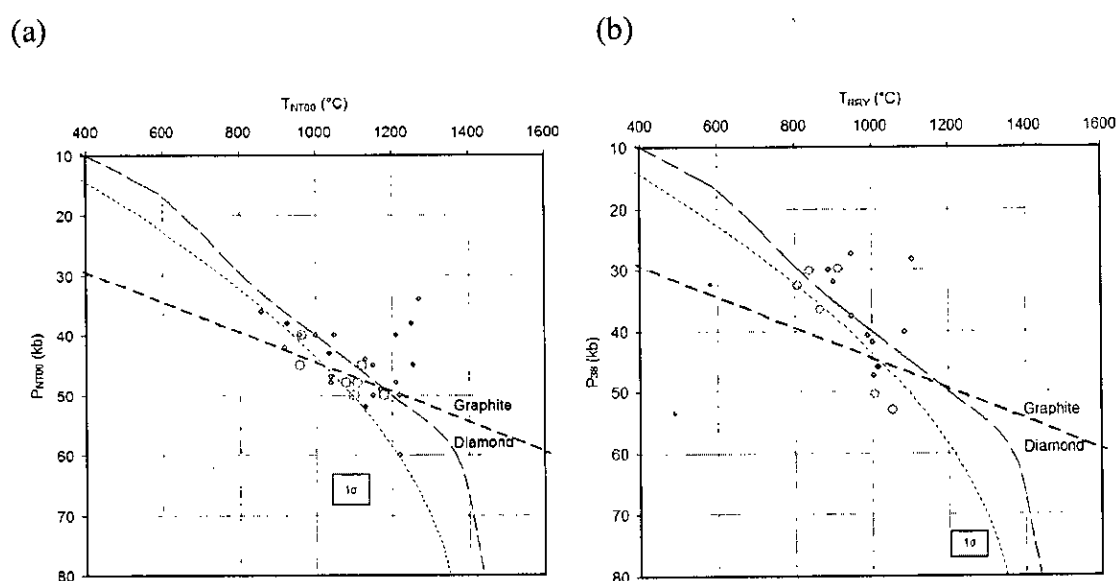


Figure 7.3: P-T estimates for Newlands (small filled circle symbols) and Bobbejaan (large open circles) samples using (a) T_{NT00} and P_{NT00} for lherzolitic samples using single clinopyroxene compositions. (b) P-T estimates for harzburgites and lherzolites using single garnet techniques of T_{RY96} and P_{38} . Errors in the formulations are shown in Table 7.1. Propagated analytical errors are contained within the size of the symbols i.e. < 10°C and < 1 kb. The combined 1σ error is shown as a box for the particular formulations. The steady state geotherm of McKenzie et al. (2005) is shown as the thin long dashed line and the conductive geotherm for a heat flow of 40mW/m² is shown from Pollack and Chapman (1977) as the thin dashed line.

Geothermometer/barometer	Estimates Range (no. of samples)
Ellis and Green (1979)	927-1373°C (30)
Krogh (1988)	842-1379°C (30)
Ai (1994)	803-1400°C (30)
Canil (1994)	904-1067°C (16)
Canil (1999)	879-1064°C (16)
Griffin et al. (1989)	804-1091°C (16)
Ryan et al. (1996)	809-1064°C (16)
Nimis and Taylor (2000)	859-1270°C (30)
Nimis and Taylor (2000)	34-60 kb (30)
Grütter et al. (2006)	26-53 kb (72)

Table 7.3: Range in pressure and temperature estimates for Newlands and Bobbejaan samples.

Newlands and Bobbejaan samples plot close to the continental conductive-convective geotherm of McKenzie et al. (2005) for old continental lithosphere and close to a 40 mW/m² conductive geotherm of Pollack and Chapman (1977). The conductive-convective geotherm is favoured relative to the conductive geotherm, because it takes into account the effects of convection below the lithosphere (McKenzie, 1989) and also the influence of temperature upon conduction. Fig. 7.3a and b show that the P-T estimates produce a relatively cool array when compared to the conductive-convective geotherm, but this is at slightly higher temperatures than the data from Menzies (2001) who reports Newlands xenoliths conforming to a 38 mW/m² conductive geotherm.

The majority of samples correspond to the medium-T xenoliths with few falling below 900°C or above 1100°C. The few high-T lherzolites that are present do not have a correspondingly high pressure and also do not have a deformed texture as is commonly observed in other xenolith suites from kimberlite (Harte, 1983).

A few high temperature estimates are generated from particular samples. For example, NEW114, NEWSP, NEW070 and NEW401 all produce T estimates > 1100°C using most grt-cpx and single clinopyroxene techniques. The T_{Ni} techniques

do not yield such high temperatures (they are closer to 1000°C) with NEW114 being close to 1100°C, but still below that of the grt-cpx Fe-Mg exchange thermometers.

Sample NEW303 has both matrix and inclusion clinopyroxene present and shows that a core garnet and core clinopyroxene yield a higher P and T estimate compared to the rims. The internal re-equilibration P and T is lower according to P_{NT00} and T_{NT00} but the temperature is intermediate according to the clinopyroxene-garnet Fe-Mg exchange thermometers. Analyses in other samples from the *cores* of garnets (instead of the contact with their particular inclusion) and using the analyses of inclusion clinopyroxenes in the same samples yield Fe-Mg garnet-clinopyroxene temperature estimates consistently a little higher (1-2°C) but within error of those calculated from rim analyses. These estimates are not reliable since the garnet core is not thought to be in equilibrium with coexisting inclusion clinopyroxenes. This is because the garnet is commonly zoned towards coexisting minerals in the way described in Chapter 5. However the higher-T at the core is thought to indicate the direction of the change to higher P-T.

Fig. 7.4a and d show that Ca content of clinopyroxenes is negatively correlated to T, whereas for garnet it appears positively correlated when using T_{A194} , but has a highly scattered relationship with T_{NT00} . The higher Ti garnets plot at $Ca/(Ca+Fe+Mg) > 0.2$ and form the higher T samples in Fig. 7.4a. All phases show a positive correlation between T and $Cr/(Cr+Al)$ (Fig. 7.4b), especially when disregarding the minerals from samples at anomalously high temperatures ($> 1300^\circ\text{C}$ for T_{A194} and $> 1120^\circ\text{C}$ for T_{NT00}). Fig. 7.4c and f show that it is only clinopyroxene that has a negative correlation between T and $Mg/(Mg+Fe)$, whereas garnet and spinel do not show any clear relationship. The high T samples (above the lines drawn in Fig. 7.4) tend to have garnets, clinopyroxenes and spinels higher in Ti and, additionally, clinopyroxenes and spinels higher in Mn.

7.3.2 Garnet, spinel and clinopyroxene compositions in lherzolites compared to P-T estimates

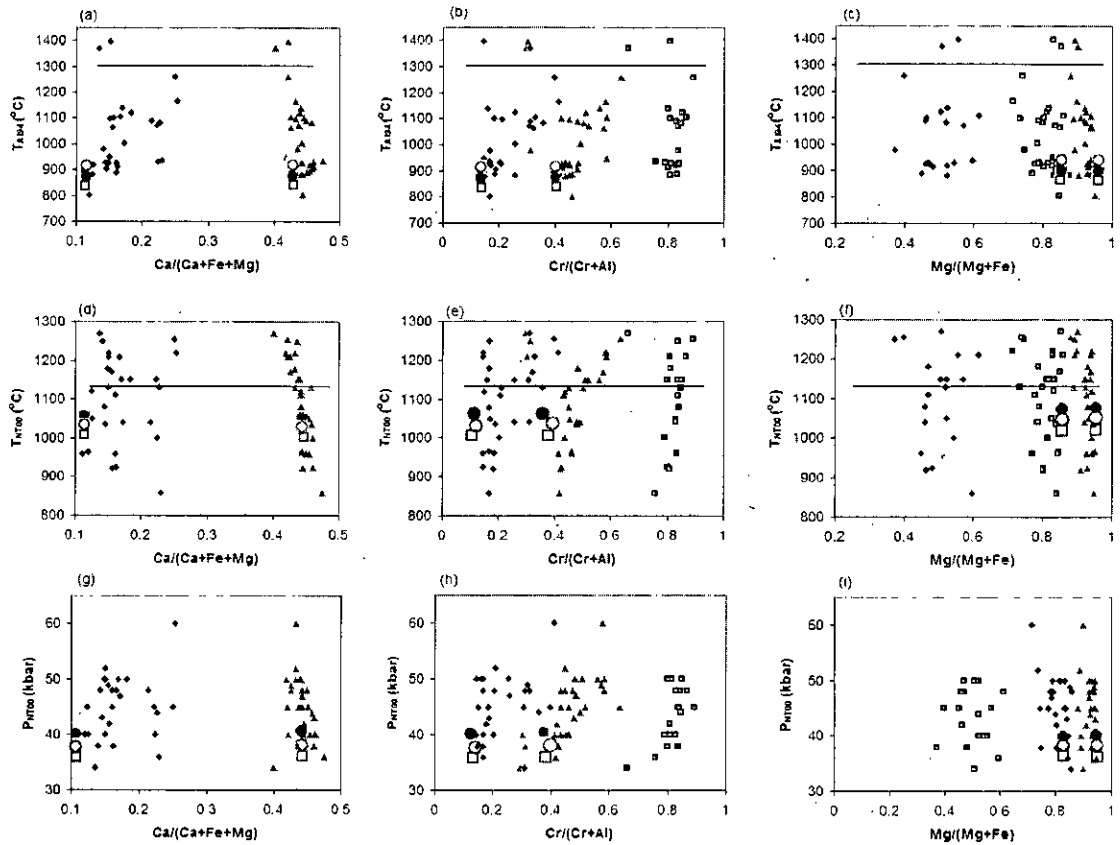


Figure 7.4: T_{A194} (a-c), T_{NT00} (d-f) and P_{NT00} (g-i) estimates for lherzolitic samples with the constituent mineral compositions plotted. Garnets (diamond symbols), spinels (square symbols) and clinopyroxenes (triangle symbols) are compared to cation ratios $Ca/(Ca+Fe+Mg)$ (a, d, g), $Cr/(Cr+Al)$ (b, e, h) and $Mg/(Mg+Fe)$ (c, f, i). Temperatures above which there is a high scatter in data are shown with a horizontal line. In each diagram the core (solid circle symbols), rim (open circle symbols) and inclusion contacts (open square symbols) are shown for the garnet (in black) and clinopyroxene (in grey) from sample NEW303 which was able to generate these three P-T estimates in a single sample.

Two trends are observable when comparing cation ratios to pressure: Firstly a negative clinopyroxene vs. $Ca/(Ca+Fe+Mg)$ trend (Fig. 7.4g); and secondly, positive trends for all minerals with $Cr/(Cr+Al)$ (Fig. 7.4h). The $Mg/(Mg+Fe)$ cation ratio in minerals is not related to P_{NT00} (Fig. 7.4i). This would be expected since Fe-Mg exchange is generally known to have a low ΔV , and hence much more T-dependent than P-dependent.

The compositions of the clinopyroxenes and garnets close to the core, rim and inclusion do not diverge from the trends in Fig. 7.4a-f. Therefore it is not expected that significant metasomatism is responsible for the core-rim external zonation in this sample. Therefore it is likely to be P-T effects that have produced the differences in composition within garnets and clinopyroxenes in the sample. Using the barometer and thermometer formulations of Nimis and Taylor (2000), consistent down P-T modification from core to rim to internal inclusion re-equilibration is shown. In terms of temperature the only difference with garnet-clinopyroxene Fe-Mg thermometry is that the rim compositions are calculated at a higher temperature than the core.

7.3.3 Garnet-spinel compositions in lherzolites and harzburgites and their relation to P-T

Experimental studies in MASCr and CMASCr show that coexisting garnet and spinel compositions both increase in Cr/(Cr+Al) as pressure increases (Fig. 7.5). The effect of Ca is to increase garnet and spinel Cr concentrations for a given pressure.

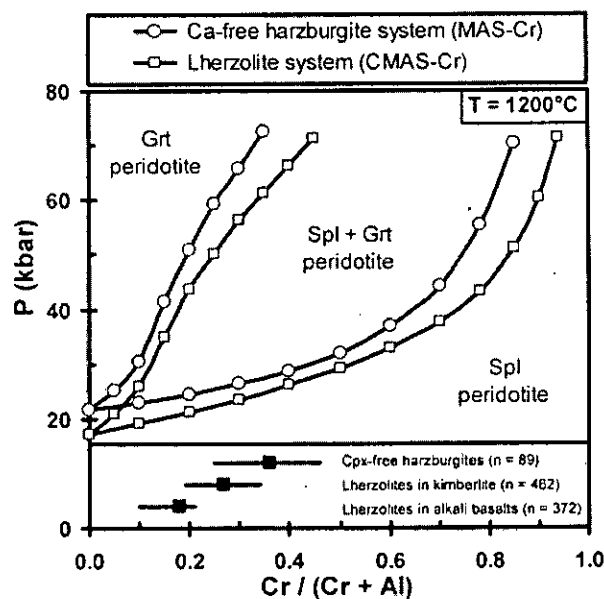


Figure 7.5: Pressure-composition section at $T = 1200^{\circ}\text{C}$ reproduced from Grütter et al. (2006). Summarising experimental studies of, Webb and Wood (1986) (lherzolitic data modified at low $\text{Cr}/(\text{Cr}+\text{Al})$ to account for experiments by Nickel (1986), Irifune (1985) (harzburgitic data) and Gasparik (2000) (harzburgitic and lherzolitic Cr-free datapoints, conforming to the original study of O'Neill, 1981).

Malinovsky and Doroshev (1977) use experimental constraints to show that, for peridotitic garnet compositions, the pyrope-knorringite composition is strongly

pressure dependent (an increase of ~10 kb for 10% Cr/(Cr+Al) in MASCr system. These authors also note a slight effect of Ca on pressure which is utilised by Grütter et al. (2006) to formulate the 'P38' single-garnet Cr/Ca barometer. Girmis and Brey (1999) provide isopleths for the FMASCr system. Fig. 7.6 shows the garnet and spinel isopleths Girmis and Brey (1999) and the range in P-T estimates gained in Newlands and Bobbejaan samples. The isopleths of Girmis and Brey (1999) are preferred because they 'anticipate' the Cr/(Cr+Al) = 1 line for the spinel-garnet transition of Klemme (2004). Note the highly pressure-sensitive nature of the garnet isopleths especially along the model geotherm line.

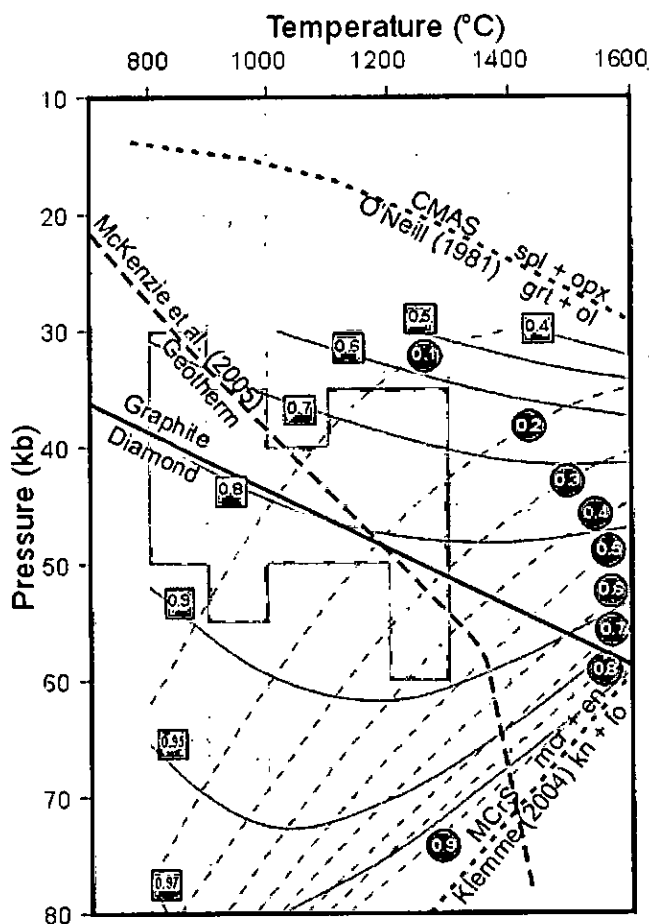


Figure 7.6: Isopleths of Cr/(Cr+Al) ratios in garnet (circles, white numbering, grey dashed lines) and spinel (squares, black numbering, thin grey lines), from Girmis and Brey (1999). Shaded grey area denotes the range in P-T estimates for Newlands and Bobbejaan samples essentially defined by lherzolitic samples using T_{NT00} - P_{NT00} . Other P-T lines as for Fig. 7.1.

The isopleths for both garnet and spinel increase in Cr/(Cr+Al) with both P and T (Fig. 7.6). Fig. 7.7 shows that there is a general trend for the Newlands and Bobbejaan spinel-garnet pairs to behave in this way since their independently

estimated P_s and T_s increase in $Cr/(Cr+Al)$. The exact $Cr/(Cr+Al)$ values for garnet and spinel are, in general, too high when compared with the isopleths, but this is expected since the Girmis and Brey (1999) data is for the Ca-free systems. The high-Ca samples shown have especially elevated garnet and spinel $Cr/(Cr+Al)$ for their particular $P-T$ estimates (see Fig. 7.7).

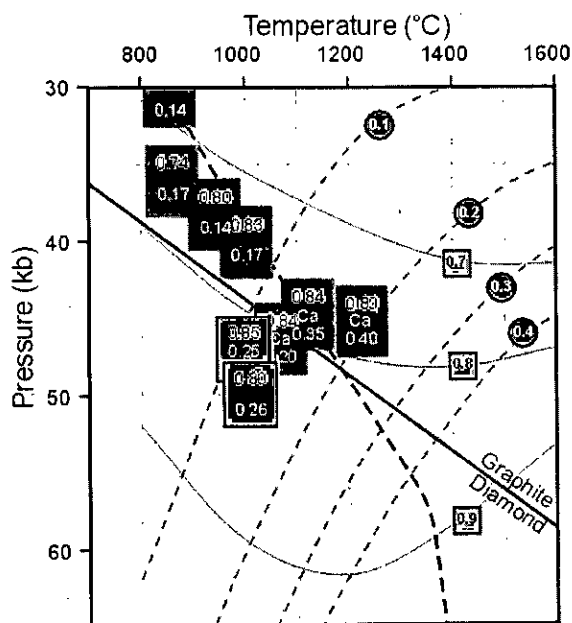


Figure 7.7: $P_{NT00}-T_{NT00}$ estimates for a selection of hercynitic samples (grey boxes) and T_{Ni} estimates for one diamond-bearing and one high pressure (P_{38}) harzburgitic sample (boxes outlined in black) that have been placed into the diamond stability field. Coexisting spinel (black) and garnet (white) $Cr/(Cr+Al)$ values are shown in these boxes with 'Ca' denoting especially Ca-rich garnets with $CaO > 7$ wt. %. Grey rectangles are proportioned according to 1σ errors quoted for the geothermometer or geobarometer used. The isopleths of Girmis and Brey (1999) are shown for garnet as grey circles (white numbering) and for spinels as grey squares (black numbering). The McKenzie et al. (2005) continental geotherm is the bold dashed line.

Spinel in most samples has $Cr/(Cr+Al)$ approximately 5 % units higher than the Girmis and Brey (1999) isopleths. Garnet is generally 10 % higher. NEW114 (the most extreme Cr and Ca enriched garnet of the samples) has its spinel $Cr/(Cr+Al)$ 10 % units high and its garnet 20 % high relative to the isopleths shown in Fig. 7.6. The low pressure samples which have lower $Cr/(Cr+Al)$ for both garnet and spinel, adhere to the isopleths most closely. The general trend in Table 7.2 indicates that as one increases Cr_2O_3 in garnet (i.e. P_{38} value) so the pressure and temperature increase in other barometers and thermometers.

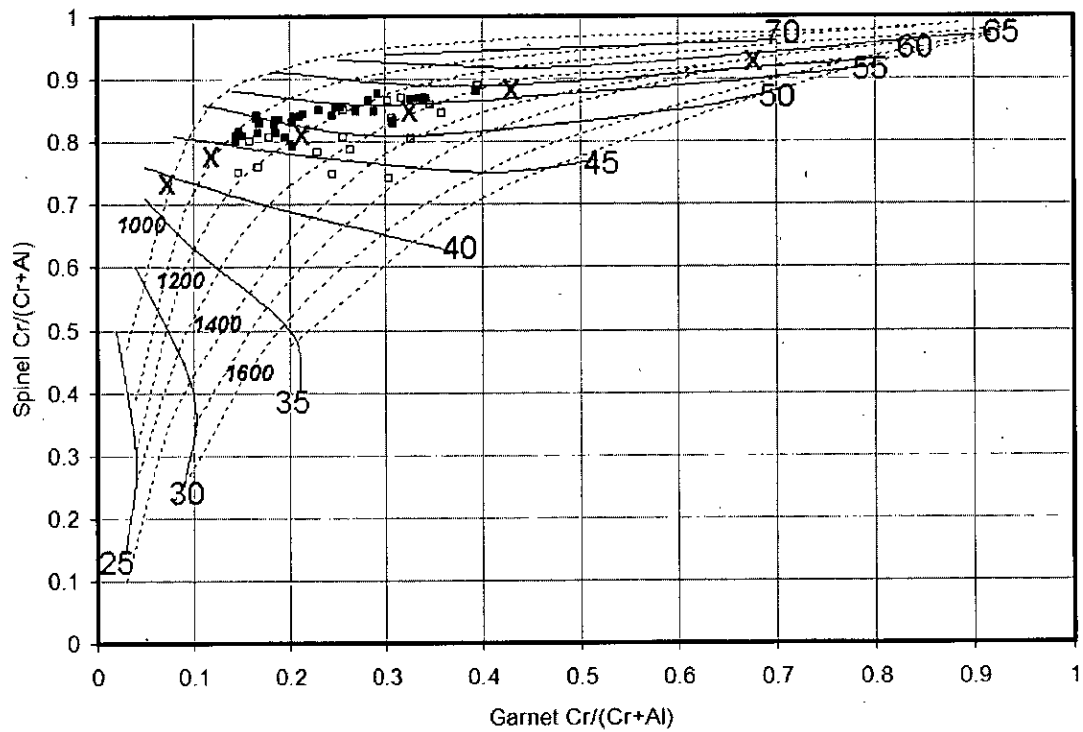


Figure 7.8: Spinel vs. garnet Cr/(Cr+Al) plot with isotherms (dashed lines at 100°C intervals, labelled every 200°C) and isobars (solid lines labelled at every 5 kbar interval) from Girmis and Brey (1999). Coexisting garnets and spinels from Newlands and Bobbejaan samples are plotted with those having high-Ti spinels shown as open squares (Ti > 1 wt. %). 1 σ analytical errors for Cr/(Cr+Al) are within the size of the symbols shown. 'X's represent the McKenzie et al. (2005) geotherm according to the isobars and isotherms shown.

Fig. 7.8 shows Cr/(Cr+Al) for coexisting garnet and spinel in relation to isobars and isotherms derived from Girmis and Brey (1999). Discounting the high-Ti spinel bearing samples (open square symbols in Fig. 7.8) the garnet-spinel pairs plot in a linear trend from Cr/(Cr+Al) values of (0.15grt, 0.8spl) to (0.4grt, 0.9spl). Data from Menzies (2001) from Newlands overlaps with data from this study. The spread of the increasing Cr/(Cr+Al) values with P and T in Fig. 7.8 correspond well with that expected along a geotherm ('X's in Fig. 7.8).

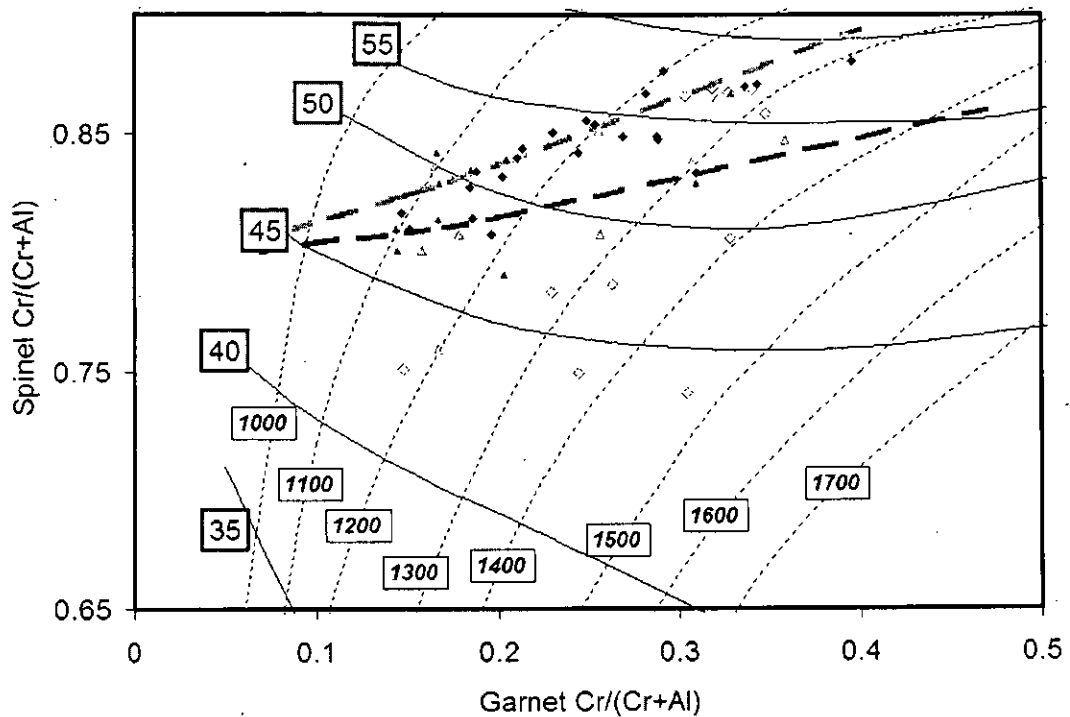


Figure 7.9: As for Fig. 7.8 but just for the Cr/(Cr+Al) values that bracket the Newlands and Bobbejaan samples. Bold black dashed line is diamond-graphite line according to the isotherms and isobars. Bold grey dashed line (at higher spinel Cr/(Cr+Al)) is the diamond-graphite line according to the independent P-T estimates for the Newlands and Bobbejaan samples from earlier in this chapter. Filled black diamond symbols are low-Ti harzburgites, filled black triangle symbols are low-Ti lherzolites, open grey diamond symbols are high-Ti harzburgites and open grey triangle symbols are high-Ti lherzolites. See text for further discussion.

Fig. 7.9 shows the data from Fig. 7.8 with the diamond-graphite line according to the Girmis and Brey (1999) isobars and isotherms. Using P-T estimates from the Newlands and Bobbejaan samples a diamond graphite line is that is at elevated garnet and spinel Cr/(Cr+Al) based on independent P-T estimates as shown. The diamond bearing sample BOB404 is the sample that plots the furthest across (on the high-P side) the diamond graphite lines shown.

The distribution of Cr between clinopyroxene and coexisting garnet and spinel is illustrated in Fig. 7.10(a and b respectively). Both garnet vs. clinopyroxene and spinel vs. clinopyroxene Cr/(Cr+Al) form a positive slope. Therefore clinopyroxene-garnet and clinopyroxene-spinel Cr partitioning appears to be pressure and temperature dependent in a similar way to garnet-spinel. Samples with high-Ti spinel overlap with low Ti spinel samples but they tend to make up the majority of the

points that plot away from the general trend. Other outliers (i.e. black filled squares away from the general trends in Fig. 7.10) tend to have the highest Ti and Mn concentration in their clinopyroxene. The high Ti in these clinopyroxenes are likely to explain their departure (vertically on the graphs in Fig. 7.10) from the Cr-, Al-based trends.

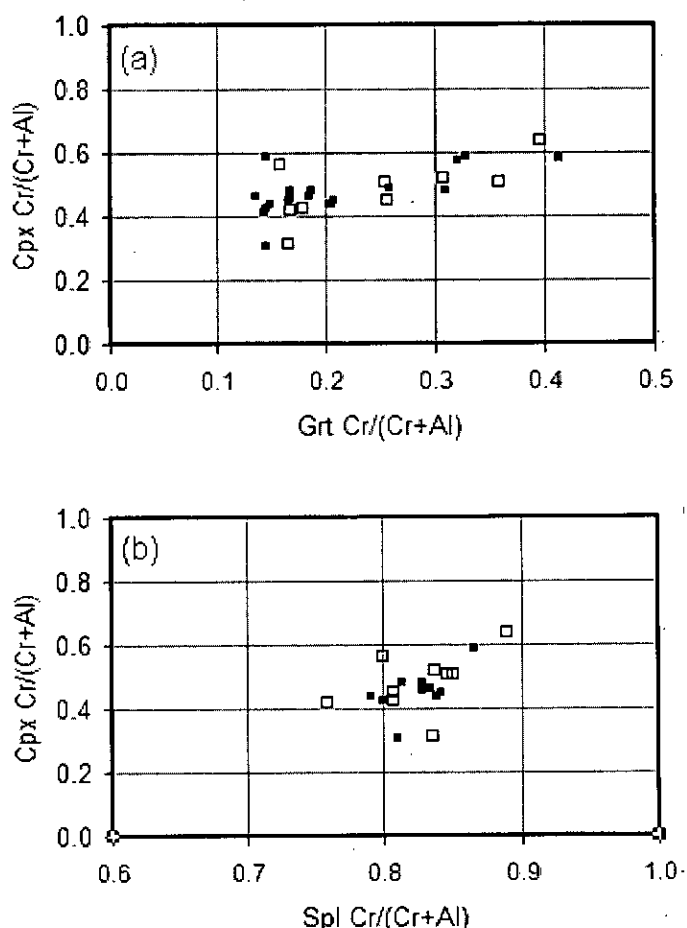


Figure 7.10: Cr/(Cr+Al) ratios for coexisting cpx-grt (a) and cpx-spl (b). Open square symbols are for samples with a coexisting high-Ti spinel.

7.3.4 Ti in coexisting phases and its relation to P-T

Figures 7.9 and 7.10 indicate that the presence of Ti in spinel at > 1 wt. % tends to draw samples away from mineral-mineral Cr/(Cr+Al) trends. Coexisting garnet-spinel, garnet-clinopyroxene and clinopyroxene-spinel are positively correlated (Fig. 7.11a-c) with garnet-clinopyroxene having the most scatter. Fig. 7.11d shows that the Ti content of each mineral is positively correlated with T_{Ni} . The diamondiferous sample BOB404 lies far away from this trend in terms of its low spinel and garnet Ti

concentration. One mechanism for generating a range of Ti concentrations is the introduction of Ti-rich metasomatic fluids which are expected from studies such as Griffin et al. (1999b). This implies that the minerals in some samples have not equilibrated with a metasomatic fluid. Sc, Y and Zr behave in a similar way to Ti except they partition into garnet > clinopyroxene > spinel and have successively weaker correlation with T_{Ni} . (Data can be found in supplementary CD, Appendix VII).

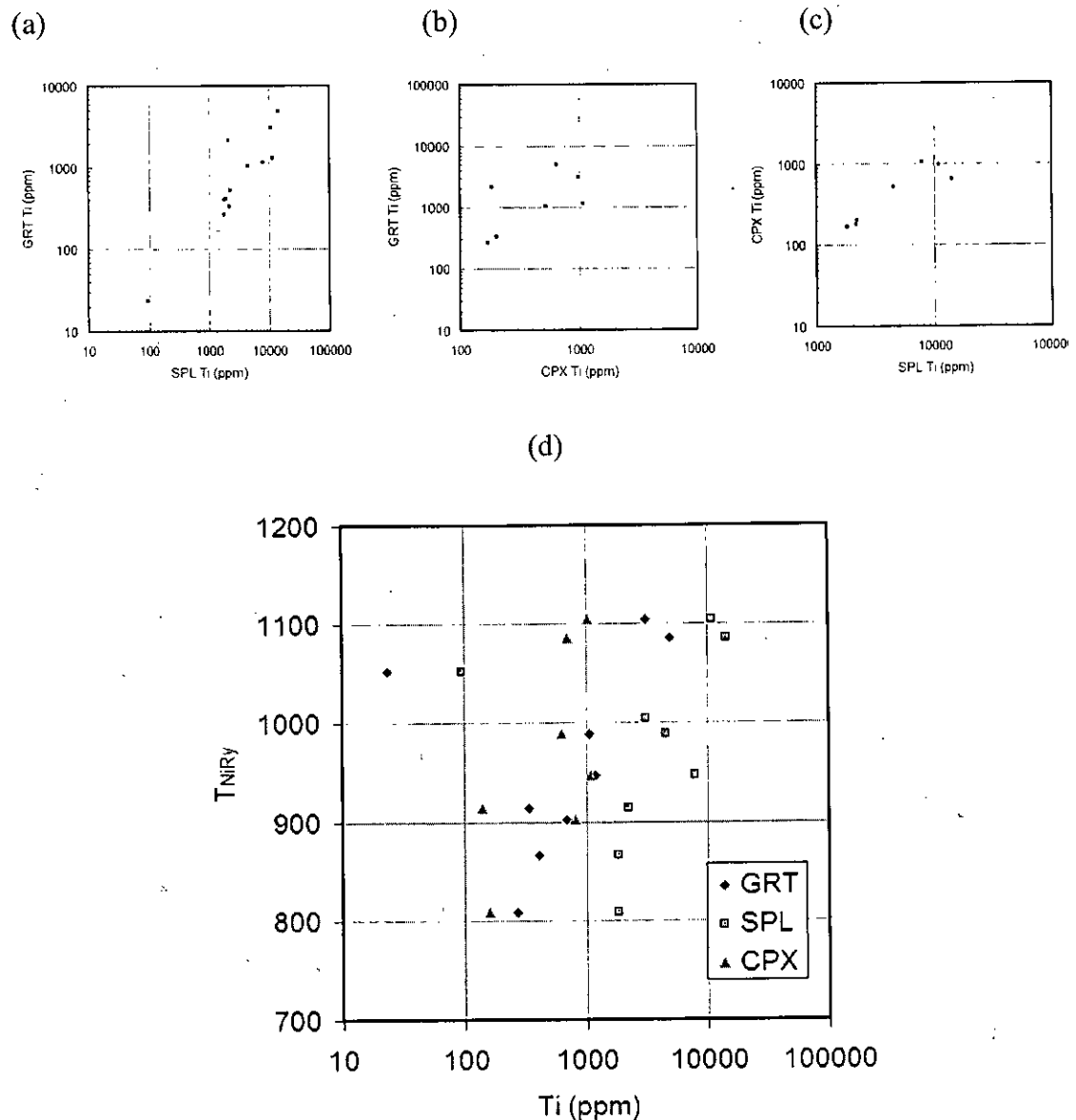


Figure 7.11: (a) coexisting spinel vs. garnet Ti concentration, (b) coexisting clinopyroxene vs. garnet Ti concentration and (c) coexisting spinel vs. clinopyroxene Ti concentrations (Ti concentrations from SIMS). (d) Ti vs. T_{NiRy} for coexisting minerals. See text for discussion.

An alternative explanation for the increasing Ti with T_{Ni} is that, according to the sliding reaction simulation [2], in Chapter 6, one would expect more dissolved spinel within the garnet at high $Cr/(Cr+Al)$ and $Ca/(Ca+Mg+Fe)$ (i.e. higher P and T), hence higher Ti in garnet. Fig. 5.4a shows that the high-Cr, high-Ca lherzolitic samples (e.g. NEW114, NEWSP) have the highest Ti concentrations. This explanation relies on there being high Ti concentrations in spinel, and where there is not then a low Ti garnet and coexisting spinel would occur like that described for BOB404.

7.4 'Perplex' Computations

'Perplex' is a collection of Fortran programs (<http://www.perplex.ethz.ch/>) that calculates petrological phase equilibria (Connolly, 1990; Connolly and Petrin, 2002). The latest database includes the thermodynamic data of Holland and Powell (1998) and Cr-end member spinels and garnets (e.g. magnesiochromite from Klemme, 2004). This allows Cr-rich peridotitic bulk rock compositions like those of the Newlands and Bobbejaan samples in this study to be modeled thermodynamically in systems with 3-5 phases and 6-7 components for the first time (Klemme pers. comm.).

BOB402 and B47 were selected for preliminary analysis with the Perplex program in order to predict how bulk rock compositions, modal mineralogy and mineral chemistry are expected to vary with changes in P and T. In order to estimate their bulk rock compositions accurately, the modes were multiplied by weight % values for minerals. These two samples are large enough so that modes are more accurately known compared to many Newlands and Bobbejaan samples.

The system CFMASCrNa was used with Fe-chromite as an excluded phase. A phase diagram was generated for each sample and then down P and down T transects were made examining changes in garnet and spinel Cr_2O_3 concentrations, garnet CaO compositions and the modal abundance of olivine, orthopyroxene, clinopyroxene, garnet and spinel. P and T were input initially according to the P-T estimate of the

particular sample (see earlier). The resultant assemblage, mineral modes and mineral compositions were calculated and compared to the modes and compositions of the natural data. BOB402 was modeled relatively successfully with Cr_2O_3 wt. % a little low in garnet and a little high in spinel. Other estimates were ± 1 wt. % and the modes were within 2 % of those input. Contour plots were made to check for the calculated variation in modal abundances and mineral compositions with pressure (20-60 kb) and temperature (1073-1673 K).

For the bulk composition of BOB402 the following features were noted:

1. The phase diagram (Fig. 7.12a) shows a change in assemblage from the 4-phase grt + ol + spl + cpx at high pressures and temperatures ($> 1200^\circ\text{C}$ and 45 kb) to the 5-phase grt + ol + spl + cpx + opx. An olivine-out line occurs at very low pressures (< 20 kb). The garnet out line is at very low P and high T.
2. The P, T, assemblage, modal abundance and mineral composition of minerals is approximated to ± 5 % of the natural data when the P-T estimate for BOB402 was input (using T_{NT00} and P_{NT00}).
3. The measured garnet zonation trend in the sample is parallel to the trend calculated for the down P-T path through the 4-phase assemblage (high P region in Fig. 7.12a, see point 1). This is also parallel to the CCGE trend¹ and simulation [2] (Chapter 6). Fig. 7.13 shows how a purely isothermal decompression path produces a trend that is too steep, therefore a combination of decreasing P and T from about 1200°C , 40 kb to 900°C , 30 kb is required.
4. As one goes down P-T the modal abundance of spinel and the two pyroxenes go up at the expense of olivine and garnet (Fig. 7.14a). This is expected since

¹ Sample B55 has a calculated zonation trend parallel to the down P-T path through the 5-phase assemblage in (1) (e.g. B55). This is also parallel to the Iherzolite line and simulation [3] (chapter 6). The strongly exsolved sample B55 is modeled particularly well (possibly due to accurate modes being known) and is located along the trend parallel to simulation [3] as shown in Fig. 6.12 (Chapter 6). P_s and T_s generated would suggest an isothermal decompression path from 30 to 27 kb or an isobaric cooling path from 1100 to 1000°C . However, if the bulk rock composition is calculated as a single garnet crystal (i.e. the situation prior to exsolution, Fig. 6.12) then pressures > 50 kb and temperatures $> 1200^\circ\text{C}$ are derived.

with lower pressures the garnet-spinel transition reaction (i.e. reaction (3), Chapter 6) favours spinel and pyroxene rather than garnet and olivine.

5. Cr isopleths in spinel show a shallow but positive P-T slope (7.12c). Cr/(Cr+Al) compositions of spinel at higher pressure are therefore higher and this correlates to lower modal spinel as one moves further away from the Cr-free spinel-garnet transition reaction.
6. Garnet has increasing Cr concentrations at higher pressures and higher temperatures with a negative P-T slope (Fig. 7.12c). This corresponds with the increase in modal garnet (Fig. 7.14a).
7. At high P and T Ca-in-garnet isopleths also have a negative P-T slope (Fig. 7.12c).

The harzburgitic B47 bulk composition produces the same kinds of features except with no clinopyroxene present (orthopyroxene is in its place, see Fig. 7.12b).

Therefore the model successfully predicts the assemblage and it approximates modes to $\pm 5\%$. It is a Na-free, CFMASCr system since the model only allows for Na in clinopyroxene. The zonation trend in garnet down P and T is close to being coincident with the actual measured Cr and Ca compositions (Fig. 7.13) and is suggestive of 60-55 kb decompression or 1450 to 1400°C cooling. The trend is not exactly parallel possibly because of the effect of small quantities of Ca in orthopyroxene that are not taken into account in the model. Modes change in a similar fashion to BOB402 (Fig. 7.14b) with orthopyroxene having a higher rate of change since there is no clinopyroxene present ('2 orthopyroxene' in reaction (2a), Chapter 6). Garnet compositions are stationary at high P and T when in the spinel-absent field as shown in Fig. 7.13d.

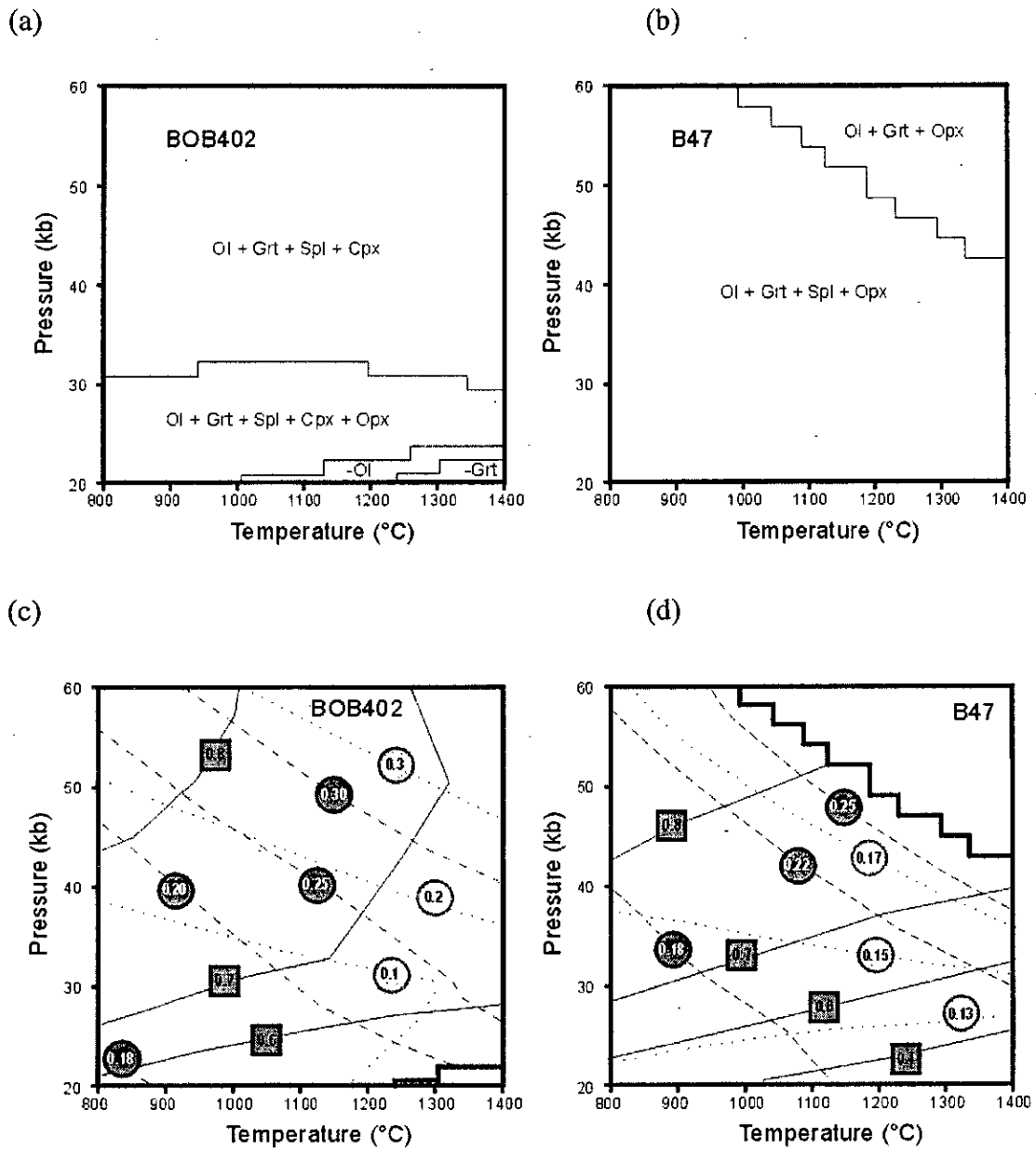


Figure 7.12: Phase diagrams generated from Perplex for bulk rock compositions BOB402 (a) and B47 (b). Ol = olivine, Spl = spinel, Grt = garnet, Cpx = clinopyroxene, Opx = Orthopyroxene, -Ol = olivine out, -Grt = garnet out. Isopleth plots generated from Perplex for bulk rock compositions BOB402 (c) and B47 (d). Garnet $Cr/(Cr+Al)$ is shown in white in a circle symbol with dashed lines, spinel $Cr/(Cr+Al)$ is shown in black in a square symbol with solid lines and garnet $Ca/(Ca+Fe+Mg)$ is shown in black as a grey circle symbol with dotted lines.

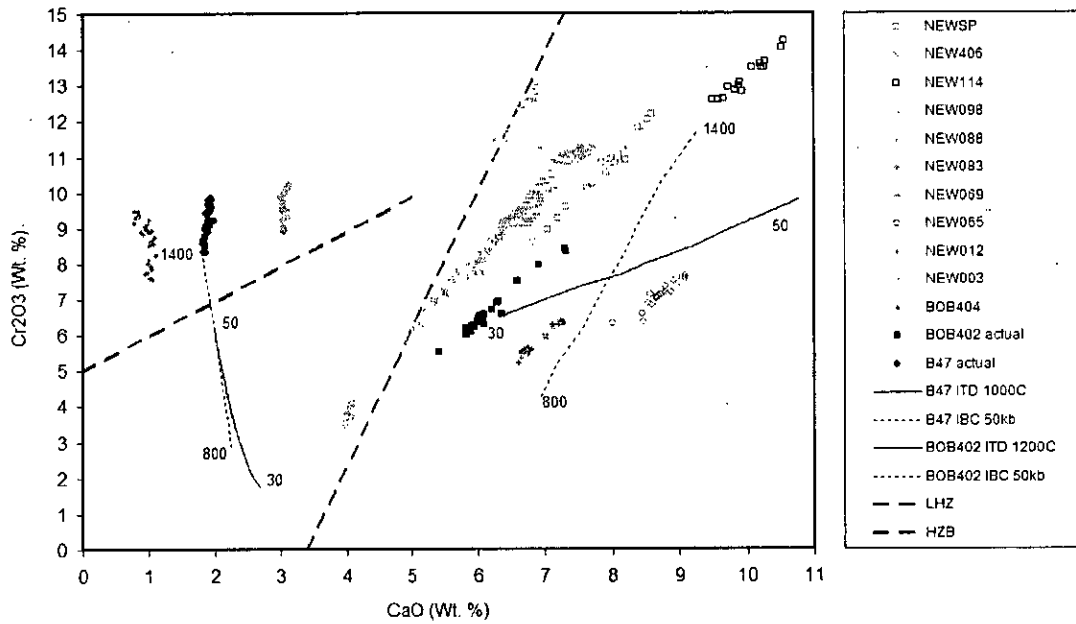


Figure 7.13: CaO vs. Cr₂O₃ wt. % plot for garnet zonation patterns from selected samples (grey) and from the samples modelled using Perplex (black filled symbols). LHZ is the Iherzolite line, HZB is the diamond-graphite constraint, thin solid lines are modelled isothermal decompression (ITD) lines and thin dashed lines are modelled isobaric cooling (IBC) lines. T estimates are used for ITD and P estimates are used for IBC in B47 (1000°C and 50 kb respectively) and BOB402 (1200°C and 50 kb respectively).

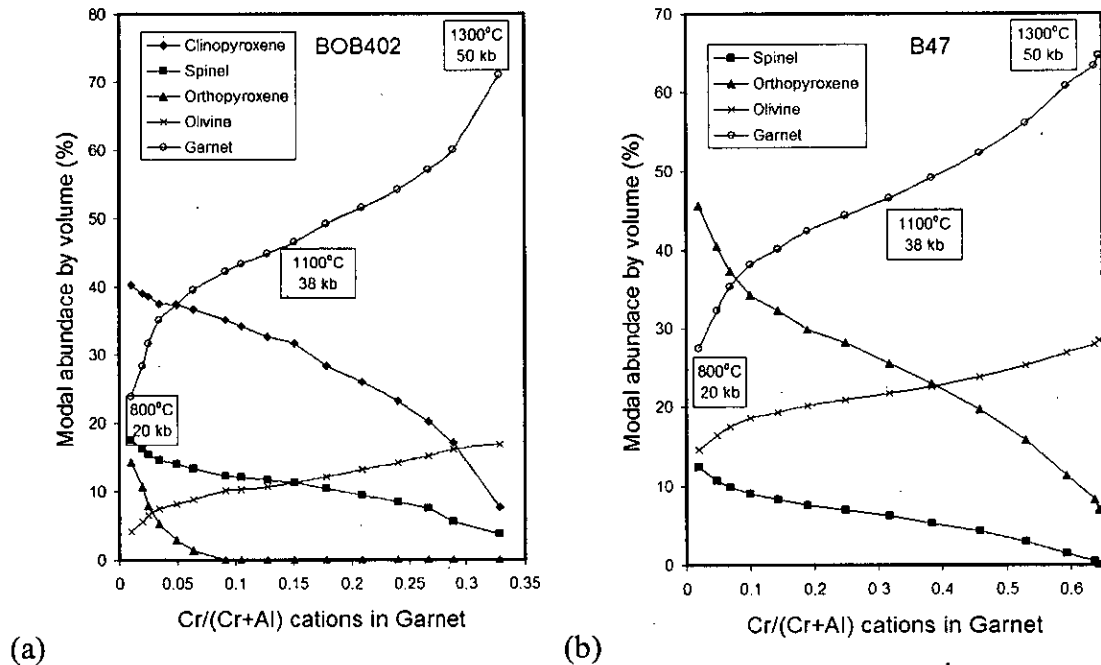


Figure 7.14: Modes for minerals in BOB402 (a) and B47 (b) as one changes Cr/(Cr+Al) in garnet. Ps and Ts are shown for a start, middle and end of the linear geotherm traversed. Note the rapid change in modes of garnet and orthopyroxene at low garnet Cr/(Cr+Al) and the relatively linear behaviour of spinel and clinopyroxene.

Overall the modelled zonation trends would suggest that the samples have undergone a pressure decrease of approximately 5 kb with a small (~50°C drop) temperature component. Since high Cr and Ca garnets coexist with higher Cr spinels (see Chapter 6), the lherzolitic samples have larger compositional variation per unit P and T. This is because higher Cr spinel is being formed in the high Cr, high Ca lherzolitic samples as one travels down P and T and so the garnet composition has to respond more dramatically to compensate for this. Perplex can be used to model a wide range of bulk rock compositions and can generate Cr and Ca isopleths for garnet spinel and clinopyroxene in P-T space.

7.5 Conclusions

The important points that have emerged from geothermobarometric considerations are as follows:

1. P-T estimates from garnet adjacent to its inclusions and the inclusions that are adjacent to the host garnet are expected to have close to equilibrium compositions. This is justified by the compositional plots in Chapter 6 where parallel tie lines between coexisting minerals are produced when plotting garnet compositions adjacent to, rather than away from, inclusions. Apart from a few high temperature samples, the P-T estimates themselves are suggestive of equilibrium since they form a relatively continuous spread of data (Fig. 7.3)
2. Using garnet compositions away from inclusions (in the interior of the garnet) yields temperatures consistently 1-2°C higher than garnet adjacent to inclusions. The one sample with clinopyroxene both in the matrix and as an inclusion in garnet suggests that early (i.e. core) matrix P and T was higher than later (i.e. rim) matrix P and T. The internal re-equilibration between garnet and clinopyroxene (as an inclusion in garnet) has a lower P-T than both of the matrix estimates according P_{NT00} and T_{NT00} and an intermediate temperature between the two matrix estimates according to garnet-clinopyroxene Fe-Mg exchange thermometers.

3. P-T estimates for Newlands and Bobbejaan lherzolites range from 803-1400°C, 30-60 kbar using the formulations of Nimis and Taylor (2000). The estimates conform to a relatively 'cold' continental geotherm compared to McKenzie et al. (2005), and equivalent to a 40 mW/m² conductive geotherm of Pollack and Chapman (1977). However the estimates are higher T than those noted by Menzies (2001) for Newlands xenoliths. Bobbejaan samples on average yield slightly lower Ts.
4. Temperature estimates using garnet-clinopyroxene Fe-Mg exchange thermometers produce lower T estimates than the Ca-Mg-Fe based pyroxene solvus thermometer used in T_{NT00}. This seems to be due to slower Ca diffusion in garnet and clinopyroxene (see Chapter 8).
5. P₃₈ single-garnet pressures are consistently low compared to P_{NT00} and Perplex models. Ni-in-garnet thermometry tends to underestimate temperatures relative to T_{NT00}. Again this is thought to be because Ca diffusion in minerals is slower than, in this case, Ni-Mg exchange.
6. Harzburgitic samples tend to yield T_{NiRy} temperatures that are narrower in range (841-1053°C) and cooler than the lherzolic samples (859-1270°C). Unlike the major elements, Ni in garnets from Newlands and Bobbejaan samples is not zoned along the same core to inclusion directions that the major elements are. Since Ni is strongly temperature dependent this would indicate that the major element zonation trends are likely to be predominantly down P re-equilibration with inclusions. However the diffusion coefficient for Ni in garnet is not well known and may be sluggish compared to Ca-Mg, so this interpretation is uncertain.
7. Coexisting garnets and spinels have higher Cr/(Cr+Al) at higher Ps and Ts. This spread of data appears to conform to a geotherm that intersects the graphite diamond line. A consequence of this is that lherzolic garnet zonation trends are longer than those of harzburgitic garnets, since lherzolic garnet Cr/(Cr+Al) decreases more rapidly as it compensates for the generation of the higher Cr Cr-spinel.

8. The effect of increasing Ca in garnet is to increase Cr/(Cr+Al) for garnet and its coexisting spinel at a given P and T.
9. Composition vs. P-T estimates in samples (and in Perplex models of samples) correlate with garnet-spinel Cr/(Cr+Al) trends expected from the experimental data of Girnir and Brey (1999) for the system FMASCr. However, consistent differences exist with actual garnet and spinel Cr/(Cr+Al) compositions being higher than those predicted for a given P and T. This is readily related to the absent Ca component in the Girnir and Brey (1999) experiments (Fig. 7.6). Therefore different isopleths are required for different bulk rock compositions.
10. According to calculations of garnet compositions using the thermodynamic model 'Perplex', garnet zonation trends correspond to down P and T re-equilibration. This correlates with increasing modal spinel and pyroxene and decreasing Cr/(Cr+Al) in spinel and conforms to reactions 2a and 3 and simulations [1-3] in Chapter 6. Isothermal decompression and isobaric cooling have similar (but not coincident) compositional trajectories in garnets. Internal and external zonation in sample BOB402 plots with a trajectory in between ITD and IBC trajectories indicative of a down-geotherm P-T path.
11. Relatively successful equilibrium thermodynamic modelling using Perplex is also evidence for the internal garnet zonation trends being the result of an equilibration process of garnet with its inclusions.

The main question emerging from this chapter is: What is the cause of the decompression and cooling documented? Isobaric cooling is difficult to envision for the lower mantle lithosphere. Several options may be considered:

- Plate tectonics-driven lithospheric compression leading to uplift and erosion and removal of the uppermost lithosphere in a mountain building process. Initially, increasing pressure would be expected, but the samples do not preserve evidence for this. The unroofing and decompression could occur relatively quickly (millions of years timescale) with cooling onto a geotherm

ensuing at a slower rate. According to P-T estimates at least 15 km would have to be eroded.

- Lithospheric stretching: This process would cause initial isothermal decompression and subsequent cooling onto the adiabat. A beta-factor of 1.05 would have to be applied as pure shear to the whole lithosphere however which is mechanically difficult to achieve without an element of simple shear. This model does not correspond to the Archaean crustal history envisioned for the Kaapvaal craton according to De Wit et al. (1992). This would also lead to kinks on the zonation trajectories as indicated by the different ITD and IBC trends shown on Fig. 7.13.
- Convective mantle movement: this would require material being trapped in overturning mantle and subsequently being heated to temperatures $>1400^{\circ}\text{C}$, before cooling along an adiabatic geotherm.
- Partial eruption (not necessarily kimberlite related): This process would transport material upwards (decompression) and heat it up in a magmatic system. Then the frozen eruption would cool to a geotherm. This process is indicated on a small scale in polymict peridotites, but in these specimens is accompanied by much melt metasomatism (Morfi, 2001).
- Kimberlite eruption: This process would also be difficult to conceive applying to the samples in question because of the extent that crystal zonation is seen: Other xenolith suites from the Newlands and Bobbejaan kimberlites do not show evidence for such a marked P-T re-equilibration.

These options are in order of speed with kimberlite being the fastest mechanism to transport material upwards. Therefore, one needs to document the time interval over which P-T change is occurring. This is dealt with in Chapter 8.

7.6 References

- Ai, Y. (1994). A revision of the garnet-clinopyroxene Fe^{2+} -Mg exchange geothermometer. *Contributions to Mineralogy and Petrology*. **115**. 467-473.
- Canil, D. (1994). An experimental calibration of the nickel in garnet geothermometer with applications. *Contributions to Mineralogy and Petrology*. **117**. 410-420.

- Canil, D. (1999). The Ni-in-garnet geothermometer: calibration at natural abundances. *Contributions to Mineralogy and Petrology*. **136**. 240-246.
- Connolly, J. A. D. (1990). Multivariable phase diagrams: An algorithm base on generalized thermodynamics. *American Journal of Science*. **290**. 666-718.
- Connolly, J. A. D. and Petrini, K. (2002). An automated strategy for calculation of phase diagram sections and retrieval of rock properties as a function of physical conditions. *Journal of Metamorphic Geology*. **20**. 697-708.
- De Wit, M. J., De Ronde, C. E. J., Tredoux, M., Roering, C., Hart, R. J., Armstrong, R. A., Green, R. W. E., Peberdy, E. and Hart, R. A. (1992). Formation of an Archaean continent. *Nature*. **357**. 553-562.
- Ellis, D. J. and Green, D. H. (1979). An experimental study of the effect of Ca upon garnet-clinopyroxene Fe-Mg exchange equilibria. *Contributions to Mineralogy and Petrology*. **71**. 13-22.
- Gasparik, T. (2000). An internally consistent thermodynamic model for the system CaO-MgO-Al₂O₃-SiO₂ derived primarily from phase equilibrium data. *Journal of Geology*. **108**. 103-119.
- Girnis, A. V. and Brey, G. P. (1999). Garnet-spinel-olivine-orthopyroxene equilibria in the FeO-MgO-Al₂O₃-SiO₂-Cr₂O₃ system: II Thermodynamic analysis. *European Journal of Mineralogy*. **11**. 619-636.
- Griffin, W. L., Cousens, D. R., Ryan, C. G., Sie, S. H. and Suter, G. F. (1989). Ni in chrome pyrope garnets: a new geothermometer. *Contributions to Mineralogy and Petrology*. **103**. 199-202.
- Griffin, W. L., Shee, S. R., Ryan, C. G., Win, T. T. and Wyatt, B. A. (1999b). Harzburgite to lherzolite and back again: metasomatic processes in ultramafic xenoliths from the Wesselton kimberlite, Kimberley, South Africa. *Contributions to Mineralogy and Petrology*. **134**. 232-250.
- Grütter, H. S., Latti, D. and Menzies, A. H. (2006). Cr-saturation arrays in concentrate garnet compositions from kimberlite and their use in mantle barometry. *J. Petrology*. **47**. 801-820.
- Harte, B. (1983). Mantle peridotites and processes: The kimberlite sample. In: Eds.: Hawkesworth, C. J. and Norry, M. J. *Continental basalts and mantle xenoliths*. Nantwick, Shiva. 46-92.
- Holland, T. J. and Powell, R. (1998). An internally consistent thermodynamic data set for phases of petrological interest. *Journal of Metamorphic Geology*. **16**. 309-343.
- Irfune, T. (1985). Experimental study of the system Mg₃Al₂Si₃O₁₂-Mg₃Cr₂Si₃O₁₂ at high pressure and high temperature. *Journal of the Faculty of Science, Hokkaido University*. **21**. 417-451.
- Kennedy, C. S. and Kennedy, G. C. (1976). The equilibrium boundary between graphite and diamond. *Journal of Geophysical Research*. **81**. 2467-2470.
- Klemme, S. (2004). The influence of Cr on the garnet-spinel transition in the Earth's mantle: experiments in the system MgO-Cr₂O₃-SiO₂ and thermodynamic modelling.

- Lithos. Selected Papers from the Eighth International Kimberlite Conference. Volume 2: The J. Barry Hawthorne Volume. **77**. 639-646.
- Kopylova, M. G., Russell, J. K., Stanley, C. and Cookenboo, H. (2000). Garnet from Cr- and Ca-saturated mantle: implications for diamond exploration. *Journal of Geochemical Exploration*. **68**. 183-199.
- Krogh, E. J. (1988). The garnet-clinopyroxene Fe-Mg geothermometer: A reinterpretation of existing experimental data. *Contributions to Mineralogy and Petrology (Historical Archive)*. **99**. 44-48.
- Malinovsky, I. Y. and Doroshev, A. M. (1977). Evaluation of P-T conditions of diamond formation with reference to chrome-bearing garnet stability. Second International Kimberlite Conference, Santa Fe, N.M. Unpaginated.
- McDade, P., Ivanic, T. J., Harte, B. and Burgess, S. R. (unpubl.). The effect of pressure on the Ni in garnet geothermometer: A SIMS study of the Jagersfontein mantle peridotites. *Journal of Petrology*. **Unpublished**.
- McKenzie, D. (1989). Some remarks on the movement of small melt fractions in the mantle. *Earth and Planetary Science Letters*. **95**. 53-72.
- McKenzie, D., Jackson, J. and Priestley, K. (2005). Thermal structure of oceanic and continental lithosphere. *Earth and Planetary Science Letters*. **233**. 337-349.
- Menzies, A. (2001). A detailed investigation into diamond-bearing xenoliths from Newlands kimberlite, South Africa. Department of Geological Sciences. Cape Town. University of Cape Town. *Unpublished PhD Thesis*
- Morfi, L. (2001). Polymict peridotites and mantle processes. *Geology and Geophysics*. University of Edinburgh. *Unpublished PhD Thesis*
- Nickel, K. G. (1986). Phase equilibria in the system $\text{SiO}_2\text{-MgO-Al}_2\text{O}_3\text{-CaO-Cr}_2\text{O}_3$ (SMACCR) and their bearing on spinel/garnet lherzolite relationships. *Neues Jahrbuch für Mineralogie, Abhandlungen*. **155**. 259-287.
- Nimis, P. and Taylor, W. R. (2000). Single clinopyroxene thermobarometry for garnet peridotites. Part I. Calibration and testing of a Cr-in-Cpx barometer and an enstatite-in-Cpx thermometer. *Contributions to Mineralogy and Petrology*. **139**. 541-554.
- O'Neill, H. S. C. (1981). The transition between spinel lherzolite and garnet lherzolite, and its use as a geobarometer. *Contributions to Mineralogy and Petrology*. **77**. 185-194.
- Pollack, H. N. and Chapman, D. S. (1977). On the regional variation of heat flow, geotherms, and lithospheric thickness. *Tectonophysics*. **38**. 279-296.
- Ryan, C. G., Griffin, W. L. and Pearson, N. J. (1996). Garnet geotherms: Pressure-temperature data from Cr-pyrope garnet xenocrysts in volcanic rocks. *Journal of Geophysical Research*. **101**. 5611-5625.
- Webb, S. A. C. and Wood, B. J. (1986). Spinel-pyroxene-garnet relationships and their dependence on Cr/Al ratio. *Contributions to Mineralogy & Petrology*. **92**. 471-480.

8. Garnet major element diffusion

8.1 Introduction

In this chapter an appraisal of the conformism of the Newlands and Bobbejaan garnets to diffusion-controlled processes shall be made. Diffusion principles in geological materials are taken from Dodson (1973), Lasaga (1978) and Philbert (1985) who also provide the shapes of experimentally generated diffusion curves which are used in this chapter to simulate diffusion profiles for the variety of zonation circumstances described in Chapter 5.

In order to quantify the spatial data for chemical zonation seen in profiles and X-ray maps, the profiles must firstly be assessed as to their mode and scale of zonation. Therefore internal and external zonations are considered and, where identifiable, given a minimum length scale over which the zonation operates (few samples have a maximum length identifiable). The length scales are minima because diffusion may have removed evidence of original composition or the sample may not contain the entire distance of zonation present in the original rock (i.e. it may comprise a non-complete garnet crystal disrupted by kimberlite magma or mining activity). Conversely, the electron microprobe traverses may be oblique to the direction of maximum zonation gradient both on the analysis surface and as the analysis surface intersects the sample in 3D, both of which produce exaggerated length scales. This last point is assumed to be effectively negligible because care was taken to make traverses parallel to maximum chemical concentration gradient. However, this data is treated with caution and used only to establish general trends and to make general predictions.

Fig. 8.1 illustrates the different profiles obtained by electron microprobe traverses depending upon whether there is a maximum inner core composition present (inner flat) and/or a known location of matrix or inclusion (the interface for diffusion). When none of these are present there is gradual change across the whole profile and only a minimum zonation distance is established. Zonation towards inclusions

(internal) as well as zonation towards matrix (external) are considered so the 'inner flats' are termed internal inner flat and external inner flat in order to be explicit (see table 8.2).

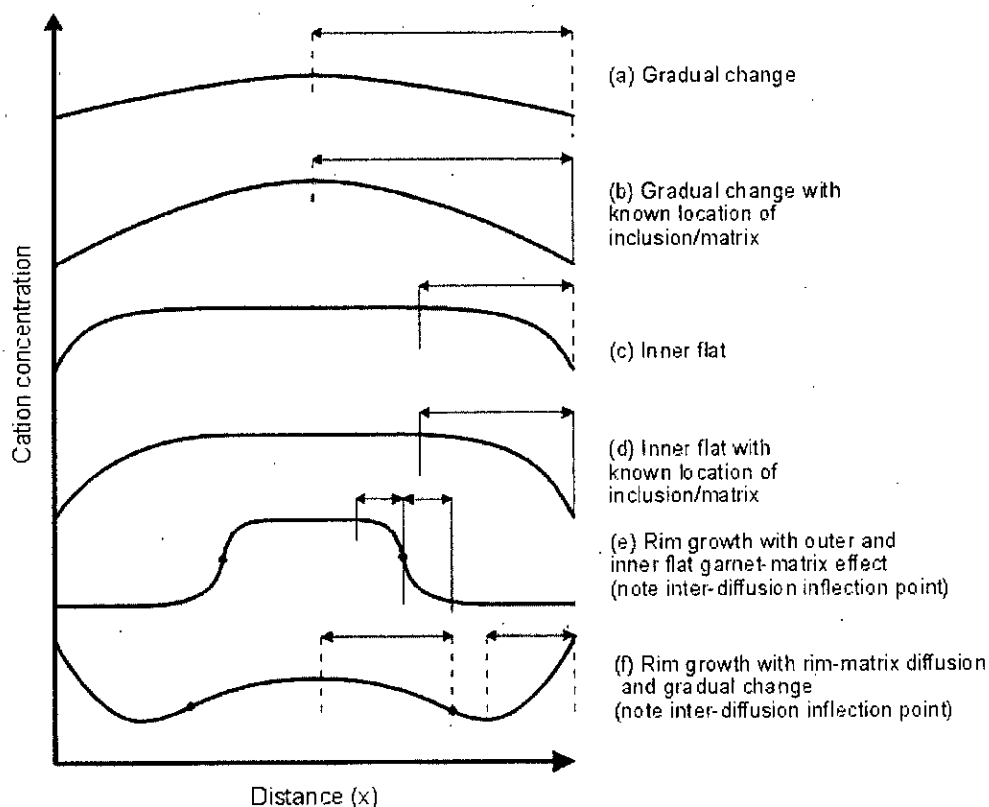


Figure 8.1: 6 Profile types observed for garnet external zonation in Newlands and Bobbejaan samples. Measurements for the zonation length scales are shown by doubly terminating arrows where dashed lines represent minimum distances and thin solid lines are maximum distances. Therefore the presence of an inner flat and knowledge of the location of the matrix are required for the maximum distance to be measured. Profiles (a) to (d) are applicable to internal zonation where an inclusion replaces the matrix as the medium the garnet is diffusing with. Profiles (e) and (f) represent a garnet with different initial core and rim compositions, where (e) has a rim in equilibrium with the matrix and an original inner core composition preserved and (f) has been affected by core-rim inter-diffusion and also rim-matrix diffusion so that there is gradual change in composition over the entire length of the profile (see Fig. 8.2 (b) t_2).

Fig. 8.2 (a) shows the progressive evolution of ideal diffusion profile shapes for a case of external diffusion-controlled zonation occurring in a homogeneous garnet with a fixed matrix composition. The profile shape may also be applied to internal zonation situations where the matrix-garnet contact becomes an inclusion-garnet contact. Fig. 8.2 (b) shows the situation for an initially heterogeneous garnet.

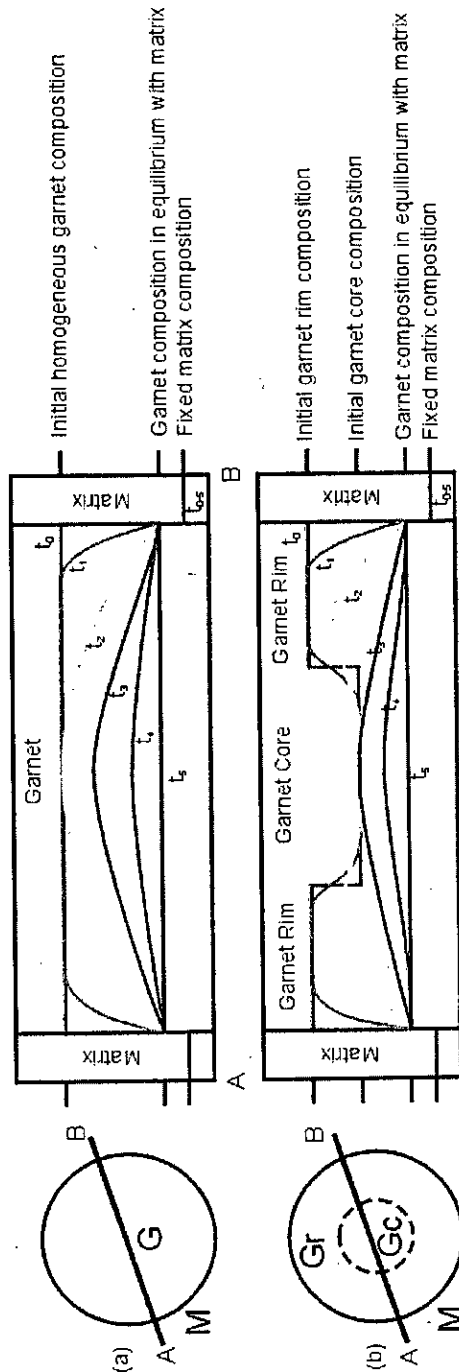


Figure 8.2: Illustration of the hypothetical evolution of diffusion profiles for end-member circumstances present in Newlands and Bobbejaan garnet-rich samples. The y-axis represents concentration of a cation in the garnet matrix where the equilibrium concentration in garnet is lower than the initial concentration. All diagrams may be flipped vertically (when upright) to illustrate the situation for the cation(s) exchanging in the opposite sense to that shown (i.e. where garnet has an initial equilibrium composition with the matrix higher than its initial concentration). The x-axis is distance along a traverse. (a) Homogeneous spherical garnet crystal where t_0 is time zero when the garnet is instantaneously grown and placed into a matrix of non-equilibrium composition. The matrix is hypothetically infinite and has a high flux of cations so that no transient profile is built up in the matrix and the matrix composition remains the same from t_0 - t_3 . The time at which the entire garnet attains equilibrium composition with the matrix is t_3 . (b) As for (a) but with a zoned spherical garnet

crystal with sharply defined initial rim compositions at higher concentrations than the core. Note the garnet inter-diffusion occurrence between core and rim regions contemporaneous with garnet-matrix diffusion, which produces an inflection point in the profile (t_1 and t_2). The potential situations at $t_{4,5}$ are essentially indistinguishable from $t_{3,5}$ in (a) since there is no 'flat' present.

8.1.1 Diffusion coefficient values

Experimental work by many authors (e.g. Elphick et al., 1985; Freer and Edwards, 1999; Chakraborty and Rubie, 1996; Ganguly et al. 1998) have derived diffusion coefficient values for a relatively narrow compositional range of pyrope-almandine garnets at a variety of pressures and temperatures. Table 8.1 summarises this data for garnets highlighting the 5 orders of magnitude over which the diffusion coefficient is calculated in different studies. Fig. 8.3 shows the data on an Arrhenius plot indicating how the diffusion coefficient varies over a temperature range with experiments carried out at a variety of pressures. Freer and Edwards (1999) describe the variation of diffusion coefficient in garnet for Fe, Mg and Ca with pressure: a 20 kb increase in pressure appears to be responsible for a drop by one order of magnitude of the diffusion coefficient. Therefore, given the wide range of measured diffusion coefficients, the differences in pressure between the experiments is not significant. Cygan and Lasaga (1985) provide a low temperature dataset for comparison.

The almandine-pyrope-grossular composition is known to have a significant effect on the diffusion coefficient but there are no obvious general trends to highlight. The majority of experiments are carried out on close to Alm₅₀Pyp₅₀ compositions except where stated in Table 8.1.

Temp.	Pressure	Elements	Diffusion coefficient	Ea (Q)	Author
950°C	40 kb	Fe-Mg inter-diffusion	$1 \times 10^{-21} \text{m}^2/\text{s}$ (extrapolated)	334±40 kJ/mol	Elphick et al. (1985)
1000°C	30 kb dependence is: 20 kb = 1 order mag D change	Fe, Ca self	$1 \times 10^{-17} \text{m}^2/\text{s}$	270.4±1 9.3 kJ/mol	Freer and Edwards (1999)
1150°C	30 kb	Fe-Mg inter-diffusion	$1 \times 10^{-16} \text{m}^2/\text{s}$	132±45 kJ/mol	Freer (1979)
1100°C 1100°C	8.5 GPa fit	Mn self Fe & Mg self	$1 \times 10^{-17} \text{m}^2/\text{s}$ $1 \times 10^{-16} \text{m}^2/\text{s}$	226±21 kJ/mol	Chakraborty and Rubie (1996)
1200°C	10 kb	Fe, Mg, Ca, Mn self	1×10^{-15} to $1 \times 10^{-17} \text{m}^2/\text{s}$	254±282 72±42 kJ/mol	Ganguly et al. (1998)
1432°C	38 kb	Mg self Fe, Ca self	$4 \times 10^{-16} \text{m}^2/\text{s}$ $2 \times 10^{-17} \text{m}^2/\text{s}$	254±282 72±42 kJ/mol	Ganguly et al. (1998)
1000°C	1 atm	Mg self	$*5 \times 10^{-20} \text{m}^2/\text{s}$	155±10 kJ/mol	Schwandt et al. (1995)
850°C	2 kb	Mg self	$1 \times 10^{-18} \text{m}^2/\text{s}$	239±16 kJ/mol	Cygan and Lasaga (1985)
1200°C	3.5 GPa	Fe-Mg inter	$1 \times 10^{-18} \text{m}^2/\text{s}$	284 ±36 kcal/mol	Chakraborty and Ganguly (1992)

Table 8.1: Summary of diffusion coefficients from experimental studies for almandine-pyropes garnets in the literature (* measured in pyrope garnet). Errors are usually in the range of ¼ of an order of magnitude. Figure 8.3 illustrates this data in graphical form with an indication of values attained to higher and lower temperatures. Ea (sometimes referred to as 'Q' in the literature) is the activation energy and affects the slope of the line in Fig. 8.3.

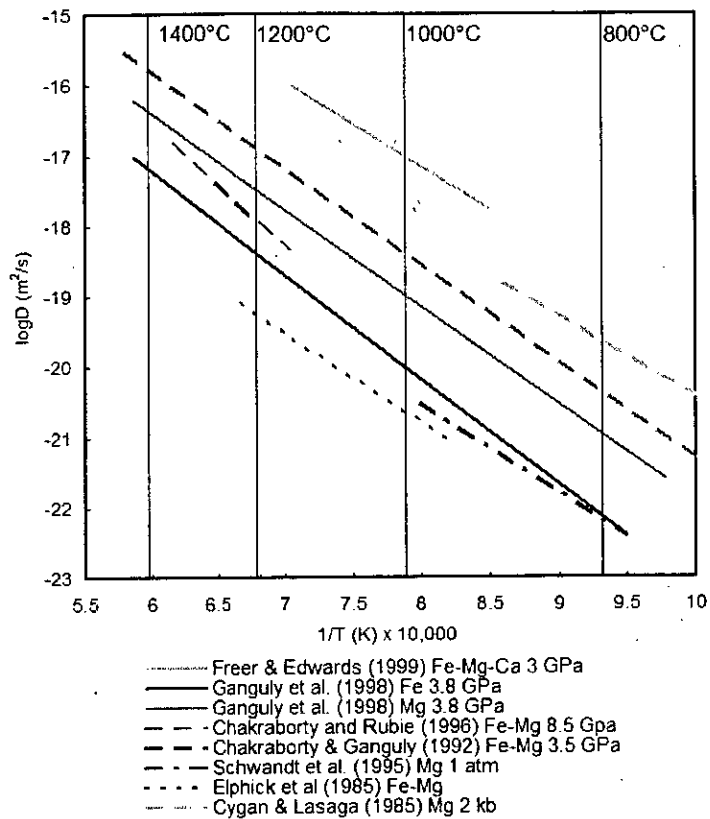


Figure 8.3: Arrhenius plot of temperature vs. diffusion coefficient for various experimental results for pyrope-almandine garnets. Reference, cations and pressure are given in the legend.

Carlson (2006) formulates a model for the variation in diffusion rates with pressure, temperature, composition and oxygen fugacity. All existing data (Table 8.1) are normalised to 1000°C, 1 GPa, graphite-oxygen buffer and almandine composition. The dependence of the diffusion coefficient on composition is found to relate directly to garnet unit cell dimension and a correction can therefore be made for any composition. Thus Mg diffusion for 1000°C, 3 GPa, graphite-oxygen buffer and pyrope composition is approximately $10^{-18} \text{m}^2/\text{s}$ and for Ca is $10^{-19} \text{m}^2/\text{s}$. Since Ca is slowest of all the divalent cations, it is expected to be the rate limiting interdiffusing ion so $10^{-19} \text{m}^2/\text{s}$ is the value that shall be used when modelling the profiles.

Many authors report much slower trivalent cation diffusion (i.e. relating to Cr^{3+} and Al^{3+} in this study) but this has not been quantified because diffusion is too slow to conduct experiments over normal timeframes. The Mg-Ca interdiffusion is therefore

the only data comparable to experimental studies and if there is dependency of Cr-Al exchange on this then the timescales are expected to be much longer.

8.2 Results

8.2.1 Length scales

Table 8.2 shows the values for measurable garnet zonation length scales in a selection of Newlands and Bobbejaan samples for zoned elements (the complete table with all samples listed is in Appendix II). The measurements are taken from profiles generated from electron microprobe traverses across garnets. Ideally the measurements should be of the perpendicular distance between the location of the deviation of the composition from the most extreme rim and core compositions for external zonation. For internal zonation it is the perpendicular distance from the inclusion's contact with garnet to the position in the garnet where the composition stabilises. A minimum distance is recorded in the majority of samples since the composition in the garnet rarely attains constancy on high and low concentration sides (Fig. 8.1).

Sample	Zonation Type	Profile Type (i.f.=inner flat)	Zonation length scale to the nearest analysis point (μm) (brackets = internal zonation)						
			Mg	Ca	Al	Cr	Ti	Fe	Mn
NEW003	Eu	Gradual change	2000	2000	2000	2000	2000	-	-
NEW039	Eu	Rim growth w. gradual change	800	1200	1000	1000	-	500	-
NEW059	Eg, Ic	External i.f.	-	-	500	500	-	-	-
	Is	Internal i.f.	(-)	(-)	(150)	(-)	(-)	(-)	(-)
NEW063	Ed, Id	External i.f.	1000	1000	500	500	400	800	-
NEW065	Eu, Is								
	Id,	Internal i.f.	(600)	(600)	(500)	(500)	(-)	(-)	(-)
NEW068	Eu	External i.f.	1250	1250	1250	1250	-	-	-
	Is	Gradual change	(900)	(900)	(900)	(900)	(-)	(-)	(-)
NEW069	Ic	Internal i.f.	(550)	(580)	(550)	(550)	(300)	(?)	(-)
NEW074	Eu,	External i.f.	2400	3200	>1000	>1000	3200	-	1000
	Is	Gradual change	(800)	(700)	(400)	(400)	(700)	(-)	(500)
NEW078	Eu, Id	Internal i.f.	(500)	(420)	(350)	(320)	(250)	(-)	(-)
NEW101	Eu	Rim Growth	700	800	800	800	500	-	-
NEW114	Eu, Id	Internal i.f.	(1000)	(850)	(750)	(750)	(550)	-	-

Sample	Zona-tion Type	Profile Type (i.f.=inner flat)	Zonation length scale to the nearest analysis point (μm) (brackets = internal zonation)						
			Mg	Ca	Al	Cr	Ti	Fe	Mn
NEW303 grt	Ed, Id	External i.f. Internal i.f.	350 (100)	350 (100)	350 (100)	350 (100)	-	-	-
NEW303 cpx	Eg	Rim growth	400	400	-	400	Na 400	-	-
NEW308	Es Is	External i.f. Internal i.f.	? (?)	1000 (500)	1000 (500)	1000 (500)	- (-)	- (-)	- (-)
NEW404	Eu Is	External i.f. Gradual change	2500 (700)	2500 (700)	2500 (700)	2500 (700)	- (-)	- (-)	- (-)
NEWSP	Id	Internal i.f.	(1000)	(1200)	(1000)	(1000)	(1000)	(-)	(-)
LEI001	Id	Internal i.f.	(500)	(500)	(500)	(500)	(-)	(500)	(-)
LEI007	Eu	I & outer flat	950	750	900	950	900	-	800
B44	Eg Id	Outer flat Gradual change	- (-)	2000 (500)	1500 (800)	1800 (800)	- (500)	1000 (500)	1800 (500)
B48	Eu	External i.f.	4000	4000	3800	4200	-	1800	-
B55	Id	Gradual change	(-)	(700)	(500)	(500)	(500)	(-)	(-)
BOB113	Eu Is	I & outer flat Internal i.f.	2300 (300)	2300 (300)	500 (400)	700 (400)	1800 (400)	- (-)	- (-)
BOB167	Eu Is	Outer flat Internal i.f.	- (500)	- (500)	4000 (-)	4000 (-)	- (-)	- (-)	- (-)
BOB301	Id, Is, Ic	Internal i.f.	(500)	(500)	(500)	(500)	(-)	(-)	(-)
BOB401	Ed Id	Outer flat Internal i.f.	2300 (500)	2400 (500)	3000 (500)	3000 (500)	1000 (-)	2400 (-)	500 (-)
BOB402	Ed Id	Gradual change Gradual change	1500 (1000)	1500 (1000)	1000 (500)	1000 (500)	- (500)	- (500)	- (-)
BOB404	Eu Is	External i.f. Gradual change	4000 (-)	4000 (-)	2000 (800)	2000 (800)	- (-)	- (-)	- (-)

Table 8.2: Selected samples analysed for major elements indicating the external and internal zonation types present with the distance of any measurable diffusion type noted in μm for zoned major elements. Internal zonation is in brackets and on the same line as the particular zonation type listed.

Fig. 8.4 shows the range of diffusion distances in single samples illustrating the shorter internal and longer external diffusion distances and Mg-Ca and Cr-Al distance relationships which are relatively independent of Ti.

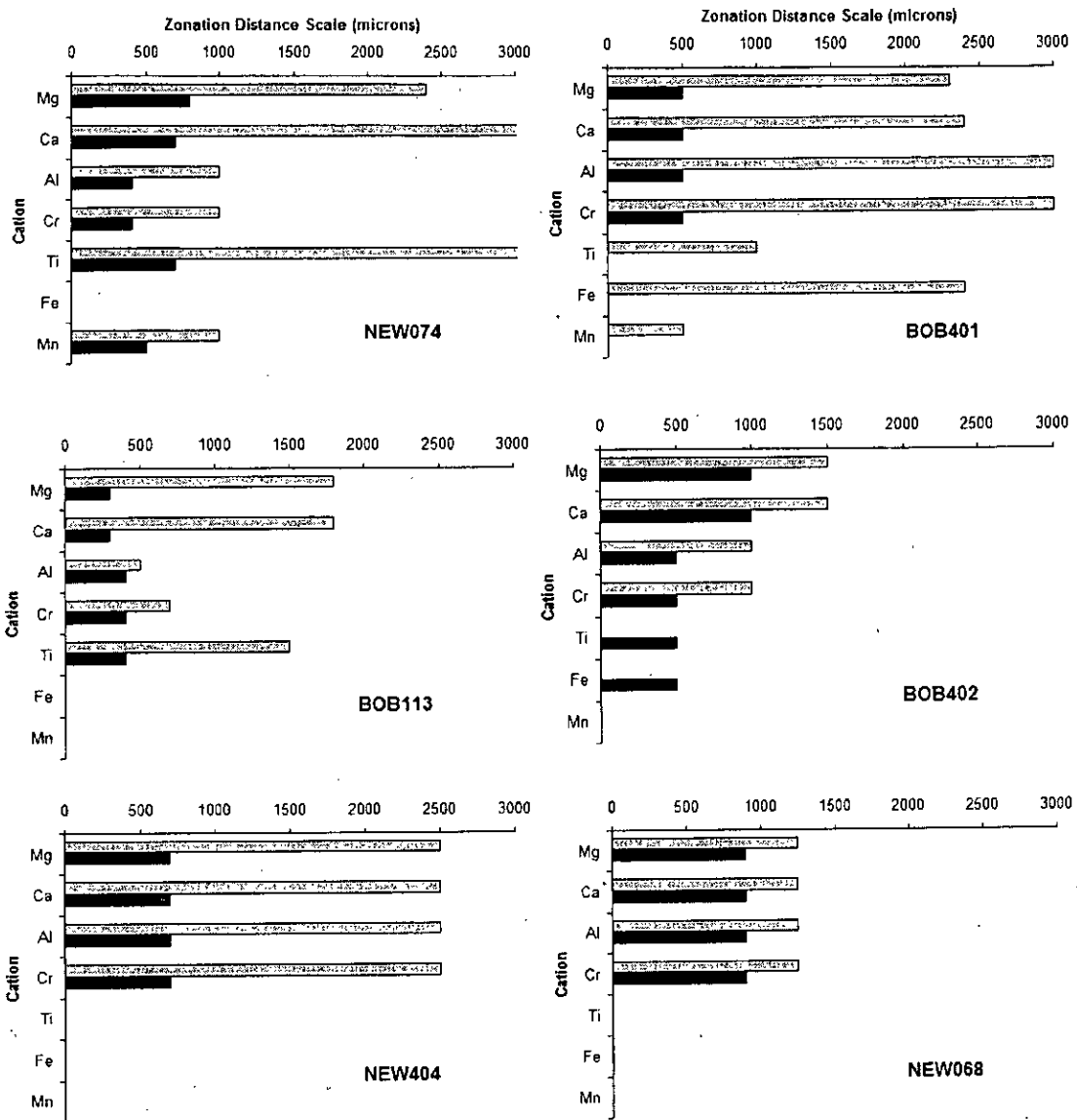


Figure 8.4: Zonation distance scale for zoned cations in six samples that show both internal (black bars) and external (grey bars) zonation.

8.2.2 Differences between cation zonation distances in individual samples

Mg and Ca and also Cr and Al appear to act as diffusion couples (inter-diffusion) since with each pair they commonly show negatively correlated cation concentrations with very similar zonation distances within individual samples. Mg and Ca tend to occur over longer length scales in both external and internal zonation types compared to Al and Cr. This observation conforms to the relatively ‘sluggish’

nature of Cr-Al diffusion mentioned. In zoned garnets Al and Cr are always zoned and Ca and Mg are only occasionally not zoned in the highly sub-calcic garnets.

Most observed Ti zonation is external (see Appendix II). In a few samples Ti is externally zoned over the greatest distance of all cations (e.g. 3200 μm in NEW074). This corresponds to samples with E_{Ca} zonation in Chapter 5, which is most likely to be a metasomatic effect. Ti is also zoned internally over shorter distances and this is interpreted to be a result of P-T re-equilibration (Chapter 6 and 7). Fe and Mn are less frequently zoned compared to the cations already mentioned. When they are zoned they only show only a slight change in cation concentration compared to the stronger zonation of Ca, Mg, Al and Cr. Fe and Mn tend to be positively correlated with each other and negatively correlated with Mg.

From NEW303 the one external clinopyroxene diffusion length scale measured (no internal zonation was discovered inside inclusions of clinopyroxene in garnet) is 400 μm for Cr, Na, Ca and Mg.

8.2.3 Differences between samples

The Newlands and Bobbejaan samples show a similar distribution of internal zonation distances (Fig. 8.5a). In general the Bobbejaan samples have a higher proportion of external zonation distances $> 1600\mu\text{m}$ (longest is $4000\mu\text{m}$) than the Newlands samples (Fig. 8.5b). This may be explained by the larger sample size at Bobbejaan which would allow greater chance that external zonations are not truncated by the kimberlitic resorption or crushing of garnet crystals in samples by mining activities.

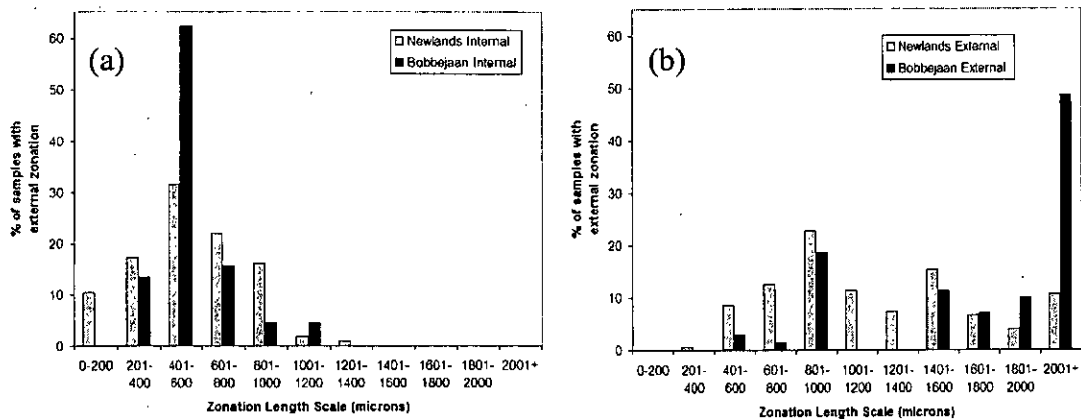


Figure 8.5: Range of garnet internal (a) and external (b) zonation distances from Newlands and Bobbejaan samples.

The longest internal zonation distances are recorded adjacent to diopside bearing inclusions (i.e. commonly 800-1400 μm at Newlands). The majority are 400-800 μm , which record serpentine \pm Cr-spinel inclusions. Since external matrix compositions are rarely known, no differences with respect to mineral type may be identified for external zonation.

8.2.4 Differences according to zonation type

The majority of external zonation occur at length scales $> 800\mu\text{m}$ whereas the internal zonation occur over a shorter length scale (200-1000 μm) (Fig. 8.6). The internal zonation length scales appear to have a normal distribution, whereas the external ones possess a weakly bimodal distribution with peaks at 900 μm and 1500 μm .

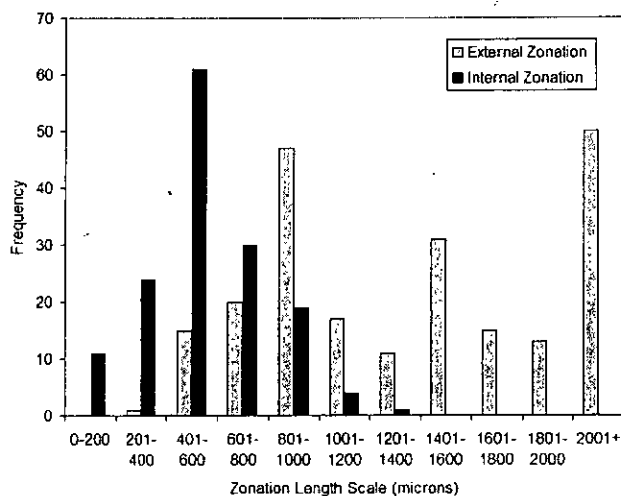


Figure 8.6: Zonation length scales for all samples separated into internal and external zonation types.

8.2.5 Conformism to ideal diffusion profiles

Various models exist to approximate the shape of diffusion profiles. Sautter and Harte (1990) used error functions (erf) to model Al diffusion in clinopyroxene utilizing the equation from Crank (1975):

$$C = C_0 + (C_x - C_0) \cdot \operatorname{erfc}\left(\frac{X}{2\sqrt{Dt}}\right) \quad (1)$$

where C is the cation concentration for a given distance along a profile (X in metres). C_0 is the initial garnet cation concentration, C_x is the y-intercept value, D is the diffusion coefficient for a particular element (m^2/s) and t is the time diffusion has occurred for (in secs.).

The time scale of zonation by diffusion may be approximated to within an order of magnitude by equation (2) which uses the diffusion coefficient and a length scale (as recorded in Table 8.1) over which a suspected diffusion profile has occurred rather than modelling the curve more precisely as required for (1):

$$t = x^2/D \quad (2)$$

where t is the time taken in seconds, x is the distance in metres and D is the diffusion coefficient in square metres per second.

Fig. 8.7a shows that internal zonations present in garnets in samples such as NEW114 conform well to curve fitting according to equation (1) by using C_x and C_0 values chosen by eye from the shape of the profiles (Appendix II). Then experimentally determined diffusion coefficient values are inserted and t is then modified until the shape of the curve fits the data, thereby yielding a value for time for each profile. NEW114 has been measured on either side of the inclusion and slightly different profiles are produced (profiles 1 and 2 in Fig. 8.7). The difference in length scale of these profiles produces a relatively small difference in the time taken according to equation (1). The time scales are one order of magnitude higher when using equation (2) given the different length scale used (see caption to Fig.

8.7). Curve fits generally produce a standard deviation of residuals from the measured values of 0.02 for 99.5% confidence limits.

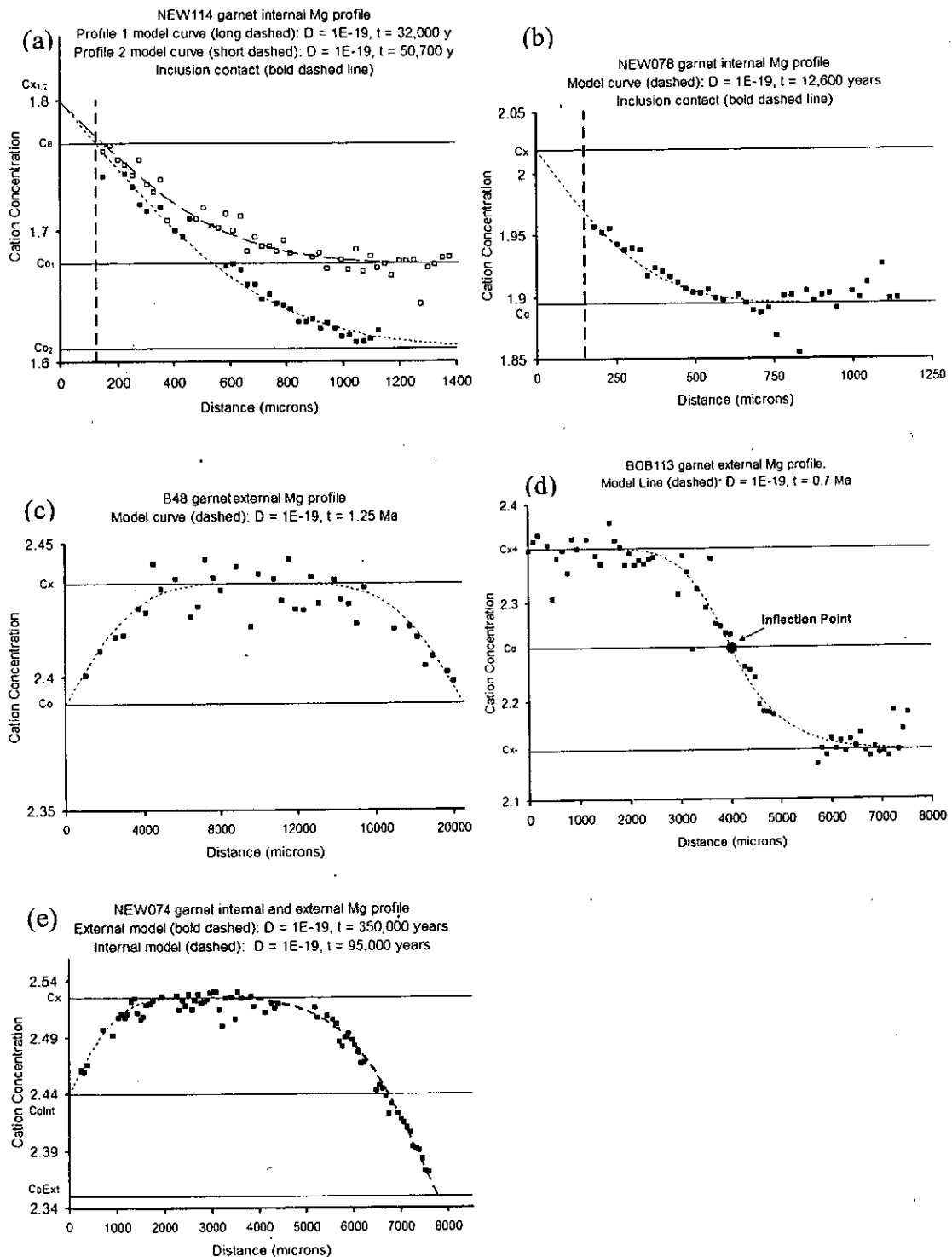


Figure 8.7: (a) Distance-concentration diagram for Mg profile of garnet in sample NEW114 (see appendix for complete profiles). The models for the two profiles shown are generated using equation 1 with the parameters on the graph. The thick dashed vertical line is the location of the contact with a 300 μ m diameter inclusion of clinopyroxene and Cr-spinel. The highest concentration horizontal line

is the concentration at the garnet-inclusion contact, the middle line is C_0 for profile 1 and the lowest line is C_0 for profile 2. y-intercept values C_{X1} and C_{X2} are shown near cation concentration 1.8. (b) as for (a) but for sample NEW078 with one profile shown. (c) as for (a) but an external zonation with an inner flat from sample B48 with single model line. (d) as for (c) but an external zonation with inner and outer flat from sample BOB113 illustrating core-rim inter-diffusion and associated inflection point on curve. (e) as for (c) but for internal and external zonations from NEW074 using two models.

The normalised Ca diffusion coefficient of $1 \times 10^{-19} \text{ m}^2/\text{s}$ (Carlson, 2006) from experimental studies (see table 8.1) was used for modelling Mg profiles with equation (1). This is because Ca diffuses more slowly compared to Mg and Ca-Mg interdiffusion is observed to occur, therefore Ca is the rate limiting cation so the D_{Ca} value is the assumed interdiffusion value $D_{Mg \leftrightarrow Ca}$. The Mg profiles were used to estimate distances because they are usually developed most clearly. The temperature of 1000°C was used because the majority of P-T estimates (see Chapter 7) yield values within 100°C of this. The plot in Fig. 8.3 shows that varying temperature by 100°C changes D values by less than 1 order of magnitude so this variation is bracketed by the range of diffusion coefficient values examined in Table 8.3.

If a $D_{Mg \leftrightarrow Ca}$ value one order of magnitude lower is chosen then the curve generated is identical if the time value is increased by one order of magnitude. Therefore each curve from Fig. 8.4 may be interpreted based on a range of $D_{Mg \leftrightarrow Ca}$ values that produce different time scales. e.g. if a $D_{Mg \leftrightarrow Ca}$ of $1 \times 10^{-20} \text{ m}^2/\text{s}$ is used in Fig. 8.7b for NEW078 the time scale would equal 126,000 years.

The range of time values generated from curve fitting of profiles to equation (1) is shown in Table 8.3; it is 0.35-1.25 Ma for external zonation and 0.01 to 0.1 Ma for internal zonation. These values are comparable (assuming one order of magnitude errors for equation (2)) with values from the more simple relationship in equation (2) and shown for all samples in Appendix II. Equation (2) generates time scales approximately but consistently one order of magnitude larger than with curve fitting using equation (1).

Sample	Profile Type	Zonation Type	Mg Zonation length scale (μm)	Equation (1) Curve fitted timescale using $D_{\text{Mg} \leftrightarrow \text{Ca}} = 1 \times 10^{-19} \text{ m}^2/\text{s}$	Equation (2) timescale using $D_{\text{Mg} \leftrightarrow \text{Ca}} = 1 \times 10^{-19} \text{ m}^2/\text{s}$	Equation (2) Max. timescale using $D_{\text{Mg} \leftrightarrow \text{Ca}} = 5 \times 10^{-20} \text{ m}^2/\text{s}$	Equation (2) Min. timescale using $D_{\text{Mg} \leftrightarrow \text{Ca}} = 1 \times 10^{-17} \text{ m}^2/\text{s}$
NEW114	Interior flat	Id	1200	50,700 y	456,000 y	913,000 y	4,560 y
NEW078	Interior flat	Id	500	12,600 y	80,000 y	158,000 y	800 y
B48	External inner flat	Eg-	5400	1.25 Ma	9.2 Ma	18.5 Ma	92,000 y
BOB113	External inner flat & outer flat	E _{Ca}	4500	0.7 Ma	1.7 Ma	3.4 Ma	16,800 y
NEW074	External inner flat	E _{Ca}	4000	350,000 y	5.1 Ma	10.1 Ma	51,000 y
	Internal inner flat	Is	1100	95,000 y	383,000 y	766,000 y	3,830 y

Table 8.3: Time scales for zonation based on modelling of well defined profiles from Fig. 8.4. Right-hand columns show the time scales for the approximation using equation (2) for comparison.

According to the last two columns in Table 8.3, bringing in the likely possible variations in $D_{\text{Mg} \leftrightarrow \text{Ca}}$, the time estimates range from 800 y to 913,000 y for internal and 51,000 y to 18.5 Ma for external zonation. This is approximately 3 orders of magnitude in each case.

The single zoned clinopyroxene yields an external zonation length scale of 400 μm and, using D_{Al} (assuming this is close to the value for Cr) of $2 \times 10^{-19} \text{ m}^2/\text{s}$ as used in Sautter and Harte (1990), a timescale of approximately 1Ma is generated, which is in the mid range of the garnet external values.

8.3 Limitations

- 1) There is a large (orders of magnitude) range in experimentally derived diffusion coefficient values that is not due to pressure effects. Experiments are dominantly for almandine-pyrope garnets, which probably yield relatively high D values where Ca diffusion is involved. For Al and Cr the diffusion coefficients are expected to be much smaller.
- 2) Diffusion profiles have been predicted from end member situations, whereas the real pre-diffusion cation distribution is not known.
- 3) Most of the length scales are minimum lengths (Fig. 8.1) so the timescale estimate may be too short (possibly by up to a factor of 2) for this reason. Conversely, the electron microprobe traverses will deviate in 3D slightly from being parallel to the line of maximum chemical gradient in a given sample. This effect is thought to be negligible.
- 4) Only Mg zonation was studied since it is the cation with the most experimental data available for garnets at high pressures. Fe diffusion data is also determined but not commonly zoned. A downside to this is that if there is a coupling effect of Mg with Ca (or even 3+ ions), then the time estimates will be incorrect since the Mg diffusion may be slowed by the slower rates of diffusion of the other cations.
- 5) $D_{\text{Mg} \leftrightarrow \text{Ca}}$ is assumed not to vary over time (i.e. P and T assumed constant) so only time-averaged values are gained from the equations.
- 6) It is impossible to know whether any diffusion has occurred in a different direction to that observed over time since the measured profiles are again essentially yielding time averaged results (e.g. t_2 to t_3 and back again in Fig. 8.2a).

8.4 Summary

- 1) Compositional zonation in garnets from all Newlands and Bobbejaan samples appears to conform to diffusion-related processes due to the shapes of the profiles measured by electron microprobe traverses. In most cases the diffusion profiles appear to be between garnet and another mineral or minerals, either included in garnet or external to garnet. Only a few samples may be identified as having a rim growth type of garnet profile that appears to show two phases of garnet growth later modified by diffusion.
- 2) The profiles have been classified according to the presence of 'flats' and whether there is evidence of rim growth of a different garnet composition.
- 3) Minimum measurements for the zonation scale of Mg, Ca, Al, Cr, Ti, Fe, Mn were made in all samples traversed by electron microprobe (table in Appendix II). Only the samples with an external inner and outer flat (for external zonation) and internal inner flats (for internal zonation) allow a maximum zonation length scale to be identified.
- 4) Al-Cr and Mg-Ca are the most clearly identifiable diffusion-couples with Mg-Ca tending to be zoned over greater distances in individual samples.
- 5) Concentrating on $D_{Mg \leftrightarrow Ca}$, the range of time values generated by curve fitting of the profiles to the Crank equation and use of the simplified equation: $x = \sqrt{Dt}$ is similar, but generally one order of magnitude greater using the simplified equation.
- 6) The range of $D_{Mg \leftrightarrow Ca}$ values used suggest external zonation has been the result of diffusion on long timescales $> 50,000$ y and < 20 Ma. This is corroborated by the single external clinopyroxene Al diffusion profile. Since this is over an order of magnitude greater timescale than internal zonation (see point 7 below), it is feasible that this reflects the total time for P-T re-equilibration including exsolution and then re-equilibration with exsolved inclusions.

- 7) The range of $D_{Mg \leftrightarrow Ca}$ values used suggest internal zonation has been the result of diffusion on short timescales > 800 y and < 1 Ma. As stated in point 6 (above) this timescale is an order of magnitude shorter than the external zonation and may just include the time for re-equilibration with inclusions.
- 8) Eg^+ , Eg^- and Ed external zonations reflect equilibration with matrix and appear to have chemically parallel trends to 'Is' (for Eg) and Id (for Ed) internal zonations. This is therefore most likely to reflect P-T re-equilibration (Chapter 6 and 7).
- 9) E_{Ca} zonation would suggest garnet equilibration with a modified matrix composition that is more Ca- and Ti-rich. This must have occurred while inclusions were present and before internal zonation happened otherwise they would overprint internal zonation patterns as seen in Appendix III (especially sheets for NEW074 and BOB113). This type of external zonation along with the Eg^- zonation of B48 represents the largest length scale of all external zonations so may be more likely to be associated with metasomatic processes rather than P-T processes (see NEW303, Chapter 7).

8.5 References

- Carlson, W. D. (2006). Rates of Fe, Mg, Mn and Ca diffusion in garnet. *American Mineralogist*. **91**. 1-11.
- Chakraborty, S. and Ganguly, J. (1992). Cation diffusion in aluminosilicate garnets: experimental determination in spessartine-almandine diffusion couples, evaluation of effective binary diffusion coefficients, and applications. *Contributions to Mineralogy and Petrology*. **111**. 74-86.
- Chakraborty, S. and Rubie, D. C. (1996). Mg tracer diffusion in aluminosilicate garnets at 750-850° C, 1 atm. and 1300° C, 8.5 GPa. *Contributions to Mineralogy and Petrology*. **122**. 406-414.
- Crank, J. (1975). *The mathematics of diffusion*. Oxford, UK, Oxford University Press.
- Cygan, R. T. and Lasaga, A. C. (1985). Self diffusion of magnesium in garnet at 750 to 900 °C. *American Journal of Science*. **285**. 328-350.
- Dodson, M. H. (1973). Closure temperature in cooling geochronological and petrological systems. *Contributions to Mineralogy and Petrology*. **40**. 259-274.
- Elphick, S. C., Ganguly, J. and Loomis, T. P. (1985). Experimental determination of cation diffusivities in aluminosilicate garnets. *Contributions to Mineralogy and Petrology*. **90**. 36-44.
- Freer, R. (1979). An experimental measurement of cation diffusion in almandine garnet. *Nature*. **280**. 220-222.
- Freer, R. and Edwards, A. (1999). An experimental study of Ca-(Fe,Mg) interdiffusion in silicate garnets. *Contributions to Mineralogy and Petrology*. **134**. 370-379.
- Ganguly, J., Cheng, W. and Chakraborty, S. (1998). Cation diffusion in aluminosilicate garnets: experimental determination in pyrope-almandine diffusion couples. *Contributions to Mineralogy and Petrology*. **131**. 171-180.
- Lasaga, A. C. (1978). Multicomponent exchange and diffusion in silicates. *Geochimica et Cosmochimica Acta*. **43**. 455-469.
- Philbert, J. (1985). *Diffusion et transport de matiere dans les solides*. Les Ulis, France, Les editions de physique.
- Sautter, V. and Harte, B. (1990). Diffusion gradients in an eclogite xenolith from the Roberts Victor kimberlite pipe: (2) kinetics and implications for petrogenesis. *Contributions to Mineralogy and Petrology*. **105**. 637-649.
- Schwandt, C. S., Cygan, R. T. and Westrich, H. R. (1995). Mg self-diffusion in pyrope garnet. *American Mineralogist*. **80**. 483-490.

9. Trace Element Mineral Chemistry

9.1 Introduction

Trace element data obtained by ion microprobe SIMS (secondary ionisation mass spectrometry) analysis have been able to contribute to the understanding of mineralogical and petrological evolution in the mantle since they provide additional means to assess processes such as enrichment and depletion in rocks and minerals. The trace elements have a wide variety of charges and ionic radii and, consequently, a wide range of compatibilities with respect to different minerals and their equilibrium melts. In addition temperature sensitive elements such as Ni and Ti may be determined to greater levels of accuracy by ion microprobe than by electron microprobe. By virtue of its high spatial resolution SIMS may be applied to define small scale features such as chemical variation at mineral contacts and across zoned crystals.

It has been recognised that the trace element composition of peridotitic DIs (diamond inclusions) is not of the depleted character that their major element compositions would suggest. The peridotitic DI garnets are very high in Cr and low in Ca and conform to the garnet-chromite harzburgitic assemblage and yet they may have extremely fractionated (incompatible element enriched) trace element compositions. Shimizu and Richardson (1987) emphasise the extent of this decoupling between major and trace element compositions for the garnet inclusions in diamond. However, such a decoupling is a common feature of many peridotite xenoliths from both basalts and kimberlites and has been widely interpreted as resulting from the enrichment of depleted peridotites by small amounts of incompatible element rich material (e.g. Harte and Hawkesworth (1989). The percolation of metasomatic fluids from the deep mantle has become the favoured agent for this effect (e.g. Burgess and Harte, 2004; Stachel et al., 2004).

Burgess and Harte (2004) identified garnet rare earth element (REE) zonation in single garnets that are also correlated with changes in garnet major element chemistry. Garnets showing major element core to rim zonation towards bulk lherzolite compositions are also shown to be zoned in trace elements towards more REE compositions at the rims. This process is also attributed to the percolation of metasomatic fluids which are believed to be silicate melts. Overall REE profiles measured in peridotitic garnets show wide variations from 'normal' (HREE strongly enriched) to types described as 'humped', 'sinusoidal', 'sinuous' and 'sigmoidal' by various authors (see Fig. 9.1). Similarly diamond inclusion garnet REE data published in the literature typically show a highly enriched (high La/Lu) 'humped' profile as illustrated:

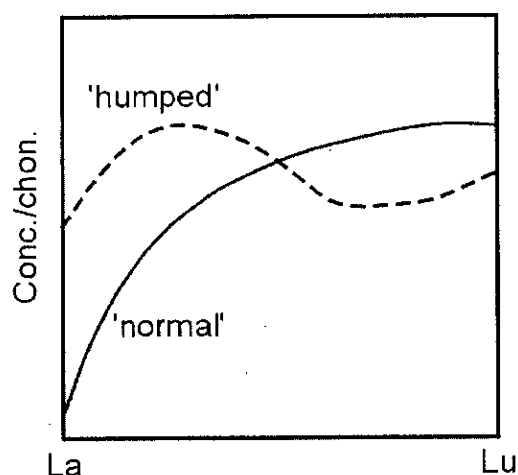


Figure 9.1: Schematic REE diagram showing the 'normal' (solid line) and 'humped' (dashed line) patterns found in mantle garnets.

Because of their curious nature and the LREE-enriched characteristic these 'humped' profiles in inclusions, like those in peridotites, have often been interpreted to be connected with some later events of metasomatism involving carbonatitic or silicate melts/fluids but this remains unresolved. In this chapter the data from the Newlands and Bobbejaan samples will be related to existing models for the formation of particular trace element characteristics in the literature for both peridotites and DIs. Previous studies have largely been on garnet alone, and thus in the absence of knowledge concerning the major and trace element chemistry of other coexisting

phases. Therefore the chromite and clinopyroxene analyses in the present study will provide broader scope for petrogenetic interpretation.

9.1.1 Nomenclature

Trace elements are the elements present in minerals that are not stoichiometrically significant and normally have concentrations < 0.1 wt. %. The measured trace elements for mantle minerals in this chapter may be divided into groups according to their properties and hence their location in the periodic table:

1. LILE (large ion lithophile elements) have large ionic radii ($>1.2\text{\AA}$) and low charge (1^+-2^+). These are Li, Na, K, Sr and Ba in order of increasing atomic number (Rb and Cs have not been measured in this study).
2. HFSE (high field strength elements) have relatively small ionic radii (0.6-0.9 \AA) and higher charge (3^+-4^+) than LILE. These are Y, Zr, Nb and Hf in order of increasing atomic number (Ta and W have not been measured in this study).
3. FSTE (first series transition elements) have small (0.4-0.7 \AA) ionic radii and variable charge usually 2^+ and 3^+ . These are Sc, Ti, V, Mn, Co, Ni and Ga in order of increasing atomic number (Cu and Zn have not been measured in this study).
4. REE (rare earth elements) comprise the heavy elements La to Lu which have atomic weight 138.91 (La) to 174.97 (Lu). The ionic radius decreases systematically with atomic number from 1.03 \AA for La to 0.86 \AA for Lu. The majority of REE have a charge of 3^+ . In this study all are measured except for the radioactive Pm. The light rare earth elements (LREE) are La to Nd, the middle rare earth elements (MREE) are Sm to Dy and the heavy rare earth elements (HREE) are Ho to Lu.

Additionally, concerning the nomenclature of *garnet REE patterns*, in this study a 'normal' profile shall represent the HREE-enriched profiles and humped shall represent any profile with a bulge in the LREE (as illustrated in Fig. 9.1). And instead of defining and distinguishing the difference between 'humped' and

'sinuous/sinusoidal/sigmoidal' patterns, the ratios of Sm/Dy, Ce/Yb and Dy/Yb (all normalised abundances) shall be used to define the variations in patterns quantitatively. Sm/Dy defines the magnitude of the 'hump', Ce/Yb defines the bulk LREE/HREE enrichment and Dy/Yb defines the MREE-HREE slope. The term 'humped' shall still be employed to refer to variants of that shown in Fig. 9.1.

Analyses are recorded as ppm values but they are also shown on 'chondrite normalised' plots. i.e. the ppm concentration is divided by that of the same element in chondritic meteorites from the data of McDonough and Sun (1995). Therefore the vertical scale on these plots is labelled 'Conc./chon.', which stands for concentration divided by chondritic concentration. The result of this is to remove unnecessary spikes from the data that are due to natural elemental abundances. Values > 1 show that the element has greater abundance than in the most primitive rock, i.e. a C1 carbonaceous chondrite meteorite. The chondrite normalised abundances are indicated by subscript notation (e.g. for 'Zr_{NORM}' read chondrite normalised Zr).

9.2 Aims

The overall purpose of the analyses is to contribute to the understanding and interpretation of the petrological and geochemical evolution of the diamond-garnet-chromite harzburgite paragenesis and the high-Cr lherzolitic assemblages identified and defined in Chapters 3 and 5. More specifically the aims are to:

1. Document the trace element variation in garnet, clinopyroxene and spinel from a selection of harzburgitic and lherzolitic bulk rock compositions from Newlands and Bobbejaan samples.
2. Define direction of chemical trends both within samples (i.e. for zonation) and between samples of different bulk rock compositions.
3. Establish which types of zonation in trace element signatures are present due to pressure-temperature effects (Chapter 7) and which are present due to changing bulk composition (i.e. metasomatism). This will be accomplished

by examining garnet zonation trends in conjunction with major element zonations (Chapter 5) and consideration of changes due to P-T re-equilibration (Chapter 6).

4. Use the data to comment on the generation of the 'humped' REE patterns in garnets.

9.3 Results

Details on sample preparation, analytical conditions, standards and techniques for ion microprobe SIMS analysis used in this study can be found in Appendix I (Section I.3). The raw data for all trace element analyses can be found tabulated in Appendix V. The results are presented below in the LILE, HFSE, FSTE and REE groups noted above. Additionally in this section, an appraisal of trace element partitioning between coexisting minerals is given for each mineral combination. Finally, divariant element plots are made for garnet, Cr-spinel and clinopyroxene in order to document those elements that provide particularly useful discriminants between samples from different P-T conditions, different bulk compositions and parageneses. Few samples show evidence for zonation so the average compositions are shown. A separate section deals with zoned samples.

9.3.1 Garnet - LILE

Large ion lithophile elements in garnet are all in very low concentration. Li concentrations in harzburgitic garnets are 0.03 +/- 0.01 ppm, in lherzolitic garnets the concentration varies from harzburgitic values up to 0.09 ppm. Na contents vary from 100 to 300 ppm with the higher concentrations belonging to lherzolitic garnets (Fig. 9.2). K in garnet is generally sub-ppm concentration but some analyses have several ppm K and appear to be affected by contamination (i.e. the analysis volume is not entirely garnet and may contain small proportions of kimberlitic material (Chapter 3)).

Sr concentrations range from 0.2 to 14 ppm. The majority of garnets have between 1 and 2 ppm Sr and only sample B47, a low-Ca G10 garnet, has a concentration > 5 ppm. This high value is compatible with analyses of diamond inclusion garnets which have high Sr concentrations in studies such as Shimizu and Richardson (1987). Ba concentration is measured as being in parts per billion in all garnets and is often close to the lower limit of detection. Elevated Ba is found in a few analyses due to contamination.

(a) Harzburgitic Garnets

(b) Lherzolitic Garnets

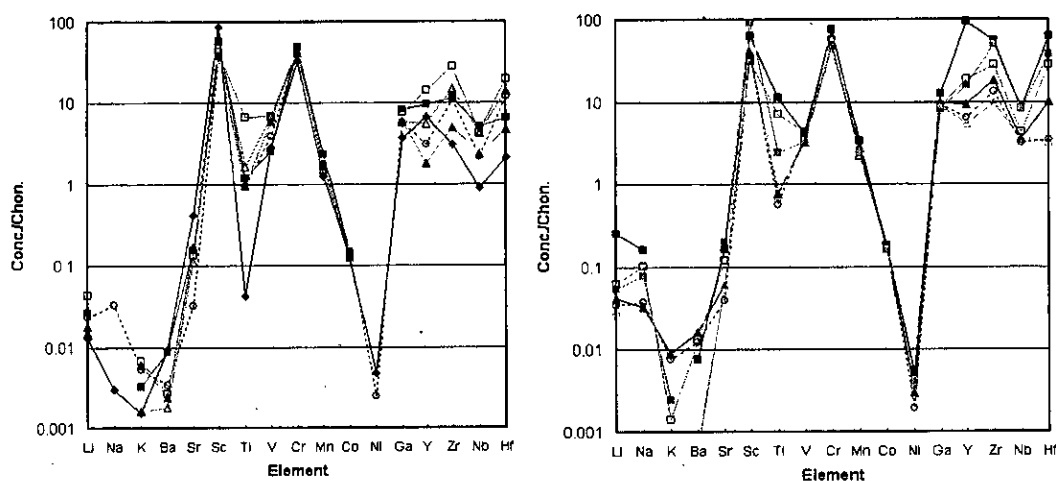


Figure 9.2: Average LILE, FSTE and HFSE compositions for (a) harzburgitic and (b) lherzolitic garnets from selected Newlands and Bobbejaan samples. Symbols are as follows: The harzburgitic samples are BOB404 (filled diamond symbols), NEW021 (open square symbols), BOB113 (open circle symbols with dashed line), NEW288 (open triangle symbols), NEW098 (filled triangle symbols) and NEW074 (filled square symbols). For lherzolites: NEW114 (filled square symbols), NEW063 (open square symbols), NEWSP (open circle symbols with dashed line), BOB402 (open triangle symbols), NEW406 (filled triangle symbols). Ion microprobe counting statistics produce a 2σ standard deviation error which is < size of the symbols used, except Ba and Hf which are approximately twice the height of the symbols used.

9.3.2 Garnet – HFSE and FSTE

The garnets in general have normalised $Zr > Hf > Y > Ti > Nb$ (all > 1 relative to chondrites) where lower values are seen in harzburgitic than lherzolitic garnets (RHS of Fig. 9.2). Zr_{NORM} and Hf_{NORM} are similar in individual samples. Ti is very variable in garnets from both harzburgites and lherzolites; samples exhibiting external zonation are not anomalously high in Ti. In harzburgites it is lowest in the most sub-

calcic garnets and higher in the higher Cr, higher Ca garnets such as NEW288. In lherzolites Ti is higher in garnets that are higher in Cr and Ca, this also corresponds to those samples yielding higher temperature estimates (Chapter 7) such as NEW114 and NEWSP. It is therefore expected that these are the samples with the higher Ni contents.

Within the transition elements, discriminants between the two garnet parageneses are a lower HFSE and transition element content and $Y < Hf$ in harzburgites. Sc contents of all garnets are consistently high at 30-900 times chondrite. Normalised abundances of the FSTE are $Cr > Ga > Mn > Co > Ni$ for all harzburgitic and lherzolitic garnets. Most samples have $Ti_{NORM} < V_{NORM}$; lherzolites that do not obey this relationship are of the high-Cr, high-Ca type and have $Ti_{NORM} > V_{NORM}$.

The samples known to have major element Ca-Ti external zonation (Chapter 5) such as BOB113, show high Na and low Sr and Ni but they are not zoned strongly in these elements. The lherzolitic sample BOB401 has external zonation of the decreasing Ca and decreasing Cr variety and does not show any unique trace element features relative to the other lherzolitic samples of similar major element composition.

9.3.3 Garnet REE compositions

Sample BD1366 is shown in Fig. 9.3 for reference because it has the lowest natural REE content that can be expected in garnet since it is exsolved from a fertile orthopyroxene as described by Dawson (2004). The rim of sample B48 from this study is also shown for reference in Fig. 9.3 because it conforms to a normal garnet REE pattern.

Fig. 9.3a and c show that garnets from harzburgitic samples have predominantly overlapping REE patterns with DIs. Only the higher Cr, higher Ca samples such as NEW288 have higher $HREE_{NORM}$ than the DIs (i.e. low Ce/Yb). The low-Ca garnets form REE profiles that are characterised by relatively high $LREE_{NORM}$ compared to a

normal profile (e.g. B48 in Fig. 9.3a). They also have a higher Ce/Yb than the normal profile. Between Pr and Sm a peak is formed and the $MREE_{NORM}$ exhibit a negative slope. Nd_{NORM}/Sm_{NORM} is always > 1 . Sm_{NORM}/Dy_{NORM} is also > 1 with the exact ratio of the latter indicating the magnitude of the hump present. The $HREE_{NORM}$ usually show an incrementally increasing trend and Dy_{NORM}/Yb_{NORM} is usually < 1 . The bulk LREE variation amongst harzburgitic garnets is < 1 order of magnitude but the bulk HREE variation is $\gg 1$ order of magnitude but < 2 . As the garnets become more Ca- and Cr-rich, the pattern becomes more like those of the lherzolitic garnets.

The most Ca-depleted harzburgitic garnets have higher LREE concentrations. NEW024 and BOB47 have the most pronounced peaks where $Sm_{NORM}/Dy_{NORM} \gg 1$ (similar to those shown in the Finsch DIs) with the peak over Pr rather than between Nd and Sm. These two profiles possess the most depleted MREE patterns of all the samples. The garnet in B47 shows MREE and HREE concentrations that are very similar to the depleted profile of BD1344, differing only in possessing a positive bulge in the LREE.

The humped curve shown in many of the lherzolitic garnets in this study (Fig. 9.3b and d) is also characterised by high $LREE_{NORM}$ (although this is not as high as the harzburgitic garnets). The profiles do not overlap with so consistently with the lherzolitic DIs although the profile for BOB402 is similar. The main difference is that the MREE and HREE are at higher concentrations than in the DIs and that Sm_{NORM}/Dy_{NORM} is more commonly < 1 . The MREE-HREE trends are highly variable; they vary from those seen in harzburgites where Dy_{NORM}/Yb_{NORM} is < 1 to trends where Dy_{NORM}/Yb_{NORM} is > 1 . The variation in bulk REE concentration is approximately one order of magnitude but again the HREE have a larger range. Low-Ca, low-Cr lherzolitic garnets tend to have the lower bulk REE concentrations, whereas higher-Ca, higher-Cr ones are progressively richer in REE. NEW114 has a

unique pattern that is extremely MREE enriched, forming a hump at Ho-Er at > 100 times chondrite.

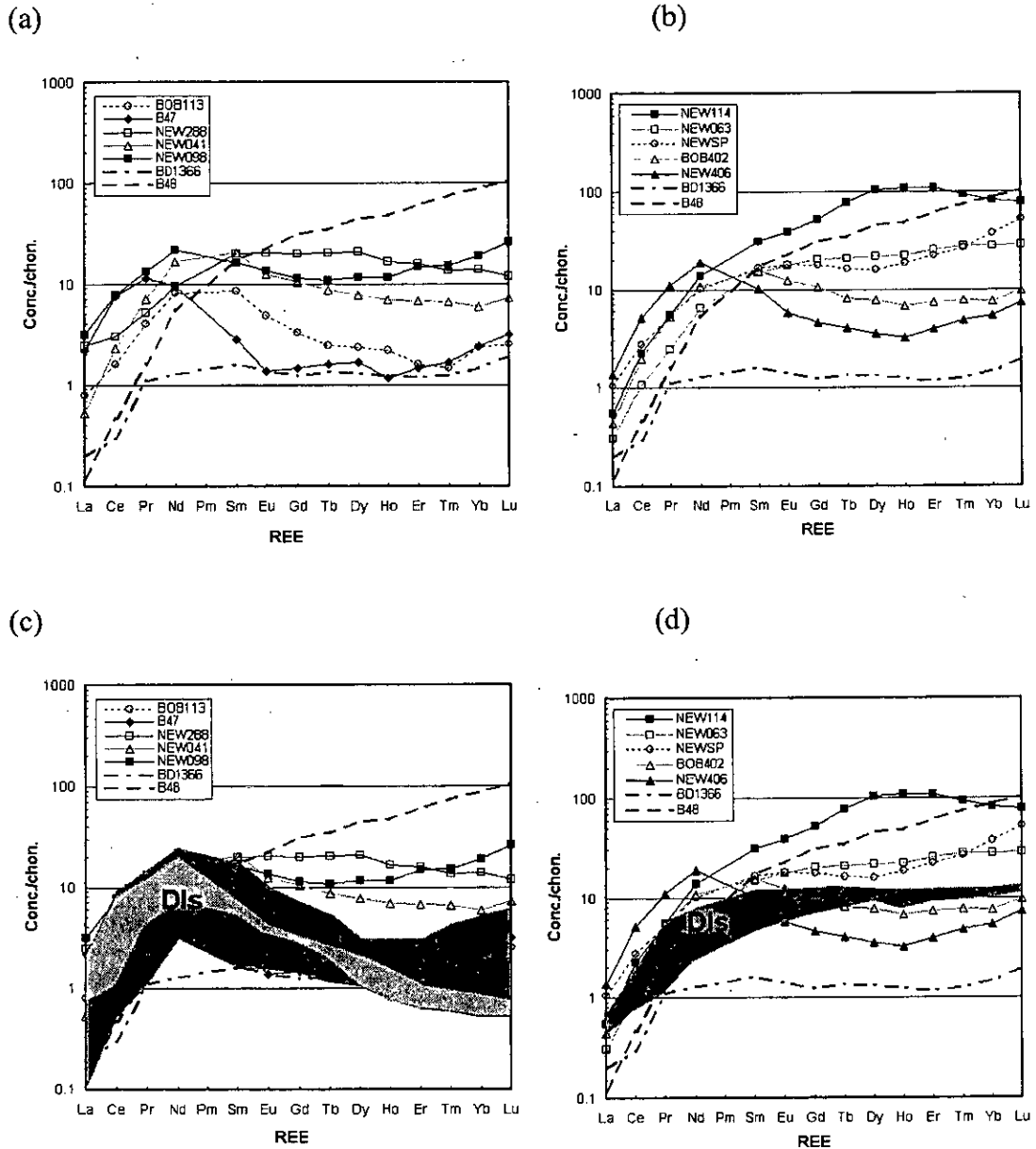


Figure 9.3: Chondrite normalised garnet REE plots for harzburgitic samples (a) and lherzolithic samples (b); (c) and (d) as for (a) and (b) respectively but with the garnet diamond inclusion field (DIs) indicated for Ghana diamonds in dark grey (data range from Stachel and Harris, 1997). The narrower range in compositions of Finsch diamond inclusions as shown in light grey (Shimizu and Richardson, 1987). Dash-dot bold line is the primitive garnet of Dawson (2004) and the dashed bold line is the profile of B48 that is most like the 'normal' profiles of megacryst garnets. Counting errors for the ion microprobe have 2σ errors smaller than the symbols used in this figure.

9.3.4 Garnet trace element zonation

Five samples with well developed external major element zonation patterns (Chapter 5) were analysed for trace elements: NEW074, BOB113, BOB401, NEW101 and B48. Of these only B48 is strongly zoned in terms of REE (Fig. 9.4a) and BOB113 has a variation in REE that does not correspond to the major element zonation pattern (Fig. 9.4b). In Chapter 5 NEW074 and BOB113 are identified as having E_{Ca} zonation i.e. an increase in Ca (\pm Ti) towards their rims but they do not show clear core-rim trends in trace elements.

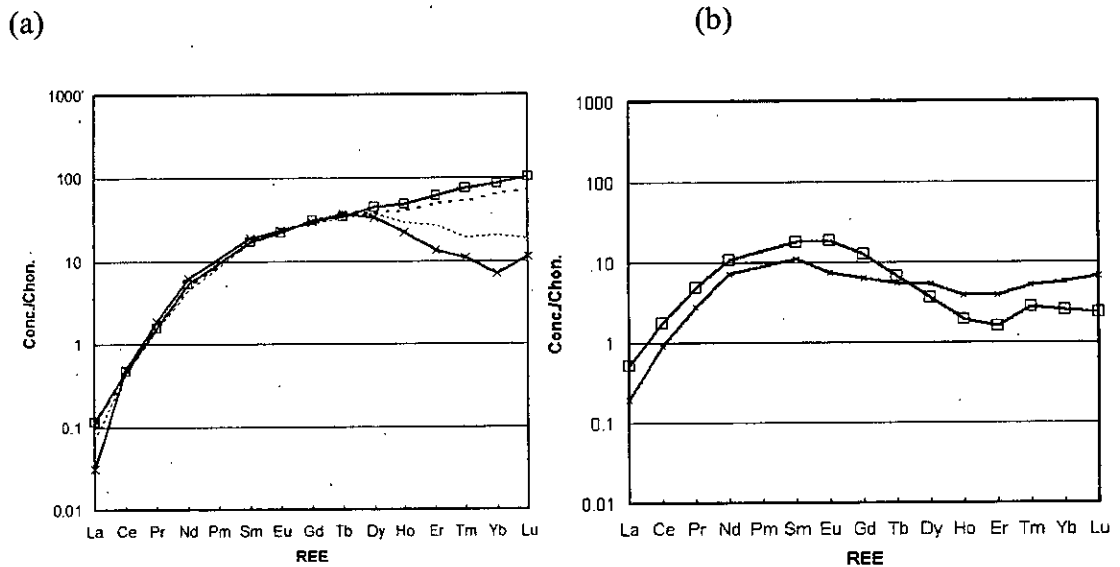


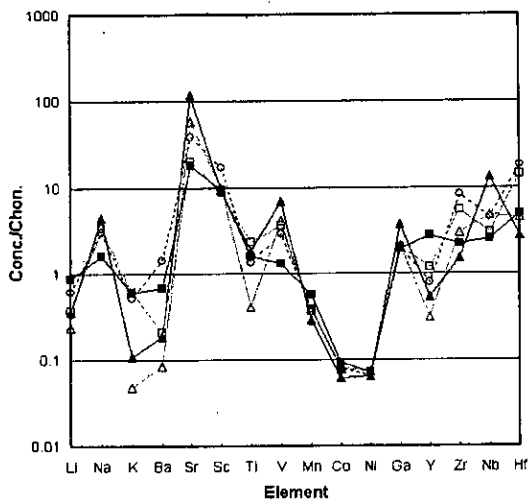
Figure 9.4: (a) REE zonation in garnet from sample B48. Core composition is the solid line with cross symbols. The rim is the solid line with square symbols and the dashed lines are for intermediate locations between core and rim. (b) REE zonation in garnet from BOB113 where the sample contains slight variations in REE patterns that do not correspond to the major element zonation pattern. The two analyses shown indicate the extent of the variation present in BOB113.

The zonation of Ni was observed in B48 alone where the core has 21 ppm and the rim has 25 ppm, which is equivalent to a change of approximately + 30-40°C at the rim compared to the core. BOB113 and NEW074 have increasing Ti towards their rims as measured by electron microprobe with a higher spatial coverage than on ion microprobe (see Chapter 5 for descriptions and Appendix II for the profiles themselves).

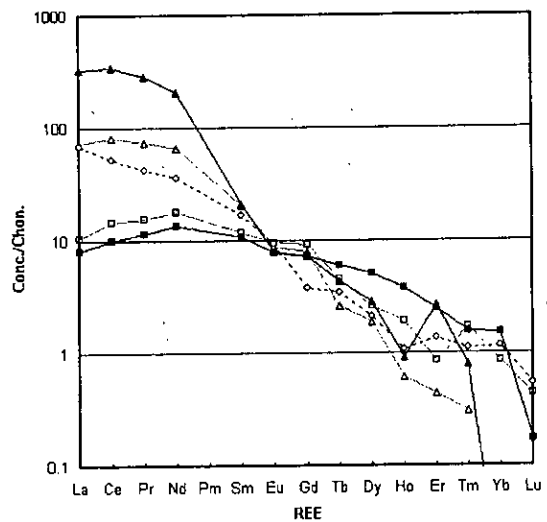
9.3.5 Clinopyroxene trace element compositions

The LHS of Fig. 9.5 (a) shows the concentration of the LIL elements in clinopyroxenes from this study. Li has ppm to sub-ppm values. Na varies from 10000-20000 ppm and K from 100-350 ppm. These values result in Na_{NORM} being > 1 with Li_{NORM} and K_{NORM} averaging 0.5. Ba_{NORM} , like K_{NORM} , is low whereas Sr is particularly high, with its highest values (> 100 times chondrite) being in the clinopyroxenes coexisting with lower-Cr, lower-Ca garnets. There is a decreasing trend through the FSTE from Sc to Ni. V is high in those clinopyroxenes with higher Sr and these tend to be the ones coexisting with lower-Cr, lower-Ca garnets. Ti seems to be variable independently of other elements. Co and Mn are slightly higher in the clinopyroxenes from the high Cr, high Ca samples. The $HFSE_{NORM}$ generally increase from Y to Hf (Fig. 9.5a). High-Cr, high-Ca samples tend to have higher Y and lower Zr, Nb and Hf than the other samples.

(a)



(b)



(c)

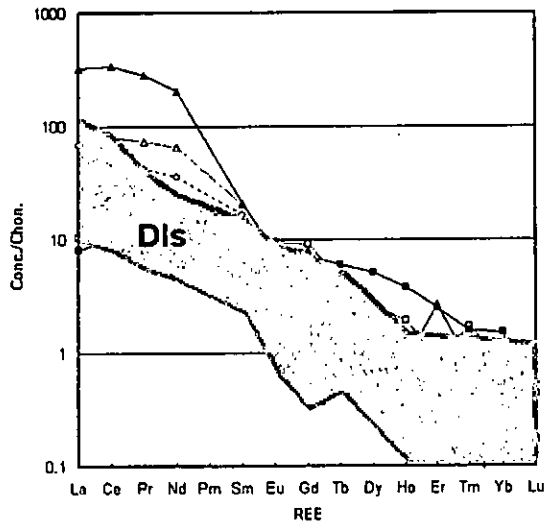


Figure 9.5: Selected clinopyroxene trace element profiles from Newlands and Bobbejaan samples. (a) LILE, FSTE and HFSE (b) REE. (c) as for (b) but with the field for diamond inclusions (DIs) shown in grey from Stachel and Harris (1997). The clinopyroxenes coexisting with the low-Cr, low-Ca garnets are shown with triangle symbols (filled triangle symbols are for NEW406 and open triangle symbols are for BOB402). The clinopyroxenes coexisting with the high-Cr, high-Ca garnets are shown with square symbols (filled square symbols are for NEW114 and open square symbols are for NEW063). Dashed line is clinopyroxene from NEWSP, which has a different LREE pattern to the other clinopyroxenes. The 2σ errors are less than the size of the symbols for La-Ho. Elements Er-Yb have progressively larger errors in clinopyroxenes with lower REE concentrations e.g. NEW406.

The REE_{NORM} (Fig. 9.5b) $La < Ce < Pr < Nd$ form a shallow positive slope for clinopyroxenes coexisting with high-Ca, high-Cr garnets, whereas the clinopyroxenes coexisting with lower Ca, lower Cr garnets have a shallow negative slope for these elements. The former have clinopyroxene $LREE_{NORM}$ as low as 10 and the latter may have values > 200 as seen in NEW406. Nd_{NORM} / Sm_{NORM} is always > 1 . Sm to Lu forms a negative slope down from ~ 10 to ~ 1 times chondrite at Lu. Tm, Yb and Lu are often near detection limit concentrations and produce scatter on the normalised plot except in the high-Cr, high-Ca garnet samples where $HREE_{NORM}$ is usually $\lesssim 1$. Higher degrees of LREE depletion are also expressed by lower Sr and $Sr > La$. NEW114 is exceptionally Cr- and Ca-rich and has a much less LREE-enriched, HREE-depleted pattern compared to common mantle clinopyroxenes. It is as though the more normal clinopyroxene REE patterns are rotated anticlockwise about Eu in order to generate this HREE-enriched pattern.

9.3.6 Clinopyroxene/garnet trace element partitioning

Fig. 9.6 shows the values for clinopyroxene/garnet trace element distribution coefficients (i.e. ppm concentration in clinopyroxene divided by ppm concentration in garnet, shorthand: ' $D^{cpx/grt}$ '). Low $D^{cpx/grt}$ values for lherzolitic samples with high-Cr high-Ca garnets show that REE, Sc, Ti and Nb partition more strongly into these garnets than into garnets of average lherzolitic compositions.

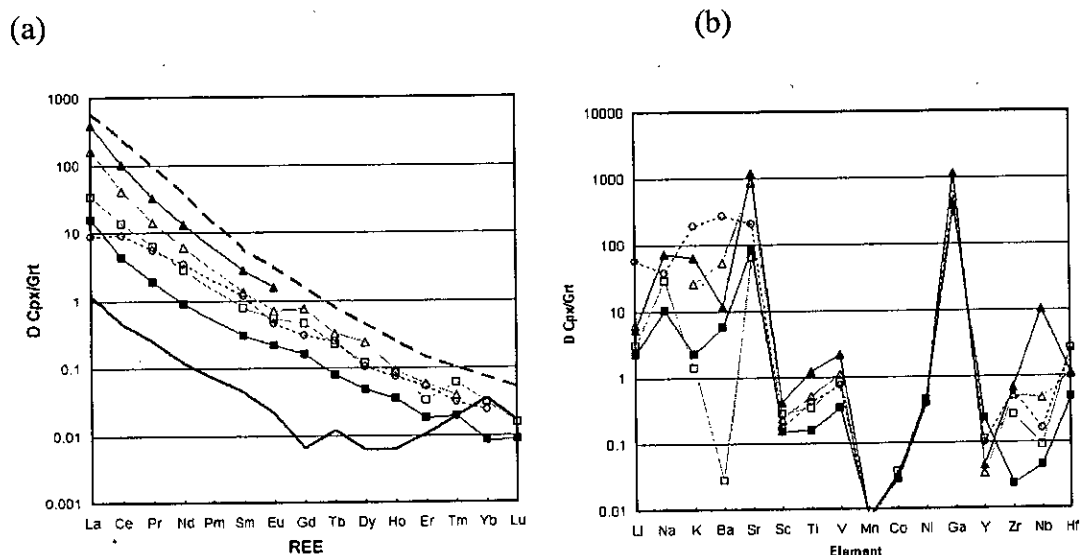


Figure 9.6: Clinopyroxene/garnet distribution ($D^{cpx/grt}$) coefficients for the samples in Fig 9.5 (symbols the same). (a) REE with solid line being $D^{cpx/grt}$ for the high-Ca garnet eclogite HRV277 and the dashed line being $D^{cpx/grt}$ for the low-Ca garnet eclogite JIG312 from Harte and Kirkley (1997). (b) LILE, FSTE and HFSE. Symbols as for Fig. 9.2b.

Fig. 9.6 (a) shows that the higher Ca the garnet in Newlands and Bobbejaan samples, the lower the $D^{cpx/grt}$ value (clinopyroxene/garnet distribution coefficient) for the REE. The values shown are bracketed by the eclogitic samples with garnets that are highly calcic (solid line) and highly sub-calcic (dashed line) from the calculations of Harte and Kirkley (1997). NEW406 has a slight disruption (not shown for clarity) of the straight to slightly concave profiles shown, which is due to clinopyroxene measurements that are approaching the detection limit for the ion microprobe in the HREE.

Fig. 9.6b shows how LILE strongly partitions into coexisting clinopyroxene in all samples. Through the FSTE, Sc, Ti, V and Ga are increasingly favoured by clinopyroxene, however those coexisting with lower Cr, lower Ca garnets have the highest $D^{\text{cpx/grt}}$ for these elements. Mn, Co and Ni partition into garnet more strongly than into clinopyroxene. In the HFSE from Zr to Nb to Hf, there is a general increasing favour towards clinopyroxene again with the high-Cr, high-Ca garnets containing more HFSE concentrations compared to their coexisting clinopyroxene.

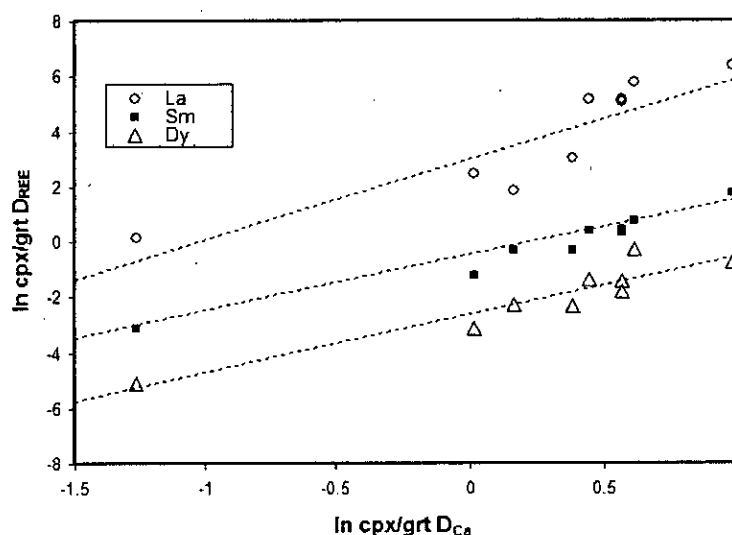


Figure 9.7: $\ln \text{cpx/grt } D_{\text{REE}}$, for La, Sm and Dy plotted against $\ln \text{cpx/grt } D_{\text{Ca}}$. Samples (from Fig. 9.5b) plot from 0 to 0.7 $\ln \text{cpx/grt } D_{\text{Ca}}$. The high-Ca sample HRV177 from Fig 9.6a plots at most negative $\ln \text{cpx/grt } D_{\text{Ca}}$ and the low-Ca sample JJG312 plots at most positive $\ln \text{cpx/grt } D_{\text{Ca}}$. Numerical parameters for the regression lines are taken from Harte and Kirkley (1997).

Fig 9.7 shows that the samples' La, Sm and Dy partitioning values fit the $1100^{\circ}\text{C} \pm 100^{\circ}\text{C}$ data from Harte and Kirkley (1997). This is indicative of the REE substituting in the Ca sites in both clinopyroxene and garnet and good evidence that this process occurs in peridotites as well as the previously studied eclogites (see also effect of $X_{\text{Grossular}}$ in van Westeren et al., 2001).

9.3.7 Spinel – FSTE and HFSE

Fig. 9.8 shows FSTE for spinels from harzburgitic (a) and lherzolititic (b) samples. The FSTE are similar in lherzolititic and harzburgitic samples although harzburgitic spinels have a wider range of Ti concentrations. The highly sub-calcic sample

BOB404 has the spinel with the lowest Ti, Ga, Y, Zr and Nb of all the samples analysed. In the HFSE the harzburgitic spinels have a wider range of Y, Zr and Nb than lherzolitic samples with consistently increasing concentrations with atomic number. The spinels have been analysed for REE and their contents were found to be sub-ppm using SOL-ICP-MS. It was not possible to accurately analyse Zn and Cu on the ion microprobe due to interferences at high energy offset with standard mass resolution.

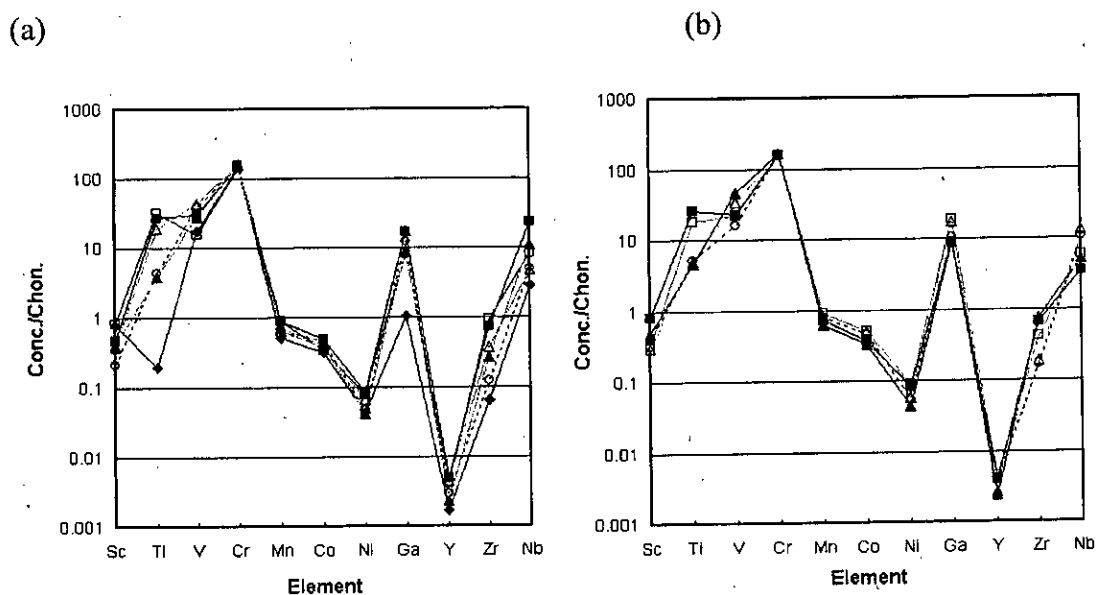


Figure 9.8: (a) FSTE and HFSE for harzburgitic spinels. (b) as for (a) but for lherzolitic spinels. Samples and symbols as for Fig. 9.2a and b. 2σ ion microprobe counting errors are less than the size of the symbols used except for Y which is approximately twice as large as the spread of data shown for these elements.

9.3.8 Spinel/garnet & spinel/clinopyroxene trace element partitioning

Fig 9.9(a) shows the distribution of elements between spinel and coexisting garnet in harzburgitic samples. The FSTE (except for Sc and Mn) partition between 1 and 20 times more strongly into spinel, whereas the HFSE (except Nb) partition favourably into garnet. This is also true in lherzolitic spinels (Fig. 9.9b) but $V/(Cr+Ti)$ is higher and Zr and Nb are on average higher in lherzolitic spinels. There is a larger range of $D^{sp/grt}$ values in lherzolitic samples for HFSE.

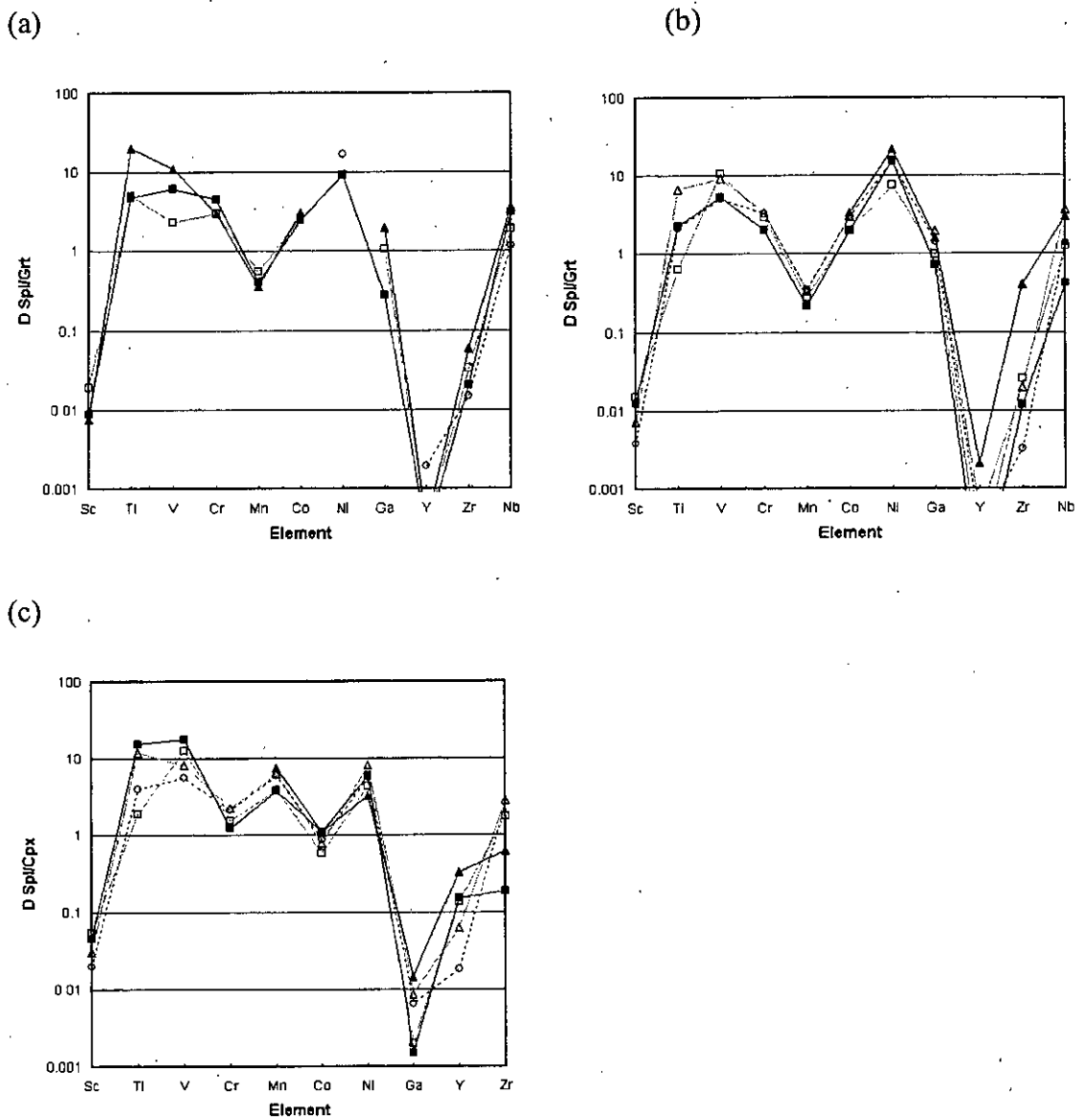


Figure 9.9: Harzburgitic spinel/garnet distribution coefficients in selected samples. (b) as for (a) but for Iherzolithic samples with symbols as for Fig. 9.2 a and b. (c) distributions of FSSTe and HFSE between spinel and clinopyroxene (symbols as for Fig. 9.2b).

Fig. 9.9(c) shows that partitioning of FSSTe, Y and Nb between spinel and clinopyroxene is very similar to that between spinel and garnet with the same trends evident. The only notable difference is that Cr and Mn are higher and Co is lower in spinel/cpx compared to spinel/garnet.

9.3.9 Divariant plots

The plots in this section are included in order to show the correlation between various trace elements in minerals. Although this data is presented in the previous section it is a useful way of presenting potential trace element discriminants between the different parageneses present in the samples. 1σ counting errors are smaller than the symbols used in the following figures unless otherwise stated. See Appendix I.3 for more details on errors.

Selected element pairs from LILE, FSTE and HFSE are plotted against each other here for garnet, clinopyroxene and Cr-spinel (Cr-spinel LILE concentrations are all at the detection limit and, hence, not shown). The symbols are divided into four populations, two lherzolitic and two harzburgitic. Lherzolites with high Cr, high Ca garnets are plotted as filled grey triangle symbols with the lower Cr and Ca ones (i.e. those similar to common mantle lherzolitic bulk compositions) as open triangle symbols. The harzburgites with low-Ca garnets are plotted as filled black square symbols and the higher-Ca ones as open square symbols. The plots are in ppm concentrations, only the Zr vs. Ti plot has logarithmic axes to conform to the 'metasomatism plot' of Griffin et al. (1999b).

9.3.9.1 LILE

Fig. 9.10a shows that a broadly positive correlation between Na and Li exists for the samples as a whole. The high-Cr lherzolitic garnets have the highest Na and Li concentrations with lower concentrations found successively in the 'normal' lherzolites, 'normal' harzburgites and are lowest in the low-Ca harzburgites. Clinopyroxene Na vs. Li concentrations do not differentiate the high and lower Cr lherzolitic samples (Fig. 9.10b).

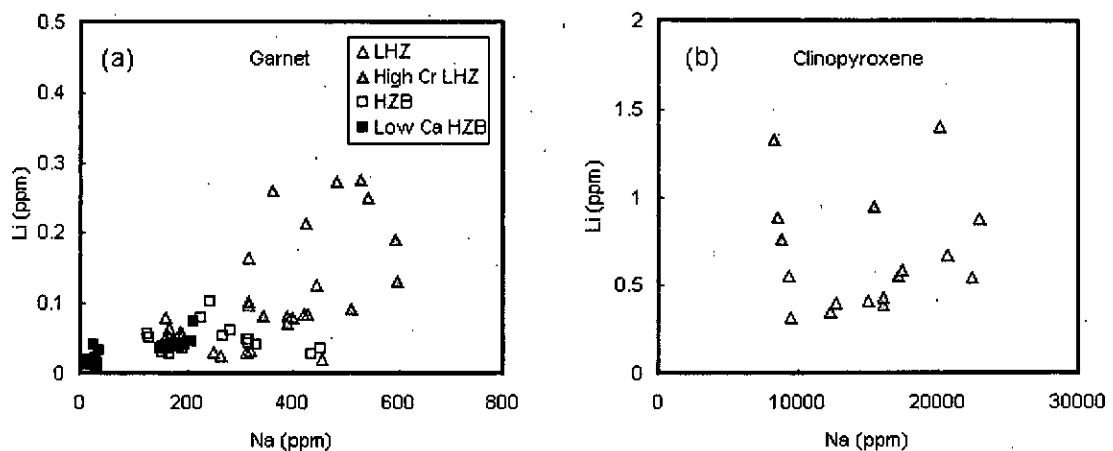


Figure 9.10: (a) Na vs. Li for garnets from harzburgitic (square symbols) and lherzolitc (triangle symbols) suites. The lherzolitc samples are divided into high-Cr ('high Cr LHZ', filled grey triangle symbols) and lower Cr lower Ca ('LHZ' open triangle symbols). The harzburgitic samples are divided into the low Ca harzburgites ('low Ca HZB', filled black square symbols) and higher Ca ones ('HZB' open square symbols). (b) Na vs. Li for clinopyroxene (symbols as for (a)).

Fig. 9.11a shows the a similar distinction between samples as with Na (Fig. 9.10a) but the K variation is more random, which is indicative of minor contamination in the analyses. However, in general the higher K garnets do tend to belong to the lherzolitc suites. Fig. 9.11b shows that clinopyroxenes from the high Cr lherzolitc samples are best separated by their K being > 200ppm. Fig. 9.11c and d show a positive correlation between Sr and La for both garnets and clinopyroxenes. The only distinction between samples is the particularly shallow trend of the low-Ca harzburgitic garnets which vary from low Sr and La towards higher La but they may have significantly higher Sr contents of up to 15 ppm.

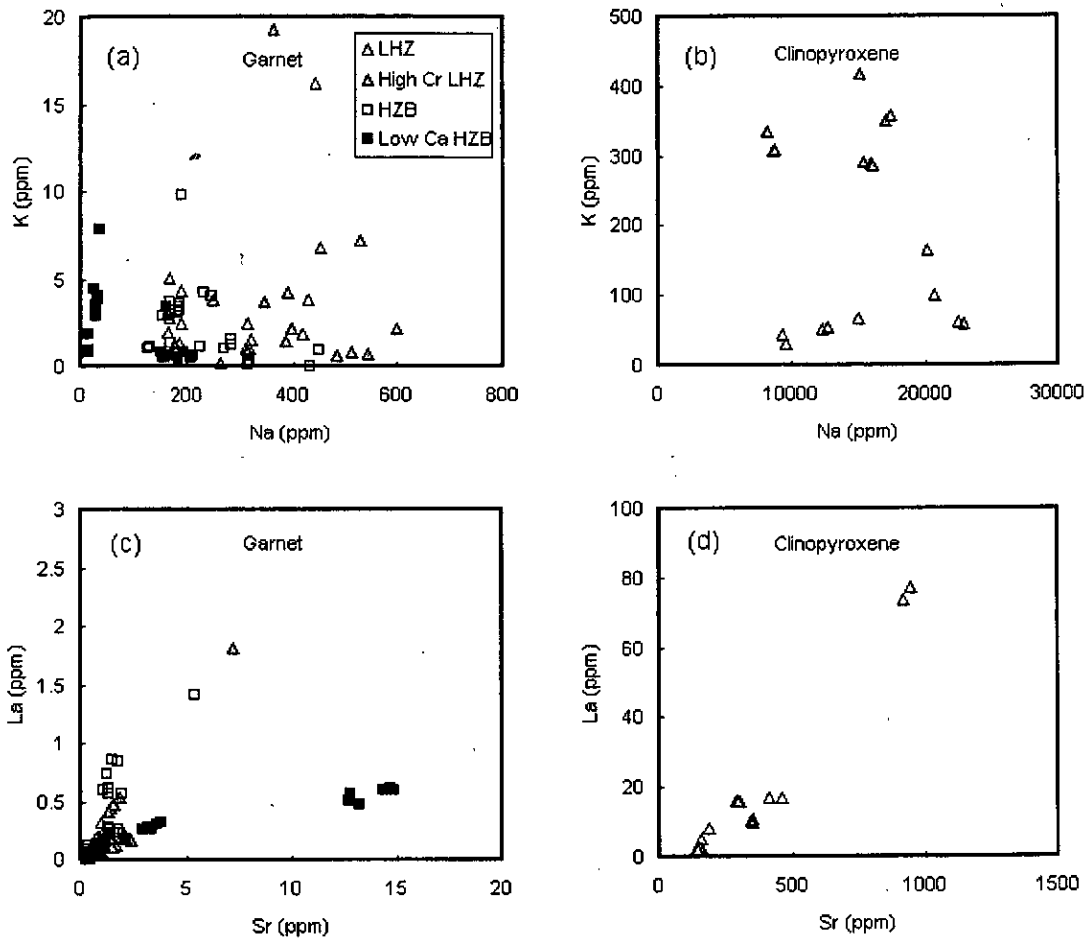


Figure 9.11: (a) Na vs. K for garnets, (b) Na vs. K for clinopyroxenes, (c) Sr vs. La for garnets, (d) Sr vs. La for clinopyroxenes. Symbols as for Fig. 9.10.

Fig. 9.12a shows that the low-Ca garnets are differentiated by both relatively high Sr (most are > 3 ppm) and low Na contents (< 200 ppm). The high-Cr lherzolitic garnets plot to high Na (> 300 ppm) and low Sr (most are < 3 ppm). Clinopyroxenes do not form any trends of note, probably due to the small number of data points (Fig. 9.12b). Fig. 9.12c shows that Ba does not discriminate the suites of garnets, however high Ba/Sr in clinopyroxenes is indicative of the high-Cr lherzolite suite and high Sr/Ba is indicative of the lower Cr lherzolites (Fig. 9.12d).

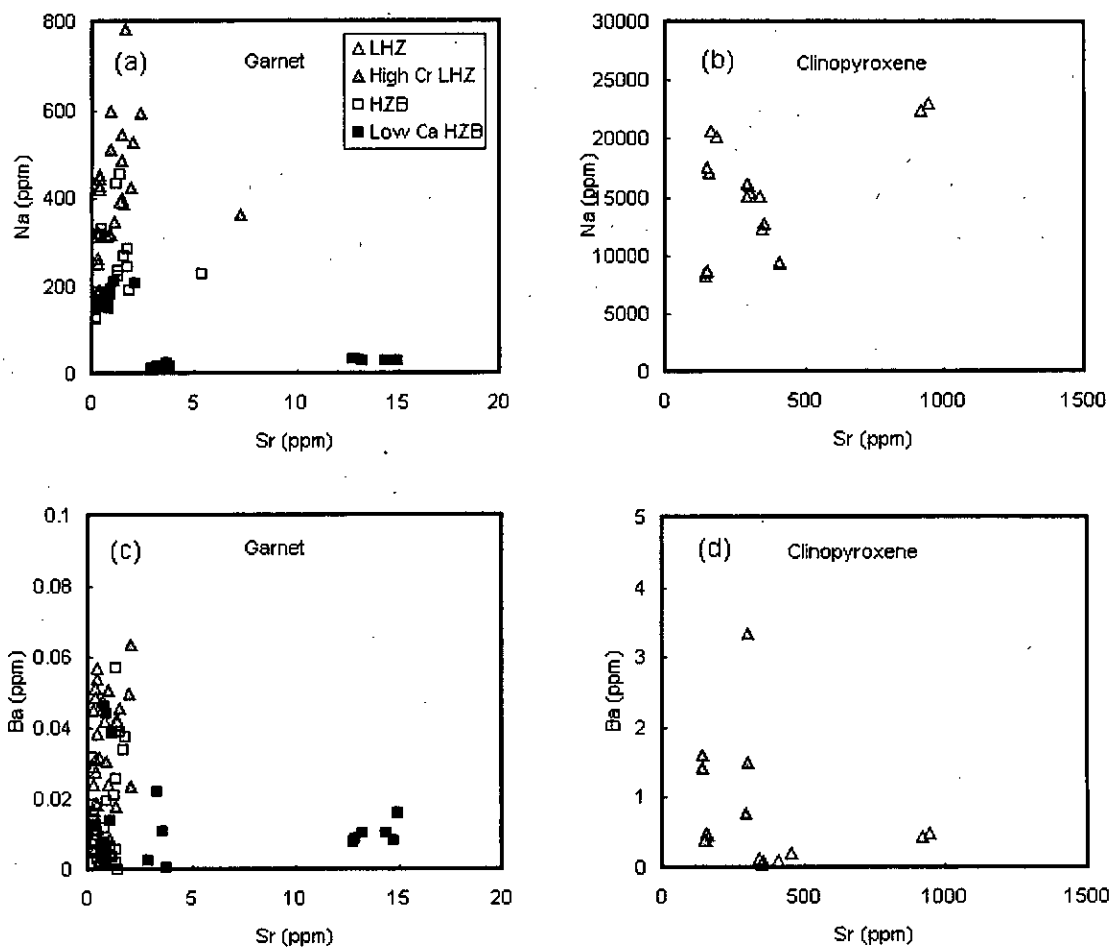


Figure 9.12: (a) Sr vs. Na for garnets, (b) Sr vs. Na for clinopyroxenes, (c) Sr vs. Ba for garnets, (d) Sr vs. Ba for clinopyroxenes. Symbols as for Fig. 9.10

9.3.9.2 HFSE

On Zr vs. Ti plots (Fig. 9.13a-c) both garnets and Cr-spinels form positive correlations with high-Cr lherzolitic samples plotting at the highest values, lower Cr lherzolites, harzburgites and low-Ca harzburgites are successively lower in both Ti and Zr. Clinopyroxenes are not distinguished clearly on the Zr vs. Ti plot. The garnet trend is coincident with the 'phlogopite metasomatism' trend of Griffin et al. (1999b) but no phlogopite is noted in these samples. Similarly on the Zr vs. Y plots (Fig. 9.13d-f) the garnets form a positive correlation with the highest Zr and Y belonging to the high-Cr lherzolite suite and successively lower Zr and Y to the lower Cr lherzolites, harzburgites and the lowest concentration in the low-Ca harzburgites. Cr-

spinel does not contain significant Y and clinopyroxenes are not separated by a Zr vs. Y plot. Fig. 9.13g-i shows Zr vs. Nb plots where a positive correlation exists for garnets and that again clinopyroxenes from the two lherzolitic suites are not distinguished. However the Cr-spinels from the lower Cr lherzolites are highest in Nb.

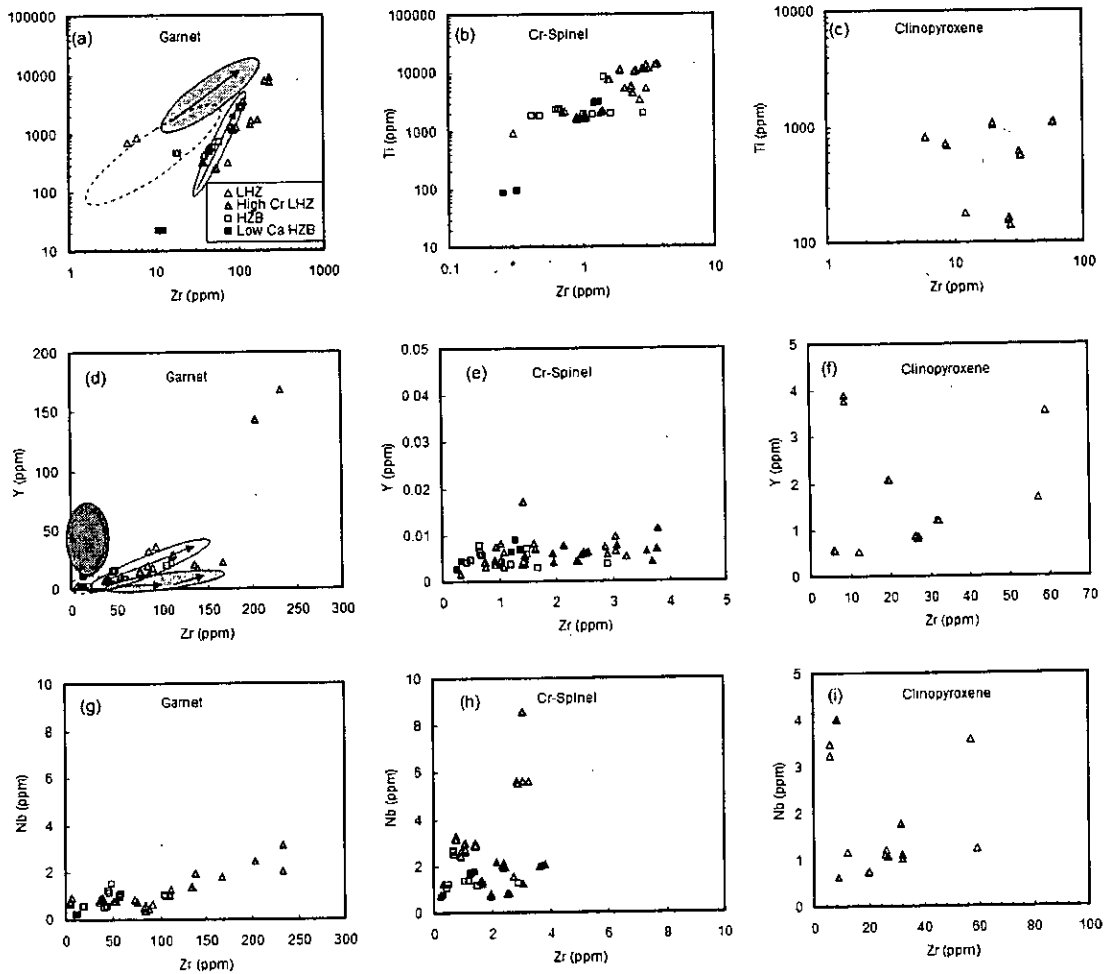


Figure 9.13: (a) Zr vs. Ti for garnets fields from Griffin et al. (1999b) with 'phlogopite metasomatism' as a filled light grey oval, 'melt metasomatism' as an unfilled oval and the 'depleted field' as a dashed-line oval shape. Arrows indicate garnet core to rim zonation trajectory. (b) Zr vs. Ti for Cr-spinels. (c) Zr vs. Ti for clinopyroxenes. (d) Zr vs. Y for garnets with the same fields as for (a) with the addition of an 'undepleted field' as a dark grey filled oval shape. (e) Zr vs. Y for Cr-spinels. (f) Zr vs. Y for clinopyroxenes. (g) Zr vs. Nb for garnets. (h) Zr vs. Nb for Cr-spinels, (i) Zr vs. Nb for clinopyroxenes. Symbols as for Fig. 9.9.

9.3.9.3 FSTE

Fig. 9.14a indicates that the high-Cr lherzolitic garnets are high in Ni and Ga, whereas the harzburgitic suites, especially, are low in Ga. A positive correlation between these two elements exists in Cr-spinel (Fig. 9.14b) with both lherzolitic suites being high in Ga and Ni. Cr-spinels from the low-Ca harzburgitic suite are especially low in Ga. High-Cr lherzolites are distinguished from lower-Cr lherzolites by their Cr-spinels and clinopyroxenes having lower Ga. Broadly positive correlations are seen between Ni and Ti for garnet and Cr-spinel and no correlation is apparent with clinopyroxenes (Fig. 9.14d-f). High-Cr lherzolitic garnets and Cr-spinels have higher Ti and Ni with the low-Ca harzburgites plotting at very low Ti and low Ni. Sc and V do not appear to discriminate the suites of samples in either mineral (Fig. 9.14g-i).

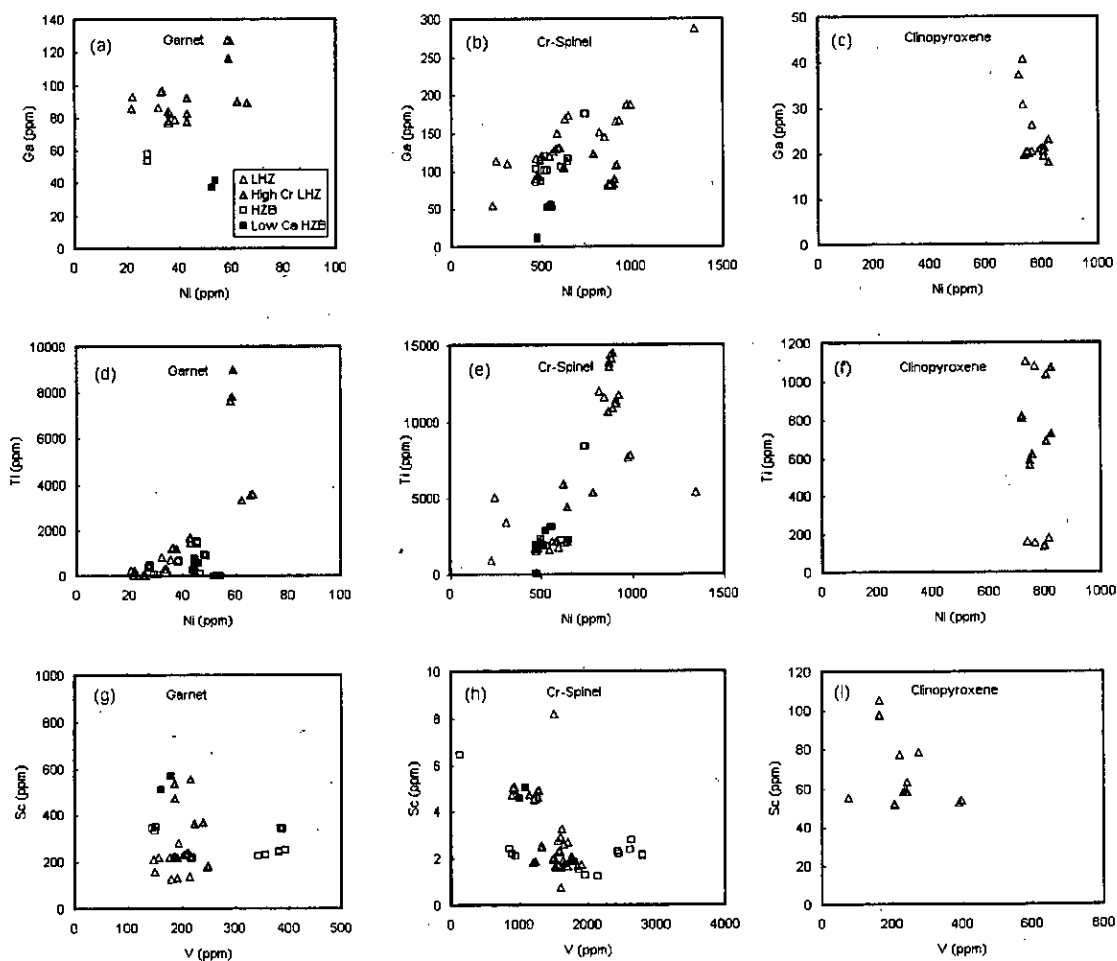


Figure 9.14: (a) Ni vs. Ga for garnets, (b) Ni vs. Ga for Cr-spinels, (c) Ni vs. Ga for clinopyroxenes, (d) Ni vs. Ti for garnets, (e) Ni vs. Ti for Cr-spinels, (f) Ni vs. Ti for clinopyroxenes, (g) V vs. Sc for garnets, (h) V vs. Sc for Cr-spinels, (i) V vs. Sc for clinopyroxenes. Symbols as for Fig. 9.9.

9.4 Summary

Trace element analysis of the Newlands and Bobbejaan samples has defined the range of trace element characteristics for a wide range of bulk rock compositions especially evident in garnet Cr-Ca space (Chapter 5). HFSE and FSTE were analysed in garnet, clinopyroxene and Cr-spinel and REE and LILE were analysed in garnet and clinopyroxene as well. The main discriminants (excluding REE) discovered between parageneses are as follows:

1. Garnets from the harzburgitic suite are distinctly higher on average in Sr and V but lower in Li, Na, Ba, Mn, Co and Ga.
2. Clinopyroxenes from the low-Cr, low-Ca lherzolitic samples are lower in LILE and HFSE compared to the high-Cr, high-Ca lherzolites. They are also higher in V and Sr.
3. Spinels from the harzburgitic suite tend to have a larger range of Ti, Ga, Y, Zr and Nb compositions than the lherzolitic suite but the majority of the transition elements are similar in both.

Focusing on the REE, a wide range of observations have been made. The patterns for garnet and clinopyroxene are shown in summary on Fig. 9.15, which shows selected garnet REE profiles for garnets of different Cr and Ca compositions. For the REE the emergent points from earlier in the chapter and from looking at Fig. 9.15 are:

1. Harzburgitic garnets generally have pronounced humps in the LREE (i.e. high Sm/Dy) that become broad at higher Ca. The profiles with pronounced humps overlap strongly with REE compositions from peridotitic diamond inclusion garnets.
2. The lherzolitic profiles tend to have a less pronounced hump (i.e. Sm/Dy is smaller) and higher HREE concentrations (i.e. Ce/Yb is lower) compared to

harzburgitic garnets. These partially overlap with REE compositions from peridotitic diamond inclusion garnets.

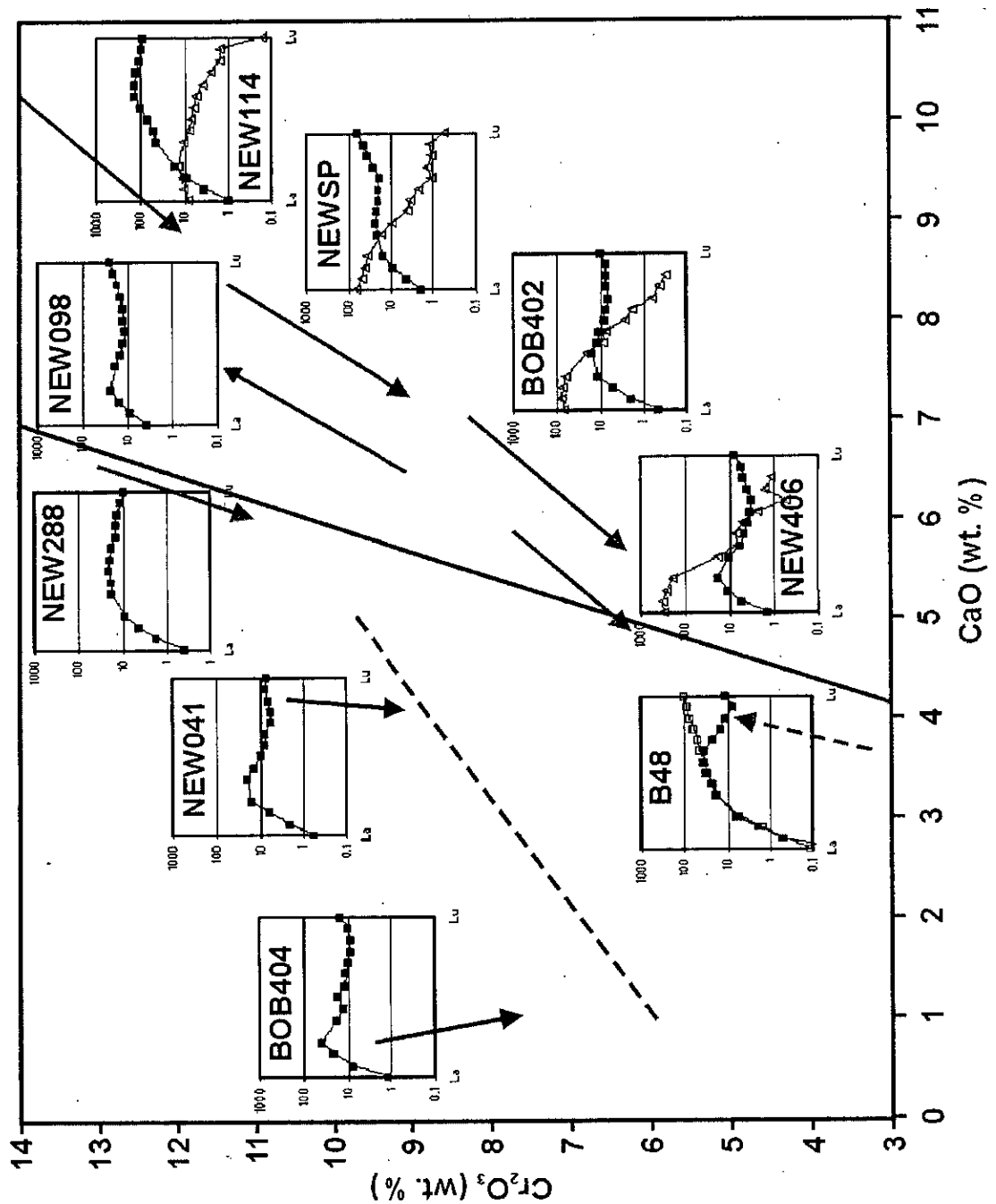


Figure 9.15: REE profiles for garnets and clinopyroxenes (triangle symbols) compared to their garnet Cr_2O_3 -CaO wt. % compositions. Arrows from Chapter 5 showing the zonation trends. Dashed arrow is the 'metasomatically zoned' B48 trend. Dashed line is the diamond-graphite constraint and the solid line is the lherzolite line (see Chapter 4).

3. Only the rim of zoned sample B48 has what could be described as a 'normal' profile. The core of this garnet has a REE profile that resembles the shape of BOB401 in Fig. 9.16.
4. Garnet and clinopyroxene REE profiles form a continuum of compositions whose apparent 'end members' are summarised in Fig. 9.16 for garnets and defined in Table 9.2.
5. The low-Cr lherzolites tend to possess highly fractionated clinopyroxene REE patterns (i.e. very high LREE and very low HREE) with coexisting garnets possessing relatively flat profiles. Whereas the high-Cr lherzolites tend to have lower LREE and higher HREE with coexisting garnets having extremely high HREE concentrations (see Fig. 9.15)
6. Clinopyroxene/garnet partitioning of REE in lherzolitic samples indicate a clear cpx/grt D_{Ca} dependency that conforms to a temperature of $1100^{\circ}\text{C} \pm 100^{\circ}\text{C}$ according to Harte and Kirkley (1997).

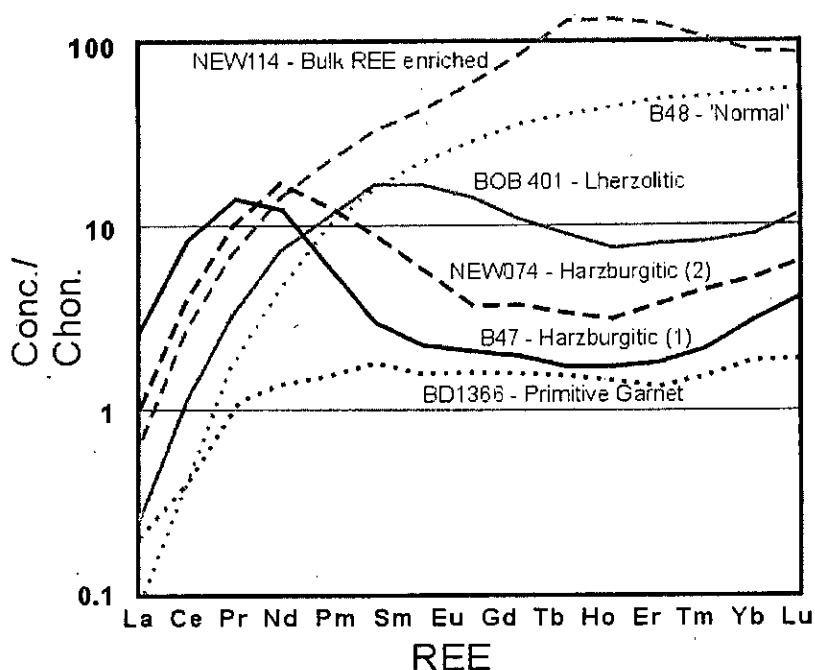


Figure 9.16: Summary of the different types of REE profiles obtained for garnets in this study with particular samples illustrating the range of profile shapes present. BD1366 is shown for comparison Dawson (2004).

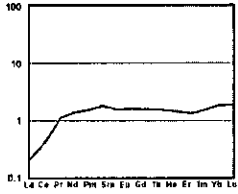
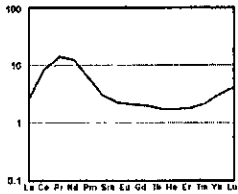
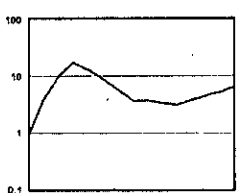
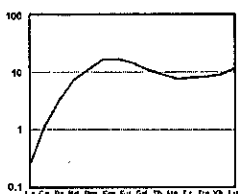
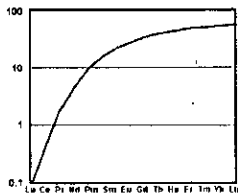
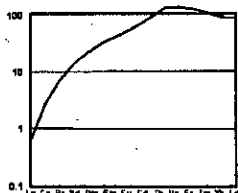
TYPE (example) (cpx present) (REE peak) (setting)	Chondrite normalised plot for type examples of Garnet REE profiles	LREE Bias (Nd/Sm)	LREE Hump magnitude (Sm/Dy)	LREE/ HREE- enrichment (Ce/Yb)	MREE/ HREE (Dy/Yb)
PRIMITIVE (BD1366) (CPX) (Yb) (Exsolved from opx)		>1	~1 Not present	No (<1)	~1
HUMPED (B47) (NO CPX) (Pr) (P-type DIs, rare in kimb conc.)		>1	>>1 Very high	Yes (>1)	<1
TRANSITION- AL (NEW074) (NO CPX) (Nd) (P-type DIs, rare in kimb conc.)		>1	>>1 Very high	Yes (>1)	<1
LHERZO- LITIC (BOB401) (CPX) (Sm-Eu) (P-type DIs, rare in kimb conc.)		<1	>1 Low	Yes (~1)	~1
NORMAL (B48) (CPX) (Lu) (common in kimb conc.)		<1	<1 Not present	No (<<1)	<1
REE- Enriched (NEW114) (CPX) (Ho) (rare in kimb conc.)		<1	<<1 Not present	No <<1	>1

Table 9.1: REE profile classification scheme with key features of the REE concentrations indicated for each profile type.

9.5 Discussion

In this section the implications of the trace element compositions of minerals from each of the parageneses are considered. The trace element patterns observed are compared to existing ideas on mantle processes from the literature based on analyses from other xenoliths, kimberlite concentrate and diamond inclusions. Some experimental data is also available on trace element behaviour at high P and T and will be taken into account. Particular attention is given to theories for the generation of garnet REE profiles.

In terms of the analyses of trace elements in Newlands and Bobbejaan samples, there are several matters that need explanation given the summary of the results (last section) and observations in the literature:

1. Why do harzburgitic garnets have a humped REE pattern, and why do lherzolitic garnets have a broader humped REE pattern given that most mantle garnets have a normal pattern?
2. What is the reason for the continuum of shapes of REE patterns across the major element compositional range of the samples? Is it to do with major element compositional effects (e.g. Ca in garnet), mineralogy, exsolution or do fluids play a role?
3. How do these patterns relate to apparently metasomatically zoned garnet crystals from previous studies?
4. What is the nature of the bulk rock trace element compositions and how are these generated?
5. How do the other trace elements fit into any explanations for the generation of the REE patterns?

Firstly, an overview of existing experimental and theoretical constraints must be made. Secondly, a presentation of the existing models for trace element behaviour in the mantle is needed before a discussion of their relative merits may be made.

9.5.1 Consideration from other authors

9.5.1.1 INITIAL CONSTRAINTS

Firstly, we must define some limits to the properties of trace elements in minerals and melts at relevant depths. This will enable a means to assess how applicable the mechanisms involved in various models will be, rather than simply showing how closely natural trace element patterns are matched. This will provide a coherent framework with which to gauge the success of the contrasting ideas on trace element behaviour in the mantle.

In terms of the properties of melts in the upper mantle, McKenzie (1989) points out that the small melt fractions (of the order of 10^{-3} %) need not ever travel to the earth's surface to become an erupted igneous rock. It is suggested that these highly potassic melts would have a very low heat capacity (and hence would transport little heat) and freeze at depth in the upper mantle between around 950-750°C (i.e. by the level of the lower crust on a continental geotherm). These melts would contain greater concentrations of LREE and less Ti than known alkali igneous rocks. It is only the re-melting of this frozen melt by adiabatic decompression (caused by lithospheric stretching) or by increased heat flux (possibly associated with plume activity) that will cause low melt fraction igneous rocks such as kimberlite, carbonatite and lamproite to reach the earth's surface.

Experiments determining trace element partitioning between garnet and melt (e.g. Simizu and Kushiro, 1975; Harrison and Wood, 1980) and clinopyroxene and melt (e.g. Harte and Dunn, 1993) enable the determination of the likely melts in equilibrium with particular trace element compositions in garnets and clinopyroxenes from natural samples. Garnet/clinopyroxene partition coefficients have been examined Harte and Kirkley (1997) in eclogites but the effect of major element composition on trace element partitioning may also be applied to peridotites.

In terms of the specific diffusion coefficients for the REE in garnet, van Orman et al. (2002) have demonstrated experimentally that it is unlikely that LREE would diffuse faster than HREE in natural pyrope at 2.8 GPa because diffusion rate can not be correlated with ionic radius.

9.5.2 Models for the generation of mantle garnet REE profiles

Models fall into 4 categories as shown in Table 9.2. Following the table is a summary of these in diagram form (Fig. 9.17).

Model Title/Variant (profile source)	References	1. Starting garnet composition and 2.-3. further modifications	Comments
DIFFERENTIAL DIFFUSION MODELS			
(a) Sub-solidus non-equilibrium modification (Diamond inclusions, diamond-bearing xenoliths)	Shimizu and Richardson (1987), Shimizu and Sobolev (1995), Shimizu et al. (1999)	1. Refractory garnet 2. Bulk system LREE depletion 3. Sub-solidus non-equilibrium modification	Diffusion coefficients for REE vary from La through to Lu in garnet
(b) Partial Equilibration with LREE metasomatic melt (Concentrate)	Hoal et al. (1994)	1. Refractory garnet 2. Partial equilibration towards metasomatic garnet composition 3. Range depends on initial garnet composition and degree of equilibration	Further definition of (a)
(b-2) LREE disequilibrium, HREE equilibrium (Other workers' data and modelling)	Khazan (2006)	1. An initial unspecified garnet composition 2. Full HREE equilibration with metasomatic fluid 3. Continuous partial equilibration (i.e. disequilibrium) of LREE	Variant of (b) using modelling from experiments
SPECIFIC METASOMATIC ENRICHMENT MODELS			
(c) 'Metasomatic Enrichment' (Diamond inclusions, diamond-bearing xenoliths)	Stachel et al. (1998), Stachel and Harris (1997)	1. Refractory garnet from melt extraction in spinel stab. field. Declining La-Dy 'enrichment' – from 'fractionated garnet-bearing source' with MREE, HREE static	Relies on very specific enrichment of LREE in garnet
(c-2) Metasomatism by carbonatitic fluid (Wesselton xenoliths)	Griffin et al. (1999b)	1. Unspecified starting composition (presumable refractory garnet). 2. HREE depleted garnet core with LREE enrichment 3. Overgrowth and annealing to produce normal HREE in rim Unlikely that REE diffuse at different rates (authors state that this requires partial equilibrium which is an inconsistency)	Variant of (c)
(d) Multiple partial melting and metasomatism events (Snap Lake xenoliths)	Promprated et al. (2003)	1. LREE depleted garnet as a relic of partial melting 2. Primary metasomatic fluid enriches garnet in LREE 3. Secondary minor partial melting reduces concentration of the lightest REE (La-Ce)	Variant of (c)

Model Title/Variant (profile source)	References	1. Starting garnet composition and 2.-3. further modifications	Comments
(e) 'Metasomatic Enrichment' (Diamond inclusions)	Stachel et al. (2004)	1. Pre-metasomatic refractory garnet 2. G10s have LREE enrichment 3. G9s have partial re-equilibration with megacryst garnet (i.e. LREE decrease, HREE increase)	Variant of (c)
(f)	Simon et al. (2003), Simon (2004)	1. Pre-metasomatic refractory bulk rock with specific melt fractions extracted in spinel and garnet stability fields 2. 'Metasomatic Enrichment'	Variant of (c) but applied to bulk rock REE composition
PERCOLATIVE INFILTRATION OF METASOMATIC FLUID GENERATED BY THE FRACTIONATION OF GARNET			
(g) Percolative Fractional Crystallisation (Jagersfontein xenoliths)	Burgess and Harte (2004)	1. Range of initial garnets in column of mantle 2. Melt percolates up melt column and is enriched in LREE/HREE as garnet fractionates 3. Garnets in rocks equilibrate with fractionating fluid	Garnet fractionation itself determines the progressive generation of the 'hump' in peridotitic garnets high in the melt column.
EXSOLUTION MODELS			
(h) Exsolution from majorite (Arnie xenoliths)	Doyle (2002)	1. Original sinusoidal (clinopyroxene-like) REE pattern. Composition of majorite derived from bulk rock reconstruction. 2. Exsolution of garnet and orthopyroxene in harzburgitic garnets progressively rotates REE pattern 3. Garnet and clinopyroxene exsolution in lherzolites produces MREE enriched profile.	Relies on pre-existing humped bulk-crystal REE profile in order to generate a humped garnet REE profile
(x) Exsolution from orthopyroxene	Lahaye and Brey (2003)	Unspecified but 'sigmoidal' REE pattern generated by exsolution of garnet from orthopyroxene	Variant of (h)

Table 9.2: Summary of existing models for the formation of humped garnet REE profiles. (a) to (i) as for Fig. 9.17.

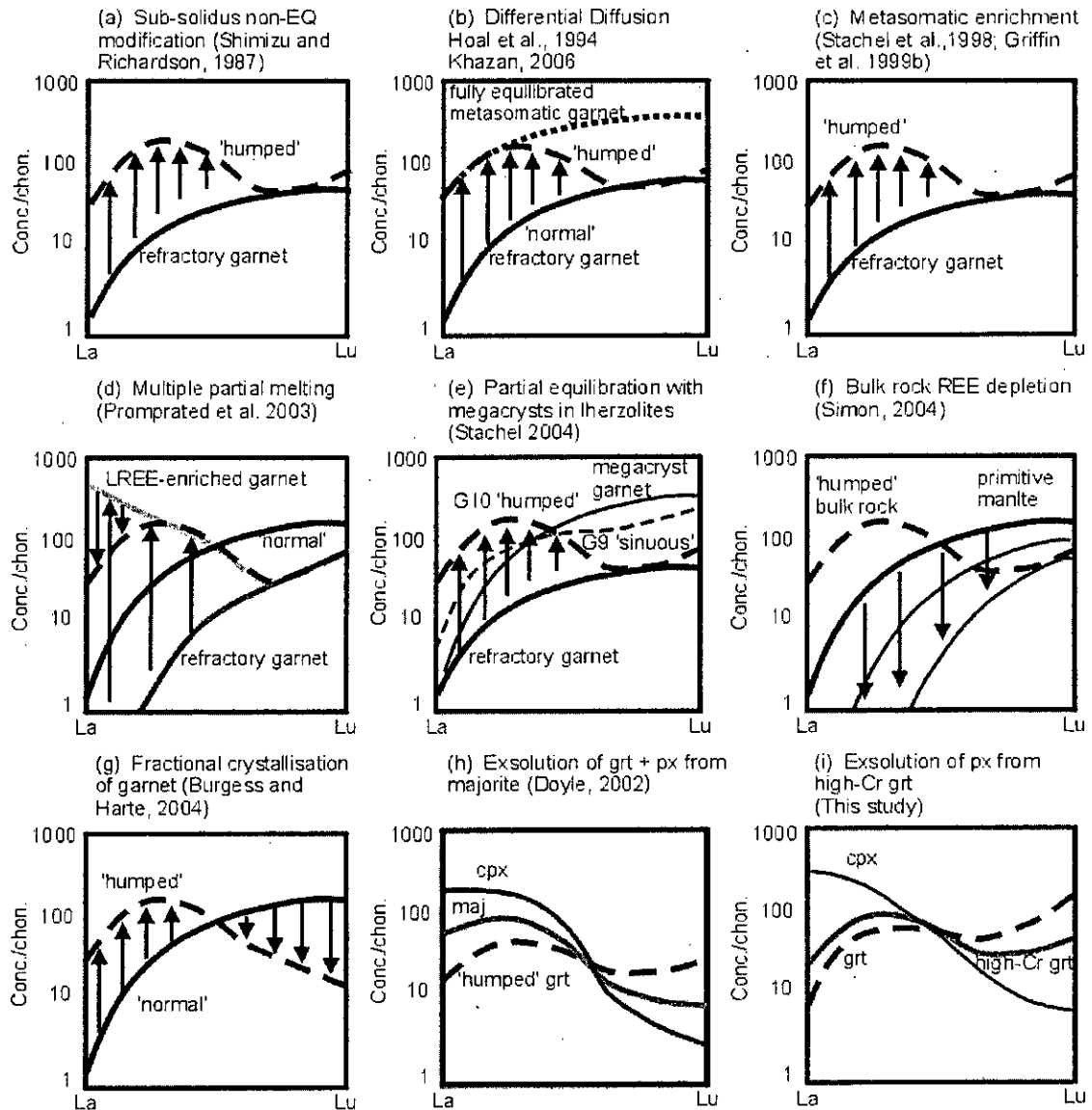


Figure 9.17: Diagrammatic summary of the various existing models for the formation of humped REE profiles in mantle garnets. Models (a) and (b) are differential diffusion models, (c) to (f) are specific metasomatic enrichment models, (g) is the model involving percolative fractional crystallisation and (h) and (i) illustrate the exsolution models. In the diagrams the dashed lines represent the resultant 'humped' garnet REE profile. Other minerals with dotted or solid lines are labelled individually. Arrows represent the differential increase/decrease involved in the modification of pre-existing REE profiles.

9.5.2.1 DIFFERENTIAL DIFFUSION MODELS

Initially suggested by Shimizu and Richardson (1987), the differential diffusion model requires that the LREE diffuse faster than the HREE so that solid state diffusion of LREE from the matrix of the rock (a metasomatic fluid) should occur

preferentially to that of the HREE forming a hump (see Fig. 9.17a). Hoal et al. (1994) analysed REE in kimberlite concentrate garnets from on- and off-craton kimberlites in southern Africa. The authors define a set of garnet REE K_d s (diffusion coefficients) that vary in orders of magnitude LREE to HREE with $LREE > MREE > HREE$. This is the principal factor affecting formation of what they call 'sinusoidal' garnet REE patterns and the process by which it is attained is the partial re-equilibration with a LREE-enriched melt (see Fig. 9.17b, with the garnet in equilibrium with the LREE-enriched melt shown as a dotted bold line).

However, the experiments of van Orman et al. (2002) show that there should be no significant difference between diffusion rates across the REE in natural pyrope at 30 kb. Therefore this would indicate that the differential diffusion models are unlikely. If the HREE diffuse sufficiently faster than the LREE (~30 times faster) then a model such as that suggested by Khazan (2006) for garnet REE would be feasible. Khazan (2006) implies that the LREE in garnet are in a constant state of partial equilibrium and only the HREE approach equilibrium with surrounding fluids. Note that this is the opposite (i.e. $HREE > MREE > LREE$) of that required for the model of Hoal et al. (1994).

9.5.2.2 SPECIFIC METASOMATIC ENRICHMENT MODELS

Stachel et al. (1998) stated that the variety of garnet REE profiles measured in harzburgitic and lherzolitic garnets cannot easily be explained by a range of K_d s as suggested by Hoal et al. (1994). Stachel et al. (1998) proposed a model of 'metasomatic overprinting' of a refractory peridotitic garnet with a LREE-enriched fluid (forming humped profiles) where lherzolitic garnets attain a lower LREE abundance through equilibration with an exsolving clinopyroxene. However, the authors did not state the exact mechanism for the generation of humped profile, only that the metasomatic enrichment decreases strongly from LREE to HREE.

Griffin et al. (1999b) suggests that the cores of garnets from the xenoliths they studied had a depleted REE pattern that partially equilibrated with a rim that was 'metasomatically overgrown' in equilibrium with a metasomatic fluid. They recognise, however, that partial equilibrium poses a problem in terms of requiring differential diffusion (see above). Promprated et al. (2003) suggest a model of 'metasomatic enrichment' of a refractory garnet by LREE-rich fluids and subsequent low degree re-melting reducing only the La and Ce concentrations. Again no mechanism for metasomatism is suggested.

Stachel et al. (2004) review trace element compositions of diamond inclusions and revise the model of Stachel et al. (1998) in order to incorporate two types of metasomatism affecting (i) harzburgites with a high LREE:MREE,HREE,HFSE ratio and (ii) lherzolites with a moderate LREE:MREE,HREE,HFSE ratio. The precise mechanisms for these 'metasomatic effects' and a definition of both metasomatic fluid compositions and also their origin are not explained. This is obviously a major problem with many metasomatic models. A metasomatic process seems likely to be involved because a super-positioning of events provides a means of generating the humped patterns. However it is often difficult to extract information which defines the pre-metasomatic composition, the metasomatic fluid composition and the influence of any partial equilibration effects.

Simon et al. (2003), Simon (2004) suggest that the bulk rock (Table 9.2f and Fig. 9.17f) HREE composition in Kimberley xenoliths corresponds to ancient melting events. The authors attribute humped bulk rock REE profiles to 'significant incompatible element addition' or 'metasomatic enrichment'. The exact mechanism for this, however, is not defined.

9.5.2.3 PERCOLATIVE FRACTIONAL CRYSTALLISATION MODEL

In the model of Burgess and Harte (2004) the mantle is treated as a column of rock with an upward percolating MORB-source melt infiltrating. Fractional crystallisation

of olivine, orthopyroxene and clinopyroxene are modelled to have little effect on the relative LREE:HREE ratio whereas fractionation of garnet does -with garnet crystallisation, the melt becomes progressively enriched in LREE/HREE as it moves up the column. Therefore it is garnet itself that generates the humped profiles as existing garnets equilibrate with the LREE-enriched percolating melt.

The advantage of this model is that the source of the melt is defined and the process of 'metasomatic enrichment' (undefined by the 'specific metasomatic enrichment models) is defined as a fractionating percolative melt. The mechanism for varying enrichment of garnets with LREE is, straightforwardly, equilibration of garnet with this melt. These processes may be defined quantitatively and conform to the ideas of McKenzie (1989) and van Orman et al. (2002). The model also suggests an explanation for garnet cores possessing more enriched REE compositions in that they may represent equilibration with pre-existing metasomatic melt percolation events superimposed by rims with a more normal REE composition during later higher-degree melts (fitting with the pattern observed in sample B48). Additionally, garnets from lower depth harzburgites have more highly fractionated REE compositions, whereas high-P lherzolites close to the base of the lithosphere tend to have garnets with more normal patterns. This conforms to the initially deep, primary mantle melt of MORB composition which generates a normal garnet REE profile, and this melt fractionates while percolating upwards, equilibrating with garnet to form a humped profile.

9.5.2.4 EXSOLUTION MODELS

The exsolution models do not involve metasomatic fluids of any kind and work backwards from the measured mineral compositions of garnets and pyroxenes in order to reconstruct the pre-exsolution REE pattern based on their modal proportions. Doyle (2002) starts with an assumed majorite composition that is similar to clinopyroxene ('sinusoidal') and, in the first case exsolves pyrope and orthopyroxene (for harzburgites) and secondly exsolves pyrope and clinopyroxene (for lherzolites).

The pyrope in each case attains a humped REE profile with the harzburgitic model yielding higher LREE compositions than the lherzolitic one. Additionally, Lahaye and Brey (2003) observe garnet exsolving from an orthopyroxenite-bearing composite xenolith. The authors suggest that this garnet will have a 'sigmoidal' REE pattern but do not provide a quantitative model for its generation.

The major disadvantage of these models is that the origin of the pre-exsolution mineral compositions (for both major and trace elements) is not justified and the resultant garnet compositions are not confirmed to agree with the precise patterns observed in the xenoliths studied.

9.5.2.5 INTERPRETATION IN RELATION TO NEWLANDS AND BOBBEJAAN SAMPLES

In this study it has been possible to document exsolution of pyroxenes and Cr-spinel from a high-Cr garnet and this is the first major event to affect the Newlands and Bobbejaan samples (see Chapter 6) that may be shown by a combination of petrographic and geochemical data. Therefore, taking sample B55 which has well constrained modal proportions, one can use garnet and clinopyroxene REE compositions in this sample to reconstruct the REE composition of the pre-existing high-Cr garnet. The result is a relatively flat profile for high-Cr garnet at around 10 times chondrite and is shown in Fig. 9.18. The harzburgites did not appear to have exsolved clinopyroxene (only orthopyroxene which is low in all REE) so their existing garnet REE profiles are modelled without further change to their REE composition. Therefore REE profiles in the harzburgitic garnets and the reconstructed lherzolitic REE profiles are thought to represent the range of ancient REE signatures prior to any exsolution and metasomatic effects.

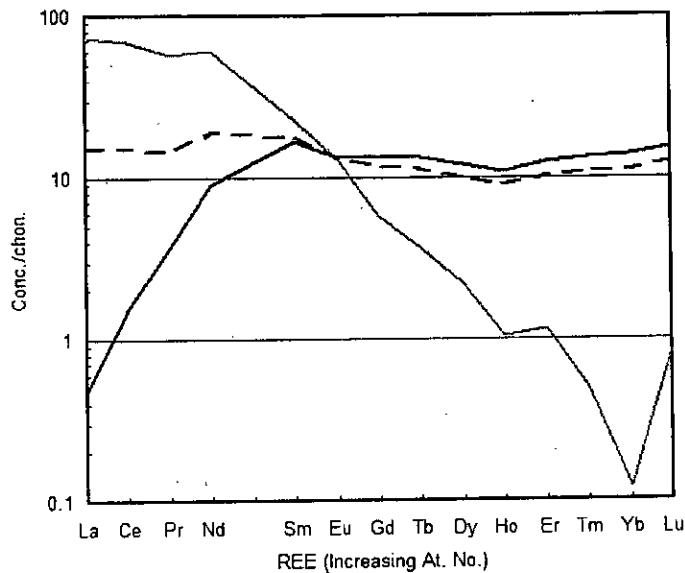


Figure 9.18: REE for analysed garnet (solid black line) and clinopyroxene (grey line) from B55. Dashed line is the mixture of garnet and clinopyroxene in the ratio 80:20 observed as the modal proportions in the sample (see modal proportions in Table 6.3), reconstructing the pre-exsolution, high-Cr garnet REE profile assuming no melt modification of either clinopyroxene and garnet.

Since Ca is known to play a role in the partitioning of REE between garnet and clinopyroxene (see section 9.3.6), particular REE ratios and ppm values for harzburgitic and lherzolitic garnets (with several reconstructed bulk REE compositions, see Fig. 9.18) are compared to Ca cations in garnet in Fig. 9.19. This figure indicates that an increase of Ca-in-garnet appears to:

1. linearly reduce the magnitude of the REE hump in garnet (Fig. 9.19a)
2. exponentially reduce the LREE/HREE ratio in garnet (Fig. 9.19b)
3. linearly increase the Sm concentration in garnet (Fig. 9.19e) and
4. exponentially increase the Yb concentration in garnet (Fig. 9.19 f)

There are three additional items of note:

1. There is a poor correlation of Ca-in-garnet with MREE/HREE ratios and Ce concentration (Fig 19.c and d, respectively).
2. B48 (identified as being affected by metasomatism) is particularly anomalous in compared to the rest of the data in Fig. 9.19a and b, whereas it is only the

rim composition (circle symbols rather than star symbols) that is anomalous in Fig.9.19c and f.

3. In general the reconstructed compositions (downward pointing triangle symbols in Fig. 9.19a,b,e and f) are not radically different to the garnet compositions (upward pointing triangle symbols). They are usually in fitting with the best fit trend lines.

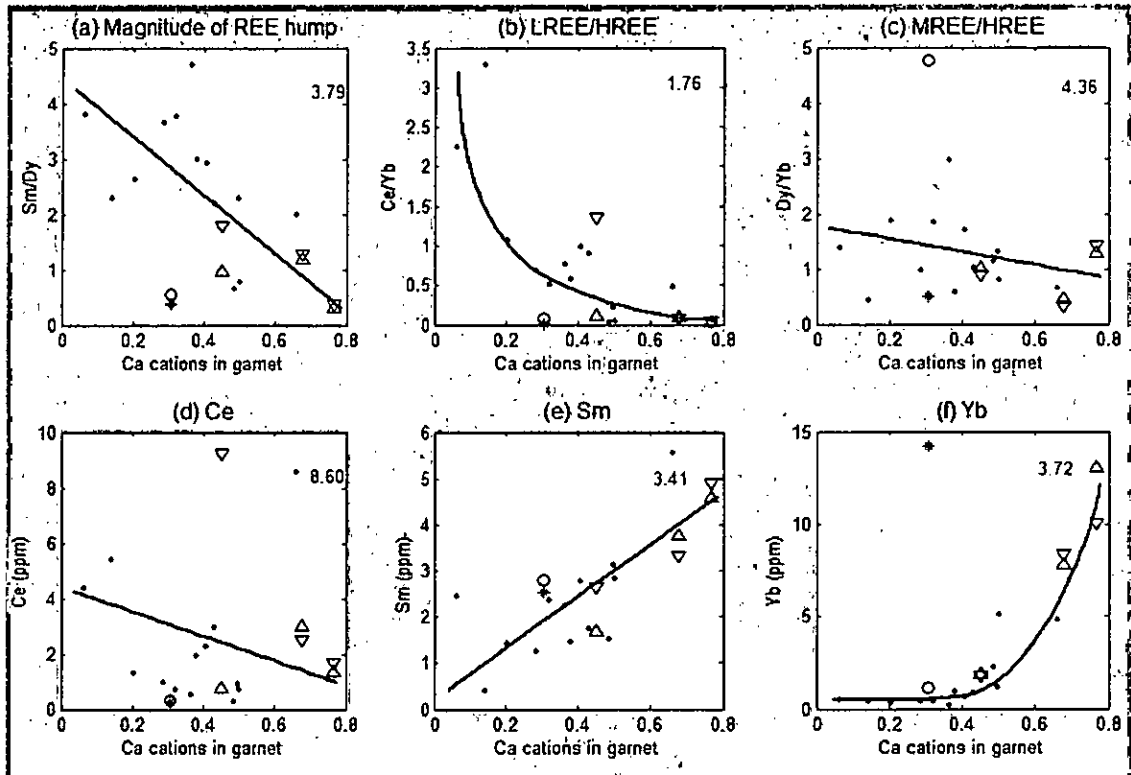


Figure 9.19: Ca in garnet (calculated on the basis of 8 cations) compared to: (a) Magnitude of REE hump defined by Sm/Dy , (b) LREE/HREE defined by Ce_{NORM}/Yb_{NORM} , (c) MREE/HREE defined by Dy_{NORM}/Yb_{NORM} , (d) Ce (ppm), (e) Sm (ppm) and (f) Yb (ppm). Lines of best fit are shown with the calculated norm of residuals in the upper right of the plots (where numbers less than 4 indicate a reasonable fit). Best fit lines ignore the sample B48, which is affected by metasomatism (B48 is plotted as a circle symbol for its rim and a star symbol for its core compositions). Downward pointing triangles are reconstructed lherzolitic bulk REE compositions (see Fig. 9.18) and upward pointing arrows are the garnets from those samples.

Therefore, the proposed sequence of events is as follows:

1. High-Cr garnet equilibrates with REE in the matrix in accordance with the Ca concentration in garnet. The pattern happens to be humped for harzburgitic garnets and more normal for lherzolitic ones, by means of having a higher

HREE content. The mechanism for this is provisionally suggested to be due to a Ca effect in garnet.

2. Exsolution of orthopyroxene + spinel in harzburgitic garnets caused only minor modification to the original garnet REE profile. And, exsolution of clinopyroxene ± orthopyroxene + spinel in lherzolitic garnets predominantly caused a reduction in LREE in garnets (see Fig. 9.18).
3. A final phase of modification in a few samples is in accordance to the percolative fractional crystallisation model of Burgess and Harte (2004). However, the Newlands and Bobbejaan samples do not provide evidence of a wide difference in depths of origin for different samples; thus it is not possible to examine changes through a percolative metasomatic column as was done for Jagersfontein by Burgess and Harte (2004).

9.6 Conclusions

A list of the conclusions of the trace element data and interpretation is as follows:

1. LILE analyses indicate that Na in garnet and K in clinopyroxene are higher in the high-Cr lherzolitic suite than in lower Cr suites. La is proportional to Sr in garnet and clinopyroxene with a higher Sr:La ratio present in the low-Ca harzburgitic garnets.
2. For HFSE positive correlations exist between Ti, Y, Zr and Nb in garnets and Cr-spinels but not clinopyroxenes. High-Cr lherzolitic garnets and Cr-spinels have the highest concentrations of HFSE and the low-Ca harzburgites have the lowest HFSE.
3. The correlation between Ga and Ni is very strong in Cr-spinels and weakly present in garnets. Cr-spinels and clinopyroxenes show lower Ga in the high-Cr lherzolite suite, whereas garnet with higher Ga and Ni is indicative of the higher Cr lherzolite and higher Ca harzburgite suite and thought to correspond to higher temperatures of equilibration.

4. In lherzolitic samples REE garnet/clinopyroxene partitioning varies with garnet Ca content due to the effect of Ca on REE partitioning described in the literature (e.g. Harte and Kirkley, 1997).
5. Reconstruction of bulk REE compositions in pre-exsolution high-Cr garnets indicates a primary REE pattern, which is humped for harzburgitic samples and approximately flat in lherzolitic ones.
6. Trace element zonation is only apparent in B48, BOB113 which have zoned REE profiles that correspond to samples with external Ti zonation. These samples appear to have been affected by metasomatism and could conform to the percolative fractional crystallisation model of Burgess and Harte (2004) since the core-to-rim, humped-to-normal feature is observed, which is especially evident in B48.
7. Initial bulk trace element compositions (i.e. those preceding the exsolution and metasomatic effects in '5' and '6') for the samples are modelled and show a correlation with the Ca concentration in garnets. Ca in garnet appears to have a progressive effect on incorporation of REE, reducing the LREE hump and increasing MREE and HREE concentrations in garnet as more Ca is present.
8. Therefore point 7 implies the possibility of a single-stage, non-disequilibrium process for the modification of existing humped profiles. Unfortunately, there is no remaining evidence in the rocks, from either petrographic features or chemical zoning preserved in minerals, to suggest further details on the generation of these primary REE patterns. An explanation for the extremely high Sr in low-Ca, high-Cr garnets remains elusive as well.
9. The application of specific models involving 'differential diffusion' or/and 'metasomatic enrichment' cannot be justified for the Newlands and Bobbejaan samples without further evidence of 'pre-primary' compositions.

9.7 References

- Burgess, S. R. and Harte, B. (2004). Tracing lithosphere evolution through the analysis of heterogeneous G9-G10 garnets in peridotite xenoliths, II: REE chemistry. *Journal of Petrology*. **45**. 609-634.
- Dawson, J. B. (2004). A fertile harzburgite-garnet lherzolite transition: possible inferences for the roles of strain and metasomatism in upper mantle peridotites. *Lithos*. **77**. 553-569.
- Doyle, P. M. (2002). A petrographic and petrochemical study of selected peridotitic and pyroxenitic xenoliths from three kimberlite localities in the Lac de Gras region, Northwest Territories, Canada. Department of Geological Sciences. Cape Town. University of Cape Town. *Unpublished Masters Thesis*
- Griffin, W. L., Shee, S. R., Ryan, C. G., Win, T. T. and Wyatt, B. A. (1999b). Harzburgite to lherzolite and back again: metasomatic processes in ultramafic xenoliths from the Wesselton kimberlite, Kimberley, South Africa. *Contributions to Mineralogy and Petrology*. **134**. 232-250.
- Harrison, W. J. and Wood, B. J. (1980). An experimental investigation of the partitioning of REE between garnet and liquid with reference to the role of defect equilibria. *Contributions to Mineralogy & Petrology*. **72**. 145-155.
- Hart, S. R. and Dunn, T. (1993). Experimental cpx/melt partitioning of 24 trace elements. *Contributions to Mineralogy & Petrology*. **113**. 1-18.
- Harte, B. and Hawkesworth, C. J. (1989). Mantle domains and mantle xenoliths. In: Eds.: Ross, J., Jaques, A. L., Ferguson, J. et al. *Kimberlites and Related Rocks*. Geological Society of Australia, Special Publication. **2**. 649-686.
- Harte, B. and Kirkley, M. B. (1997). Partitioning of trace elements between clinopyroxene and garnet: data from mantle eclogites. *Chemical Geology*. **136**. 1-24.
- Hoal, K. E. O., Hoal, B. G., Erlank, A. J. and Shimizu, N. (1994). Metasomatism of the mantle lithosphere recorded by rare earth elements in garnets. *Earth and Planetary Science Letters*. **126**. 303-313.
- Khazan, Y. (2006). Distribution of trace elements between the mantle rocks minerals: Observational evidences of diffusive equilibrium and its implications. European Geophysical Union Conference, Vienna, Poster.
- Lahaye, Y. and Brey, G. P. (2003). Scale and timing constraints on chemical redistribution between minerals of a composite garnet peridotite/orthopyroxenite. 8th International Conference Abstracts, CD Unpaginated.
- McDonough, W. F. and Sun, S.-s. (1995). The composition of the Earth. *Chemical Geology*. **120**. 223-253.
- McKenzie, D. (1989). Some remarks on the movement of small melt fractions in the mantle. *Earth and Planetary Science Letters*. **95**. 53-72.

- Promprated, P., Taylor, W. R., Anand, M., Malkovets, V. G., Floss, C. and Griffin, W. L. (2003). Diamond inclusions from Snap Lake, Northwest Territories, Canada. 8th International Conference Abstracts.
- Shimizu, N. and Kushiro, I. (1975). The partitioning of rare earth elements between garnet and liquid at high pressures: Preliminary experiments. *Geophysical Research Letters*. **2**. 413-416.
- Shimizu, N., Pokhilenko, N. P., Boyd, F. R. and Pearson, D. G. (1999). Trace element characteristics of garnet dunites/harzburgites, host rocks for Siberian peridotitic diamonds. 7th International Kimberlite Conference. 773-782.
- Shimizu, N. and Richardson, S. H. (1987). Trace element abundance patterns of garnet inclusions in peridotite-suite diamonds. *Geochimica et Cosmochimica Acta*. **51**. 755-758.
- Shimizu, N. and Sobolev, N. V. (1995). Young peridotitic diamonds from the Mir kimberlite pipe. **375**. 394-397.
- Simon, N. S. C. (2004). The formation and modification of cratonic lithospheric roots: A petrological and geochemical study of xenoliths from the Kaapvaal craton. Department of isotope geochemistry. Amsterdam. Vrije Universiteit Amsterdam. *Unpublished PhD Thesis*
- Simon, N. S. C., Irvine, G. J., Davies, G. R., Pearson, D. G. and Carlson, R. W. (2003). The origin of garnet and clinopyroxene in "depleted" Kaapvaal peridotites. *Lithos*. **71**. 289-322.
- Stachel, T., Aulbach, S., Brey, G. P., Harris, J. W., Leost, I., Tappert, R. and Viljoen, K. S. F. (2004). The trace element composition of silicate inclusions in diamonds: a review. *Lithos*. **77**. 1-19.
- Stachel, T. and Harris, J. W. (1997). Syngenetic inclusions in diamond from the Birim field (Ghana) - a deep peridotitic profile with a history of depletion and re-enrichment. *Contributions to Mineralogy and Petrology*. **127**. 336-352.
- Stachel, T., Viljoen, K. S., Brey, G. and Harris, J. W. (1998). Metasomatic processes in lherzolitic and harzburgitic domains of diamondiferous lithospheric mantle: REE in garnets from xenoliths and inclusions in diamonds. *Earth and Planetary Science Letters*. **159**. 1-12.
- van Orman, J. A., Grove, T. L., Shimizu, N. and Layne, G. D. (2002). Rare earth element diffusion in a natural pyrope single crystal at 2.8 GPa. *Contributions to Mineralogy and Petrology*. **142**. 416-424.
- van Westrenen, W., Wood, B. J. and Blundy, J. D. (2001). A predictive thermodynamic model of garnet-melt trace element partitioning. *Contributions to Mineralogy & Petrology*. **142**. 219-234.

10. Synthesis, Wider Implications and Further Work

The aim of this chapter is to synthesise the conclusions from Chapters 3 to 9 into a coherent and integrated model for the evolution of the Newlands and Bobbejaan samples representing the chromite-garnet peridotite assemblages. This will enable an assessment of how well the initial aims of the project have been achieved and it will also allow discussion of the 'wider implications' of the findings and how they contribute to existing understanding of the evolution of the mantle lithosphere. The final section, entitled 'further work', will address directions for additional research resulting from the findings of this thesis.

10.1 Synthesis: A Multistage History for the Evolution of Newlands and Bobbejaan Samples

This section is divided into the 5 identifiable evolutionary events (stages) for Newlands and Bobbejaan samples in chronological order. Evidence for the details of the events and their relative chronology is integrated from the observations and conclusions in Chapters 3-9, and summary figures of the garnet zonations and the chronology of events are produced in Figs. 10.1 and 10.2:

10.1.1 Stage 1: Earliest known mineralogy

The Newlands and Bobbejaan samples comprise garnet-rich xenocrysts (monogranular) and xenoliths (polygranular) (Chapter 3), with either harzburgitic or lherzolititic rock compositions. Within the polygranular samples, the main texture evident is granuloblastic with crystals generally in the range 2-5mm. Modally, the polygranular samples indicate that the samples originate from garnet-rich (>50% garnet in most cases), rocks of peridotitic affinity with rare examples of garnetite (>90% garnet). It is expected that other matrix minerals will have been olivine with or without minor pyroxene and Cr-spinel although probable olivine and orthopyroxene are always altered. Bulk garnet compositions are high in Cr (see Fig. 10.1, Stage 1) and are suggestive of higher P-T than calculated for the subsequent stages.

Little is known in detail about this stage and any prior events leading to the generation of the earliest known mineralogy since the later events have modified mineral compositions. However, given that exsolution-generated inclusions in garnets do not have measurably different compositions, it appears that the pre-exsolution garnets were relatively homogeneous chemically in terms of major elements (e.g. see sample B55, X-ray map). According to thermodynamic modelling of several samples using the Perplex program, the majority of them are calculated to have pre-exsolution P_s and $T_s > 65\text{kb}$ and $> 1300^\circ\text{C}$. The pre-exsolution, primary trace elements patterns in garnets are also thought to have formed before or during Stage 1 and normalised REE plots are humped in LREE for harzburgites and relatively flat for lherzolites (Chapter 9).

10.1.2 Stage 2: Exsolution of pyroxene and spinel from garnet

Within individual garnet crystals the internal texture grades from pristine to annealed exsolution textures to one with no inclusions at all (Chapter 3). The exsolution forms orthopyroxene and Cr-spinel in harzburgitic garnets and clinopyroxene and Cr-spinel \pm orthopyroxene in lherzolititic garnets. Calculated bulk rock compositions conform to the composition of high-Cr garnets (they have 8 cations with 12 oxygens), which appears to represent a pre-exsolution bulk crystal composition. When plotted on a $\text{Ca}/(\text{Ca}+\text{Mg}+\text{Fe}_t)$ vs. $\text{Cr}/(\text{Cr}+\text{Al})$ diagram the initial compositions plot at higher $\text{Ca}/(\text{Ca}+\text{Mg}+\text{Fe}_t)$ and higher $\text{Cr}/(\text{Cr}+\text{Al})$ for lherzolititic samples and at higher $\text{Cr}/(\text{Cr}+\text{Al})$ for harzburgitic samples (Fig. 10.1, Stage 2). Garnet core compositions in samples with multiple inclusions reveal that the lower-Cr garnet produced by exsolution was relatively homogeneous (e.g. sample B55, Chapter 5). According to the sliding reactions postulated (see Chapter 6) and the geothermobarometric modelling (see Chapter 7) the exsolution event represents a substantial lowering of P and T (probably close to a normal continental geotherm) for the samples.

The primary trace element patterns in garnet are thought to be redistributed amongst pyroxenes and spinels as exsolution occurs, modifying the REE patterns in garnet as

described in Chapter 9. The textural features within garnet indicate a certain degree of disequilibrium even though the rocks they comprise are texturally relatively equilibrated (i.e. granuloblastic). The extent of annealing of exsolution textures present signifies that the samples were at residing over a diverse range of temperatures (probably for an extensive length of time i.e. in the order of millions of years). This is confirmed by the range of temperature estimates (e.g. garnet-clinopyroxene Fe-Mg exchange thermometers) reported in Chapter 7. For example, B55 a sample with a pristine exsolution texture is lower temperature than many samples that show annealed textures.

10.1.3 Stage 3a: External zonation - P-T re-equilibration and metasomatism

Major element external zonation in the majority of garnets and additionally in two clinopyroxenes studied (Chapter 5) indicates an event (~0.5-5 Ma from diffusion constraints, Chapter 8) producing major element external zonation from garnet to matrix and clinopyroxene to matrix. In NEW303 the matrix clinopyroxene (core) and matrix garnet (core) pair generate a higher P-T estimate than the one produced using rim compositions (Chapter 7). Therefore 'Ed' garnet zonation (external zonation to a matrix of diopside \pm serpentine \pm Cr-spinel) is expected to represent P-T re-equilibration of garnet with matrix (this overlaps compositionally with type Ib zonation of Burgess and Harte, 1999). It is also expected that Eg⁺ zonation (external zonation towards a matrix of garnet where Cr decreases towards the rim) and Es zonations (zonation towards a matrix of serpentine \pm Cr-spinel) are indicative P-T re-equilibration since they follow the down P-T reaction simulations in Chapter 6 (these are shown in Fig. 10.1). External P-T re-equilibration is expected to be contiguous with Stage 2. This P-T re-equilibration is at least 25°C and 2kb (NEW303, Chapter 7) and probably up to 100°C and 6kb (see Perplex simulation for BOB402, Chapter 7).

E_{Ca} zonation (external zonation towards the matrix involving an increase in Ca \pm Ti from core to rim) and Eg⁻ zonation (external zonation towards a matrix of garnet where Cr increases towards the rim) are the only external zonation types that

conform to metasomatic modification since they may be accompanied by strong Ti and REE zonation (Chapters 5 and 9). These conform to the zonation types IIIb and II respectively from Burgess and Harte (1999). Additionally these represent the two vectors on the $\text{Ca}/(\text{Ca}+\text{Fe}+\text{Mg})$ vs. $\text{Cr}/(\text{Cr}+\text{Al})$ that are at odds with the sliding reaction simulations (Fig. 10.1, lowermost plot). These zonations generate the longest diffusion profiles and calculations yield time scales at the high end of all external zonations (up to 10s of Ma, Chapter 8). However, it is not possible to comment on whether metasomatism occurred prior to, or after external P-T re-equilibration (in Fig. 10.1, Stage 3a, the situation for metasomatism occurring at a later stage is shown).

Sample B48 is zoned in Ni and has concentrations in its core and rim, which, according to Ni-in-garnet thermometry, indicate that metasomatism affecting the rim of the sample occurred at $\sim 40^\circ\text{C}$ above the ambient mantle temperature for this sample (Chapter 9). This is the only sample to indicate REE zonation where the HREE are enriched above the concentration expected for the particular Ca content of the garnet. REE in garnet and clinopyroxene are not thought to be affected by the P-T re-equilibration since they are not zoned.

10.1.4 Stage 3b: Internal zonation - P-T re-equilibration

Internal zonation towards exsolution-generated inclusions clearly overprints external metasomatic zonation (see BOB113, illustrated in Fig. 10.1, Stage 3b). External P-T re-equilibration zones are also apparently overprinted by internal zonation. However, the initiation of internal zonation may have occurred during some of the time interval over which the external zonation operated (see summary points 6 and 7 from Chapter 8, Section 8.4). Fig. 10.2 indicates that some internal P-T re-equilibration may have occurred at the final stages of exsolution as well but this is not preserved in the garnet crystals since some textural annealing, post exsolution, is thought to have occurred (see Stage 2, in 10.1.2). It is also possible that inclusions may have overgrown internally zoned garnet during Stage 2

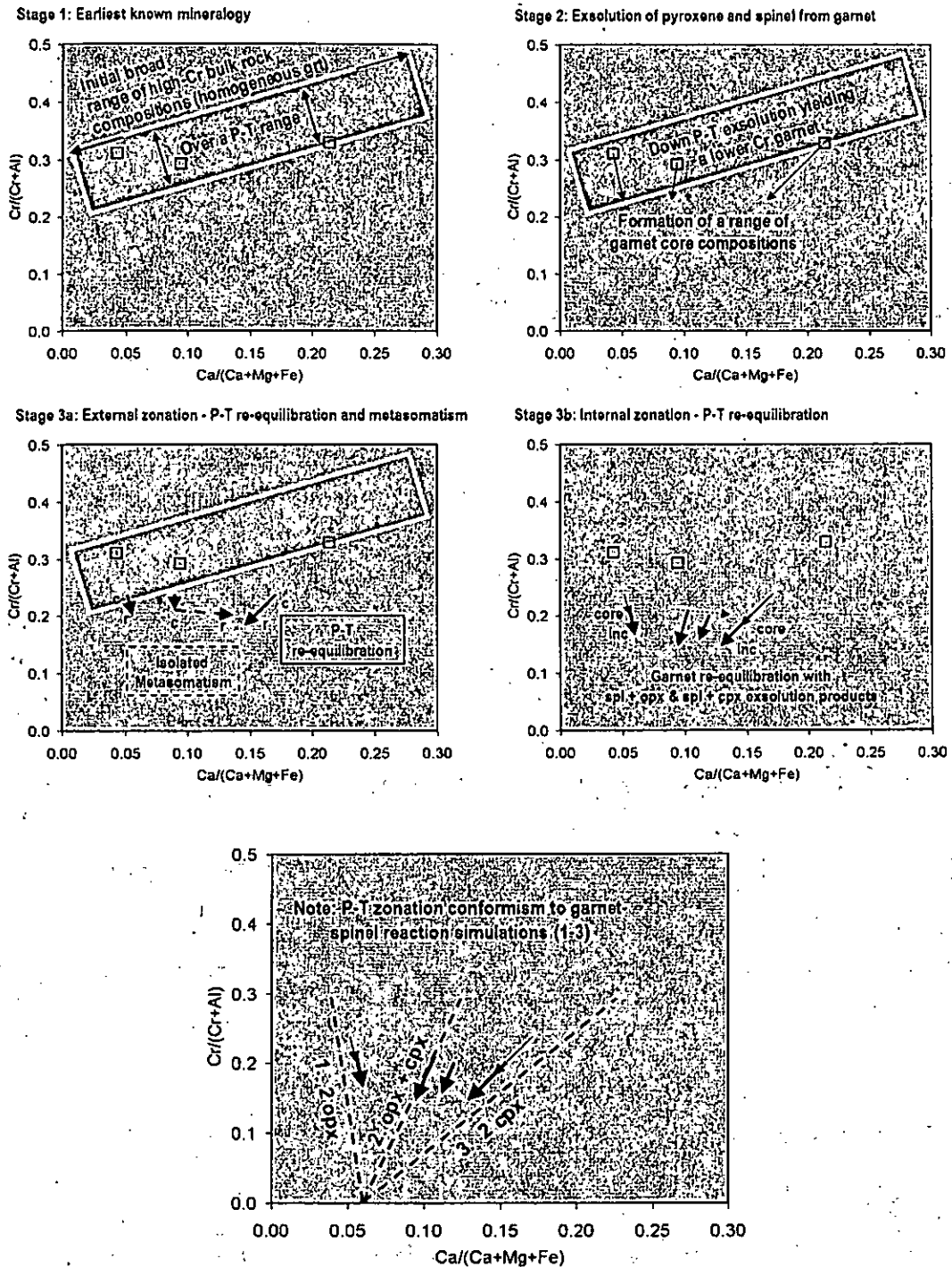


Figure 10.1: Illustrative $\text{Ca}/(\text{Ca}+\text{Mg}+\text{Fe})$ vs. $\text{Cr}/(\text{Cr}+\text{Al})$ plots for Stages 1-3b described above and below, applicable to the Newlands and Bobbejaan samples. Square symbols represent examples of three pre-exsolution bulk garnet compositions shown for reference. Note: it is assumed that metasomatism occurred at a later stage than external P-T re-equilibration during Stage 3a.

As with external P-T re-equilibration zonation, internal zonation follows very specific trajectories on a $\text{Ca}/(\text{Ca}+\text{Mg}+\text{Fe}_t)$ vs. $\text{Cr}/(\text{Cr}+\text{Al})$ plot (see Chapter 5). These form a continuum of trajectories (i.e. zonation types Is and Id) and conform to the down P-T sliding reactions (garnet-spinel transition reactions) as described in Chapter 6. Therefore this is interpreted as down P-T re-equilibration of garnet with its inclusions.

Geothermobarometry using existing formulations yield P-T estimates consistently a little higher using garnet cores rather than using garnet adjacent to inclusions (Chapter 7). And also P-T estimates from clinopyroxene inclusions and garnet adjacent to the clinopyroxene inclusion yield P-T estimates lower than both core and rim external P-T estimates. These indicate similar values to those of Stage 3a: a decrease of at least 40°C and 4kb (NEW303, Chapter 7) and possibly as high as 100°C and 6kb (see Perplex simulation for BOB402, Chapter 7). Diffusion distances indicate that internal re-equilibration was shorter lived (< 0.5 Ma) than external P-T re-equilibration (> 0.5Ma) and external metasomatic re-equilibration (~10Ma) (Chapter 8). It appears that this internal chemical modification could not be associated with the kimberlite magma itself since one would expect, in addition, to detect some diffusion towards the kelyphite rims of garnets of a similar magnitude and this is not the case. However uplift associated with kimberlite genesis cannot be ruled out (see gap with unknown time interval between kimberlite eruption and end of internal zonation event in Fig. 10.2).

Additionally, the REE in garnet and clinopyroxene are not thought to be significantly affected by the P-T re-equilibration since garnet zonation in REE is not detected in accordance with their proximity to inclusions. The samples do not appear to have been chemically modified again until kimberlite eruption – presumably because the closure temperature for diffusion had been crossed.

10.1.5 Stage 4: Kimberlite eruption

The age of the “Bellsbank” kimberlite eruption is 118 ± 2.8 Ma 2σ using a Rb-Sr isochron of kimberlite whole rock and phlogopite macrocrysts (Smith et al., 1985b). For the Newlands kimberlite an age of 114.1 ± 1.6 Ma 2σ is obtained (Smith et al., 1985b utilising the method as above). The effect of the kimberlite magma itself may be seen as micro- and macro-veining in samples and also as kelyphytic rims on garnet (see Chapter 3). The kimberlite mechanically disrupted the samples into predominantly monogranular garnet macrocrysts and was most probably the agent that retrogressed olivine and orthopyroxene by hydration into serpentine. The rapid decompression and cooling of the samples as xenoliths and xenocrysts within the kimberlite magma appears to have been fast enough not to have instigated any significant chemical diffusion in garnet, Cr-spinel or clinopyroxene, preserving the previous major and trace element chemical distribution in these minerals. Once near the surface the samples will have suffered hydrothermal alteration by carbonated fluids until the kimberlite dyke/blow had cooled to a shallow sub-surface temperature ($\ll 100^\circ\text{C}$). The samples will have been in the kimberlite host rock for a further ~ 100 Ma and will have been affected by the percolation of meteoric fluids until mining activity commenced.

10.1.6 Ages for the stages

There are few time markers for the stages of the history of the Newlands and Bobbejaan samples described above (see Fig. 10.2). Most recently there is the kimberlites' eruption ages over the period 112-121Ma (Smith et al., 1985b) and the dates for the Newlands peridotites themselves (conducted by Menzies, 2001 using Re-Os isotopes), which indicate a wide range of ages spanning from the Proterozoic (minimum $T_{\text{Rhenium depletion}} = 1.77\text{Ga}$) to the mid-Archæan (maximum $T_{\text{Model age}} = 3.52\text{Ga}$). The oldest T_{RDS} and T_{MAS} overlap with the 3.2-3.3Ga Sm-Nd and Rb-Sr model ages of Richardson et al. (1984) for diamond inclusion garnets.

Using the diffusion coefficient of Si in olivine at 1000°C (extrapolated from Dohem et al., 2002) as an upper limit for the diffusion of Cr in garnet, it is feasible that the samples remained at this temperature (i.e. post Stage 3b) for > 1.77Ga and up to 3.54Ga. Therefore the Menzies data may apply to the earliest stages of the formation of the samples in this study from Newlands (Bobbejaan peridotitic samples have not been analysed for Re-Os).

Fig 10.2 shows the time window for events observed in the Newlands and Bobbejaan samples (i.e. Stages 2-3b) and indicates that the age and overall time interval for the main down P-T events (i.e. exsolution and re-equilibration) and also metasomatism is not known. The age of these events could be close to the more ancient Stage 1 (pre-exsolution) or, equally, they could be close to the recent Stage 5 (kimberlitic). In terms of relative timings for these events, exsolution occurred in a pre-existing garnet and olivine-rich rock type and the garnets were relatively homogeneous (see section 10.1.1 and 10.1.2) but there is no handle on the time interval between the generation of the earliest known mineralogy and the start of exsolution.

Multiple inclusions of the same mineral within garnet are not significantly different in their compositions, therefore inclusion formation must have been occurring prior to the external P-T and metasomatic modifications. Since metasomatism is known, firstly, to predate internal P-T re-equilibration and, secondly, to occupy a time period greater than external P-T re-equilibration, it has to predate and post date external P-T re-equilibration (this is shown as a dotted line in Fig. 10.2 since it only affects a few samples). Internal P-T re-equilibration is known to post date metasomatic zonation from the clear geometry of chemical variation found in samples such as BOB113.

Age	3.52-1.77Ga ¹	??		??	-120Ma ²
Prograde Reactions					
Earliest known mineralogy					
Exsolution of pyroxene and spinel from garnet					
External zonation - P-T re-equilibration					
Metasomatism					
Internal zonation - P-T re-equilibration					
Past diffusion closure temperature					
Kimberlite eruption					
Mineralogy, texture and zonation (Px in harzburgites = Opx, in lherzolites = Cpx ± Opx)					
Cr-Ca in garnet					
REE in harzburgitic garnet REE in lherzolitic garnet					
P max T max P min T max	>65kb >1350°C > 50kb > 1100°C		<65kb <1350°C <50kb <1100°C	56kb 1250°C 44kb 1000°C	50kb 1150°C 38kb 900°C

Figure 10.2: Chronological summary of the events affecting Newlands and Bobbejaan samples.

¹Dating from Menzies (2001), ²dating from Smith et al. (1985b) (see text for discussion). The final max. and min. P-T values are derived from a final internal P-T estimates whereas pre-exsolution and pre-external P-T re-equilibration P-T values are indicative only and derived from Perplex modelling.

10.2 Wider Implications

The implications of the sequence of stages events described in the previous section (section 10.1) may be seen in a wider mantle-lithosphere context. With comparison to a wide range of previous research, there are some important links and disparities that should be highlighted as a final part to this thesis. Firstly the generation of the specific compositions of the samples shall be addressed, secondly the implications for the major down P-T and metasomatic events of Stages 2-3b, shall be discussed and finally the parts of this study relevant to diamond exploration shall be outlined.

10.2.1 Generation of the bulk rock major element compositions of Newlands and Bobbejaan samples

The events prior to the 'documented story' presented in this thesis remain unknown but several considerations may be made: Firstly, justifying the presence of a highly garnetiferous rock type is, itself, difficult to conceive in the upper mantle. The Cr-content of many of the samples is very high (see Chapter 4) and therefore the bulk rock requires a large melt extraction volume % since Cr is refractory and will be concentrated in a residue. Melt extraction in the spinel stability field would allow for a Cr-spinel to remain in the residue, enriching it significantly in Cr and Al.

Ringwood (1977) suggests the formation of an olivine, orthopyroxene, Cr-spinel cumulate in a large igneous plutonic rocks and Bulatov et al. (1977) suggest Cr-spinel harzburgite formation in an oceanic lithosphere setting. Many authors, e.g. Stachel et al. (2004) and Simon (2004), have also used 'ultra-depleted' aspects of trace element patterns in diamond inclusions and harzburgitic xenoliths (respectively) to justify the presence of an Archaean depletion event. Here there are possible links to komatiite formation in the Archaean, since there is abundant evidence for large volumes of these lava flows in Archaean greenstone belts (e.g. Viljoen and Viljoen, 1969), which would have created highly depleted residues in the upper mantle (e.g. Walter, 1998). These residues would be highly magnesian but the

extent of Cr-enrichment is unknown and dependent on whether garnet or spinel was fractionating in the source.

Bulatov et al. (1977) and Ringwood (1977) suggest subsequent burial of their depleted ultramafic rock types via subduction since this would be one mechanism that would allow this rock to be converted to a garnet-rich rock type at pressures at least those of the Al-peridotite spinel-garnet transition (15kb, 45km) for a typical continental geotherm and probably at considerably higher pressure if Cr/(Cr+Al) is high (Klemme, 2004). However, it may be possible to have a melt depletion event at deeper levels and negate the need for an extreme burial event altogether.

Harte et al. (1980) suggest a model for the generation of low-Ca, high Cr/Al and high Mg/Fe bulk rock compositions observed for peridotitic diamond inclusions via interaction with a melt. The melt hypothesised has a high CO₂ content which provides a mechanism for removing more CaO than with CO₂-absent melting. Thus in situ deep melting can account for the diamond-chromite-harzburgitic assemblage is feasible without need for direct subduction of lithosphere. However, this is not applicable to the lherzolithic compositions in the Newlands and Bobbejaan samples.

From the evidence preserved in the Newlands and Bobbejaan samples it is not possible to discern absolutely which of the above hypotheses is most applicable. Since the bulk rock compositions are so close to Cr-garnet + olivine, it is difficult to rule out a depletion event that left spinel or garnet in the residue and this could relate to komatiitic melt extraction events in the Archaean. Additional diversity of Ca compositions observed may be potentially be explained by subsequent and differential interaction with a CO₂-rich fluid which may also amplify the high Cr/Al and Mg/Fe ratios. The maximum P-T is expected to have been in excess of 65kb and 1350°C, therefore, unless initial depletion occurred at enormous depths, burial of some kind is required for the peak metamorphic mineral assemblage. A possible

mechanism for this would be a continental accretionary process, where lithosphere with >150km depth is formed relatively rapidly with a similar age for all depths (see models of Pearson, 1999). The Newlands and Bobbejaan samples would then represent further evidence for crust and mantle coupling in lithospheric roots for billions of years.

10.2.2 Generation of the bulk rock REE compositions of Newlands and Bobbejaan samples

The finding in Chapter 9 that the humped REE compositions of garnets in the Newlands and Bobbejaan samples are strongly dependent on Ca concentration in garnet allows a range of humped and normal REE profiles to be formed across a range of compositions in a single event. This potentially conflicts with a two-stage (i.e. bulk REE depletion + LREE enrichment) process, favored by many authors e.g. Stachel et al. (2004), and a single stage formation process requires some attention. One possible explanation is that the incorporation of REE (and other trace elements) into garnet occurred at the time of first formation of garnet as it crystallised from a series of melts of variable Ca/(Ca+Mg+Fe) ratio. Such a situation might arise in a model like that proposed in Hart et al. (1980) (see above) where a range of Ca compositions are produced under the influence of varying from a CO₂-content in the melts. Without further constraints, the origin and precise composition of this melt is not identifiable.

A second possibility is that the bulk rock attained an approximately 10 times chondrite REE concentration during initial melting in the spinel stability field (see last section, model of Ringwood, 1977), but the problem with this is that there is no known mineral in a spinel-peridotite that can contain sufficient HREE to explain the levels seen in garnets in the samples from this study. Therefore if a single stage formation of bulk rock REE concentrations is required, then a primary melting event would have to have been in the garnet stability field. Again from the evidence preserved in the Newlands and Bobbejaan samples it is not possible to discern absolutely which of the above hypotheses is most applicable.

10.2.3 Mantle evolution

Having discussed the chemical constitution of the samples the processes responsible for mantle decompression, cooling and metasomatism in the stages described section 10.1 must be addressed with any quantitative or qualitative constraints available placed upon them. With regard to the down P-T events, there are several possible explanations (mentioned at the end of Chapter 7) which are dependent on the duration of the observed events, for which some diffusion constraints exist (see Chapter 8). Therefore, the 0.5 – 5 Ma timescale for external P-T re-equilibration (Stage 3a, ~ 5kb = ~ 15 km uplift) would suggest a lower uplift rate of ~ 3 mm/year for a 5 Ma timescale and a higher uplift rate of 30 mm/year for a 0.5 Ma timescale. This rate of uplift may allow for an associated cooling along a geotherm of 100°C (i.e. 20°C/Ma for a 5 Ma timescale) if the longer timescale is used, resulting in an uplift that is not geologically instantaneous. Since Stages 2-4 are thought to be contiguous, this is most likely part of a longer lived (~10 Ma), down P-T event (see Fig. 10.2).

Such a continual decompression-with-cooling history expressed in these different ways (i.e. exsolution and major element zonations) has not been described for natural samples before. An uplift rate in the order of 3mm/year might be due to collisional tectonics, since these kinds of uplift rates have been observed in the recent geological past (e.g. associated with continent-continent collision in continental lower crustal granulites, Harley, 1989, and also uplift rates of > 6mm/year have been calculated in the Nanga Parbat syntaxis, Karakoram massif, NW Himalaya Treloar et al., 1991). If a 3mm/year uplift rate acted over the proposed 10Ma, then up to 30km total unroofing/erosion at the surface would be required. From the examination of the crustal cratonic rock units in southern Africa, it is known that assembly of the Kaapvaal craton was occurring in the late Archaean (De Wit et al., 1992). Re-Os dating of eclogitic diamond inclusion sulphides from kimberlites adjacent to the Colesberg magnetic lineament (Richardson et al., 2004) suggest multiple timings for diamond formation with the oldest at around 2.9Ga. The authors imply that these

diamond formation events were caused by upward migration of C-bearing fluids derived from subducted slabs of oceanic lithosphere just prior to continent-continent collision. The Colesberg magnetic lineament is thought to represent the suture zone between the eastern and western blocks of the Kaapvaal craton.

In terms of the metasomatism, which is only observed in a few samples from Newlands and Bobbejaan, it seems that this episode of chemical modification was not temporally distinct from the main down P-T event. Therefore this would conform to the diamond formation event described above with regard to syn-orogenesis timing and also the evidence for modification of the sub-continental lithospheric mantle by means of subduction-related fluids. Additionally, the Jagersfontein kimberlite pipe contains xenoliths that have abundant evidence for metasomatic modification (see Burgess, 1997; Burgess and Harte, 1999; Burgess and Harte, 2004) and this pipe is situated directly over the Colesberg lineament.

The study of Leost et al. (2003) highlights instances of diamond growth history (found in placer deposits in Namibia) that preserves the highest P-T inclusions closer to the core and successively lower P-T inclusion assemblages at their rims. That study documents a down P-T diamond growth history for eclogitic diamonds but would be in accordance with the syn-orogenesis, metasomatic event proposed here for the Newlands and Bobbejaan samples. The humped REE compositions of peridotitic diamond inclusion garnets (Shimizu and Richardson, 1987) would potentially result from encapsulation of the primary mineralogy and chemistry of Stage 1 with metasomatic modification occurring in isolated, non-encapsulated garnets only (Stage 3a).

10.2.4 Relationship of Newlands and Bobbejaan samples to diamond

One sample from this study was observed to contain diamond; it is the lowest Ca harzburgitic garnet of all the samples (BOB404) and it is from the Bobbejaan kimberlite. Therefore the harzburgitic connection is confirmed and the result

conforms to the study by Menzies (2001) where the diamondiferous samples from Newlands were predominantly of the harzburgitic paragenesis. Therefore, in the Newlands and Bobbejaan samples, high-Cr garnet without regard to Ca does not necessarily imply a strong correlation to diamond, whereas it is the high Cr AND low Ca garnet that does (Gurney and Switzer, 1973; Gurney, 1984). This conforms to the harzburgitic field in diamond facies (G10D) Grütter et al., 2006).

10.2.5 Implications for diamond exploration

A list of points concerning implications of this study for diamond exploration is as follows:

1. From Cr-Al partitioning between garnet and spinel (Fig. 7.7 and 7.9) and Perplex modelling (Fig. 7.12c and d) the garnet compositions that indicate equilibration in the diamond stability field are those with $\text{Cr}/(\text{Cr}+\text{Al}) > 0.2$ with accompanying low $\text{Ca}/(\text{Ca}+\text{Fe}+\text{Mg}) (< 0.3)$. This is predominantly found in high-Cr harzburgitic samples, i.e. those plotting in the G10D field (Gurney, 1984; Grütter et al., 2006).
2. The lherzolitic samples in this study tend to plot at too high temperatures for diamond stability, hence the presence of clinopyroxene tends to indicate higher temperatures of equilibration. However, along a continental geotherm, garnet $\text{Cr}/(\text{Cr}+\text{Al}) > 0.25$ and $\text{Ca}/(\text{Ca}+\text{Fe}+\text{Mg}) > 0.2$ with spinel $\text{Cr}/(\text{Cr}+\text{Al}) > 0.7$ should place minerals in the diamond stability field according to Perplex modelling.
3. A new finding from this study is that Cr-spinels from the lherzolitic paragenesis have lower $\text{Mg}/(\text{Mg}+\text{Fe})$ and higher Ti than the harzburgitic Cr-spinels, but they also have overlapping $\text{Cr}/(\text{Cr}+\text{Al})$ contents. Spinel compositions indicative of the diamond stability field are $\text{Cr}/(\text{Cr}+\text{Al}) > 0.75$ but also with high $\text{Mg}/(\text{Mg}+\text{Fe})$ ratios, and are again generally found in the harzburgitic samples. Therefore in terms of diamond exploration, if it is the harzburgitic diamond paragenesis that is sought, then one should place

particular importance on the high-Mg and lower Ti parts of the DI fields of Fipke et al. (1995) (see Fig.4.33a and b in Chapter 4).

4. Negative Clapeyron-sloped isopleths (Fig. 7.12c and d) show that an increase of temperature has the effect to increase garnet Cr/(Cr+Al) and Ca/(Ca+Fe+Mg) in lherzolitic samples and to increase Cr/(Cr+Al) in harzburgitic samples. Therefore knowledge of coexisting Cr-spinel compositions are useful because it generally has positively sloped isopleths for Cr/(Cr+Al) and should help to constrain the pressure of the garnet-spinel pair.
5. In Chapter 7 it is shown that Perplex computation of phase diagrams for peridotitic bulk rock compositions in CrCFMASNa may be used to generate petrogenetic grids from which P and T may be inferred for particular garnet, spinel and clinopyroxene mineral compositions. This may be applied to xenolith suites from kimberlites to see if diamond stability field mantle has been sampled.
6. In terms of P-T estimates (Chapter 7), Ni-in-garnet thermometry (Ryan et al., 1996), single garnet barometry (P38 in Grütter et al., 2006) and single clinopyroxene thermometry and barometry (Nimis and Taylor, 2000) do not predict pressures and temperatures with sufficient assurance to place significance on a verdict of whether the minerals equilibrated in the diamond stability field or the graphite stability field. It is the composition of coexisting minerals in equilibrium that allows tighter bounds to be placed upon both pressure and temperature (see relationship in Fig. 7.8). Therefore an approach for geothermobarometry that involves examination of polymineralic peridotite xenoliths is endorsed.

10.3 Further Work

10.3.1 Further work on the Newlands and Bobbejaan samples

The sample set for this study provides a wide range of peridotitic bulk rock compositions in terms of Cr/(Cr+Al) and Ca/(Ca+Fe+Mg), they provide an ideal means to assess both crystal chemical effects (such as the Ca-in-garnet effect on REE incorporation into garnet and pyroxene, see Chapter 9) and also particular aspects of mineral chemistry and phase relations in 4-phase (harzburgitic and wehrlitic) and 5-phase (lherzolitic) assemblages. The samples also provide evidence for a unique set of features representing a down P-T event.

Therefore further study of these samples is recommended for the following:

1. Further analysis of trace element compositions of garnet, Cr-spinel and clinopyroxene compared to Ca-in-garnet would widen the dataset generated in this study.
2. Use the full range of bulk rock compositions of the samples to calculate more petrogenetic grids using Perplex. Further testing of the accuracy of this method is required.
3. Isotopic data, especially Lu-Hf dating of the garnets, in the Newlands and Bobbejaan samples would be especially beneficial to the chronology of the down P-T event and metasomatism, relative to the Archaean formation time and the kimberlite eruption age.

10.3.2 Further work on lines of investigation generated by findings in this study

1. Since olivine and orthopyroxene major and trace element compositions are not known in this study it would be extremely interesting to find similar garnet-spinel-bearing samples (possibly from other kimberlites) that have fresh olivine and orthopyroxene to analyse. This would provide better P-T constraints and also establish phase relations more clearly.

2. In terms of the down P-T event, it would be very interesting if other xenoliths could be found in southern Africa that also document this type of history.
3. Further definition of the Ca-in-garnet effect on trace element compositions of garnet and clinopyroxene would be an interesting line of investigation to follow given the preliminary findings in this study (Chapter 9). It would be beneficial to find similar correlations in other peridotitic garnets from diamond inclusions and also from non-metasomatic xenolith samples.
4. The Perplex program should be further tested on natural samples (especially Cr-bearing peridotite xenoliths) for which independent geothermobarometry may be applied.

10.4 References

- Bulatov, V., Brey, G. P. and Foley, S. F. (1977). Origin of low-Ca, high-Cr garnets by recrystallization of low-pressure harzburgites. Second International Kimberlite Conference, Santa Fe, N.M.
- Burgess, S. R. (1997). The evolution of the sub-cratonic mantle seen in mantle xenoliths. Grant Institute of Earth Science. Edinburgh. University of Edinburgh. *Unpublished PhD*
- Burgess, S. R. and Harte, B. (1999). Tracing lithosphere evolution through the analysis of heterogeneous G9/G10 garnets in peridotite xenoliths, I: Major element chemistry. 7th International Kimberlite Conference, Cape Town, Red Roof Designs. 66-80.
- Burgess, S. R. and Harte, B. (2004). Tracing lithosphere evolution through the analysis of heterogeneous G9-G10 garnets in peridotite xenoliths, II: REE chemistry. *Journal of Petrology*. **45**. 609-634.
- De Wit, M. J., De Ronde, C. E. J., Tredoux, M., Roering, C., Hart, R. J., Armstrong, R. A., Green, R. W. E., Peberdy, E. and Hart, R. A. (1992). Formation of an Archaean continent. *Nature*. **357**. 553-562.
- Dohmen, R., Chakraborty, S. and Becker, H. S. (2002). Si and O diffusion in olivine and implications for characterizing plastic flow in the mantle. *Geophysical Research Letters*. **29**. 1-4.
- Fipke, C. E., Gurney, J. J. and Moore, R. O. (1995). Diamond exploration techniques emphasising indicator mineral geochemistry and Canadian examples. Geological Survey of Canada. **423**. 1-86.

- Grütter, H. S., Latti, D. and Menzies, A. H. (2006). Cr-saturation arrays in concentrate garnet compositions from kimberlite and their use in mantle barometry. *J. Petrology*. **47**. 801-820.
- Gurney, J. J. (1984). A correlation between garnets and diamonds in kimberlites. In: Ed. Glover, J. E., Harris, P. G. *Kimberlites: Occurrence and origin: A basis for conceptual models in exploration*. Perth, University of Western Australia, Extension Services. **8**. 143-166.
- Gurney, J. J. and Switzer, G. S. (1973). The Discovery of Garnets Closely Related to Diamonds in the Finsch Pipe, South Africa. *Contributions to Mineralogy & Petrology*. **39**. 103-116.
- Harley, S. L. (1989). The origins of granulites: a metamorphic perspective. *Geological Magazine*. **126**. 215-247.
- Harte, B., Gurney, J. J. and Harris, J. W. (1980). The formation of peridotite suite inclusions in diamonds. *Contributions to Mineralogy & Petrology*. **72**. 181-190.
- Klemme, S. (2004). The influence of Cr on the garnet-spinel transition in the Earth's mantle: experiments in the system MgO-Cr₂O₃-SiO₂ and thermodynamic modelling. *Lithos. Selected Papers from the Eighth International Kimberlite Conference. Volume 2: The J. Barry Hawthorne Volume*. **77**. 639-646.
- Leost, I., Stachel, T., Brey, G. P., Harris, J. W. and Ryabchikov, I. D. (2003). Diamond formation and source carbonation: mineral associations in diamonds from Namibia. *Contributions to Mineralogy and Petrology*. **145**. 15-24.
- Menzies, A. (2001). A detailed investigation into diamond-bearing xenoliths from Newlands kimberlite, South Africa. Department of Geological Sciences. Cape Town. University of Cape Town. *Unpublished PhD Thesis*
- Nimis, P. and Taylor, W. R. (2000). Single clinopyroxene thermobarometry for garnet peridotites. Part I. Calibration and testing of a Cr-in-Cpx barometer and an enstatite-in-Cpx thermometer. *Contributions to Mineralogy and Petrology*. **139**. 541-554.
- Pearson, D. G. (1999). The age of continental roots. *Lithos*. **48**. 171-194.
- Richardson, S. H., Gurney, J. J., Erlank, A. J. and Harris, J. W. (1984). Origin of diamonds in old enriched mantle. *Nature*. **310**. 198-202.
- Richardson, S. H., Shirey, S. B. and Harris, J. W. (2004). Episodic diamond genesis at Jwaneng, Botswana, and implications for Kaapvaal craton evolution. *Lithos*. **77**. 143-154.
- Ringwood, A. E. (1977). Synthesis of pyrope-knorringite solid solution series. *Earth and Planetary Science Letters*. **36**. 443-448.
- Ryan, C. G., Griffin, W. L. and Pearson, N. J. (1996). Garnet geotherms: Pressure-temperature data from Cr-pyrope garnet xenocrysts in volcanic rocks. *Journal of Geophysical Research*. **101**. 5611-5625.

- Shimizu, N. and Richardson, S. H. (1987). Trace element abundance patterns of garnet inclusions in peridotite-suite diamonds. *Geochimica et Cosmochimica Acta*. **51**. 755-758.
- Simon, N. S. C. (2004). The formation and modification of cratonic lithospheric roots: A petrological and geochemical study of xenoliths from the Kaapvaal craton. Department of isotope geochemistry. Amsterdam. Vrije Universiteit Amsterdam. *Unpublished PhD Thesis*
- Smith, C. B., Gurney, J. J., Skinner, E. M. W., Clement, C. R. and Ebrahim, N. (1985b). Geochemical character of southern African kimberlites: a new approach based on isotopic constraints. *Transactions of the Geological Society of South Africa*. **88**. 267-280.
- Stachel, T., Aulbach, S., Brey, G. P., Harris, J. W., Leost, I., Tappert, R. and Viljoen, K. S. F. (2004). The trace element composition of silicate inclusions in diamonds: a review. *Lithos*. **77**. 1-19.
- Treloar, P. J., Potts, G. J., Wheeler, J. and Rex, D. C. (1991). Structural evolution and asymmetric uplift of the Nanga Parbat syntaxis, Pakistan Himalaya. *International Journal of Earth Sciences*. **80**. 411-428.
- Viljoen, M. J. and Viljoen, R. P. (1969). Evidence for the existence of a mobile extrusive peridotitic magma from the Komati formation of the Onverwacht group. *Special Publication of the Geological Society of South Africa*. **2**. 27-112.
- Walter, M. J. (1998). Melting of garnet peridotite and the origin of komatiite and depleted lithosphere. *Journal of Petrology*. **39**. 29-60.

Appendix I: Analytical Techniques

For this project I used optical microscopy initially to examine the samples; further analysis was carried out on electron and ion microprobes. The following sections describe these in more detail with additional information provided in the last section on the preparation and use of a new chromite glass standard in ion microprobe analysis. In addition Appendix IV contains information on the scanning electron microprobe analysis of particular samples, which was used to test for garnet crystal orientation by applying the electron backscatter diffraction technique.

1.1 *Optical Microscopy*

Initially a binocular microscope was used with a 'goose neck lamp' to examine the range of features visible on the surface of intact and cracked samples. The mineral colouration, grain size, mineralogy and texture present was noted to provide context for more detailed investigations. The samples that were large enough to display textural features were preferentially selected for mounting and microanalysis. Heavy mineral concentrate was also examined in a glass dish under the microscope and the mantle phases were selected and sorted for mounting and electron microprobe analysis.

Once the selected samples were mounted and polished or made into polished thin sections they were examined using a reflected light microscope. The thin sections were also examined on a petrographic microscope in plane polarised and cross polarised light on a rotating stage providing information on the orientation of anisotropic minerals. At this stage photographs were taken of all the polished samples in reflected light. More detailed photographs were taken of the distinctive features visible and a catalogue of these thin section images was produced including both secondary (alteration-type features) and primary features.

Primary mineralogy and mineral modal abundance was recorded for all the polished samples along with mineral grain sizes. As far as possible polygranular samples were distinguished from monogranular ones (see Chapter 3) but those that were ambiguous were selected for mineral orientation analysis (see Appendix IV).

1.2 Electron Microprobe

Analysis was carried out on Cameca SX100 Electron Microprobe, School of GeoSciences, University of Edinburgh and was supervised primarily by Dr. Pete Hill. The instrument is part of EMMAC (Edinburgh Materials and Micro-Analysis Centre). A description of the sample mounting, electron microprobe beam and spectrometer setup and the standards used is as follows:

1.2.1 Mounting

The samples ranged in size from 2-60 mm (long axis) to approximately 2 mm (short axis). The larger samples (> 20 mm short axis) were cut to the size of a rectangular thin section (35 x 15 mm), or circular thin section (25.4 mm diameter) using a diamond studded saw, mounted on glass slide using araldite, ground to thickness of 50 μm on 40 μm , 20 μm , 10 μm , and 5 μm diamond studded laps. They were then polished using 3 μm , 1 μm , 0.3 μm diamond paste on motorised laps.

The medium sized samples (<20 mm short axis, > 2 mm long axis) and coarse concentrate grains were positioned directly onto lubricated base plate of 25.4 mm (1") round Teflon containers. Araldite poured onto samples and allowed to set on hot plate so that air bubbles escaped. Samples were cut using circular diamond studded saw to expose the plane of interest. Grinding and polishing as above.

The small samples (< 2 mm long axis) and fine concentrate grains were positioned directly into 2 mm holes in 25.4 mm diameter x 5 mm aluminium discs (20 holes per disc). Araldite was poured onto samples and allowed to set on hot plate so that air bubbles escaped. Grinding and polishing as above.

I.2.1.1 CARBON COATING

Carbon coating was used to prevent charging for samples inserted into the Electron Microprobe. All polished samples were carbon coated. Coating was carried out at high vacuum using current, through touching and sprung carbon rods (one sharp against the other blunt one). This was carried out at a distance of 250 mm, to generate carbon sputtering until a current of 0.5 A was attained across a glass slide tester. Aquadag (colloidal graphite) was applied to the edges of sample holders to allow conduction between sample and its metal holder.

I.2.2 Beam and spectrometer setup for EDS analysis

A beam current of 20 nA was used at 20 kV, accelerating voltage, in order to maximise counts whilst maintaining a small beam size of approximately 4-5 μm. A beam regulator is installed to insure that the current does not fluctuate during an analysis. Table I.1 shows the setup of the 5 spectrometers for EDS analysis (Energy Dispersive Spectrometry):

Spectrometer	1	2	3	4	5
Crystal	TAP	LPET	LLIF	LIF	LTAP
Pass 1	Si	K	Cr	Fe	Na
Pass 2	Al	Ca	Ni	-	Mg
Pass 3	-	Ti	Mn	(Zn)	-
Count Time per pass (s)	20	20	20	40	20
Bias (V)	1272	1890	1858	1276	1296
Gain	2482	1111	430	396	2597
Dead Time (μs)	3	3	3	3	3
Mode	Integral	Integral	Integral	Integral	Integral
Base Line (mV)	1842	1310	1266	785	2469
Window (mV)	3608	2548	1638	2548	2250
Count Preset	2.15E9	2.15E9	2.15E9	2.15E9	2.15E9

Table I.1: Spectrometer setup, Zn was measured for certain chromite analyses on spectrometer 4 using LIF crystal.

In house standards were used for all elements to be analysed and a calibration was made for every 4 days of analysis, as well as at the start of an analysis session if it had been more than 1 week since the previous calibration for 20ηA and 20 KV.

Table I.2 summarises the calibration setup.

Standard name	Standard type	Element	Spectrometer	Crystal	Background Offset (-)	Background Offset (+)	Peak Time (s)	Bg Time	Scanning
SiK3	Wollastonite	Si	1	TAP	none	750	20	10	off
SiK3	Wollastonite	Si	5	LTAP	none	750	20	10	off
SiK3	Wollastonite	Ca	2	LPET	none	750	20	10	off
AlK2	Corundum	Al	1	TAP	none	750	20	10	off
TiK2	Rutile	Ti	2	LPET	-1000	None	20	10	off
CrK1	Cr-metal	Cr	3	LLIF	none	750	20	10	off
NiK1	Ni-metal	Ni	3	LLIF	none	750	20	10	off
MnK1	Mn-metal	Mn	3	LLIF	none	1000	20	10	off
FeK1	Fe-metal	Fe	4	LIF	none	1000	40	20	off
ZnK1	Zn-metal	Zn	4	LIF	none	1000	20	10	off
MgK3	SJI Olivine	Mg	5	LTAP	none	1250	20	10	off
NaK3	Jadeite	Na	5	LTAP	none	750	20	10	10μm
KK3	Orthoclase	K	2	LPET	none	1000	20	10	10μm

Table I.2: Calibration standards summary. The standard name comprises the element, line and concentration e.g. MgK2 refers to the magnesium standard, K line with the second highest concentration of Mg i.e. olivine rather than periclase, which would be MgK1 for the latter.

During a routine analysis session the spectrometer positioning was verified on the andradite standard and a St. John's Island olivine standard was analysed periodically (both at least twice a day). This enabled a check to be made on Mg analysis because it was most susceptible to small instrument fluctuations. An andradite was also analysed occasionally to check that no major fluctuations occurred on each of the spectrometers.

I.2.3 Error statistics and lower limit of detection

Equations and explanations in this section are similar to those of Burgess (1997).

$$\%Error = \frac{100}{\sqrt{T} \left((\sqrt{R_p}) - (\sqrt{R_b}) \right)}$$

where T is the count time on peak on the sample, R_p counts per second on peak on the sample, R_b counts per second on background. Typical error, calculated using the above equation, for point analysis of garnet, clinopyroxene and Cr-Spinel, at 20nA, are given in Table I.3. Error is typically indistinguishable from the symbols plotted in graphs from Chapters 4 and 5. Absolute values for precision vary depending on the phase and the abundance of an element in that phase. Actual precision is certainly worse than the ideal precision calculated from counting statistics. This is because of the role of other errors in the analysis process. Analysis repeatability indicates a relative standard deviation of <1% for major elements (> 1 wt. % oxide) and < 5 % for minor elements (<1 wt. % oxide.).

In addition, the theoretical detection limit can also be calculated from counting times and count rates for typical elemental concentrations in the minerals analysed.

$$\text{Detection Limit at a } 2\sigma \text{ confidence level} = \frac{3}{m} \sqrt{\frac{R_b}{T_b}}$$

Where, m = cts/sec/% element in the standard material, R_b = the background count rate (cts/sec) and T_b = the count time on background. The factor m is calculated using the count rates obtained on the standard of the element in question. This is done instead of using the count rates obtained on the unknown, because of the very poor precision resulting from the low count rates involved. Detection limits for elements, calculated with the above equation, for individual point analysis of garnet, clinopyroxene and Cr-spinel are given in Table I.3.

The lower limit of detectability (LLD) is defined by the relationship:

$$\text{LLD} = (6/m) * (R/T)^{1/2}$$

where: $R = R_B + R_P$ (and R_B, R_P are Background and Peak *counts per second* on the sample respectively), $T = T_B + T_P$ (and T_B, T_P are Background and Peak *counting times* on the sample respectively), $m = (R_P - R_B)/\text{concentration (in wt\%)}$. LLD for elements, calculated with the above equation, for individual point analysis of garnet, clinopyroxene and Cr-spinel are given in Table I.3.

Oxide	Detection limit (wt. % oxide)			Lower limit of detectability (wt. % oxide)			% Error or relative standard deviation (2 σ)		
	Grt	Cpx	Chr	Grt	Cpx	Chr	Grt	Cpx	Chr
SiO ₂	0.009	0.010	0.010	0.099	0.112	0.003	0.04	0.04	0.53
TiO ₂	0.038	0.036	0.046	0.007	0.003	0.012	0.15	0.36	0.07
Al ₂ O ₃	0.008	0.007	0.008	0.057	0.015	0.038	0.08	0.28	0.14
Cr ₂ O ₃	0.014	0.012	0.020	0.070	0.027	0.136	0.09	0.24	0.04
FeO	0.018	0.011	0.023	0.051	0.029	0.084	0.09	0.17	0.05
MnO	0.012	0.015	0.015	0.012	0.005	0.010	0.35	0.65	0.37
MgO	0.005	0.005	0.005	0.037	0.039	0.035	0.04	0.04	0.06
CaO	0.031	0.033	0.031	0.026	0.038	0.001	0.04	0.03	0.42
Na ₂ O	0.007	0.007	0.007	0.002	0.014	0.001	0.70	0.18	0.91
K ₂ O	0.006	0.005	0.007	0.001	0.002	0.001	0.76	0.52	0.64
NiO	0.014	0.013	0.016	0.001	0.002	0.004	0.67	0.60	0.44
(ZnO)	0.018	0.016	0.019	0.004	0.005	0.008	0.76	0.82	0.61

Table I.3: Detection limits, lower limits of detectability and errors for the various oxides in garnet (grt), clinopyroxene (cpx) and chromite (chr) based on electron microprobe counting statistics for typical analysis.

1.2.4 Point analyses

Point analyses were used for analysis of the kimberlite concentrate where only one or two points were required for each grain. These analyses could be queued up with x, y and z co-ordinates stored for each point. Approximately 2 % of these points produced bad analyses because of unseen flaws in the surface or incorrect stage adjustment. The concentrate analyses may be found in their entirety in Appendix X. Appendix II contains summary tables of coexisting mineral compositions in samples.

1.2.5 Traverses

Automatic traverses were used to analyse a series of points with even spacing along a straight line of interest on a sample surface. The focussing was graduated evenly from the start point to the end point, to counteract sample loading tilt. Approximately 15 % of these traverse points produced bad analyses with low/high totals, because the automatically selected location happened to be in a crack or pit within the sample. These analyses were discarded by inspection afterwards without losing the

spatial distance along the traverse. Appendix II contains graphs of the traverses and Appendix X contains all traverse data in spreadsheet form.

1.2.6 X-ray mapping (EDS)

The X-ray mapping technique is a qualitative mode of analysis that records the counts per second intensities of particular elements (one per spectrometer per pass) as the stage moves underneath a fixed beam to generate a series of transects. This allows a 2-dimensional picture of pixels to be made up, with each pixel recording integrated X-ray counts that can be assigned a particular colour or brightness based on a spectral chart. The scaling can then be changed so that particular parts of the spectrum of counts can be emphasised.

A variety of setups were used for X-ray mapping of samples, depending on the desired elements to be analysed and the sensitivity to be achieved (summarised in Table I.3). The spectrometer positioning was verified on the andradite standard before each mapping session.

	Spectrometer	1	2	3	4	5
Setup 4: Increased Ti sensitivity	Crystal	PET	LPET	LLIF	TAP	LTAP
	Element	Ti	Ca	Cr	Al	Mg
Setup 3: Lower performance found with PET on Spec. 4	Crystal	TAP	LPET	LLIF	PET	LTAP
	Element	Al	Ca	Cr	Ti	Mg
Setup 2: LIF less effective than PET	Crystal	TAP	LPET	LLIF	LIF	LTAP
	Element	Al	Ca	Cr	Ti	Mg
Setup 1: Fe found not to vary	Crystal	TAP	LPET	LLIF	LIF	LTAP
	Element	Al	Ca	Cr	Fe	Mg

Table I.4: ray mapping spectrometer settings. Setup 4 was the setup that achieved the maximum count rates from each spectrometer given the concentrations of elements within the majority of the samples.

In order to setup an automated map of a sample, or part of a sample the maximum and minimum stage co-ordinates in x and y must be known and used to find the mid-point of a square or rectangular mapping zone. The focussing height of each corner of the zone must also be entered so that a 'four corner correction' can be used to correct for sample tilt. The, line length, points per line and number of lines must be selected to produce a zone with the correct dimensions. The dwell time and step

length must be chosen to produce a suitable density of data. Finally the stage is set to move underneath a fixed beam; this produces much more consistent data than a setup where the beam is allowed to scan across the zone with a fixed stage, which introduces variable beam intensity at different positions on the sample surface. Table I.4 summarises the variety of beam and analytical conditions utilised for X-ray mapping. Appendix III contains all successful maps with details of their specific setups.

	Minimum	Normal	Maximum
Beam current	50nA	100nA	100nA
Accelerating voltage	20KV	20KV	20KV
Dwell time per pixel	50ms	100ms	200ms
Step (μm)	4 μm	10 μm	25 μm
Line length (μm)	2048 μm	5120 μm	12800 μm
Points per line	512	512	640
No. of lines	210	384	512

Table I.5: Summary of the range of parameters utilised for X-Ray mapping.

1.2.7 Other EMP techniques

WDS (Wavelength Dispersive Spectrometry). This technique provides a qualitative measurement of counts per second intensity vs. wavelength of X-rays generated from particular minerals. It was used to identify minerals rapidly, according to the relative amplitude of their major element peaks, prior to quantitative analysis if necessary.

BSE (Back-Scattered Electron) images of particular features in samples were acquired. Since the intensity of back-scattered electrons is proportional to the mean atomic number of the material, this approach enabled the imaging of the precise location of minerals in samples (e.g. Fig. 3.20, in sample B55, Chapter 3). Some Cr-spinels were zoned strongly to high-Cr rims which produces a higher intensity of backscatter than the more Al-rich core (Fig. 5.5, Chapter 5). The technique was also used to capture textural features and to provide maps for further microanalysis (used as navigational aids). Initial scanning for image composition was scanned at 0.5s for 320 x 240 pixels and the brightness and contrast set accordingly. Once composed, the

image was acquired for 30s at 1024 x 768 pixels and finally saved as a bitmap image file.

1.2.8 Data processing

For each quantitative analysis point, the software for the Cameca SX100 electron microprobe uses counts per second intensities for each of the elements analysed to calculate weight percent oxide concentrations based on the calibration file and using a 'PAP' correction. From these weight % oxide values, the number of cations within each mineral was calculated in a spreadsheet on a cation basis (i.e. so that cations summed to the number present in the formula of a given mineral). The number of charges was then summed assuming all Fe as Fe²⁺. Then the charges were corrected by creating the appropriate amount of Fe³⁺. The formulation follows Ryburn et al. (1975) using the formula (e.g. for clinopyroxenes with a 12 oxygen formula) where:

$$\text{Fe}^{3+} = 4 - (2\text{Si} + 2\text{Ti} + \text{Al} + \text{Cr}) + (\text{Na} + \text{K}) \quad \text{and} \quad \text{Fe}^{2+} = \text{Fe}^{\text{t}} - \text{Fe}^{3+}$$

This method was preferred to that of Droop (1987) because numbers of cations and oxygens are not removed away from their whole number values. However it was found that errors on the Si analyses (i.e. $\pm \sim 1$ wt. %) were enough to render the resultant Fe³⁺ and Fe²⁺ concentrations unreliable. Therefore all Fe was calculated as Fe²⁺ and the formula calculated to the formula sum of cations as described above. All analyses in Appendix II are shown with all Fe as FeO (i.e. Fe²⁺).

1.2.8.1 INCONSISTENCIES IN MINERAL FORMULAE CALCULATIONS

For garnet and spinel the mean weight percent totals are > 100 %, whereas clinopyroxenes yield on average just under 100 wt. % oxide totals since they have some Na and K of which minor amounts may be lost whilst under the beam.

For cation concentrations it is apparent that the different datasets present in Chapter 4 have been analysed using different electron microprobes and different beam and spectrometer setups. An example of the resultant cation site occupancy in garnet is shown below but similar inconsistencies exist for pyroxene and spinel as well. The

sites are theoretically occupied by the following cations (Deer et al. (1962)) with the formula unit total shown:

X site [8]: Ca^{2+} Fe^{2+} Mg^{2+} Mn^{2+} Ni^{2+} Na^+ Total 3 cations per formula unit

Y site [6]: Al^{3+} Cr^{3+} Fe^{3+} Ti^{4+} Total 2 cations per formula unit

Z site [4]: Si^{4+} Total 3 cations per formula unit

Therefore, in the X site, the sum of the main 2+ ions (Ca+Fe+Mg) should total just < 3, assuming small amounts of Mn and very low amounts of Ni and Na. In the Y site the sum of the 3+ ions Al and Cr should total just < 2 assuming small amounts of Fe^{3+} and Ti present. The Z site should be close to completely filled by Si (summing to 3 cations). Overall a cluster of garnet data should form a negatively sloping line passing through (or just below due to varying small amounts of Fe^{3+} and Mn) the ideal cation sum values of 3 (for 2+ ions) and 2 (for 3+ ions). The negative slope should be due to the presence of Fe^{3+} and also Na, since its substitution will cause lower 2+ and higher 3+ cation concentrations in order to compensate for its single charge.

Figure I.1 shows the difference in analyses from NWT sampling and analyses from this study, other Frank Smith data (from the Kimberlite Research Group (KRG), University of Cape Town) and data from Menzies (2001).

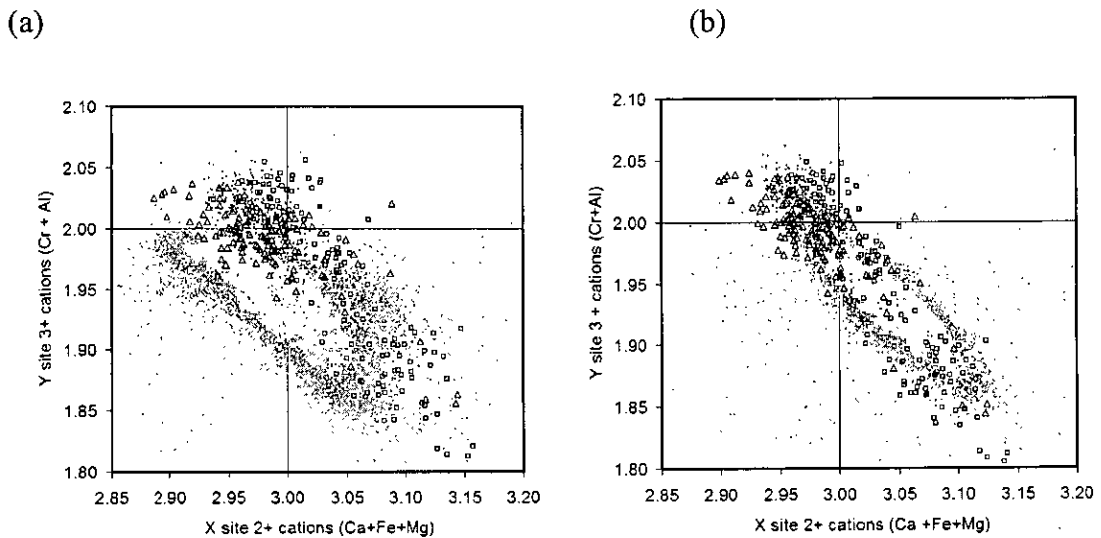


Figure I.1: (a) 3+ ions (Cr + Al) vs. 2+ ions (Ca + Mg + Fet) with the ideal 3 and 2 formula units shown as straight lines. Cations calculated on a 12 oxygen basis. Analyses from NWT till sampling (grey dots, cloud), this study (triangles), other KRG data (squares) and data from Menzies (2001) as black dots. (b) as for (a) except cations calculated on an 8 cation basis.

Calculation to 8 cations (Fig. I.1 b), rather than to 12 oxygens yields a better cross-dataset correlation with most data explained by the Fe and Na substitutions. The discrepancy in the NWT data using the 12 oxygen method (Fig. I.1a) appears mainly due to the higher Na values obtained in the analytical method used (see Chapter 4). Additionally the NWT dataset appears to have more points that lie far away from the general cluster of data. These are likely to be the result of using unfiltered data that has not had bad analysis points removed.

1.3 Ion Microprobe (SIMS)

Analyses of Newlands and Bobbejaan samples for trace elements was carried out on the Cameca IMS-4f Ion Microprobe using the SIMS (secondary ion mass spectrometry) technique. The instrument is part of EMMAC (Edinburgh Materials and Micro-Analysis Centre). The total analysis time for all desired elements required approximately 45 mins per analysis spot. Samples were analysed during 3 week-long sessions over the period 2004 to 2005 and analytical conditions are summarised in Table I.6.

	Session 1 - Light elements	Session 1 - Heavy elements	Session 2 - Ni	Session 3 - Transition elements
Elements	Li, Na, Si, K, ⁴⁶ Ca, Sc, Ti, Fe, Ni	Si, Sr, Y, Zr, Nb, Ba, REE, Hf	⁴⁷ Ti, ⁵⁷ Fe, ⁶⁰ Ni	Si, Ca, Sc, Ti, V, Cr, Fe, Mn, Ni, Ga, Sr, Y, Zr, Nb
Primary beam polarity	Negative	Negative	Negative	Negative
Primary ion beam	¹⁶ O ⁻	¹⁶ O ⁻	¹⁶ O ⁻	¹⁶ O ⁻
Net Accelerating voltage	15 keV	15 keV	15 keV	15 keV
Secondary Accelerating voltage	4.5 keV	4.5 keV	4.5 keV	4.5 keV
Beam current	10 nA	10 nA	10 nA	20 nA
Secondary beam polarity	Positive	Positive	Positive	Positive
Offset	~75 eV	~75 eV	0 eV	~75 eV
Energy window	40 eV	40 eV	40 eV	40 eV
Number of cycles	5	10	10	5
Count time per cycle	5s	10s	10s	5s
Deadtime	~12 ns	~12 ns	~12 ns	~12 ns
Glass Standards (frequency of analysis/day)	SRM610 (2)	SRM610 (2)	SRM610 (1)	SRM610 (1)
Garnet Standards	DDI (1) Shimizu (1)	DDI (1) Shimizu (1)	Diamantkop (2) DDI (2) Gore Mtn (2) LBM11 (2) MNAG (1) Spriggs 1 (2) Spriggs 2 (2) Spriggs 3 (2) PN (2) PN2A (2) PN2B (2) Shimizu (2)	DDI (1)
Clinopyroxene Standards	KH1 Kilburn Hole (1)	KH1 Kilburn Hole (1)	-	-
Chromite Standards	-	-	-	Bushveld: R1b (2), LG6 (1), M1 (1)

Table I.6: Ion Microprobe operating conditions and standards used for the four analysis setups.

Session 1 focussed on LILE (Large Ion Lithophile Elements), HFSE (High Field Strength Elements) and REE (Rare Earth Elements) within garnets and clinopyroxenes. Elemental concentrations were calculated by utilising relative ion yields that were determined using standards of known concentration. The method of

Hinton (1990) was employed and a 500 ppm trace element glass (SRM610) was analysed twice each day to calculate silicate ion yields. Concentrations were calculated using these ion yields and were checked periodically (twice daily) against standard garnet and clinopyroxene standards.

Session 2 was entirely used to establish a method for Ni analysis in garnet based on that carried out by Paula McDade in 2002 (McDade et al. (unpubl.)) using the Ni-in-garnet standard block housed at EMMAC. The Jagersfontein xenolith suite was studied with additional texturally equilibrated samples from Matsoku. Spots analysed for the Newlands and Bobbejaan samples were chosen to be close to those analysed in Session 1. See I.3.2 for further details.

Session 3 was devoted to the transition and high field strength element analysis of Cr-spinels, making use of a chromite standard developed for this purpose (see last section in Appendix I for details). Garnet and clinopyroxene transition elements were also measured at adjacent locations to the other trace element analyses of session 1.

I.3.1 Procedure for routine trace element analysis

The procedure closely follows that of Harte and Kirkley (1997). Clean polished samples (see electron probe sample preparation) were coated with a 10 - 30 nm thick gold coat to prevent charging. Gold is also beneficial to use because it is removed quickly by the ion beam. It is also mono-isotopic, poorly ionising and of high mass (so as not to create species that cause interference for the vast majority of masses). The sample chamber vacuum was always between 10^{-8} to 10^{-9} mbar during analysis. A 10 μ A duoplasmatron O^- beam accelerated at 15 kV (impact energy) was used to sputter positively-charged atomic and molecular secondary species from an area 15 to 20 μ m in diameter (with a $\sim 5\mu$ m deep pit generated). The sample was maintained at a voltage of +4425 V, producing a voltage offset of 75 eV to ensure only high energy ions are measured. This procedure has the advantage of decreasing the matrix

effect and simplifies the correction procedures for molecular interferences (Hinton (1995)). A beam burn-in time of 30 s was used in all sessions for consistency.

Analytical uncertainties are typically: $\sim \pm 1\%$ or less for concentrations above 10 ppm; $\pm 10\text{-}15\%$ for concentrations in the range 1.0 to 0.1 ppm; and $\sim 50\%$ for concentrations of 0.01-0.005 ppm. Fig. I.2 shows the typical counting statistics errors for the normalised abundance of all elements analysed for garnet clinopyroxene and Cr-spinel. The lower limit of detection is essentially zero because no counts were registered for the mass 130.5 which was chosen for a blank.

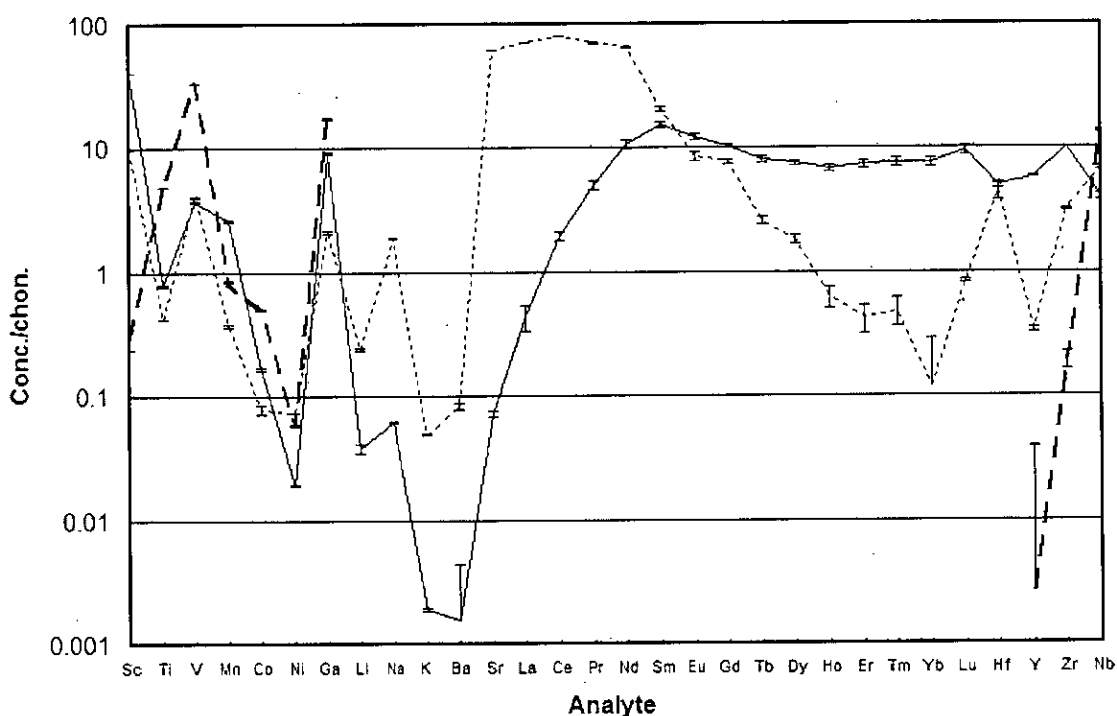


Figure I.2: 1σ above and 1σ below error bars are shown for each element measured in garnet (thin solid line), clinopyroxene (thin dashed line) and Cr-Spinel (bold dashed line) on a chondrite normalised plot.

I.3.2 Procedure for Ni-in garnet determination (McDade et al. (unpubl.))

I.3.2.1 ANALYTICAL CONDITIONS

Samples were coated with a 10 - 30 nm thick gold coat to prevent charging. A 7 nA O^+ beam accelerated at 15 kV was used to sputter positively-charged atomic and

molecular secondary species from an area 20 to 30 μm in diameter. The sample was maintained at a nominal voltage of +4500 V.

During many SIMS trace element analysis routines, a voltage offset (typically ~ 75 eV) is employed to ensure only high energy ions are measured. This procedure has the advantage of decreasing the matrix effect and simplifies the correction procedures for molecular interferences (Hinton (1995)), but it has the disadvantage of lowering count rates and thus reducing precision. In the present case we used zero energy offset (± 50 eV) and a high mass resolution ($m/\mu\text{m}$) of ~ 3000 to eliminate interferences. For this a $150\mu\text{m}$ image field and a contrast aperture number of 3 were employed. The entrance slits and exit slits were closed sufficiently to provide the appropriate mass resolution (see below).

The isotopes ^{60}Ni , ^{47}Ti and ^{57}Fe were measured on each of the standards and unknowns. Measurement of the Ti and Fe accompanying elements allows calculation of the relative ion yield (RIY) of Ni ($\text{RIY} = (\text{cps}/\text{conc})_{\text{standard}}^{\text{Ni}} / (\text{cps}/\text{conc})_{\text{standard}}^{\text{reference}}$). Using RIY elemental ratios rather than single element count-rates minimises any errors which may be introduced as a result of instrumental fluctuation, such as primary beam variation.

Iron and titanium were selected as suitable elements to ratio ^{60}Ni counts to for several reasons: i. Iron and titanium are present in sufficiently high concentrations to be accurately measured by electron microprobe and hence are independently quantifiable; ii. The chosen isotopes are present in sufficiently low concentrations as not to overload the electron multiplier; iii. ^{47}Ti and ^{57}Fe are resolvable under the analytical constraints ($m/\mu\text{m} \sim 3000$) required for accurate Ni determination; iv. Minimum movement of the magnetic field from the ^{60}Ni position is required to deflect ^{47}Ti and ^{57}Fe masses towards the electron multiplier and thus instrument instability is minimised; v. Titanium and iron ion yields were found to vary directly with their concentrations, as did ^{60}Ni , within the compositional range analysed.

Measurements were made in cycles where ^{47}Ti and ^{57}Fe counts were collected for 1 s, ^{60}Ni counts were collected for 5 s. Such cycles were repeated a minimum of 20 times for each analysis, with the number of cycles being increased for samples with lower Ni contents. Manipulation of the entrance and exit slits to the magnetic prism ensured that flat-topped peaks of each species were transmitted to the electron multiplier thus enabling accurate peak jumping during repeated cycling.

The use of zero voltage offsets in high-resolution ion microprobe analysis requires particularly careful attention to detect any potential interfering molecular species. This was facilitated by collection of mass spectrums at high mass resolution over ^{47}Ti , ^{57}Fe and ^{60}Ni peak positions (Fig. 1). Molecular species potentially capable of interfering with detection and measurement of the ^{47}Ti , ^{57}Fe and ^{60}Ni ions are listed in Table 1, along with their displacement from the relevant peaks in millimass units, and the resolution required to discriminate these molecular species from those of interest. In theory, the most difficult species to discriminate between are ^{57}Fe and $^{56}\text{Fe}^1\text{H}$, requiring a resolution of 7800. However, such very high mass resolution and accompanying reduction in count rate was avoided by extended (> 12 hours) pumping of the multi-sample airlock to high vacuum conditions in order to minimise the abundance of $^{56}\text{Fe}^1\text{H}$. Calculation of Ni concentration using Ti ion yields in addition to ^{57}Fe provided a secondary check that $^{56}\text{Fe}^1\text{H}$ interference was minimal.

1.3.2.2 CALIBRATION OF STANDARDS

Garnet standards, spanning a comparable major element compositional range to potential unknowns, were selected in an attempt to quantify and minimise the effect of garnet major element composition on Ni ion yield during ion microprobe analysis. Major element analysis of each of the garnet standard materials was undertaken at the Grant Institute of Earth Sciences, School of GeoSciences, University of Edinburgh using the Cameca Camebax electron microprobe. The analysis procedure utilised an accelerating potential of 20 kV, and a beam current of 25 nA. The count

time on K α peaks for each element was 30 s with backgrounds measured for 15 s. At least 20 analyses were made on each standard to ensure homogeneity.

The concentration of Ni in each of the standards was independently determined both by ICP-OES at the Department of Geology, University of Leicester and by laser ablation ICP-MS at the Department of Geological Sciences, University of Cape Town. Wet chemical analyses of standard materials were undertaken using a Philips PV 8060 ICP-OES. Complete dissolution of the sample (30 to 50 mg) was achieved by addition of hydrofluoric and perchloric acids, with the resultant solution being subjected to microwave digestion at 100 psi for 2 hours. Subsequent to digestion the samples were evaporated to dryness and taken up in a small volume of 10% HCl for analysis. High spatial resolution analyses were undertaken using a Perkin Elmer Elan 6000 ICP-MS attached to a Cetac LSX-200 laser. Each standard was analysed between 5 and 9 times. Only the standards for which the ICP-OES and LA-ICP-MS Ni estimates fell within 1 σ error were selected as suitable for ion microprobe calibration. Fig. II illustrates the calibration curve established. NOTE: intercept does not equal 0.

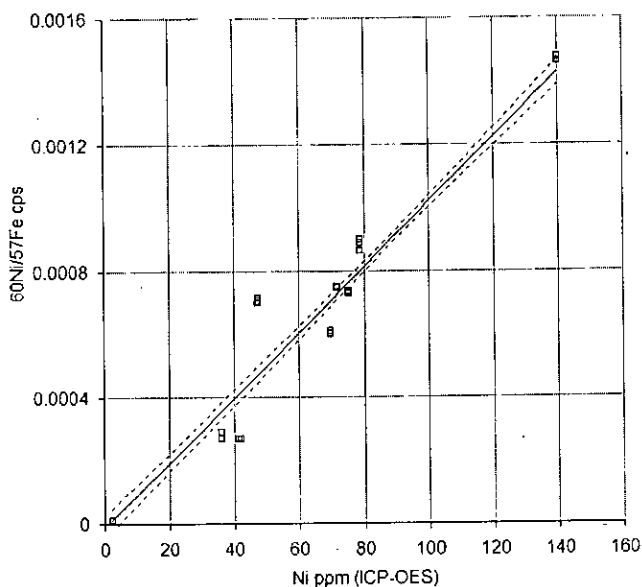


Figure 1.3: Calibration curve using garnet Ni standards for IMP Ni/Fe vs. Ni concentration established using ICP-OES analysis. Solid line is least squares best fit R^2 97.7 % with $\pm 1 \sigma$ un-weighted error on the best fit line shown as dashed lines.

Major element and cation compositions together with the Ni concentration for each garnet standard are compiled in Table 2, and their relative compositions are illustrated in Fig. 2 along with the Jagersfontein garnet compositions analysed in this study. The composition of the garnet standards ranged from Mg# ($\text{Mg}/(\text{Mg} + \text{Fe}^{2+})$) 0.48 to 0.83, and $\text{Ca}/(\text{Ca} + \text{Mg} + \text{Fe}^{2+})$ from 0.12 to 0.15. In addition to pyrope-rich compositions the non-peridotitic 'Gore Mountain' almandine garnet (Mg# 0.48, $\text{Ca}/(\text{Ca} + \text{Mg} + \text{Fe}^{2+})$ 0.12) was included to aid quantification of the matrix effect. However the effect was found to be small because Ni_{RIY}s from this sample did not deviate from those of the other garnets. The standard suite also includes garnet from LBM11, a peridotite xenolith from Matsoku, Lesotho. This xenolith, originally studied by Cox et al. (1973), has previously been subjected to proton microprobe Ni analysis by Griffin et al. (1989). Our Ni value (47 ± 3 ppm) falls within error of that proposed by Griffin et al. (1989) at 43 ± 4 ppm. Additionally, Griffin et al. (1989) reported the garnet rims from the high-temperature sheared peridotite PHN 1611 to contain 126 ± 11 ppm Ni. This concurs with our value of 130 ± 6 ppm demonstrating the reproducibility between proton and ion microprobe analysis.

A plot of Ni contents versus Ni_{RIY} produces a working curve (Fig. 3) from which the Ni content of unknowns can be determined. The reported Ni contents were primarily obtained using ion yields relative to ^{57}Fe rather than ^{47}Ti , since estimates of Fe content by EMPA are likely to be more accurate than those of Ti because of the higher concentrations of iron typically found in pyrope garnet. However Ti aided in more precise relative peak positioning on particularly low Ni samples, and always provided a secondary check on Fe ion yield calculations.

1.3.2.3 ENERGY DISTRIBUTIONS

During the course of the study analyses at varying energy offsets were also attempted, in order to examine whether the small deviation of standard data from the ideal working curve in Fig. 3 were the result of a matrix effect or natural compositional variation. The variation of ^{47}Ti , ^{57}Fe , and ^{60}Ni counts per second relative to sample voltage are illustrated in Fig. 4. The energy distribution profiles for

^{47}Ti , ^{57}Fe and ^{60}Ni are shown in Fig. 4. During ion microprobe analysis samples may accumulate a negative charge due to incomplete removal of O^- ions via conduction by the thin gold coat on the sample surface. This results in the shifting of the energy curves in Figure 4 towards the right, resulting in a loss of counts, and a change in the relative count rates of different species at high offsets (e.g. -50 volts or more). However the similarity in shape of the high energy ^{47}Ti , ^{57}Fe and ^{60}Ni ion profiles in Figure 4 shows close consistency in count rate ratios for the elements from zero offset up to ~ -30 V offset. This demonstrates that significant charging can be accommodated during analysis of the sample before significant loss of counts, and precision occurs. In many cases, particularly in the case of samples with $< \sim 40$ ppm Ni, the use of a voltage offset made it more difficult to calibrate the magnet accurately on the Ni peak prior to analysis during the peak-centring routine. Thus use of a voltage offset could, in cases, give a lower than expected Ni concentrations due to counts being collected 'off-peak'. Overall, the best estimates of Ni concentration in garnet were obtained using zero offset.

1.3.2.4 ACCURACY AND PRECISION OF Ni ANALYSES

Counting statistics were optimised by increasing the voltage across the electron multiplier prior to analysis, in order to obtain the maximum ^{60}Ni count-rate : voltage ratio from a particular sample. The standard error of the mean (1σ) on a typical 20 cycle analysis was found to be generally $< 1\%$ of the total counts. The detection limit for Ni in garnet was found to be less than 1 ppm.

ICP-OES analysis assumed a detection limit of 6 ppm, and an accuracy of $\pm 5\%$ determined from repeated analysis of W1 and JH1 international reference standards containing 75 and 56 ppm Ni respectively. These concentrations are comparable with typical Ni contents of peridotitic garnets. Errors on Fe and Ti contents in the garnet standards by electron microprobe are of the order of ± 0.10 and ± 0.01 wt% (3σ) respectively.

Overall the error for Ni determination in a typical garnet possessing 60 ppm Ni, utilising the standard working curve method illustrated in Fig. 3, would be $\sim \pm 3.5$

ppm Ni. This results in a temperature error of between 10 and 22°C depending on which Ni in garnet thermometer calibration is employed.

I.4 Chromite Standard Preparation and Use in Analysis

Chromite standard preparation took place in May 2003, October 2003 and March 2004. The IMP analysis session was in May 2004.

I.4.1 Standard material selection

The chromitite layers of the Bushveld Intrusion, RSA, were chosen as standards because of their abundance, major element homogeneity and relatively large grain size. Mantle Cr-spinels have grain sizes usually <0.5mm and are too rare in xenoliths to make a useful standard. Sample MR1 (R1b) is a 0.5 kg specimen from Ben Harte and Robin Lee (Univ. of Edin.) and was selected for high trace element content of bulk rock, which contains a 1cm undulose layer of chromitite grading into an orthopyroxene + minor plagioclase matrix. One block was used for the production of a polished mount (2.54cm disc) and a polished thin section of the same dimensions was borrowed from Robin Lee.

I.4.2 Chromite separation procedure:

The following steps (in note form) were followed to derive a pure chromite separate, which can be dissolved into a homogeneous glass. Problems encountered are indicated in sequence.

I.4.2.1 CRUSHING

- Saw cut R1b into 15mm slabs
- Drill blocks of chromitite richest in chromite out from rock sample
- Crush and pull out aggregates of chromite + plagioclase and chromite + orthopyroxene and crush so that they separate
- Crush further in WC (tungsten carbide) percussion mortar (steel base, cardboard shield) to 50 mesh size then sieve to recover -50+100, -100+200 and -200 mesh sizes

- Then examine to find the largest sieve size that contains essentially cleavage fragments only with minimal surface contamination
- Ultrasonic for 30 mins in D.I. water. Dry overnight at 50°C.

I.4.2.2 MAGNETIC SEPARATION

Magnetic separation to remove most non-chromite material from a crushed sample was undertaken on the Franz Isodynamic Separator, Model L1:

- Slope of 15°, an angle of sideways tilt 12°, a current 0.20 Amps
- Acid wash in HF overnight at 60°C to dissolve remaining non-chromite material and dry for 3 hours in evacuation chamber
- Hand pick any non-chromite fragments under microscope
- Sieve at 0.177 mm to remove undissolved pellets of plagioclase and orthopyroxene.

I.4.2.3 HEAVY LIQUID SEPARATION

Magnetically separated samples were further purified by use of heavy liquids:

- Diiodomethane (CH_2I_2) was not dense enough at 3.31 g/cc and would not differentiate composite orthopyroxene + minor chromite grains (~ 3.4 g/cc) from chromite only grains
- Pure chromite is 4.6 g/cc so if it is present in grains of orthopyroxene it will raise the particle's density
- Clerici's solution (a mixture of thallium formate ($\text{Tl}(\text{CHO}_2)$) and thallium malonate ($\text{Tl}(\text{C}_3\text{H}_3\text{O}_4)$) was used
- Dissolve Clerici crystals by heating glass bottle and adding DI water
- Pour into evaporating dish containing density tablets (3.8 g/cc, 3.9 g/cc and 4.04 g/cc) and graphite chips to sequester impurities
- Heat to evaporate water until solution density is 4 g/cc

- Put sample (~ 1 cc) and Clerici solution (30 ml) into pinched 50 ml test tube and agitate for 30 s so that light grains are liberated
- Place tube into centrifuge at 2000 rpm for 20 mins
- Insert teflon stopper into pinched part of tube and pour out light fraction into a filtered (50 μm) vacuum drainer whilst washing the tube with DI water
- Rinse stopper into collection flask with DI water
- Pour heavy fraction into separate filtered vacuum drainer and wash test tube and filter funnel thoroughly with DI water and subsequently acetone
- Remove filter funnels and dry on paper for 1 hour
- Examine under microscope for impurities (grains are charged and jump around)
- Re-evaporate Clerici wash to desired density

I.4.3 Fluxing Procedure (1)

Separated samples were then fluxed using the following procedure (chromite is particularly refractory so it requires a high flux:chromite ratio):

- Grind to flour sized particles in automated agate mortar
- Weigh out 0.3g packets
- Mix with ultrapure lithium tetraborate ($\text{Li}_2\text{B}_4\text{O}_7$) flux
- Fuse 0.015g sample with 1.5g flux at 1100°C for 20 mins in Pt crucible
- Pour onto metal plate and press into disc with metal weight
- Allow to cool on hotplate for 30 mins
- The result is chromite particles remain as fragments in green/brown glass
- This procedure left chromite residue at base of crucible.

1.4.4 Fluxing Procedure (2)

Parallel procedure run with 'Spec pure' SiO₂ in place of sample for use as a blank test hereafter called 'Si-blank'.

- Grind to flour sized particles in agate mortar
- Keep dry in oven at 100°C
- Measure 0.15 g sample into Pt crucible
- Mix thoroughly with
 - 0.15 g SiO₂
 - 0.075 g Na₂CO₃
 - 4.5 g Li₂B₄O₇/Li₂BO₂ (50:50 mix)
- Fuse at 1200°C for 30 mins
- Pour onto metal plate (200°C)
- Recover remaining drops from crucible
- Allow to cool on hotplate for 10 mins

The result is a low viscosity dark green glass with *no residue*

1.4.5 Solution procedure for ICPMS (boron removal required)

- Break glass disc R1b (and run parallel procedure for Si-blank) and select ~0.3g chip for dissolution
- Dissolve weighed chips in 9ml HF and 1ml HNO₃ for 5 hours on a hotplate and check there is no undissolved material, then dry and dissolve in ultrapure water.
- Prepare boron columns (following method of Tonarini et al. (1997)):
 - 0.3 ml Amberlite 743 (50 mesh) boron-specific ion-exchange resin loaded into Teflon columns (h = 20mm, r = 2mm), flow-rate adjusted to < 0.5ml/min
 - Clean twice with 5 ml 6M HCl

- Clean twice with 5 ml ultrapure water
- Condition with 2ml 3M NH₄OH and 3ml ultrapure water
- Dry samples for 24hrs

For REE analysis on TIMS, Y and Re standards were added so that the REEs are bracketed in terms of mass, thus allowing a check for the overall REE yield of the method. In order to concentrate the REEs, the dissolved sample was loaded into ion exchange columns and a light to middle REE elution and a HREE elution were collected, dried and dissolved in nitric acid. The samples were analysed using standard analytical procedure on TIMS at SUERC, East Kilbride. This yielded sub ppb REE concentrations and only ppb concentrations when multiplied up to gain the original pure chromite concentration. Therefore, this was deemed too low to provide viable regular analyses on most analytical instruments and certainly too low for use as a standard. Analysis was directed towards the transition elements.

1.4.6 Solution procedure for ICP-OES

- Break glass disc R1b (and run parallel procedure for Si-blank) and select ~ 0.3g chip. Dissolve in 10 ml 2% nitric acid
- Prepare 10ml of standards for grouped Co, Ca, Sr, Y, Zr, Nb, Hf in 2% nitric with 0.1, 1 and 10ppm concentrations
- Prepare 10ml of standards for grouped Cu, Sc, V, Ga, Ni, Zn, Mn in 2% nitric with 1, 10 and 100ppm concentrations
- Prepare 10ml of standards for grouped Fe, Cr in 2% nitric with 10, 100 and 500ppm concentrations.

The resultant solutions were run using standard procedure on ICP-OES (inductively coupled plasma optical emission spectrometer, School of Chemistry, University of Edinburgh) for analytes as listed in Table I.7. This used in house standards (Ca, Sc, V, Cr, Mn, Fe, Co, Ni, Cu, Zn, Ga, Y and Zr) as mentioned above to create working calibration curves. Sr, Nb, Hf were also analysed using standards supplied by SUERC. Zn and Ca were high in the Si-blank glass analysed in parallel with the standard itself on ICP-OES, therefore, reliable standard concentrations could not be

obtained for these elements. Hf, Sr, Sc returned anomalously high values in the glass standard, which is thought to be due to poor calibration curves on ICP-OES. Since this only concerns three elements and since development time on ICP-OES was not available due to staffing, this was not pursued further. Finally, the ppm values in the glass were multiplied up to yield ppm concentrations in the pure chromite from R1b, so that the chromite block itself could be used as a standard.

The chromite standard glass contained the following concentrations of trace elements as determined by ICP-OES (Table I.7):

Analyte	R1b Standard Glass (ppm)	R1b standard mineral (ppm)	Si-blank glass (ppm)
Ca	0.095	89.11	12.13
Co	0.301	282.35	5.36
Cr	309	289851	n.d.
Cu	0.179	168	n.d.
Fe	251.9	236289	n.d.
Ga	0.296	1225	24.56
Hf	1.306	2062	1.99
Mn	2.198	199.8	n.d.
Nb	0.213	1213.8	1.79
Ni	1.294	0.09	n.d.
Sc	n.d	n.d	n.d
Sr	n.d	n.d	0.18
V	2.034	1908	n.d.
Y	0.005	4.69	n.d.
Zn	1.266	1188	3205.34
Zr	0.01	9.38	3.42

Table I.7: Concentrations of standard glass, standard and Si-blank glass measured by ICP-OES.

1.4.7 SIMS analyses of spinel trace elements in standards and unknowns

The ion yields for transition elements in chromites are very close to the NIST610 glass (used for silicate analysis) and higher than the FeSi glass of Kilburn and Hinton (2001). This was checked using Ti, Cr, Mn, Fe values, since these were known independently. Therefore the 'matrix effect' for analysing Cr-spinels is negligible,

relative to garnet and pyroxene. The predominantly lithium tetraborate glass, which contained the standard material R1b, has not produced comparable ion yields and was not used to generate ion yield files. The standard block used contains large chromite grains that produced repeatable counts per second intensities within counting statistics error. Therefore counts per second per ppm were calculated in the R1b standard block so that the elements known from electron probe and ICP-OES analysis were faithfully reproduced. Cr was the primary normalisation element.

Zn and Cu have particularly high mass interference on SIMS and were not analysed in this ion microprobe study. Hf, Sr and Sc were analysed on SIMS without characterisation by ICP-OES. Therefore, these values have not been checked for reliability, since concentration in the standard was not known. For the unknowns an ion yield file was created, using the NIST SRM610 glass and counts per second intensities were converted to elemental wt. % ppm in unknown Cr-spinel grains from Newlands and Bobbejaan samples.

1.5 References

- Burgess, S. R. (1997). The evolution of the sub-cratonic mantle seen in mantle xenoliths. Grant Institute of Earth Science. Edinburgh. University of Edinburgh. *Unpublished PhD*
- Deer, W. A., Howie, R. A. and Zussman, J. (1962). *Rock Forming Minerals*. London, Longmans.
- Droop, G. T. R. (1987). A general equation for estimating Fe^{3+} concentrations in ferromagnesian silicates and oxides from microprobe analyses, using stoichiometric criteria. *Mineralogical Magazine*. **51**. 431-435.
- Harte, B. and Kirkley, M. B. (1997). Partitioning of trace elements between clinopyroxene and garnet: data from mantle eclogites. *Chemical Geology*. **136**. 1-24.
- Hinton, R. W. (1990). Ion microprobe trace element analysis of silicates: Measurement of multi-element glasses. *Chemical Geology*. **83**. 11-25.
- Hinton, R. W. (1995). Ion microprobe analysis in geology. In: Eds.: Potts, P. J., Bowles, J. F. W., Reed, S. J. B. and Cave, M. R. *Microprobe Techniques in Earth Sciences*. London, Chapman and Hall. 235-275.
- Kilburn, M. R. and Hinton, R. W. (2001). Relative ion yields for SIMS analysis of trace elements in metallic Fe, Fe-Si alloy, and FeSi. *International Journal of Mass Spectrometry*. **207**. 153-165.

McDade, P., Ivanic, T. J., Harte, B. and Burgess, S. R. (unpubl.). The effect of pressure on the Ni in garnet geothermometer: A SIMS study of the Jagersfontein mantle peridotites. *Journal of Petrology*. **Unpublished**.

Menzies, A. (2001). A detailed investigation into diamond-bearing xenoliths from Newlands kimberlite, South Africa. Department of Geological Sciences. Cape Town. University of Cape Town. *Unpublished PhD Thesis*

Ryburn, R. J., Råheim, A. and Green, D. H. (1975). Determination of P,T paths of natural eclogites during metamorphism - record of subduction. *Lithos*. **9**. 161-164.

Tonarini, S., Pennisi, M. and Leeman, W. P. (1997). Precise boron isotopic analysis of complex silicate (rock) samples using alkali carbonate fusion and ion-exchange separation. *Chemical Geology*. **142**. 129-137.

Appendix II: Summary Tables and EMPA Traverses*

(*see also data CD)

Contents:

Table II.1: Sample summary table with petrographic sample type, number of profiles, number of X-Ray maps and the type of internal and/or external zonation observed.

Table II.2: Sample zonation distances presented for Mg, Ca, Al, Cr, Ti, Fe and Mn with the type of profile according to definitions in Chapter 8.

Table II.3: Core-rim and inclusion garnet (and 2 clinopyroxenes in grey) compositions for the samples.

Table II.4: Coexisting mineral inclusions and their host garnet (adjacent to inclusions) compositions for the samples.

Traverses: Introduction to the traverses referring to the data CD (Appendix II):

Electron microprobe traverses across garnets, Cr-spinels and clinopyroxenes included on the data CD (see inside back cover)

Sample	Petrographic Class	Profiles	X-Ray Maps	External Zonation	Internal Zonation
N16	Ms	(1)	0	<i>Eu</i>	-
N23	M	(1)	0	<i>Eu</i>	-
N30	Ms	1	0	Eu	-
N87	Ps	(1)	0	-	-
N97	M	(1)	0	-	-
N158	Ms	(1)	0	-	Is
NEW003	M	2	1	Eu	-
NEW005	Ms	(1)	1	Eu	Is
NEW007	Pdsc	1	1	<i>Ed</i>	<i>Id</i>
NEW012	-	(1)	0	Eu	Ic
NEW014	-	1	0	Eu	-
NEW019	Msc	1	0	Eu	-
NEW022	-	(1)	0	Eu	-
NEW023	-	1	0	Eu	-
NEW024	Msc	2	1	<i>Eu</i>	Is, Ic
NEW025	Ms	1	0	Eu	-
NEW026	Msc	(1)	0	-	Is
NEW032	M	1	0	Eu	-
NEW038	Mc	1	0	Eu	-

Sample	Petrographic Class	Profiles	X-Ray Maps	External Zonation	Internal Zonation
NEW039	-	1	0	Eu	-
NEW042	Msc	(1)	0	Eu	-
NEW046	-	(1)	0	Eu	-
NEW047	M	1 (1)	1	Eu?	Is
NEW058	Mdc	(2)	0	Eu	Id
NEW059	Psc	1 (1)	.1	Eg	Is, Ic
NEW063	Pdcs	1 (1)	3	Ed	Id
NEW065	Mdsc	2	2	Eu	Id, Is
NEW068	Msd	1	0	Eu	Is
NEW069	Mc	2 (2)	1	-	Ic
NEW070	Ps	1 (1)	1	Eg	Is, Id
NEW071	Mds	1 (1)	0	Eu	Is
NEW073	-	(1)	0	Eu	-
NEW074	Msc	1 (1)	1	Eu	Is
NEW078	Mdc	1 (2)	2	-	Id
NEW079	Msc	(1)	0	Eu	Is
NEW083	Mc	1	1	Eu?	Ic
NEW086	Ms	(1)	0	Eu	Is
NEW088	Ps	1	0	Eu	Is
NEW094	-	1	0	Eu	-
NEW095	-	(1)	0	Eu	-
NEW096	-	(1)	0	?	-
NEW098	Msc	1	0	Eu	Is
NEW101	M	1	1	Eu	-
NEW107	Mdsc	1	0	Eu	-
NEW109	Msc	1	0	Eu	Is
NEW110	Ms	(1)	0	-	-
NEW111	Md	(1)	0	Eu	-
NEW114	Mdc	2 (1)	1	Eu	Id
NEW115	Mds	1	0	Eu	?Id
NEW119	Ms	(1)	0	?	?
NEW288	Mc	1 (1)	1	-	Ic
NEW301	Pgsc	1 (2)	1	Eg	Is
NEW302	Msc	2	0	Eu	Is
NEW303	Psd	1	1	Eu	Is
NEW307	Psd	(1)	1	Ed	Id

Sample	Petrographic Class	Profiles	X-Ray Maps	External Zonation	Internal Zonation
NEW308	Ps	(1)	1	Es	Is
NEW402	Ms	1	1	Eu	Is
NEW403	Ms	1	0	Eu	Is
NEW404	Ms	1	1	Eu	Is
NEW405	Ps	1	0	-	-
NEW406	Ms	1	0	Eu	Is
NEW407	Ps	1	0	-	-
NEW408	Ms	(1)	0	Eu	-
NEW409	Ms	(1)	0	Eu	-
NEW410	Ps	(1)	1	Es	-
NEW420	Pds	(1)	0	Es	-
NEW421	Pd	1	0	Ed	Id
NEW422	Ms	(1)	0	-	-
NEWOPX	Mgc	1 (2)	2	Eopx	-
NEWSP	Mdc	2 (1)	2	-	Id
LEI001	Mdc	(1)	1	-	Id
LEI002	M	(1)	0	-	-
LEI003	M	(1)	0	-	-
LEI004	M	(1)	0	-	-
LEI005	M	(1)	0	Eu	-
LEI006	M	(1)	0	Eu	-
LEI007	M	1	0	Eu	-
LEI008	M	(1)	0	-	-
LEI009	M	(1)	0	-	-
LEI010	M	(1)	0	Eu	-
LEI011	M	(1)	0	Eu	-
LEI012	M	(1)	0	-	-
B2	M	1	0	Eu?	?
B3	M	1	0	Eu	-
B4	M	(1)	0	-	-
B5	-	(1)	0	Eu	-
B44	Pds	1 (2)	1	Eg	Id
B48	Mdr.	1	1	Eu	-
B55	Mdcs	1 (2)	2	-	Id
B152	-	1	0	Eu	Is
BOB027	Ps	(1)	0	Es	-

Sample	Petrographic Class	Profiles	X-Ray Maps	External Zonation	Internal Zonation
BOB050	Ps	(1)	0	<i>Es</i>	-
BOB076	M	1	0	Eu	-
BOB113	Msc	3 (1)	2	Eu	Is
BOB167	Ps	(1)	1	Eu	Is
BOB168	Ps	1	0	-	-
BOB301	Mdsc	1	1	-	Id, Is, Ic
BOB304	Ms	(1)	1	-	<i>Is</i>
BOB305	Ps	(1)	0	<i>Es</i>	<i>Is</i>
BOB306	Mdc	(1)	0	Eu	<i>Id</i>
BOB307	Ps	(1)	0	<i>Es</i>	-
BOB308	Ps	(1)	0	<i>Es</i>	-
BOB401	Pdcs	1	2	Ed	Id
BOB402	Pdcs	1	2	Ed	Id
BOB403	Pdsc	1	0	Ed	Id
BOB404	Ms	1 (1)	1	Eu	Is
BOB405	Md	1	0	Eu	Id
BOBKIMB	Ps	(1)	1	Es	Is

Table II.1 All samples analysed for major elements indicating the petrographic classification from chapter 3, the number of traverses made in appendix II with the number on CD in brackets, the number of X-ray maps in appendix III, external and internal zonation types if evident. Italics indicate only a slight manifestation of zonation type and bold indicates strong manifestation of zonation type. '-' = observation not made.

Sample	Zonation Type	Profile Type (i.f. = inner flat)	Zonation Length Scale to the nearest analysis point (μm) (brackets denote internal zonation)						
			Mg	Ca	Al	Cr	Ti	Fe	Mn
N16	Eu	Rim Growth	1100	-	-	-	1100	1100	1100
N23	Eu		750	-	750	750	-	-	-
N30	Eu		~1000	~1000	1560	1560	-	-	1560
N87	-		-	-	-	-	-	-	-
N97	-		-	-	-	-	-	-	-
N158	Is		(250)	(250)	(250)	(250)	(-)	(-)	(-)
NEW003	Eu	Gradual change	2000	2000	2000	2000	2000	-	-
NEW005	Eu, Is		(500)	(-)	(770)	(770)	(-)	(-)	(-)
NEW007	Ed, Id	Internal i.f.	(500)	(500)	(500)	(500)	(-)	(-)	(-)
NEW012	Eu, Ic		(100)	(100)	(100)	(100)	(100)	(-)	(-)
NEW014	-		-	-	-	-	-	-	-
NEW019	Eu	Gradual change	2200	2200	-	-	-	-	-
NEW022	Eu		-	-	-	-	-	-	-
NEW023	Eu		580	580	580	580	-	580	-
NEW024	Eu, Ic	External i.f.	450	450	1490	1490	-	-	-
	Is	Internal i.f.	(-)	(250)	(-)	(250)	(-)	(-)	(-)
NEW025	Eu		-	-	800	800	-	-	-
NEW026	Is		(700)	(700)	(700)	(700)	(-)	(-)	(-)
NEW032	Eu	Rim Growth	1000	1000	1650	1650	-	-	-
NEW038	Eu	External i.f.	1100	1400	1400	1400	1400	-	-
NEW039	Eu	Rim Growth	800	1200	1000	1000	-	500	-
NEW041	Eu, Ic		-	-	800	800	-	-	-
NEW042	Eu		-	-	1200	1200	-	-	-
NEW046	Eu		1750	1750	1310	1310	-	-	-
NEW047	Eu?, Is	Rim Growth?	-	-	1200	1200	-	-	-
NEW058	Eu, Id		(130)	(-)	(-)	(100)	(-)	(-)	(-)
NEW059	Eg, Ic	External i.f.	-	-	500	500	-	-	-
	Is	Internal i.f.	(-)	(-)	(150)	(-)	(-)	(-)	(-)
NEW063	Ed, Id	External i.f.	1000	1000	500	500	400	800	-
NEW065	Eu, Is								
NEW068	Id,	Internal i.f.	(600)	(600)	(500)	(500)	(-)	(-)	(-)
	Eu	External i.f.	1250	1250	1250	1250	-	-	-
NEW069	Is	Gradual change	(900)	(900)	(900)	(900)	(-)	(-)	(-)
	Ic	External i.f.	(550)	(580)	(550)	(550)	(300)	(?)	(-)
NEW070	Eg, Id	Gradual change	(800)	(800)	(750)	(750)	(-)	(-)	(800)
NEW071	Eu, Is	Gradual change	(-)	(560)	(280)	(280)	(-)	(-)	(-)
NEW073	Eu		-	-	-	-	-	-	-
pto									

Sample	Zonation Type	Profile Type (i.f. = inner flat)	Zonation Length Scale to the nearest analysis point (μm) (brackets denote internal zonation)						
			Mg	Ca	Al	Cr	Ti	Fe	Mn
NEW074	Eu, Is	External i.f. Gradual change	2400 (800)	3200 (700)	>1000 (400)	>1000 (400)	3200 (700)	- (-)	1000 (500)
NEW078	Eu, Id	Internal i.f.	(500)	(420)	(350)	(320)	(250)	(-)	(-)
NEW079	Eu, Is		3000	3000	3000	3000	1000	1000	1000
NEW083	Eu?Ic	Gradual change	(500)	(500)	(500)	(500)	(-)	(-)	(-)
NEW086	Eu, Is		1500	-	1500	1500	-	-	-
NEW088	Eu, Is	External i.f.	-	-	1800	1800	-	-	-
NEW094	Eu	Outer flat	-	-	2000	2100	-	-	-
NEW095	Eu		-	-	-	500	-	-	-
NEW096	Eu		2500	-	-	2500	-	-	-
NEW098	Eu, Is	External i.f.	1100	1800	1700	1700	-	-	-
NEW101	Eu	Rim Growth	700	800	800	800	500	-	-
NEW107	Eu	Rim Growth?	700	700	800	800	-	-	-
NEW109	Eu, Is	Rim Growth - I & outer flat	-	1000	1500	1500	700	-	-
NEW110	-		-	-	-	-	-	150	-
NEW111	Eu		1000	1000	1000	1000	-	-	-
NEW114	Eu, Id	Internal i.f.	(1000)	(850)	(750)	(750)	(550)	-	-
NEW115	Eu	Rim growth	1500	1500	1500	1500	-	-	-
NEW119	-		-	-	-	-	-	-	-
NEW288	Ic	I & outer flat	(450)	(400)	(450)	(450)	(500)	(400)	-
NEW301	Eg, Is	External i.f.	1100	1100	1000	1000	-	-	-
NEW302	Eu, Is	Internal i.f.	-	-	-	-	-	-	-
NEW303	Eu Is	Gradual change Internal i.f.	- (-)	1000 (300)	1000 (300)	1000 (300)	- (-)	- (-)	- (-)
NEW307	Ed Id		(300)	-	(800)	(700)	-	-	-
NEW308	Es Is	External i.f. Internal i.f.	- (-)	1000 (500)	1000 (500)	1000 (500)	- (-)	- (-)	- (-)
NEW401	Is	Internal i.f.	-	(1400)	(550)	(550)	-	-	-
NEW402	Eu, Is	External i.f. Internal i.f.	1500 (-)	- (-)	- (1000)	- (1000)	- (-)	- (1000)	- (-)
NEW403	Eu, Is	External i.f.	2100	1800	1400	1500	-	-	-
NEW404	Eu Is	External i.f. Gradual change	2500 (700)	2500 (700)	2500 (700)	2500 (700)	- (-)	- (-)	- (-)
NEW405	-	Gradual change	-	-	-	-	-	-	-
NEW406	Eu Is	External i.f. Gradual change	1000 (200)	1000 (200)	500 (200)	700 (200)	1000 (1000)	-	-
pto									

Sample	Zonation Type	Profile Type (i.f. = inner flat)	Zonation Length Scale to the nearest analysis point (μm) (brackets denote internal zonation)						
			Mg	Ca	Al	Cr	Ti	Fe	Mn
NEW407	-		-	-	-	-	-	-	-
NEW408	Eu		1600	1600	1600	1600	-	-	-
NEW409	Eu		1000	-	1600	1600	-	-	-
NEW410	Es		1000	1000	1000	1000	-	-	-
NEW420	Es		-	-	-	-	-	-	-
NEW421	-		-	-	-	-	-	-	-
NEW422	-		-	-	-	-	-	-	-
NEWOPX	Eopx	External i.f.	300	300	200	200	300	300	300
NEWSP	Id	Internal i.f.	(1000)	(1200)	(1000)	(1000)	(1000)	(-)	(-)
LEI001	Id	Internal i.f.	(500)	(500)	(500)	(500)	(-)	(500)	(-)
LEI002	-		-	-	-	-	-	-	-
LEI003	-		-	-	-	-	-	-	-
LEI004	-		-	-	-	-	-	-	-
LEI005	Eu		500	500	-	-	-	-	-
LEI006	Eu		1000	-	700	500	-	500	-
LEI007	Eu	I & outer flat	950	750	900	950	900	-	800
LEI008	-		-	-	-	-	-	-	-
LEI009	-		-	-	-	-	-	-	-
LEI010	Eu		-	-	-	-	-	-	-
LEI011	Eu		-	-	500	500	-	500	-
LEI012	-		-	-	-	-	-	-	-
B2	Eu	External i.f.	2500	2500	2500	2500	-	-	-
B3	Eu	Rim Growth – core flat	1500	1500	1000	1000	-	-	1500
B4	-		-	-	-	-	-	-	-
B5	Eu		1000	1000	1000	1000	-	-	-
B44	Eg	Outer flat	-	2000	1500	1800	-	1000	1800
	Id	Gradual change	(-)	(500)	(800)	(800)	(500)	(500)	(500)
B47	Eu	External i.f.	2100	-	2000	2000	-	-	-
	Is	Gradual change	(-)	(-)	(1200)	(1200)	(-)	(-)	(-)
B48	Eu	External i.f.	4000	4000	3800	4200	-	1800	-
B55	Id	Gradual change	(-)	(700)	(500)	(500)	(500)	(-)	(-)
B152	Eu	Rim growth -	2000	2000	1600	1600	2000	-	-
	Is	core flat	(700)	(700)	(600)	(600)	(500)	(-)	(-)
		Gradual change							
BOB027	Es		-	-	-	-	-	-	-
BOB050	Es		-	-	-	-	-	-	-
BOB065	Es, Is		-	-	-	-	-	-	-
pto									

Sample	Zonation Type	Profile Type (i.f. = inner flat)	Zonation Length Scale to the nearest analysis point (μm) (brackets denote internal zonation)						
			Mg	Ca	Al	Cr	Ti	Fe	Mn
BOB076	Eu	Rim Growth	1600	1700	1800	1800	-	-	2500
BOB113	Eu	I & outer flat	2900	3400	500	800	3000	-	-
	Is	Internal i.f.	(300)	(300)	(400)	(400)	(400)	(-)	(-)
BOB167	Eu	Outer flat	-	-	4000	4000	-	-	-
	Is	Internal i.f.	(500)	(500)	(-)	(-)	(-)	(-)	(-)
BOB168	-		-	-	-	-	-	-	-
BOB301	Id,	Internal i.f.	(500)	(500)	(500)	(500)	(-)	(-)	(-)
	Is, Ic								
BOB304	Is		(700)	(-)	(500)	(-)	(-)	(-)	(-)
BOB305	Es, Is		-	-	-	-	-	-	-
BOB306	Eu, Id		2400	2400	2400	2400	-	-	-
BOB307	Es		-	-	-	-	-	-	-
BOB308	Es		-	-	-	-	-	-	-
BOB401	Ed	Outer flat	2300	2400	3000	3000	1000	2400	500
	Id	Internal i.f.	(500)	(500)	(500)	(500)	(-)	(-)	(-)
BOB402	Ed	Gradual change	1500	1500	1000	1000	-	-	-
	Id	Gradual change	(1000)	(1000)	(500)	(500)	(500)	(500)	(-)
BOB403	Ed, Id	Gradual change	(2000)	(2000)	(1500)	(1500)	(-)	(-)	(1500)
BOB404	Eu	External i.f.	4000	4000	2000	2000	-	-	-
	Is	Gradual change	(-)	(-)	(800)	(800)	(-)	(-)	(-)
BOB405	Eu	External i.f.	2300	2400	2100	2200	2000	2000	-
	Id	Internal i.f.	(500)	(700)	(300)	(500)	(-)	(500)	(-)
BOBKIM	Es		1000	-	1000	-	-	-	-
B	Is		(-)	(700)	(300)	(500)	(-)	(-)	(-)

Table II.2: All samples analysed for major elements indicating the external and internal zonation types present with the distance of any measurable diffusion type noted in μm for zoned major elements. Internal zonation is in brackets and on the same row as the particular zonation type listed.

	SiO ₂	Al ₂ O ₃	CaO	NO ₃	NO ₂	K ₂ O	Na ₂ O	Fe ₂ O ₃	MgO	MnO	Ca	Na	K	MMF	CCA	Al-Cr	Ca-Mg
BOB405 core	40.028	0.050	18.488	6.962	10.004	0.864	18.038	0.000	6.919	0.030	0.004	0.115	2.888	0.003	0.748	0.202	1.976
BOB405 inc	39.570	0.058	18.168	5.783	9.851	0.900	18.786	0.005	5.725	0.044	0.008	0.091	2.884	0.003	0.773	0.186	1.979
LE1001 homog	40.188	0.221	19.528	4.047	13.872	0.704	15.588	0.005	6.074	0.044	0.002	0.067	2.887	0.001	0.001	0.122	3.568
LE1002 homog	41.557	0.162	20.837	4.250	22.255	0.012	5.268	0.019	5.868	0.005	0.005	0.011	3.277	0.011	0.001	0.001	0.509
LE1003 homog	41.448	0.238	19.828	5.696	6.528	0.384	22.327	0.019	4.868	0.057	0.003	0.011	3.876	0.001	0.001	0.001	0.493
LE1004 core	40.849	0.209	21.352	2.237	13.204	0.609	18.084	0.638	4.568	0.067	0.006	0.006	1.021	0.002	0.001	0.001	0.308
LE1005 core	41.659	0.271	21.078	3.658	6.666	0.358	22.393	0.014	4.878	0.068	0.004	0.004	1.021	0.002	0.001	0.001	0.483
LE1006 rim	42.015	0.268	21.272	3.683	6.531	0.404	21.750	0.012	4.927	0.062	0.009	0.009	1.021	0.002	0.001	0.001	0.524
LE1008 core	41.362	0.084	18.310	6.423	6.531	0.404	21.750	0.012	4.927	0.062	0.009	0.009	1.021	0.002	0.001	0.001	0.524
LE1007 core	41.688	0.404	20.174	3.309	13.572	0.648	17.752	0.003	4.823	0.045	0.010	0.010	1.021	0.002	0.001	0.001	0.524
LE1009 rim	41.565	0.454	20.633	4.707	13.671	0.307	13.671	0.003	4.823	0.045	0.010	0.010	1.021	0.002	0.001	0.001	0.524
LE1008 homog	40.526	0.161	20.864	4.708	6.968	0.308	22.902	0.015	4.911	0.062	0.000	0.000	1.021	0.002	0.001	0.001	0.524
LE1010 homog	41.478	0.244	21.443	2.870	6.735	0.333	20.890	0.018	4.911	0.062	0.000	0.000	1.021	0.002	0.001	0.001	0.524
LE1011 homog	41.619	0.020	20.493	4.220	6.716	0.378	22.010	0.018	4.948	0.022	0.007	0.007	1.021	0.002	0.001	0.001	0.524
LE1012 homog	40.853	0.385	22.997	3.996	12.562	0.378	18.951	0.018	4.720	0.064	0.000	0.000	1.021	0.002	0.001	0.001	0.524
N158 homog	42.688	0.000	23.373	2.181	5.460	0.317	25.226	0.002	4.712	0.071	0.014	0.014	1.021	0.002	0.001	0.001	0.524
N18 homog	42.545	0.281	22.448	2.862	8.560	0.332	22.367	0.002	4.712	0.071	0.014	0.014	1.021	0.002	0.001	0.001	0.524
N30 core	42.525	0.000	19.812	7.811	5.357	0.304	26.181	0.000	4.712	0.071	0.014	0.014	1.021	0.002	0.001	0.001	0.524
N30 rim	42.525	0.000	19.812	7.811	5.357	0.304	26.181	0.000	4.712	0.071	0.014	0.014	1.021	0.002	0.001	0.001	0.524
N87 homog	41.907	0.000	20.072	6.891	8.200	0.357	25.286	0.002	4.712	0.071	0.014	0.014	1.021	0.002	0.001	0.001	0.524
N87 Aln Cr	42.052	0.000	20.072	6.891	8.200	0.357	25.286	0.002	4.712	0.071	0.014	0.014	1.021	0.002	0.001	0.001	0.524
N87 core	41.781	0.004	18.408	8.580	8.672	0.331	24.482	0.000	4.712	0.071	0.014	0.014	1.021	0.002	0.001	0.001	0.524
N87 rim	42.156	0.006	18.757	8.078	5.745	0.342	24.662	0.023	4.712	0.071	0.014	0.014	1.021	0.002	0.001	0.001	0.524
NEW003 core	40.823	0.241	14.887	12.424	5.278	0.350	20.745	0.014	6.285	0.066	0.004	0.004	1.021	0.002	0.001	0.001	0.524
NEW007 core	41.389	0.241	14.887	12.424	5.278	0.350	20.745	0.014	6.285	0.066	0.004	0.004	1.021	0.002	0.001	0.001	0.524
NEW007 rim	41.659	0.240	20.201	5.368	7.724	0.506	19.227	0.023	6.178	0.062	0.003	0.003	1.021	0.002	0.001	0.001	0.524
NEW012 core	40.181	0.049	18.702	8.033	8.685	0.610	17.852	0.017	7.227	0.023	0.003	0.003	1.021	0.002	0.001	0.001	0.524
NEW012 rim	40.840	0.055	18.643	5.722	8.815	0.659	18.351	0.011	6.612	0.033	0.013	0.013	1.021	0.002	0.001	0.001	0.524
NEW014 max cr	40.968	0.397	15.354	11.181	5.809	0.372	20.800	0.010	5.745	0.085	0.007	0.007	1.021	0.002	0.001	0.001	0.524
NEW014 min cr	39.963	0.398	15.296	10.884	5.825	0.376	20.800	0.010	5.745	0.085	0.007	0.007	1.021	0.002	0.001	0.001	0.524
NEW018 max cr	40.322	0.083	18.202	10.097	7.140	0.517	17.865	0.018	7.508	0.048	0.000	0.000	1.021	0.002	0.001	0.001	0.524
NEW018 min cr	41.343	0.068	18.582	7.325	7.117	0.491	19.061	0.013	6.482	0.037	0.003	0.003	1.021	0.002	0.001	0.001	0.524
NEW022 core	40.278	0.278	14.460	12.147	5.594	0.370	19.069	0.004	6.810	0.064	0.010	0.010	1.021	0.002	0.001	0.001	0.524
NEW023 core	41.342	0.000	19.128	6.884	8.984	0.508	20.038	0.011	6.193	0.012	0.000	0.000	1.021	0.002	0.001	0.001	0.524
NEW023 rim	41.024	0.007	18.708	6.998	6.968	0.505	18.620	0.001	6.528	0.027	0.005	0.005	1.021	0.002	0.001	0.001	0.524
NEW024 core	39.772	0.066	18.153	8.156	6.723	0.473	21.886	0.028	3.424	0.032	0.022	0.022	1.021	0.002	0.001	0.001	0.524
NEW024 inc	41.238	0.180	15.980	10.330	6.830	0.380	21.969	0.025	4.424	0.053	0.013	0.013	1.021	0.002	0.001	0.001	0.524
NEW025 core	42.032	0.170	18.844	9.747	5.783	0.369	22.231	0.025	4.356	0.043	0.013	0.013	1.021	0.002	0.001	0.001	0.524
NEW026 core	41.405	0.111	18.608	10.578	6.068	0.369	21.488	0.022	5.031	0.036	0.003	0.003	1.021	0.002	0.001	0.001	0.524
NEW026 inc	40.728	0.172	18.028	9.703	6.352	0.451	20.894	0.010	5.575	0.040	0.000	0.000	1.021	0.002	0.001	0.001	0.524
NEW032 core	41.075	0.178	18.284	10.482	8.231	0.347	21.141	0.033	4.301	0.068	0.008	0.008	1.021	0.002	0.001	0.001	0.524
NEW032 rim	41.075	0.178	18.284	10.482	8.231	0.347	21.141	0.033	4.301	0.068	0.008	0.008	1.021	0.002	0.001	0.001	0.524
NEW033 core	40.238	0.104	18.654	8.237	8.398	0.541	18.227	0.008	6.837	0.044	0.004	0.004	1.021	0.002	0.001	0.001	0.524
NEW033 rim	40.858	0.104	18.654	8.237	8.398	0.541	18.227	0.008	6.837	0.044	0.004	0.004	1.021	0.002	0.001	0.001	0.524
NEW038 core	40.748	0.538	15.179	11.487	5.845	0.355	19.794	0.018	6.189	0.095	0.012	0.012	1.021	0.002	0.001	0.001	0.524
NEW039 core	40.418	0.518	15.419	10.850	6.168	0.355	20.283	0.000	5.992	0.098	0.008	0.008	1.021	0.002	0.001	0.001	0.524
NEW041 core	41.090	0.255	15.960	10.915	5.352	0.351	21.569	0.000	4.418	0.045	0.000	0.000	1.021	0.002	0.001	0.001	0.524
NEW041 rim	41.227	0.144	16.060	10.728	5.352	0.372	21.429	0.016	4.418	0.045	0.000	0.000	1.021	0.002	0.001	0.001	0.524
NEW042 core	40.938	0.138	18.073	10.653	5.567	0.331	20.947	0.032	5.513	0.068	0.000	0.000	1.021	0.002	0.001	0.001	0.524
NEW042 rim	41.557	0.142	18.604	10.180	5.548	0.338	21.304	0.025	5.684	0.069	0.020	0.020	1.021	0.002	0.001	0.001	0.524

Table II.3: Core-rim and inclusion garnet (clinopyroxene with gray background) compositions for the Newlands and Bobbejan samples

	SiO ₂	TiO ₂	Al ₂ O ₃	Cr ₂ O ₃	FeO	MnO	MgO	NiO	CaO	Na ₂ O	K ₂ O	Total	Si	Al	Cr	Fe	Mn	Mg	Ni	Ca	Mg	Total	MMF	CCA	CCM	Al-Cr	Ca-Mg-Fe		
NEW046 core	41.529	0.053	16.507	7.732	5.331	0.430	18.655	0.018	5.164	0.049	0.008	98.961	3.004	0.578	0.442	0.395	0.026	2.120	0.001	0.423	0.007	0.001	8.0	0.843	0.219	0.144	2.020	2.838	
NEW046 rim	41.750	0.054	16.384	6.718	5.381	0.406	19.357	0.018	5.092	0.052	0.008	100.02	3.006	0.645	0.382	0.346	0.025	2.142	0.001	0.393	0.007	0.001	8.0	0.844	0.189	0.134	2.027	2.931	
NEW047 core	41.061	0.119	15.802	9.881	5.672	0.401	21.391	0.026	4.911	0.053	0.008	100.22	2.972	0.636	0.347	0.328	0.025	2.307	0.002	0.362	0.007	0.001	8.0	0.871	0.318	0.120	1.875	3.012	
NEW047 rim	41.272	0.127	16.599	9.884	5.683	0.370	21.502	0.012	4.811	0.059	0.012	100.10	2.978	0.607	0.411	0.363	0.023	2.313	0.001	0.356	0.005	0.001	8.0	0.871	0.289	0.118	1.974	3.012	
NEW058 core	40.963	0.265	16.534	10.473	5.648	0.376	21.278	0.025	5.288	0.074	0.003	101.021	2.937	0.614	0.388	0.338	0.023	2.273	0.001	0.410	0.012	0.000	8.0	0.870	0.289	0.136	1.990	3.022	
NEW058 rim	41.105	0.267	16.696	9.988	5.524	0.350	20.517	0.022	5.348	0.088	0.004	100.461	2.961	0.615	0.427	0.373	0.021	2.187	0.001	0.411	0.011	0.000	8.0	0.857	0.286	0.138	2.000	2.970	
NEW059 core	41.713	0.123	18.072	7.463	5.602	0.343	23.844	0.040	3.173	0.041	0.008	100.350	2.933	0.572	0.479	0.341	0.020	2.148	0.000	0.239	0.006	0.001	8.0	0.870	0.208	0.078	1.987	3.046	
NEW059 rim	40.513	0.620	14.961	11.121	7.235	0.450	18.018	0.019	7.862	0.081	0.007	101.250	2.968	0.584	0.279	0.394	0.020	2.587	0.002	0.235	0.007	0.001	8.0	0.860	0.203	0.076	1.941	3.064	
NEW063 core	40.746	0.168	17.020	7.761	5.632	0.343	18.103	0.032	7.822	0.078	0.007	101.250	2.968	0.584	0.279	0.394	0.020	2.587	0.002	0.235	0.007	0.001	8.0	0.860	0.203	0.076	1.941	3.064	
NEW063 rim	40.746	0.168	17.020	7.761	5.632	0.343	18.103	0.032	7.822	0.078	0.007	101.250	2.968	0.584	0.279	0.394	0.020	2.587	0.002	0.235	0.007	0.001	8.0	0.860	0.203	0.076	1.941	3.064	
NEW065 core	40.746	0.168	17.020	7.761	5.632	0.343	18.103	0.032	7.822	0.078	0.007	101.250	2.968	0.584	0.279	0.394	0.020	2.587	0.002	0.235	0.007	0.001	8.0	0.860	0.203	0.076	1.941	3.064	
NEW065 rim	40.746	0.168	17.020	7.761	5.632	0.343	18.103	0.032	7.822	0.078	0.007	101.250	2.968	0.584	0.279	0.394	0.020	2.587	0.002	0.235	0.007	0.001	8.0	0.860	0.203	0.076	1.941	3.064	
NEW068 core	41.637	0.088	18.855	7.230	7.106	0.479	18.288	0.001	6.210	0.041	0.011	100.165	3.022	0.603	0.373	0.623	0.023	1.979	0.000	0.498	0.006	0.000	8.0	0.862	0.162	0.205	1.987	3.018	
NEW068 rim	41.637	0.088	18.855	7.230	7.106	0.479	18.288	0.001	6.210	0.041	0.011	100.165	3.022	0.603	0.373	0.623	0.023	1.979	0.000	0.498	0.006	0.000	8.0	0.862	0.162	0.205	1.987	3.018	
NEW069 core	40.302	0.597	15.235	10.623	7.005	0.411	18.629	0.012	7.817	0.070	0.011	100.344	2.949	0.629	0.317	0.628	0.028	2.208	0.001	0.573	0.010	0.001	8.0	0.828	0.272	0.188	1.825	3.152	
NEW069 rim	39.571	0.458	15.478	9.179	7.005	0.428	20.529	0.012	7.817	0.070	0.011	100.344	2.949	0.629	0.317	0.628	0.028	2.208	0.001	0.573	0.010	0.001	8.0	0.828	0.272	0.188	1.825	3.152	
NEW070 core	41.848	0.106	19.042	9.918	6.265	0.347	22.455	0.010	3.909	0.030	0.000	101.444	2.935	0.608	0.487	0.503	0.022	2.371	0.001	0.297	0.004	0.001	8.0	0.865	0.253	0.098	1.990	3.039	
NEW070 rim	41.439	0.155	17.808	8.891	6.271	0.354	22.455	0.010	3.909	0.030	0.000	101.444	2.935	0.608	0.487	0.503	0.022	2.371	0.001	0.297	0.004	0.001	8.0	0.865	0.253	0.098	1.990	3.039	
NEW074 core	40.314	0.196	16.399	9.892	5.220	0.755	18.278	0.033	5.253	0.049	0.020	101.460	2.974	0.615	0.517	0.402	0.660	0.038	1.902	0.002	0.471	0.005	0.000	8.0	0.742	0.203	0.155	1.979	3.032
NEW074 rim	40.346	0.263	17.462	7.642	5.114	0.883	17.960	0.000	5.261	0.068	0.002	101.460	2.974	0.615	0.517	0.402	0.660	0.038	1.902	0.002	0.471	0.005	0.000	8.0	0.742	0.203	0.155	1.979	3.032
NEW078 core	40.825	0.241	17.529	8.822	6.531	0.380	22.968	0.010	3.063	0.010	0.000	100.200	2.966	0.613	0.265	0.372	0.698	0.035	1.865	0.000	0.416	0.010	0.001	8.0	0.736	0.186	0.141	1.997	2.949
NEW078 rim	40.825	0.241	17.529	8.822	6.531	0.380	22.968	0.010	3.063	0.010	0.000	100.200	2.966	0.613	0.265	0.372	0.698	0.035	1.865	0.000	0.416	0.010	0.001	8.0	0.736	0.186	0.141	1.997	2.949
NEW079 core	41.655	0.094	17.529	8.822	6.531	0.380	22.968	0.010	3.063	0.010	0.000	100.200	2.966	0.613	0.265	0.372	0.698	0.035	1.865	0.000	0.416	0.010	0.001	8.0	0.736	0.186	0.141	1.997	2.949
NEW079 rim	41.655	0.094	17.529	8.822	6.531	0.380	22.968	0.010	3.063	0.010	0.000	100.200	2.966	0.613	0.265	0.372	0.698	0.035	1.865	0.000	0.416	0.010	0.001	8.0	0.736	0.186	0.141	1.997	2.949
NEW083 core	40.891	0.114	16.448	10.246	6.543	0.348	21.465	0.016	4.561	0.044	0.007	100.005	2.985	0.607	0.421	0.561	0.021	2.323	0.001	0.345	0.007	0.000	8.0	0.873	0.268	0.118	1.932	3.039	
NEW083 rim	40.891	0.114	16.448	10.246	6.543	0.348	21.465	0.016	4.561	0.044	0.007	100.005	2.985	0.607	0.421	0.561	0.021	2.323	0.001	0.345	0.007	0.000	8.0	0.873	0.268	0.118	1.932	3.039	
NEW088 core	41.373	0.131	16.711	9.834	5.555	0.347	21.696	0.022	4.519	0.054	0.005	101.21	2.973	0.608	0.451	0.552	0.339	0.021	2.323	0.001	0.345	0.007	0.000	8.0	0.863	0.097	0.068	1.877	3.067
NEW088 rim	41.373	0.131	16.711	9.834	5.555	0.347	21.696	0.022	4.519	0.054	0.005	101.21	2.973	0.608	0.451	0.552	0.339	0.021	2.323	0.001	0.345	0.007	0.000	8.0	0.863	0.097	0.068	1.877	3.067
NEW089 core	41.197	0.222	21.431	3.447	6.425	0.371	22.666	0.025	3.960	0.068	0.000	99.844	2.984	0.612	0.722	0.383	0.021	2.398	0.000	0.300	0.008	0.000	8.0	0.863	0.120	0.100	1.956	3.107	
NEW089 rim	40.729	0.232	20.555	4.165	6.442	0.345	22.772	0.000	4.055	0.068	0.000	99.844	2.984	0.612	0.722	0.383	0.021	2.398	0.000	0.300	0.008	0.000	8.0	0.863	0.120	0.100	1.956	3.107	
NEW094 core	41.111	0.064	14.605	11.733	5.514	0.389	19.762	0.000	6.971	0.035	0.000	100.22	3.001	0.604	0.257	0.677	0.337	0.024	2.173	0.000	0.345	0.005	0.000	8.0	0.865	0.150	0.180	1.934	3.033
NEW094 rim	41.111	0.064	14.605	11.733	5.514	0.389	19.762	0.000	6.971	0.035	0.000	100.22	3.001	0.604	0.257	0.677	0.337	0.024	2.173	0.000	0.345	0.005	0.000	8.0	0.865	0.150	0.180	1.934	3.033
NEW094 core	41.111	0.064	14.605	11.733	5.514	0.389	19.762	0.000	6.971	0.035	0.000	100.22	3.001	0.604	0.257	0.677	0.337	0.024	2.173	0.000	0.345	0.005	0.000	8.0	0.865	0.150	0.180	1.934	3.033
NEW094 rim	41.111	0.064	14.605	11.733	5.514	0.389	19.762	0.000	6.971	0.035	0.000	100.22	3.001	0.604	0.257	0.677	0.337	0.024	2.173	0.000	0.345	0.005	0.000	8.0	0.865	0.150	0.180	1.934	3.033
NEW095 core	41.268	0.076	16.984	9.765	5.839	0.363	21.571	0.003	4.054	0.041	0.006	100.07	2.978	0.604	0.444	0.558	0.352	0.022	2.320	0.000	0.343	0.006	0.001	8.0	0.868	0.276	0.105	2.002	2.986
NEW095 rim	40.716	0.109	15.983	11.201	6.375	0.440	17.528	0.005	6.144	0.035	0.065	99.48	3.000	0.606	0.327	0.652	0.383	0.029	2.097	0.001	0.484	0.005	0.006	8.0	0.862	0.330	0.151	1.965	2.974
NEW096 core	41.823	0.089	16.070	10.600	6.937	0.440																							

II.1 Traverses

Garnet, chromite and clinopyroxene traverses are shown on the data CD with the different elements plotted on the y-axes (scale in cations, calculated by summing to 8 cations for garnet and clinopyroxene and 6 for Cr-spinel) and horizontal distance plotted on the x-axis (scale in μm , calculated from stage positions output from SX100 instrument). The entire numerical tabulation of each traverse, including their weight percent values, may also be found on the data CD. Garnet traverse profiles are presented in alphabetical order. Ti, Al, Cr, Fet, Mn, Mg, Ca and Na concentrations are graphed for garnet where iron is calculated as total iron (Fet). Si is not shown due to inaccuracies in its measurement. K, V, Zn and Ni concentrations are not shown as traverses due to their low abundance in garnet. Chromite profiles are graphed as for garnet without Na and with Zn when analysed. Clinopyroxene profiles have K in addition to the elements presented for garnet.

Due to cracking and kimberlite veining in the samples an average of ~20 % of the automated traverse analyses had to be discarded. These were distinguished by having high or low (> 102.0 and < 98.0 wt. %) analysis totals indicating a pit and high K_2O values (> 0.05 wt. %) indicating partial kimberlitic contamination of the analysis.

At the tops of the following pages are the sample names, the type of zonations observed (i.e. 'Id', 'Es' etc), the analysis spacings in μm and note as to whether there is an X-ray map of the samples. There is also a description of the parts of crystal analysed along the traverse in sequence e.g. 'Rim-core-rim' indicates that the traverse starts at the rim, goes through the centre of the mineral which may be, but is not necessarily, close to the true core and finishes at the opposite rim. 'Edge-inclusion-core' is used for monocranular samples containing inclusions and would indicate that the traverse started at the edge of the sample (in a garnet), passed over an inclusion and ended at a core-region of the garnet that is far from inclusions. Labels on graphs show the location in terms of horizontal distance of features such as rim, core and inclusions.

Appendix III: X-Ray Maps (see data CD)

Appendix I details the X-ray mapping technique itself. Each of the Corel Draw files in Appendix III (data CD) contains 4-5 maps of different elements and sometimes a backscattered electron map of a sample. Some maps are smaller scale and do not contain the whole sample and are referred to as 'zoom maps'. The locations of these smaller scale maps are shown on the whole sample maps if present. The locations of any profiles from Appendix II are also indicated on the maps. Additionally information as to the spectrometer setup for the maps are shown at the lower right of the pages. Note that samples displaying zonation in X-ray maps will tend to show greater variation than that measured by traverses because of the limited spatial coverage (i.e. one or two 1-D traverses per sample).

Appendix IV: EBSD Results

The EBSD (electron backscatter diffraction) technique was used on the SEM (scanning electron microscope) at University of Edinburgh. The purpose was to establish the number of garnet grains present in certain samples where the polygranular/monogranular sample type was ambiguous. i.e. if the garnet across the entire sample is oriented in one direction then it is deemed monogranular and if there are more than one orientations, polygranular.

The EBSD technique collects diffraction patterns from a highly polished sample surface. Selected samples were reground flat using a 20 μm diamond lap and 'Siton polished' for 6 minutes to produce a clean, flat and unscratched sample surface. Siton polishing chemically erodes the sample surface to create a flat crystal surface to generate well defined diffraction patterns. Samples were then placed into a holder and silver dag was applied to the edge of the sample and its contact with the holder to prevent charging.

The sample was placed into the SEM analysis chamber and a workable vacuum achieved. A pre-existing calibration was used for 20 mm distance from analysis spot to camera so the camera was positioned accordingly and the sample was brought into focus at 20 mm. Once the beam was placed onto suitable spots, the magnification was increased to 500 X and a background diffraction pattern was gathered whilst rotating the sample. Then a stationary diffraction pattern was gathered and the software told that the phase concerned is a pyrope garnet. The 'stationary' diffraction patterns are matched to those expected for an ideal pyrope garnet (model exists on software) and the best fit orientation is automatically recorded for each analysis point.

The number of analysis points per sample varied from 14 to 45 depending on the area of the garnet that was needed to be covered. Following are the stereonet plots of garnet {100} directions in individual samples. Since garnet is cubic, the (100) direction is identical crystallographically to (010) and (001) and so a single garnet orientation is represented by three clusters of points (there is about a 3° error with

this technique), two orientations by six clusters of points and three orientations by nine clusters of points. The number of data points on the right hand panel. The results are summarised in Table IV.1.

Sample	Number of garnet orientations present	Polygranular/monogranular designation
B55	1	Monogranular
BOB065	3	Polygranular
BOB113	1	Monogranular
BOB168	2	Polygranular
BOB308	1	Monogranular
BOB310	1	Monogranular
BOB401	1	Monogranular
NEW059	3	Polygranular
NEW307	2	Polygranular
NEW308	1	Monogranular
NEW422	1	Monogranular

Table IV.1

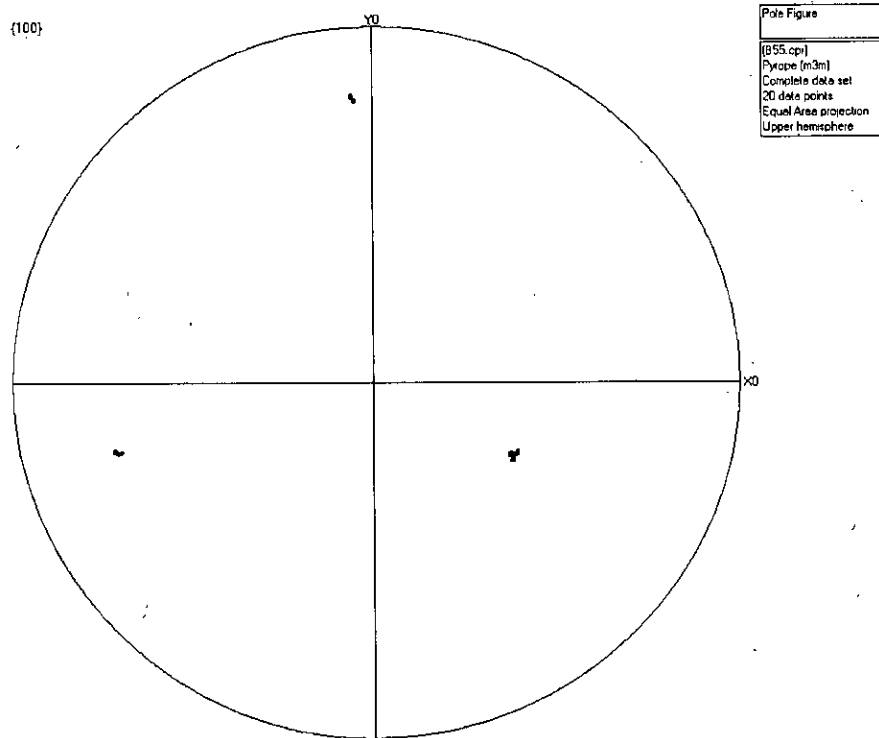


Figure IV.1: B55

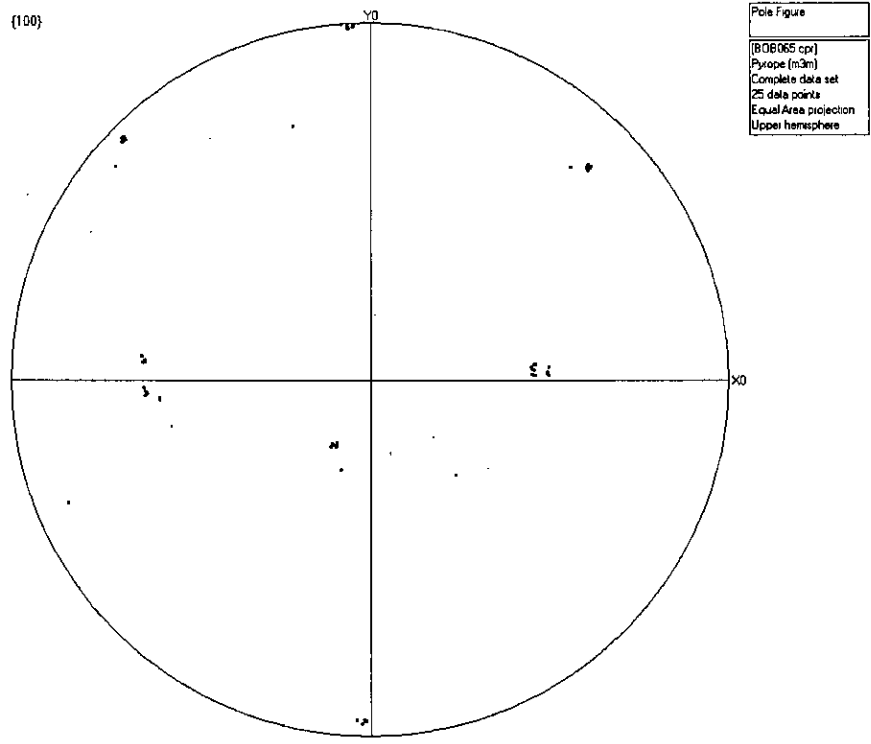


Figure IV.2: BOB065

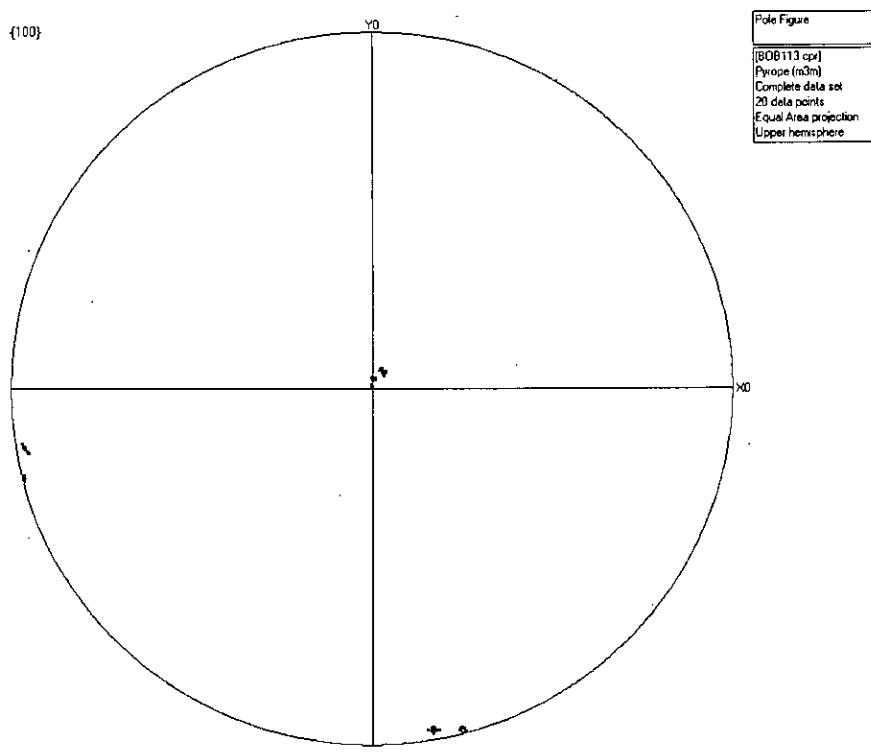


Figure IV.3: BOB113

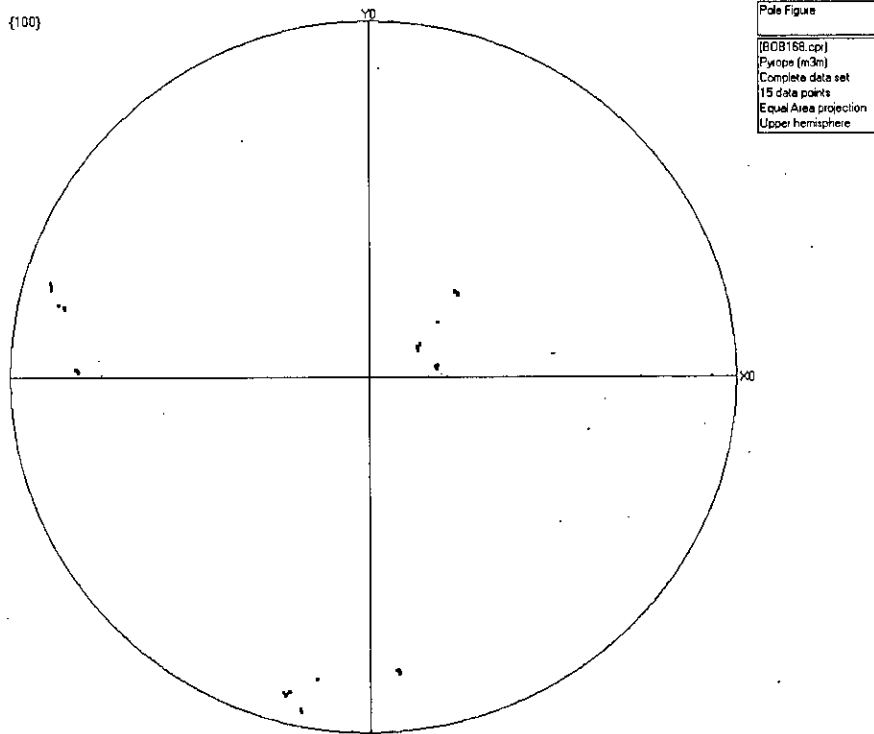


Figure IV.4: BOB168

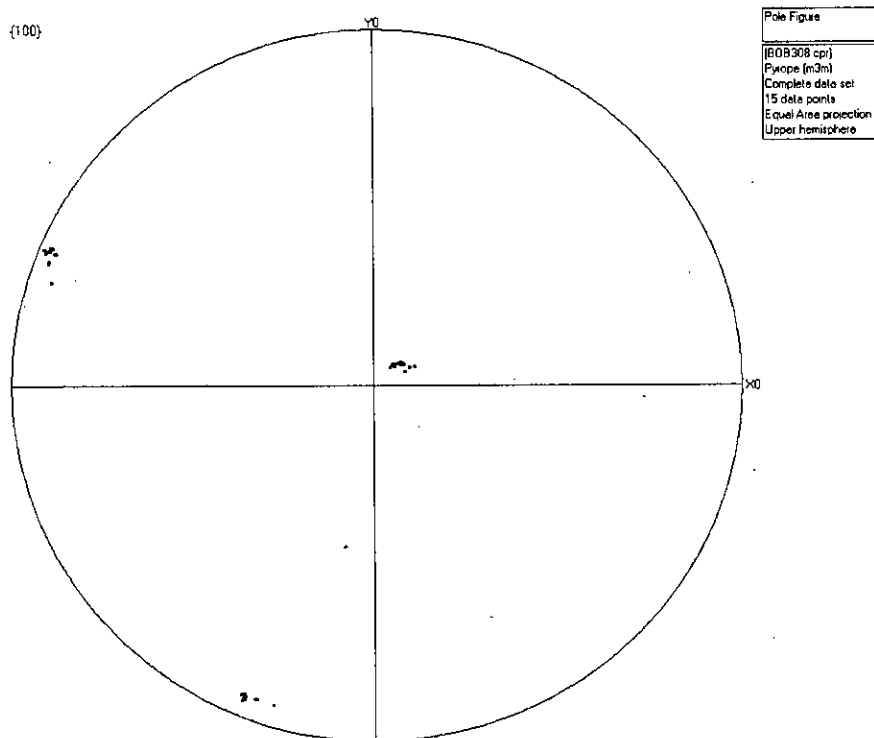
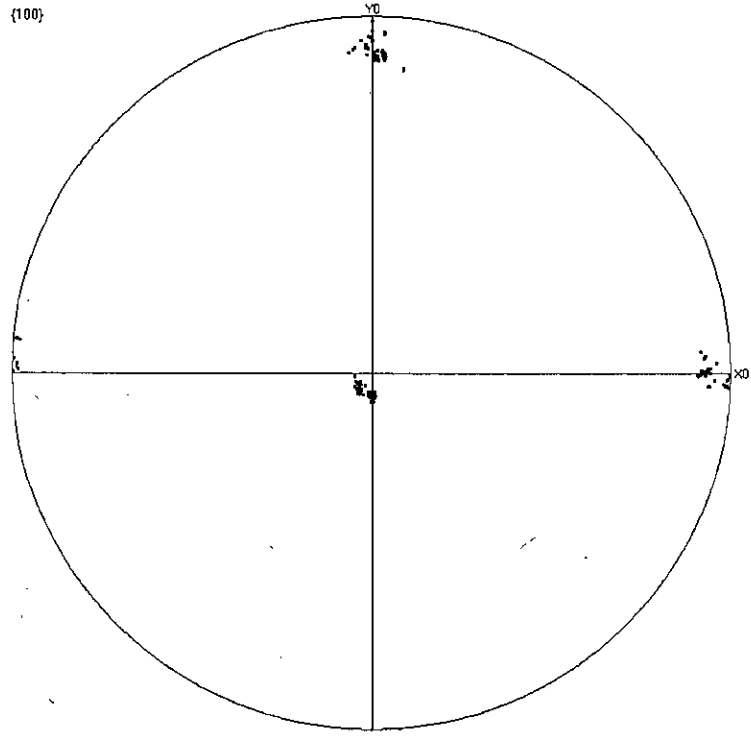


Figure IV.5: BOB308

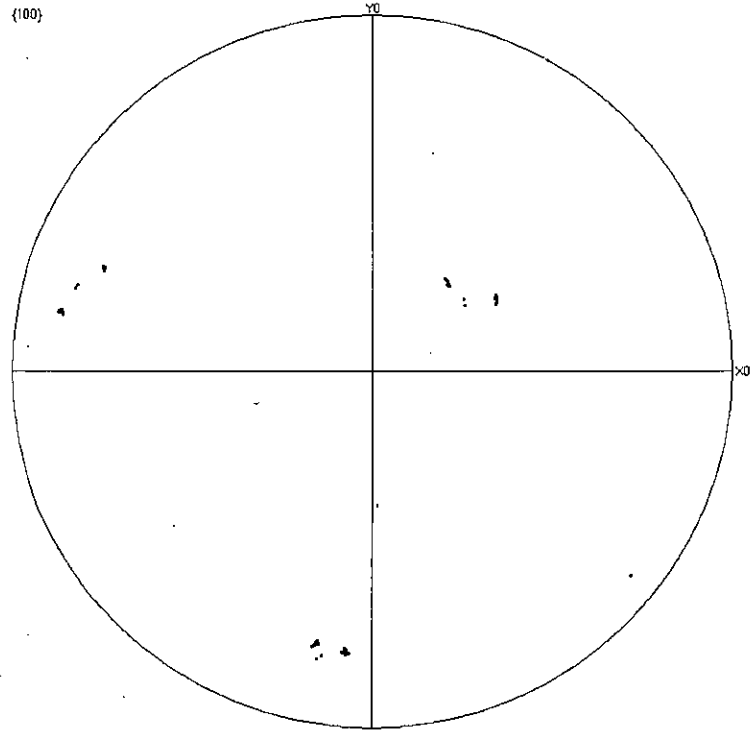
{100}



Pole Figure
[BOB310.cpr]
Pyrope (m3m)
Complete data set
45 data points
Stereographic projection
Upper hemisphere

Figure IV.6: BOB310

{100}



Pole Figure
[BOB401.cpr]
Pyrope (m3m)
Complete data set
16 data points
Equal Area projection
Upper hemisphere

Figure IV.7: BOB401

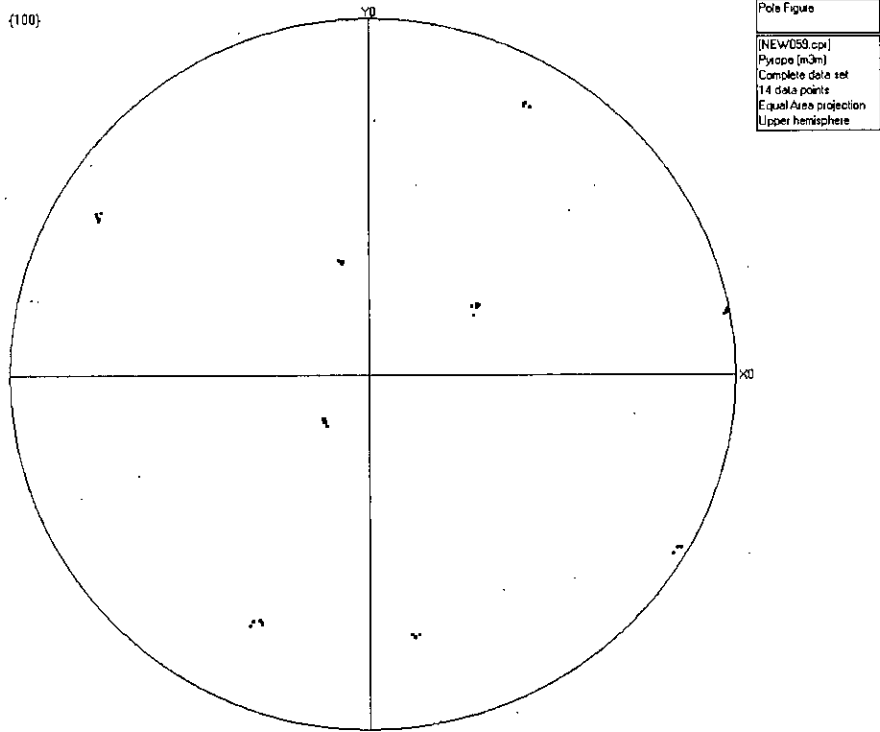


Figure IV.8: NEW059

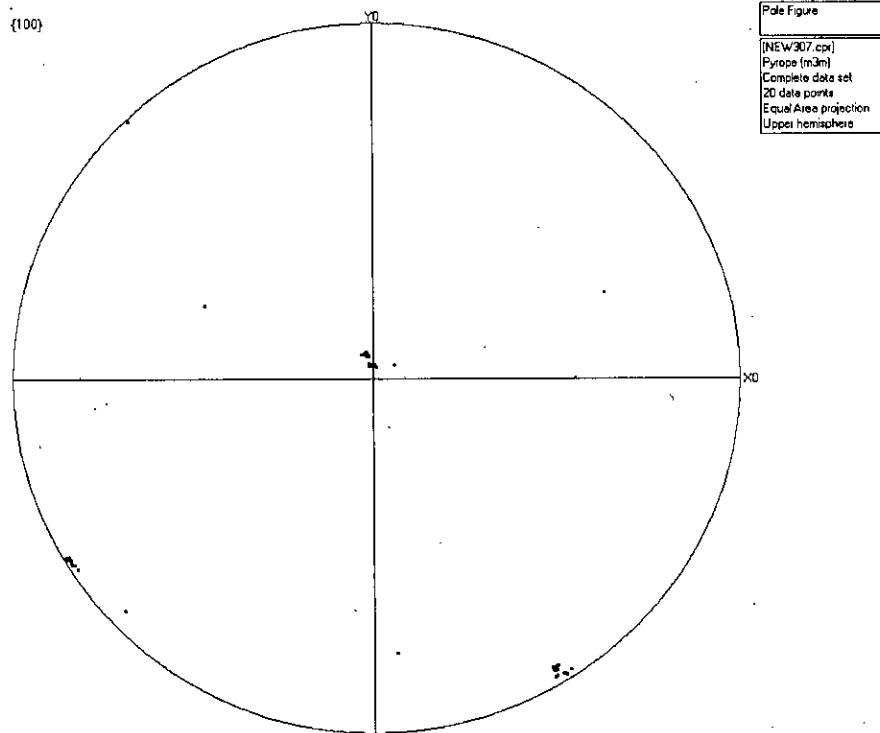


Figure IV.9: NEW307

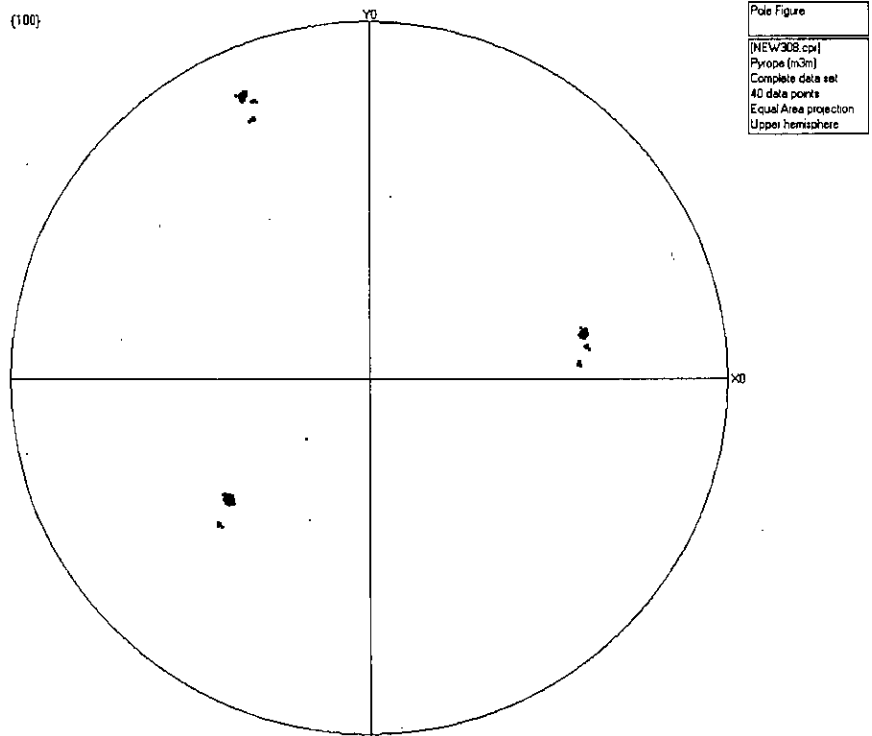


Figure IV.10: NEW308

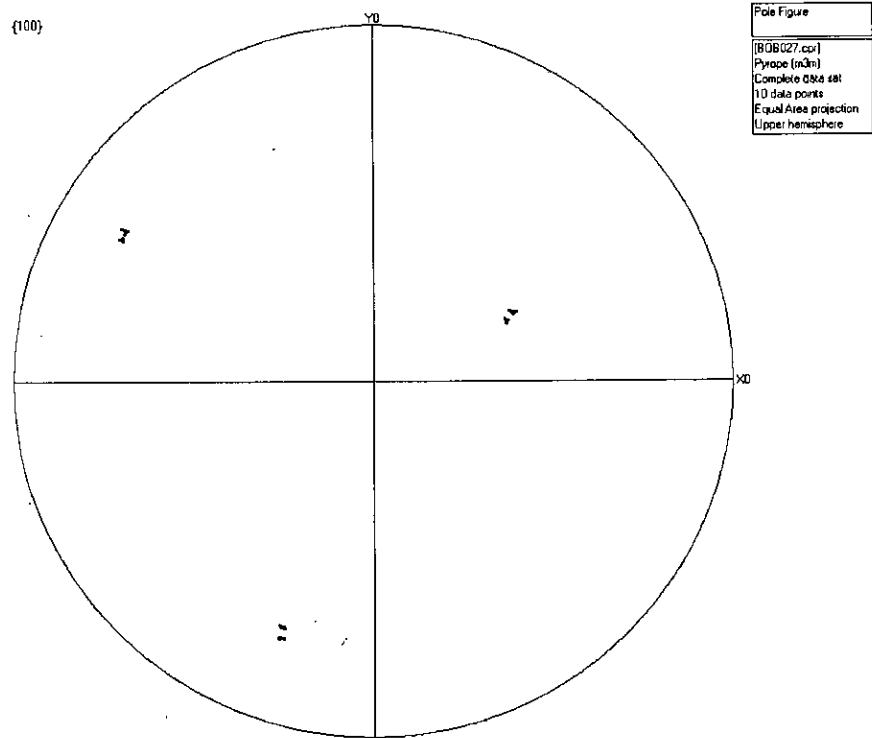


Figure IV.11: NEW422

Appendix V: Trace Element Analyses

On the following page is the average trace element ppm values for garnet, clinopyroxene and Cr-spinel in samples selected for ion microprobe SIMS analysis. See Appendix I for details on the analytical techniques and see data CD for the complete trace element analyses in spreadsheet form.

	Li	Na	K	Sc	Ti	V	Mn	Co	Ni	Ga	Se	Y	Zr	Nb	Ba	La	Ce	Pr	Nd	Sm	Eu	Gd	Tb	Dy	Ho	Er	Tm	Yb	Lu	Hf	
B46cor	0.0038	218.55	3.8304	160.09	11.767				21.2	0.2753	28.283	140.17	0.4152	0.0453	0.0074	0.3016	0.1655	2.8317	2.771	1.3132	5.8622	1.3062	1.3066	2.1234	2.1366	0.2649	1.1608	0.2739	2.7377		
B46brm	0.0023	320.42	1.3217	385.03	65.785			25.1	0.2804	65.653	100.9	0.4987	0.0263	0.0273	0.2858	0.1411	2.4118	2.3272	1.2576	1.0262	10.965	9.9728	10.965	9.9728	18.177	14.206	2.5355	1.4254			
BOB113	0.0028	180.99	10.118	215.18	428.93	217.7	55.717	68.904	27.7	65.368	12.645	15.358	48.837	1.3242	0.0083	0.738	4.712	1.2435	4.6603	1.7444	0.7514	2.2698	0.3927	0.8041	0.1463	0.4581	0.0688	0.5006	0.085	1.0004	
NEW638	0.0451	0.059	278.43	1.2977	122	1459.9		45.548		1.6643	5.4608	23.641	0.9007	0.0239	2.4077	2.8178	0.9265	6.5777	1.7548	0.0068	1.9739	0.2156	3.3033	0.4233	0.6788	0.098	0.6289	0.1478	0.58		
NEW218	0.1638	154.66	233.75	2784.18	398.81	324.2	68.818		76.583	1.2698	21.294	107.32	1.0527	0.2721	0.2807	1.5143	0.4381	4.2825	2.83	1.1108	0.0651	0.7418	4.7656	0.6916	2.4586	0.322	1.9628	0.2861	2.1957		
BOB404	0.0218	16.597	1.7731	6.0004	200.74	489.66		44.537	39.573	0.9997	2.8224	12.614	0.8487	0.0255	0.1	1.1735	1.1286	5.6663	1.4027	0.4082	1.3653	0.3813	0.3813	0.2018	0.3506	0.9892	0.1461	1.2413	0.2851	2.4592	
B47	0.0187	30.036	4.22	388.44	86.452				13.708	1.7283	7.253	25.32	0.2532	0.0102	0.5814	0.1	1.1735	1.1286	5.6663	1.4027	0.4082	1.3653	0.3813	0.3813	0.2018	0.3506	0.9892	0.1461	1.2413	0.2851	2.4592
NEW074	0.0451	318.77	0.0977	225.24	866.71			45.464		0.4048	3.7839	17.264	0.8474	0.0068	0.01	0.3306	1.3397	3.9004	7.804	2.9787	0.7294	1.9633	0.29	1.8907	0.371	1.0051	0.1652	1.042	0.1835	1.3528	
NEW032	0.023	2.8682	0.0714	327.5	717.54	387.32	3017.2	66.42	56.811	1.3458	2.9719	18.948	0.034	0.1702	2.8158	0.104	0.3306	1.3397	3.9004	7.804	2.9787	0.7294	1.9633	0.29	1.8907	0.371	1.0051	0.1652	1.042	0.1835	1.3528
NEW024	0.028	442.73	0.4334	308.31	1466.7			44.01	33.332	0.6688	80.01	0.3527	18.383	0.4725	0.0388	0.0301	0.338	1.449	1.8172	1.5165	2.3545	0.2754	1.4504	0.2466	0.6526	0.1075	0.2503	0.3368	1.6742		
NEW007	0.0787	438.86	1.1201	198.45	1248.8	150.86	44.01	33.332	36.668	80.01	0.3527	18.383	0.4725	0.0388	0.0301	0.338	1.449	1.8172	1.5165	2.3545	0.2754	1.4504	0.2466	0.6526	0.1075	0.2503	0.3368	1.6742			
NEW047	0.0544	128.47	1.2001	113.26	26.722			30.054	1.788	1.8008	38.132	0.1768	0.0106	0.0548	0.0548	0.0548	0.0548	0.0548	0.0548	0.0548	0.0548	0.0548	0.0548	0.0548	0.0548	0.0548	0.0548	0.0548	0.0548	0.0548	
B35	0.0569	184.18	6.6967	218.13	322.21	189.72	554.7	65.83	33.489	0.4151	14.802	72.079	0.2701	0.0155	0.1036	0.055	0.6571	0.1322	3.173	1.543	2.096	0.8378	0.4892	1.021	0.6569	0.2675	0.31	2.1482	0.3522	0.9878	
NEW079	0.1076	318.24	1.4589	128.13	758.74	154.75	382.8	72.93	104.2	0.602	33.23	87.698	0.863	0.0066	0.029	0.8003	0.274	1.165	1.6894	1.2541	4.4945	0.8461	1.173	1.4097	0.6401	0.7800	8.3387	1.1121	1.8407		
NEW408	0.1218	1.4589	128.13	758.74	154.75	382.8	72.93	104.2	0.602	33.23	87.698	0.863	0.0066	0.029	0.8003	0.274	1.165	1.6894	1.2541	4.4945	0.8461	1.173	1.4097	0.6401	0.7800	8.3387	1.1121	1.8407			
BOB401	0.0175	2700	60.009	58.18	757.84	983.88	574.92	31.383	38.768	562.03	20.032	341.18	0.8726	28.149	1.0238	0.9878	10.289	30.781	11.0088	23.601	3.4657	0.7354	1.6848	0.1177	0.5691	0.0614	0.1328	0.0229	0.001	0.001	
BOB402	0.0175	2700	60.009	58.18	757.84	983.88	574.92	31.383	38.768	562.03	20.032	341.18	0.8726	28.149	1.0238	0.9878	10.289	30.781	11.0088	23.601	3.4657	0.7354	1.6848	0.1177	0.5691	0.0614	0.1328	0.0229	0.001	0.001	
NEW063	0.5601	17288	353.04	52.027	861.5	207.02	180.72	41.111	823.86	21.728	158.55	0.2685	12.143	1.024	1.097	16.945	48.055	11.0088	23.601	3.4657	0.7354	1.6848	0.1177	0.5691	0.0614	0.1328	0.0229	0.001	0.001		
NEW064	1.6073	15073	320.78	100.6	583.29	184.68	773.09	39.133	749.21	20.968	205.66	1.288	35.691	1.2308	30.882	2.105	15.962	3.863	15.712	2.2123	0.4745	0.287	5.012	0.4684	0.042	0.2171	0.023	0.225	0.023		
NEW114	10.8892	8614.8	317.15	55.281	659.85	75.487	1138	47.181	948.8	18.765	128.12	3.8381	8.8388	1.8896	2.134	1.839	5.9687	0.8612	3.9829	1.4808	0.4578	1.4808	0.4578	1.4808	0.4578	1.4808	0.4578	1.4808	0.4578	1.4808	
NEW038	2.2077	2847.1	909.92	1595.6	92691	221.58	598.33	108.04	0.0053	0.668																					
NEW038	2.2077	2847.1	909.92	1595.6	92691	221.58	598.33	108.04	0.0053	0.668																					
BOB404	4.8189	90.533	1049	1042.9	56353	158.08	473.5	11.544	0.2956	0.0034	0.288																				
NEW074	1.8238	3056.7	1749.2	1157.4	75393	158.35	545.56	52.958	52.958	52.958	52.958	52.958	52.958	52.958	52.958	52.958	52.958	52.958	52.958	52.958	52.958	52.958	52.958	52.958	52.958	52.958	52.958	52.958	52.958	52.958	52.958
NEW024	2.3559	1962.3	2717.9	1328.8	82803	173.24	498.3	93.898	0.0397	0.0037	1.7028																				
NEW007	1.8975	7778.7	1718.5	1784.1	117230	254.3	580.68	188.15	0.078	0.6124																					
B55	1.7008	2193.9	1597.7	1813.6	99957	218.83	580.99	21.598	0.1568	0.0066	1.4309																				
BOB401	9.1984	9232.0	1607.9	2428.1	160702	225.68	676.34	142.32	5.3368	0.3364	6.1079																				
BOB402	1.5315	1910.7	1568.3	1400.1	90307	209.56	534.26	139.71	0.0355	0.0032	0.6534																				
NEW063	3.7787	11091	1274.3	1403.9	104378	177.58	897.88	95.07	0.8324	0.0588	2.901																				
NEW064	4.65	5259.3	1223.5	1634.9	102678	204.05	661.32	112.08	0.0491	0.0053	3.3968																				
NEW114	4.8363	14108	912.42	1818.6	120764	173.82	881.58	82.378	0.0826	0.0074	3.59																				

Table V.1: ppm averages (except Ba) core and rim) for all samples analysed on ten Microprobe SIMS. Chondrite-normalized values in grey and Cr-spinel in italics. Gemat Ni values determined by high mass resolution technique.